

Viktor P. Astakhov

Springer Series in  
Advanced Manufacturing

# Geometry of Single-point Turning Tools and Drills

Fundamentals and  
Practical Applications

 Springer

# **Springer Series in Advanced Manufacturing**

## Series Editor

Professor D.T. Pham  
Manufacturing Engineering Centre  
Cardiff University  
Queen's Building  
Newport Road  
Cardiff CF24 3AA  
UK

## Other titles in this series

*Assembly Line Design*

B. Rekiek and A. Delchambre

*Advances in Design*

H.A. ElMaraghy and W.H. ElMaraghy (Eds.)

*Effective Resource Management in Manufacturing Systems: Optimization Algorithms in Production Planning*

M. Caramia and P. Dell'Olmo

*Condition Monitoring and Control for Intelligent Manufacturing*

L. Wang and R.X. Gao (Eds.)

*Optimal Production Planning for PCB Assembly*

W. Ho and P. Ji

*Trends in Supply Chain Design and Management: Technologies and Methodologies*

H. Jung, F.F. Chen and B. Jeong (Eds.)

*Process Planning and Scheduling for Distributed Manufacturing*

L. Wang and W. Shen (Eds.)

*Collaborative Product Design and Manufacturing Methodologies and Applications*

W.D. Li, S.K. Ong, A.Y.C. Nee and C. McMahon (Eds.)

*Decision Making in the Manufacturing Environment*

R. Venkata Rao

*Reverse Engineering: An Industrial Perspective*

V. Raja and K.J. Fernandes (Eds.)

*Frontiers in Computing Technologies for Manufacturing Applications*

Y. Shimizu, Z. Zhang and R. Batres

*Automated Nanohandling by Microrobots*

S. Fatikow

*A Distributed Coordination Approach to Reconfigurable Process Control*

N.N. Chokshi and D.C. McFarlane

*ERP Systems and Organisational Change*

B. Grabot, A. Mayère and I. Bazet (Eds.)

*ANEMONA*

V. Botti and A. Giret

*Theory and Design of CNC Systems*

S.-H. Suh, S.-K. Kang, D.H. Chung and I. Stroud

*Machining Dynamics*

K. Cheng

*Changeable and Reconfigurable Manufacturing Systems*

H.A. ElMaraghy

*Advanced Design and Manufacturing Based on STEP*

X. Xu and A.Y.C. Nee (Eds.)

*Artificial Intelligence Techniques for Networked Manufacturing Enterprises Management*

L. Benyoucef and B. Grabot (Eds.)

Viktor P. Astakhov

# Geometry of Single-point Turning Tools and Drills

Fundamentals and Practical Applications

 Springer

Viktor P. Astakhov, PhD  
Michigan State University  
Department of Mechanical Engineering  
2453, Engineering Building  
East Lansing  
MI 48824-1226  
USA  
astvik@gmail.com

ISSN 1860-5168  
ISBN 978-1-84996-052-6 e-ISBN 978-1-84996-053-3  
DOI 10.1007/978-1-84996-053-3  
Springer London Dordrecht Heidelberg New York

British Library Cataloguing in Publication Data  
A catalogue record for this book is available from the British Library

Library of Congress Control Number: 2010930010

© Springer-Verlag London Limited 2010

RaCon<sup>®</sup> is a registered trademark of R&M Materials Handling, Inc., 4501 Gateway Blvd., Springfield, OH 45502, [www.rmhoist.com](http://www.rmhoist.com)  
Shear Geometry<sup>®</sup> is a registered trademark of ROBERTSON PRECISION, Inc., 2971 Spring Street, Redwood City, CA 94063-3935, [www.robertsonprecision.com](http://www.robertsonprecision.com)

Apart from any fair dealing for the purposes of research or private study, or criticism or review, as permitted under the Copyright, Designs and Patents Act 1988, this publication may only be reproduced, stored or transmitted, in any form or by any means, with the prior permission in writing of the publishers, or in the case of reprographic reproduction in accordance with the terms of licences issued by the Copyright Licensing Agency. Enquiries concerning reproduction outside those terms should be sent to the publishers.

The use of registered names, trademarks, etc. in this publication does not imply, even in the absence of a specific statement, that such names are exempt from the relevant laws and regulations and therefore free for general use.

The publisher makes no representation, express or implied, with regard to the accuracy of the information contained in this book and cannot accept any legal responsibility or liability for any errors or omissions that may be made.

*Cover design:* eStudioCalamar, Figueres/Berlin

Printed on acid-free paper

Springer is part of Springer Science+Business Media ([www.springer.com](http://www.springer.com))

---

## Preface

Although almost any book and/or text on metal cutting, cutting tool design, and manufacturing process discusses to a certain extent the tool geometry, the body of knowledge on the subject is scattered and confusing. Moreover, there is no clear objective(s) set in the selection of the tool geometry parameters so that an answer to a simple question about optimal tool geometry cannot be found in the literature on the subject. This is because a criterion (criteria) of optimization is not clear, on one hand, and because the role of cutting tool geometry in machining process optimization has never been studied systematically, on the other. As a result, many practical tool/process designers are forced to use extremely vague ranges of tool geometry parameters provided by handbooks. Being at least 20+ years outdated, these data do not account for any particularities of a machining operation including a particular grade of tool material, the condition of the machine used, the cutting fluid, properties and metallurgical condition of the work material, requirements to the integrity of the machined surface, etc.

Unfortunately, while today's professionals, practitioners, and students are interested in cutting tool geometry, they are doomed to struggle with the confusing terminology. When one does not know what the words (terms) mean, it is easy to slip into thinking that the matter is difficult, when actually the ideas are simple, easy to grasp, and fun to consider. It is the terms that get in the way, that stand as a wall between many practitioners and science. This book attempts to turn those walls into windows, so that readers can peer in and join in the fun of proper tool design.

So, why am I writing this book? There are a few reasons, but first and foremost, because I am a true believer in what we call technical literacy. I believe that everyone involved in the metal cutting business should understand the essence and

importance of cutting tool geometry. In my opinion, this understanding is key to improving efficiency of practically all machining operations. For the first time, this book presents and explains the direct correlations between tool geometry and tool performance. The second reason is that I felt that there is no comprehensive book on the subject so professionals, practitioners, and students do not have a text from which to learn more on the subject and thus appreciate the real value of tool geometry. Finally, I wanted to share the key elements of tool geometry that I felt were not broadly understood and thus used in the tool design practice and in optimization of machining operations in industry. Moreover, being directly involved in the launch of many modern manufacturing facilities equipped with state-of-the-art high-precision machines, I found that the cutting tool industry is not ready to meet the challenge of modern metal cutting applications. One of the key issues is the definite lack of understanding of the basics of tool geometry of standard and application-specific tools.

The lack of information on cutting tool geometry and its influence on the outcome of machining operations can be explained as follows. Many great findings on tool geometry were published a long time ago when neither CNC grinding machines capable of reproducing any kind of tool geometry were available nor were computers to calculate parameters of such geometry (using numerical methods) common. Manual grinding using standard 2- and 3-axis simple grinding features was common so the major requirement for tool geometry was the simpler the better. Moreover, old, insufficiently rigid machines, aged tool holders and part fixtures, and poor metal working fluid (MWF) selection and maintenance levered any advancement in tool geometry as its influence could not be distinguished under these conditions. Besides, a great scatter in the properties of tool materials in the past did not allow distinguishing of the true influence of tool geometry. As a result, studies on tool geometry were reduced to theoretical considerations of features of twist drills and some gear manufacturing tools such as hobs, shaving cutters, shapers, etc.

Gradually, once mighty chapters on tool geometry in metal cutting and tool design books were reduced to sections of few pages where no correlation between tool geometry and tool performance is normally considered. What is left is a general perception that the so-called “positive geometry” is somehow better than “negative geometry.” As such, there is no quantitative translation of the word “better” into the language of technical data although a great number of articles written in many professional magazines discuss the qualitative advantages of “positive geometry.” For example, one popular manufacturing magazine article read “Negative rake tools have a much stronger leading edge and tend to push against the workpiece in the direction of the cutter feed. This geometry is less free cutting than positive rakes and so consumes more horsepower to cut.” Reading these articles one may wonder why cutting tool manufacturers did not switch their tool designs completely to this mysterious “positive geometry” or why some of them still investigate and promote negative geometry.

During recent decades, the metalworking industry underwent several important changes that should bring cutting tool geometry into the forefront of tool design and implementation:

1. For decades, the measurement of the actual tool geometry of real cutting tools was a cumbersome and time consuming process as no special equipment besides toolmakers microscopes was available. Today, automated tool geometry inspection systems such as ZOLLER “Genius 3”, Helicheck<sup>®</sup> & Heli-Toolcheck<sup>®</sup>, etc. are available on the market. The common problem, however, is that tool manufactures do not really understand what they measure.
2. Today's tool grinder is typically a CNC machine tool, usually of 4, 5, or 6 axes. Extremely hard and exotic materials are generally no problem for today's grinding systems and multi-axis machines are capable of generating complex geometries.
3. Advanced cutting insert manufacturing companies perfected the technology of inserts pressing (for example, spray drying) so practically any desirable shape of cutting insert can be produced with a very close tolerance. The introduction of micro- and sub-micrograin carbide grades, characterized by great fracture toughness, strength, and hardness, allows lifting of the last possible limitation on tool geometry, namely the sufficient strength of the cutting wedge. Earlier, the implementation of “exotic” geometries was restricted by the properties of the tool materials.
4. Many manufacturing companies updated their machines, fixtures, and tool holders. Modern machines used today have rigid high-speed spindles. Hydraulic and shrink-fit tool holders, pre-setting machines, and non-contact automatic control of tool geometry features find widespread use in many manufacturing facilities. In other words, many traditional “excuses” for poor tool performance and known scatter in tool life are eliminated so that tool design and geometry can be directly correlated with tool performance. Unfortunately, many tool manufacturers are not ready to meet this new challenge as the basic designs and geometries of their cutting tools did not change although new tool materials with superior properties as well as new opportunities of applying advanced tool geometries were developed.
5. Many manufacturing companies established tight controls and maintenance of their MWF units. Tight control of the MWF (coolant) concentration, temperature, chemical composition, pH, particle count, contaminations as tramp oil, bacteria, etc. is becoming common. Many production line and manufacturing cells are equipped with high-pressure and micron-filtration units with digital readouts of the MWF pressure and temperature (in and out). All of these impose even higher requirements of the tool geometry and design (location) of the coolant outlet nozzles.

All this pushed tool design including primarily the selection of tool materials and geometry to the forefront as no more traditional excuses for poor tool performance could be accepted. One might think that this happy marriage of CNC grinders and advanced tool materials should result in the wide introduction of advanced tool geometries. However, this is not the case in reality as many tool designers do not possess proper knowledge on the subject and the available literature provides little help on the matter. Co-existence of two basic standards, namely *ASME B94.50* -



*1975 Basic Nomenclature and Definitions for Single-Point Cutting Tools and ISO 3002-1:1982, Basic quantities in cutting and grinding - Part 1: Geometry of the active part of cutting tools - General terms, reference systems, tool and working angles, chip breakers*, which use non-interchangeable terminology and definitions, adds a great deal to the confusion in understanding the basic parameters of the cutting tool geometry.

## Why One Needs to Know Cutting Tool Geometry

Although any book and textbook on metal cutting, cutting tool, or manufacturing processes discuss to a certain extent the subject matter, no one known to the author provides any explanation of the necessity of knowing tool geometry. At best, the influence of the components of tool geometry on tool performance is considered in quantitative terms (better, higher, longer, greater, etc.) with no quantifications to make any intelligent choice of tool geometry parameters.

It is a natural perception that tool geometry affects tool life. However, in accordance with ANSI/ASME Tool life testing with single-point turning tools (B94.55M-1985), standard tool-life testing and representation includes Taylor's tool life formula

$$vT^n = C_T$$

where  $T$  is tool life in minutes, and  $C_T$  is a constant into which all cutting conditions affecting tool life must be absorbed. Although Taylor's tool life formula is still in wide use today and is the very core of many studies on metal cutting including the level of National and International standards, this formula does not suggest that tool geometry affects tool life. The reason for this is simple as one should always remember that it was introduced in 1907 as a generalization of many-year experimental studies conducted in the nineteenth century using work and tool materials and experimental technique available at that time. Since then, each of these three components underwent dramatic changes. Unfortunately, the validity of the formula has never been verified for these new conditions. Nobody proved so far that it is still valid for any other cutting tool materials than carbon steels and HSS.

Analysis of the standard methodology of tool life testing, available criteria of tool wear, and tool life assessment clearly indicates that these assessments are insufficient, and very subjective. They do not account for cutting tool geometry (flank, rake, cutting edge angles, for example) so they are not suitable to compare cutting tools having different geometries. Moreover, they do not account for the cutting regime and thus do not reflect the real amount of work material removed by the tool during the time over which the measured rake or flank wear is achieved. As a result, they can hardly be used for optimization of the cutting tool geometry, any process improvements and optimization, as well as the process adaptive intelligent control.

Understanding tool geometry is a key to improving efficiency of practically all machining operations. This general statement should be extensively elaborated with clear specific details as no one known to the author book, paper, manual or any other technical publication/material provides the answer to an array of simple yet practical questions: “why does one need to know the cutting tool geometry?”, “what are those parameters of tool geometry one needs to use in a particular case of machining?”, “to what extent does the tool geometry affect tool life, cutting force, tool wear, integrity of the machined surface?”, “what is effect of the tool geometry on the accuracy and efficiency of machining operations?” Therefore, a need is felt to clarify the issues and thus provide practical help to the practitioners (tool designers, manufacturing/process engineers) and methodological help to the researchers. This is the main objective of this book. It argues that one needs to know the tool geometry because it allows determination of:

1. *Uncut chip thickness.* Only when one knows and understands tool geometry he can properly determine the uncut chip thickness for each and every cutting element (wedge) involved. Knowing this probably the most important parameter, one can:
  - *Maximize productivity of machining.* Productivity of machining can be thought of as the tool penetration rate defined as the product of the rotation speed (r.p.m.) and cutting feed per revolution. The cutting speed is normally limited by the properties of the tool material (red hardness) while feed per revolution is considered as the major resource in increasing productivity. This is because it can be significantly increased though tool design and geometry. Any cutting insert (solid, brazed, or mechanically clamped) is characterized by the so-called breaking uncut chip thickness known in industry as the maximum chip load. As such, an increase in the number of cutting inserts working simultaneously, the feed rate can be proportionally increased. For example, if a two-flute reamer is replaced by a four-flute reamer then the penetration rate can be increase twofold. Another method of feed rate increasing that can be used concurrently with the first is adjusting the so-called lead angle of the cutting edge. Increasing the lead angle of a cutting insert leads to so-called “chip thinning” (decreasing the uncut chip thickness under a given feed per revolution). As a result, the feed per revolution can be increased with increasing lead angle to keep the maximum allowable uncut chip thickness for the inserts. For example, the most common use of this feature in milling where the lead angle is increased to  $45^\circ$  is that it allows increasing the feed rate by 1.4-fold. As such, a wiper insert is introduced to reduce the feed marks left on the machined surface due to the increased feed.
  - *Prevent burnishing and galling instead of cutting.* In simple terms, the cutting edge is not a perfect line of intersection of the rake and flank surfaces. Rather, it is characterized by the radius of the cutting edge. This radius is common and applied (at the insert sintering or by special edge preparation techniques) to prevent chipping of the cutting edge. The problem arises when this radius becomes less than five uncut chip

thicknesses. In this case, the cutting becomes rather difficult, and significant burnishing or even galling takes place causing a significant increase of the cutting temperature and reduction of tool life. Moreover, the quality including surface integrity of the machined surface deteriorates rapidly. Knowing the uncut chip thickness, however, one can select the proper radius of cutting edge to prevent this from happening.

- *Calculate the chip compression ratio.* Measuring the chip thickness and dividing it by the uncut chip thickness, one can determine the uncut chip thickness. Knowing this fundamental of metal cutting theory and practice parameter, one can calculate practically all other process parameters and characteristics such as the power spent in plastic deformation of the layer being removed in its transformation into the chip, the tool-chip contact length, contact stresses (both normal and shear) at the tool-chip and tool-workpiece interfaces, and can calculate tool-chip contact temperature, etc. All this allows selecting the proper tool materials and machining regime. This facilitates the only practical way to optimize the cutting process. This method can be used at different levels – from the research laboratory to the shop floor.
2. *Direction of the chip flow.* The simplest yet very practical aspect of tool geometry is that this geometry defines the direction of chip flow. This direction is important to control chip breakage and evacuation. Although knowledge of chip control was available a long time ago, it can be properly utilized only at the present stage when advancements in the technology of insert manufacturing and properties of the tool materials allow one to make virtually any intricate shape of cutting inserts. The so-called “helical tool geometry” that allows preventing chip re-cutting, reduction in cutting forces, improving quality of machining surface, etc., becomes the key design and marketing feature of some tool manufacturers.
  3. *Cutting force on each cutting element as well as the total cutting force.* The cutting force is primarily determined by the mechanical properties of the work material, machining regime, and uncut chip thickness. Together with four other components of cutting tool geometry, namely, the rake angle, tool cutting edge angle, tool minor cutting edge angle, and inclination angle, the uncut chip thickness defines the magnitudes of the orthogonal components of the cutting force. Knowing the correlation among the mentioned angles and force components, one can design efficient cutting tools with inserts where no force acts on the locating pins, insert tilting under the action of the cutting force is eliminated, inserts are self-locked in the pockets of the holder for an efficient process where the cutting force does not cause excessive bending, buckling and deformations of long and non-rigid workpieces. This knowledge allows designing effective clamping mechanisms and insert pockets, and locating and clamping fixtures for the workpiece to assure the required accuracy of machining at minimum cost.

4. *Quality (surface integrity and machining residual stress) of machined surfaces.* Quality of the machined surface increasingly becomes one of the important parameters of the machined parts. Although only recently the only specified parameter on part drawings was surface finish, the direction of surface roughness and the shape of valleys and peaks, superficial and in-depth machining residual stresses as well as other parameters of the integrity of the machined surface became common requirements on part drawings. The geometry and the cutting tool together with machining regime define the mentioned surface integrity. First of all, tool geometry defines surface finish (surface topography). The influence of cutting geometry on machining residual stress is easily realized if one recalls that this geometry defines to a great extent the state of stress in the deformation zone, i.e., around the tool. This state of stresses combined with the thermal energy released due to plastic deformation and fracture of the layer being removed, as well as due to friction on the tool flank, presents the background of the formation of the machining residual stress both superficial and in-depth.
5. *Tool life.* The geometry of the cutting tool affects tool life directly as this geometry defines the magnitude and direction of the cutting force and its components, sliding velocity at the tool-chip interface, the distribution of the thermal energy released in machining, the temperature distribution in the cutting wedge, etc.

### **Uniqueness of this Publication**

This book is intended to be the first comprehensive book on cutting tool geometry of single point cutting tools and drills although the methodologies presented are valid for the geometry of any cutting tool.

The book subject matter is covered in a systemic and systematic way that covers the most of the common and special single-point cutting tools and drills as most common tools used in various industries. The uniqueness of the book is in its manner of coverage of key items as they are covered from the very simple basic geometry level, slowly adding layers of complexity up to the advanced vector geometry level. It explains with multiple examples how to select the proper geometry for a given particular case, how to design, adjust (set), and re-sharpen cutting tools. Bridging the gap between theory and practice, the book goes to the most advanced level of kinematic tool geometry as the summation of several simultaneously-occurring motions to achieve the desired shape of the machined part while maintaining optimal tool geometry. In practical terms, it means that the book clearly shows what seems to be “rocket science” as differential topology or vectorial analysis can do to solve real-life problems on the shop floor and/or in the design of standard and application-specific cutting tools. It provides valuable help in utilizing the ability of modern CNC tool sharpening machines (for example ANKA and Walter CNC grinding systems). It provides methodological guidance for properly using automated tool geometry inspection systems such as ZOLLER “Genius 3”, Helicheck® & Heli-Toolcheck®, etc., because the major obstacles in the wide implementation of these tool geometry measuring systems are:

(a) convincing new potential customers on the potential benefits of knowing real tool geometry, (b) proper machine setting with respect to the tool-in-hand coordinate system, and (c) interpretation of the output in terms of its correlation with the geometry parameters assigned by the tool drawing.

The key features and advantages of the book that sets it apart from all known subject matter can be summarized as follows:

- For the first time, clear objectives of cutting tool geometry section/optimization are formulated and explained with multiple examples.
- Individual and combined influences of the parameters of cutting tool geometry on cutting tool performance and outcomes of a machining operation are revealed through establishing clear bridges between cutting theory, tool geometry, and shop practice.
- The three basic systems of consideration of the tool geometry, namely, tool-in-hand, tool-in-machine (holder), and tool-in-use are considered and the transformations between these systems are established.
- For the first time, the book discusses the system outlook of common problems and solutions in cutting tools implementation practice in the setting of automotive powertrain plant. It addresses several urgent problems that many present-day tool manufacturers, tool application specialists, and tool users in the automotive industry are facing. First, the book is meant to be a source of instant solutions, including pieces of useful practical suggestions that one can just implement into one's own applications, providing the solutions of common problems. Second, it is meant to be a useful reference to the most important aspects of the cutting tool design, application and troubleshooting practices. Finally, it covers emerging trends in the cutting tool geometry, machining regimes, and optimization of machining operations.
- For the first time, the book provides a comprehensive analysis of the design and geometry of deep-hole machining tools. The book provides practical recommendations for the proper selection of the components of deep-hole machining system to assure system coherency.

After reading the book and reviewing the many practical examples included, a potential reader should gain solid knowledge and understanding of tool geometry, namely, the shapes, angles, and other geometric aspects of single-point and multi-point cutting tools. He should be well equipped for all the facets of geometry related tool business management starting with design and/or selection of the proper geometry and finishing with troubleshooting of failed tools.

### **How this Book is Organized**

The chapters that follow and their contents are listed here:

#### *Chapter 1: What Does It Mean “Metal Cutting”?*

To design a cutting tool and thus to assign its proper geometry, select the proper tool material and machining regime, one needs to know the physical essence of the

metal cutting process starting with its definition and finishing with the easiest way to accomplish the objective of this process. This chapter provides guidelines to distinguish the metal cutting process commonly referred to as metal cutting among other closely related manufacturing processes and operations. It presents the known results and compares them with those used in other forming processes/operations. It argues that if the usual notions are used, the metal cutting process does not have any distinguishing feature. Analyzing what and when went wrong with the existing notions in metal cutting, this chapter provides a physically-based definition of the metal cutting process. Using the introduced definition, this chapter for the first time describes explicitly the role of cutting tool geometry in the metal cutting process that sets the stage for a better understanding of other chapters in this book. Because in the development and implementation of any cutting tool the experiment remains essential, the complete hierarchical system of tool testing is also discussed and the most useful similarity numbers used in testing are introduced and explained.

#### *Chapter 2: Basic Definitions and Cutting Tool Geometry, Single Point Cutting Tools*

This chapter presents the basic terms and their definitions related to cutting tool geometry according to ISO and AISI standards. It considers tool geometry and inter-correlation of geometry parameters in three basic systems: tool-in-hand, tool-in-machine, and tool-in-use. It also reveals and resolves the common issues in the selection of geometry parameters including those related to indexable inserts and tool holders. The chapter introduces the concept and basics of advanced representation of cutting tool geometry using vector analysis. A step-by-step approach with self-sufficient coverage of terms, definitions, and rules (in Appendixes) makes this complicated subject simple as considerations begin with the simplest geometry of a single-point cutting tool and finish with summation of several motions. Extensive exemplification using practical cases enhances understanding of the covered material.

#### *Chapter 3: Fundamentals of the Selection of Cutting Tool Geometry Parameters*

This chapter presents a general methodology for the selection of optimal tool geometry based upon minimization of the work of plastic deformation in metal cutting. It argues that the chip compression ratio is the most objective yet simple ‘gage’ that should be used for the assessment of this work and thus to optimize tool geometry. Individual and system influences of the major parameters of the cutting tool geometry are discussed. The tool cutting edge, rake, flank and inclination angles, as well as edge preparation are included in considerations because these parameters have a multi-faced influence on practically all aspects of the metal cutting process and greatly affects the outcomes of a machining operation. The chapter offers explanations and rationales for many common perceptions and experimental knowledge concerning the listed parameters.

#### *Chapter 4: Straight Flute and Twist Drills*

This chapter discusses classification, geometry, and design of straight flute and twist drills. It argues that the design, manufacturing, and implementation practices of drills are lagging behind the achievements in tool materials, powerful, high-

speed-spindles rigid machines, and high-pressure MWF (coolant) supply. Although the wide availability of CAD design tools and CNC precision grinding machines make it possible to reproduce any drill geometry, there are not many new drill designs becoming available recently. The chapter points out that the prime objective of the drilling system is an increase in the drill penetration rate, i.e., in drilling productivity as the prime source for potential cost savings. As the major problem is in understanding particularities of drill geometry and its components, this chapter walks the reader from simple concepts starting from the basic terminology in drill design and geometry to the most complicated concepts in the field, keeping the context to the simplest possible fashion and providing practical examples. It provides an overview of important results concerning drill geometry and synthesizes the most relevant findings in the field with the practice of tool design.

#### *Chapter 5: Deep-hole Tools*

This chapter discusses classification, geometry, and design of deep-hole drills. The concept of self-piloting is explained. The system approach to deep-hole machining is introduced and common system issues are discussed with examples. The major emphasis is placed on gundrills. A number of simple design rules are proposed and explained with examples. The conditions of free penetration of the drill into the hole being drilled are explained. The geometry consideration systemically related to MWF flow and thus the concept of the optimum MWF flow rate are explained. A number of novel design concepts are revealed. This chapter also discusses system consideration in experimental study of gundrill parameters. It is demonstrated that tool life is a complex function of not only geometry parameters and machining regime alone but also of their combination. Tool geometry optimization using the Hooke and Jeeves method is also discussed.

#### *Appendix A: Basic Kinematics of Turning and Drilling*

This appendix discusses basic turning and drilling operation and presets the definitions of the basic terms used in kinematics of turning, boring, and drilling. The cutting speed, cutting feed, feed rate, depth of cut and material removal rate are considered with practical examples of calculations. Based on the chip compression ratio (CCR) discussed in Chap. 1, a simple practical methodology to calculate the cutting power (force) and its partition in the cutting system is considered with examples. It is shown that the greatest part of the energy needed for cutting is spent in plastic deformation of the layer being removed.

#### *Appendix B: ANSI and ISO Turning Indexable Inserts and Holders*

This appendix aims to help specialists in tool design and end users to make proper selection of the standard cutting inserts, and tool holders. It walks a potential reader through particularities of ISO and ANSI standards explaining differences between these standards and clarifying specific issues. It points out important discrepancies between these standards and their interpretations found in the catalogs of tool manufacturers. Examples provided in this appendix help to understand the selection process and its results clearly.

*Appendix C: Basics of Vector Analysis*

This appendix presents the basics of vector analysis to help readers to comprehend the analysis of the tool geometry as made in the book. The concepts of vector and scalar quantities are explained. Starting with trivial vector operations as vector summation and subtraction, the text walks a potential reader to the dot and cross and scalar triple products of vectors as the fundamental operations used in the analysis of tool geometry. Suitable exemplifications are provided for each of these vector operations.

*Appendix D: Hydraulic Losses: Basics and Gundrill Specifics*

This appendix discusses MWF pressure losses in the hydraulic circuit of the gundrilling system. An electrical analogy of this hydraulic system is used to explain the essence of these losses. To fulfil *Design Rule No. 3* introduced in Chap. 5, namely, to maximize the MWF pressure in the bottom clearance space, all hydraulic losses are distinguish as ‘bad’ (reduce the pressure) and ‘good’ (increase the pressure in the bottom clearance space) losses. The concept and significance of the critical and optimal MWF velocity and flow rate as applicable to chip transportation in the V-flute are introduced and explained with an example.

*Appendix E: Requirements and Examples of Cutting Tool Drawings*

This appendix argues that probably the most important stage in the implementation of the optimized tool geometry is its assigning on the tool drawings. To assign this tool geometry properly, a tool designer should be a well-seasoned specialist with an advanced degree having a broad knowledge of the design, manufacturing, implementation, failure analysis and many other surrounding subjects. As this is not the case today, the common flaws with exemplification of some common tool drawings are discussed. The appendix sets the basic requirements to tool drawings with examples of proper tool drawings.

**Acknowledgments**

I am indebted to the administration of Faculty of Engineering of Michigan State University and to the faculty and staff of its Mechanical Engineering Department for their support of my efforts in writing this book and for providing me with the yearlong refuge from teaching and administrative duties that allowed me the time to formulate my technical notes into a coherent whole.

I wish to thank all my former and present colleagues and students who have contributed to my knowledge of cutting tool geometry. A special note of thanks goes to the late professor Y.N. Sukhoruckhov, professors M.O.M. Osman, I.S. Jawahir, J.S. Outeiro, S.P. Radzevich, G. M. Petrosian, A.L. Airikyan, and A. Y. Brailov, Dr. NL Slafman for their valuable help, friendship, and continuous support.

I appreciate the support by my colleagues on the executive board of SME Chapter 69, on the board of International Journal of Advances in Machining and Forming Operations (Editor-in-Chief Professor V.P. Astakhov) and International Journal of Machining and Machinability of Materials (Editor-in-Chief Professor J. Paulo Davim). A special note of thanks to Professor J. Paulo Davim for his



constant support and encouragement, his unlimited energy and vision in the field of machining

I wish to express my gratitude to my colleagues and management of Production Service Management Inc. (PSMi) for their patient support of my metal cutting and tool application activities in the automotive industry.

Last and most of all, I offer a special word of thanks to my wife Professor Xinran (Sharon) Xiao (Michigan State University) for her constructive criticism, tolerance, endless support, encouragement, and love as well as to my young son Andrew and grown daughter Iren. Despite the numerous days, evenings and weekends devoted to writing this book and business trips near, and far devoted to developing the material, they provided the loving family environment that afforded me the tranquility and peace of mind that made writing it possible. This book is dedicated to them.

Okemos, Michigan, USA  
March, 2010

*Viktor P. Astakhov*

---

# Contents

<b>1</b>	<b>What Does It Mean “Metal Cutting”?</b>	<b>1</b>
1.1	Introduction	1
1.2	Known Results and Comparison with Other Forming Processes	2
1.2.1	Single-shear Plane Model of Metal Cutting	2
1.2.2	Metal Cutting vs. Other Closely Related Manufacturing Operations	5
1.3	What Went Wrong in the Representation of Metal Cutting?	22
1.3.1	Force Diagram	23
1.3.2	Resistance of the Work Material in Cutting	25
1.3.3	Comparison of the Known Solutions for the Single-shear Plane Model with Experimental Results	27
1.4	What is Metal Cutting?	28
1.4.1	Importance to Know the Right Answer	28
1.4.2	Definition	28
1.4.3	Relevance to the Cutting Tool Geometry	29
1.5	Fundamental Laws of Metal Cutting	32
1.5.1	Optimal Cutting Temperature – Makarow’s Law	32
1.5.2	Deformation Law	35
	References	50
<b>2</b>	<b>Basic Definitions and Cutting Tool Geometry,</b>	
	<b>Single Point Cutting Tools</b>	<b>55</b>
2.1	Basic Terms and Definitions	55
2.1.1	Workpiece Surfaces	57
2.1.2	Tool Surfaces and Elements	57
2.1.3	Tool and Workpiece Motions	57
2.1.4	Types of Cutting	58
2.2	Cutting Tool Geometry Standards	60
2.3	Systems of Consideration of Tool Geometry	61
2.4	Tool-in-hand System (T-hand-S)	64

2.4.1	Tool-in-hand Coordinate System .....	64
2.4.2	References Planes .....	66
2.4.3	Tool Angles.....	68
2.4.4	Geometry of Cutting Tools with Indexable Inserts .....	74
2.5	Tool-in-machine System (T-mach-S).....	84
2.5.1	Angles .....	84
2.5.2	Example 2.3 .....	88
2.6	Tool-in-use System (T-use-S) .....	90
2.6.1	Reference Planes .....	91
2.6.2	The Concept.....	92
2.6.3	Modification of the T-hand-S Cool Geometry .....	92
2.6.4	Kinematic Angles.....	98
2.6.5	Example 2.4 .....	100
2.7	Avalanched Representation of the Cutting Tool Geometry in T-hand-S.....	102
2.7.1	Basic Tool Geometry .....	102
2.7.2	Determination of Cutting Tool Angles Relation for a Wiper Cutting Insert .....	108
2.7.3	Determination of Cutting Tool Angles for a Single-point Tool.....	110
2.7.4	Flank Angles of a Dovetail Forming Tool .....	117
2.7.5	Summation of Several Motions.....	119
	References.....	125
<b>3</b>	<b>Fundamentals of the Selection of Cutting Tool Geometry Parameters...</b>	<b>127</b>
3.1	Introduction .....	127
3.2	General Considerations in the Selection of Parameters of Cutting Tool Geometry .....	129
3.2.1	Known Results .....	129
3.2.2	Ideal Tool Geometry and Constrains.....	130
3.2.3	Practical Gage for Experimental Evaluation of Tool Geometry ...	132
3.3	Tool Cutting Edge Angles .....	132
3.3.1	General Consideration.....	132
3.3.2	Uncut ChipT in Non-free Cutting .....	134
3.3.3	Influence on the Surface Finish.....	142
3.3.4	Tools with $\kappa_r > 90^\circ$ .....	144
3.3.5	Tool Minor Cutting Edge Angle .....	147
3.4	Edge Preparation .....	161
3.4.1	General .....	161
3.4.2	Shape and Extent.....	163
3.4.3	Limitations .....	163
3.4.4	What Edge Preparation Actually Does.....	169
3.5	Rake Angle.....	171
3.5.1	Introduction.....	171
3.5.2	Influence on Plastic Deformation and Generazliations .....	175

3.5.3	Effective Rake Angle .....	183
3.5.4	Conditions for Using High Rake Angles.....	189
3.6	Flank Angle.....	191
3.7	Inclination Angle.....	193
3.7.1	Turning with Rotary Tools.....	195
3.7.2	Helical Treading Taps and Broaches.....	197
3.7.3	Milling Tools.....	198
	References.....	201
<b>4</b>	<b>Straight Flute and Twist Drills .....</b>	<b>205</b>
4.1	Introduction .....	205
4.2	Classification.....	206
4.3	Basic Terms.....	208
4.4	System Approach .....	211
4.4.1	System Objective .....	212
4.4.2	Understanding the Drilling System .....	212
4.4.3	Understanding the Tool.....	212
4.5	Force System Constrains on the Drill Penetration Rate .....	213
4.5.1	Force-balance Problem in Conventional Drills .....	213
4.5.2	Constrains on the Drill Penetration Rate.....	218
4.5.3	Drilling Torque .....	219
4.5.4	Axial Force.....	220
4.5.5	Axial Force (Thrust)-torque Coupling .....	221
4.6	Drill Point.....	223
4.6.1	Basic Classifications .....	223
4.6.2	Tool Geometry Measures to Increase the Allowable Penetration Rate .....	224
4.7	Common Design and Manufacturing Flaws.....	259
4.7.1	Web Eccentricity/ Lip Index Error.....	260
4.7.2	Poor Surface Finish and Improper Tool Material/Hardness.....	261
4.7.3	Coolant Hole Location and Size.....	263
4.8	Tool Geometry .....	267
4.8.1	Straight-flute and Twist Drills Particularities.....	269
4.8.2	Geometry of the Typical Drill Point .....	270
4.8.3	Rake Angle.....	272
4.8.4	Inclination Angle .....	280
4.8.5	Flank Angle.....	281
4.8.6	Geometry of a Cutting Edge Located at an Angle to the $y_0$ -plane .....	292
4.8.7	Chisel Edge .....	295
4.8.8	Drill Flank is Formed by Two Planes: Generalization .....	306
4.8.9	Drill Flank Angle Formed by Three Planes .....	310
4.8.10	Flank Formed by Quadratic Surfaces.....	313
4.9	Load Over the Drill Cutting Edge .....	324

4.9.1	Uncut Chip Thickness in Drilling .....	325
4.9.2	Load Distribution Over the Cutting Edge .....	327
4.10	Drills with Curved and Segmented Cutting Edges .....	328
4.10.1	Load of the Cutting Part of a Drill with Curved Cutting Edges .....	329
4.10.2	Rake Angle .....	332
	References.....	337
<b>5</b>	<b>Deep-hole Tools.....</b>	<b>341</b>
5.1	Introduction .....	341
5.2	Generic Classification of Deep-hole Machining Operations .....	343
5.3	What Does ‘Self-piloting Tool’ Mean? .....	345
5.3.1	Force Balance in Self-piloting Tools.....	345
5.4	Three Basic Kinematic Schemes of Drilling .....	350
5.4.1	Gundrill Rotates and the Workpiece is Stationary .....	351
5.4.2	Workpiece Rotates and the Gundrill is Stationary .....	352
5.4.3	Counterrotation .....	352
5.5	System Approach .....	353
5.5.1	Handling Tool Failure .....	353
5.5.2	System Considerations .....	354
5.6	Gundrills.....	362
5.6.1	Basic Geometry .....	362
5.6.2	Rake Surface .....	365
5.6.3	Geometry of Major Flanks .....	370
5.6.4	System Considerations in Gundrill Design .....	390
5.6.5	Exemplification of Significance of the High MWF Pressure in the Bottom Clearance Space .....	423
5.6.6	Example of Experimental Study .....	425
5.6.7	Optimization of Tool Geometry .....	439
	References.....	440
 <b>Appendix A</b>		
<b>Basic Kinematics of Turning and Drilling.....</b>		
A.1	Introduction .....	443
A.2	Turning and Boring .....	444
A.2.1	Basic Motions in Turning.....	444
A.2.2	Cutting Speed in Turning and Boring .....	448
A.2.3	Feed and Feed Rate .....	448
A.2.4	Depth of Cut.....	449
A.2.5	Material Removal Rate .....	449
A.2.6	Resultant Motion.....	450
A.3	Drilling and Reaming .....	450
A.3.1	Basic Motions in Drilling.....	450
A.3.2	Machining Regime .....	451
A.4	Cutting Force and Power.....	453

A.4.1 Force System in Metal Cutting.....	453
A.4.2 Cutting Power .....	454
A.4.3 Practical Assessment of the Cutting Force.....	455
References.....	461

## Appendix B

<b>ANSI and ISO Turning Indexable Inserts and Holders.....</b>	<b>463</b>
B.1 Indexable Inserts .....	463
B.1.1 ANSI Code .....	464
B.1.2 ISO Code.....	471
B.2 Tool Holders for Indexable Inserts (Single Point Tools) .....	491
B.2.1 Symbol for the Method of Holding Horizontally Mounted Insert – Reference Position (1) .....	492
B.2.2 Symbol for Insert Shape – Reference Position (2) .....	493
B.2.3 Symbol for Tool Style – Reference Position (3) .....	493
B.2.4 Letter Symbol Identifying Insert Normal Clearance – Reference Position (4).....	494
B.2.5 Symbol for Tool Hand – Reference position (5) .....	494
B.2.6 Symbol for Tool Height (Shank Height of Tool Holders and Height of Cutting Edge) - Reference Position (6) .....	494
B.2.7 Number Symbol Identifying Tool Holder Shank Width – Reference Position (7).....	495
B.2.8 Number Symbol Identifying Tool Length – Reference Position (8).....	495
B.2.9 Letter Symbol Identifying Indexable Insert Size – Reference Position (9).....	497

## Appendix C

<b>Basics of Vector Analysis .....</b>	<b>499</b>
C.1 Vectors and Scalars .....	499
C.2 Definition and Representation.....	500
C.2.1 Definitions.....	500
C.2.2 Basic Vector Operations .....	503
C.3 Application Conveniences.....	509
C.4 Rotation: Linear and Angular Velocities.....	511
C.4.1 Planar Linear and Angular Velocities .....	511
C.4.2 Rotation: The Angular Velocity Vector .....	515
References .....	518

## Appendix D

<b>Hydraulic Losses: Basics and Gundrill Specifics.....</b>	<b>519</b>
D.1 Hydraulic Pressure Losses – General .....	519
D.1.1 Major Losses: Friction Factor .....	520
D.1.2 Minor Losses (Losses Due to Form Resistance) .....	521

- D.2 Concept of the Critical MWF Velocity and Flow Rate ..... 521
  - D.2.1 MWF Flow Rate Needed for Reliable Chip Transportation..... 522
  - D.2.3 Example D.1..... 527
- D.3 Inlet MWF pressure..... 528
- D.4 Analysis of Hydraulic Resistances ..... 532
  - D.4.1 Analysis of Hydraulic Resistances Over Which the Designer Has No or Little Control ..... 532
  - D.4.2 Variable Resistances Over Which the Designer Has Control .... 535
- D.5 Practical Implementation in the Drill Design ..... 539
- References ..... 543
  
- Appendix E**
- Requirements and Examples of Cutting Tool Drawings..... 545**
  - E.1 Introduction ..... 545
  - E.2 Tool Drawings – the Existent Practice ..... 546
  - E.3 Tool Drawing Requirements ..... 548
  - E.4 Examples of Tool Drawing ..... 553
- References ..... 559
  
- Index..... 561**

## What Does It Mean “Metal Cutting”?

*Theory helps us bear our ignorance of facts.*

George Santayana (1863–1952), *The Sense of Beauty*, 1896

**Abstract.** To design a cutting tool and thus to assign its proper geometry, select the proper tool material and machining regime, one needs to know the physical essence of a metal cutting process starting with its definition and finishing with the easiest way to accomplish the objective of this process. This chapter provides guidelines to distinguish the metal cutting process commonly referred to as metal cutting among other closely related manufacturing processes and operations. It presents the known results and compares them with those used in other forming processes/operations. It argues that, if the usual notions are used, the metal cutting process does not have any distinguishing features. Analyzing what went wrong with the existing notions in metal cutting, this chapter provides a physically-based definition of the metal cutting process. Using the introduced definition, this chapter for the first time describes explicitly the role of cutting tool geometry in the metal cutting process that sets the stage for better understanding of other chapters in this book. Because in the development and implementation of any cutting tool experiment remains essential, the complete hierarchical system of tool testing is also discussed and the most useful similarity numbers used in testing are introduced and explained.

### 1.1 Introduction

As discussed in the Preface, the geometry of cutting tools affects the quality and productivity of machining operations, chip control, magnitude, and direction of the cutting force and its components. Although these correlations are known phenomenologically, i.e., from the testing and implementation practice of various tools, little is known about their physical nature. Unfortunately, these experience-based facts are often incomplete and contradicting as they are normally considered



ignoring system properties of the cutting system. As a result, they cannot provide much guidance in tool design in terms of selection of the optimal for a given application, tool geometry. The theory of metal cutting as taught in student's texts is of little help as it does not consider correlations between essential parameters of the cutting tool geometry and the physics of this process. Only when the physics of the metal cutting process is understood and the system properties of the metal cutting system are accounted for, can the proper tool geometry be selected. This, however, can happen if the proper answer a simple question: What is metal cutting? is known so one can answer the following questions:

1. What is the difference between metal cutting and cutting?
2. If a polymer or any other non-metal (wood, stone) material is cut by means of turning, milling, drilling, etc., what should this process be called?
3. What kind of cutting is performed by a knife or by a pair of scissors?

This chapter aims to provide the answers to these questions. These answers should help to distinguish metal cutting from other closely related manufacturing operations, revealing its unique physical features controlling this process. As a result, the essence of the metal cutting process can be understood so the parameters of the cutting tool geometry can then be selected to optimize this process.

## **1.2 Known Results and Comparison with Other Forming Processes**

To distinguish one manufacturing operation from other closely related operations, one should consider the most important process parameters, namely the prime deformation mode, and force (energy) needed to accomplish an operation as well as the tool design to realize this deformation mode.

### **1.2.1 Single-shear Plane Model of Metal Cutting**

#### *1.2.1.1 Deformation Mode*

When one tries to learn the basics of metal cutting or even metal cutting theory, he/she takes a textbook on metal cutting (manufacturing, tool design, etc.) and then learns that this seemingly complicated subject is normally reduced to a model of chip formation that constitutes the very core of theory and practice [1, 2]. Although a number of various models of chip formation are known to specialists in this field, the single-shear plane model is still the only option for studies on metal cutting [3], computer simulations programs including the most advanced FEA packages (e.g., [4]) and students' textbooks (e.g., [2, 5]). A simple explanation of this fact is that the model is easy to teach, to learn, and simple numerical examples to calculate cutting parameters can be worked out for student's assignments [1]. The simple geometrical relations used in this model seem to be logical and straightforward so FEA and simulation packages were developed with rather simple user interfaces and colorful outputs that have been preventing attention of many practitioners with shallow understanding of metal cutting principles.

The single-shear plane model shown in Fig. 1.1 was developed using simple observations of the simplest case of machining known as orthogonal free cutting (discussed in Chap. 2). Figure 1.1 indicates that the tool is actually a cutting wedge having the rake and the flank faces that meet to form the cutting edge. The cutting force is applied to the tool so that it removes the stock of thickness  $t_1$  (known as the uncut or undeformed chip thickness) by shearing (as assumed and widely accepted in the literature on metal cutting [6–8]) it ahead of the tool in a zone that is quite thin compared to its length, and can thus be well represented by the shear plane AB. The position of the shear plane is customarily defined by means of the so-called shear angle  $\phi$ , as shown in Fig. 1.1. Since this model was originally introduced in 1870 by Time [9], the theoretical determination of the shear angle  $\phi$  has been attracting the attention of many researchers. Despite all the effort that have been made, however, it has not happened yet.

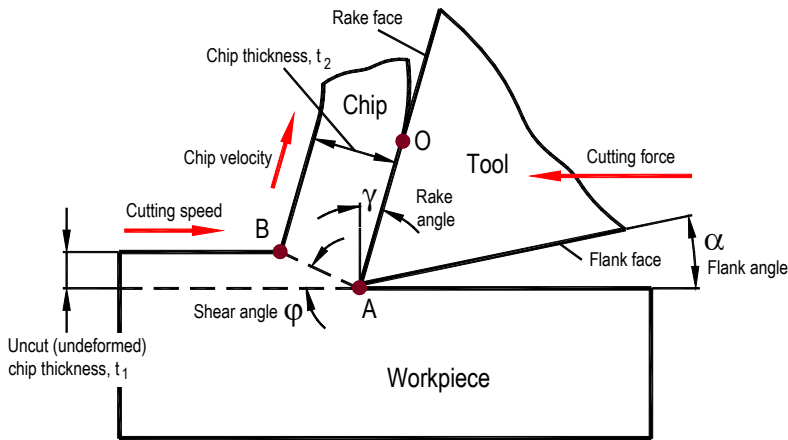


Fig. 1.1. Single-shear plane model

After being sheared, the layer being cut becomes the chip, which slides first along the tool rake face, following its shape (the straight portion of the chip in Fig. 1.1), and then, beyond a particular point O on the tool face, it curls away from that tool face. Two important facts have been established experimentally:

1. The metallographic structure (texture) of the chip is not the same as that of the workpiece. In other words, the work material undergoes severe plastic deformation though the entire cross-section of the layer being removed.
2. The formed chip becomes thicker compared to the uncut chip thickness, i.e.,  $t_2 > t_1$  while the volume of the cut layer is preserved. It means that the length of chip becomes shorter than that of the cut. Zvorykin [10] introduced the chip compression ratio  $\zeta$  as the ratio of the chip thickness and the uncut chip thickness, i.e.,

$$\zeta = \frac{t_2}{t_1} = \frac{v}{v_1} \tag{1.1}$$

It follows from Eq. 1.1 that the chip compression ratio correlates the cutting velocity (speed)  $v$  and the chip velocity  $v_1$ .

It directly follows from Eq. 1.1 and geometry of the diagram shown in Fig. 1.1 that the shear angle calculates as

$$\phi = \arctan \frac{\cos \gamma}{\zeta - \sin \gamma} \tag{1.2}$$

Researchers in the field have been using the model shown in Fig. 1.1 almost exclusively. In some work a few changes were made when studying the plastic deformation in the shear zone or when taking into account the presence of the built-up edge. The deformation mode, namely simple shearing, is assumed to be the prime deformation mode without exception.

*1.2.1.2 Force (Energy) Needed to Accomplish a Machining Operation*

Merchant added a force diagram to the model shown in Fig. 1.1, considering forces acting in metal cutting and arrived at the force system shown in Fig. 1.2a (Fig. 7 in [11]). In this figure, the total force is represented by two equal opposite forces (action and reaction)  $R$  and  $R'$ , which hold the chip in equilibrium. The force  $R'$  which the tool exerts on the chip is resolved into the tool face-chip friction force  $F$  and normal force  $N$ . The angle  $\mu$  between  $F$  and  $N$  is thus the friction angle. The force  $R$  which the workpiece exerts on the chip is resolved along the shear plane into the shear(ing) force,  $F_s$ , which, in Merchant's opinion, is responsible for the work expended in shearing the metal, and into normal force,  $F_n$ , which exerts compressive stress on the shear plane. Force  $R$  is also resolved along the direction of tool motion into  $F_c$ , termed by Merchant as the cutting force, and into  $F_T$ , the thrust force.

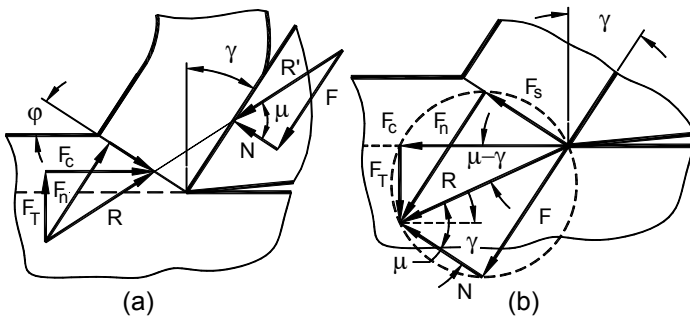


Fig. 1.2. (a) Original and (b) modified force diagrams

The force and energy calculations in metal cutting are based upon determination of the shearing force,  $F_s$  using the equation proposed by Ernst and Merchant in 1941 [12]:

$$F_s = s_s A_c = s_s \frac{t_1 d_w}{\sin \phi} \quad (1.3)$$

where  $s_s$  is the shear strength of the work material,  $A_{sh}$  is the shearing area, and  $d_w$  is the width of cut in orthogonal cutting.

According to Ernst and Merchant, the work material deforms when the stress on the shear plane reaches the ultimate shear strength of the work material. Later researchers published a great number of papers showing that  $s_s$  should be thought of as the shear flow stress, which is somehow higher than the shear strength of the work material depending on particular cutting conditions [13]. Still, this stress remains today the only relevant characteristic of the work material characterizing its resistance to cutting [14].

It follows from Fig. 1.2b that

$$F_c = \frac{F_s \cos(\mu - \gamma)}{\cos(\phi + \mu - \gamma)} \quad (1.4)$$

and combining Eqs. 1.3 and 1.4, one can obtain

$$F_c = \frac{s_s A_c \cos(\mu - \gamma)}{\sin \phi \cos(\phi + \mu - \gamma)} \quad (1.5)$$

The cutting power  $P_c$  then calculates as

$$P_c = F_c v \quad (1.6)$$

This power defines the energy required for cutting, cutting temperatures, plastic deformation of the work material, machining residual stress, and other parameters.

The foregoing considerations show that the shear strength, or in its modern interpretation known as the shear flow stress, is the only relevant characteristic of the work material that defines its resistance to cutting and thus the power used in this process.

### 1.2.2 Metal Cutting vs. Other Closely Related Manufacturing Operations

The above-discussed single-shear plane constitutes the very core of metal cutting theory, which can be represented, in the simplest terms, as a cutting tool *deforming* a particular part of the workpiece by means of shearing. However, there are a number of other, closely-related manufacturing processes known as forming and shearing press operations [5] that can be characterized using the identical

definition. Although forming operations as, for example, roll forming and spinning may not resemble the machining process visually, they completely resemble this process in their representation of the major process parameters. On the other hand, the shearing operation may not completely satisfy the known definition of the metal cutting process while resembling this process closely. Therefore, the differences and similarities of the above-mentioned manufacturing operations and metal cutting have to be analyzed in an attempt to distinguish metal cutting from other closely-related manufacturing processes and operations.

### 1.2.2.1 Comparison with Shear and Tube Spinning

Also known as power spinning, flow turning, hydrospinning, and spin forging, shear spinning is an old process. It produces an axisymmetrical conical or curvilinear shape while maintaining the part's maximum diameter and reducing the part's thickness [5]. The principle of this process is shown in Fig. 1.3a. The process involves forming over a mandrel while the workpiece, held rigidly against one end of the mandrel, rotates. The process involves about 50% or more reduction of area. Because the large plastic deformation takes place, a considerable amount of the thermal energy released due to deformation results in high part and tool temperatures, necessitating the use of MWF.

A detailed examination of the roller-workpiece contact area shown in Fig. 1.3b reveals that the plastically deformed instantaneous cross-sectional area (analogue of the uncut chip thickness in metal cutting)  $A_{sp}=ABDA$ . It follows from the geometry shown in Fig. 1.3 that

$$A_{sp} = (t_1 - t_2) f - \frac{f^3}{16\rho_{rl}} = \left( \frac{t_1 - t_2}{t_1} \right) t_1 f - \frac{f^3}{16\rho_{rl}} \quad (1.7)$$

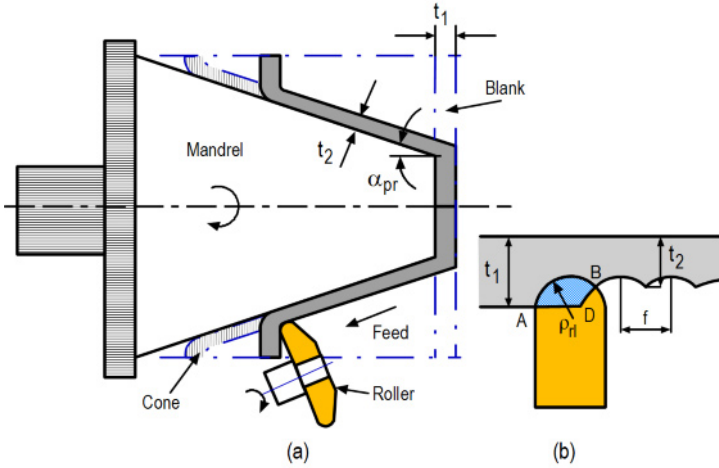
or

$$A_{sp} \cong q_{sp} \cdot t_1 \cdot f \quad (1.8)$$

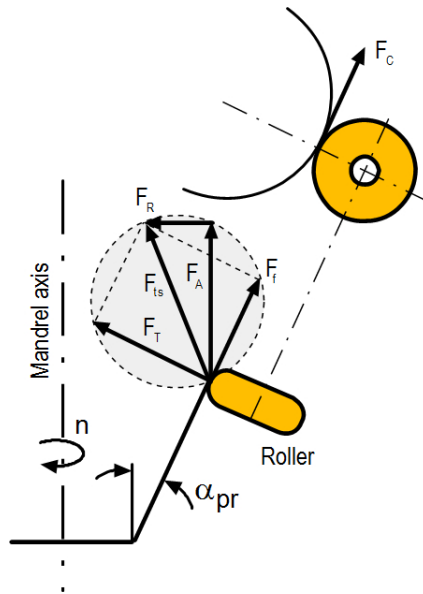
where  $t_1$  is the disk thickness,  $t_2$  is the wall thickness of the part after the process,  $f$  is the feed per revolution of the workpiece,  $\rho_{rl}$  is the corner radius of the roller, and  $q_{sp} = (t_1 - t_2)/t_1$  is the so-called thickness reduction [15].

Figure 1.4 shows the force system in spinning. As seen, it is very similar to that constructed for metal cutting (Fig. 1.2b). In full analogy with metal cutting, the main force is the extrusion force  $F_c$  that acts in the direction of the extrusion speed, the normal force  $F_T$  is the thrust force trying to push the roller off the cone surface. The force  $F_f$  along the surface feeds the roller against the remaining disc flange.

The second force system is also shown in Fig. 1.4. It includes the tangential force  $F_c$ , axial force  $F_A$ , and radial  $F_R$ . In full analogy with the so-called Merchant's force circle shown in Fig. 1.2b, these forces are related by a dashed line circle shown in Fig. 1.4. However, there is a significant difference in calculating these forces.



**Fig. 1.3.** (a) Schematic illustration of the shear-spinning process and (b) the roller-workpiece contact area



**Fig. 1.4.** Spinning force system

Cutting force calculations are based on the determination of the shear strength of the work material ( $s_s$  in Eqs. 1.3 and 1.5) and do not include any strain component. In other words, the cutting forces (under the identical cutting conditions) calculated for two work materials with the same shear strength but considerably different strain are the same. This is not the case, however, for the extrusion force as it

calculates accounting on the amount of plastic deformation achieved in the process (i.e., strain). The extrusion force calculates as [15]

$$F_c \cong 5s_m A_{sp} \ln \frac{t_1}{t_2} = 5s_m q_{st} t_1 f \ln \frac{t_1}{t_2} \quad (1.9)$$

where  $s_m = (\sigma_{UTS} + \sigma_y)/2$  is the mean stress value between the ultimate tensile  $\sigma_{UTS}$  and 0.2% offset yield  $\sigma_y$  strengths of the work material.

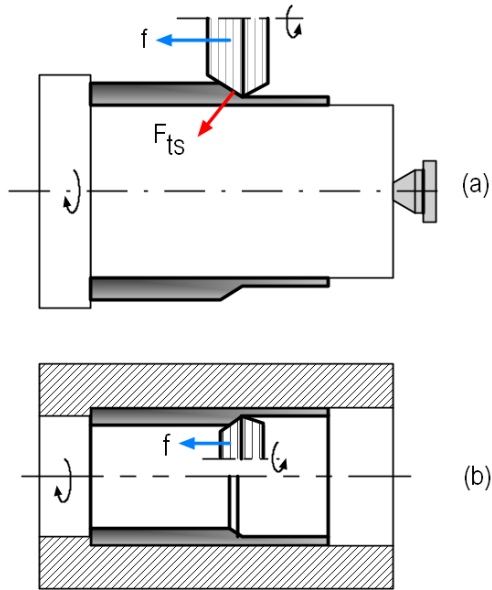
An analysis of Eq. 1.9 reveals that this equation includes the stress factor which is assumed to be somewhere in the middle of the flow curve of the work material ( $s_m$ ), unreformed spinning area  $A_{as}$  (analogous to the uncut chip cross-sectional area), and the strain achieved in spinning ( $\ln(t_1/t_2)$ ), i.e., it properly accounts for the energy spent in spinning. As mentioned, this is not the case in the known methodology of the metal cutting force determination.

A very similar process is tube spinning [5] where the thickness of the cylindrical parts is reduced by spinning on a cylindrical mandrel using a special tool known as rollers (Fig. 1.5). As in shear spinning, the tool applies a certain force  $F_{ts}$  to the workpiece, causing its plastic deformation in shear to accomplish the process. A significant amount of heat is released due to this plastic deformation, necessitating the use of the coolant. The force  $F_{ts}$  needed to accomplish the process calculates identical to metal cutting, i.e., as the product of the shear strength (the shear flow stress) of the work material times the area of shear deformation.

Comparing these processes with metal cutting, one can point out the obvious similarities:

- Both processes involve the workpiece, clamped in the spindle which rotates at a certain speed. Tool, moving with respect to the workpiece with certain feed.
- Both accomplished by heavy plastic deformation of the work material.
- The force needed to accomplish the process for both processes is calculated similarly as the flow stress of the work material times the area of shear deformation. The energy needed for the process calculates as the product of this force and the rotating speed.
- Thermal energy realized due to plastic deformation causes high process temperatures affecting the workpiece and tool that requires the use of the coolant.
- Tool life defined mainly by the rotating speed, feed and properties of the work material.

Therefore, if the notion of metal cutting prevailing today as a process that accomplished by pure plastic deformation of the work material is used, there is no difference between metal cutting and spinning.



**Fig. 1.5.** Examples of (a) external and (b) internal tube-spinning processes

A more objective deeper analysis of the physics of spinning and metal cutting where no common notions prevail in today’s metal cutting field are used, reveals, however, some essential differences:

- The volume of the workpiece is preserved in spinning while that in metal cutting is always reduced.
- The principle difference that exists between machining and spinning is the chip. In machining, the physical separation of the layer being removed (in the form of chips) from the rest of the workpiece must occur. By definition, the physical separation of a solid into two or more fragments is *fracture* [16]. To achieve this fracture, the corresponding stresses and thus forces should be applied in metal cutting.
- The requirements of the work material to achieve the best spinability and machinability are directly opposite. The spinability of metal is defined as the maximum reduction in thickness to which a part can be subjected by spinning without fracture [5]. In other words, the work material should be soft and highly ductile to prevent it from fracturing during large plastic deformation. In metal cutting, plastic deformation is a nuisance [14], i.e., machining of a brittle cast iron requires much less cutting forces and thus power than machining of a highly plastic stainless steel.

These differences suggest that fracture in metal cutting must occur. However, this is in direct contradiction with the most common notion of metal cutting as a process accomplished by plastic deformation of the work material. The idea of fracture was the most criticized in the history of metal cutting. The next section explains the issue.



### 1.2.2.2 Crack (Fracture) or No Crack (No Fracture) in Metal Cutting?

One of the best minds of his time famed for his engineering studies, Franz Reuleaux of the Berlin Royal Technical Academy, suggested in 1890 that fracture occurs in metal cutting and thus a crack forms ahead of the tool [17]. This was confirmed by observations made by Kingsbury as stated in an ASME report [18], who claimed that a crack ran ahead of the tool. MWFs (coolants) were apparently reaching the point of the tool and it was felt that this would be impossible without a crack. This idea of Franz Reuleaux was as revolutionary in the field of metal cutting just the same as the idea of Nicolaus Copernicus, the first astronomer to formulate a scientifically based heliocentric cosmology that displaced the Earth from the center of the Universe in the contrary official doctrine Ptolemaic model of the heavens, which placed the Earth at the center of the Universe, in astronomy. The reaction of the scientific and engineering community on Reuleaux's idea was the same as on the Copernicus idea because the theory of metal cutting established at the beginning of twenty century was entirely based on the ideas of Mallock [19] according to which plastic deformation by simple shearing is the prime deformation mode in metal cutting. Ungrounded destruction or denigration of this idea has been carried out since 1901 [20] till today [8, 21].

Finnie in his review paper [22] devoted a section "A Misconception" to criticize this idea. He stated that the "crack" idea was immediately refuted by Kick [20] in a paper a year after Reuleaux's. Kick pointed out what Reuleaux had seen was probably an optical illusion. Experiments were made by Kick to show that there was no crack ahead of the tool. Because Kick did not find a crack ahead of the tool using his ancient experimental apparatuses, it was proclaimed that there is not a crack and nobody else for more than a century has attempted to find one. This resembles the "Malta Yok" syndrome. The saying is credited to a Turkish admiral, who was leading a fleet towards Malta, but failed to find the island in the relatively small Mediterranean Sea due to the lack of basic navigation skills and obsolete equipment. On return, he thus reported to the sultan (the ruler) that "Malta Yok", "There is no Malta."

In the author's opinion, the section "A Misconception" in Finnie's paper [22] does not appear to be very convincing. It fails to point out the cutting conditions under which Reuleaux and Kingsbury observed cracks (the work material, machining regime, tool geometry) as well as the cutting conditions and experimental apparatus used in Kick's experimentation. It has to be pointed out, however, that the time at which Finnie's paper was written was very special in the history of metal cutting. It was the time when the theory of engineering plasticity developed by Hill [23, 24] was flourishing so that the general impression was that the metal cutting problem would be solved soon using this theory. Because "the crack" was a disturbing factor that makes it impossible to apply the theory of engineering plasticity in metal cutting, the researchers of this time "closed" their eyes and minds to obvious facts that can be observed experimentally.

Since then, practically all books on metal cutting (monographs and texts) repeat the statement about the misconception of Reuleaux referring to the Finnie paper. For example, the recent text on metal cutting (as well as its previous two editions) by Boothroyd and Knight [8] in Introduction to Chapter 2 Mechanics of Metal Cutting states: "Finnie [22] reports that a step backward in the understanding of the

metal cutting process was taken in 1990 when Reuleaux [17] suggested that a crack occurred ahead of the tool and that the process could be linked to splitting of wood.” It was never explained, however, why Reuleaux’s result was a step backwards (from which reference point and established by whom exactly?) or who, when and how disproved this result. Moreover, the idea of Reuleaux, gained by visual observation of the metal cutting process, became a theory according to this text.

### 1.2.2.3 Obvious Contradiction of the “No Crack” Notion

Although there are a number of physical contradiction with the “no crack” notion [13, 25, 26], three of them are outstanding and thus obvious. They are given below.

#### *Unrealistically High Shear Strain*

Merchant [11, 27, 28] derived the following equation for the final shear strain in metal cutting:

$$\varepsilon = \frac{\cos \gamma}{\cos(\varphi - \gamma) \sin \varphi} = \frac{\zeta^2 - 2\zeta \sin \gamma + 1}{\zeta \cos \gamma} \quad (1.10)$$

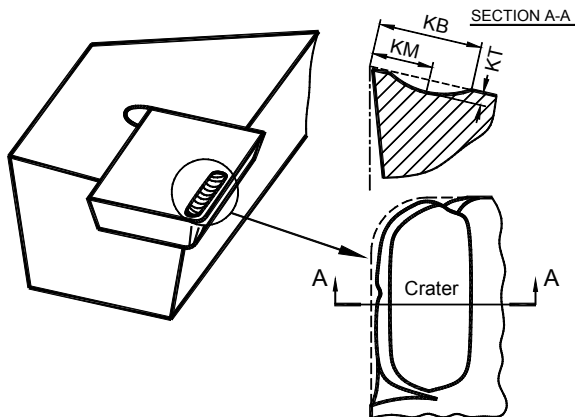
which is actually a form of the continuity conditions for a single-shear plane model [14]. In other words, Eq. 1.10 valid if metal cutting involves pure plastic deformation without cracking. Although Eq. 1.10 appears in almost any book on metal cutting, no one probably calculated a strain using this equation. The problem is that the calculated shear strain in metal cutting is much greater than the strain at fracture achieved in the mechanical testing of materials under various conditions. Moreover, when the chip compression ratio  $\zeta = 1$ , i.e., the uncut chip thickness is equal to the chip thickness, no plastic deformation occurs in metal cutting [29], the shear strain, calculated by the model remains very significant without any apparent reason that it is physically impossible.

#### *Wear Pattern*

As well known and secured at the level of national and international standards [30, 31], one of the two prime wear regions of cutting tools is so-called crater wear that occurs on the tool rake face as shown in Fig. 1.6. As seen, the maximum crater wear occurs at a certain distance KM from the cutting edge.

However, this wear pattern does not follow from the single-shear plane model shown in Fig. 1.1 as there is no apparent reason for a crater to occur in the middle of the tool-chip contact. This is because if no crack occurs in front of the cutting edge, the distributions of the normal and shear contact stresses along the tool-chip interface of length  $l_c$  (Fig. 1.7a) are as shown in Fig. 1.7b known after Zorev [32] and adopted by all “no crack” notion specialists (for example, Fig. 2.25, page 99 in the discussed text by Boothroyd and Knight [8]). It directly follows from Fig. 1.7b that the maximum combined stress (normal plus shear) occurs at the cutting edge so there is no apparent reason for crater wear to occur at the middle of the tool-chip interface. Moreover, Zorev had pointed out [32] that a singularity of the normal contact stress exists at the cutting edge, i.e., this stress tends to infinity at the

cutting edge although the subsequent “no crack” notion specialists ascribed finite value to this stress presenting the mentioned distribution in a qualitative manner, i.e. to hide the issue. Therefore, the two discussed issues, namely the crater wear pattern and singularity of the normal contact stress, have never been resolved.



**Fig. 1.6.** Crater wear on turning tools according to ANSI/ASME Tool Life Testing with Single-Point Turning Tools (B94.55M–1985)

### *Chip Structure*

The simplest, straightforward and self-explanatory way to validate any metal cutting model (including FE model) is to compare the chip shape and its structure obtained in modeling and in a verification test carried out under the same conditions. It has never been done, however for obvious reason explained below.

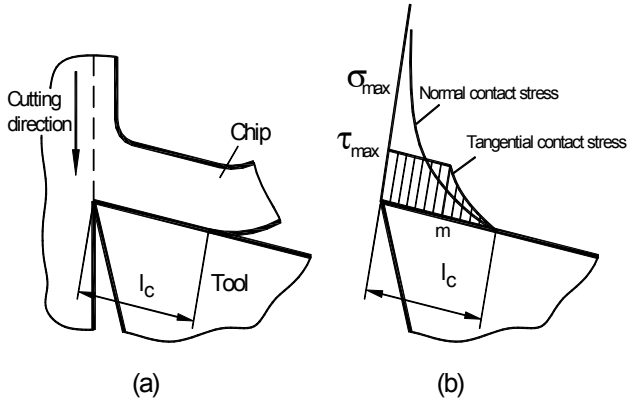
According to Merchant, the so-called card model of the cutting process proposed by Piispanen [33] is very useful to illustrate the physical significance of shear strain and to develop the velocity diagram of the cutting process. This model is shown in Fig. 1.8. The card-like elements displaced by the cutting tool were assumed to have a finite thickness  $\Delta x$ . Then each element of thickness  $\Delta x$  is displaced through a distance  $\Delta s$  with respect to its neighbor during the formation of the chip.

Although the card model appears in almost every textbook on metal cutting to explain chip formation, two obvious problems have never been pointed out. First is that the separation of each chip fragment should conveniently take place along line  $ab$  which then becomes  $a'b'$ , i.e., a chip fragment should fracture from the rest of the workpiece in the direction of the feed motion which is impossible physically under the force model shown in Fig. 1.2 and conceptually as the idea of the model does not include fracture. Second, it is unclear how to deal with empty spaces (triangle  $ba'b'$  in Fig. 1.8) as they have never been observed in practice. To solve these contradiction, Merchant [11] assumed that thickness of an individual chip fragment  $\Delta x \rightarrow 0$  in the real cutting process so there would be no fracture and no empty spaces. As such, the chip structure should be uniform. However, this assumption not only failed to solve the problems as the fracture would take place

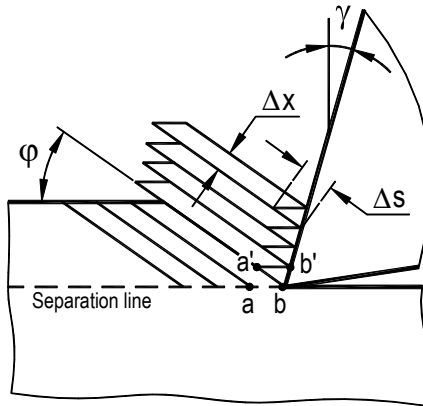
even for infinitesimal thickness of a chip fragment but also created two more severe problems. According to Merchant [11], shear strain  $\epsilon$  calculates as

$$\epsilon = \frac{\Delta s}{\Delta x} \tag{1.11}$$

If  $\Delta x \rightarrow 0$  then strain should tend to infinity.

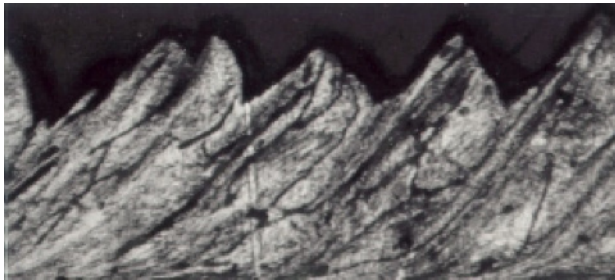


**Fig. 1.7.** (a) Tool-chip interface and (b) distribution of the normal and shear stress over this interface



**Fig. 1.8.** Card model to represent chip formation

The real chip structure does include the chip fragments and separators as shown in Fig. 1.9. Moreover, as the cutting speed increases, these separators become more pronounced even for highly ductile material [29].



**Fig. 1.9.** Typical structure of medium-carbon steel chip

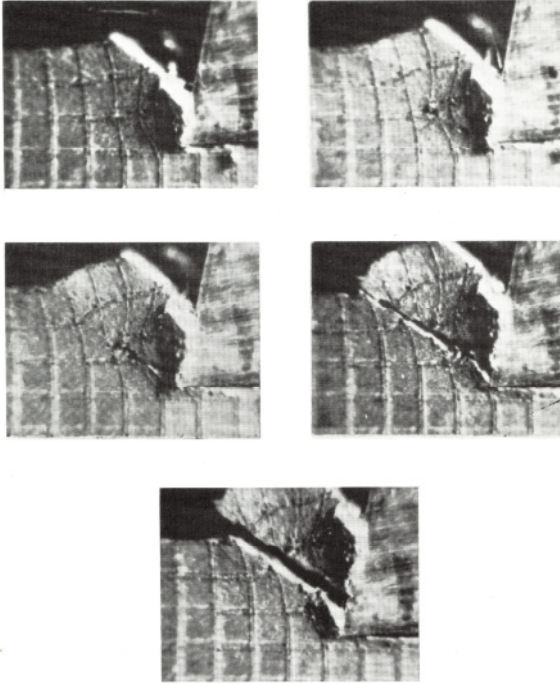
#### *1.2.2.4 Computational “Crack”*

Although thousands of specialists in metal cutting still believe that there is no crack associated with the single-shear plane model, the word “believe” does not work well with computers when it comes to numerical modeling of the metal cutting process. As soon as decent FEM programs had become available to specialists in metal cutting modeling, the problem of chip separation came into existence. Researchers were forced to induce a crack between the chip and the workpiece to make models work. A great number of numerical techniques to model chip separation from the rest of the work material were developed. The node-splitting technique is the oldest where chip separation is modeled by the separation of nodes of the mesh ahead of the tool cutting edge along the pre-defined cutting line. This technique is usually used with the Lagrangian formulation to simulate steady-state cutting. A number of separation criteria grouped as geometrical and physical were developed [34–40].

#### *1.2.2.5 Ductile and Brittle Work Materials*

It was recognized even by most orthodox proponents of “no crack” metal cutting that a crack forms in front of the cutting edge in machining of “brittle” work materials. For example, Finnie in the above-mentioned paper where he discussed “misconception” of the crack notion in metal cutting [22] presented a micrograph of a partially formed chip where a crack can be readily observed. He attributed such a case to the machining of “brittle” materials. “The dynamics” of the formation of discontinuous chip was presented by Ernst as early as 1938 [41]. As seen in Fig. 1.10, a distinctive crack forms in front of the cutting edge and then runs to the workpiece free surface separating a chip fragment from the rest of the workpiece.

The foregoing consideration reveals that simple real life evidence forced specialists to admit that cracks do occur in metal cutting in machining brittle work materials. What was never discussed in the publications is how brittle the work material should be for crack occurrence. Unfortunately, nobody ever quantified the exact location of the border “Brittle/Ductile” in metal cutting although, in general, measurements of ductility are of interest to indicate the extent to which a metal can be deformed without fracture in metalworking operations [16].



**Fig. 1.10.** Formation of a typical discontinuous chip. Work material: high lead bronze; depth of cut: 2.7 mm; rake angle:  $10^\circ$ ; cutting speed: 25.4 mm/min; no coolant [41]

The conventional measures of ductility that are obtained from the tension test are the engineering strain at fracture  $e_f$  (usually called elongation) and the reduction of area at fracture  $q$ ;

$$e_f = \frac{L_f - L_0}{L_0} \quad (1.12)$$

$$q = \frac{A_0 - A_f}{A_0} \quad (1.13)$$

where  $L$  is the original gage length of the specimen,  $L_f$  is the gage length at fracture,  $A_0$  is the original area of the cross section of the specimen, and  $A_f$  is this area at fracture. Both elongation and reduction of the area are expressed as a percentage [16]. A ductile material is usually classified as a material that has a yield strength and that exhibits more than 5% elongation in the standard tension test [42, 43].

According to this standard classification, the work materials used in cutting test (Fig. 1.10) is ductile as it has more than 12% of elongation and very distinctive yield strengths. As clearly seen in this figure, a great deal of plastic deformation of the layer being removed is achieved before a crack appears. The grid distortion due

to plastic deformation (as can be seen in Fig. 1.10) is a direct indication that the work material used is ductile. Note that ANSI 1045 as-rolled steel has elongation 12% and it is always considered as to be a ductile material. Moreover, many cast irons have elongation more than 10%. For example, Ductile Iron grade 60–40–18 (ASTM A395–76, ASME SA395) has elongation at break of 18%.

Therefore, formation of a visible crack and the so-called discontinuous chip should be attributed to brittle work materials. In other words, the standard set of tensile properties, obtained in the standard tensile test or in SHPB testing, are not relevant in metal cutting. A considerable different set of physical properties should be considered if one tries to understand this process.

#### *1.2.2.6 Support of the “Crack” (Fracture) Notion*

Atkins, who supported the “crack” (fracture) notion for years [44], in his very extensive analysis of the problem [45] pointed out that fracture must occur along the surface separating the layer being removed and the rest of the workpiece. As early as in 1983, Sampath and Shaw [46], studying an elastic-plastic finite element stress field based on an assumed continuum and experimentally observed chip geometry and cutting forces, have found it to be inconsistent with physical conditions that must pertain along the shear plane (constant stress on the shear plane equal to the flow shear stress of the heavy pre-strained hardened work material). It was concluded that the material does not behave as a continuum and that microcracks along the shear plane play a significant role just as they do on the tool face. Although this very important finding explains many known contradictory results, it has not been noticed by the further researchers.

When more sophisticated experimental technique emerged, the presents of cracks in chip formation was conclusively proven in the machining of a wide variety of work material at macro and micro levels [47, 48]. Conducting a very detailed study of chip formation, Itawa and Ueda proved that the continuous chip forms only under relatively specific (or exotic) cutting conditions such as when pure single crystal aluminum is machined [47]. Under common cutting conditions, crack(s) are the real phenomenon in chip formation which is classified to be:

- Quasi-continuous chip formation that takes place in machining ductile materials such as steels under favorable cutting conditions. The crack occurs along the shear direction.
- Discontinuous chip formation that occurs typically when machining brittle materials. As such, the crack nucleates below the flank face and then propagates ahead of the cutting tool due to void coalescence.
- Chip formation with built-up edge that takes place in machining “materials which can adhere to the tool face.” The crack forms initially below the flank face and then ahead of the tool.

Similar phenomena were observed by Didjanin and Kovac [48]. Because most of the work materials are alloys and thus have different phases and inclusions, cracking in metal cutting occurs between different phases and voids [16].

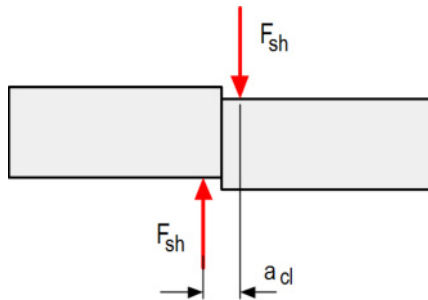
Therefore, metal cutting should be considered in comparison with other shearing manufacturing processes where cracks and then fractures occur in due course of the process. Besides, the word “shearing” is one of the most used words

in describing the metal cutting process in books and research papers and articles. Particularly, Trent and Wright pointed out that a punch method can be used to obtain yield strength in metal cutting (page 348 in [49]).

### 1.2.2.7 Comparison with Shearing Manufacturing Operations

#### *What are Shearing and Shear Strength?*

Shearing is the deformation of a material substance in which parallel internal surfaces slide past one another. In shearing, one layer of a material is made to move on the adjacent layer in a linear direction due to action of two parallel forces  $F_{sh}$  located at distance  $a_{cl}$  known as the clearance distance as shown in Fig. 1.11. A typical example of shearing is cutting with a pair of scissors (Fig. 1.12). Scissors are cutting instruments consisting of a pair of metal blades connected in such a way that the blades meet and cut materials placed between them when the handles are brought together.



**Fig. 1.11.** Shearing

Shear strength is the maximum observed load divided by the cross-sectional area that is sheared. Standard ASTM D732 defines a procedure for testing the shear strength for sheet materials. In the determination of the shear strength, it is very important to account for the clearance  $a_{cl}$  (Fig. 1.11) because, when this clearance increases, the opposing forces producing shear forces do not act in the same plane or line, bending stresses are set up. On the other hand, if the forces act along the same line, the test becomes a compression test. Because in any real shearing there is always a considerable clearance between two parallel forces, shearing should be considered as a combined load consisting of compression and bending. This explains why the shear strength is much lower than the ultimate compression strength. For example, according to Latrobe Specialty Steel Co, the ultimate compressive strength is approximately 130% of the ultimate tensile strength while the shear strength is approximately 60% of the ultimate tensile strength for tool steels [50]. It shows the effectiveness of the combined load in cutting of materials as this load reduces the force needed to separate the two parts of the work material.

#### *Shearing Operations*

Many sheet-metal parts are made from a blank of suitable dimension which is first removed from a large sheet or coil using a variety of manufacturing processes called shearing operations as they are all based on the shearing process. In these



operations, the sheet is cut by subjecting it to shear stress typically between a punch and a die as shown in Fig. 1.13. Shearing usually starts with the formation of the shear planes and then cracks on both the top and bottom edges of the workpiece (A and B, and C and D in Fig. 1.13). These cracks eventually meet each other and separation occurs. The rough fracture surfaces are due to these cracks. The smooth and shiny surface on the hole results from the burnishing of the flank edge of the punch.



**Fig. 1.12.** Cutting with a pair of scissors

In punching, the sheared slug is discarded while in blanking this slug is the part and the rest is scrap as seen in Fig. 1.14. Die cutting includes perforating, or punching a number of holes in a sheet; parting, or shearing the sheet into two or more pieces; notching, or removing pieces of various shapes from the edges; lancing, or leaving the tab without removing any material.

Generally, the punching force calculates as the product of the shear strength of the work material and the shearing area [15], i.e.

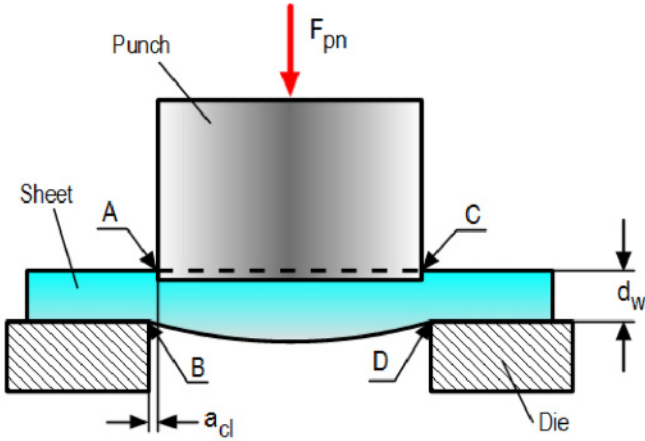
$$F_{pn} = A_{sh}s_s = L_{pn}d_w s_s \quad (1.14)$$

where  $A_{sh}$  is the shearing area,  $s_s$  is the ultimate shear strength of the work material,  $L_{pn}$  is the length or perimeter of cut, and  $d_w$  is the thickness of sheet being sheared.

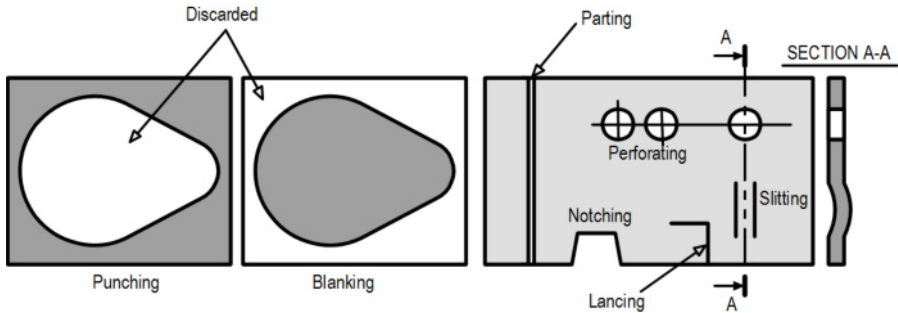
As seen, the punching force can be significant if a flat punch similar to that shown in Fig. 1.13 is used because the length or perimeter of cut in this case can be great. Thus the punch force builds up rapidly during shearing because the entire thickness is sheared at the same time. As a result, multi-ton presses have been used for many years for punching.

As the tool materials, presses and accuracy of the tooling improved, new design of punch and die appeared. Figure 1.15 shows a beveled punch which is widely used nowadays for punching a wide variety of materials including steel

coils and paper sheets (a paper punch used in any office). This geometry is particularly suitable for shearing thick blanks because it reduces the punching force and operation noise level. The area being sheared at any moment can be controlled by angle  $\phi_{pn}$  shown in Fig. 1.15. The greater this angle, the smaller the punching force. As such, the punching stroke is increased. However, it should be obvious that the total work done in shearing a blank is independent of angle  $\phi_{pn}$ .



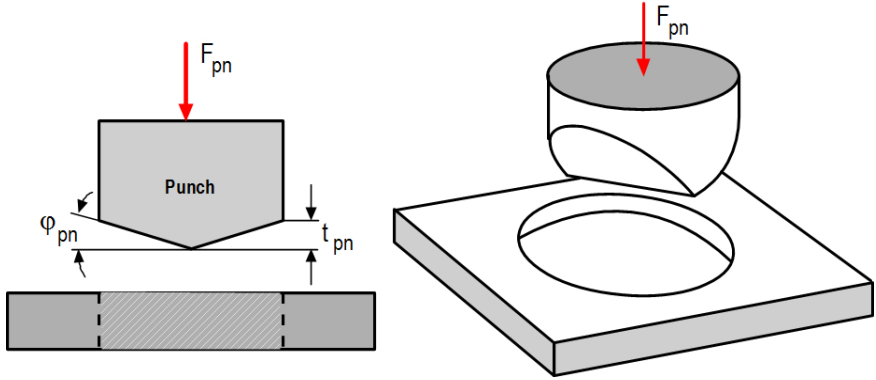
**Fig. 1.13.** Schematic illustration of shearing with punch and die, indicating some of the important process variables



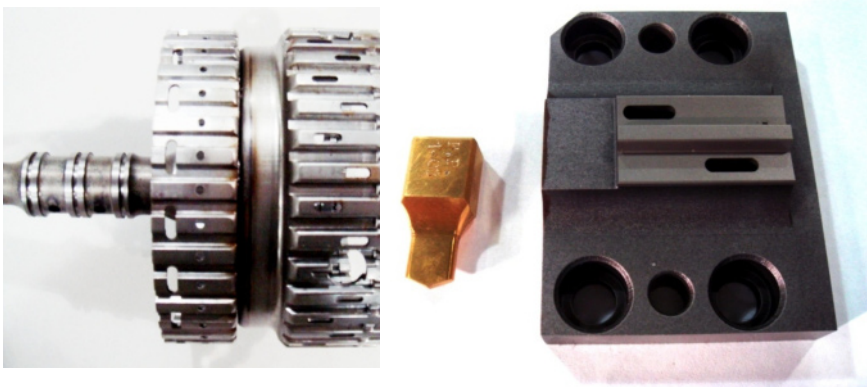
**Fig. 1.14.** Examples of various shearing operations

Figure 1.16 shows the clutch housing of a RWD automatic transmission – a typical automotive part as well as a punch and a die used to make slots in this part.

Figure 1.17 the areas of wear of the punch. The flank wears due to contact of the flank surface with the punched surface while the rake wears due to the contact of the punch with the slug.



**Fig. 1.15.** Example of the use of shear angles in punch design

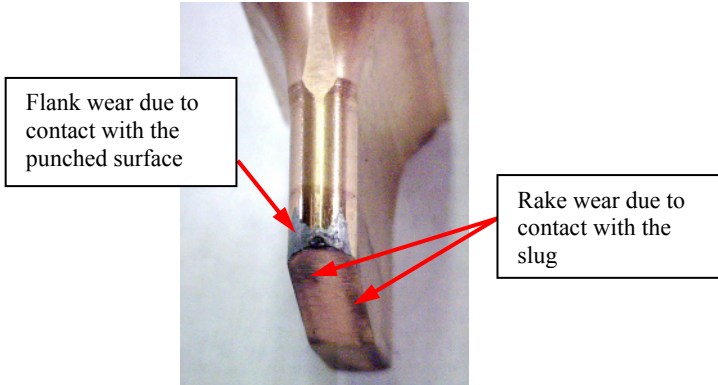


**Fig. 1.16.** Clutch housing with punched slots, a punch, and a die used for punching these slots

### *Comparison with Metal Cutting*

Surprisingly, the shearing process (as it is considered in the literature [5]) is practically identical to the metal cutting process as it is considered in the literature [6, 8, 28, 49, 51]. This is because:

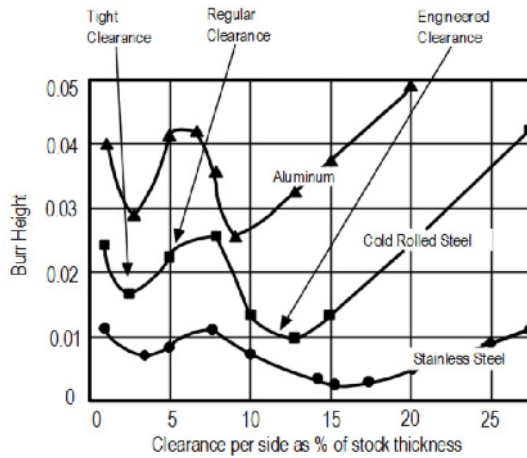
1. Both processes are presumably accomplished by simple shearing.
2. The shearing force in machining and in punching calculate using the same formulas, i.e., as the product of the shear strength of the work material and the shearing area (compare Eqs. 1.3 and (1.14)). One may argue, the shearing area in punching is normally much greater than that in machining. It is true that it was like that for many years. Nowadays, beveled punches are used for wide variety of work materials (from steel to paper punching), where the shearing area is rather small so it is similar to that found in machining.



**Fig. 1.17.** Wear areas of the punch

3. The wear patterns of the punch and the cutting tool are the same. Flank wear for both is due to the rubbing of the flank force with the machined surface (the punched hole) while the rake wear is due to the contact of the rake face with the chip (slug). The shearing process starts with the formation of shear plane.
  
4. The same set of assumptions is used in FE modeling of both processes. For example, the constant friction coefficient is assumed to be constant along the contact areas; the Johnson-Cook material constitutive model is used for the characterization of the work material behavior in deformation and fracture [52]. As a result, the known results of such modeling have the same problems showing poor agreement with the results of observations [53]. Particularly for shearing, for many years toolmakers used 5% of stock thickness per side as a standard, or regular, punch-to-die clearance. This provided an acceptable burr height and slug control. FEA was “adjusted” correspondingly so it proved that this is the best clearance in terms of burr control, minimum tool wear, and smallest punching force [52]. Experimental studies, however, proved otherwise. Research and testing have revealed that a radical increase in punch-to-die clearance can reduce burr height to the lowest point as shown in Fig. 1.18 and increases tool life exponentially. This increased clearance is referred to as engineered clearance [54]. This discrepancy of FEM and test results is a direct consequence of improper modeling of the work material behavior and fracture. The Johnson-Cook model used in both metal cutting and shearing modeling does not account for the combined stress and cannot handle the fracture behavior of the work material. As clearances increases, the failure of the work material takes place under combined stress (shear and bending stresses). The failure of the work material requires the minimum energy (thus plastic deformation and punching force) at a certain combination of

these stresses depending on a particular work material. This combination is defined by the clearance.



**Fig. 1.18.** Influence of the clearance per side on the burr height in punching of different materials

The foregoing considerations suggest that there is no difference between metal cutting and shearing manufacturing operations. It may be concluded then that metal cutting has been attracting much more attention than other shearing press operations only because it is a very important component in the overall manufacturing activity.

### 1.3 What Went Wrong in the Representation of Metal Cutting?

As discussed in Sect. 1.1, the single-shear plane model is still the only option for studies on metal cutting [3] although a number of various models of chip formation are known to specialists in this field. Therefore, this model will be considered in this section. This is because Zorev [32], using pure geometrical considerations, conclusively proved that all other known models of metal cutting are just particular cases of the single-shear plane model.

The major drawbacks of the single-shear plane model pointed out by Astakhov [26] are as follows:

Inherent drawbacks

- *Infinite strain rate.* Infinite deceleration and thus strain rate of a microvolume of the work material passing through the shear plane.
- *Unrealistically high shear strain.* The calculated shear strain in metal cutting is much greater than the strain at fracture achieved in the mechanical testing of materials under various conditions. Moreover, when the chip compression ratio (Eq. 1.1)  $\zeta = 1$ , i.e., the uncut chip thickness is equal to the chip thickness, no plastic deformation occurs in metal cutting.

However, the shear strain, calculated using the model (Eq. 1.10) remains very significant without any apparent reason for that.

- *Unrealistic behavior of the work material.* Rigid perfectly plastic work material is assumed which is not the case in practice.
- *Improper accounting for the resistance of the work material to cutting.* The shear strength or the shear flow stress cannot be considered as an adequate characteristic in this respect because the stress does not account for the energy spent in cutting.
- *Unrealistic representation of the tool-workpiece contact.* The cutting edge is perfectly sharp and no contact takes place on the tool flank surface. This is in obvious contradiction to the practice of machining where the flank wear (due to the tool flank-workpiece contact) is a common criterion of tool life [30].
- *Inapplicability for cutting brittle work materials.* The model is not applicable for the case of the cutting of brittle materials, which exhibit no or very little plastic deformation. Nevertheless, the single-shear model is still applied to model the machining of gray cast iron [55], cryogenic water ice [56], etc.

Ernst and Merchant induced drawbacks

- *Incorrect velocity diagram.* In the known considerations of velocities in metal cutting, the common coordinate system is not set, so that the existing velocity diagram consists of the velocity components from different coordinate systems. As a result, unrealistic velocity components are considered.
- *Incorrect force diagram.* The bending moment due to the parallel shift of the resultant cutting force is missed in the force diagram. As was shown [14], this missed moment is the prime cause for chip formation and thus it distinguishes the cutting process among other deforming processes. Moreover, the state of stress imposed by this moment in the chip root causes chip curling.
- *Constant friction coefficient.* Because the friction coefficient at the tool–chip interface can be thought as the ratio of the shear and normal force on this interface, the distributions of the normal and shear stresses should be equidistant over this interface. The available theoretical and experimental data [29] do not conform this assumption.

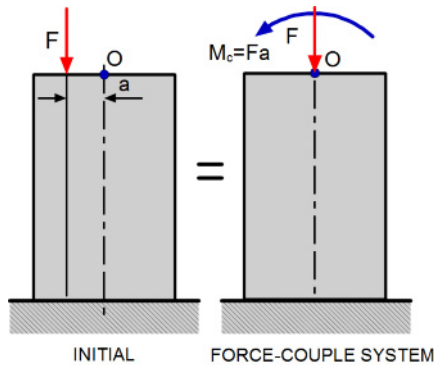
Among these drawbacks, the force diagram and resistance of the work material in cutting are most relevant to the foregoing analysis.

### 1.3.1 Force Diagram

As discussed in Sec. 1.1, Merchant, considering forces acting in metal cutting, arrived at the force system shown in Fig. 1.2a (Fig. 7 in [11]). Although this diagram looks logical, there are a number of serious concerns about its physical justification. Probably the main item is that, for this diagram to exist in the fashion shown in Fig. 1.2(a), the normal force should be less than the friction force at the

tool-chip interface and the shear angle should be rather greater. In reality, the opposite is true [29] so angle  $\mu$  does not exceed  $25^\circ$ . Because the force  $R'$  applied to the cutting tool must act within the tool-chip contact length (distance  $AO$  in Fig. 1.1), its line of action does not intersect the shear plane  $AB$  so that the balancing force  $R$  is applied somewhere at the point of intersection of the line of action of  $R'$  and the imaginary continuation of the shear plane.

A far more important issue is that Merchant shifted the resultant cutting force  $R'$  parallel to itself, applying it to the cutting edge “for convenience” (p. 272 [11]) as shown in Fig. 1.2b. As such, the moment equal to this force times the shift distance was overlooked. As well known from statics [57], any force  $F$  can be replaced by a parallel force of the same magnitude applied at an arbitrary point  $O$  and a couple of magnitude  $M_c = F \cdot a$ , where  $a$  is a moment arm from  $O$  to the original position of the force. Such a representation shown in Fig. 1.19 is called force-couple system.



**Fig. 1.19.** Displacement of a force parallel to itself

Unfortunately, this simple flaw was not noticed by the subsequent researchers who just copied these two pictures. Moreover, the force diagram shown in Fig. 1.2b became known as the classical Merchant force circle and this diagram is discussed today in any book on metal cutting. No wonder that all attempts to apply the fundamental principles of engineering plasticity [24], the principle of minimum energy [58], or define the uniqueness of the chip formation process [24, 59] did not yield in any meaningful results because the incomplete force system, shown in Fig. 1.2b was used as the model.

According to the force diagram shown in Fig. 1.2b, the chip sliding over the rake face should never separate from this face because no one force factor is responsible for the chip curling away. Moreover, if the concept of the so-called secondary deformation zone adjacent to the tool rake face is used in the considerations of the single-shear plane model as in practically all known publications on metal cutting [32, 51, 60, 61] starting from Ernst [41], then the chip contact layer is subjected to further plastic deformation up to seizure as suggested by Trent [62, 63]. As such, the formed chip should curve “inside” the tool rake face because the chip layers adjacent to the chip free surface move freely, i.e., without

any further plastic deformation while the flow of the chip contact layer is restricted. Unfortunately, these deductions from the single-shear plane model fail even remotely to resemble reality. The chip has rather limited contact area with the tool rake face so chip curling always occurs even in the simplest case of orthogonal cutting. This well-known observation of any metal cutting process cannot be explained by the discussed force diagram.

### 1.3.2 Resistance of the Work Material in Cutting

#### *1.3.2.1 Mechanical Properties of the Work Material in Force Calculations*

As discussed in Sect. 1.1.2, the basic material mechanical property used to calculate the cutting force is its shear strength. According to Ernst and Merchant, the work material deforms when the stress on the shear plane reaches the shear strength of the work material. Later researches published a great number of papers showing that  $\tau_y$  in Eq. 1.5 should be thought of as the shear flow stress [7, 51] which, is somehow higher than the shear strength of the work material depending on particular cutting conditions. If one recalls that the ultimate shear strength  $S_s$  is 0.75 of the ultimate tensile  $\sigma_{UTS}$  for steels then one realizes that the maximum shear flow stress cannot exceed  $\sigma_{UTS}$ .

However, everyday practice of machining shows that these considerations do not match reality. For example, machining of medium carbon steel AISI 1045 (tensile strength, ultimate  $\sigma_{UTS} = 655\text{MPa}$ , tensile strength, yield  $\sigma_Y = 375\text{MPa}$ ) results in a much lower total cutting force (Fig. 1.20), greater tool life, lower required energy, cutting temperature, and machining residual stresses than those obtained in the machining of stainless steel AISI 316L ( $\sigma_{UTS} = 517\text{MPa}$ ;  $\sigma_Y = 218\text{MPa}$ ) [64]. The prime reason is that any strength characteristic of the work material in terms of its characteristic stresses cannot be considered alone without corresponding strains, which determine the energy spent in deformation of the work material [14, 65, 66]. Only when the stress and corresponding strain are known, can the other parameters-outcomes of the metal cutting process be calculated [66].

#### *1.3.2.2 Mechanical Properties of the Work Material Involved in FE Modeling of the Metal Cutting Process*

Experimental studies in metal cutting are expensive and time consuming. Moreover, their results are valid only for the experimental conditions used and depend greatly on the accuracy of calibration of the experimental equipment and apparatus used. An alternative approach is numerical methods. Several numerical methods have been used in metal cutting studies, for instance, the finite difference method, the finite element method (FEM), the boundary element method etc. Amongst the numerical methods, FEM is the most frequently used in metal cutting studies. The goal of finite element analysis (FEA) is to predict the various outputs and characteristics of the metal cutting process such as the cutting force, stresses, temperatures, chip geometry, etc.



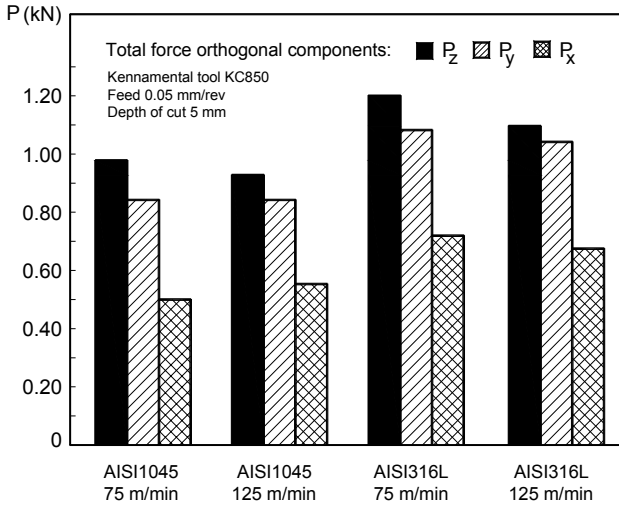


Fig. 1.20. Comparison of cutting force components (courtesy Prof. J.C. Outeiro)

Several material constitutive models are used in FEM of metal cutting, including rigid-plastic, elasto-plastic, viscoplastic, elasto-viscoplastic, etc. These models take into account the high strains and temperatures reportedly found in metal cutting. Among others, the most widely used is the Johnson and Cook model [67]. This is a thermo-elasto-visco-plastic material constitutive model represented as

$$\sigma_{eq} = \left( A + B \epsilon_{eq}^n \right) \left( 1 + C \ln \left( \frac{\dot{\epsilon}_{eq}}{\dot{\epsilon}_{eq}^0} \right) \right) \left[ 1 - \left( \frac{T - T_0}{T_F - T_0} \right)^m \right] \quad (1.15)$$

where  $\epsilon_{eq}^n$  is the equivalent plastic strain,  $\dot{\epsilon}_{eq}$  is the equivalent plastic strain rate,  $\dot{\epsilon}_{eq}^0$  is the reference equivalent plastic strain rate (normally  $\dot{\epsilon}_{eq}^0 = 1s^{-1}$ ),  $T$  is the temperature,  $T_0$  is the room temperature,  $T_F$  is the melting temperature and  $A, B, C, n$  and  $m$  are constants, which depend on the material. These constants are determined through material tests.

Because the strain rates in conventional material tests (tensile, compressive or torsion) are in the range of  $10^{-3} - 10^{-1} s^{-1}$ , non-conventional material tests, referred to as dynamic tests, are usually preferred by many researchers. Split Hopkinson Pressure Bar (SHPB) impact testing is the most common. This test is used to determine the material behavior at strain rates up to  $10^5$ . This test can be conducted at an elevated temperature (500°C or even more). There are, however, some major problems with the use of the discussed model and the method of the determination of its constants:

- Only a few laboratories and specialists in the world can conduct SHPB testing while properly assuring the condition of dynamic equilibrium.

- It is completely unclear how to correlate the properties of the work materials obtained in SHPB uniaxial impact testing with those in metal cutting with a strong degree of stress triaxiality. As known [16], the deformation and fracture modes as well as the strain at fracture depend on a given state of stress, which is defined in metal cutting by the tool geometry, friction conditions on the tool-chip and tool-workpiece interfaces, machining regime, etc. Even when only the cutting speed varies while all other cutting conditions are kept the same, the deformation in metal cutting changes significantly which is reflected in the chip structure [29].
- The model does not account for the formation of cracks and fracture.
- The model coefficients are very sensitive to any change in the metallurgical conditions of the work material. According to the existent standards on the composition and properties of various work materials, their properties vary significantly even within the same grade, not to mention heat treatment, grain size, residual stresses, and many other factors. Unfortunately, the many known FEM of metal cutting used the coefficients of the Johnson and Cook model taken from literature sources. As such, the discussed particularities of a particular work material are not mentioned

### **1.3.3 Comparison of the Known Solutions for the Single-shear Plane Model with Experimental Results**

The next logical question is: How good is the single shear plane model? In other words, how far is this model from reality? Naturally, during the period of 1950–1960, when decent dynamometers and metallographic equipment became widely available, a number of fundamental works were carried out to answer this important question. The results of these extensive researches are well summarized by Pugh [68] and Chisholm [69]. In the author’s opinion, the best research results and a detailed description of the experimental methodology were presented by Pugh [68]. The results obtained by Pugh [68] was discussed by Bailey and Boothroyd 10 years later [70]. In his study, all the possible ‘excuses’ for ‘inadequate’ experimental technique were eliminated. Zorev also presented clear experimental evidence that the discussed solutions are inadequate [71]. He showed that Merchant’s solution is not valid even in the simplest case of cutting at low cutting speeds. The experimental results are conclusively proved that for every work material tested, there is a marked disagreement between experiment and the predictions made using the single-shear model and its derivatives [29].

Hill, one of the founders of engineering plasticity [23], noticed [72] that “it is notorious that the extent theories of mechanics of machining do not agree well with experiment.” Other prominent researchers in the field conclusively proved that the experimental results are not even close to those predicted theoretically [68, 69, 71, 73]. Recent researchers further clarified this issue, presenting more theoretical and experimental evidence [29, 74]. As one might expect, knowing these results, the single-shear plane model would become history. In reality, however, this is not the case and the single-shear plane model managed to “survive” all these conclusive facts and is still the first choice for practically all the textbooks on metal cutting used today [2, 5, 6, 8, 49, 75]. In contrast, all the excellent works showing

complete disagreement of this model with reality are practically forgotten and not even mentioned in modern metal cutting books, which still discuss the single-shear plane model as the very core of metal cutting theory. Moreover, the book “Application of Metal Cutting Theory” [1] is entirely based on this model, showing how to apply it in practical calculations, although other research works complain about the absence of “predictive theory or analytical system which enables us, without any cutting experiment, to predict cutting performance such as chip formation, cutting force, cutting temperature, tool wear and surface finish [76].” It should become clear that any progress in the prediction ability of metal cutting theory could not be achieved if the single-shear plane model were still used.

## **1.4 What is Metal Cutting?**

### **1.4.1 Importance to Know the Right Answer**

The right answer to this question has enormous significance, both theoretical and practical. It should allow the development of the correct models of metal cutting that can be used as parts of CAD/CAM systems, reducing the necessity for expensive and time consuming experimental studies and increasing the first-time success rate in the implementation of the cutting tools. The “guessing” part in the design and selection of cutting tools can thus be significantly reduced. Machinability of various work materials can be assessed properly so the right tool geometry and material as well as appropriate machining regime can be assigned in each given case. Moreover, work materials can be brought to the conditions where their machinability is at maximum without compromising their service quality. Objective, physics-based criteria of optimization of machining operation can be worked out so simple optimization that can be used even on the shop floor can be developed that should increase efficiency of machining operations.

### **1.4.2 Definition**

The system concept in metal cutting was first introduced by Astakhov and Shvets [77]. According to this concept, the process of metal cutting is defined as a forming process, which takes place in the components of the cutting system that are so arranged that the external energy applied to the cutting system causes the purposeful fracture of the layer being removed. This fracture occurs due to the combined stress including the continuously changing bending stress causing a cyclic nature of this process. The most important property in metal cutting studies is the system time. The system time was introduced as a new variable in the analysis of the metal cutting system and it was conclusively proven that the relevant properties of the cutting system’s components are time dependent. The dynamic interactions of these components take place in the cutting process, causing a cyclic nature of this process.

It follows from this definition that, considered together (the system approach), the following features distinguish metal cutting among other closely related manufacturing processes and operations:

1. *Bending moment.* The bending moment forms the combined stress in the deformation zone that significantly reduces the resistance of the work material to cutting. As a result, metal cutting is the most energy efficient material removal process (energy per removed volume accounting for the achieved accuracy) compare to other closely related operations.
2. *Purposeful (micro)fracture* of the layer being removed under combined stress. The fracture occurs in each successive cycle of chip formation.
3. *Stress singularity at the cutting edge.* The maximum combined stress does not act at the cutting edge compared to other closely related forming operations. Rather, a (micro) crack forms in front of the cutting edge. As a result, when the cutting system is rigid and the cutting tool is made and run properly, the wear occurs at a certain distance from the cutting edge that allows maintaining the accuracy of machining over the entire time of tool life.
4. *Metal cutting is a cold-working process.* The maximum temperature in the deformation zone normally does not exceed 200°C [29] although the chip leaving the tool rake face can be cherry-red because of high temperature developed due to its friction at the tool-chip interface. However, this high temperature does not affect chip deformation in the deformation zone. The high temperature generated in the region of the tool-chip interface does not affect the temperature in the deformation zone ahead of the tool because the chip velocity is much higher than that of heat conduction [29]. Although the energy spent in the deformation zone is higher than that at the tool-chip interface due to friction (see Appendix A), a significant difference in the mass in the bodies that dissipate these thermal energies causes the mentioned temperature difference, i.e., because the chip is of relatively small mass, it heats up much faster, requiring much less thermal energy to reach high temperatures.
5. *Cyclical nature.* Metal cutting is inherently a cyclic process. As such, a single chip fragment forms in each chip formation cycle. As a result, considered at the appropriate magnification, the chip structure is not uniform. Rather, it consists of chip fragments and connectors. The frequency of the chip formation process (Appendix A) primarily depends on the cutting speed and on the work material. The cutting feed and the depth of cut ( $> 1$  mm) have very small influence on this frequency.

### 1.4.3 Relevance to the Cutting Tool Geometry

The definition of the cutting process allows formulating the ultimate objective of cutting tool geometry which is the reduction of the energy required by the cutting system. This is because:

1. The physical resource of the cutting tool that includes the tool life is reverse proportional to this energy [29]. The smaller the energy required by the cutting system, the greater the tool life.
2. The level and the depth of the machining residual stress are directly proportional to this energy. The smaller the energy required by the cutting system, the lower the machining residual stresses.
3. The successful implementation of near dry machining (also know as MQL machining) requires the physically possible minimum of this energy.

There are a number of ways by which the cutting tool geometry can affect the energy required by the cutting system, the process outcomes and efficiency. Many of them are traditional although quite often not that obvious in terms of correlation between geometry parameters and process outcomes. They are listed and explained in the Preface.

The most important, however, is that the tool geometry directly affects the amount of plastic deformation in metal cutting. As discussed by the author earlier [78], this energy is the largest part of the energy required by the cutting system for its existence. This energy defines the cutting force, tool life, and other outcomes of the machining (Appendix A). It should be very clear that plastic deformation in metal cutting is a nuisance so that it should be reduced in order to increase the process efficiency. The rule of thumb here is: the less the plastic deformation, the better the cutting process.

The tool geometry defines to a large extent the triaxial state of stress in the deformation zone and the degree of triaxiality. This triaxiality in the body which undergoes plastic deformation affects the fracture strain, i.e., the extent of plastic deformation. One of the best parameters used to characterize the triaxiality of the state of stress in a deforming body is  $\Pi$ -factor [79] represented in the following form:

$$\Pi = \frac{3I_1(\sigma)}{2\sqrt{I_1^2(\sigma) - 3I_2^3(\sigma)}} \quad (1.16)$$

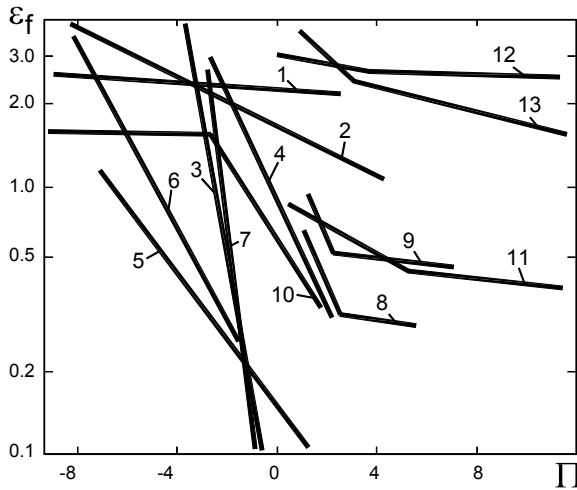
where  $I_1(\sigma)$  and  $I_2(\sigma)$  are the stress invariants which may be expressed in terms of principal stress  $\sigma_1$ ,  $\sigma_2$ , and  $\sigma_3$  as

$$I_1(\sigma) = \sigma_1 + \sigma_2 + \sigma_3 \quad (1.17)$$

$$I_2(\sigma) = -(\sigma_1\sigma_2 + \sigma_2\sigma_3 + \sigma_3\sigma_1) \quad (1.18)$$

Figure 1.21 shows the relationships between the fracture strain and of the state of stress represented by  $\Pi$ -factor. As seen, the degree of triaxiality has a great influence on the fracture strain. In the author's opinion, this is the major lead in the

optimization of the tool geometry, which can be thought of as having the objective function – the minimum fracture strain with the set of real-life constraints.



**Fig. 1.21.** Effect of  $\Pi$ -factor of the fracture strain: 1–niobium, 2–iron, 3–tungsten, 4–molybdenum, 5–beryllium, 6–magnesium, 7–zinc, 8–tin alloy, 9–brass, 10–brass, 11–tin bronze, 12–deformed lead, 13–cast lead (after Astakhov [14])

The list of the real-life constraints on the optimized tool geometry includes:

1. Dimensional and form accuracy of the parts produced. This constrain should be specified for each and every tool because the tool geometry defines the direction and magnitude of the cutting force and its components that, in turn, affect the deformations of the workpiece and its fixture, tool, tool holder, spindle and machine structure deformations.
2. Surface integrity of the machined surface in terms of its surface finish, machining residual stress, etc.
3. Properties of the tool materials. The optimized tool geometry should utilize the strong properties to the full extent while preventing the situation where the tool materials weaknesses can compromise tool performance and reliability.
4. Efficiency of machining. One should realize that the optimum cutting process does not necessarily mean the most efficient one as the cutting tool and machining process are part of the machining system.

The quantitative analysis of the influence of the tool geometry parameters on the cutting process and their correlations with the listed constraints is one of the objectives and thus an inherent part of this book.

## 1.5 Fundamental Laws of Metal Cutting

### 1.5.1 Optimal Cutting Temperature – Makarow’s Law

#### 1.5.1.1 Formulation

The First Metal-Cutting Law (Makarow’s law) formulated by Astakhov in the following form:

*For a given combination of the tool and work materials, there is the cutting temperature, referred to as the optimal cutting temperature  $\theta_{opt}$ , at which the combination of minimum tool wear rate, minimum stabilized cutting force, and highest quality of the machined surface, is achieved. This temperature is invariant to the way it has been achieved (whether the workpiece was cooled, pre-heated, etc).*

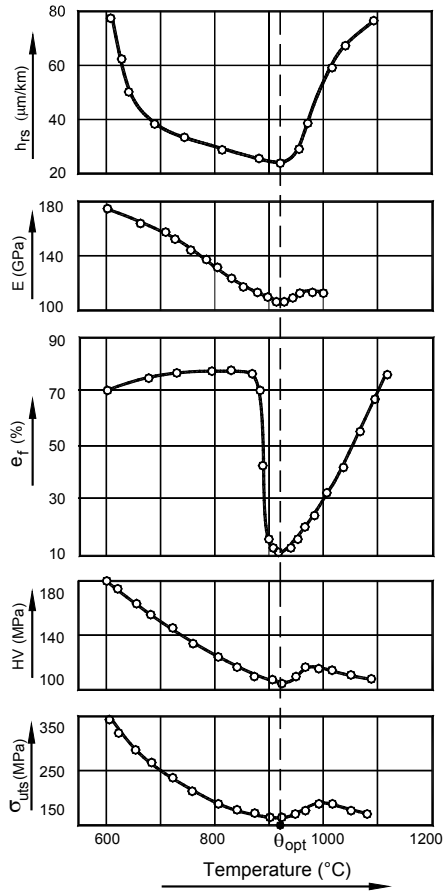
The Makarow’s law, established initially for longitudinal turning of various work materials, was then experimentally proven for various machining operations. The cutting temperature is determined as the average integral temperature on the tool-chip interface so that it can be measured by the tool-work thermocouple technique. Therefore, the optimum cutting temperature for a given combination “work material-tool material” should be established and used as the only criterion for the suitability of this particular tool material for this particular work material. This temperature is a physical property and thus does not depend on the intrinsic details of tool design and geometry as well as on the parameters of a particular test setup. The methodology of determination of the optimum cutting temperature is well discussed by the author earlier [29].

#### 1.5.1.2 Physical Background

To understand the technical and physical background of the optimal cutting temperature, one should understand what happens with the work material at this temperature. Figure 1.22 presents the answer to this question at the technical level. This figure shows what happens with the most relevant (to machining) mechanical characteristics of the work material when this material is brought to the temperature equal to the optimal cutting temperature. Particularly, the minima of the ultimate strength,  $\sigma_{UTS}$ , and elongation,  $e_f$ , (which represents the strain at fracture) result in the minimum work done in the fracture of the layer being removed [80]. The minimum microhardness,  $HV$ , assures the minimum of the normal stress at the tool-chip interface [29]. The minimum Young’s modulus assures the minimum work of elastic deformation while the minimum of wear rate  $h_{r-s}$  results in minimum tool flank wear [81].

To understand the discussed phenomena at the level of physical metallurgy, one should recognize that metal cutting is the purposeful fracture of the work material as defined by Astakhov [14]. The work spent in purposeful fracturing of the layer being removed, i.e., its fracture toughness, should be considered as the prime parameter in determining the cutting force and the energy spent in machining. Therefore, one should consider the mechanics of fracture [44] and the importance of the process temperature in this mechanics. Another important aspect discussed

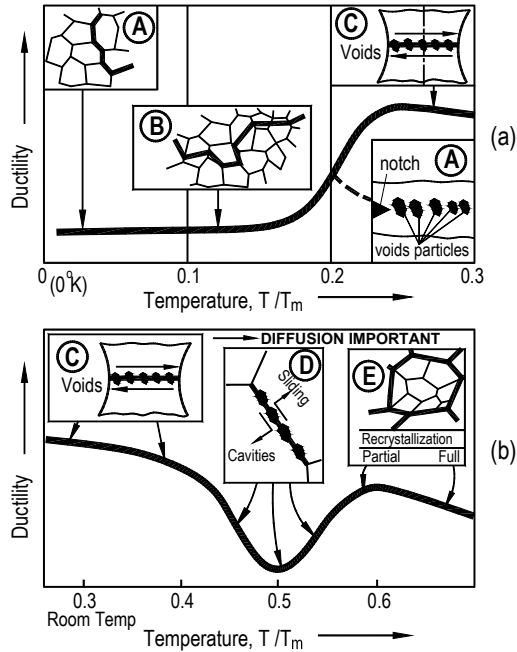
in the deformation law is that the lower the ductility of the work material, the longer the tool life.



**Fig. 1.22.** Temperature influence on the properties of pure iron (after Astakhov [29])

According to Atkins and Mai [44] and Komarovskiy and Astakhov [80], there is a marked increase in the strain at fracture and also in the work of fracture, at about 0.18–0.25 of the melting point ( $T_m$ ); similar changes occur in other measures of ductility such as Charpy values ( $CVN$ ) as shown in Fig. 1.23(a). It explains a number of “strange” results obtained by Zorev in his tests at low cutting speeds [32]. This phenomenon also explains the great size of the zone of plastic deformation observed at low cutting speeds and incorporated in the model discussed by Astakhov [14]. The known built-up edge is the result of the discussed high plasticity region in front of the tool rake face within the contact length. Exceptions are certain *fcc* metals and alloys (Al, Cu, Ni, Pb) that do not normally cleave. As such, there is no transition in values, which gradually rises with temperature.





**Fig. 1.23.** Changes in ductility and typical associated mechanisms of fracture for bcc materials: (a) at temperatures  $<0.3T_m$ : (A) low-temperature intergranular cracks, (B) twinning or slip leading to cleavage, (C) shear fracture at particles, (D) low energy shear at particles, (b) at temperatures  $>0.3T_m$ : (C) shear at particles, (D) cavities along grain faces, (E) recrystallization suppresses cavitation (after Astakhov [29])

The increase in ductility over the ‘transition temperature range’ is followed by a gradual drop beyond approximately  $0.35T_m$ . It is believed that it happens due to the continuing fall in the Peierls-Nabarro stress which opposes dislocation movement, coupled with the emergence of cross-slip (as opposed to Frank-Read sources) as a dislocation generator as the temperature is raised [44]. In the author’s opinion the cause is in dilations-compressions reactions as explained in [80].

At high temperatures, grain boundaries become significant. Below approximately  $0.45T_m$  grain boundaries act principally as barriers, inhibiting cleavage and causing dislocation pile-ups. At higher temperatures, the regions of intense deformation, which are contained within the grains at lower temperatures, now shift to the grain boundaries themselves. Voids are nucleated and cracks then develop on the grain boundaries. Shear stresses on the boundaries cause relative sliding of the grains, and voids are reduced in region of stress concentrations (see Fig. 1.23b – position D). Therefore, around this temperature region can be referred as *the ductility valley*. Experiments showed [82] that the reduction of plasticity may reach twofold and even more for high alloys. The presence of this valley is the physical cause of the existence of the optimal cutting temperature.

At temperatures  $(0.5-0.6)T_m$ , recovery and recrystallization processes set in (recovery relates to a re-distribution of dislocation sources so that dislocation movement is easier, and in recrystallization, the energy of dislocations generated

during prior deformation is used to nucleate and grow new grains, thus effecting an annealed structures over a long time). The net effect is increased ductility causing a bump shown in the Fig. 1.23.

### 1.5.1.3 Consequences

The following consequences of the first metal cutting law are of great importance:

1. For cutting tools with various combinations of cutting geometry parameters – rake, flank, inclination, tool cutting edge angles, nose and cutting edge radii, etc. – the optimal cutting temperature corresponds to the points of minima on the curves representing the dependence of tool wear rate on the cutting speed while the optimal cutting speed corresponding to each and every particular case varies over a wide range.
2. The minimum tool wear rate is achieved at the same optimal temperature in dry cutting and in cutting with various cutting fluids (media) using various methods of cutting fluid supply.
3. The optimal cutting temperature is the same for various combinations of the temperature of the pre-heated workpiece and uncut chip thicknesses.
4. Variation of the workpiece diameter in turning and boring leads to the significant change in the optimal cutting speed (i.e., the cutting speed corresponding to the minimum tool wear rate). The reason for this is discussed by the author in [29]. The optimal temperature, however, remains the same.
5. If the structure and/or hardness of the work material are changed, the optimal cutting speed is changed correspondingly, but the optimal temperature remains the same.

It was also shown that machining at optimal cutting temperature results not only in the minimum tool wear rate but also leads to obtaining the minimum cutting force and smallest roughness of the machined surface [29].

## 1.5.2 Deformation Law

### 1.5.2.1 Formulation

The second law of metal cutting named as the deformation law is formulated by the author as

*Plastic deformation of the layer being removed in its transformation into the chip is the greatest nuisance in metal cutting, i.e., while it is needed to accomplish the process, it does not add any value to the finished part. Therefore, being by far the greatest part of the total energy required by the cutting system, this energy must be considered as a waste which should be minimized to achieve higher process efficiency.*

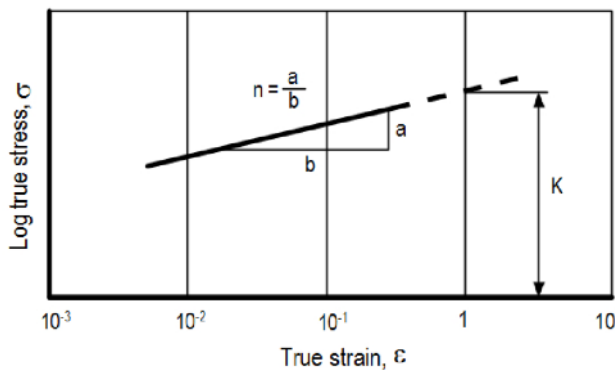
The examples of energy partition in the cutting system presented in Appendix A clearly show that the energy of plastic deformation is the greatest in machining of a steel and aluminum alloy. The greater the energy of plastic deformation, the lower the tool life, quality of the machined surface, and process efficiency. Therefore, the prime objective of the cutting process design is to reduce this energy to its lowest possible minimum by the proper selection of the tool geometry, tool material, machining regime, MWF, and other design and process parameters. To accomplish this clear objective, i.e., to make the introduced law of practical significance, a reliable measure of this energy should be readily available to be used at various levels from a research laboratory to the shop floor.

*1.5.2.2 Characterization of Plastic Deformation in Materials Testing*

Two basic mechanical properties are used to characterise the strength of a material – the true fracture stress and the true fracture strain. The loading history to arrive at these characteristic is known as the flow curve. The flow curve for many metals in the region of plastic deformation can be expressed by the simple power curve relation [16, 83]

$$\sigma = K \epsilon^n \tag{1.19}$$

where  $n$  is the strain-hardening exponent, and  $K$  is the strength coefficient. A log-log plot of true stress and true strain up to the strain at fracture will result in a straight line if Eq. 1.19 that allows determining of  $n$  and  $K$  in the manner shown in Fig. 1.24. As can be seen, the linear slope is  $n$ , and  $K$  is the true stress at  $\epsilon = 1$ . As shown in Fig. 1.25, the strain-hardening exponent may have values from  $n = 0$  (perfectly plastic material) to  $n = 1$  (perfectly elastic material). For common work materials,  $n$  has values between 0.10 and 0.50 as indicated in Table 1.1.



**Fig. 1.24.** Log-log plot of true stress-true strain curve to determine strain-hardening exponent  $n$  and the strength coefficient  $K$

Some important deductions relevant to metal cutting directly follow from the above consideration:

1. The strength of a material is defined by the stress at fracture while the energy required to fracture a unit volume of a material is determined by the both stress and strain at fracture and is represented by area under the stress–strain curve.
2. The flow curve of a given material reflects the manner in which the material deforms, i.e., in which the strain hardening of the material takes place.
3. The flow curve characteristics  $n$  and  $K$  are very sensitive to even small changes in the material composition, structure, inclusions, metallurgical characteristics, and other parameters. For example, the data for 0.6% carbon steel show that changing the tempering temperature changes these characteristics significantly.
4. A simple standard tensile test can be used to obtain  $n$  and  $K$  for most work materials.

### 1.5.2.3 Known Characterisations of Plastic Deformation in Metal Cutting

There are two characteristics of plastic deformation in metal cutting, namely, the chip compression ratio (CCR) and shear strain.

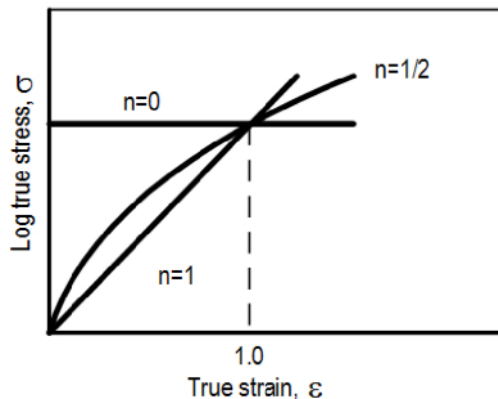


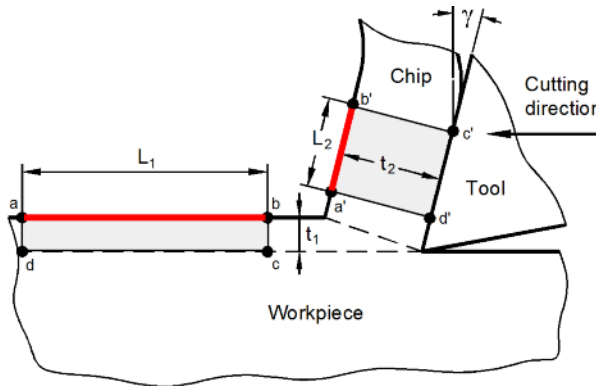
Fig. 1.25. Various forms of power curve  $\sigma = \epsilon^n$

Table 1.1. Values for  $n$  and  $K$  for metals at room temperature [83]

Materials	Conditions	$n$	$K$ (MPa)
0.05% Carbon steel	Annealed	0.26	530
SAE 4340 Steel	Annealed	0.15	641
0.6% Carbon steel	Quenched and tempered at 540°C	0.10	1572
0.6% Carbon steel	Quenched and tempered at 705°C	0.19	1227
Copper	Annealed	0.54	320
70/30 Brass	Annealed	0.49	896

Historically, CCR was introduced in the earlier studies on metal cutting as a measure of plastic deformation of the work material in its transformation into the chip [14, 32]. A model of chip deformation in the simplest case of cutting (orthogonal cutting) is shown in Fig. 1.26. A flat section  $abcd$  having length  $L_1$  and thickness  $t_1$  is distinguished in the layer to be removed by the cutting tool. Once the distinguished section is deformed on its transformation into the chip, the section  $abcd$  transforms into section  $a'b'c'd'$ . In this transformation, called plastic deformation, the area of the initial section does not change due to conservation of work material volume. However, the dimensions of its sides do change. Length  $L_1$  of side  $ab$  becomes length  $L_2$  of side  $a'b'$  while thickness  $t_1$  (uncut chip thickness) becomes chip thickness  $t_2$ . The chip compression ratio (CCR) represents such a transformation due to plastic deformation as

$$\zeta = \frac{L_1}{L_2} = \frac{t_2}{t_1} \quad (1.20)$$



**Fig. 1.26.** Simple model of chip plastic deformation in orthogonal cutting

Although this parameter was widely used in metal cutting tests of the past [32], it was always considered as a secondary parameter to provide only qualitative support to certain conclusions. Since the real physical meaning of this parameter has never been revealed, it was gradually abandoned in metal cutting studies because nobody could explain the results obtained. For example, when one obtained  $\zeta = 2.5$  in machining of a steel while in machining of a copper alloy  $\zeta = 4.5$  at the same cutting speed, he should conclude that the plastic deformation and thus energy required for this deformation in the latter case is much greater than that in the former. However, the cutting force in machining of the steel is much greater than that in machining of the copper alloy. As the total energy required by the cutting system can be thought of as the product of the cutting force and the cutting speed, then unexplained contradiction between the values of the cutting force and chip compression ratio is obvious. That is why CCR is practically abandoned in modern metal cutting studies. For example, although Shaw in his book [9]

dedicated a full chapter to the analysis of plastic deformation in metal cutting, this parameter is not even mentioned. The same can be said about books by Trent and Trent and Wright [49], Oxley [51], and Gorczyca [1]; Altintas [84] just mentioned its definition in the consideration of the single shear plane model; Childs et.al. [75] mentioned this parameter as related to the friction coefficient at the tool-chip interface. Not a single modern study on metal cutting correlates this parameter with the amount of plastic deformation in metal cutting.

The shear strain is another characteristic of plastic deformation in metal cutting. It calculates as

$$\varepsilon = \frac{\cos \gamma}{\cos(\varphi - \gamma) \sin \varphi} = \frac{1 - 2\zeta \sin \gamma + \zeta^2}{\zeta \cos \gamma} \quad (1.21)$$

Although Eq. 1.21 is used in practically all books on metal cutting, there are some obvious problems with these equations in terms of their physical meaning and experimental confirmation [29]. If one calculates shear strain using Eq. 1.21 (it can be easily accomplished by measuring the actual chip compression ratio) and then compares the result with the shear strain at fracture obtained in standard materials tests (tensile or compression), one easily finds that the calculated shear strain is much greater than that obtained in the standard materials tests. Moreover, when the chip compression ratio  $\zeta = 1$ , i.e., the uncut chip thickness is equal to the chip thickness so no plastic deformation occurs in metal cutting [66], the shear strain, calculated by Eq. 1.21 remains very significant, with no apparent reason for that. For example, when  $\zeta = 1$ , the rake angle  $\gamma = -10^\circ$ , Eq. 1.21 yields  $\varepsilon = 2.38$ ; when  $\zeta = 1$ , the rake angle  $\gamma = 0^\circ$  then  $\varepsilon = 2$ ; when  $\zeta = 1$ ,  $\gamma = +10^\circ$  then  $\varepsilon = 1.68$ . As shown by the author earlier, this severe physical contradiction is caused by the incorrect velocity diagram used to derive Eq. 1.21.

The foregoing analysis suggests that, apparently, there is no reliable measure of plastic deformation in metal cutting that can be used in tool and process designs as suggested earlier.

#### 1.5.2.4 Proper Characterization of Plastic Deformation in Metal Cutting

The chip compression ratio (CCR) is the only post-process parameter of plastic deformation that objectively reflects the reality. Therefore, to make this parameter useful, its physical meaning and correlation with work material mechanical properties discussed in Sect. 1.5.2.2 should be revealed.

Consider an infinitesimal element in the form of a parallelepiped with its faces oriented parallel to the coordinate planes as shown in Fig. 1.27. When body and inertia forces are insignificant then the following three differential equations of force (stress) equilibrium are obtained [14, 85]:

$$\frac{\partial \sigma_x}{\partial x} + \frac{\partial \tau_{xy}}{\partial y} + \frac{\partial \tau_{xz}}{\partial z} = 0 \quad (1.22)$$

$$\frac{\partial \tau_{xy}}{\partial x} + \frac{\partial \sigma_y}{\partial y} + \frac{\partial \tau_{zy}}{\partial z} = 0 \tag{1.23}$$

$$\frac{\partial \tau_{xz}}{\partial x} + \frac{\partial \tau_{yz}}{\partial y} + \frac{\partial \sigma_z}{\partial z} = 0 \tag{1.24}$$

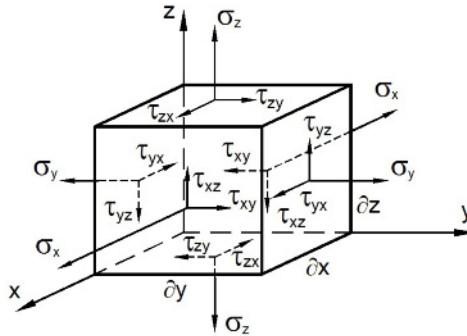


Fig. 1.27. Stresses acting on elemental free body

When a stress field applied to a body and, as a result, the relative position of its parts is changed, then the body is said to be deformed or strained. A deformed state in a point can be represented by the strain components if the projections  $u_x$ ,  $u_y$ , and  $u_z$  of the displacement of this point into corresponding coordinate planes are known:

$$e_x = \frac{\partial u_x}{\partial x}, e_y = \frac{\partial u_y}{\partial y}, e_z = \frac{\partial u_z}{\partial z} \tag{1.25}$$

$$\gamma_{xy} = \frac{\partial u_x}{\partial y} + \frac{\partial u_y}{\partial x}, \gamma_{yz} = \frac{\partial u_y}{\partial z} + \frac{\partial u_z}{\partial y}, \gamma_{zx} = \frac{\partial u_z}{\partial x} + \frac{\partial u_x}{\partial z} \tag{1.26}$$

where  $e_x$ ,  $e_y$ , and  $e_z$  are the direct strains,  $\gamma_{xy}$ ,  $\gamma_{yz}$ , and  $\gamma_{zx}$  are the engineering shear strains.

Using the generalized Hooke’s law, one can write the following relationship between strains and stresses [85]:

$$e_x = \frac{1}{E} [\sigma_x - \nu_s (\sigma_y + \sigma_z)] \tag{1.27}$$

$$e_y = \frac{1}{E} [\sigma_y - \nu_s (\sigma_z + \sigma_x)] \tag{1.28}$$

$$e_z = \frac{1}{E} [\sigma_z - \nu_s (\sigma_x + \sigma_y)] \tag{1.29}$$

$$e_{xy} = \frac{2}{E}(1 + \nu_s)\tau_{xy} \quad (1.30)$$

$$e_{yz} = \frac{2}{E}(1 + \nu_s)\tau_{yz} \quad (1.31)$$

$$e_{zx} = \frac{2}{E}(1 + \nu_s)\tau_{zx} \quad (1.32)$$

where  $E$  is the modulus of elasticity and  $\nu_s$  is the Poisson's ratio.

The imbalanced external forces applied to a body cause its deformation and thus lead to the displacement of its points until the equilibrium is established. As such, a certain amount of energy is absorbed. This energy depends on the work done in displacement of all points of the body. Such work can be calculated by integrating the work per unit volume. The work per unit volume done in the displacement of each point of the body is calculated as the product of the generalized force acting on a point and the change of the generalized displacement of this point caused by this force.

The Von-Mises' stress [85]

$$\sigma_i = \frac{1}{\sqrt{2}} \left[ (\sigma_x - \sigma_y)^2 + (\sigma_y - \sigma_z)^2 + (\sigma_z - \sigma_x)^2 + 6(\tau_{xy}^2 + \tau_{yz}^2 + \tau_{zx}^2) \right]^{1/2} \quad (1.33)$$

was considered as the generalized force and the equivalent strain

$$e_i = \frac{\sqrt{2}}{3} \left[ (e_x - e_y)^2 + (e_y - e_z)^2 + (e_z - e_x)^2 + 6(e_{xy}^2 + e_{yz}^2 + e_{zx}^2) \right]^{1/2} \quad (1.34)$$

can be considered as the generalized displacement.

Because the elementary work is  $dA = \sigma_i e_i$ , the total work done over a volume  $V$  then calculates as [14]

$$A = \int_V \sigma_i e_i dV \quad (1.35)$$

In the further derivations, the distribution of the mechanical energy over the chip cross section is assumed to be uniform, i.e., strains in Eqs. 1.33 – (1.35) have homogeneous distribution.

To correlate CCR with the amount of plastic deformation in metal cutting, the xyz coordinate system is set so that the y-axis is directed along the chip length,  $L_I$  (Fig. 1.26), the x-axis is directed along the chip width,  $b$ , and the z-axis is directed along its thickness,  $t_2$ . As such, the following expressions for the components of the true strain along the introduced coordinate axes can be written accounting for the definition of CCR [14]:



$$\varepsilon_z = \ln \zeta_t, \quad \varepsilon_x = \ln \zeta_b, \quad \varepsilon_y = -\ln \zeta_L \quad (1.36)$$

As shown by Astakhov [14], in orthogonal cutting, the direction of the principal stress coincides with the introduced coordinate system. Then, Eq. 1.34 could be rewritten accounting for Eq. 1.36 as

$$\varepsilon_i = \frac{\sqrt{2}}{3} \left[ (-\ln \zeta_L - \ln \zeta_t)^2 + (\ln \zeta_t - \ln \zeta_b)^2 + (\ln \zeta_b + \ln \zeta_L)^2 \right]^{1/2} \quad (1.37)$$

As shown in [14], if the chip parameters are properly measured in the orthogonal cutting test, then  $\zeta_b = 1$  as the chip width is equal to the width of cut,  $\zeta_t = \zeta_L = \zeta$ ; thus the plane strain condition is the case in such a process. Therefore

$$\varepsilon_i = 1.15 \ln \zeta \quad (1.38)$$

In the considered coordinate system, stress components  $\sigma_z$  and  $\sigma_y$  do not depend on the x coordinate (measured along chip width) and the  $\sigma_z$  component is determined as [83]

$$\sigma_x = 0.5(\sigma_z + \sigma_y) \quad (1.39)$$

Substituting these results in Eq. 1.33, one can obtain

$$\sigma_i = \frac{1}{\sqrt{2}} \left\{ \left[ \sigma_z - 0.5(\sigma_z + \sigma_y) \right]^2 + \left[ 0.5(\sigma_z + \sigma_y) - \sigma_y \right]^2 + (\sigma_y - \sigma_z)^2 \right\}^{1/2} \quad (1.40)$$

or after simplification

$$\sigma_i = 0.87(\sigma_z - \sigma_y) \quad (1.41)$$

Substituting representation of the flow curve given by Eq. 1.19 in Eq. 1.41, one obtains

$$\begin{aligned} \sigma_i &= 0.87(K\varepsilon_z^n - K\varepsilon_y^n) = 0.87K(\varepsilon_z^n - \varepsilon_y^n) = \\ &0.87K \left[ (\ln \zeta_t)^n - (\ln \zeta_L)^n \right] = 0.87K2(\ln \zeta)^n = 1.74K(\ln \zeta)^n \end{aligned} \quad (1.42)$$

Because it was assumed that the chip has uniform deformation, the elementary work spent over plastic deformation of a unit volume of the work material is calculated as

$$A_u = \int_0^{\varepsilon_f} \sigma d\varepsilon = \frac{K(1.15 \ln \zeta)^{n+1}}{n+1} \quad (1.43)$$

The result obtained is of great significance to the experimental studies in metal cutting because it correlates in a simple and physically-grounded manner the work of plastic deformation done in cutting with a measurable, post-process characteristic of the cutting process such as CCR. Knowing the elementary work, the total work done by the external force applied to the tool is then calculated as

$$A = A_u v f d_w \tau_{ct} \quad (1.44)$$

where  $\tau_{ct}$  is time of cutting.

The power spent on the plastic deformation of the layer being removed,  $P_{pd}$ , can be calculated knowing the chip compression ratio and parameters of the flow curve of the work material as

$$P_{pd} = \frac{K(1.15 \ln \zeta)^{n+1}}{n+1} v A_w \quad (1.45)$$

A series of tests were carried out to resolve the above-mentioned contradiction between CCR and the cutting force in the machining of steel and copper. All the tests were conducted using the same cutting feed  $f = 0.07 \text{ mm/rev}$  and the depth of cut  $d_w = 1 \text{ mm}$ . Three different types of the work material listed in Table 1.2 were used in the tests. For each work material, the influence of the cutting speed on CCR was determined and the elementary work spent over plastic deformation of the work material was calculated using Eq. 1.43.

The test results are shown in Fig. 1.28. As seen, although CCR is the greatest in the machining of copper and lowest in the machining of steel, the elementary work is the greatest for steel. In other words, the energy per unit volume spent on plastic deformation in the machining of steel is the greatest, which results in a much higher cutting force, amount of heat generated, and in more significant tool wear. This conclusion is supported by multiple facts known from the everyday practice of machining.

The accuracy of the estimation of the work done in plastic deformation can be improved if, instead of just generic approximation for the flow curve given by Eq. 1.19 used in Eq. 1.42, a more comprehensive approximation of material flow curve that includes the work material specific parameters is used.

**Table 1.2** Work materials and flow curve constants used in the tests

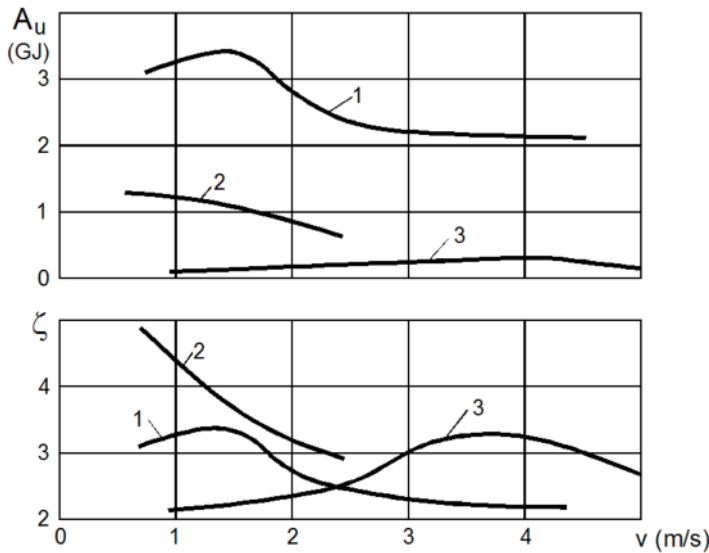
Material	K (GPa)	n
AISI steel E52100, HB280 (0.981.10%C, 1.45%Cr, 0.35%Mn)	1.34	0.25
Copper (99.7%)	0.40	0.24
Aluminum 1050-0, HB 21	0.14	0.27

1.5.2.5 Significance of CCR in Metal Cutting

The proposed method for determination of the work of plastic deformation in metal cutting gives new meaning to CCR. The chip compression ratio (or its reciprocal, the chip ratio) is the most reliable, physically grounded yet simple to determine measure of plastic deformation in metal cutting. In the author’s opinion, anyone involved in the field should clearly understand its meaning, applications, and methods of its determinations because the value of this characteristic in metal cutting and cutting tool studies, development, testing, and applications cannot be overstated.

Knowing CCR, one can directly determine:

1. Power spent on plastic deformation of the layer being removed (see Appendix A) which is the largest portion of the power required by the cutting system and which is the major contributor to the cutting force
2. The so-called natural length of tool-chip interface using Eqs. 3.40 and 3.41 (Chap. 3)
3. The chip velocity relative to the cutting tool as the cutting speed divided by CCR



**Fig. 1.28.** Influence of the cutting speed on CCR and the work done in plastic deformation: 1 – AISI steel E52100, 2 – Copper, 3 – Aluminum 1050-0 (after V.P. Astakhov and Shvets [66])

Knowing these parameters, CCR together with parameters of the machining system and properties of the materials involved can be used to determine:

1. The cutting force (see Appendix A)

2. Tribological conditions at the tool-chip interface used in the design of chipbreakers, selection of tool materials and coatings as well as the selection of optimal cutting regime [29]
3. The maximum temperature and temperature distribution over the tool-chip interface [14, 29]

Because CCR is very sensitive to any change in tool design, geometry, material, coating, MWF, etc, it is an invaluable parameter to be used in tool testing and tool troubleshooting. Tool tests including machinability test can be significantly reduced to measuring CCR and determining the optimum tool parameters. By measuring CCR in the shop floor, the root cause of many tooling related problems can easily be determined with no special and expensive equipment and apparatuses involved.

The great advantage of CCR is simplicity of its experimental determination. Figure 1.29 shows its definition for turning. In *any* machining operation the determination of CCR includes two important steps:

- Proper determination of the uncut (undeformed) chip thickness. Chapter 3, Sect. 3.3.2 explains determination of this parameter in turning and Chap. 4, Sect. 4.9.1.
- Measurement of the chip thickness.

Simple methods for CCR determination are presented by in earlier works [29, 66].

#### *1.5.2.6 CCR and Properties of the Work Material*

The properties and structure of the work material strongly and directly affect tool wear, quality of the machined surface, and thus the cost per unit of the machined part. Unfortunately this simple and self-obvious fact did not prevent sufficient attention of researchers and practitioners in the field of metal machining. The properties of the tool materials and coatings are subjects of a great number of theoretical and experimental studies from shop floor level (for example [86, 87]) to high level applied physics (for example [88–90]), while among the properties and conditions of the work material in many studies in the field are only mentioned generic (not actual) chemical composition (or AISI (SAE, ASM) designation as AISI steel 1045, for example), hardness and metallurgical state in material dealer’s language (for example, as rolled, annealed, hot rolled, cold rolled, extruded, etc.). In the author’s experience, these are not sufficient even to the first approximation to characterize the machinability of the work material. As a result, a great scatter in experimental data is a nuisance in experimental metal cutting.

When it comes to industry, one expects that high costs of poor machinability, great scatter in tool life (that particularly hurts production on automated lines and manufacturing cells with no or minimum human attendance), and great scrap rate prevented at least some attention from practical manufacturing engineers to the properties of the work material. Unfortunately, this is not the case even at the most advanced industries and manufacturing facilities. This is particularly true in the automotive industry where the losses due to misunderstanding and/or underestimation of the discussed issue result in losses of tens of millions of dollars.

In the author's experience the hidden losses are even greater than that, as a number of premature failures of powertrain components (first of all, transmissions) are due to the burr and chips left after machining.

Manufacturing has been reluctant to hold materials suppliers to a narrow range of chemical composition and hardness variation in the materials supplied. The variations in the chemical composition and hardness, amount of inclusions and porosity, grain size and grain boundary conditions including microcracks, make it very difficult to specify the optimum tool geometry, suitable grade of the tool material, and optimal machining regime.

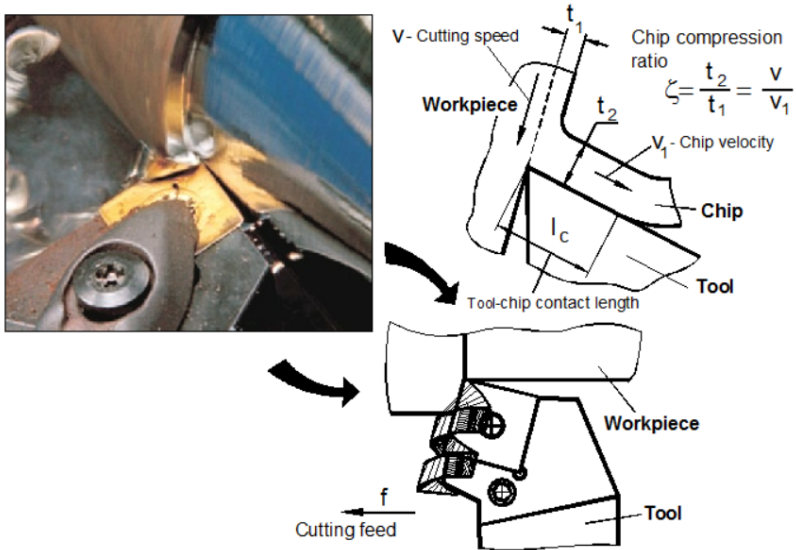


Fig. 1.29. CCR in turning

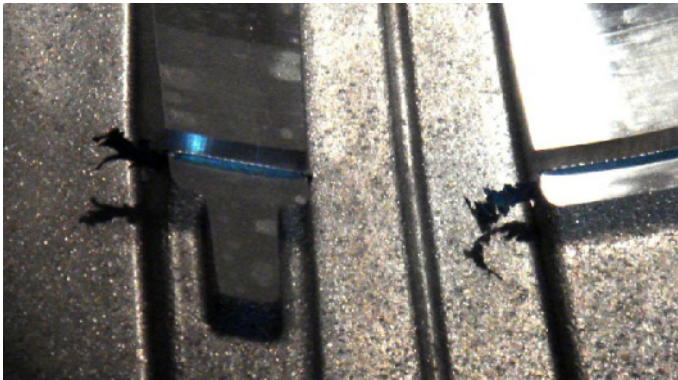
Moreover, it is next to impossible to implement the results of many test and optimization studies under these conditions as the modeled and experimentally obtained data cannot be relevant for the whole allowable range of properties of the work materials. Some common causes for poor material specification in manufacturing and research practices are as follows:

- Prime cause is the lack of knowledge and readily available data on the correlation of the properties (both mechanical and metallurgical) of work materials and their machinability
- False perception that tighter specification and control of metallurgical properties would always result in higher cost of blanks (castings, forgings, etc.), and materials. There are two major misunderstandings: (a) often, the tightened specification reduces the usage of some very expensive materials such as for example in gray cast iron; requirements to increase the hardness of gray cast iron lead to reduced annealing time that, in turn, reduces the energy (natural gas or electricity) spent, (b) the automotive industry rapidly shifts from the consideration the cost of individual components (blanks,

tool, parts, etc.) to that of the cost per unit including reliability of the processes and the final products. In such a context, even if the cost of blanks or raw materials grows, the overall saving on the much higher tool and process costs, process stability, chip disposal, and better quality of the machined part and assembly structures would overlap this increase cost a hundred times.

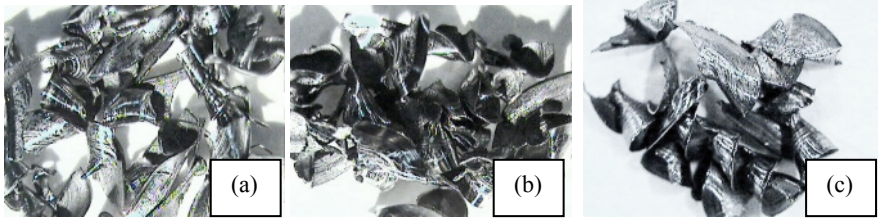
- Many automotive companies developed standards on material specification more than 30 years ago so these standards do not reflect the advances made in materials production and control. To change any particular specification is a cumbersome process that requires insistence and consumes a lot of time. Moreover, since the automotive industry outsourced the tooling management, this originator – the tooling application specialist – is an outsider that makes this task next to impossible.

To exemplify these statements, consider a few common flaws due to variation of properties of the work material. Figure 1.30 shows tearing in slot boring due to excessive ductility of the work material. Figure 1.31 shows the variation in chip shape with variation of the properties of the work material within the allowable range (drilling the turbine shaft discussed in Chap. 4, Fig. 4.4). Figure 1.32 shows that the exit burr in drilling does not occur (Fig. 1.32a) when the hardness of the work material is in the middle of the allowable range while an acceptable burr occurs (Fig. 1.32b) when this hardness is at the low limit of this range (drilling the turbine shaft, discussed in Chap. 4, Fig. 4.4).

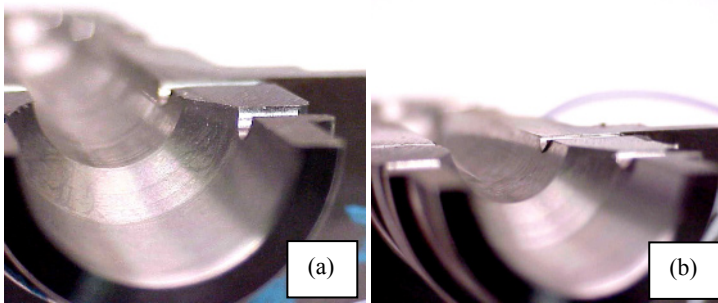


**Fig. 1.30.** Tearing in slot boring

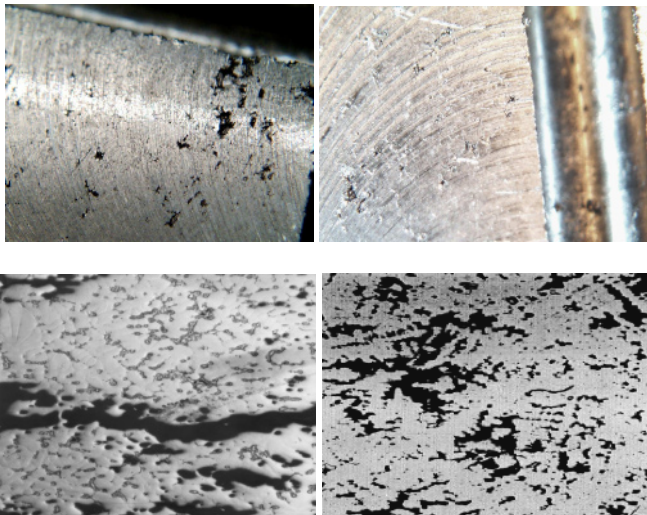
A common cause of tool poor performance in terms of achieving the required parameters of surface finish and diametric accuracy is porosity which normally occurs in castings. Figure 1.33 shows various appearances of porosity at different magnifications. Often, the pores can be filled out by silicon clusters which are highly abrasive that lowers tool life in machining. When pores filled with silicon clusters reach a certain size, they are considered as inclusions. Figure 1.34 shows what happens with a drill when it drills through such an inclusion. Normally, the part is not sectioned so that the drill is blamed for the failure.



**Fig. 1.31.** Variation in the shape of the chip with the variation of the properties of the work material: (a) soft at the low limit of hardness, (b) in the middle of the allowable hardness range, (c) hard, at the upper limit of hardness

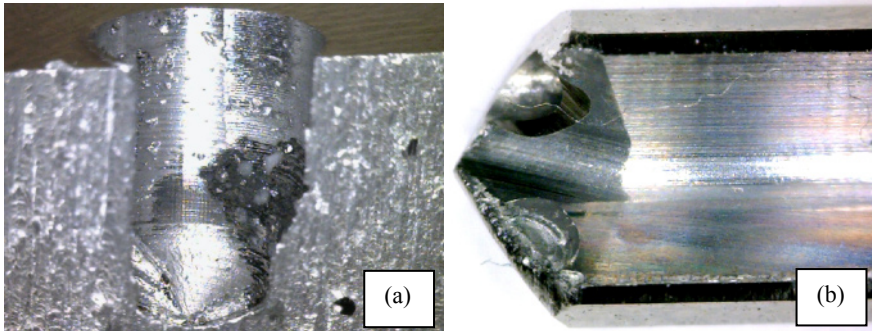


**Fig. 1.32.** Exit burr formation depends on the hardness of the work material



**Fig. 1.33.** Appearance of porosity in die casting aluminum alloys used in the automotive industry

In the author’s opinion, the simplest and most reliable way to deal with the problem of variation of properties of the work materials in terms of their influence on machinability is to establish reference database of CCR for critical machining operations. As such, the ‘normal’ chip appearance should be a part of this database (see Fig. 1.35). When machinability problem occurs, the actual CCR should be measured and the chip should be collected. These two should then be compared with the reference data to find which components of the machining system are responsible for the problem.

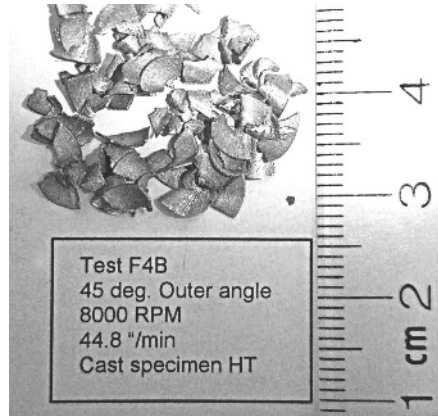


**Fig. 1.34.** (a) Hard inclusion in die casting and (b) worn drill

If the work material properties variation is found to be responsible for the problem then the machining regime is adjusted to bring CCR to the reference level that assures similarity of deformation processes between the reference work material and that in current use. Once tuned up and optimized, the production line or manufacturing cell can run in the intended automated regime with the intended efficiency.

To determine actual CCR, the parameters of the flow curve of the work material should be known. They can be obtained using a simple tensile test on a simple tensile machine or even computerized MTS are widely available in many modern manufacturing facilities. When such a machine is not available, a simple test can be carried out on any simple press using a pair of flat dies which can be used to obtain parameters of the flow curve. This very simple tooling may be accommodated in production equipment in order to obtain accurate results concerning the stress-strain relationship [91].





**Fig. 1.35.** Example of reference chip appearance

## References

- [1] Gorczyca FY (1987) Application of metal cutting theory. Industrial Press, London
- [2] DeGarmo EP, Black JT, Kohser RA (2007) Materials and processes in manufacturing. 10th Ed., Wiley, New York
- [3] Shaw MC (2004) Metal cutting principles. 2nd Edition, University Press, Oxford
- [4] *AdvantEdge 4.6*. (2004) Available from: <http://www.thirdwavesys.com/>
- [5] Kalpakjian S, Schmid SR (2001) Manufacturing engineering and technology. 4th ed, Prentice–Hall, New Jersey
- [6] Shaw MC (1984) Metal cutting principles. University Press, Oxford
- [7] Stephenson DA, Agapiou JS (1996) Metal cutting theory and practice. Marcel Dekker, New York
- [8] Boothroyd G, Knight WA (2006) Fundamentals of machining and machine tools, Third ed. CRC, Boca Raton
- [9] Time I (1870) Resistance of metals and wood to cutting (in Russian). Dermacow, St.Petersburg, Russia
- [10] Zvorykin KA. (1896) On the force and energy needed to separate the chip from the workpiece (in Russian). *Tekhnicheskii Sbornik i Vestnic Promyslinosty*, 123: 57–96
- [11] Merchant ME (1945) Mechanics of the metal cutting process. I. Orthogonal cutting and a type 2 chip. *J. of App. Phys.* 16: 267–275
- [12] Ernst H, Merchant ME (1941) Chip formation, friction and high quality machined surfaces. *Surface Treatment of Metals*, ASM 29: 299–378
- [13] Astakhov VP (1999) A treatise on material characterization in the metal cutting process. Part 1: A novel approach and experimental verification. *J. Mat. Proc. Tech* 96(1–3): 22–33
- [14] Astakhov, V.P. (1998/1999) Metal cutting mechanics. CRC, Boca Raton
- [15] Vidosic JP (1964) Metal machining and forming technology. Roland Press, New York
- [16] Dieter G (1976) Mechanical metallurgy. 2 ed. McGraw–Hill, New York
- [17] Reuleaux F (1900) Über den taylor whiteschen werkzeugstahl verein sur berforderung des gewerbeleissen in preussen. *Sitzungsberichte* 79(1): 179–220
- [18] (1924) Report of the present status and future problems in the art of cutting and forming metals. ASME Committee Report. *Mechanical Engineering* 46: 20–30

- [19] Mallock A (1881–1882) The action of cutting tools. Proc. of the Royal Soc. of London 33:127
- [20] Kick F (1901) Zur folge der wirkungsweise des taylor–white and der bohler–rapid–stahles. Baumaterialkunde 6: 227
- [21] Byers JP (2006) Metalworking fluids, CRC, Boca Raton
- [22] Finnie I (1956) Review of the metal–cutting analysis of the past hundred years. Mech. Engr. 78:715–721
- [23] Hill R (1950) The mathematical theory of plasticity, University Press, London
- [24] Hill R (1954) The mechanism of machining: a new approach. J. of the Mech. and Phys. of Solids 3:47–53
- [25] Astakhov VP (1999) A treatise on material characterization in the metal cutting process. Part 2: cutting as the fracture of workpiece material. J. Mat. Proc. Tech. 96(1–3):34–41
- [26] Astakhov VP (2005) On the inadequacy of the single-shear plane model of chip formation. Int. J. Mech. Science 47:1649–1672
- [27] Merchant ME (1944) Basic mechanics of metal cutting process. J. of App. Mech. 11: A168–A175
- [28] Merchant ME (1945) Mechanics of the metal cutting process. II. Plasticity conditions in orthogonal cutting. J. of App Physics 16:318–324
- [29] Astakhov VP (2006) Tribology of metal cutting. Elsevier, London
- [30] American National Standard "Tool life testing with single-point turning tools" *ANSI/ASME B94.55M–1985*. 1985, ASME: New York
- [31] (1993) *Tool-life testing with single-point turning tools*. ISO Standard 3685
- [32] Zorev NN (1966) Metal cutting mechanics. Pergamon Press, Oxford
- [33] Piispanen V (1937) Lastunmuodostumisen teoriaa. Teknillinen Aikakauslehti 27: 315–322
- [34] Carroll JT, Strenkowski JS (1988) Finite element models of orthogonal cutting with application to single point diamond turning. Int. J. of Mech. Sciences 30:899–920
- [35] Komvopoulos K, Erpenbeck SA (1991) Finite element modeling of orthogonal metal cutting. ASME J. of Eng. for Ind. 113(3):253–267
- [36] Zhang B, Bagchi A (1994) Finite element simulation of chip formation and comparison with machining experiment. ASME J. of Eng. for Ind. 116(3): 289–297
- [37] Shih AJ (1995) Finite element simulation of orthogonal metal cutting. ASME J. of Eng. for Ind. 117(1):84–93
- [38] Hashemi J, Tseng, AA, Chou PC (1994) Finite element modeling of segmental chip formation in high-speed orthogonal cutting. J. of Materials Engineering and Performance 3(5):712–721
- [39] Lin, ZC, Lin, SY (1992) A coupled finite element model of thermo-elastic-plastic large deformation for orthogonal cutting. J. of Engineering Materials and Technology 114:218–226
- [40] Mackerle J. (2001) 2D and 3D finite element meshing and remeshing: A bibliography (1990–2001). Engineering Computations: Int. J. for Computer-Aided Engineering 18(8):1108–1197
- [41] Ernst H (1938) Physics of metal cutting. The Cincinnati Milling Machine Co., Cincinnati OH, USA
- [42] Blake A (1985) Handbook of mechanics, materials, and structures. Wiley New York
- [43] Hamrock BJ, Schmid SR, Jacobson BO (2005) Fundamentals of machine elements. McGraw–Hill, Boston
- [44] Atkins AG, Mai YW (1985) elastic and plastic fracture: metals, polymers, ceramics, composites, biological materials. Wiley, New York

- [45] Atkins AG (2003) Modelling metal cutting using modern ductile fracture mechanics: qualitative explanations for some longstanding problems. *Int. J. of Mech. Science* 45:373–396
- [46] Sampath WS, Shaw MS (1983) Fracture on the shear plane in continuous cutting. In: *Proc. 11th NAMRI Conference, Dearborn, MI 1983*
- [47] Itava K, Ueda K (1976) The significance of the dynamic crack behavior in chip formation. *Annals of the CIRP* 25:65–70
- [48] Didjanin L, Kovac P (1997) Fracture mechanisms in chip formation processes. *Materials Science and Technology* 13:439–444
- [49] Trent EM, Wright PK (2000) *Metal cutting, Fourth Edition*. Butterworth–Heinemann, Woburn, MA
- [50] *Strength vs. Hardness of Tool Steels (2007), Bulletin 112*. Latrob Speciality Steel Company: Latrobe, PA
- [51] Oxley PLB (1989) *Mechanics of machining: an analytical approach to assessing machinability*. Wiley, New York
- [52] Al-Momani E, Rawabdeh I (2008) An application of finite element method and design of experiment in the optimization of sheet metal blanking process. *Jordan Journal of Mechanical and Industrial Engineering* 2(1):53–63
- [53] Astakhov VP, Outeiro JC (2008) *Metal cutting mechanics, finite element modeling*. In Davim PJ(ed) *Machining: fundamentals and recent advances*, Springer: London
- [54] Tarkany N (2004) Improving perforating die performance: the effect of stress, clearance and material. *The Fabricator*, 2004, 2–7
- [55] Eleftherion E, Bates CE (1999) Effect of inoculation on machinability of grey cast iron. *ASF Transactions* 122:659–669
- [56] Garry JRC, Wright IP (2000) The cutting strength of cryogenic water. <http://www.lpi.usra.edu/meetings/lpsc2000/pdf/1982.pdf>.
- [57] Muvdi BB, Al-Khafaji AW, McNabb JW (1997) *Dynamics for engineers: with 1118 illustrations*. Springer, New York
- [58] Rubenstein SA (1983) A note concerning the inadmissibility of applying of minimum work principle to metal cutting. *ASME J. of Eng. for Ind.* 105:294–296
- [59] Dewhurst W (1978) On the non-uniqueness of the machining process. *Proc. of the Royal Society of London, A* 360:587–609
- [60] Shaw MC (2008) *Metal cutting principles*. Science Publications. Oxford.
- [61] Shaw MC (1988) *Metal removal*. In: Booser ER (ed) *CRC handbook of lubrication: theory and practice of tribology*, CRC Boca Raton
- [62] Trent EM (1988) *Metal cutting and the tribology of seizure. Part1. Seizure in metal cutting*. *Wear* 128:29–37
- [63] Trent EM (1991) *Metal cutting, 3rd ed*. London, Butterworth Heinemann
- [64] Outeiro JC (2003) *Application of recent metal cutting approaches to the study of the machining residual stresses Dissertation*. University of Coimbra
- [65] Astakhov VP (2004), *Tribology of metal cutting*, In: Toten G, Lieang H (ed) *Mechanical tribology. material characterization and application*. MarcelDekker, New York
- [66] Astakhov VP, Shvets S. (2004) The assessment of plastic deformation in metal cutting. *J. of Mat. Proc. Tech.* 146:193–202
- [67] Johnson GR, Cook WH (1983) A constructive model and data for metals subjected to large strains, high strain rates and high temperatures. In: *Proc. of the 7th International Symposium on Ballistics*. 1983
- [68] Pugh HLD (1958) *Mechanics of metal cutting process*. In: *Proc. IME Conf. Tech. Eng. Manufacture, London*
- [69] Chisholm AWJ (1958). *A review of some basic research on the machining of metals*. n: *Proc. IME Conf. Tech. Eng. Manufacture, London*.

- [70] Bailey JA, Boothroyd G (1969) Critical review of some previous work on the mechanics of the metal-cutting process. *ASME J. of Eng. for Ind.* 90: 54–62
- [71] Zorev NN (1958) Results of work in the field of the mechanics of the metal cutting process. In: *Proc. IME Conf. Tech. Eng. Manufacture*, London.
- [72] Hill R (1954) The mechanics of machining: a new approach. *Journal of the Mechanics and Physics of Solids* 3:47–53
- [73] Creveling JH, Jordon TF, Thomsen EG. (1958) Some studies on angle relationship in metal cutting. *ASME Journal of Applied Mechanics* 79:127–138
- [74] Atkins AG (2003) Modelling metal cutting using modern ductile fracture mechanics: quantitative explanations for some longstanding problems. *International Journal of Mechanical Science* 43:373–396
- [75] Childs THC, Maekawa K, Obikawa T, Yamane Y (2000) *Metal machining. theory and application*. Arnold, London
- [76] Usui E (1988) Progress of "predictive" theories in metal cutting. *JSME International Journal* 31:363–369
- [77] Astakhov VP, Shvets SV (1998) A system concept in metal cutting. *J. Mat. Proc. Tech.* 79(1–3):189–199
- [78] Astakhov VP, Xiao XR (2008) A methodology for practical cutting force evaluation based on the energy spent in the cutting system. *Machining Science and Technology, An International Journal* 12(3):325–347
- [79] Johnson W, Mellor PB (1973) *Engineering plasticity*. Ingleterra London
- [80] Komarovskiy AA, Astakhov VP (2002) *Physics of strength and fracture control: fundamentals of the adaptation of engineering materials and structures*. CRC, Boca Raton
- [81] Astakhov VP, Davim PJ (2008) Tools (geometry and material) and tool wear. In Davim PJ(ed) *Machining: fundamentals and recent advances*, Springer: London
- [82] Makarov AD (1976) *Optimization of cutting processes (in Russian)*, Mashinostroenie, Moscow
- [83] Davis JR (2004) *Tensile testing*. 2nd ed. ASTM, Materials Park, OH
- [84] Altintas Y (2000) *Manufacturing automation. metal cutting mechanics, machine tool vibrations, and CNC design*. University Press, London
- [85] Slater RAC (1977) *Engineering plasticity: theory and application to metal forming processes*. Macmillan, London
- [86] Saletri R.A, Sisler DE (1992) Cutting tool geometries: a user perspective. *SME Paper MR92–360:1–10*
- [87] Ezugwu EO (2005) Key improvements in the machining of difficult-to-cut aerospace superalloys. *Int. J. of Mach. Tools and Manufact.*, 40:1353–1367
- [88] Qi Y, Hector LG (2003) Hydrogen effect on adhesion and adhesive transfer at aluminum/diamond interfaces. *Physical Review B* 68:201403–1 – 201403–4
- [89] Qi Y, Hector LG (2004) Adhesion and adhesive transfer at aluminum/diamond interfaces: A first-principles study. *Physical Review B* 69: 235401–1 – 235401–13
- [90] Qi Y, Hector LG, Ooi N, Adams JB (2005) A first principles study of adhesion and adhesive transfer at AL(111)/graphite(0001). *Surface Engineering* 581:155–168
- [91] Gelin JC, Oudin J, Ravalard Y (1981) Determination of the flow stress-strain curves for metals from axisymmetric upsetting. *J. of Mechanical Working Technology* 5(3–4):297–308

## Basic Definitions and Cutting Tool Geometry, Single Point Cutting Tools

*Give us the tools, and we will finish the job.*  
Winston Churchill's message to President Roosevelt  
in a radio broadcast on 9 February 1941.

**Abstract.** This chapter presents the basic terms and their definitions related to the cutting tool geometry according to ISO and AISI standards. It considers the tool geometry and inter-correlation of geometry parameters in three basic systems: tool-in-hand, tool-in-machine, and tool-in-use. It also reveals and resolves the common issues in the selection of geometry parameters including those related to indexable inserts and tool holders. The chapter introduces the concept and basics of advanced representation of cutting tool geometry using vector analysis. A step-by-step approach with self-sufficient coverage of terms, definitions, and rules makes this complicated subject simple as considerations begin with the simplest geometry of a single-point cutting tool and finish with summation of several motions. Extensive exemplification using practical cases enhances understanding of the covered material.

### 2.1 Basic Terms and Definitions

The geometry and nomenclature of cutting tools, even single-point cutting tools, are surprisingly complicated subjects [1]. It is difficult, for example, to determine the appropriate planes in which the various angles of a single-point cutting tool should be measured; it is especially difficult to determine the slope of the tool face. The simplest cutting operation is one in which a straight-edged tool moves with a constant velocity in the direction perpendicular to the cutting edge of the tool. This is known as the two-dimensional or orthogonal cutting process illustrated in Fig. 2.1. The cutting operation can best be understood in terms of orthogonal cutting parameters. Figure 2.2 shows the application of a single-point cutting tool in a turning operation. It helps to correlate the terminology used in orthogonal and oblique non-free cutting.

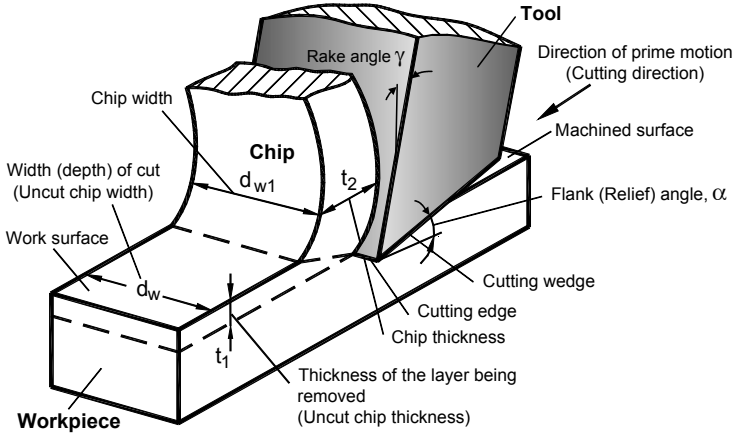


Fig. 2.1. Visualization of basic terms in orthogonal cutting (after Astakhov[2])

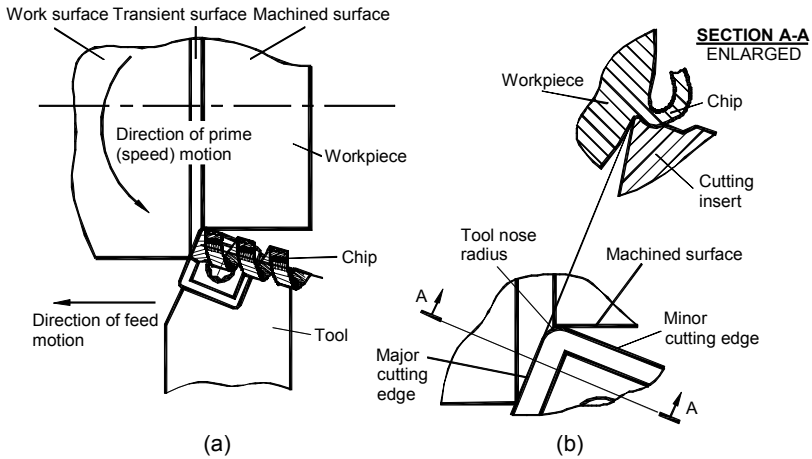


Fig. 2.2. Visualization of basic terms in turning: (a) general view and (b) enlarged cutting portion (after Astakhov [2])

This section aims to introduce the basic definitions of the terms and notions involved in tool geometry considerations. Proper definitions and illustrations of these items are important for comprehension of the basic and advanced concept of the tool geometry. This is particularly true because a wide diversity of terms used in the books, texts, research papers, tool companies catalogs, trade materials, and even standards (National and International) combined with the so-called “machine shop terminology” makes it difficult to understand even the basic concepts of the tool geometry.

### 2.1.1 Workpiece Surfaces

In orthogonal cutting (Fig. 2.1), the two basic surfaces of the workpiece are considered:

- Work surface is the surface of the workpiece to be removed by machining
- Machined surface is the surface produced after the cutting tool pass

In many practical machining operations additional surface is considered. The transient surface is the surface being cut by the major cutting edge (Fig. 2.2a). Note that the transient surface is always located between the work surface and machined surface. It presents distinguished orthogonal cutting and other machining operations besides simple shaping, planning and broaching where the cutting edge is perpendicular to the cutting speed and the only edge involved in machining.

In most real machining operations, the cutting edge does not form the machined surface. As clearly seen in Fig. 2.2b, the machined surface is formed by the tool nose and minor cutting edge. Unfortunately, not much attention is paid to these two important components of tool geometry although their parameters directly affect the integrity of the machined surface including the surface finish and machining residual stresses. Misunderstanding of the above discussed matter causes a great mismatch in the results of known modeling of the cutting process and reality.

### 2.1.2 Tool Surfaces and Elements

The design components of the cutting tool are defined as follows:

- *Rake face* is the surface over which the chip, formed in the cutting process, slides
- *Flank face* is the surface(s) over which the surface, produced on the workpiece, passes
- *Cutting edge* is a theoretical line of intersection of the rake and the flank surfaces
- *Cutting wedge* is the tool body enclosed between the rake and the flank faces
- *Shank* is the part of the tool by which it is held

### 2.1.3 Tool and Workpiece Motions

According to ISO 3002/1 standard [3], all motions, directions, and speeds are defined relative to the workpiece.

The primary motion is the main motion provided by a machine tool or manually to cause relative motion between the tool and workpiece so that the face of the tool approaches the workpiece material. Appendix A discusses the primary motion for various machining operations as well as its direction and speed known as the cutting speed. It is important to realize that the primary motion is only able to cause chip removal for more than one revolution or stroke (of workpiece or tool) if there is a feed motion applied.

The feed motion is a motion provided by a machine tool or manually or built in the design of the cutting tool (for example, in broaching) to cause the additional relative motion between the tool and the workpiece, which, when added to the primary motion, leads to repeated or continuous chip removal and thus creation of a machined surface with the desired geometric characteristics. This motion may be provided by steps or continuously. Appendix A discusses the feed motion(s) for various machining operations as well as its direction and speed known as the feed speed (often referred to as the feed rate).

The resultant cutting motion is the motion resulting from simultaneously applying the primary and feed motions. Appendix A discusses the direction and velocity of this motion for various machining operations.

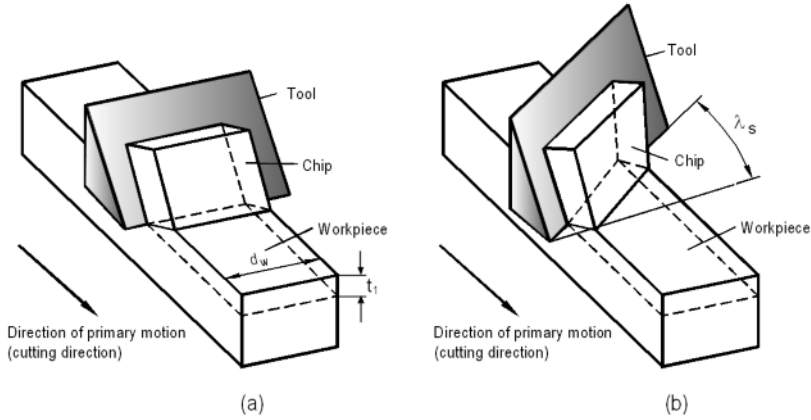
### 2.1.4 Types of Cutting

Orthogonal cutting is that type of cutting where the straight cutting edge of the wedge-shaped cutting tool is at right angle to the direction of cutting as shown in Fig. 2.1. The additional distinctive features of orthogonal cutting are:

- The cutting edge is wider than the width of cut.
- No side spread of the layer being removed occurs on its transformation into the chip.
- Plane strain condition is the case, i.e., a single “slice” (by a plane perpendicular to the cutting edge) of the model shown in Fig. 2.1 can be considered in the analysis of the chip formation model.
- The cutting edge does not pass the previously machined surface by this cutting edge so there is no influence of the previous cutting passes on the current pass. This is not the case in tube end turning, which is often used to simulate orthogonal cutting, because the temperatures and machining residual stresses built on the previous pass might significantly affect the cutting conditions on the current pass. Moreover, this influence depends on many cutting parameters as the rotational speed of the tubular workpiece (which defines the time difference between two successive positions of the cutting edge and the intensity of the residual heat), axial feed (which defines the machining residual stresses left from the previous pass of the cutting tool), etc. In the author’s opinion, this makes end tube turning unsuitable to simulate orthogonal cutting [1].

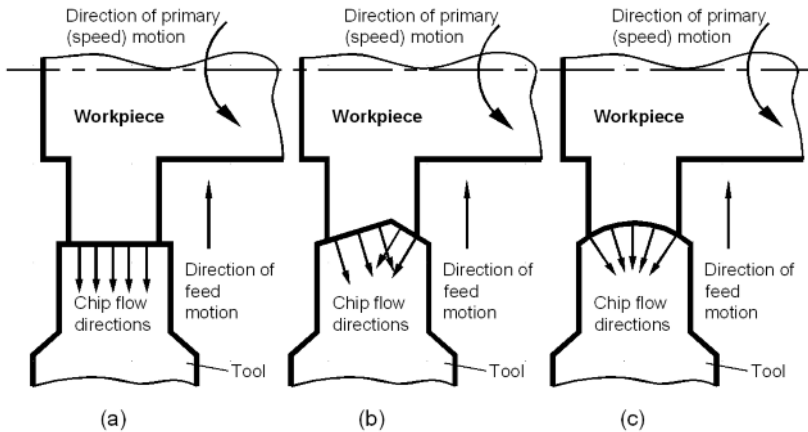
Oblique cutting is that type of cutting where the straight cutting edge of the wedge-shaped cutting tool is not at right angle to the direction of cutting. Figure 2.3 illustrates the difference between orthogonal and oblique cutting. In orthogonal cutting (Fig. 2.3a), the cutting edge is perpendicular to the direction of primary motion while in oblique cutting (Fig. 2.3b) it is not. The angle which the straight cutting edge makes with the direction of the cutting speed is known as the cutting edge inclination angle  $\lambda_s$ . The plastic deformation of the layer being removed in oblique cutting is more complicated than that in orthogonal cutting [4]. Therefore, this type of cutting cannot be represented by a 2D model.





**Fig. 2.3.** Orthogonal (a) and oblique (b) cutting

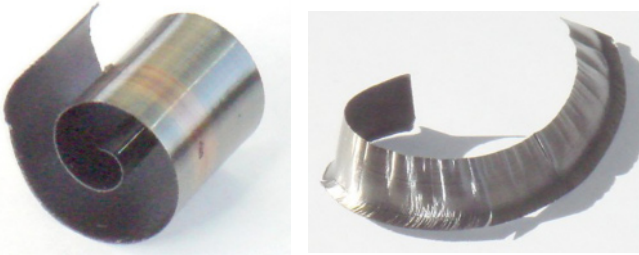
Free cutting is that type of orthogonal or oblique cutting when only one cutting edge is engaged in cutting. Although this definition is widely used in the literature on metal cutting [4-6], it does not provide the proper explanation to the idea of free cutting. For example, if a cutting edge is not straight, it does not perform free cutting. In contrast, a number of cutting edges can be simultaneously engaged in cutting in surface broaching but each edge is engaged in free cutting. In the definition, ‘free’ means that the elementary chip flow vectors from each point of the cutting edge are parallel to each other and do not intersect any other chip flow vectors. An example of free cutting is shown in Figure 2.4a. If more than one adjacent cutting edges are involved in cutting (Figure 2.4b shows an example of two cutting edges) or when the cutting edge is not straight (Figure 2.4c), the chip flows formed at different cutting edges or at different points of the same cutting edges cross each other causing greater chip deformation and thus a greater cutting force than in free cutting.



**Figure 2.4.** Model showing: (a) free and (c)(d) non-free cutting

Non-free cutting is that type of cutting where more than one cutting edge is engaged in cutting so that the chip flows from the engaged cutting edges interact with each other (Figure 2.4b,c).

Figure 2.5 shows a comparison of chips obtained in orthogonal cutting (a) and that obtained in non-free cutting (turning) (b). For a turning test tool with a nose radius similar to that shown in Fig. 2.2b was used and the uncut chip thickness was chosen to be small so the chip almost conforms to the shape of the major cutting edge, nose radius, and the minor cutting edge. As seen, non-free cutting causes non-uniform chip deformation.



**Figure 2.5.** Shapes of chips obtained in (a) free and (b) non-free cutting

## 2.2 Cutting Tool Geometry Standards

There are two established tool geometry standards, namely ISO Standard [3] and ANSI Standard [7]. A simple comparison of these standards shows that the ISO Standard is much more advanced as it contains much more clear and functional definitions. Moreover, the basic notions of the ISO Standard are well explained and shown with multiple examples as applied to various cutting tools while the ANSI Standard concentrates only on single-point cutting tools. Both standards, however, failed to answer a simple yet the most important question: “Why should one know the tool geometry?” The educated and thus complete answer to this question is not simple and straightforward. The simplest answer can be thought of as follows: “To be able to reproduce *the same* tool geometry from one tool re-sharpening to another, from one cutting insert to the next, etc.” so in the author’s opinion it should be stated as both standards.

The ISO Standard [3] is widely used worldwide while the ANSI Standard [7] is used in parallel with the ISO Standard in North America. Similarity of some terms and definitions and differences of others creates a number of confusions in publications of various types starting from textbooks and research papers and finishing with flyers of various tool companies for new tools. For example, the term “the depth of cut” widely used in practice and properly defined by the ISO Standard, is termed “Back engagement” in the ANSI Standard. The terms “the approach angle” and “tool orthogonal clearance” defined by the ISO Standard termed “the lead angle” and “tool base clearance” by the ANSI Standard. Although further considerations are based on the notions and definitions of the ISO Standard

(with some corrections of some obvious flaws [8]), the basic notions of the ANSI Standard and explanations of the correspondence of the basic terms of both standards are given in further text wherever it is important.

### 2.3 Systems of Consideration of Tool Geometry

Both the above-mentioned tool geometry standards discuss two systems of consideration of the cutting tool geometry, namely, the tool-in-hand and tool-in-use systems (hereafter, T-hand-S and T-use-S, respectively). The former relates to the so-called static geometry while the latter is based on consideration of tool motions with respect to the workpiece. In the author's opinion, however, these two systems are insufficient for the proper consideration of cutting tool geometry. Another system, namely, the tool-in-machine system [1] (hereafter, T-mach-S) should also be considered.

Introduction of an additional system of consideration may be thought of as a kind of overcomplicating of the cutting tool geometry and its practical applications so that it is suitable only for ivory academicians as it has little practical value at the shop floor level. In the author's opinion, the opposite is actually the case. Namely, misunderstanding the tool geometry in the above-mentioned system leads to improper selection of the tool geometry parameters and humps optimization of practical machining operations. Moreover, tool life and quality of the machined surface are often not as good as they could be if the tool geometry were selected properly. In other words, the proposed consideration does not complicate but rather simplifies the analysis of tool geometry.

The cutting tool geometry includes a number of angles measured in different planes. Although the definitions of the standard planes for consideration of tool geometry are the same for all of the three above-mentioned systems of consideration, these planes are not the same in these systems. This is because a set of the standard planes in each particular system is defined in a certain coordinate system. Thus, it is of crucial importance to set the proper coordinate system in each system of consideration. Such a coordinate system distinguishes one system under consideration from others within the three basic systems of consideration. Note that if the coordinate systems of two or more systems of consideration coincide then there is no need to consider these systems separately as the set of the reference planes would be the same.

The choice of a particular system and/or their combinations depends on the tool and toolholder design, tool post, and tool fixing in the machine, direction of the tool motion with respect to the workpiece or axis of rotation and other factors. Such a choice, however, should always have a clear objective, namely, to be correlated in simple fashion to the cutting tool geometry needed for optimum tool performance. In the case of a cutting tool with indexable inserts, the objective is to select the proper inserts and available tool holder to assure the tool geometry required by the optimal performance of the machining operation. Therefore, the starting point of tool design (selection) is the optimum cutting geometry and the finishing point is the tool grinding geometry or specifically selected tool holders and inserts to assure this optimal cutting geometry. To do this, a tool designer (tool

layout, tool application and tool optimization specialists, manufacturing and process engineers) should know the basic definitions and parameters of tool geometry, the above-mentioned three systems of consideration of tool geometry, as well as the correlations among these systems. One of the prime objectives of this book is to introduce these items showing their practical implementation in single point and in drilling tools with multiple real-world examples.

Being simple, logical, and straightforward, the above-stated representation of the tool geometry is not common while being indirectly used for years in various books and research papers. Therefore, a simple exemplification can clarify the essence of the proposed three systems.

To demonstrate a necessity of a third additional system, the geometry of a common cutting insert shown in Fig. 2.6 is considered as an example. The geometry of this insert is as follows: rake angle is  $20^\circ$ , flank angle is  $3^\circ$ , assumed tool cutting edge angle is  $0^\circ$ . These angles together with some other parameters (as for example, the nose radius) do not constitute the T-hand-S tool geometry as this insert is not a tool.



**Fig. 2.6.** A square indexable insert

Obviously this insert can be placed in various available standard and special tool holders as shown in Fig. 2.7. Once the insert is placed, the tool holder sets the assumed directions of the prime and feed motions and thus the T-hand-S can be established. Moreover, the tool holder sets the assumed tool cutting edge angle. It is shown later that this angle is of vital importance in metal cutting as it defines the uncut chip thickness and contact conditions at the tool-chip interface.

Moreover, the tool holder often changes the rake and flank angles. If this insert is used with a Seco Tool MSRNR-20-5D tool holder then the tool cutting edge angle would be  $75^\circ$ , the normal rake angle would be  $15^\circ$ , while the normal flank angle would be  $5^\circ$ . If this insert is used with a MSRNR-20-6D tool holder then the tool cutting edge angle would be  $45^\circ$ , the normal rake angle would be  $17^\circ$ , while the normal flank angle would be  $4^\circ$ .

Figure 2.8 shows milling tools with square inserts. As seen, all geometry parameters of the discussed inserts can be altered over a wide range depending upon the particular tool holder used. Therefore, it is necessary to know the geometry of the insert and the tool holder to understand and thus calculate properly the tool geometry in T-hand-S. Unfortunately, this is rarely done.

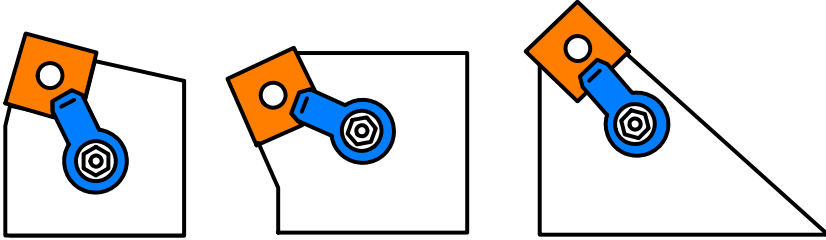


Fig. 2.7. Tool holders with different tool cutting edge angles



Fig. 2.8. Square insert can be placed in various milling tool holders

The tool-in-machine system (T-mach-S) can be fully appreciated if one realizes that the holder can be installed in the machine in a number of different ways. In the simplest case, it can be installed below or above the axis of rotation. Moreover, modern CNC machine and manufacturing cells allow the position of the tool holder to be varied with respect to the axis of rotation to increase versatility of the cutting tool, i.e., to perform more operations with the same tool.

Yes another pictorial example of the different tool geometries in T-hand-S and T-mach-S is the geometry of a straight-flute drill. Figure 2.9 shows the geometry of such a drill in T-hand-S. As seen, the T-hand-S is set at a point of the cutting edge geometry which is to be considered. Such a representation is the standard in the practice of tool design and manufacturing. A common notion is that this drill has a zero rake angle and a small positive angle of the web-thinning part (edge 2–3). The normal flank angle  $\alpha_n$  is selected depending on the work material following usual recommendations for flank angles. This angle is used as the major re-sharpening feature and is indicated on the tool drawing. The distinguishing feature of the drill geometry in T-hand-S is that the rake and flank angles do not change along the considered cutting edges.

In reality, however, parameters as the tool geometry shown in Fig. 2.9, have only remote correlation with the those involved in cutting as is shown later in Chap. 4. Figure 2.10 presents the T-mach-S coordinate system. In this coordinate system, the drill geometry parameters, including rake and flank angles, vary along the cutting edges. The flank and rake angle of a point  $a$  of the cutting edge 1–2 depend on the distance  $c_{ct}$ , radius  $Oa$ , and point angle  $\Phi$ . It will be shown later in

Chap. 4 that the rake angle becomes highly negative at point 2 while it is  $0^\circ$  in T-mach-S. The opposite is true for the flank angle. Therefore, the lack of knowledge on the correlations of the geometry parameters in T-hand-S and T-mach-S often leads to improper design of such drills as will be shown later.

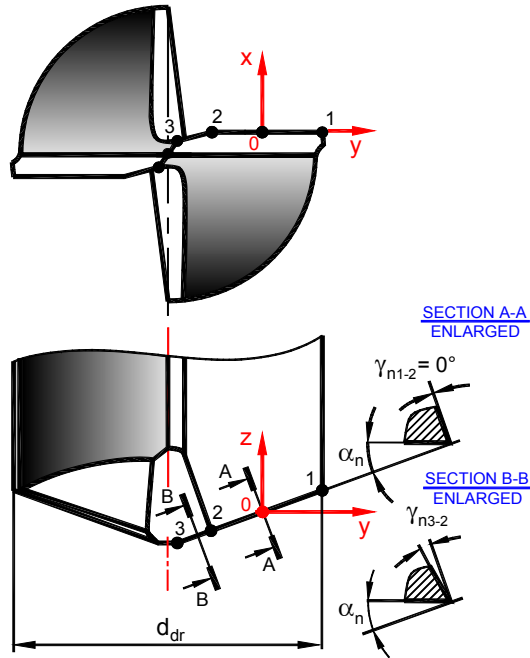


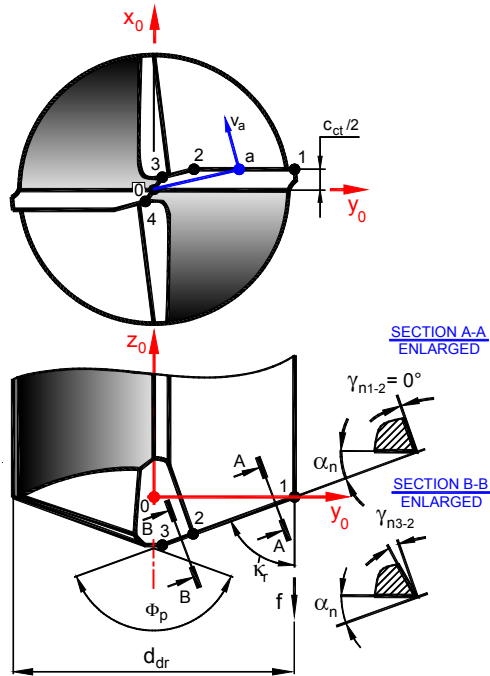
Fig. 2.9. Geometry of a straight-flute drill in T-hand-S

The tool-in-use system (T-use-S) accounts for the actual directions and velocities of the speed and feed motions. Its essence and necessity are well-discussed in the above-mentioned ISO and ANSI Standards.

## 2.4 Tool-in-hand System (T-hand-S)

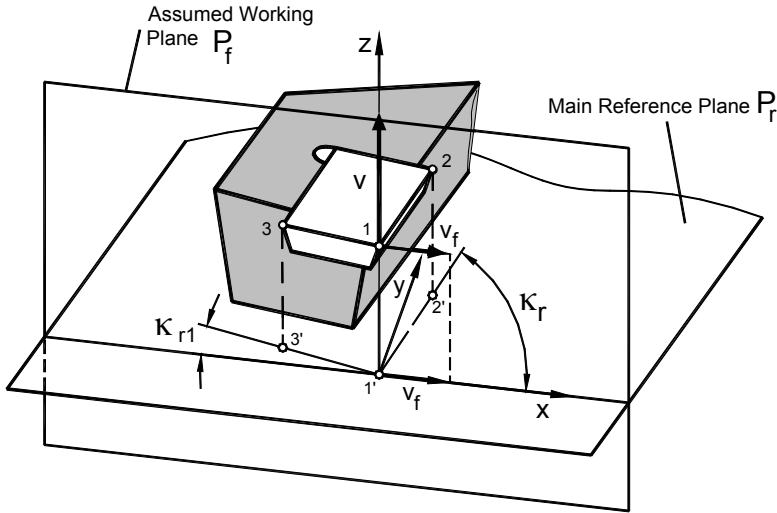
### 2.4.1 Tool-in-hand Coordinate System

The cutting tool geometry includes a number of angles measured in different planes. Although the definitions of the standard planes of consideration of the tool geometry are the same for all four above-mentioned systems under consideration, these planes are not the same in these systems. This is because a set of the standard planes in each particular system is defined in a certain coordinate system. Thus, it is of crucial importance to set the proper coordinate system in each system of consideration.



**Figure 2.10.** Tool-in-Holder (Tool-in-Machine) coordinate system

Figure 2.11 sets the T-hand-S. The origin of this coordinate system is always placed at a point on the cutting edge. The z-axis is always in the assumed direction of the prime motion while the x-axis is in the direction of the assumed direction of the feed motion. The y-axis is perpendicular to the z- and x-axes to form a right-hand Cartesian coordinate system. It is extremely important not to associate this coordinate system with the actual holders, location of this holder in the machine, and with the actual speed and feed directions, assuming that a cutting element (for example a tooth of a gear hob) is a single point cutting tool considered below in this section. The corresponding transformations to the geometry in T-use-S (through T-hand-S and T-mach-S) is then accomplished accounting for the actual location of the this cutting element in the tool holder (for example, the placement of the mentioned tooth of the gear hob on the body), location of this holder in the machine (for example, the actual location of the gear hob with respect to the workpiece-gear blank), and speeds and feeds in machining.



**Fig. 2.11.** Tool-in-hand coordinate system and basic geometry parameters of a single point cutting tool (after Astakhov [2])

## 2.4.2 Reference Planes

In Fig. 2.11,  $\mathbf{v}$  is the assumed direction of primary motion, known as the direction of the cutting velocity (customarily referred to as the cutting speed),  $\mathbf{v}_f$  is the assumed direction of the cutting feed, line 1–2 is the major cutting edge, and 1–3 is the minor cutting edge. Figure 2.11 visualizes the definition of:

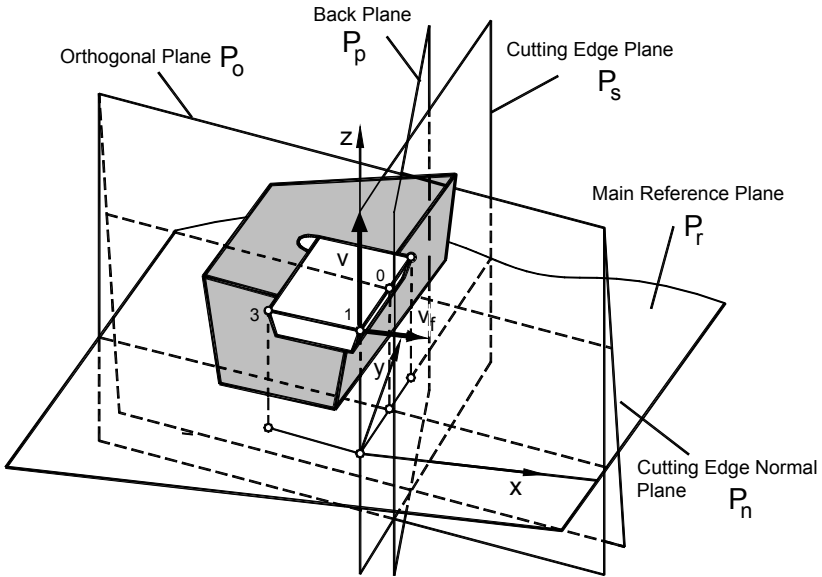
- *Main reference plane*  $P_r$  as to be perpendicular to the assumed direction of primary motion (the  $z$ -direction in Fig. 2.11).
- *Assumed working plane*  $P_f$  as to be perpendicular to the reference plane  $P_r$  and containing the assumed direction of feed motion.
- *Tool cutting edge angle*,  $\kappa_r$  as the acute angle between the projection of the main cutting edge into the reference plane and the  $x$ -direction. Angle  $\kappa_r$  is always positive and it is measured in a counter-clockwise direction from the position of the assumed working plane.
- *Tool minor (end) cutting edge angle*,  $\kappa_{r1}$  as the acute angle between the projection of the minor (end) cutting edge into the reference plane and the  $x$ -direction. Angle  $\kappa_{r1}$  is always positive (including zero) and it is measured in a clockwise direction from the position of the assumed working plane.

The angles of the cutting tool are defined in a series of reference planes. A system of these planes in T-hand-S is shown in Fig. 2.12. This system consists of five basic planes defined relative to the reference plane  $P_r$ :

- *The tool cutting edge plane*  $P_s$  is perpendicular to  $P_r$ , and contains the major cutting edge. It is important for the proper analysis of the cutting tool geometry to understand that: (a) if the major cutting edge is a straight line,



then the tool conning edge plane is the same for any point on this edge. This plane is fully defined by two intersecting lines, namely, by the straight cutting edge and the vector of the cutting speed; (b) if the major cutting edge is not straight then a tool cutting edge plane should be determined for each point on the curved cutting edge thus being the plane which is tangent to the cutting edge at the point of consideration and which contains the vector of the cutting speed (or perpendicular to the main reference plane).



**Fig. 2.12.** Visualization of a system of reference planes to define tool geometry

- The tool back plane  $P_p$  is perpendicular to  $P_r$  and  $P_f$ .
- Perpendicular to the projection of the cutting edge into the reference plane is the orthogonal plane  $P_o$ . When the cutting edge is not straight, there are an infinite number of orthogonal planes defined for each point of the curved cutting edge. For a given point of the curved cutting edge, the orthogonal plane is defined as the plane which is perpendicular to the tangent to the projection of the cutting edge into the reference plane edge at the point of consideration.
- The cutting edge normal plane  $P_n$  is perpendicular to the cutting edge. When the cutting edge is not straight, a normal plane is defined for each point of the curved cutting edge. For a given point of the curved cutting edge, the cutting edge normal plane is defined as the plane perpendicular to the tangent to the cutting edge at the point of consideration.

### 2.4.3 Tool Angles

#### 2.4.3.1 Definitions

The geometry of a cutting element is defined by certain basic tool angles and thus precise definitions of these angles are essential. A system of tool angles is shown in Fig. 2.13 and is known as the tool-in-hand system (T-hand-S) [1]. Rake, wedge, and flank angles are designated by  $\gamma$ ,  $\beta$ , and  $\alpha$ , respectively, and these are further identified by the subscript of the plane of consideration. The definitions of basic tool angles in the T-hand-S are as follows:

- $\psi_r$  is the tool approach angle; it is the acute angle that  $P_s$  makes with  $P_p$  and is measured in the reference plane  $P_r$  as shown in Fig. 2.13.
- The rake angles are defined in the corresponding planes of measurement. The rake angle is the angle between the reference plane (the trace of which in the considered plane of measurement appears as the normal to the direction of primary motion) and the intersection line formed by the considered plane of measurement and the tool rake face. The rake angle is defined as always being acute when looking across the rake face from the selected point and along the line of intersection of the face and plane of measurement. The viewed line of intersection lies on the opposite side of the tool reference plane from the direction of primary motion in the measurement plane for  $\gamma_f$ ,  $\gamma_p$ ,  $\gamma_o$ , or a major component of it appears in the normal plane for  $\gamma_n$ . Angle  $\gamma_f$  is known as the tool side rake,  $\gamma_p$  is known as the tool back rake, and  $\gamma_n$  is known as the normal rake. The sign of the rake angles is well defined (Fig. 2.13).
- The flank angles are defined in a similar way to the rake angles, though here if the viewed line of intersection lies on the opposite side of the cutting edge plane  $P_s$  from the direction of feed motion, assumed or actual as the case may be, then the flank angle is positive. The flank (sometimes referred to as the clearance) angle is the angle between the tool cutting edge plane  $P_s$  and the intersection line formed by the tool flank plane and the considered plane of measurement as shown in Fig. 2.13. Angles  $\alpha_f$ ,  $\alpha_p$ ,  $\alpha_o$ ,  $\alpha_n$  are clearly defined in the corresponding planes as seen in Fig. 2.13. Angle  $\alpha_f$  is known as the tool side flank,  $\alpha_p$  is known as the tool back flank, and  $\alpha_n$  is known as the normal flank.
- The wedge angles  $\beta_f$ ,  $\beta_p$ ,  $\beta_o$ ,  $\beta_n$  are defined in the planes of measurements. The wedge angle is the angle between the two intersection lines formed as the corresponding plane of measurement intersects with the rake and flank faces. For all cases, the sum of the rake, wedge and clearance angles is  $90^\circ$ , i.e.

$$\gamma_p + \beta_p + \alpha_p = \gamma_n + \beta_n + \alpha_n = \gamma_o + \beta_o + \alpha_o = \gamma_f + \beta_f + \alpha_f = 90^\circ \quad (2.1)$$

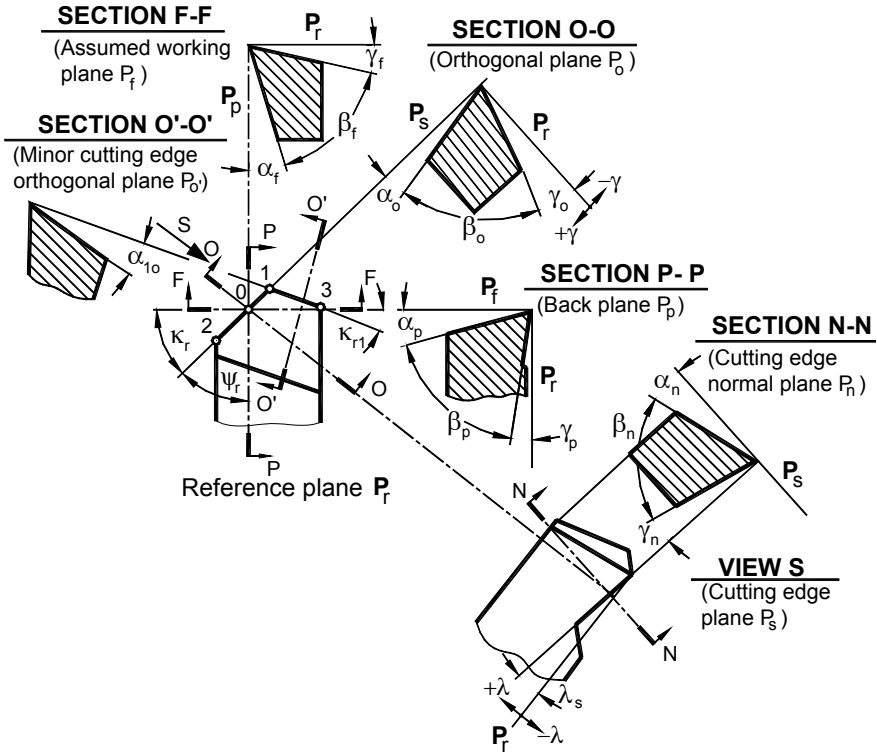


Fig. 2.13. System of tool angles in the defined planes in T-hand-S (after Astakhov [2])

- The orientation and inclination of the cutting edge are specified in the tool cutting edge plane  $P_s$ . In this plane, the cutting edge inclination angle  $\lambda_s$  is the angle between the cutting edge and the reference plane. This angle is defined as always being acute and positive if the cutting edge, when viewed in a direction away from the selected point at the tool corner being considered, lies on the opposite side of the reference plane from the direction of primary motion. This angle can be defined at any point of the cutting edge. The sign of the inclination angle is well defined in Fig. 2.13.

2.4.3.2 Basic Relationship Among Angles in T-hand-S

It is important to know the basic relationships between the rake and flank angles in various section planes. As known [2], the normal or orthogonal flank and rake angles are selected based upon cutting conditions (primarily, tool life and chip breakability), the tool cutting edge angle,  $\kappa_r$  is selected based upon the contour of the machined part, and the cutting edge inclination angle  $\lambda_s$  is selected based upon the desired direction of the chip flow. The tool angles in the assumed working plane  $P_f$  and in the assumed back plane,  $P_p$ , namely, the tool side rake,  $\gamma_f$ , the tool back rake  $\gamma_p$ , the tool side flank,  $\alpha_f$ , and the tool back flank  $\alpha_p$ , do not directly

affect the cutting process. Rather, they serve some useful purposes in the tool manufacturing (assembly) and in preventing tool interference with the workpiece.

Figure 2.14 shows a model used to correlate the orthogonal rake and flank angles with those in  $P_f$  and  $P_p$  [9]. In this model, the cutting edge is represented by line  $ab$  (Fig. 2.14a). The cutting edge plane  $P_s$  contains this edge  $ab$  and is perpendicular to the reference plane  $P_r$ . A plane  $P_{s1}$  is parallel to  $P_s$  and set at a certain distance  $l_1$  from  $P_s$ . Line  $cd$  is the line of intersection of  $P_{s1}$  and the tool rake face. A point  $M$  is selected on the cutting edge  $ab$ . The following planes are drawn through point  $M$ :

1. Orthogonal plane  $P_o$  (SECTION A–A). The line of intersection of this orthogonal plane with the rake face included between planes  $P_s$  and  $P_{s1}$  is  $MM_1$ .
2. Assumed back plane,  $P_p$  (SECTION B–B). The line of intersection of this plane with the rake face included between planes  $P_s$  and  $P_{s1}$  is  $MM_2$ .
3. Assumed working plane,  $P_f$  (SECTION C–C). The line of intersection of this plane with the rake face included between planes  $P_s$  and  $P_{s1}$  is  $MM_3$ .

The rake angles in the corresponding planes are defined as the angle between the reference plane through point  $M$  the rake face in these section planes as shown in Fig. 2.14a–c.

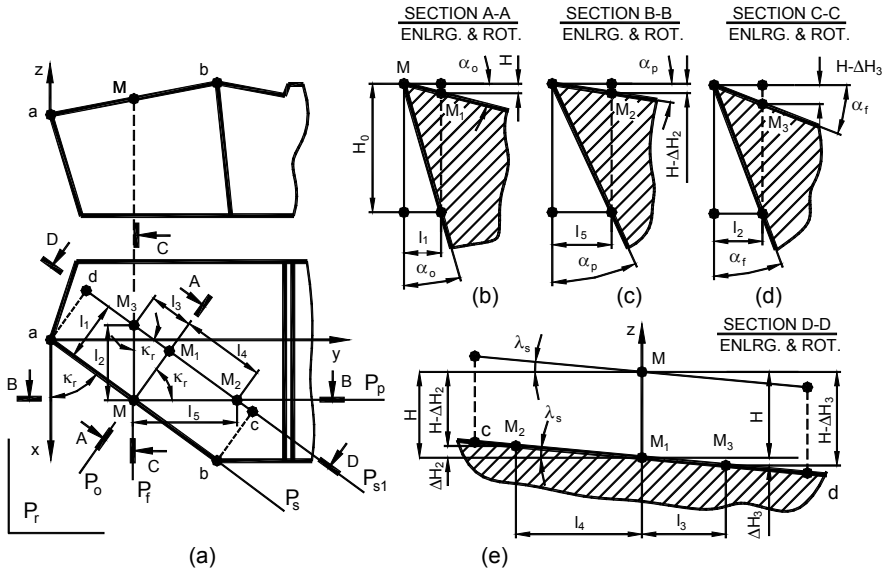
Figure 2.14a shows the sense of distances  $l_2$  (between points  $M$  and  $M_3$ ),  $l_3$  (between points  $M_1$  and  $M_3$ ),  $l_4$  (between points  $M_1$  and  $M_2$ ), and  $l_5$  (between points  $M$  and  $M_2$ ) along the rake face. Figure 2.14d shows a cross-section view (SECTION D–D) where  $H$  is defined as the vertical distance between points  $M$  (the reference plane  $P_r$  through point  $M$ ) and  $M_1$ . As seen in this figure, the vertical distance between point  $M_2$  and the reference plane ( $H - \Delta H_2$ ) is smaller than  $H$ , while that between point  $M_3$  and the reference plane ( $H + \Delta H_3$ ) is greater than  $H$  due to cutting edge inclination by angle  $\lambda_s$ . Obviously,  $\Delta H_2 = l_4 \tan \lambda_s$  and  $\Delta H_3 = l_3 \tan \lambda_s$ .

As follows from Fig. 2.14b–d

$$\tan \gamma_o = \frac{H}{l_1} \quad (2.1)$$

$$\tan \gamma_f = \frac{H + \Delta H_3}{l_2} = \frac{H + l_3 \tan \lambda_s}{l_2} \quad (2.2)$$

$$\tan \gamma_p = \frac{H - \Delta H_2}{l_5} = \frac{H - l_4 \tan \lambda_s}{l_5} \quad (2.3)$$



**Fig. 2.14.** Model to correlate the orthogonal rake and flank angles with those in the working and back planes

As follows from Eq. 2.2  $H = l_1 \tan \gamma_o$  and it directly follows from Fig. 2.14a that

$$l_1/l_2 = \sin \kappa_r, \quad l_2/l_2 = \cos \kappa_r, \quad l_1/l_5 = \cos \kappa_r, \quad \text{and} \quad l_4/l_5 = \sin \kappa_r \quad (2.4)$$

Substituting these results into Eqs. 2.3 and 2.4, one obtains

$$\tan \gamma_f = \tan \gamma_o \sin \kappa_r + \tan \lambda_s \cos \kappa_r \quad (2.5)$$

and

$$\tan \gamma_p = \tan \gamma_o \cos \kappa_r - \tan \lambda_s \sin \kappa_r \quad (2.6)$$

Similar consideration can be applied for the flank angles. It follows from Fig. 2.14b that the flank angle in the orthogonal plane,  $\alpha_o$  calculates as

$$\tan \alpha_o = \frac{H_o}{l_1} \quad (2.7)$$

the flank angle in the assumed working plane as

$$\tan \alpha_f = \frac{H_o}{l_2} \quad (2.8)$$

and the flank angle in the assumed working plane as

$$\tan \alpha_p = \frac{H_o}{l_5} \quad (2.9)$$

It follows from Eq. 2.8 that  $H_o = l_1 \tan \alpha_o$ . Substituting this results into Eqs. 2.9 and 2.10 and accounting for Eq. 2.5, one can obtain

$$\tan \alpha_f = \tan \alpha_o / \sin \kappa_r \quad (2.10)$$

and

$$\tan \alpha_p = \tan \alpha_o / \cos \kappa_r \quad (2.11)$$

Although the model shown in Fig. 2.14 is constructed assuming positive rake and inclination angles, the results obtained are also valid for negative rake and/or inclination angles provided that these angles are substituted into the resulting Eqs. 2.6 and 2.7 with the corresponding signs.

Figure 2.15 shows a model that helps to correlate the tool angles in the orthogonal,  $P_o$  and in the normal,  $P_n$  planes. The cutting edge  $ab$  provided with the rake and flank angles is inclined at angle  $\lambda_s$ . The orthogonal rake,  $\gamma_o$  and flank,  $\alpha_o$  angles are considered in the orthogonal plane,  $P_o$  while the normal rake,  $\gamma_n$  and flank,  $\alpha_n$  angles are considered in the orthogonal plane,  $P_n$ . As seen

$$\tan \alpha_o = dc/Mc \text{ and } \tan \alpha_n = fe/Me \quad (2.12)$$

As  $dc = fe$  and  $Mc = Me \cdot \cos \lambda_s$ , one can obtain

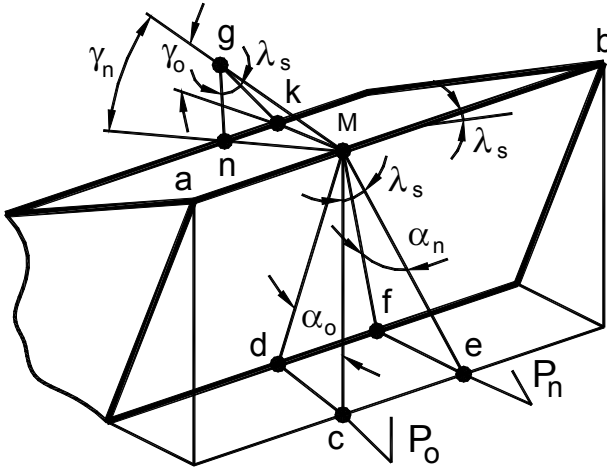
$$\cot \alpha_n = \cos \lambda_s \cot \alpha_o \quad (2.13)$$

Similarly,

$$\tan \gamma_o = gk/Mg \text{ and } \tan \gamma_n = ng/Mg \quad (2.14)$$

As  $gk = ng/\cos \lambda_s$ , one can obtain

$$\tan \gamma_n = \cos \lambda_s \tan \gamma_o \quad (2.15)$$



**Fig. 2.15.** Model to correlate the tool angles in the orthogonal and normal planes

Simple relationships exist among the considered angles in T-hand-S. These relationships have been derived using the results obtained in this section:

$$\tan \lambda_s = \sin \kappa_r \tan \gamma_p - \cos \kappa_r \tan \gamma_f \quad (2.16)$$

$$\tan \gamma_o = \cos \kappa_r \tan \gamma_p + \sin \kappa_r \tan \gamma_f \quad (2.17)$$

$$\cot \alpha_o = \cos \kappa_r \cot \alpha_p + \sin \kappa_r \cot \alpha_f \quad (2.18)$$

It must be stated, however, that these relationships apply only when the cutting edge angle  $\kappa_r$  is less than  $90^\circ$ . Nowadays, it is becoming common practice to use cutting tools having  $\kappa_r$  greater than  $90^\circ$ . Moreover, most drills are made in the same way. For these tools, the following relationships are valid

$$\tan \lambda_s = -\sin \kappa_r \tan \gamma_p - \cos \kappa_r \tan \gamma_f \quad (2.19)$$

$$\tan \gamma_o = -\cos \kappa_r \tan \gamma_p + \sin \kappa_r \tan \gamma_f \quad (2.20)$$

$$\cot \alpha_o = -\cos \kappa_r \cot \alpha_p + \sin \kappa_r \cot \alpha_f \quad (2.21)$$

#### 2.4.3.3 Example 2.1

**Problem:** The optimal cutting performance of a single-point tool for turning was found when this tool has the following geometry: Normal flank angle  $\alpha_n = 12^\circ$ , normal rake angle  $\gamma_n = 8^\circ$ , cutting edge inclination angle  $\lambda_s = 10^\circ$ , tool cutting

edge angle  $\kappa_r = 60^\circ$ . Find the corresponding angles in the orthogonal, back, and assumed working planes that used in tool design and manufacturing.

Solution: The flank angle in the orthogonal plane calculates using Eq. 2.14 as

$$\alpha_o = \arctan(\cos \lambda_s \tan \alpha_n) = \arctan(\tan 10^\circ \tan 12^\circ) = 11.82^\circ$$

The rake angle in the orthogonal plane calculates using Eq. 2.16 as

$$\gamma_o = \arctan(\tan \gamma_n / \cos \lambda_s) = \arctan(\tan 8^\circ / \cos 10^\circ) = 8.12^\circ$$

The flank angle in the assumed working plane calculates using Eq. 2.11 as

$$\alpha_f = \arctan(\tan \alpha_o / \sin \kappa_r) = \arctan(\tan 11.82^\circ / \sin 60^\circ) = 13.59^\circ$$

The flank angle in the back plane calculates using Eq. 2.12 as

$$\alpha_p = \arctan(\tan \alpha_o / \cos \kappa_r) = \arctan(\tan 11.82^\circ / \cos 60^\circ) = 22.71^\circ$$

The rake angle in the assumed working plane calculates using Eq. 2.6 as

$$\begin{aligned} \gamma_f &= \arctan(\tan \gamma_o \sin \kappa_r + \tan \lambda_s \cos \kappa_r) = \\ &\arctan(\tan 8.12^\circ \sin 60^\circ + \tan 10^\circ \cos 60^\circ) = 11.96^\circ \end{aligned}$$

The rake angle in the back plane calculates using Eq. 2.7 as

$$\begin{aligned} \gamma_p &= \arctan(\tan \gamma_o \cos \kappa_r - \tan \lambda_s \sin \kappa_r) = \\ &\arctan(\tan 8.12^\circ \cos 60^\circ - \tan 10^\circ \sin 60^\circ) = -4.65^\circ \end{aligned}$$

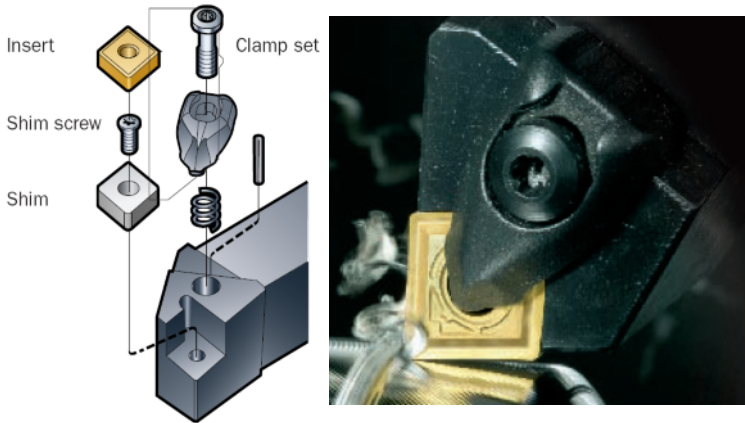
#### 2.4.4 Geometry of Cutting Tools with Indexable Inserts

Indexable cutting inserts (solid and tipped) are available in a great variety of shapes, dimensions, and geometries. The tool is assembled when a particular insert is placed and clamped in a tool holder as shown in Fig. 2.16. The geometry of this assembled tool in T-hand-S depends on both geometry of the cutting insert and on the design and geometry of the selected tool holder. Therefore, it is of practical importance to have a proper methodology to assess this resultant geometry.

Looking through the colorful catalogs of various tool companies, one may develop a kind of perception that such a methodology should be very simple and straightforward as all the geometry parameters of indexable inserts are standard



and well presented in these catalogs. These parameters together with their tolerances are uniquely described by the insert code (Appendix B). Cutting tool catalogs also present codes for tool holders which, as readers anticipate, are the uniquely defined geometry parameters of the tool holders (Appendix B). Therefore, it should not be a challenging task to calculate T-hand-S tool geometry when a certain insert and the corresponding tool holder are selected. In reality, however, this is not nearly the case.


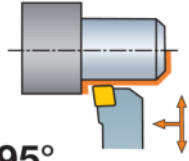

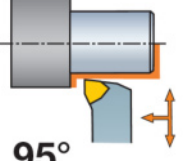

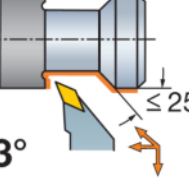

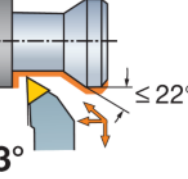

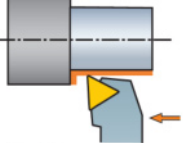

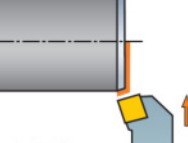

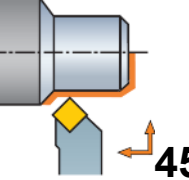

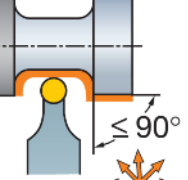

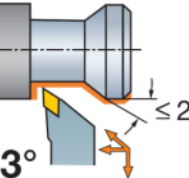

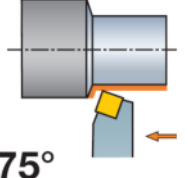

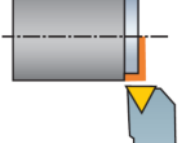

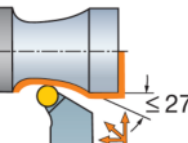


**Fig. 2.16.** Insert is installed and clamped in a tool holder

Reading this, one may wonder what seems to be the problem. To understand the essence of the problem, one should consider how the geometry parameters of the indexable inserts and tool holders are selected and then what is the actual geometry of a single-point cutting tool as an assemblage, i.e., when the chosen insert is placed and clamped into the selected tool holder.

Although the tool catalogs of various tool manufacturers and suppliers present seemingly different approaches to the selection of the indexable inserts and tool holders, the basic logic of these approaches is practically the same. The first step is the selection of the cutting tool as the whole. The only rationale behind the choice of a suitable tool is the tool cutting edge angles of the major,  $\kappa_r$  and minor,  $\kappa_{r1}$  (Fig. 2.1) cutting edges. Table 2.1 shows an example of a common approach to such a selection. As seen, the contour of the part to be machined is the major factor in the selection. A process engineer/technician tries to machine the complete contour with a single tool to reduce the time and increase apparent efficiency of machining (minimize tool changing, simplify programming, reduce inventory of tool holders and inserts, and so on). Even though a selected tool may not be optimal for each particular part of the part contour, a common perception is that the overall efficiency is higher if a tool change can be avoided. Once a suitable tool is chosen, the particular indexable insert (shape) is then selected. Then the insert material, shape of chipbreaker, nose radius, and/or wiper edge (depending on surface finish requirements) and coating are added to the selection depending on the particular merchantability group the work materials falls to (many tool manufacturers and

**Table 2.1.** Selection of the cutting tool based upon the contour of the part

Insert	Tool cutting edge angle	Insert	Tool cutting edge angle
<p>C</p> 	 <p>95°</p>	<p>W</p> 	 <p>95°</p>
<p>V</p> 	 <p>93°</p> <p>≤ 25°</p>	<p>T</p> 	 <p>93°</p> <p>≤ 22°</p>
<p>T</p> 	 <p>91°</p>	<p>S</p> 	 <p>75°</p>
<p>S</p> 	 <p>45°</p>	<p>R</p> 	 <p>≤ 90°</p>
<p>B</p> 	 <p>93°</p> <p>≤ 27°</p>	<p>S</p> 	 <p>75°</p>
<p>T</p> 	 <p>91°</p>	<p>R</p> 	 <p>≤ 27°</p>

suppliers provide their own classification of work materials). Once the insert is finalized, a suitable tool holder to accommodate this insert is then selected.

Note that in the selection process, the tool rake and flank angles are not considered. One may wonder if there is any way to know these angles after the tool is assembled.

#### 2.4.4.1 Geometry Parameters of Indexable Inserts

Appendix B presents the classification of the indexable and tipped cutting inserts according to ANSI and ISO standards. The following parameters of the cutting tool geometry are distinguished by these standards:

- The shape of inserts (Tables B.1 and B.12). This may give only a very vague idea of the tool cutting edge angle because this angle is mainly determined by the tool holder. However, the shape of insert indicates a possible range of the tool cutting edge angle and the tool cutting edge angle of the minor cutting edge variations which is the starting point in the selection of a particular shape. For an insert with a wiper cutting edge, however, the tool cutting edge angle of the major and minor cutting edges are clearly indicated as follows from Tables B.7 and B.20.
- Flank angle. There are eight possible flank angles of standard inserts as follows from Tables B.2 and B.13. Clearly cutting is not possible with a zero clearance angle (N) so the holder *must* provide a certain flank angle needed in practical machining operations. To provide this flank angle, the insert is tilted in the holder so that the rake face becomes “negative” and thus the clearance along the cutting edge is assured. Needless to say, indexable inserts with zero flank angle (N) are the most popular in practice because both sides of the insert can be used, i.e., the number of useful corners doubles. However, this advantage can only be gained if the tool holder is selected properly to provide the optimal flank angle.
- *Rake angle*. This angle is not specified by both standards. Therefore, the words “negative”/“positive” inserts do not have rationale behind them and are thus conditional for indexable inserts with chipbreakers. As seen in Tables B.4 and B.17, inserts are available with flat faces or with a chipbreaker made on one or both rake faces. Although this will be discussed later in the consideration of the influence of the rake angle on the cutting process and its outcome, it is worth mentioning here that an indexable insert of the same shape, size, tolerance, etc. can be made with considerably different chip breakers as shown in Fig. 2.17. It is understood that the rake angle and chip deformation is not the same for all shown inserts.



Fig. 2.17. Various chip breakers made on a square insert

- Nose (corner) radius. Tables B.7 and B.20 shown designation of the nose radius. The ANSI Standard defines this radius in a more accurate way as seen in Fig. B.3.
- Edge preparation. Both standards define edge preparation shapes as shown in Table B.8 and Sect. B.1.2.3. However, the ISO Standard provides the exact shapes and dimensions for edge preparation while the ANSI Standard leaves it to the discretion of insert manufacturers.

#### 2.4.4.2 Geometry Parameters of Tool Holders for Indexable Inserts

Appendix B, Sect. B2 presents the standard classification of the tool holders for indexable inserts. Out of nine compulsory and one optional symbols in this designation, only one directly and one conditionally relate to the tool geometry. Tool style symbol (reference position (3)) defines the tool cutting edge angle as shown in Table A.16 that simplifies the choice of the tool style after the analysis of the part contour (Table 1.1) is done.

Insert clearance symbol (reference position (4)) relates to the insert flank angle. It is not clear, however, how the tool holder supports or modifies this angle. Although, as mentioned above, indexable inserts with zero flank angle (N) are the most popular in practice, it does not follow from the toolholders standard designation what the flank angle (if any) they provide in this most common case. The next section that deals with the tool geometry of the assemblage “insert-toolholder” aims to clarify this important issue.

#### 2.4.4.3 Geometry Parameters of Single Point Tools with Indexable Inserts

The above-discussed process of selection of indexable inserts and toolholders defines the following parameters of the tool geometry:

- The tool cutting edge angles of the major and minor cutting edges
- The nose radius
- The shape of the cutting edge and particularities of edge preparation if used
- The shape of the chipbreaker if used

Three other major parameters of the tool geometry (when the insert is mounted into the toolholder), namely, the rake, flank, and cutting edge inclination angle, are not defined. The next sections are clarify the issue.

#### Rake Angle

Tools manufacturers made distinction between the so-called negative and positive insert geometry as shown in Fig. 2.18. According to this perception, a negative

insert has the normal wedge angle of 90 degrees while this angle is of less than 90 degrees for a positive insert. The negative insert has to be inclined negatively in the toolholder so as to provide a suitable flank angle (clearance) while the positive insert has this clearance built-in.

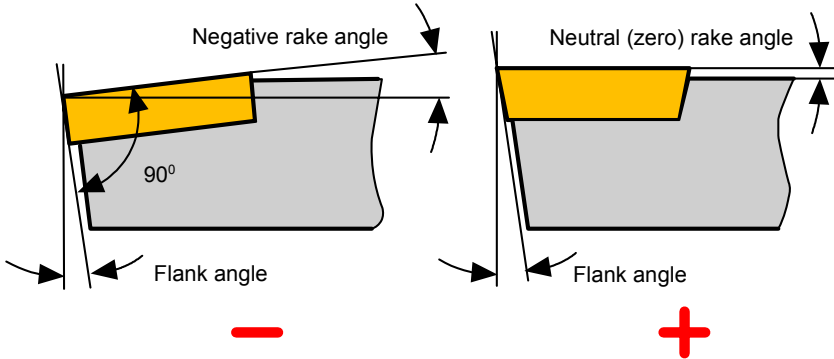


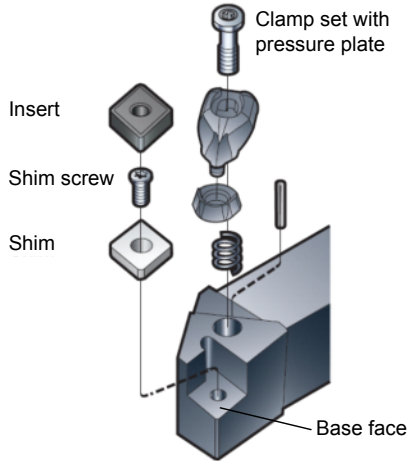
Fig. 2.18. Common perception of negative and positive geometry

In the author's opinion, this perception is misleading. First of all, an insert itself does not have "negative rake." Rather, a presumably negative rake angle is formed only if the insert is set in a tool holder. Second, the so-called positive inserts do not form even apparent positive rake angle. As shown in Fig. 2.18, a zero rake angle cannot be regarded as positive. Moreover, the so-called built-in flank angle (clearance) is often insufficient in many practical applications so that even "a positive insert" must be "inclined negatively" to achieve the optimal flank angle.

### *Flank Angle*

Apart from the rake angle, the actual value of the flank angle (clearance) should be known exactly as this angle strongly affects tool performance. Obtaining this real value for a single-point tool with an indexable insert may present some challenge because this value does not appear in the tool holder designation or in its specifications in the catalogs of tool and toolholder manufacturers. Not only are there no explanations provided on the selection of this important angle in these catalogs and in other training/advertisement brochures, materials, flyers, but also this angle is not even mentioned. Therefore, a need is felt to clarify the issue.

The flank angle of a single-point cutting tool with an indexable insert depends on both the flank angle of the insert (if any) and on the inclination of the base face (Fig. 2.19) of the tool holder. As the flank angle of the insert is always known (Tables B.2 and B.13) as a part of insert designation code, the determination of the flank angle of the tool should not be a problem as far as the inclination of the base face is known. The latter, however, presents a challenge demonstrated by few examples in the following paragraphs.



**Fig. 2.19.** Base face of the tool holder

Sandvik Coromant uses in its toolholder parameters tables two columns designates as  $\gamma$  and  $\lambda_s$ . Each table has a footnote explaining that  $\gamma$  = rake angle (valid with flat insert) and  $\lambda_s$  = angle of inclination. No explanations or clarifying figures are provides for these two angles. Moreover:

- Toolholder does not have the rake angle as it does not have the rake face defined in Sect. 2.1.2 as the surface over which the chip formed in the cutting process slides. Besides, Sect. 2.4.3.1 defines three different rake angles in the corresponding plane of measurement. It is not clear, which particular rake angle is meant.
- Angle of inclination is not defined. Section 2.4.2 defined the cutting edge inclination angle (Fig. 2.13) as the angle between the cutting edge and the reference plane. As tool holders do not have the cutting edge, it is not clear what kind of “angle of inclination” is meant.

Valenite in its catalog (2008) in the dimensions of tool holder lists, without any explanations, two parameters “axial” and “radial” that have the angular dimensions. Although the catalog presents two designation systems for toolholders, none of them corresponds to ISO 5608:1995 (see Appendix A) even to the first approximation. Moreover, the designation for inch inserts (Page B4) implies that the clearance angle can even be negative.

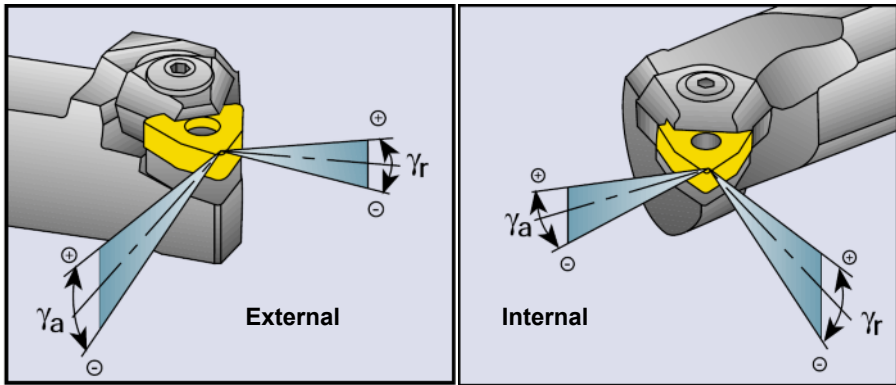
Seco Tools in the list of its toolholder parameters provides two angles, namely  $\gamma_o^\circ$  and  $\gamma_p^\circ$ . Under the picture of the tool in each tool group,  $\gamma_o^\circ$  is defined as the cutting rake and  $\gamma_p^\circ$  as the back rake. The coordinate system, planes, lines, and directions of measurement of these features are not set/explained. Moreover, the term “the cutting rake” is not identified in the above-mentioned ISO and ANSI tool geometry standards and literature on metal cutting.

According to the Bohler turning catalog, practically all of its toolholders are suitable for neutral inserts (N). However, it is not mentioned how the flank angle

(relief) is provided by these tool holders. The same can be said about the Ingersoll turning tool catalog.

Kennametal combines Sandvik Coromant and Seco designations, namely, for some toolholders  $\lambda S^\circ \gamma O^\circ$  and for others  $\gamma F^\circ \gamma P^\circ$  are listed in its catalog. The mentioned angles are not clearly defined or explained.

ISCAR provides an explanation to angles  $\gamma_a$  and  $\gamma_r$  as they appear in its toolholders catalog as shown in Fig. 2.20. Although it is probably the best explanation compare to other companies, it still refers to the rake angle which is true only in a very limited and unpractical case when the insert does not have any chipbreaker. Moreover, it is possible but not easy to correlate these angles with the flank angle of the single-point tool.



**Fig. 2.20.** The meaning of axial,  $\gamma_a$  and radial  $\gamma_r$  angles for external and internal turning according to ISCAR

As the majority of tool manufacturers indicate in their catalogs the axial and radial “rake angles” in the manner shown in Fig. 2.20, these two angles should be regarded as:

- The inclination angle  $\Delta_f$  of the toolholder base face (Fig. 2.19) in the assumed working plane  $P_f$  (Fig. 2.11) that corresponds to the axial inclination angle  $\gamma_a$  for external turning and to radial inclination angle  $\gamma_r$  for internal turning (boring) shown in Fig. 2.20
- the inclination angle  $\Delta_p$  of the toolholder base face (Fig. 2.19) in the assumed back plane  $P_p$  (Fig. 2.12) that corresponds to the radial inclination angle  $\gamma_r$  for external turning and to axial inclination angle  $\gamma_a$  for internal turning (boring) shown in Fig. 2.20

Once a particular tool holder and a suitable cutting insert are chosen, the tool cutting edge angle,  $\kappa_r$  and angles  $\Delta_f$  and  $\Delta_p$  are known. Using Eq. 2.20, one can calculate the tool inclination angle as

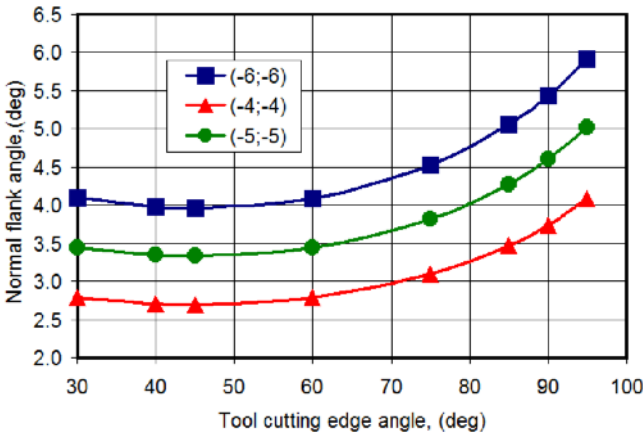
$$\tan \lambda_s = -\sin \kappa_r \tan \Delta_p - \cos \kappa_r \tan \Delta_f \tag{2.22}$$

Using this calculated value, one can combine Eqs. 2.14 and 2.18 to calculate the normal flank angle as

$$\alpha_n = \arctan \frac{1}{\cos \lambda_s (-\cos \kappa_r \cot \Delta_p - \sin \kappa_r \cot \Delta_f)} \tag{2.23}$$

Note that if the selected insert is not neutral (N) but rather has a flank angle, this angle should be added to that calculated using Eq. 2.24.

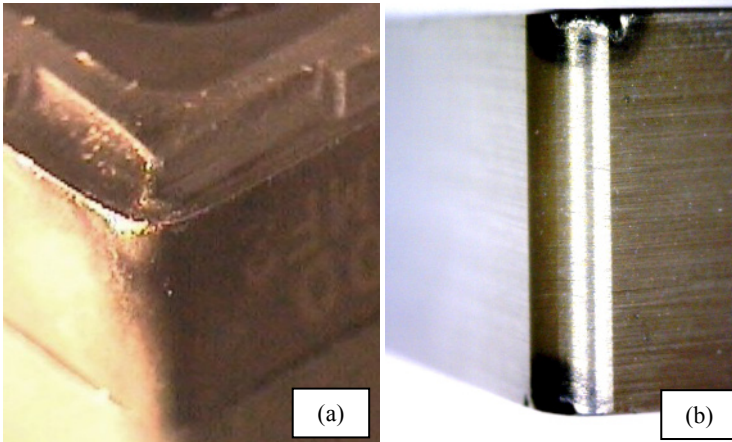
Figure 2.21 shows the results of calculation (using Eq. 2.23) of the T-hand-S normal flank angle for neutral inserts (N) as the function of the tool cutting edge angle,  $\kappa_r$  for various standard  $\Delta_p$  and  $\Delta_f$  ( $-4^\circ, -4^\circ; -5^\circ, -5^\circ; -6^\circ, -6^\circ$ ) commonly used for tool holders. As seen, the normal flank angle is sub-optimal, i.e. it is  $4^\circ-5^\circ$  while the optimal flank angle for machining of many steel grades is  $7^\circ-9^\circ$  and  $10^\circ-12^\circ$  for finishing operations. This causes burn marks on the flank surfaces of many standard inserts as shown in Fig. 2.22. Although such marks are common, tool manufacturers did not correct the flank angle.



**Fig. 2.21.** T-hand-S normal flank angle for various  $\Delta_p$  and  $\Delta_f$  ( $-4^\circ, -4^\circ; -5^\circ, -5^\circ; -6^\circ, -6^\circ$ ) vs the tool cutting edge angle

The issue with insufficient flank angles is very severe in the automotive industry in the boring of cast iron liners. The problem is the high residual stresses imposed by the boring operation. These stresses may cause cracking of the liner during engine assembly which is costly as the manufacturing cost of an engine block is high. The machining residual stresses are caused primarily by two sources: 1) cutting forces, 2) tool flank temperature [10].





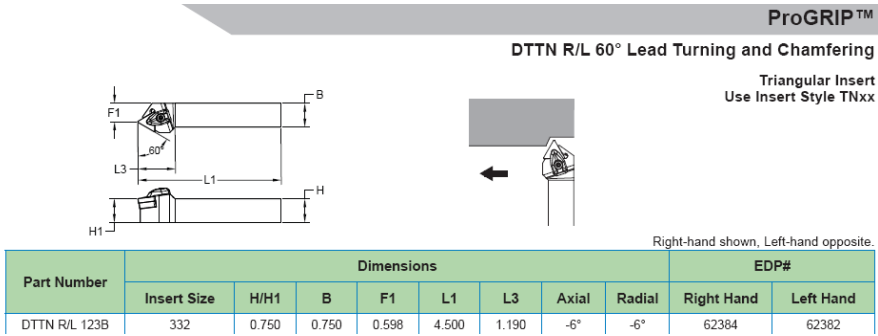
**Fig. 2.22.** Burn marks common for indexable inserts: (a) carbide, and (b) ceramic

In machining of high-yield strength brittle materials such as cast iron, the machining residual stresses due to cutting force are mainly superficial. This is because the amount of heat generated due to plastic deformation is small and the powder-like chip does not create high temperature at the tool chip interface as there is almost no sliding and rubbing between the chip and the tool rake face. This allows machining of cast irons even without MWF. Moreover, these small superficial residual stresses are easily removed by the finishing honing. In contrast, the residual stresses due to high temperature are high. These stresses normally cause distortion and cracking of the machined parts. A logical question rises: “Where is this high temperature coming from in machining of cast iron (engine block liners particularly) when the high-pressure coolant is applied?”

The explanation is surprisingly simple. This phenomenon is known in machining as “springback” (explained in Chap. 3). Because cast iron is of high-yield strength and brittle, it is first deformed by the cutting force just ahead of the cutting edge and then, because the plastic deformation is very small, the material immediately bounces back. When the flank angle is small, the rubbing between this material and tool flank occurs that is the prime cause for high temperature and thus high residual stresses. The only way to reduce these stresses is to increase the normal flank angle. The standard cartridges with neutral inserts, however, do not allow this increase. This “simple” geometry issue costs a lot of money and creates a lot of troubles for automotive companies.

#### 2.4.4.4 Example 2.2

**Problem:** Let a Valenite single point tool with a triangle insert for general turning be selected based on the part configuration. The parameters of the selected tool are shown in Fig. 2.23. Determine the cutting edge inclination and normal flank angles.



**Fig. 2.23.** Parameters of the selected single point tools (from Valenite 2007 catalog)

Solutions:

As seen in Fig. 2.23,  $\Delta_p = -6^\circ$ ,  $\Delta_f = -6^\circ$  and  $\kappa_r = 60^\circ$ . Using Eqs. 2.23 and 2.24, one can calculate that

$$\lambda_s = -\sin \kappa_r \tan \Delta_p - \cos \kappa_r \tan \Delta_f = -\sin 60^\circ \tan(-6^\circ) - \cos 60^\circ \tan(-6^\circ) = 8.17^\circ$$

and

$$\alpha_n = \arctan \frac{1}{\cos \lambda_s (-\cos \kappa_r \cot \Delta_p - \sin \kappa_r \cot \Delta_f)} =$$

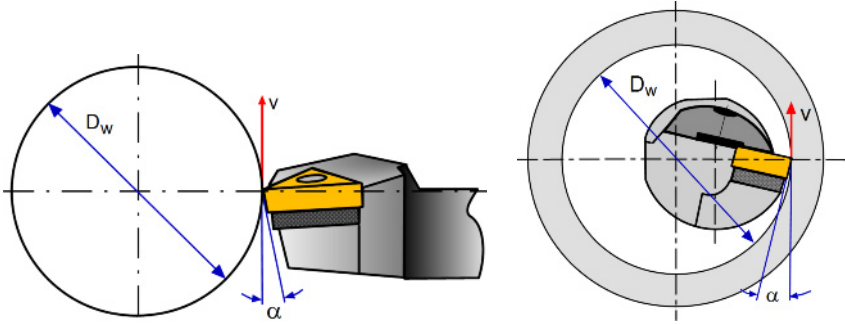
$$\arctan \frac{1}{\cos 8.17^\circ (-\cos 60^\circ \cot(-6^\circ) - \sin 60^\circ \cot(-6^\circ))} = 4.44^\circ$$

## 2.5 Tool-in-machine System (T-mach-S)

### 2.5.1 Angles

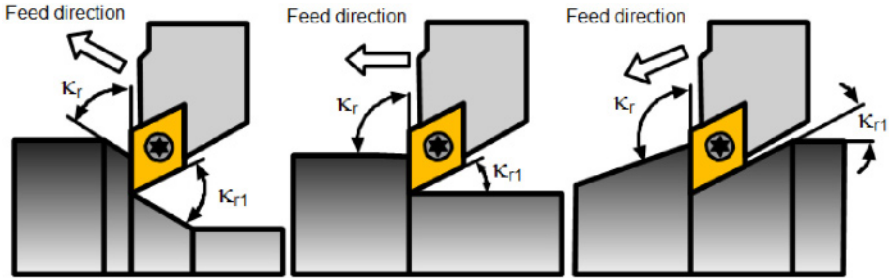
The previous considerations of the cutting tool geometry are related to the T-hand-S in which the tool tip (point 1 in Fig. 2.11) and the axis of rotation of the workpiece are located on the same reference plane as shown in Fig. 2.24. As the direction of the cutting feed  $v_f$  is parallel to the axis of rotation of the workpiece, the cutting edge angles of the major and the minor cutting edge is determined as shown in Fig. 2.11.

In reality, however, the position of the cutting insert in the toolholder and setting of the tool holder in the machine can change the T-hand-S geometry of the cutting insert. It is the common practice of tool design that the insert is manufactured with a zero flank angle and then the flank angle is achieved by locating the insert in the tool holder. Moreover, in modern CNC machines the direction of the feed motion may vary with the tool path depending upon the



**Fig. 2.24.** Tool tip and the axis of rotation locate at the same reference plane

configuration of the machined part so that of the cutting tool angles change according to the actual direction of the cutting feed as shown in Fig. 2.25.



**Fig. 2.25.** Showing the variation of the tool cutting edge angles of the major and minor cutting edges with the direction of the cutting feed in a typical CNC copying operation

Besides the considered case of CNC machining, the T-mach-S (also known as the setting system) is used when the tool is set in the machine or a cartridge is set in the tool body (milling cutter, boring bar) so that the tool geometry established in the T-hand-S is altered, i.e., one or more important tool angles are changed. Although there can be a great number of various scenarios, two most common are:

- Tool re-positioning in the reference plane that changes the tool cutting edge angle  $\kappa_r$
- Tool re-positioning in the back plane that changes the rake and the flank angles

Experience shows that all other cases are combinations of these two basic cases.

Figure 2.26a shows the case where the geometrical axis of the cutter is perpendicular to the axis of rotation of the workpiece. Obviously, the cutting edge angles  $\kappa_r$  and  $\kappa_{r1}$  of the major and minor cutting edges are as in T-hand-S. Figure 2.26b,c shows two cases where the tool, installed in the machine, is rotated by an angle  $\omega_r$  in the clockwise and counterclockwise directions. When the former is the case then the cutting edge angles in T-mach-S is calculated as

$$\kappa_{r\omega} = \kappa_r - \omega_r \text{ and } \kappa_{r1\omega} = \kappa_{r1} + \omega_r \tag{2.24}$$

and when the latter is the case then

$$\kappa_{r\omega} = \kappa_r + \omega_l \text{ and } \kappa_{r1\omega} = \kappa_{r1} - \omega_l \tag{2.25}$$

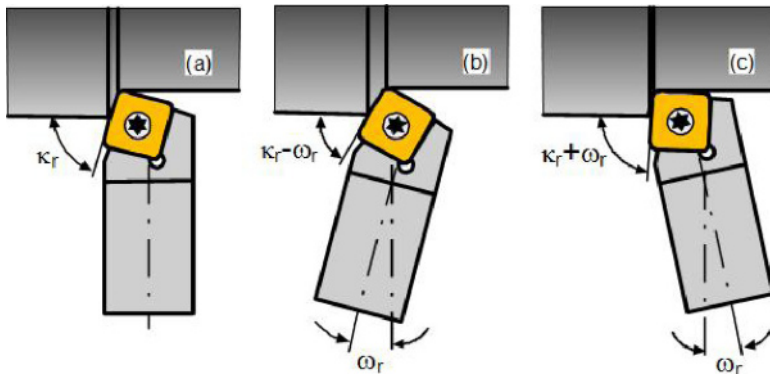


Fig. 2.26. The tool cutting edge angle depends on the setting angle

As mentioned, in T-hand-S, the tool tip is assumed to be in the same reference plane as the axis of rotation of the workpiece (Fig. 2.24). In practice, however, it is not always the case. The tool tip, after being installed in the machine, is often found to be shifted in the vertical direction with respect to the mentioned reference plane (Fig. 2.27). In many axial tools, the cutting edge(s) is intently located with a certain shift from this reference plane (i.e., in twist drills). This shift causes changes in the cutting angles which should be accounted for.

The modified angles are calculated using two additional angles [1, 9] calculated using models shown in Fig. 2.27:

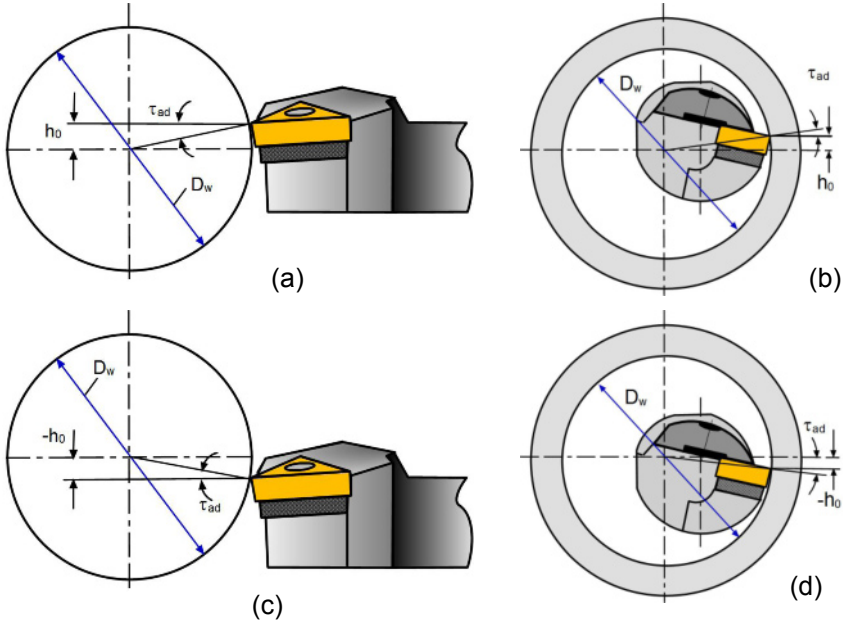
The surplus angle  $\tau_{ad}$  is calculated as

$$\tau_{ad} = \arctan \frac{h_o}{D_w/2} \tag{2.26}$$

where  $h_o$  is vertical shift of the drill point,  $D_w$  is the diameter of the workpiece.

The modification angle  $\tau_{ap}$  is calculated as

$$\tau_{ap} = \arctan \frac{\tan \lambda_s}{\sin \kappa_r} \tag{2.27}$$



**Fig. 2.27.** Vertical shift of the tool tip with respect to the reference plane through the axis of rotation of the workpiece for single-point turning and boring tools

Knowing these two angles due to the tool vertical shift, one can calculate the modified angles of the cutting tool geometry as:

The modified tool cutting edge angle

$$\kappa_{r-m} = \arctan \left( \frac{\tan \kappa_r \cos(\tau_{ap} - \tau_{ad})}{\cos \tau_{ap}} \right) \quad (2.28)$$

and Eq. 2.29 is general as it is valid for any sign of the inclination angle  $\lambda_s$  (including  $\lambda_s = 0$ ) and vertical shift  $h_o$ . In fact, when  $\lambda_s = 0$ ,  $\tau_{ap} = 0$  according to Eq. 2.28 so Eq. 2.29 becomes

$$\kappa_{r-m} = \arctan(\tan \kappa_r \cos \tau_{ad}) \quad (2.29)$$

When  $h_0=0$  (no vertical shift) then  $\tau_{ad} = 0$  according to Eq. 2.27, so that  $\kappa_{r-m} = \kappa_r$  according to Eq. 2.30. It also follows from Eq. 2.29 that when the inclination angle  $\lambda_s$  and vertical shift  $h_o$  are of opposite signs then  $\kappa_{r-m} < \kappa_r$  while when these signs are the same then  $\kappa_{r-m} > \kappa_r$ .

The modified cutting edge inclination angle

$$\lambda_{s-m} = \arctan(\sin \kappa_{r-m} \tan(\tau_{ap} - \tau_{ad})) \quad (2.30)$$

Equation 2.31 is valid for any sign of the inclination angle  $\lambda_s$  (including  $\lambda_s = 0$ ) and vertical shift  $h_o$ .

The modified orthogonal rake angle

$$\gamma_{o-m} = \arctan \left( \tan \kappa_{r-m} \tan \lambda_{s-m} + \frac{\tan(\gamma_p + \tau_{ad})}{\cos \kappa_{r-m}} \right) \quad (2.31)$$

where the back rake angle  $\gamma_p$  calculates using Eq. 2.7. Equation 2.32 is valid for any sign of the inclination angle  $\lambda_s$  (including  $\lambda_s = 0$ ) and vertical shift  $h_o$ . When  $h_o = 0$  (no vertical shift) then  $\tau_{ad} = 0$  according to Eq. 2.27,  $\kappa_{r-m} = \kappa_r$  and  $\lambda_{s-m} = \lambda_s$  so that  $\gamma_{o-m} = \gamma_o$  according to Eq. 2.18.

The modified orthogonal flank angle

$$\alpha_{o-m} = \arctan \left( \tan(\alpha_p - \tau_{ad}) \cos \kappa_{r-m} \right) \quad (2.32)$$

where the back rake angle  $\alpha_p$  calculates using Eq. 2.19. Equation 2.33 is valid for any sign of the inclination angle  $\lambda_s$  (including  $\lambda_s = 0$ ) and vertical shift  $h_o$ . When  $h_o = 0$  (no vertical shift) then  $\tau_{ad} = 0$  according to Eq. 2.27,  $\kappa_{r-m} = \kappa_r$  and  $\lambda_{s-m} = \lambda_s$  so that  $\alpha_{o-m} = \alpha_o$  according to Eq. 2.19.

Figure 2.28 shows deviations  $\Delta\alpha_n$  of the tool cutting edge angle,  $\Delta\kappa_r$ , orthogonal rake angle,  $\Delta\gamma_o$ , orthogonal flank angle,  $\Delta\alpha_o$ , and cutting edge inclination angle,  $\Delta\lambda_s$  as functions of the tool cutting edge angle when a single point cutting tool having normal rake angle,  $\gamma_n = 10^\circ$ , normal flank angle,  $\alpha_n = 8^\circ$ , and cutting edge inclination angle,  $\lambda_s = 10^\circ$ , is installed with  $h_o = 2mm$  (Fig. 2.27a). The diameter of the workpiece  $D_w = 30mm$ .

As seen in Fig. 2.28, the cutting tool inclination angle changes significantly while deviations of the orthogonal rake and flank angles diminish in the region of the widely used tool cutting edge angle. However, the deviation of the flank angle cannot be ignored for tools with neutral (N) indexable inserts.

### 2.5.2 Example 2.3

**Problem:** Let the cutting tool discussed in Example 2 be elevated by  $h_o = 1mm$  with respect to the reference plane containing the axis of rotation of the workpiece (Fig. 2.27) in machining of a workpiece having diameter  $D_w = 40mm$ . Determine the geometry of this tool in the tool-in-machine system.

**Solution:** The tool selected in Example 2 has the following geometrical parameters: normal flank angle  $\alpha_n = 44.4^\circ$ , cutting edge inclination angle  $\lambda_s = 8.17^\circ$ , tool cutting edge angle  $\kappa_r = 60^\circ$ , back rake angle  $\gamma_p = -6^\circ$ .

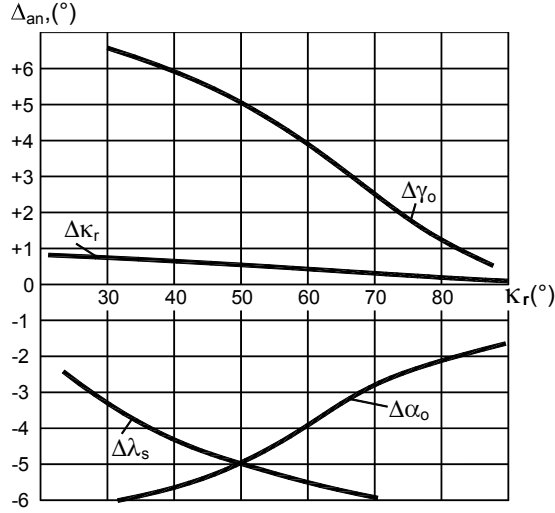


Fig. 2.28. Influence of the tool cutting edge angle on the tool geometry parameters

The surplus angle calculates as per Eq. 2.27

$$\tau_{ad} = \arctan \frac{h_o}{D_w/2} = \arctan \frac{1}{40/2} = 2.86^\circ$$

The modification angle  $\tau_{ap}$  calculates using Eq. 2.28 as

$$\tau_{ap} = \arctan \frac{\tan \lambda_s}{\sin \kappa_r} = \arctan \frac{\tan 8.17^\circ}{\sin 60^\circ} = 9.41^\circ$$

The modified tool cutting edge angle calculates using Eq. 2.29 as

$$\kappa_{r-m} = \arctan \left( \frac{\tan \kappa_r \cos(\tau_{ap} - \tau_{ad})}{\cos \tau_{ap}} \right) = \arctan \left( \frac{\tan 60^\circ \cos(9.41^\circ - 2.86^\circ)}{\cos 9.41^\circ} \right) = 60.17^\circ$$

Modified cutting edge inclination angle calculates using Eq. 2.31 as

$$\lambda_{s-m} = \arctan \left( \sin \kappa_{r-m} \tan(\tau_{ap} - \tau_{ad}) \right) = \arctan \left( \sin 60.17^\circ \tan(9.41^\circ - 2.86^\circ) \right) = 5.68^\circ$$

The modified orthogonal rake angle calculates using Eq. 2.32 as

$$\gamma_{o-m} = \arctan \left( \tan \kappa_{r-m} \tan \lambda_{s-m} + \frac{\tan(\gamma_p + \tau_{ad})}{\cos \kappa_{r-m}} \right) =$$

$$\arctan \left( \tan 60.17^\circ \tan 5.68^\circ + \frac{\tan((-6^\circ) + 2.86^\circ)}{\cos 60.17^\circ} \right) = -2.20^\circ$$

The modified normal rake angle calculates using Eq. 2.16 as

$$\gamma_{n-m} = \arctan(\tan \gamma_{o-m} \cos \lambda_{s-m}) = \arctan(\tan(-2.20^\circ) \cos 5.68^\circ) = -2.19^\circ$$

The back flank angle calculates using Eq. 2.12 as

$$\alpha_p = \arctan \left( \frac{\tan \alpha_n}{\cos \kappa_r} \right) = \arctan \left( \frac{\tan 4.44^\circ}{\cos 60^\circ} \right) = 8.83^\circ$$

The modified orthogonal flank angle calculates using Eq. 2.33 as

$$\alpha_{o-m} = \arctan(\tan(\alpha_p - \tau_{ad}) \cos \kappa_{r-m}) =$$

$$\arctan(\tan(8.83 - 2.85) \cos 60.17) = 2.98^\circ$$

And finally, the modified normal flank angle calculates using Eq. 2.14 as

$$\alpha_{n-m} = \arctan \left( \frac{\tan \alpha_{o-m}}{\cos \lambda_{s-m}} \right) = \arctan \left( \frac{\tan 3.07^\circ}{\cos 5.68^\circ} \right) = 3.08^\circ$$

## 2.6 Tool-in-use System (T-use-S)

The T-use-S considers the geometry of the cutting tool accounting for machining kinematics. When the cutting tool is being used, the actual direction of the primary motion and the feed motion may differ from the assumed directions in the T-hand-S and T-mach-S. Moreover, the actual tool path may be different compare to that assumed in the T-hand-S and T-mach-S due to several feed motions applied simultaneously as multi-axis machines are widely used. As the parameters of the tool geometry are affected by the actual resultant motion of the cutting tool relative to the workpiece, a new system, referred to as the tool-in-use system (T-use-S) coordinate system should be considered and the corresponding tool angles, referred to as the working angles, should be established in this new system.



Although such a system has been known for years, its importance is growing due to the following facts:

- Demand for increasing productivity of machining has been resulting in the development of stronger tool materials with advanced coatings that allow higher feed rates. Today, these rates, particularly in machining aluminum alloys in the aerospace and automotive industries, are so great that they can significantly affect the direction of the resultant cutting motion.
- Wide use of multi-axis machines results in the utilization of multi-feed cutting to produce the so-called sculptured surfaces. These feeds also change the direction of the resultant motion that affects the cutting tool geometry.
- Wide use of CNC machines and production lines gave rise to so-called contour machining where the same tool is used to machine the complete contour or profile of a part as shown in Fig. 2.25. As such, the tool geometry parameters vary depending upon a particular segment of the contour because the tool cutting edge angles of the major and minor cutting edges vary as well as the cutting feed.

### 2.6.1 Reference Planes

The basis of the T-use-S is the tool in use reference plane  $P_{re}$ . Similar to  $P_r$ , the position of this reference plane is defined as being perpendicular to the vector of the resultant motion. Once  $P_{re}$  is defined, the following system of planes (similar to that shown in Fig. 2.12) can be defined:

- The T-use-S *working plane*,  $P_{ef}$  is perpendicular to the reference plane  $P_{re}$  and contains the direction of the resultant motion.
- The T-use-S *cutting edge plane*  $P_{se}$  is perpendicular to  $P_{re}$ , and contains the major cutting edge. Similar to the T-hand-S, if the major cutting edge is a straight line then the tool cutting edge plane is the same for any point of this edge. This plane is fully defined by two intersecting lines, namely, by the straight cutting edge and the vector of the cutting speed. If, however, the major cutting edge is not straight then there are an infinite number of tool cutting edge planes. As such, a tool cutting edge plane should be determined for each point of the curved cutting edge as the plane which tangent to the cutting edge at the point of consideration and which contains the vector of the cutting speed (or perpendicular to the main reference plane).
- The T-use-S *back plane*  $P_{pe}$  is perpendicular to  $P_{re}$  and  $P_{fe}$ .
- Perpendicular to the projection of the cutting edge into the reference plane is the T-use-S *orthogonal plane*  $P_{oe}$ . When the cutting edge is not straight, there are an infinite number of orthogonal planes defined for each given point of the curved cutting edge, and the orthogonal plane is defined as the plane which is perpendicular to the tangent to the projection of the cutting edge into the reference plane edge at the point of consideration.

- The T-use-S *cutting edge normal plane*  $P_{ne}$ . According to ISO and ANSI standards [3, 7], this plane is identical to the cutting edge normal plane defined in the T-hand-S, i.e.,  $P_{ne} \equiv P_n$ . In the author's opinion, this notion is incorrect as it is not based on the physics of the metal cutting process. This physics implies that the proper rake and flank angles in the T-use-S are measured in a plane containing the resultant direction of chip flow. As  $P_{ne}$  defined by the abovementioned standards does not contain this direction, it lacks physical sense. In the author's opinion,  $P_{ne}$  should be defined as to be perpendicular to the equivalent cutting edge (discussed later).

The angles of the cutting tool in the T-use-S are defined in these planes in the same manner as in the T-hand-S.

### 2.6.2 The Concept

The foregoing analysis implies that the basis of the T-use-S is the proper determination of the reference plane  $P_{re}$ . To do that, the direction of the resultant motion should be identified. As discussed in Appendix A (Fig. A.7), this direction, defined by the directional vector  $\mathbf{v}_e$  is the vectorial sum of the directional vector of prime motion  $\mathbf{v}$  and the directional vector of the resultant feed motion  $\mathbf{v}_f$  [9], i.e.,

$$\mathbf{v}_e = \mathbf{v} + \mathbf{v}_f \quad (2.33)$$

This directional vector is always tangential to the trajectory of the resultant tool motion.

As the flank angle (clearance) is to clear a certain motion, the following equation for the T-use-S flank angle can be written on the basis of Eq. 2.34

$$\alpha_e = \alpha \pm \alpha_{vf} \quad (2.34)$$

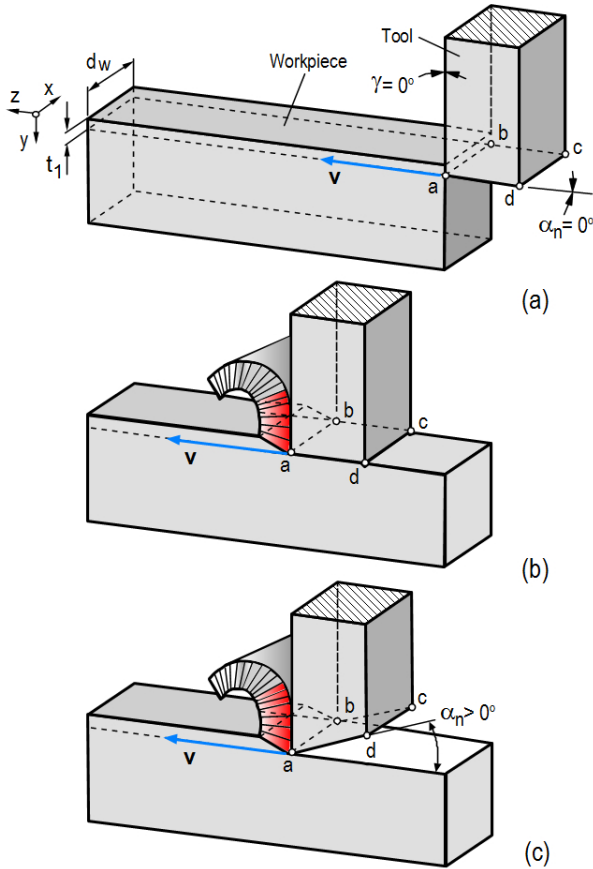
Depending on particular direction(s) of feed motion(s), the kinematic flank angle due to these motions may increase or decrease the T-hand-S flank angle. This is accounted for by the  $\pm$  sign in Eq. 2.35.

### 2.6.3 Modification of the T-hand-S Tool Geometry

Figure 2.29 presents the simplest example of a shaping operation where the prime motion is straight having velocity  $\mathbf{v}$ . As seen in Fig. 2.29a, a square bar stock is used as a tool. The side face of this bar stock is used as the rake face having cutting edge  $ab$  and thus the rake angle  $\gamma$  is zero. The square face of this bar stock  $abcd$  is used as the flank face so the flank angle  $\alpha$  is also zero. The tool thus formed is set to cut the chip having chip thickness  $t_f$ .

When the tool moves in the direction of the prime motion (along the z-axis) with velocity  $\mathbf{v}$  and the chip is formed (Fig. 2.29b), the force (energy) needed for tool penetration into the workpiece consists of three parts: (1) the force (energy)

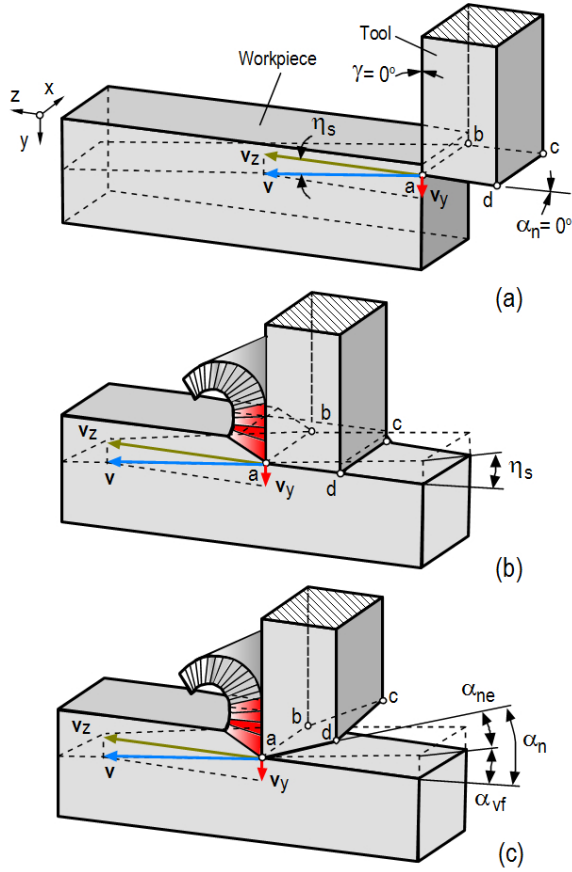
needed for chip formation, i.e., for separation of the layer being removed (having width  $d_w$  and height  $t_1$ ) from the rest of the workpiece, (2) the friction force (energy) due to friction at the tool-chip interface over the rake face and (3) the friction force (energy) due to friction of the flank face  $abcd$  and the machined surface. Note that such machining is possible only theoretically where it can be assumed for the sake of discussion that no elastic recovery (springback) of the work material occurs (the work material is perfectly plastic).



**Fig. 2.29.** Formation of the tool from a square bar stock in planing

Out of these three forces (energies), the first and second are unavoidable as it represents the essence of the cutting process. In contrast, the friction force on the tool flank  $abcd$  must be significantly reduced for the very existence of the process. To do that, the flank surface should always be made with a certain flank angle (relief)  $\alpha > 0^\circ$  as shown in Fig. 2.29c. The square bar stock having  $\alpha > 0^\circ$  thus becomes the cutting tool.

The above example implies that the major distinguishing feature of the cutting tool is the flank face having a flank angle  $\alpha > 0^\circ$ . The rake angle can be positive,



**Figure 2.30.** Sense of the kinematic flank angle

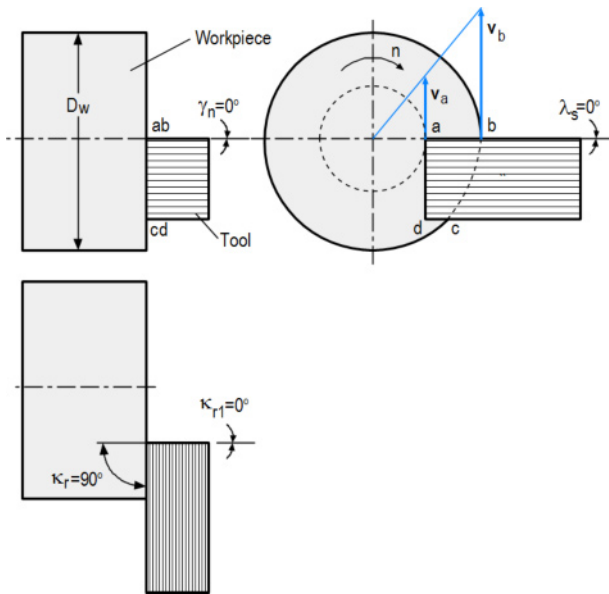
zero, or negative (the practical range of  $\gamma$  is from  $-40^\circ$  to  $+30^\circ$ ) as this angle does not affect the very existence of the cutting process.

Consider the next scenario, where the tool and workpiece are the same as shown in Fig. 2.29a, but the direction of the prime motion is as shown in Figure 2.30a. As can be seen, this direction is no more along the z-axis so the velocity  $v$  of this motion can be considered as the vectorial sum of the velocities along the z- and y-axes. The motion having velocity  $v_y$  can be thought of as the feed velocity. Figure 2.30(b) shows why the machining is impossible in principle with that tool having a zero T-hand-S flank angle. As clearly seen, the T-hand-S zero flank angle becomes negative, i.e., interference of the flank face  $abcd$  and the machined surface takes place. Therefore, the feed motion modifies the T-hand-S flank angle. It is clear, however, that if the velocity  $v_z$  is directed upward, the T-hand-S zero flank angle would be positive and machining is quite possible with this tool having the T-hand-S zero flank angle. This explains the sign  $\pm$  of  $\alpha_{vf}$  in Eq. 2.35.

Figure 2.30c shows a case where the tool is provided with a positive T-hand-S normal flank angle (relief)  $\alpha_n$ . Due to the motion  $v_y$ , the T-use-S normal flank angle calculates as

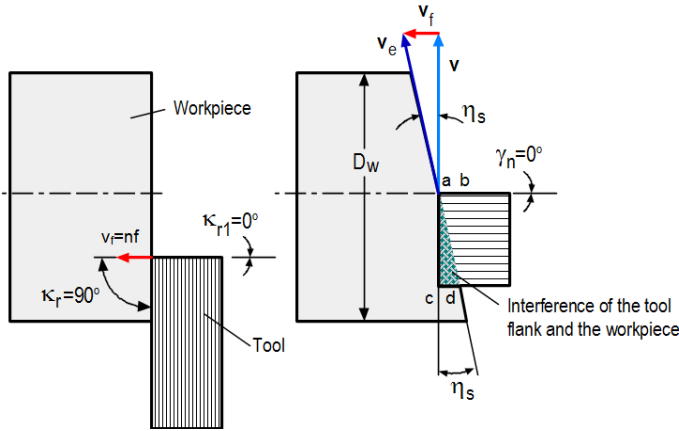
$$\alpha_{ne} = \alpha_n - \alpha_{vf} \tag{2.35}$$

To understand a modification of the T-hand-S geometry due to the feed motion in practice of machining, one can consider turning with the same tool made of a square bar stock [9]. Figure 2.31 shows an arrangement in turning where a hypothetical tool made of a square bar stock is clamped in the tool post of a lathe so that its side edge  $ab$  is horizontal and passes through the center of rotation of the workpiece. The workpiece of  $D_w$  diameter is clamped in the spindle and rotates with  $n$  r.p.m. in the direction indicated in Fig. 2.31. In this arrangement (kinematics of turning is discussed in Appendix A), the following parameters of the T-hand-S tool geometry are achieved: the normal flank angle  $\alpha_n = 0^\circ$ , the normal rake angle  $\gamma_n = 0^\circ$ , the tool cutting edge angle  $\kappa_r = 90^\circ$ , the tool cutting edge angle of the minor cutting edge  $\kappa_{r1} = 0^\circ$ , the cutting edge inclination angle  $\lambda_s = 0^\circ$ . In this arrangement, surface  $abcd$  plays a role of the flank face. As long as there is no feed motion, this surface just rubs against the face of the workpiece.



**Fig. 2.31.** Initial arrangement of a hypothetical tool made of a square bar stock and the workpiece in turning

Figure 2.32 shows what happens if the feed motion with velocity  $v_f = fn$  (known as the feed rate as discussed in Appendix A) is applied to the tool-workpiece arrangements shown in Fig. 2.31. As clearly seen, the T-hand-S zero flank angle



**Fig. 2.32.** Interference of the tool flank *abcd* and the workpiece when the feed is applied

becomes negative, i.e., interference of the flank face *abcd* and the machined surface takes place, that makes machining physically impossible in full analogy with Figure 2.30b.

In full analogy with the discussion on Figure 2.30c, Figure 2.30 shows a case when the tool is provided with a positive T-hand-S normal flank angle (relief)  $\alpha_n$ . Due to the motion  $v_y$ , the T-use-S normal flank angle calculates as

$$\alpha_{ne} = \alpha_n - \alpha_{vf} = \alpha_n - \eta_s \tag{2.36}$$

where angle  $\eta_s$  calculates as [1]

$$\tan \eta_s = \frac{v}{v_f} = \frac{f}{\pi D_w} \tag{2.37}$$

where  $f$  and  $D_w$  are the feed per revolution and diameter of the workpiece. Equation 2.38 is a reasonable approximation for most practical machining application where cutting tools have small inclination angles  $\lambda_s$ .

Note that Eq. 2.37 is valid only for the considered case, i.e., when a tool with  $\kappa_r = 0^\circ$ . In the general case, a model shown in Fig. 2.34 should be considered. As follows from this model, the rake and the flank angles in the T-use-S in the working plane  $P_f$  as shown in Fig. 2.34 is calculated as

$$\gamma_{fe} = \gamma_f + \eta_s \tag{2.38}$$

$$\alpha_{fe} = \alpha_f - \eta_s \tag{2.39}$$

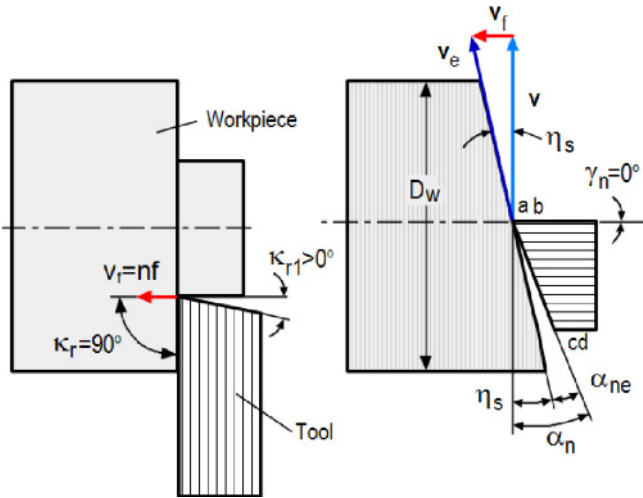


Fig. 2.33. Sense of the kinematic flank angle due to feed motion

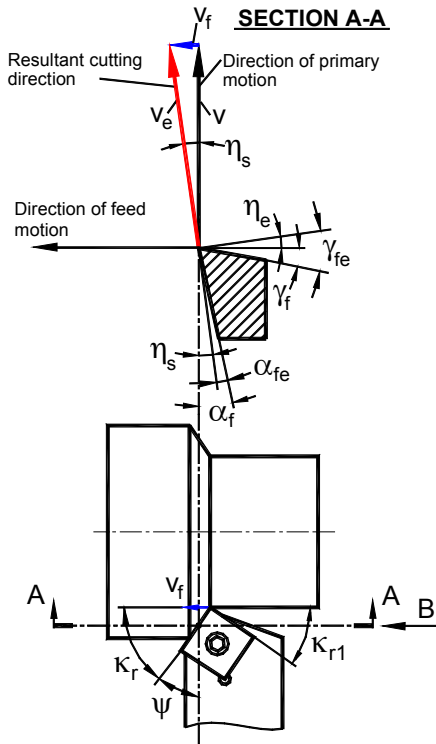
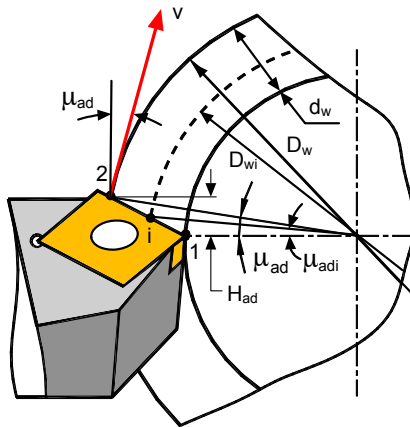


Fig. 2.34. Sense of kinematic rake and flank angles in the general case

**2.6.4 Kinematic Angles**

Three kinematic angles are normally considered [9] as they might play an important role in the formation of the state of stress in the deformation zone, direction of chip flow and tool-workpiece contact conditions. Figure 2.34 shows the sense of the kinematic angles in turning.

Figure 2.35, which is VIEW B on Fig. 2.34 (enlarged and revolved 90° clockwise for clarity) reveals another aspect of the T-use-S, namely that the vector of the cutting speed,  $v$  does not follow the vertical direction (the z-axis). In Fig. 2.35 it is shown for the tool periphery point 2. Being always perpendicular to the radius of rotation, this vector makes a certain angle  $\mu_{ad}$  with the z-axis. It also follows from Fig. 2.35 that this angle varies over the cutting edge. Being zero at point 1, it gradually increases reaching it maximum at point 2. As a result, the kinematic angles vary over the cutting edge as they are functions of this angle.



**Fig. 2.35.** VIEW B in Fig. 2.32

Figure 2.35 allows one to calculate the angle between the vector of the cutting speed and the z-axis for any point I located on the cutting edge 1–2 as

$$\mu_{adi} = acr \sin \left[ \sin \tau_{\mu} \left( \sqrt{1 - e_{\mu i}^2 \sin^2 \tau_{\mu}} - e_{\mu i} \cos \tau_{\mu} \right) \right] \tag{2.40}$$

where auxiliary angles  $\tau_{\mu}$  and  $e_{\mu}$  are calculated as

$$\tau_{\mu} = \arctan \left( \frac{\tan \lambda_s}{\sin \kappa_r} \right) \tag{2.41}$$

and



$$e_{\mu_i} = 1 - \frac{2d_w}{D_{wi}} \quad (2.42)$$

The cutting edge inclination angle  $\lambda_{sei}$  is the angle between the cutting edge and the plane perpendicular to the resultant cutting direction. It is calculated as [1]

$$\lambda_{sei} = \cos \kappa_r \cos \lambda_s \sin \eta_{si} + \sin \kappa_r \cos \lambda_s \sin \mu_{adi} \cos \eta_{si} + \sin \lambda_s \cos \eta_{si} \cos \mu_{adi} \quad (2.43)$$

where

$$\eta_{si} = \arctan \left( \frac{v_f}{v_i} \right) = \arctan \left( \frac{f}{\pi D_{wi}} \right) \quad (2.44)$$

In practice, however, this angle is calculated for periphery point 2 (Fig. 2.35). In this case, Eq. 2.41 becomes

$$\mu_{ad} = \arctan \left( \frac{2d_w \sin \lambda_s}{D_w \sin \kappa_r \cos \lambda_s} \right) \quad (2.45)$$

In practice, the inclination angle  $\lambda_s$  is small for general turning tools so the variation of  $\lambda_{se}$  over the cutting edge can be safely neglected. This is not the case, however, with many other tools such as drills, milling tools, hobs, etc., where this variation must be considered in an analysis of cutting tool geometry and its influence on the cutting process.

In a particular case when  $\lambda_s = 0$ , as it follows from Eq. 2.46,  $\mu_{ad}$  then it follows from Eq. 2.44 that

$$\lambda_{se} = \cos \kappa_r \sin \eta_s \quad (2.46)$$

Kinematic rake angle calculates as

$$\gamma_{ei} = \arcsin \sqrt{1 - \sin^2 \gamma_n \cos^2 \lambda_{sei}} \left[ \sin \left( \kappa_r + \arctan \left( \frac{\tan \lambda_s}{\cos \gamma_n} \right) \right) \sin \eta_{si} + \cos \left( \kappa_r + \arctan \left( \frac{\tan \lambda_s}{\cos \gamma_n} \right) \right) \cos \eta_{si} \sin \mu_{adi} \right] + \sin \gamma_n \cos \lambda_s \cos \eta_{si} \sin \mu_{adi} \quad (2.47)$$

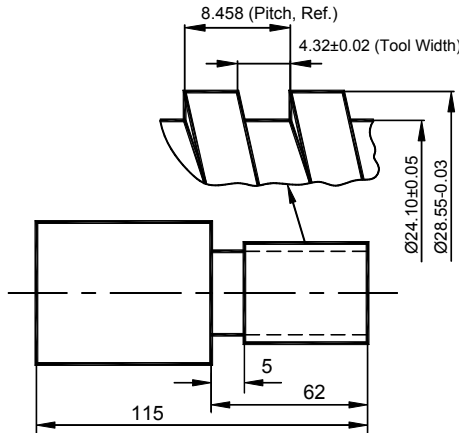
Kinematic flank angle calculates as

$$\alpha_{ei} = \arccos \frac{2\pi \sin \kappa_r + \cos \kappa_r \sin \mu_{adi} - \tan \alpha_n \cos \mu_{di}}{\sqrt{(1 + 4\pi^2) (\sin^2 \kappa_r + (\cos \kappa_r \sin \mu_{adi} - \tan \alpha_n \cos \mu_{di})^2)}} \quad (2.48)$$

The use of the T-use-S makes sense when one of the kinematic parameters in a particular machining operation is unusually great. For example, the velocity of the cutting feed ( $v_f$  in Fig. 2.34) is normally small compare to the cutting speed. However, in thread cutting operations, this velocity is great and significantly affects the cutting geometry causing possible interference if no special measures were taken in the design of the flanks of the thread cutter. The same can be said when the direction of the feed velocity changes significantly in machining. Often this happens in machining of so-called sculpture surfaces having complicated shapes. One has to remember that, once unique, machining of sculptured surfaces has become a common operation on many CNC machines and machining centers. As such, tool layouts should be carefully analyzed to avoid the interference of the tool with the workpiece and to follow up significant changes in the cutting tool geometry which may result in tool failure.

**2.6.5 Example 2.4**

Problem: Determine the flank angle which should be applied for the leading side edge of a tool for cutting a square-shaped thread with parameters shown in Fig. 2.36 if the recommended flank angle for the work material is  $\alpha_{rc}=8^\circ$ .



**Fig. 2.36.** Profile of the thread to be cut

Solution: We should note that the outside diameter of thread is  $D_o = 28.55\text{mm}$  and its inside diameter is  $D_i = 24.1\text{mm}$ . The pitch of the thread is  $P = 8.458\text{mm}$ .

The kinematic angle  $\eta_s$  is given by Eq. 2.45 where the feed velocity calculates (see Appendix A) as  $v_f = \frac{nf}{1000}$  (m/min) if  $f$  in mm/rev or  $v_f = \frac{nf}{12}$  (fpm) if  $f$  in ipr;  $n$  is the rotational speed of the workpiece (r.p.m.); the cutting speed calculates as (see Appendix A)  $v = \frac{\pi Dn}{1000}$  (m/min) if  $D$  in mm or  $v = \frac{\pi Dn}{12}$  fpm if  $D$  in inches.

In thread machining, the feed per revolution is always equal to the thread lead. For one-start threads, the lead is equal to the pitch, therefore  $f = 8.458\text{mm/rev}$  and, therefore, finally

$$\eta_s = \arctan \frac{P}{\pi D_i} = \arctan \frac{8.458}{3.14 \cdot 24.1} = 6.38^\circ \approx 7^\circ$$

Note that the inside diameter is  $D_i = 24.1\text{mm}$  was used to calculate  $\eta_{ad}$  as the most critical diameter where  $\eta_{ad}$  is at maximum.

The flank angle in the tool in the T-hand-S which should be applied to the leading side edge calculates as

$$\alpha_{fe} = \alpha_f + \eta_s = 7 + 8 = 15^\circ$$

Figure 2.37 shows the profile of the cutting tool and the flank angle in the T-use-S system. Note that the flank angle is considered in the tool orthogonal plane  $P_o$  which for the considered case coincides with the cutting edge normal plane since  $\lambda_s=0$ .

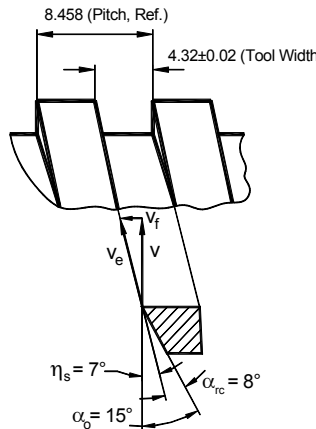


Fig. 2.37. The flank angle in the T-hand-S

## 2.7 Avalanched Representation of the Cutting Tool Geometry in T-hand-S

The advanced representation of the cutting tool geometry is based upon the vector analysis that allows one to simplify significantly the analysis of the tool geometry. The use of the vector analysis allows one to:

2. Visualize and generalize tool geometry representation. This is of prime importance for programming automated tool sharpening machines as well as tool inspection machines.
3. Simplify significantly the derivations and final formulae for tool geometry calculations. This is particularly true for complicated cutting geometries involving 3D considerations and complicated rake and flank surfaces.
4. Include simple and complicated tool (workpiece) motions in the geometry (both tool and machined part) analysis. This is particularly important when several feed motions are involved or when the parameters of the prime motion are results of a combination of several motions. This will be demonstrated further in the consideration of the advanced tool geometry analysis on T-use-S.

According to Radzevich [11], Mozhaev [12] was the first who applied the elements of vector analysis to the consideration of the geometry of cutting tools. Further significant developments are achieved due to fundamental works by Rodin [13] and Radzevich [14]. Application of this technique to the comprehensive analysis of gundrill geometry resulted in the development of a new line of such tools [15, 16].

Before proceeding further, the reader might find it useful to revise some basics of vector analysis presented in Appendix C. This appendix contains the complete information the reader needs to understand the following sections.

### 2.7.1 Basic Tool Geometry

Consider the tool geometry parameters discussed in Sect. 2.4.2.1 using the method of vector analysis. Figure 2.38 shows the basic parameters in the T-hand-S. The first and foremost step in any application of vector analysis is to establish a suitable coordinate system. In Fig. 2.38, the right-hand coordinate system is set as shown: the z-axis is perpendicular to the reference plane, the x-axis is along the projection of the cutting edge 1–2 into the reference plane, and the y-axis is perpendicular to this projection.

To consider the relationships between rake angles in the standard section planes, the following vectors are introduced in the xyz coordinate system:

- Vector  $\mathbf{p}$  is directed along the cutting edge. The length of this vector is selected so that its projection into the x-axis is

$$\mathbf{p} = \mathbf{i} - \mathbf{k} \tan \lambda_s \quad (2.49)$$

- Vector  $\mathbf{n}$  is directed along the rake face following the line of intersection of this plane with the orthogonal plane drawn through point  $O$  of the cutting edge. The length of this vector is selected so that its projection into the  $y$ -axis is

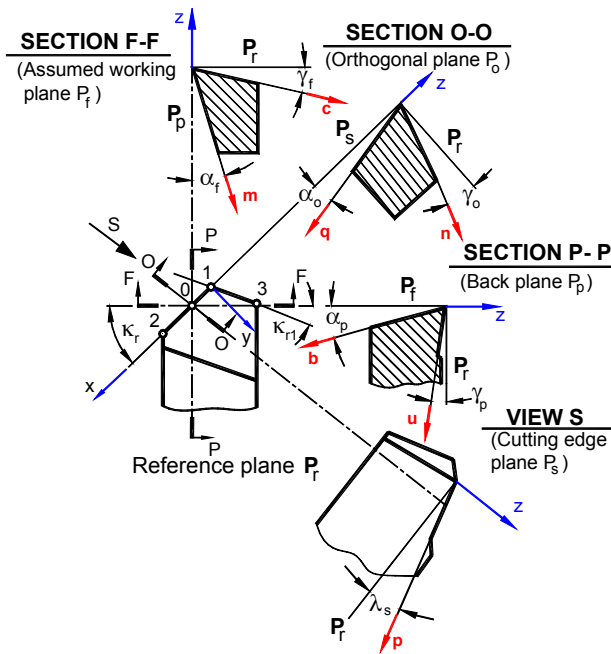
$$\mathbf{n} = \mathbf{j} - \mathbf{k} \tan \gamma_o \tag{2.50}$$

- Vector  $\mathbf{c}$  is directed along the rake face following the line of intersection of this plane with the working plane drawn through point  $O$  of the cutting edge. The length of this vector is selected so that its projection into the  $z$ -axis is  $\tan \gamma_f$ , then

$$\mathbf{c} = -\mathbf{i} \cos \kappa_r + \mathbf{j} \sin \kappa_r - \mathbf{k} \tan \gamma_f \tag{2.51}$$

- Vector  $\mathbf{u}$  is directed along the rake face following the line of intersection of this plane with the back plane drawn through point  $O$  of the cutting edge. The length of this vector is selected so that its projection into the  $z$ -axis is  $\tan \gamma_p$ , then

$$\mathbf{u} = \mathbf{i} \sin \kappa_r + \mathbf{j} \cos \kappa_r - \mathbf{k} \tan \gamma_p \tag{2.52}$$



**Fig. 2.38.** System of tool angles in the defined planes in T-hand-S used in the vector analysis of the major cutting edge

Consider vectors  $\mathbf{p}$ ,  $\mathbf{n}$ , and  $\mathbf{c}$ . Because these vectors belong to the same plane (the rake face), their triple product is zero, i.e.,

$$(\mathbf{p} \times \mathbf{n}) \cdot \mathbf{c} = \begin{vmatrix} 1 & 0 & \tan \lambda_p \\ 0 & 1 & -\tan \gamma_o \\ -\cos \kappa_r & \sin \kappa_r & -\tan \gamma_f \end{vmatrix} = \quad (2.53)$$

$$-\tan \gamma_f + \tan \gamma_o \sin \kappa_r + \tan \lambda_s \cos \kappa_r = 0$$

that yields

$$\tan \gamma_f = \tan \gamma_o \sin \kappa_r + \tan \lambda_s \cos \kappa_r \quad (2.54)$$

Equation 2.55 correlates the rake angles in the orthogonal and in the working planes.

Consider vectors  $\mathbf{p}$ ,  $\mathbf{n}$ , and  $\mathbf{u}$ . Because these vectors belong to the same plane (the rake face), their triple product is zero, i.e.,

$$(\mathbf{p} \times \mathbf{n}) \cdot \mathbf{u} = \begin{vmatrix} 1 & 0 & \tan \lambda_p \\ 0 & 1 & -\tan \gamma_o \\ \sin \kappa_r & \cos \kappa_r & -\tan \gamma_p \end{vmatrix} = \quad (2.55)$$

$$-\tan \gamma_p + \tan \gamma_o \cos \kappa_r - \tan \lambda_s \sin \kappa_r = 0$$

that yields

$$\tan \gamma_p = \tan \gamma_o \cos \kappa_r - \tan \lambda_s \sin \kappa_r \quad (2.56)$$

Equation 2.57 correlates the rake angles in the orthogonal and in the back planes.

To consider the relationships between flank angles in the standard section planes, the following vectors are introduced in the xyz coordinate system:

- Vector  $\mathbf{q}$  is directed along the flank face following the line of intersection of this plane with the orthogonal plane drawn through point  $O$  of the cutting edge. If the length of this vector is selected so that its projection into y-axis is equal to 1, then

$$\mathbf{q} = \mathbf{j} - \mathbf{k} \cot \alpha_o \quad (2.57)$$

- Vector  $\mathbf{m}$  is directed along the flank face following the line of intersection of this plane with the working plane drawn through point  $O$  of the cutting edge. The length of this vector is selected so that its projection into the z-axis is  $\cot \alpha_f$ , then

$$\mathbf{m} = -\mathbf{i} \cos \kappa_r + \mathbf{j} \sin \kappa_r - \mathbf{k} \cot \alpha_f \quad (2.58)$$

- Vector  $\mathbf{b}$  is directed along the flank face following the line of intersection of this plane with the back plane drawn through point  $O$  of the cutting edge. The length of this vector is select so that its projection into the  $z$ -axis is  $\cot \alpha_p$ , then

$$\mathbf{b} = \mathbf{i} \sin \kappa_r + \mathbf{j} \cos \kappa_r - \mathbf{k} \cot \alpha_p \quad (2.59)$$

Consider vectors  $\mathbf{p}$ ,  $\mathbf{q}$ , and  $\mathbf{m}$ . Because these vectors belong to the same plane (the flank face), their triple product is zero, i.e.,

$$\begin{aligned} (\mathbf{p} \times \mathbf{q}) \cdot \mathbf{m} &= \begin{vmatrix} 1 & 0 & \tan \lambda_p \\ 0 & 1 & -\cot \alpha_o \\ -\cos \kappa_r & \sin \kappa_r & -\cot \alpha_f \end{vmatrix} = \\ & -\cot \alpha_f + \cot \alpha_o \sin \kappa_r + \tan \lambda_s \cos \kappa_r = 0 \end{aligned} \quad (2.60)$$

that yields

$$\cot \alpha_f = \cot \alpha_o \sin \kappa_r + \tan \lambda_s \cos \kappa_r \quad (2.61)$$

Equation 2.62 correlates the flank angles in the orthogonal and in the working planes.

Consider vectors  $\mathbf{p}$ ,  $\mathbf{q}$ , and  $\mathbf{b}$ . Because these vectors belong to the same plane (the flank face), their triple product is zero, i.e.,

$$\begin{aligned} (\mathbf{p} \times \mathbf{q}) \cdot \mathbf{b} &= \begin{vmatrix} 1 & 0 & \tan \lambda_p \\ 0 & 1 & -\cot \alpha_o \\ \sin \kappa_r & \cos \kappa_r & -\cot \alpha_p \end{vmatrix} = \\ & -\cot \alpha_p + \cot \alpha_o \cos \kappa_r - \tan \lambda_s \sin \kappa_r = 0 \end{aligned} \quad (2.62)$$

that yields

$$\cot \alpha_p = \cot \alpha_o \cos \kappa_r - \tan \lambda_s \sin \kappa_r \quad (2.63)$$

Equation 2.64 correlates the flank angles in the orthogonal and in the back planes.

To consider the relationships between angles of the minor cutting edge 1–3 in the standard section planes, the following vectors are additionally introduced in the  $xyz$  coordinate system as shown in (Fig. 2.39):

- Vector  $\mathbf{p}_1$  is directed along the minor cutting edge. The length of this vector is selected so that its projection into the  $z$ -axis is  $\tan \lambda_{1s}$ . Therefore

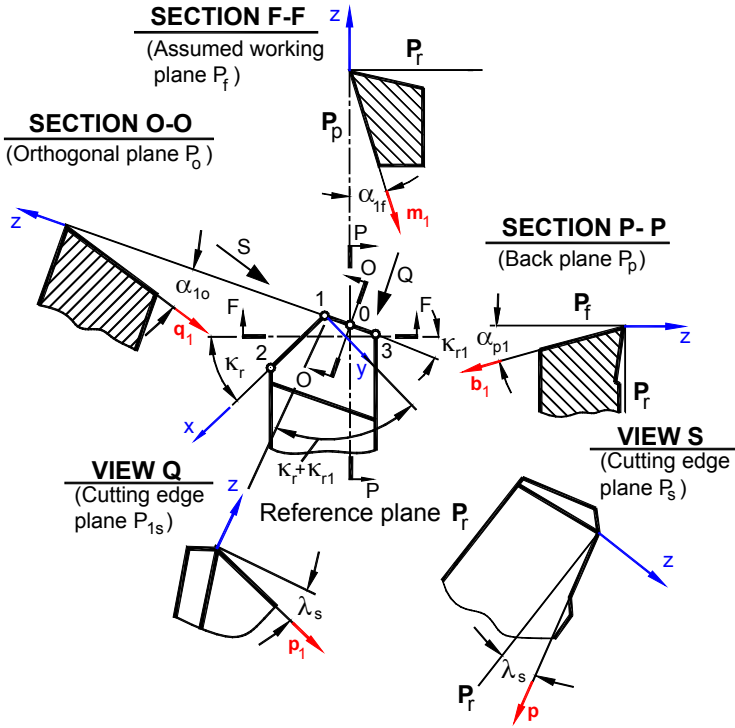


Fig. 2.39. System of tool angles in the defined planes in T-hand-S used in the vector analysis of the minor cutting edge

$$p_1 = -i \cos(\kappa_r + \kappa_{r1}) + j \sin(\kappa_r + \kappa_{r1}) - k \tan \lambda_{1s} \tag{2.64}$$

- Vector  $q_1$  is directed along the flank face of the minor cutting edge following the line of intersection of this plane with the orthogonal plane drawn through point  $\theta$  of the cutting edge. If the length of this vector is selected so that its projection into y-axis is equal to  $\tan \alpha_{1o}$ , then

$$q_1 = i \sin(\kappa_r + \kappa_{r1}) + j \cos(\kappa_r + \kappa_{r1}) - k \cot \alpha_{1o} \tag{2.65}$$

- Vector  $m_1$  is directed along the flank face of the minor cutting edge following the line of intersection of this plane with the working plane drawn through point  $\theta$  of the cutting edge. The length of this vector is selected so that its projection into the z-axis is  $\cot \alpha_{1f}$ , then

$$m_1 = i \cos \kappa_r - j \sin \kappa_r - k \cot \alpha_{1f} \tag{2.66}$$

- Vector  $b_1$  is directed along the flank face of the minor cutting edge following the line of intersection of this plane with the back plane



through point  $O$  of the cutting edge. The length of this vector is select so that its projection into the  $z$ -axis is  $\cot\alpha_{1p}$ , then

$$\mathbf{b}_1 = \mathbf{i} \sin \kappa_r + \mathbf{j} \cos \kappa_r - \mathbf{k} \cot \alpha_{1p} \quad (2.67)$$

Consider vectors  $\mathbf{p}$  (Eq. 2.50),  $\mathbf{n}$  (Eq. 2.51) and  $\mathbf{p}_1$ . Because these vectors belong to the same plane (the rake face), their triple product is zero, i.e.,

$$\begin{aligned} (\mathbf{p} \times \mathbf{n}) \cdot \mathbf{p}_1 &= \begin{vmatrix} 1 & 0 & \tan \lambda_p \\ 0 & 1 & -\tan \gamma_o \\ -\cos(\kappa_r + \kappa_{r1}) & \sin(\kappa_r + \kappa_{r1}) & -\tan \lambda_{1p} \end{vmatrix} = \\ & -\tan \lambda_{1p} + \tan \gamma_o \sin(\kappa_r + \kappa_{r1}) + \tan \lambda_s \cos(\kappa_r + \kappa_{r1}) = 0 \end{aligned} \quad (2.68)$$

Using Eq. 2.69 one can write an equation that correlates the inclination angle of the minor cutting edge,  $\lambda_{1s}$  with the known parameters of the tool geometry as

$$\tan \lambda_{1s} = \tan \gamma_o \sin(\kappa_r + \kappa_{r1}) + \tan \lambda_s \cos(\kappa_r + \kappa_{r1}) \quad (2.69)$$

Consider vectors  $\mathbf{p}_1$ ,  $\mathbf{q}_1$  and  $\mathbf{m}_1$  (Fig. 2.39). Because these vectors belong to the same plane (the flank face of the minor cutting edge), their triple product is zero, i.e.,

$$\begin{aligned} (\mathbf{p}_1 \times \mathbf{q}_1) \cdot \mathbf{m}_1 &= \begin{vmatrix} -\cos(\kappa_r + \kappa_{r1}) & \sin(\kappa_r + \kappa_{r1}) & -\tan \lambda_{1s} \\ \sin(\kappa_r + \kappa_{r1}) & \cos(\kappa_r + \kappa_{r1}) & -\cot \alpha_{1o} \\ \cos \kappa_r & -\sin \kappa_r & -\cot \alpha_{1f} \end{vmatrix} = \\ \cos^2(\kappa_r + \kappa_{r1}) \cot \alpha_{1f} + \sin \kappa_r \cos(\kappa_r + \kappa_{r1}) \cot \alpha_{1o} + \sin^2(\kappa_r + \kappa_{r1}) \cot \alpha_{1f} + \\ \tan \lambda_{1s} \sin \kappa_r \sin(\kappa_r + \kappa_{r1}) + \tan \lambda_{1s} \cos \kappa_r \cos(\kappa_r + \kappa_{r1}) &= 0 \end{aligned} \quad (2.70)$$

Using Eq. 2.71 one can write an equation that correlates the flank angle of the minor cutting edge in the working plane,  $\alpha_{1f}$  with other known parameters of the tool geometry as

$$\cot \alpha_{1f} = \cot \alpha_{1o} \sin \kappa_{r1} - \tan \lambda_{1s} \cos \kappa_{r1} \quad (2.71)$$

Consider vectors  $\mathbf{p}_1$ ,  $\mathbf{m}_1$ , and  $\mathbf{b}_1$  (Fig. 2.39). Because these vectors belong to the same plane (the flank face of the minor cutting edge), their triple product is zero, i.e.

$$(\mathbf{p}_1 \times \mathbf{m}_1) \cdot \mathbf{b}_1 = \begin{vmatrix} -\cos(\kappa_r + \kappa_{r1}) & \sin(\kappa_r + \kappa_{r1}) & -\tan \lambda_{1s} \\ \sin(\kappa_r + \kappa_{r1}) & \cos(\kappa_r + \kappa_{r1}) & -\cot \alpha_{1o} \\ \sin \kappa_r & \cos \kappa_r & -\cot \alpha_{1p} \end{vmatrix} = \tag{2.72}$$

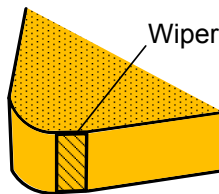
$$\begin{aligned}
 & \cos^2(\kappa_r + \kappa_{r1}) \cot \alpha_{1p} + \cos \kappa_r \cos(\kappa_r + \kappa_{r1}) \cot \alpha_{1o} + \sin^2(\kappa_r + \kappa_{r1}) \cot \alpha_{1p} - \\
 & \sin \kappa_r \sin(\kappa_r + \kappa_{r1}) \cot \alpha_{1o} + \tan \lambda_{1s} \cos \kappa_r \sin(\kappa_r + \kappa_{r1}) \\
 & + \tan \lambda_{1s} \sin \kappa_r \cos(\kappa_r + \kappa_{r1}) = 0
 \end{aligned}$$

Using Eq. 2.73, one can write an equation that correlates the flank angle of the minor cutting edge in the back plane,  $\alpha_{1p}$  with other known parameters of the tool geometry as

$$\cot \alpha_{1p} = \cot \alpha_{1o} \cos \kappa_{r1} - \tan \lambda_{1s} \sin \kappa_{r1} \tag{2.73}$$

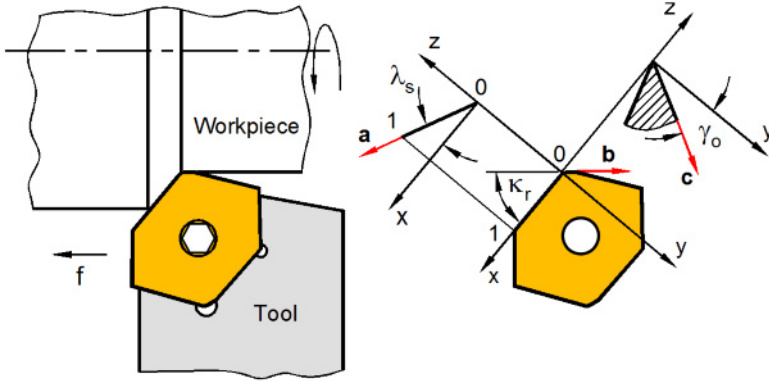
**2.7.2 Determination of Cutting Tool Angles Relation for a Wiper Cutting Insert**

The idea behind wiper inserts is not new. It has been used for years on face milling operations and finds its application in turning. The principle behind a wiper insert for turning concerns the use of a modified tool nose radius. A standard insert will, under magnification, leave a series of peaks and troughs across the cut surface; a wiper uses trailing radii that follow the cutting nose as shown in Fig. 2.40. These remain in contact with the workpiece and 'wipe' or smooth the peaks to leave an improved finish. Therefore, in terms of the tool geometry, a distinctive feature of such an insert is that the minor cutting edge must be parallel to the axis of rotation of the workpiece in turning or must be parallel to the machined surface in face milling. This section considers the conditions to assure such a feature.



**Fig. 2.40.** The wiper part of the modified nose radius of a turning insert

Figure 2.41 shows a cutting tool with a wiper-type insert. The objective of the present analysis is to establish the basic geometrical relationship between the tool cutting edge angle  $\kappa_r$ , inclination angle  $\lambda_s$  and normal rake angle  $\gamma_n$  to assure that the wiper edge is parallel to the axis of rotation of the workpiece. To do that, the xyz coordinate system is set with the origin in point  $\theta$  which is the point of intersection of the major and minor cutting edges. The x-axis of this coordinate



**Figure 2.41.** Geometry of a wiper type cutting insert

system is directed along the major cutting edge. The minor cutting edge is parallel to the rotational axis of the workpiece.

Let vector  $\mathbf{a}$  be directed along the major cutting edge. Its magnitude is selected so that its projection on the  $x$ -axis is equal to 1. Then this vector can be expressed through its components as

$$\mathbf{a} = \mathbf{i} + \mathbf{k} \tan \lambda_s \quad (2.74)$$

Let vector  $\mathbf{b}$  be directed along the wiper (minor) cutting edge. Its magnitude is selected so that its projection on the  $x$ -axis is equal to 1. Then this vector can be expressed through its components as

$$\mathbf{b} = -\mathbf{i} + \mathbf{j} \tan \kappa_r \quad (2.75)$$

Let vector  $\mathbf{c}$  be directed along the intersection line between the rake face and the  $zy$  plane (the orthogonal plane) as shown in Figure 2.41. Its magnitude is selected so that its projection on the  $y$ -axis is equal to 1. Then this vector can be expressed through its components as

$$\mathbf{c} = \mathbf{j} - \mathbf{k} \tan \gamma_o \quad (2.76)$$

Because vectors  $\mathbf{a}$ ,  $\mathbf{b}$ , and  $\mathbf{c}$  lie in the same plane (the  $xy$  plane), their triple product is zero, i.e.,

$$(\mathbf{a} \times \mathbf{c}) \cdot \mathbf{b} = \begin{vmatrix} 1 & 0 & \tan \lambda_s \\ 0 & 1 & -\tan \gamma_o \\ -1 & \tan \kappa_r & 0 \end{vmatrix} = \tan \kappa_r \tan \gamma_o + \tan \lambda_s = 0 \quad (2.77)$$

Equation 2.78 gives the geometrical relationships between the tool cutting edge angle  $\kappa_r$ , inclination angle  $\lambda_s$ , and orthogonal rake angle  $\gamma_o$ . Out of these three

angles, only two can be selected independently and the third has to be determined using this equation. For example, if, as usually found in practice, angles  $\kappa_r$  and  $\gamma_o$  are selected by the tool designer, then angle  $\lambda_s$  is calculated as

$$\lambda_s = -\tan \kappa_r \tan \gamma_o \tag{2.78}$$

In a particular case, when  $\kappa_r \neq 0$  and  $\lambda_s = 0$ ,

$$\tan \kappa_r \tan \gamma_o = 0 \tag{2.79}$$

So  $\gamma_o = 0$  as expected to assure that the wiper cutting edge is parallel to the axis of rotation.

It should be pointed out that Eq. 2.79 is valid for any kind of cutting tools with wiper inserts including face milling cutters and axial end tools. In the latter, the side cutting edge plays the role of the wiper insert.

### 2.7.3 Determination of Cutting Tool Angles for a Single-point Tool

In Sect. 2.5, the geometry of a single-point cutting tool installed or designed so that its point locates above or below the reference plane contacting the axis of rotation of the workpiece is discussed. Consider the same case using vector analysis.

Figure 2.42 shows a single-point tool with a zero inclination angle ( $\lambda_s = 0$ ) in the T-hand-S (i.e., the major cutting edge 1-2 is horizontal). In the T-mach-S, the tool is installed so that its tip 1 locates at distance  $h_0$  to the reference plane containing the axis of rotation of the workpiece. The problem is to determine the cutting edge inclination angle  $\lambda_{sp}$  due to this shift and the angles in the T-mach-S.

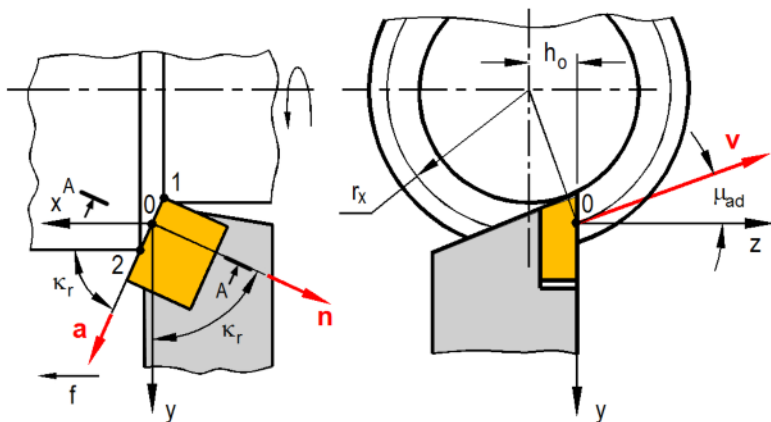


Fig. 2.42. Geometrical model of a single-point cutting tool having  $0 < \kappa_r < \pi/2$

The right-hand xyz coordinate system with the origin in the point of interest  $\theta$  is set up as follows: the x-axis is directed along with the feed motion; the y-axis is

chosen to be perpendicular to the axis of rotation of the workpiece and thus to the x-axis with sense as shown in Fig. 2.42; the z-axis is perpendicular to the x- and y-axes, with sense as shown in Fig. 2.42. Let vector  $\mathbf{a}$  be directed along the major cutting edge. Its magnitude is selected so that its projection on the x-axis is equal to 1. Then, this vector can be expressed through its components as

$$\mathbf{a} = \mathbf{i} + \mathbf{j} \tan \kappa_r \quad (2.80)$$

As shown in Fig. 2.42, the vertical shift of the cutting edge is  $h_o$  and the radius of the point  $O$  is  $r_x$ . The vector of the cutting velocity,  $\mathbf{v}$  in the point  $O$  is perpendicular to the line connecting this point with the axis of the workpiece as shown in Fig. 2.42. Let  $\mu_{ad}$  be the angle between  $\mathbf{v}$  and the z-axis. This angle is calculated as

$$\sin \mu_{ad} = \frac{h_o}{r_x} \quad (2.81)$$

If the magnitude of vector  $\mathbf{v}$  is selected so that its projection on the z-axis is equal to 1, then this vector can be expressed through its components as

$$\mathbf{v} = -\mathbf{j} \tan \mu_{ad} + \mathbf{k} \quad (2.82)$$

Angle between vectors  $\mathbf{a}$  and  $\mathbf{v}$  is  $\pi/2 - \lambda_{sp}$  so one can write

$$\cos \angle(\mathbf{a}\mathbf{v}) = \cos \left( \frac{\pi}{2} + \lambda_{sp} \right) = -\sin \lambda_{sp} = \frac{\mathbf{a} \cdot \mathbf{v}}{\|\mathbf{a}\| \cdot \|\mathbf{v}\|} \quad (2.83)$$

Expressing the scalar product and vector modules through the vectors' components given by Eqs. 2.81 and 2.83, one can obtain

$$\sin \lambda_{sp} = \frac{-\tan \mu_{ad} \tan \kappa_r}{\pm \sqrt{(1 + \tan^2 \mu_{ad})(1 + \tan^2 \kappa_r)}} = \mp \sin \kappa_r \sin \mu_{ad} \quad (2.84)$$

Equation 2.85 allows one to calculate the inclination angle for any given point of the cutting edge 1-2 in the T-mach-S.

Two important conclusions can be drawn from Eq. 2.85. First, although the inclination angle in the T-hand-S is zero, in the T-mach-S it is negative and it varies along the cutting edge due to the variation of angle  $\mu_{ad}$ . As seen, the maximum  $\lambda_{sp}$  is in point 1 and the minimum is in point 2. Second, if the tool is installed below the discussed reference plane then angle  $\mu_{ad}$  is negative. As such,  $\lambda_{sp}$  is positive changing from its maximum in point 1 to its minimum at point 2.

As discussed earlier in Sect. 2.5, if a single-point tool is installed as shown in Fig. 2.42, its rake and flank angles in the T-mach-S would not be the same as those defined in the T-hand-S. This is because the main reference plane  $P_r$  defined to be

perpendicular to the assumed direction of primary motion is no more horizontal because the vector of the cutting speed  $\mathbf{v}$  is not perpendicular to the tool base as shown in Fig. 2.42. The normal rake angle is defined earlier as the angle between the reference plane and the rake face plane in the direction of the cutting edge normal plane.

Therefore, to appreciate the change in the rake and flank angles in the T-mach-S, one should consider the angle  $\xi_{ad}$  between the tool cutting edge planes in the T-hand-S and the T-mach-S as shown in Fig. 2.43. Knowing this angle, one can determine the normal rake and flank angles in the said T-mach-S as

$$\gamma_{nw} = \gamma_n + \xi_{ad} \tag{2.85}$$

$$\alpha_{nw} = \alpha_n - \xi_{ad} \tag{2.86}$$

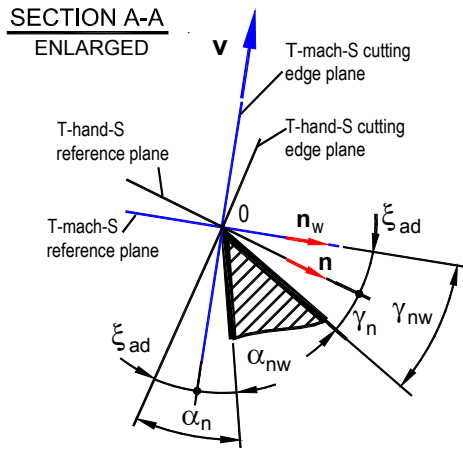


Fig. 2.43. SECTION A-A in Fig. 2.42

Angle  $\xi_{ad}$  can be determined as the angle between the normals to the tool cutting edge planes in the T-hand-S and the T-mach-S. Its magnitude of a normal  $\mathbf{n}$  to the tool cutting edge plane in the T-hand-S is selected so that its projection on the y-axis is equal to 1, then this vector can be expressed through its components as

$$\mathbf{n} = -\mathbf{i} \tan \kappa_r + \mathbf{j} \tag{2.87}$$

A normal  $\mathbf{n}_w$  to the tool cutting edge plane the T-mach-S is determined by the cross product of vectors  $\mathbf{v}$  and  $\mathbf{a}$  located in this plane:

$$\mathbf{n}_w = \mathbf{v} \times \mathbf{a} = \begin{vmatrix} \mathbf{i} & \mathbf{j} & \mathbf{k} \\ 0 & -\tan \mu_{ad} & 1 \\ 1 & \tan \kappa_r & 0 \end{vmatrix} = \mathbf{i}(-\tan \kappa_r) + \mathbf{j} + \mathbf{k} \tan \mu_{ad} \tag{2.88}$$

Angle  $\xi_{ad}$  is determined then as the angle between normals  $\mathbf{n}$  and  $\mathbf{n}_w$ .

$$\tan \xi_{ad} = \frac{\|\mathbf{n} \times \mathbf{n}_w\|}{\mathbf{n} \cdot \mathbf{n}_w} \quad (2.89)$$

The vector product of  $\mathbf{n}$  and  $\mathbf{n}_w$  is calculated as

$$\mathbf{n} \times \mathbf{n}_w = \begin{vmatrix} \mathbf{i} & \mathbf{j} & \mathbf{k} \\ -\tan \kappa_r & 1 & 0 \\ -\tan \kappa_r & 1 & \tan \mu_{ad} \end{vmatrix} = \mathbf{i}(-\tan \mu_{ad}) + \mathbf{j} \tan \kappa_r \tan \mu_{ad} \quad (2.90)$$

and so its magnitude is

$$\|\mathbf{n} \times \mathbf{n}_w\| = \sqrt{\tan^2 \kappa_r + \tan^2 \kappa_r \tan^2 \mu_{ad}} = \frac{\tan \mu_{ad}}{\cos \kappa_r} \quad (2.91)$$

The scalar product of  $\mathbf{n}$  and  $\mathbf{n}_w$  is calculated as

$$\|\mathbf{n} \cdot \mathbf{n}_w\| = \tan^2 \kappa_r + 1 = \frac{1}{\cos^2 \kappa_r} \quad (2.92)$$

Substituting Eqs. 2.92 and 2.93 into 2.90, one can obtain

$$\tan \xi_{ad} = \frac{\tan \mu_{ad} / \cos \kappa_r}{1 / \cos^2 \kappa_r} = \tan \mu_{ad} \cos \kappa_r \quad (2.93)$$

Analysis of Eq. 2.94 shows that angle  $\xi_{ad}$  varies along the cutting edge as it depends on angle  $\mu_{ad}$ , which is a function of current radius  $r_x$  (Fig. 2.42). Thus, the rake and flank angles also vary along the cutting edge (Eqs. 2.86 and 2.87). As such, the maximum  $\gamma_{nw}$  and the minimum  $\alpha_{nw}$  are at point 1 while the opposite is true at point 2. The opposite is the case when the cutting tool shown in Fig. 2.42 is installed below the centerline.

Consider the case with a single-point tool having angle  $\kappa_r > \pi/2$  while other parameters and designations are kept the same as shown in Fig. 2.44. In this model, the approach angle  $\varphi_p = \kappa_r - \pi/2$  is set for convenience of our further consideration of the drill geometry.

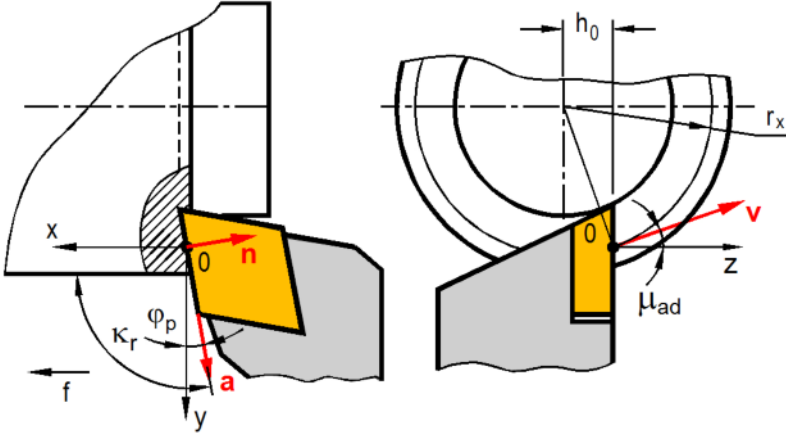


Fig. 2.44. Geometrical model of a single-point cutting tool having  $\kappa_r > \pi/2$

The magnitude of a normal  $\mathbf{n}$  to the tool cutting edge plane in the T-hand-S is selected so that its projection on the y-axis is equal to 1, then this vector can be expressed through its components as

$$\mathbf{n} = -\mathbf{i} \tan \varphi_p - \mathbf{j} \quad (2.94)$$

Vectors along the cutting speed and the cutting edge can be represented as

$$\mathbf{v} = -\mathbf{j} \tan \mu_{ad} + \mathbf{k} \quad (2.95)$$

$$\mathbf{a} = -\mathbf{i} + \mathbf{j} \tan \varphi_p \quad (2.96)$$

A normal  $\mathbf{n}_w$  to the tool cutting edge plane the T-mach-S is determined by the cross product of vectors  $\mathbf{v}$  and  $\mathbf{a}$  located in this plane:

$$\mathbf{n}_w = \mathbf{v} \times \mathbf{a} = \begin{vmatrix} \mathbf{i} & \mathbf{j} & \mathbf{k} \\ 0 & -\tan \mu_{ad} & 1 \\ -\tan \varphi_p & 1 & 0 \end{vmatrix} = -\mathbf{i} - \mathbf{j} \tan \varphi_p - \mathbf{k} \tan \mu_{ad} \tan \varphi_p \quad (2.97)$$

Angle  $\xi_{ad}$  is determined then as the angle between normals  $\mathbf{n}$  and  $\mathbf{n}_w$ :

$$\tan \xi_{ad} = \frac{\|\mathbf{n} \times \mathbf{n}_w\|}{\mathbf{n} \cdot \mathbf{n}_w} \quad (2.98)$$

The vector product of  $\mathbf{n}$  and  $\mathbf{n}_w$  calculates as



$$\mathbf{n} \times \mathbf{n}_w = \begin{vmatrix} \mathbf{i} & \mathbf{j} & \mathbf{k} \\ -\tan \varphi_p & -1 & 0 \\ -1 & -\tan \varphi_p & -\tan \mu_{ad} \tan \varphi_p \end{vmatrix} = \mathbf{i} \tan \mu_{ad} \tan^2 \varphi_p - \mathbf{j} \tan \varphi_p \tan \mu_{ad} \quad (2.99)$$

and its magnitude is

$$\|\mathbf{n} \times \mathbf{n}_w\| = \sqrt{\tan^2 \mu_{ad} \tan^2 \varphi_p + \tan^2 \varphi_p \tan^2 \mu_{ad}} = \frac{\tan \mu_{ad} \tan \varphi_p}{\cos \varphi_p} \quad (2.100)$$

The scalar product of  $\mathbf{n}$  and  $\mathbf{n}_w$  calculates as

$$\|\mathbf{n} \cdot \mathbf{n}_w\| = 1 + \tan^2 \varphi_p = \frac{1}{\cos^2 \varphi_p} \quad (2.101)$$

Finally

$$\tan \xi_{ad} = \frac{\tan \mu_{ad} / \cos \varphi_p}{1 / \cos^2 \varphi_p} = \tan \mu_{ad} \cos \varphi_p \quad (2.102)$$

Analysis of the second case shown in Fig. 2.44 results in the following conclusion. Equations 2.86 and 2.87 are no longer valid when  $\kappa_r > \pi/2$ , i.e., when  $\kappa_r = \pi/2 + \varphi_p$ . This follows from Eq. 2.103 because  $\cos \kappa_r = \cos(\pi/2 + \varphi_p) = -\sin \varphi_p$  so angle  $\xi_{ad}$  becomes negative. It also follows from Eq. 2.98 that normal  $\mathbf{n}_w$  to the tool cutting edge plane goes 'down' (since the  $\mathbf{k}$ -term is negative) with respect to the horizontal normal  $\mathbf{n}$  (compared with the first case where this normal goes up (Eq. 2.89) because the  $\mathbf{k}$ -term is positive). As a result, Eqs. 2.86 and 2.87 should be re-written for the considered case as

$$\gamma_{nw} = \gamma_n - \xi_{ad} \quad (2.103)$$

$$\alpha_{nw} = \alpha_n + \xi_{ad} \quad (2.104)$$

Equations 2.104 and 2.105 are of extreme importance in the considerations of the geometry of all kinds of drills because currently the opposite result (as per Eqs. 2.86 and 2.87) is used in the analysis of their the rake and flank angles. The location of the cutting edge above the reference plane through the drill rotation axis leads to increased rake and decreased flank angles along the major cutting edges if and only if  $\kappa_r < \pi/2$ . When  $\kappa_r > \pi/2$  (and this is the common case for most drills), such a location leads to decreased rake and increased flank angles. When the drill's cutting edge is located below the mentioned reference plane, the opposite is true.

To complete the analysis, consider a special case when  $\kappa_r = \pi/2$  as shown in Fig. 2.45. Following the same methodology, one can write the equation of a normal  $\mathbf{n}$  to the tool cutting edge plane in the T-hand-S as

$$\mathbf{n} = -\mathbf{i} \tag{2.105}$$

Vectors along the cutting speed and the cutting edge, respectively

$$\mathbf{v} = -\mathbf{j} \tan \mu_{ad} + \mathbf{k} \tag{2.106}$$

$$\mathbf{a} = \mathbf{j} \tag{2.107}$$

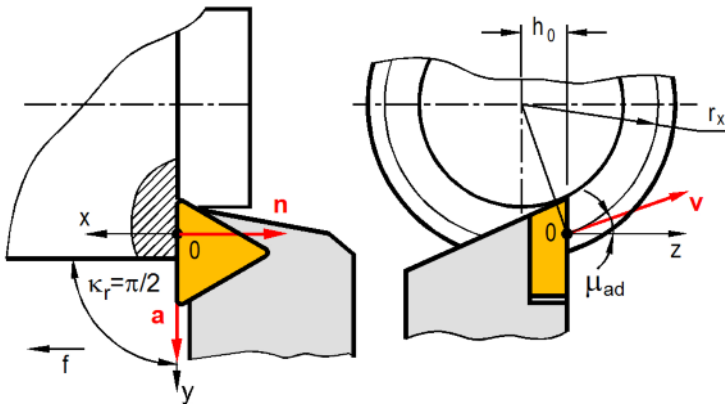


Fig. 2.45. Geometrical model of a single-point cutting tool having  $\kappa_r = \pi/2$

A normal  $\mathbf{n}_w$  to the tool cutting edge plane the T-mach-S is determined by the cross product of vectors  $\mathbf{v}$  and  $\mathbf{a}$  located in this plane:

$$\mathbf{n}_w = \mathbf{v} \times \mathbf{a} = \begin{vmatrix} \mathbf{i} & \mathbf{j} & \mathbf{k} \\ 0 & -\tan \mu_{ad} & 1 \\ 0 & 1 & 0 \end{vmatrix} = -\mathbf{i} \tag{2.108}$$

Angle  $\xi_{ad}$  is determined then as the angle between normals  $\mathbf{n}$  and  $\mathbf{n}_w$ :

$$\tan \xi_{ad} = \frac{\|\mathbf{n} \times \mathbf{n}_w\|}{\mathbf{n} \cdot \mathbf{n}_w} \tag{2.109}$$

The vector product of  $\mathbf{n}$  and  $\mathbf{n}_w$  calculates as

$$\mathbf{n} \times \mathbf{n}_w = \begin{vmatrix} \mathbf{i} & \mathbf{j} & \mathbf{k} \\ -1 & 0 & 0 \\ -1 & 0 & 0 \end{vmatrix} = 0 \quad (2.110)$$

and its magnitude is

$$\|\mathbf{n} \times \mathbf{n}_w\| = 0 \quad (2.111)$$

The scalar product of  $\mathbf{n}$  and  $\mathbf{n}_w$  calculates as

$$\|\mathbf{n} \cdot \mathbf{n}_w\| = 1 \quad (2.112)$$

Finally

$$\tan \xi_{ad} = \frac{0}{1} = 0 \text{ thus } \xi_{ad} = 0 \quad (2.113)$$

It follows from Eq. 2.114 that when  $\kappa_r = \pi/2$ , the vertical shift of a tool (with respect to the reference plane through the workpiece axis of rotation) does not affect the rake and flank angles of the cutting edge.

### 2.7.4 Flank Angles of a Dovetail Forming Tool

Consider the analysis of the tool geometry of a dovetail forming tool shown in Fig. 2.46. As seen in this figure, the rake face of this tool is made with zero rake and inclination angles so the combined three-part cutting edge  $BCDE$  of the tool lies in the horizontal plane through the axis of part rotation. If the tool base of such a tool is parallel to the rotational axis then the flank angle of cutting edge  $CD$  is zero. To avoid this zero flank angle, the base of the tool is inclined at a certain locating angle  $\delta_{lc}$  as shown in Fig. 2.46. As such, the flank angles on cutting edges  $BC$ ,  $CD$ , and  $DE$  would depend on this angle. Therefore, the objective of the present analysis is to determine  $\delta_{lc}$  for which the normal flank angles of all three cutting edges are equal [13].

The flank angle  $\alpha$  is the known angle obtained due to the location of the tool in the tool holder. The relationship between this angle and the normal flank angle,  $\alpha_{n1}$ , of cutting edge  $BC$  is derived as follows. Three vectors  $\mathbf{a}$ ,  $\mathbf{a}_1$ , and  $\mathbf{p}$  are introduced in the flank plane of cutting edge  $BC$ . Vector  $\mathbf{a}$  is in SECTION A–A, vector  $\mathbf{a}_1$  is a section normal to the cutting edge, and vector  $\mathbf{p}$  is along the cutting edge. In the coordinate system shown in Fig. 2.46, these vectors are defined as

$$\mathbf{a} = \mathbf{i} \sin \delta_{lc} + \mathbf{j} \cos \delta_{lc} - \mathbf{k} \cot \alpha \quad (2.114)$$

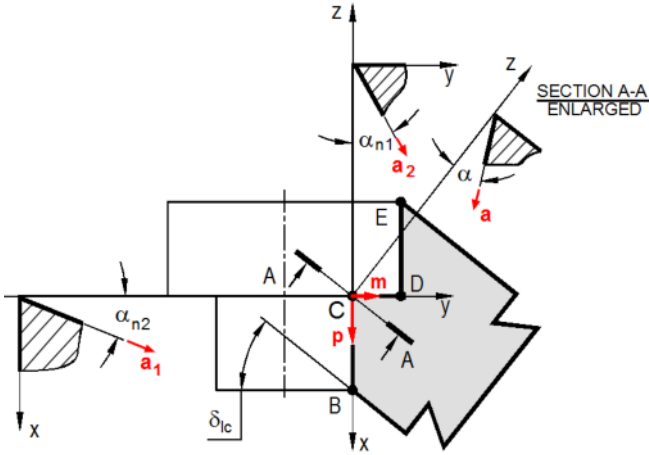


Fig. 2.46. Flank angles of a dovetail forming tool

$$\mathbf{a}_1 = \mathbf{j} \tan \alpha_{n1} - \mathbf{k} \quad (2.115)$$

$$\mathbf{p} = \mathbf{i} \quad (2.116)$$

As these vectors are coplanar (belong to the same plane), their scalar triple product (Appendix C) is equal to zero, i.e.,

$$\mathbf{p} \cdot (\mathbf{a} \times \mathbf{a}_1) = \begin{vmatrix} \mathbf{i} & \mathbf{j} & \mathbf{k} \\ \sin \delta_{lc} & \cos \delta_{lc} & -\cot \alpha \\ 0 & \tan \alpha_{n1} & -1 \end{vmatrix} = 0 \quad (2.117)$$

from where

$$\tan \alpha_{n1} = \tan \alpha \cos \delta_{lc} \quad (2.118)$$

Equation 2.119 allows calculation of the normal flank angles of cutting edge  $DC$  as a function of the locating angle  $\delta_{lc}$ .

Three vectors  $\mathbf{a}$ ,  $\mathbf{a}_2$ , and  $\mathbf{m}$  are introduced in the flank plane of cutting edge  $CD$ . Vector  $\mathbf{a}$  is in SECTION A-A, vector  $\mathbf{a}_2$  is a section normal to the cutting edge, and vector  $\mathbf{m}$  is along the cutting edge from the coordinate origin as shown in Fig. 2.46. These vectors are defined as

$$\mathbf{a} = \mathbf{i} \sin \delta_{lc} + \mathbf{j} \cos \delta_{lc} - \mathbf{k} \cot \alpha \quad (2.119)$$

$$\mathbf{a}_2 = \mathbf{i} \tan \alpha_{n2} - \mathbf{k} \quad (2.120)$$

$$\mathbf{m} = \mathbf{j} \quad (2.121)$$

As these vectors are coplanar (belong to the same plane), their scalar triple product (Appendix C) is equal to zero, i.e.,

$$\mathbf{m} \cdot (\mathbf{a}_2 \times \mathbf{a}) = \begin{vmatrix} 0 & 1 & 0 \\ \tan \alpha_{n1} & 0 & 0 \\ \sin \delta_{lc} & \cos \delta_{lc} & -\cot \alpha \end{vmatrix} = 0 \quad (2.122)$$

from where

$$\tan \alpha_{n2} = \tan \alpha \sin \delta_{lc} \quad (2.123)$$

Equation 2.124 allows calculation of the normal flank angles of cutting edge  $DC$  as a function of the locating angle  $\delta_{lc}$ .

According to the objective set earlier, the normal flank angles of all three cutting edges are equal. Therefore, from Eqs. 2.119 and 2.124 one can write

$$\tan \alpha \cos \delta_{lc} = \tan \alpha \sin \delta_{lc} \quad (2.124)$$

from which it follows that  $\tan \delta_{lc} = 1$  and hence  $\delta_{lc} = \pi/4 = 45^\circ$ . Using this locating angle and selecting the optimal (for a given work materials and cutting conditions) normal flank angle, one can assure the uniform tool geometry (and thus, uniform tool wear and machining quality) over the cutting edge.

This discussed example shows that the tool geometry can be altered over a wide range by changing the design and setting parameters of the tool. The simple and straightforward vector method of analysis used equips a tool designer with the ability to understand the mentioned interrelationships.

### 2.7.5 Summation of Several Motions

The common case in the summation of motions in metal cutting is the summation of the rotational and translational simultaneous relative motions of the tool and the workpiece. The simplest yet common case is the summation of the rotation of the workpiece and translation of the tool, for example in turning. As such, the resultant velocity  $\mathbf{v}_R$  is calculated as the vector sum of the feed velocity  $\mathbf{v}_f$  (translation along the longitudinal axis of the workpiece) and the linear velocity of the workpiece having radius  $r_w$  and rotating with the angular velocity  $\boldsymbol{\omega}_w$  (Appendix C) known as the cutting speed as

$$\mathbf{v}_R = \mathbf{v}_f + \boldsymbol{\omega}_w \times \mathbf{r}_w \quad (2.125)$$

This velocity causes a spiral tool path that generated the cylindrical workpiece. Summation of two rotations with equal and oppositely directed angular velocities (rotational pair) results in a translation. The velocity of this translation is perpendicular to the plane containing vectors of angular velocities and is directed to from the vector head viewpoint that one can see this rotational pair as rotating counterclockwise.

Lets consider the result of summation of two motions [13]. One is rotation and the second is translation with velocity directed perpendicular to the axis of rotation. Let body  $A$  rotates about axis  $O$  with angular velocity  $\omega$ . Axis  $O$  moves translationally with velocity  $v$  which is perpendicular to  $\omega$  as shown in Fig. 2.47a. The translation motion with velocity  $v$  can be replaced by a rotational pair. Let's select the modules of the angular velocities in this pair as

$$\|\omega_1\| = \|\omega_2\| = \|\omega\| \tag{2.126}$$

Let's direct one of these two angular velocities,  $\omega_2$  along the axis of rotation  $O$  opposite to  $\omega$ . Then, vector  $\omega_1$  is directed parallel to  $O$  at distance  $r_{ct} = \|v\|/\|\omega\|$  measured in a plane perpendicular to  $v$  as shown in Fig. 2.47b. The sum of  $\omega_2$  and  $\omega$  is zero so the resultant motion is rotation with angular velocity  $\omega$  about the instantaneous axis of rotation shifted from axis  $O$  by  $r_{ct}$ . In other words, it is rolling of cylinder  $A$  on plane  $W$ . The mutual tangent of these two surfaces at any given instant is the instantaneous axis of rotation.

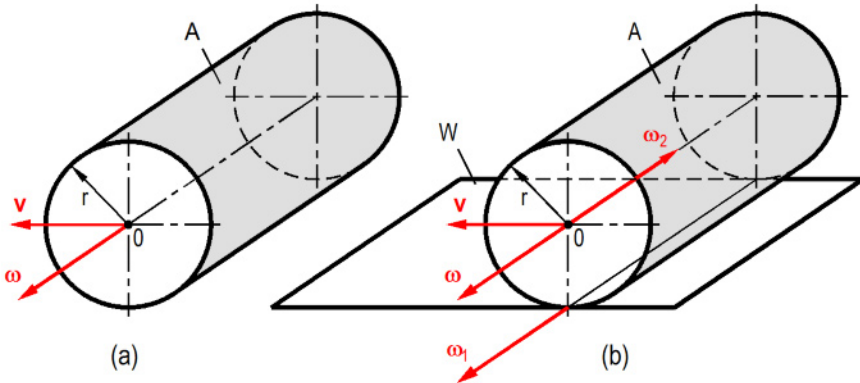


Fig. 2.47. Model showing the combining of rotation and translation

2.7.5.1 Frank Angles of the Tooth Profile of a Gear Hob

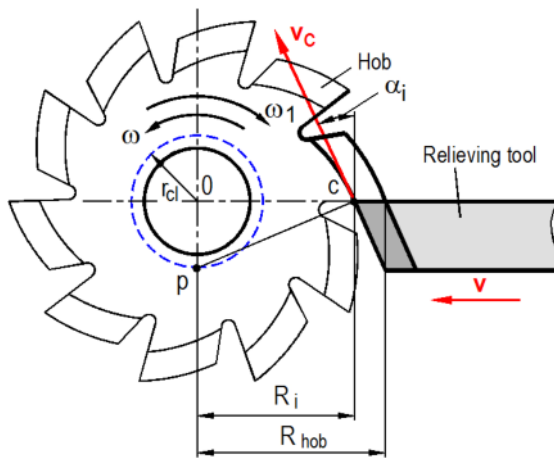
The considered setting is similar to that in relieving a hob or a shape milling cutter by turning as shown in Fig. 2.48 [13]. The relieving lather tool is installed so that its rake face locates in the axial plane of the hob and its cutting edge has the profile of a hob tooth. As such,  $\gamma = 0^\circ$  and  $\lambda_s = 0^\circ$ . When operating, the hob rotates with angular velocity  $\omega_1$  and the relieving tool moves perpendicular to the axis of

rotation with translational velocity  $\mathbf{v}$ . The relief (flank) surface on the tooth forms as a result of these two coordinated motions.

The motion of the relief tool with respect to the hob can be represented as the translation with velocity  $\mathbf{v}$  and rotation with angular velocity  $\boldsymbol{\omega}$  about the axis of the hob. As such,  $\boldsymbol{\omega} = -\boldsymbol{\omega}_1$ , that is these angular velocity have equal magnitudes and opposite directions. Accounting for the result obtained above in the considerations of the rolling cylinder (Fig. 2.47), this motion is represented as rotation about instantaneous axis  $p$  located in the plane perpendicular to  $\mathbf{v}$  and thus along the longitudinal axis of the hob. The distance between axes  $\theta$  and  $p$  is calculated as  $r_{cl} = \|\mathbf{v}\|/\|\boldsymbol{\omega}\| = v/\omega$ .

In Fig. 2.48,  $R_i$  is the distance between point  $c$  of the cutting edge and the hob axis  $\theta$ . The distance between point  $c$  and instantaneous axis  $p$  is calculated as

$$pc = \sqrt{R_i^2 + r_{cl}^2} = \sqrt{R_i^2 + \frac{v^2}{\omega^2}} \tag{2.127}$$



**Fig. 2.48.** Model for determining flank angles generated by a relieving tool on a gear hob

The cutting velocity  $\mathbf{v}_c$  is the velocity of point  $c$  relative to the hob. It can be represented as the linear velocity of this point in its rotation about instantaneous axis  $p$  with angular velocity  $\boldsymbol{\omega}$ . Then the magnitude of this velocity is calculated as

$$\|\mathbf{v}_c\| = \omega \sqrt{R_i^2 + \frac{v^2}{\omega^2}} = \sqrt{(R_i \omega)^2 + v^2} \tag{2.128}$$

Vector  $\mathbf{v}_c$  is perpendicular to the instantaneous radius  $pc$  and lays in the plane perpendicular to axis  $\theta$ . It originates from point  $c$  and thus is tangential to the hob relief (flank surface) in its generation by the relieving tool. Therefore, the position

of  $v_c$  determines flank angle  $\alpha_i$  of the hob at point  $c$  of its cutting edge. As follows from Fig. 2.48, this flank angle is equal to  $\angle pc\theta$  thus it is calculated as

$$\tan \alpha_i = \frac{r_i}{R_i} = \frac{v}{\omega R_i} \tag{2.129}$$

Particularly, for the top of a tooth of the hob, this angle calculates as

$$\tan \alpha_{top} = \frac{v}{\omega R_{hob}} \tag{2.130}$$

where  $R_{hob}$  is the radius of the hob.

Combining Eqs. 2.130 and 2.131, one can obtain the equation to calculate the flank angle  $\alpha_i$  in any point of radius  $R_i$  of the hob tooth profile as

$$\tan \alpha_i = \frac{R_{hob}}{R_i} \tan \alpha_{top} \tag{2.131}$$

2.7.5.2 Summation of Two Rotations About Parallel Axes

Consider the summation of two rotations with continuous and oppositely-directed angular velocities about parallel axes [13]. Let a body rotates about axis  $O_1$  with angular velocity  $\omega_1$  and axis  $O_2$  rotates about axis  $O_2$  with angular velocity  $\omega_2$  as shown in Fig. 2.49. Lets  $\|\omega_1\| > \|\omega_2\|$ .

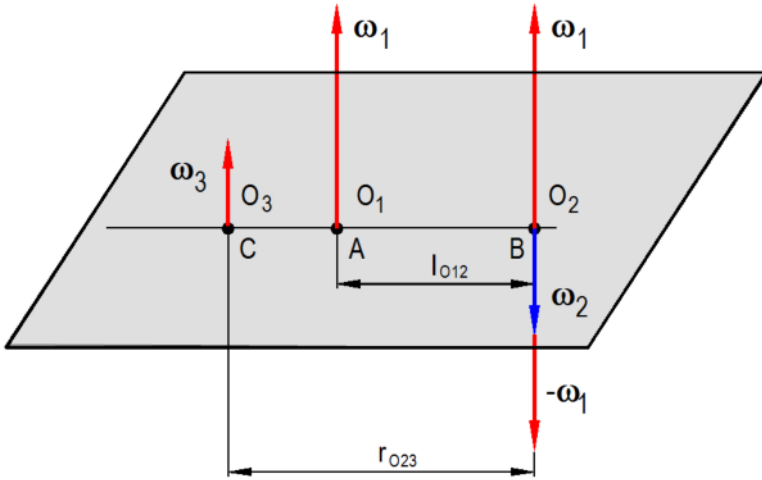


Fig. 2.49. Summation of two rotations about parallel axes



Let's apply two opposite vectors  $\omega_1$  and  $-\omega_1$  at point B located on axis  $O_2$  as shown in Fig. 2.49. As seen, vector  $\omega_1$  applied at point A located on axis  $O_1$  and vector  $\omega_1$  at point B located on axis  $O_2$  constitute a rotational pair, which is equivalent to translation with velocity:

$$\|\mathbf{v}\| = \|\omega\|l_{O12} \quad (2.132)$$

where  $l_{O12}$  is the distance between axes  $O_1$  and  $O_2$ .

Vectors  $\omega_1$  and  $\omega_2$  applied at B add and the resulting vector is  $\omega_3 = \omega_1 - \omega_2$ . As follows from the previous sections, two rotations about parallel axes can be represented as the rotation about axis  $O_2$  with angular velocity  $\omega_3$  and translation with velocity  $\mathbf{v}$  which is perpendicular to  $O_2$ . As such, these two motions can be represented by one instantaneous rotation with angular velocity  $\omega_3$  with respect to axis  $O_3$  which is parallel to axis  $O_2$  and the distance  $r_{O12}$  between these two axes is given as

$$r_{O23} = \frac{\|\mathbf{v}\|}{\|\omega_3\|} = \frac{\omega_1 l_{O12}}{\omega_1 - \omega_2} \quad (2.133)$$

As follows, the result of two opposite rotations about parallel axes  $O_1$  and  $O_2$  is the rotation about axis  $O_3$  which is parallel to  $O_1$  and  $O_2$  and lies in the same plane as these two axes. The resultant angular velocity  $\omega_3$  is the geometrical sum of the angular velocities ( $\omega_1$  and  $\omega_2$ ). The considered motion can be thought of as the rolling (without slipping) of a cylinder with axis  $O_1$  and of radius  $r_{O23} - l_{O12} = AC$  over a cylinder with axis  $O_2$  and of radius  $r_{O23} = BC$  (Fig. 2.49). As such, the first cylinder locates in the second (as a planet and a ring gear in an epicyclic gear train). If, however,  $\omega_1$  and  $\omega_2$  have the same direction then the first cylinder is outside the second (as a planet gear and a sun gear in an epicyclic gear train). In both cases, the mutual tangent to the said cylinders is the instantaneous axis of rotation.

The summation of two rotations about parallel axes takes place in machining shafts of a polygonal cross section on a lathe [13]. The schematic of such machining is shown in Fig. 2.50. The angular velocities of workpiece  $\omega_w$  and tool  $\omega_T$  have the same directions and are located along the parallel axes of rotations  $O_1$  and  $O_2$ , respectively. The distance between  $O_1$  and  $O_2$  is  $l_{O12}$ . The ratio of the magnitude of these angular velocities is selected as

$$\frac{\|\omega_T\|}{\|\omega_w\|} = \frac{\omega_T}{\omega_w} = \frac{N}{m} \quad (2.134)$$

where  $N$  is number of faces (polygons) on the shaft and  $m$  is the number of teeth made on the tool head.

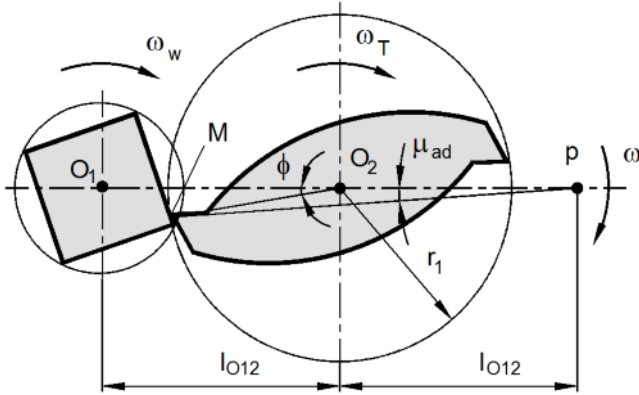


Fig. 2.50. Model of machining a polygonal shaft on a lathe

In the tool/work relative motion, the tool cutting edge (point  $M$ ) produces a curve that is very close to a straight line so polygonal shafts of high accuracy can be produced using this method.

The motion of the tool about the workpiece is the instantaneous rotation with angular velocity

$$\omega = \omega_T - \omega_w \quad (2.135)$$

When a shaft of a square cross section is machined and the tool has two teeth then it follows from Eq. 2.135 that

$$\omega_T = 2\omega_w \quad (2.136)$$

so

$$\omega = 2\omega_w - \omega_w = \omega_w \quad (2.137)$$

It follows from Eq. 2.134 that for a shaft of a square cross section

$$r_{23} = \frac{2\omega_w l_{O12}}{2\omega_w - \omega_w} = 2l_{O12} \quad (2.138)$$

The cutting velocity  $v_c$  of any point of the tool cutting edge, for example point  $M$  (Fig. 2.50), is defined as the linear velocity of this point as this point rotates about axis  $p$  with angular velocity  $\omega$ . This cutting velocity is perpendicular to radius  $pM = R_M$ . It follows from the model shown in Fig. 2.50 that this radius calculates as

$$R_M = \sqrt{(l_{O12} + r_1 \cos \phi)^2 + (r_1 \sin \phi)^2} \quad (2.139)$$

so that the cutting speed of point  $M$  at any instant (determined by angle  $\phi$ ) is calculated as

$$\|\mathbf{v}_c\| = v_c = \|\boldsymbol{\omega}\| R_M = \|\boldsymbol{\omega}\| \sqrt{(l_{O12} + r_1 \cos \phi)^2 + (r_1 \sin \phi)^2} \quad (2.140)$$

The variations of the of the rake and flank angles in the tool back plane (the plane of consideration shown in Fig. 2.50) can be represented as

$$\gamma_{pM} = \gamma_p \pm \mu_{ad} \quad (2.141)$$

$$\alpha_{pM} = \alpha_p \mp \mu_{ad} \quad (2.142)$$

where  $\gamma_p$  and  $\alpha_p$  are the rake and flank angles in the tool back plane in the T-hand-S,  $\mu_{ad}$  is the angle between  $R_M$  and the axis connecting all three centers of rotation (axis  $pO_I$ ) as shown in Fig. 2.50. It is calculated as

$$\mu_{ad} = \frac{r_1 \sin \phi}{R_M} \quad (2.143)$$

As seen, the rake angle  $\gamma_p$  is increased and the flank angle  $\alpha_p$  is decrease by  $\mu_{ad}$  when point  $M$  is below axis  $pO_I$  while the opposite is true when this point is above this axis.

The maximum cutting speed is when angle  $\phi=0$ . As such, it calculates as

$$\|\mathbf{v}_c\|_{\max} = \|\boldsymbol{\omega}\| (l_{O12} + r_1) \quad (2.144)$$

As follows from Eqs. 2.142–2.145, the tool geometry and the cutting speed vary in machining (in the T-use-S). However, the rage of variation of  $\mu_{ad}$  is rather small so the rake and flank angles as well as the cutting speed variations are small which is a definite advantage of the described machining operation.

## References

- [1] Astakhov VP (1998/1999) Metal cutting mechanics. CRC, Boca Raton
- [2] Astakhov VP (2006) Tribology of metal cutting. Elsevier, London
- [3] International Standard ISO 3002–1 Basic quantities in cutting and grinding. Part 1: Geometry of the active part of cutting tools - general terms, reference systems, tool and working angles, chip breakers. 1982
- [4] Shaw MC (2005) Metal cutting principles. University Press, Oxford
- [5] Zorev NN (1966) Metal cutting mechanics. Pergamon Press, Oxford
- [6] Armarego EJ, Brown RH (1969) The machining of metals. Prentice-Hall, New Jersey
- [7] American National Standard ANSI B94.50–1975 Basic nomenclature and definitions for single-point cutting tools. 1975 (reaffirmed 1993)

- [8] Astakhov VP (2005) Comments and suggestions to International Standard ISO 3002/1 “Basic quantities in cutting and grinding – Part1: Geometry of the active part of cutting tools – General terms, reference systems, tool and working angles, chip breakers (<http://www.astvik.com/MC/ISOStand3002c.pdf>)
- [9] Granovsky GE, Granovsky VG (1985) Metal cutting (in Russian). Vishaya Shkola, Moscow
- [10] Outeiro JC, Dias AM, Lebrun JL, Astakhov VP (2002) Machining residual stresses in AISI 316L steel and their correlation with the cutting parameters. *Machining Science and Technology* 6(2):251–270
- [11] Radzevich SP (2006) Geometry of the active part of cutting tools (in the tool-in-hand system). *SME Paper TPO 6PUB37:10*
- [12] Mozhaev SS (1948) Analytical theory of twist drills (in Russian). Mashgiz, Moscow
- [13] Rodin PR (1972) The basics of shape formation by cutting (in Russian). Visha Skola, Kyev
- [14] Radzevich SP (2001) Shape generation – theoretical fundamentals (in Russian). Rastan, Kyev
- [15] Astakhov VP, Galitsky VV, Osman MOM (1995) A novel approach to the design of self-piloting drills. Part 1. Geometry of the cutting tip and grinding process. *ASME J. of Eng for Ind.* 117:453–463
- [16] Astakhov VP, Galitsky VV, Osman MOM (1995) A novel approach to the design of self-piloting drills with external chip removal, Part 2: Bottom clearance topology and experimental results. *ASME J. of Eng. for Ind.* 117:464–474

## Fundamentals of the Selection of Cutting Tool Geometry Parameters

*Not everything that counts can be counted and  
not everything that can be counted counts.*

Sign hanging in Albert Einstein's office at Princeton

**Abstract.** This chapter presents a general methodology for the selection of the optimal tool geometry based upon minimization of the work of plastic deformation in metal cutting. It argues that the chip compression ratio is the most objective yet simple 'gage' that should be used for the assessment of this work and thus to optimize the tool geometry. Individual and system influences of the major parameters of cutting tool geometry are discussed. The tool cutting edge, rake, flank and inclination angles, as well as edge preparation are included in considerations because these parameters have multi-faced influence on practically all aspects of the metal cutting process and greatly affect the outcome of a machining operation. The chapter offers explanations and rationales for many common perceptions and experimental knowledge concerning the listed parameters.

### 3.1 Introduction

Tool geometry selection and optimization of the selected parameters are complex tasks owing to a great number of considerations involved. A broad range of tool geometries is available today to suit various practical applications and machining systems. As a consequence, the tool/process designer has to wade through voluminous machining data handbooks and catalogs of tool manufacturers to select the proper tool geometry parameters for a given application. In the author's opinion, one of the major obstacles in such a selection is the great scatter in the recommendations provided by mostly outdated handbooks containing recommendations which do not account for the significant changes that the metalworking industry has experienced over the last few decades. These changes

concern substantial improvements in the whole machining system including machine tools, tool materials and designs, tools pre-setting and mounting in machines, process control, etc.

Unfortunately, the current level of understanding of the subject provides no systematic guidance or algorithm to make such a selection clear and straightforward. It is common that a tool designer does not know what is the starting point in the tool geometry selection due to a multi-faced influence of the geometry parameters which also depends on many other conditions particular to a given machining operation and quality requirements to the machined parts [1]. The pressure to reduce the cost of the tool or cost per unit of the machined part while competing with the other tool manufacturers for the job just adds another dimension to this complicated problem.

Each geometry component defined in the previous chapter has its individual influence on the various facets of the machining process (cutting force, power, tool life, etc.) and machining operation (chip breakage and removal, surface finish and accuracy of the machined parts, etc.) as well as the combined influence depending upon particular values of other geometry and process parameters. It is important to understand these multiple correlations and influences in the selection of the optimal geometrical parameters for a given application. Besides very general and often misleading trends and notions (for example, positive geometry, helical design), the known literature sources do not provide help to a tool/process designer/planner in such understanding.

Unfortunately, there been not been many known attempts to help tool/process designers in the selection of the proper tool geometry. In the author's opinion, the prime mistake made in the known studies is that the influence of one geometry parameter, for example, the rake angle, is considered while completely ignored the system consideration in the selection process. As a consequence, the known results are contradicting. For example, Shaw concluded [2] that the so-called specific cutting energy (and thus the cutting force) decreases about 1% per degree increase in the rake angle while a detailed experimental study by Gunay et al. [3] showed that the influence of the rake angle on the cutting force is within the normal scatter of experimental results. Gunay et al. [4] studied the influence of the rake angle on cutting forces while other parameters as for example tool life or chip shape are ignored. Rodrigues and Coelho [5] studied influence of the geometry of the chip breaker on the specific cutting energy while other parameters as tool life, surface finish, chip shape (in terms of its suitability for easy removal from the machining zone) and many other were not addressed.

Very often in research papers and books, improper terms for the tool geometry parameter are used. Moreover, it almost never mentioned what kind of angle is listed (normal, orthogonal, for example) and in what particular system (T-hand-S, T-mach-S) is considered. Little attention is paid to the fact that many parameters of tool geometry are interrelated. For example, when one studies the influence of the drill (reamer) point angle, the T-hand-S normal rake and flank angles remain the same in such a study. However, the fact that the T-mach-S (T-use-S) rake and flank angles change significantly with the drill point angle (see Chap. 4) is normally neglected.

Little attention is paid to the selection of the machining regime for the study (assessment) of a given tool geometry. The cutting feed is routinely selected to be of the same level as the cutting edge radius that completely undermines the real tool geometry. The depth of cut is frequently selected equal to or less than the tool nose radius that undermines the influence of the tool cutting edge angles of the major and minor cutting edges.

Besides these mistakes, the importance of micro-geometry is often neglected. Although cutting edge preparation type and its geometry has significant (up to 400%) influence on tool life and quality of machined parts [6, 7], these are rarely reported in the known studies.

## **3.2 General Considerations in the Selection of the Parameters of Cutting Tool Geometry**

### **3.2.1 Known Results**

There have not been many attempts to develop a methodology that might help a tool/process designer to select the proper tool geometry. Multiple books on metal cutting and tool design provide very general and impractical recommendation on the selection of tool geometry parameters. Although there is a great deal of available information on a role and significance of tool geometry parameters for particular conditions, these research reports are scattered over many journal and edited books. This situation is frustrating for many specialists in the field. It is increasingly difficult to perceive links between different research approaches to identify the results relevant to a given case of cutting tool design. This fragmentation of publication of relevant research obviously has rather negative effects in terms of integration of research finding from different approaches.

Having limited experience, time, and access to information, a practical tool/process designer is normally left at the mercy of the information provided by the catalogs of tool manufacturers and sales/technical representatives of tool manufacturers. As a result, the whole foundation of selection and optimization of tool geometry becomes shaky. It is common that a tool/process designer fails to answer simple questions about the rationale behind the selection of the parameters of tool geometry.

Among very few known approaches, the so-called macro-level optimization of the tool geometry approach developed by Kaldor and Venuvinod [1] attempted to provide some help. The intention of this approach is to simplify tool geometry selection by incorporating only the most essential cutting variables and identifying a generalized relationship amongst them, which satisfies the condition of maximum tool life and is consistent with as much empirical data as possible [8, 9]. This relationship is capable of yielding a set of tool geometries which are all optimized in a coarse sense in the context of the limited number of input variables considered. The process designer may then subject a chosen subset of these macro-level solutions to finer optimization, or modify these suitably to take into account some variables which were ignored during the macro-level analysis but are

suspected to be of importance in view of the desired level of accuracy of the solution.

In due course of the approach development, however, the discussed macro-level approach became a cutting process rather than tool geometry optimization. It was pointed out by the authors [8, 9] that a need for such a macro-level approach to cutting process optimization seems to be supported by machining experience and wisdom. For instance, in recent times, tool manufacturers are becoming increasingly concerned with the development and recommendation of a wide range of alternative tool geometries which are deemed to be equally effective over a range of cutting applications for given tool/work material pairs. A similar situation usually prevails in the early stages of process planning for machined components. Given the enormous complexity of the machining process and the inability, as yet, of researchers to come up with a comprehensive model (i.e., a model encompassing all the input variables) of the machining process, it seems currently impossible to optimize simultaneously all the input variables.

There are two principle errors in the foundation of the proposed method. First, it uses a very outdated characterization of the tool material as a non-dimension number equal to the ratio of the bending strength of the tool material to its elastic modulus introduced by Sandvik Coromant in 1967 [10]. It is pointed out, however, that Shaw has also used this parameter to characterize tool materials in his dimensional analysis of the fracture of metal cutting tools [11]. His approach was based on fracture failure of the cutting insert which normally is not observed in the normal metal cutting process.

The second error is even more severe. According to the proposed method, the critical step two (out of four) in the selection of the proper tool geometry reads as “Select the magnitude of specific cutting energy from machining data handbooks (or, from prior measurement or experience) which is broadly consistent with the cutting conditions proposed to be used.” In other words, the authors assumed the existence of the specific cutting energy that is the sole property of the work material which does not depend on the tool geometry and process parameters. In reality, it is not true. Shaw [2] pointed out “In general, cutting speed and depth of cut have a small influence on specific cutting energy, but rake angle and undeformed chip thickness have an appreciable influence.” Boothroyd and Knight [12] pointed out “The specific cutting energy can vary considerably for a given material and is affected by changes in cutting speed, feed, tool rake, and so on.” Rodrigues and Coelho found that the specific cutting energy decreased 15.5% when cutting speed was increased up to 700%. An increase of 1° in the chip breaker chamfer angle led to a reduction in the specific cutting energy about 13.7% and 28.6% when machining at HSC and conventional cutting speed respectively [5].

### 3.2.2 Ideal Tool Geometry and Constrains

It is discussed in Chap. 1 (Sect. 1.3.3) that the tool geometry directly affects the amount of plastic deformation in metal cutting, which is the plastic deformation of the layer being removed in its transition into the chip. Because, this energy is the largest part of the energy required by the cutting system for its existence, it defines



the cutting force, tool life, and other outcomes of a machining operation. Therefore, the prime objective in the selection of the tool geometry parameters is to minimize plastic deformation in metal cutting as this deformation should always be considered as a nuisance. The rule of thumb in such a selection is: the less the plastic deformation, the better the cutting process.

Because tool geometry plays a decisive role in the formation of the triaxial state of stress in the deformation zone, it defines the fracture strain, i.e., the extent of plastic deformation in metal cutting. Therefore, if the correlation between state of stress and fracture strain of the work material is known (see Fig. 1.21), then using a simple FEM analysis which nowadays is part of many standard CAD programs, one can find the combinations of the tool geometry parameters that result in the minimum plastic deformation in metal cutting. Although this way is the ultimate aim in the proper selection of the tool geometry parameters, it requires some specific information that is not readily available yet. Moreover, some constraints on the selected geometry parameters in their optimization should also be considered.

There are two major obstacles in the full implementation of the discussed methodology of the selection of the geometrical parameters. The first is that the relationships similar to those shown in Fig. 1.21 are not yet common in material testing although computer-controlled MTSs have become readily available. This is because the results of mechanical testings used in the design are not required to be exact as the so-called safety factor covers all discrepancies between testing and real-world conditions. In metal cutting, this safety factor is zero as the work material must be brought to fracture, and thus the strain at fracture should be known exactly. Therefore, a new work material testing methodology (a new machinability test) should be developed. Such a development does not present any problem. It is not yet developed only because there is no understanding and thus no demand.

The second obstacle is much more severe as it relates to the allowable variation of the real-world work materials properties as discussed in Chap. 1. These variations are caused by wide ranges of the so-called secondary alloying elements in the work materials. A good example of the influence of minor components on the machinability of a gray cast iron widely used in the automotive industry was presented by Griffin and co-workers [13]. They found that within the range allowed for manganese (0.3–0.8%), the longest tool life corresponds to 0.3% and it reduces more than twice when the content of manganese is 0.8%. The same result was obtained for the allowable range of tin. An even more pronounced influence of volume percent of hard inclusion was found in this study. Unfortunately, the conclusive results obtained did not affect the way the automotive industry specifies composition of gray, ductile, and malleable cast irons although significant cost saving can be achieved with minimum effort. Moreover, quality and reliability of cars can be improved by reduction of the number of defective transmissions and engines due to metallic chips and burrs left in veins and gates of case body, pump cover, upper and lower valve bodies, etc.

The major constraint in the optimization of tool geometry using the proposed methodology is the quality of the machined part in terms of the required surface finish, dimensional accuracy, form accuracy (for example, flatness, cylindricity), and machining residual stresses (both superficial and in-depth). Other constraints

may include the shape of the chip and the direction of its flow, vibrations due to dynamic properties of the machining system, available power, speed and feed ranges on the machine, and many others.

Regardless of real-world obstacles and constraints, the proposed way of tool geometry selection provides clear and objective so-called ideal tool geometry that can then be corrected, accounting for the discussed constraints. This ideal geometry should be considered as cutting tool related while the optimized geometry is machining system related. It is clear that the better the machining system, the closer the ideal cutting tool geometry is to the optimized.

### **3.2.3 Practical Gage for Experimental Evaluation of Tool Geometry**

To assess the influence of tool geometry and its individual parameters on the cutting process, a proper criterion or simple gage must be used. Commonly, the cutting force, temperature, tool life, surface finish, and many other output parameters are used for such an assessment. This, in the author's opinion, presents the major problem. As discussed in Appendix A, the cutting force and cutting temperature cannot be measured with reasonable accuracy for multiple reasons as these parameters are metal cutting system dependant. Moreover, their determination requires special expensive measuring equipment that is not readily available in many manufacturing facilities, not to mention specially trained personnel.

A tool life test is extremely expensive and time consuming. For example, in the automotive industry in machining of aluminum alloy powertrain components, tool life is measured in the hundreds of thousands of holes which requires more than half a year to obtain just one experimental point. Therefore, another, more accurate, inexpensive and practical output parameter that directly correlates with major output characteristics of the cutting process should be used. As discussed in Chap. 1, the chip compression ratio (CCR) can be used as such a parameter as it correlates with practically all parameters of the cutting process and can be measured with reasonable accuracy even on the shop floor. Although it is a simple parameter, one should understand the physical meaning of this parameter discussed in Chap. 1 in order to use it properly.

This chapter discussed the influence of the parameters of the cutting tool geometry on the machining operation outcomes. Understanding of these correlations should equip a tool designer with the knowledge to select the parameters of tool geometry properly and/or to correct the selected parameters after tool testing.

## **3.3 Tool Cutting Edge Angles**

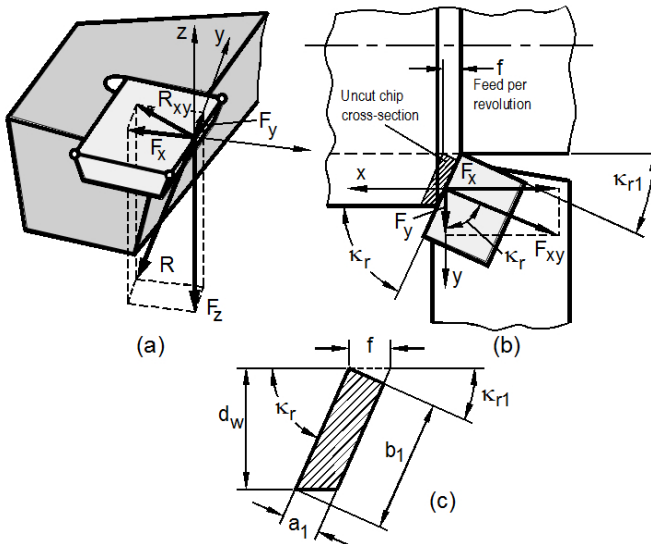
### **3.3.1 General Consideration**

The tool cutting edge angle is probably the most important angle of tool geometry as it has multi-faced influence on practically all aspects of the metal cutting process and greatly affects the outcome of a machining operation. This is because

it defines the magnitudes of the radial and tangential components of the cutting force and, for given feed and cutting depth, it defines the uncut chip thickness, width of cut, and thus tool life. The physical background of this phenomenon can be explained as follows: when  $\kappa_r$  decreases, the chip width increases correspondingly because the active part of the cutting edge increases. The latter results in improved heat removal from the tool and hence tool life increases. For example, if tool life of a high speed steel face milling tool having  $\kappa_r = 60^\circ$  is taken to be 100%, then when  $\kappa_r = 30^\circ$  its tool life is 190%, and when  $\kappa_r = 10^\circ$  its tool life is 650%. An even more profound effect of  $\kappa_r$  is observed in the machining with single point cutting tools. For example, in rough turning of carbon steels, the change of  $\kappa_r$  from  $45^\circ$  to  $30^\circ$  leads sometimes to a fivefold increase in tool life.

The reduction of  $\kappa_r$ , however, has its drawbacks. One of them is the corresponding increase of the radial component of the cutting force. As discussed in Appendix A (Sect. A.4.1, Fig. A.11), the cutting force,  $R$ , is a 3D vector which is normally resolved into three orthogonal components, namely the power (tangential, torque) component,  $F_z$ , axial component,  $F_x$ , and radial component,  $F_y$ . For simplicity, these are often called tangential, axial, and radial forces, respectively. As shown in Fig. 3.1, the radial and axial forces are related as

$$\frac{F_x}{F_y} = \tan \kappa_r \quad (3.1)$$



**Fig. 3.1.** The cutting force system and the uncut chip thickness for a single point cutting tool (after Astakhov [14])

As follows from this equation, lowering  $\kappa_r$  from  $45^\circ$  to  $20^\circ$  results in more than a twofold increase in the radial force that increases the bending force acting on the workpiece and thus may reduce the accuracy of machining because the rigidity of

the workpiece varies along its length. When the workpiece is machined between centers, an increased radial force causes so-called barreling, and when the workpiece is clamped only in the chuck, tapering may occur. Besides, because lowering  $\kappa_r$  leads to an increased radial force, this force often causes vibrations so that the advantages of small tool cutting edge angle may not become too profound.

### Example 3.1

*Problem:* In machining a long workpiece, it was found that the excessive radial force causes barreling of the workpiece which results in the variation of the diameter of the workpiece along its length exceeding the assigned tolerance. The tool used has the cutting edge angle  $\kappa_r = 45^\circ$ . Provided that the machining regime is still the same, i.e., the magnitude of  $F_{xy}$  (Fig. 3.1) does not change, find  $\kappa_r$  that reduces the radial force  $F_y$  twofold.

*Solution:* As follows from  $F_y = F_{xy} \cos \kappa_r$ . With the existing  $\kappa_r = 45^\circ$ ,  $F_y = F_{xy} \cos 45^\circ = 0.71F_{xy}$ . To lower  $F_y$  twofold, it should be  $F_y = F_{xy} \cos \kappa_{r(new)} = 0.35F_{xy}$ . Hence  $\cos \kappa_{r(new)} = 0.35$  so that  $\kappa_{r(new)} = 69.5^\circ$ . Counting on the availability of standard cutting inserts and tool holders,  $\kappa_{r(new)} = 70^\circ$  was chosen.

End of Example 3.1.

The tool cutting edge angle has direct influence on the uncut (undeformed) chip cross-sectional shape, uncut chip cross-sectional area, and thus on the uncut chip thickness which is by far the most important parameter of a machining operation because it determines (for a given work material) the cutting force, plastic deformation of the work material in its transformation into the chip, allowable feed, tool-chip contact length, etc. Therefore, the correlations between  $\kappa_r$  and the uncut chip thickness (known in the practice of metal cutting as the chip load) should be established.

In orthogonal cutting, the concept of the uncut chip thickness is self-obvious as it is equal to the thickness of the layer being removed (Fig. 2.1). Figure 3.1b,c helps to comprehend the concept of the uncut chip thickness in the simplest case of turning. As seen, the uncut chip cross section is represented by polygon ABCD. Side AD is formed by the major cutting edge, side AB is formed by the minor cutting edge, side DC is a part of the workpiece surface to be machined. The uncut chip thickness  $t_1$  is the thickness of the layer to be removed per one revolution of the workpiece as measured perpendicular to the cutting edge. As follows from Fig. 3.1c,

$$t_1 = f \sin \kappa_r \quad (3.2)$$

where  $f$  is the cutting feed per revolution.

It follows from Eq. 3.2 that, under a given feed  $f$ , the uncut chip thickness can be varied over a wide range by changing the angle  $\kappa_r$ . When this angle becomes

zero, the uncut chip thickness is also zero (no cutting) and when  $\kappa_r = 90^\circ$ , the uncut chip thickness reaches its maximum, becoming  $t_1 = f$  as in orthogonal cutting. Therefore,  $t_1 \in (0, f)$ .

The following equation for the uncut chip area correlates the feed,  $f$ , and the depth of cut,  $d_w$ , with the uncut chip thickness  $t_1$  and non-orthogonal chip width  $d_{wl} = b_l$ :

$$d_w f = t_1 d_{wl} = A_w \quad (3.3)$$

and

$$d_{wl} = \frac{d_w}{\sin \kappa_r} \quad (3.4)$$

where  $A_w$  is the uncut chip cross-sectional area.

It follows from Eq. 3.4 that, under a given feed and depth of cut, any change of  $t_1$  causes a corresponding change in  $d_{wl} = b_l$ . As seen, when  $t_1 \in (0, f)$ , the chip width  $d_{wl} \in (\infty, d_w)$ .

In general, the specific cutting force (the force that is acting on the unit length of the cutting edge) is proportional to the uncut chip thickness. For this reason, the uncut chip thickness is often referred to as the chip load in literature on metal cutting (Appendix A). As for a given cutting insert, the maximum allowable chip load is the same, and any change in the tool cutting edge angle changes the maximum allowable cutting feed. For example, according to Eq. 3.4, a change in  $\kappa_r$  from  $90^\circ$  to  $45^\circ$  allows a 30% increase in the allowable feed rate while keeping the chip load the same. This is often used in face milling where  $\kappa_r = 45^\circ$  is used when it is possible by the part geometry.

As discussed by Astakhov [14], this parameter is of great importance in determining many tribological characteristics of the cutting process. The smaller the chip load, the higher the tool life, and *vice versa*. However, there is the minimum uncut chip thickness (under other given cutting parameters) below which the opposite effect is true.

Two factors primary limit the minimum allowable uncut chip thickness:

- Decreasing the uncut chip thickness, one should increase the width of cut according to Eq. 3.4. When  $t_1 \rightarrow 0$ ,  $d_{wl} \rightarrow \infty$ , i.e., the length of the cutting edge should be increased to infinity. Obviously this is not practical.
- Decreasing the uncut chip thickness is limited by the radius of the cutting edge (discussed later).

### 3.3.2 Uncut Chip Thickness in Non-free Cutting

Real cutting cannot be regarded as free cutting (see Chap. 2 for definitions) because, apart from some specific machining operations, real tools almost always

have more than one cutting edge engaged in cutting. There have been a number of attempts to allow for the inter-influence of the neighboring cutting edges in determining the direction of chip flow. They are well summarized in [15]. Klushin [16] and Stabler [17] suggested that one should determine the true uncut chip thickness  $t_{IT}$  in the plane perpendicular to the direction of chip flow and the true uncut chip width  $b_{IT}$  ( $d_{wIT}$ ) in the perpendicular direction and equal to the length of the segment  $AB$ , which joins the ends of the major and minor cutting edges engaged in cutting, as shown in Fig. 3.2. In this figure, the directions  $AC$  and  $BC$  are orthogonal chip flow directions of the major and minor cutting edges, respectively, and direction  $AB$  is the resultant chip flow direction. The angle between  $AC$  and  $AB$  is referred to as the chip flow angle  $\eta_{ch}$ . The segment  $AB$  is often referred to as the equivalent cutting edge as suggested by Colwell [18]. Therefore, in non-free cutting, the uncut chip thickness depends on the orientation of the equivalent cutting edge.

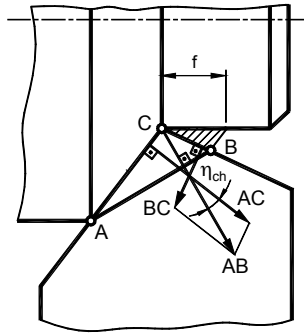


Fig. 3.2. Chip flow direction (after Astakhov [14])

Figure 3.3 shows a model for determining the chip flow direction for one of common configuration in turning where the tool has  $\lambda_s=0^\circ$  and  $\gamma_n=0^\circ$ . For this case the chip flow direction is determined as

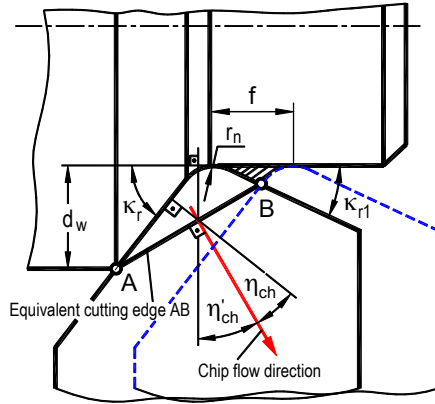
$$\eta_{ch} = \kappa_r - \eta'_{ch} \tag{3.5}$$

where

$$\eta'_{ch} = \begin{cases} \arctan \left[ \frac{c_\eta}{[1 - a_\eta(1 - \cos \kappa_r)] \cot \kappa_r + a_\eta(\sin \kappa_r + b_\eta)} \right] & \text{if } d_w \geq r_n(1 - \cos \kappa_r) \text{ and } f \leq 2r_n \sin \kappa_{r1} \\ \arctan \left[ \frac{c_\eta}{\sqrt{2a_\eta - 1} + a_\eta \cdot b_\eta} \right] & \text{if } d_w < r_n(1 - \cos \kappa_r) \text{ and } f \leq 2r_n \sin \kappa_{r1} \end{cases} \tag{3.6}$$

where

$$a_\eta = \frac{r_n}{d_w}, \quad b_\eta = \frac{d_w}{2r_n}, \quad c_\eta = 1 - a_\eta \left(1 - \sqrt{1 - b_\eta}\right) \quad (3.7)$$



**Fig. 3.3.** Model to determine the chip flow direction for a common configuration in turning

Figure 3.4 presents four basic configurations in non-free cutting. The first configuration, shown in Fig. 3.4, represents the most common single point tools in use today. The cutting tool is made with a nose radius  $r_n$  and set so that the depth of cut is greater than the nose radius. When

$$d_w \geq r_n (1 - \cos \kappa_r) \quad \text{and} \quad f \leq 2r_n \sin \kappa_{r1} \quad (3.8)$$

the formulas for calculation of  $t_{1T}$  and  $b_{1T}$  are as follows:

$$t_{1T} = \frac{f}{c_1} \sin \arctan \frac{c_1}{[1 - e_1 (1 - \cos \kappa_r)] \cot \kappa_r + e_1 (\sin \kappa_r + g_1)} \quad (3.9)$$

$$b_{1T} = \frac{c_1 d_w}{\sin \arctan \frac{c_1}{[1 - e_1 (1 - \cos \kappa_r)] \cot \kappa_r + e_1 (\sin \kappa_r + g_1)}} \quad (3.10)$$

where

$$c_1 = 1 - e_1 \left(1 - \sqrt{1 - g_1^2}\right), \quad e_1 = \frac{r_n}{t_1}, \quad g_1 = \frac{f}{2r_n} \quad (3.11)$$

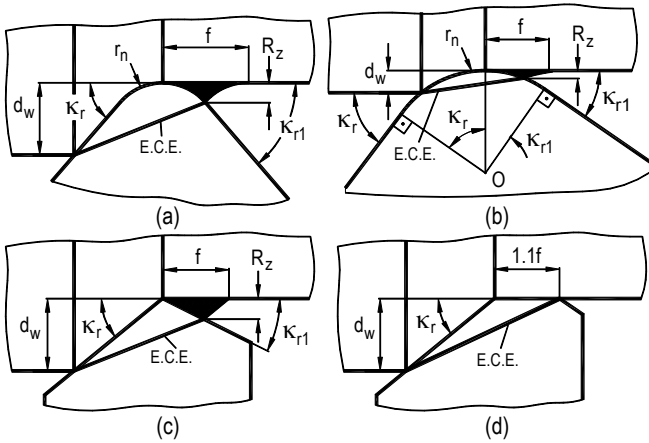
The second configuration shown in Fig. 3.4b is similar to the first except that only the radius part of the cutting edge is engaged in cutting. If the following relationships are justified:

$$d_w < r_n (1 - \cos \kappa_r) \text{ and } f \leq 2r_n \sin \kappa_{r1} \tag{3.12}$$

the formulas for calculation of  $t_{1T}$  and  $b_{1T}$  are as follows:

$$t_{1T} = \frac{f}{c_1} \sin \arctan \frac{c_1}{\sqrt{2e_1 - 1} + e_1 g_1} \tag{3.13}$$

$$b_{1T} = \frac{c_1 d_w}{\sin \arctan \frac{c_1}{e_1 g_1 + \sqrt{2e_1 - 1}}} \tag{3.14}$$



**Fig. 3.4.** Four basic configurations in non-free cutting (E.C.E is the equivalent cutting edge) (after Astakhov [14])

In the third configuration shown in Fig. 3.4c, the nose radius is rather small compared to the depth of cut, so that only the straight parts of the major and minor cutting edges are considered. Then the formulas for calculation of  $t_{1T}$  and  $b_{1T}$  are as follows:

$$t_{1T} = \frac{f}{q_1} \sin \arctan \frac{q_1}{1 + \cot \kappa_r - q_1} \tag{3.15}$$



$$b_{1T} = \frac{c_1 d_w}{\sin \arctan \frac{c_1}{e_1 g_1 + \sqrt{2e_1 - 1}}} \quad (3.16)$$

where

$$q_1 = 1 - \frac{f}{d_w} \frac{1}{\cot \kappa_r + \cot \kappa_{r1}} \quad (3.17)$$

### Example 3.2

**Problem:** Determine the true uncut chip thickness  $t_{1T}$  and the true uncut chip width  $b_{1T}$  for a turning operation with the cutting feed  $f = 0.25$  mm/rev and depth of cut  $d_w = 3$  mm. A standard square insert SNMG 432 having nose radius  $r_n = 1$  mm was mounted in a tool holder with  $\kappa_r = 45^\circ$  and  $\kappa_{r1} = 45^\circ$ .

**Solution:** As the considered cutting insert has two straight cutting edges and nose radius, case (a) in Fig. 3.4 is considered.

First, the conditions set by Eq. 3.8 should be verified

$$d_w \geq r_n (1 - \cos \kappa_r) \quad 2 \geq 1(1 - \cos 45^\circ) = 0.29 \quad \text{— justified}$$

$$f \leq 2r_n \sin \kappa_{r1} \quad 0.25 \leq 2 \sin 45^\circ = 1.41 \quad \text{— justified.}$$

The apparent uncut chip thickness is calculated according to Eq. 3.2

$$t_1 = f \sin \kappa_r = 0.25 \sin 45^\circ = 0.177 \text{ mm}$$

Variables set by Eq. 3.11 are calculated as

$$e_1 = \frac{r_n}{d_w} = \frac{1}{3} = 0.333 \quad g_1 = \frac{f}{2r_n} = \frac{0.25}{2 \cdot 1} = 0.125$$

$$c_1 = 1 - e_1 (1 - \sqrt{1 - g_1}) = 1 - 0.333 (1 - \sqrt{1 - 0.125^2}) = 0.902$$

The true uncut chip thickness is calculated using Eq. 3.9 as

$$t_{1T} = \frac{f}{c_1} \sin \arctan \frac{c_1}{[1 - e_1 (1 - \cos \kappa_r)] \cot \kappa_r + e_1 (\sin \kappa_r + g_1)} =$$

$$\frac{0.25}{0.997} \sin \arctan \frac{0.977}{[1 - 0.333(1 - \cos 45^\circ)] \cot 45^\circ + 0.333(\sin 45^\circ + 0.125)} = 0.162 \text{ mm}$$

As seen  $t_{IT} < t_I$  and this is the case in many practical machining operations.

The true uncut chip width calculates using Eq. 3.10 as

$$b_{IT} = \frac{c_1 d_w}{\sin \arctan \frac{c_1}{[1 - e_1(1 - \cos \kappa_r)] \cot \kappa_r + e_1(\sin \kappa_r + g_1)}} = \frac{0.977 \cdot 3}{\sin \arctan \frac{c_1}{[1 - 0.333(1 - \cos 45^\circ)] \cot 45^\circ + 0.333(\sin 45^\circ + 0.125)}} = 4.538 \text{mm}$$

End of Example 3.2.

In the fourth configuration shown in Fig. 3.4d, the nose radius is rather small so that only the straight parts of the major and minor cutting edges are considered. To improve the machined surface finish, the minor cutting edge is positioned parallel to the axis of rotation of the workpiece so that  $\kappa_{r1} = 0$ . As such, the length of the minor cutting edge is usually selected to be equal to  $1/f$ . The formulas for calculation of  $t_{IT}$  and  $b_{IT}$  are as follows

$$t_{IT} = f \sin \arctan \frac{1}{\cot \kappa_r + 2.2e_1g_1} \quad (3.18)$$

$$b_{IT} = \frac{d_w}{\sin \arctan \frac{1}{\cot \kappa_r + 2.2e_1g_1}} \quad (3.19)$$

Although the fourth configuration has been known for many years and its advantages are well documented, its implementation has often been accompanied by vibration and thus was restricted by the rigidity of machine tools. Only recently, when machine tools became rigid enough, did it become possible to use tools with such geometry on rigid milling machines. Using the rather shallow knowledge of users in the cutting tool history, cutting tool companies claim that they “invented” new inserts of innovative geometry which became known as “wiper” inserts (see Chap. 2, Sect. 2.7.2).

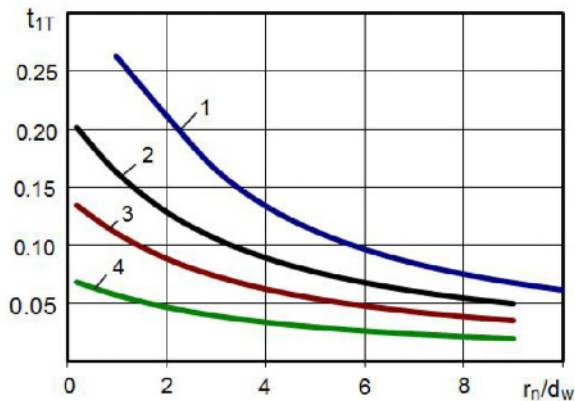
In operation, “wiper” technology is designed to improve surface finishes in milling applications. It works by positioning an insert with a flat just below (10–20 microns depending on the work material) the other ordinary parallel land inserts on a face mill. As the “wiper” insert passes through the cut, it smoothes the machined surface. For large diameter milling tools with many cutting inserts (cartridges), two or more wiper inserts can be used.

Sandvik Coromant has managed to create “wiper” technology for use on turning operations. What Sandvik has done is take an insert with a standard nose radius and added additional geometry behind the lead cutting edge. In operation, this geometry follows the tool nose with a “wiping” effect that knocks off the

peaks of the scallops created by the leading edge. Wiper geometries are often promoted as giving a mirror finish, but the real benefit, according to tool suppliers, is reduced cycle times resulting from increased feed rates. Users may even be able to double feed rates and maintain the same surface finish as that obtained using a standard insert. The company claims that the production advantages for these new inserts are dramatic. Shops have a choice of how to use the wiper to achieve either double the current feed rates used on a job or run the job at current feed and reduce by half the surface finish number of the current process.

Although the wiper geometry can be used to improve surface finish, it has some limitations. Wiper geometries are not for every application. They are not suited to light finishing operations, because they require more stock and slightly heavier depths of cut to work correctly. Also, they must be run at higher feeds to take full advantage of the wiper geometry. Moreover, they can be used only if the static and dynamic rigidities of the machine tool are high enough to prevent the vibration associated with the use of the geometry. Second, the presetting of the tool should be very accurate, preferably using a digital cutting tool pre-setter to achieve the tool minor cutting edge angle  $\kappa_{r1} = 0$ . This is because if  $\kappa_{r1} > 0$ , the efficiency of the wiper geometry reduces and if  $\kappa_{r1} < 0$ , the cutting force rises significantly may break the cutting insert. Third, the wiper geometry is not suitable in machining of some difficult-to-machine work materials having significant yield strength. This is due to elastic recovery (sometimes referred to as springback) of the machined surface. So-called re-cutting may occur in this case [19].

Numerical analysis of the formulas to calculate the true uncut chip thickness  $t_{1T}$  shows that  $t_{1T}$  in non-free cutting increases with the cutting feed,  $f$ , and the tool cutting edge angles of the major and minor cutting edges. It decreases with the ratio  $r_n/d_w$ . Figure 3.5 shows an example. The influence of  $r_n/d_w$  on  $t_{1T}$  is significant when  $r_n/d_w$  is small for great cutting feeds.



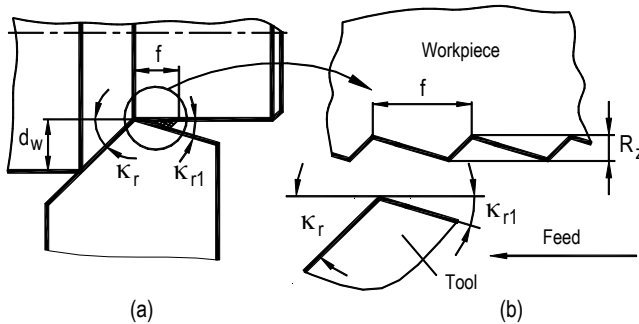
**Fig. 3.5.** Influence of  $r_n/d_w$  and the cutting feed on the true uncut chip thickness. First case when  $\kappa_r = 45^\circ$ ,  $r_n = 1\text{mm}$ . Cutting feeds: 1 – 0.4mm/rev, 2 – 0.3, 3 – 0.2, 4 – 0.1

**3.3.3 Influence on the Surface Finish**

Another important yet often ignored aspect of interest is the influence of the cutting edge angles  $\kappa_r$  and  $\kappa_{r1}$  on the surface finish of the produced parts [11]. As seen in Fig. 3.1, the tool leaves on the machined surface a profile the height of which is  $R_z$  which is considered theoretical surface finish. As seen in this figure,  $R_z$  depends on the cutting tool approach angles as well as on the tool nose radius and cutting feed.

Consider the simplest case when the nose radius is zero as shown in Fig. 3.6a. As seen in Fig. 3.6b, the height  $R_z$  and profile of this roughness (theoretical resulting from the feed marks) depends on the cutting feed, the cutting edge angles and the major and minor cutting edges. This roughness can easily be computed in terms of maximum peak-to-valley distance as

$$R_z = \frac{f}{\cot \kappa_r + \cot \kappa_{r1}} \tag{3.20}$$



**Fig. 3.6.** Model of roughness left on the machined surface

When a full-radius cutting insert is used, the discussed roughness can be calculated as:

$$R_z = r_n - \sqrt{r_n^2 - \frac{f^2}{4}} \tag{3.21}$$

Though exact, Eq. 3.21 is very sensitive to small values of nose radius  $r_n$  and feed  $f$ . A more practical equation can be derived. It follows from Eq. 3.21 that

$$(r_n - R_z) = r_n^2 - \frac{f^2}{4} \text{ or } 4R_z^2 - 8r_n R_z + f^2 = 0 \tag{3.22}$$

If the term  $4R_z^2$  is assumed negligible compared to remaining terms, then

$$R_z \approx \frac{f^2}{8r_n} \quad (3.23)$$

*Example 3.3*

*Problem:* Determine the maximum peak-to-valley distance (theoretical surface roughness) in turning using the single point tool with a small nose radius (Fig. 3.4c), the cutting feed  $f = 0.25\text{mm/rev}$  and depth of cut  $d_w = 3\text{mm}$ . A standard diamond-shaped insert CEJN 2525M is mounted in a tool holder with  $\kappa_r = 95^\circ$  and  $\kappa_{r1} = 7.5^\circ$ .

How would this distance change if a standard RCMX 1204MO round insert having diameter of 16 mm is used instead?

*Solution:* With a standard diamond-shaped insert CEJN 2525M, one can calculate the maximum peak-to-valley distance using Eq. 3.20

$$h_m = \frac{f}{\cot \kappa_r + \cot \kappa_{r1}} = \frac{0.15}{\cot 95^\circ + \cot 7.5^\circ} = 0.049\text{mm}$$

When a standard RCMX 1204MO round insert is used, the maximum peak-to-valley distance is calculated using Eq. 3.23

$$R_z \approx \frac{f^2}{8r_n} = \frac{0.15^2}{8 \cdot 16} = 0.0018\text{mm}$$

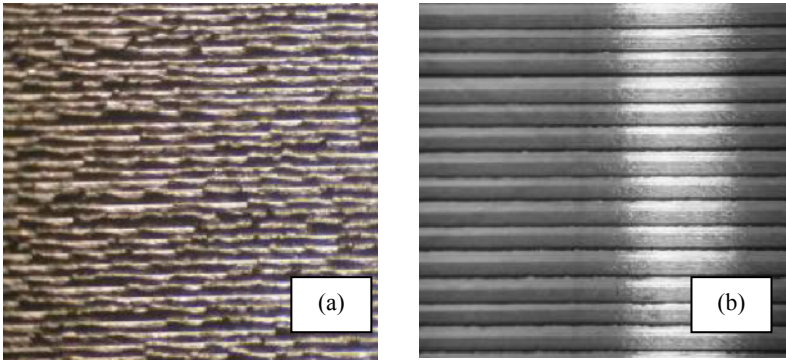
A comparison shows that the maximum peak-to-valley distance (theoretical surface roughness) decreases significantly when the latter insert is used.

End of Example 3.3.

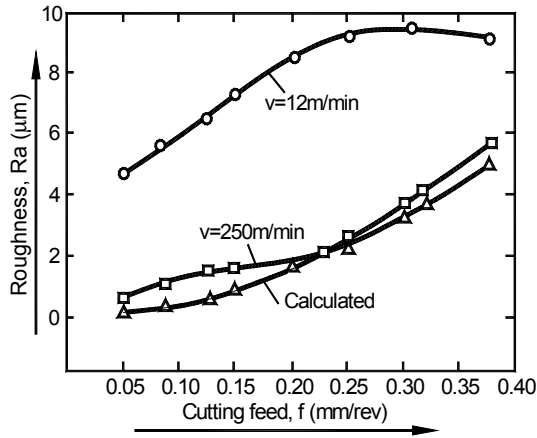
A logical question to be answered is: How far is the geometrical (theoretical) roughness of the machined surface from that obtained in the real cutting? As discussed by Astakhov [14], if the cutting process takes place at the optimal cutting temperature, the BUE does not form at all so it does not have any effect on the surface finish. Figure 3.7 exemplifies this statement. As seen, the BUE affects the surface finish only when working with low cutting speeds when the cutting temperature is below the optimal cutting temperature (Fig. 3.7a). When the cutting temperature is close or equal to the optimal cutting temperature, the BUE does not form at all so the surface roughness is practically equal to the so-called theoretical surface roughness determined by tool geometry and the cutting feed as seen in Fig. 3.7b [14].

Figure 3.8 shows the comparison of the surface finish calculated through the tool geometry and the cutting feed with that obtained experimentally at two different cutting speeds. As seen, when the cutting speed is selected so that the cutting temperature is close to the optimal cutting temperature (depending upon the particular cutting feed as it also affects the cutting temperature), the actual and the

calculated surface roughnesses are close to each other. When the combination of the cutting speed and feed results in the optimal cutting temperature, they are the same.



**Fig. 3.7.** Surface finish in logitudinal turning. Work material - ANSI 1045 steel, tool material - Carbide P10 (14%TiC,8%Co), rake angle  $\gamma_n = 7^\circ$ , flank angle  $\alpha_n = 9^\circ$ , tool cutting edge angle  $\kappa_r = 93^\circ$ , tool cutting minor cutting edge angle  $\kappa_{r1} = 27^\circ$ , tool nose radius  $r_n = 1\text{mm}$ , depth of cut  $d_w = 0.3\text{mm}$  at different cutting conditions: (a) cutting speed  $v = 12\text{m/min}$ , feed  $f = 0.38\text{mm/rev}$ , and (b)  $v = 250\text{m/min}$ ,  $f = 0.45\text{mm/rev}$



**Fig. 3.8.** Calculated and actual surface roughness at two different cutting speeds (the cutting tool and work material are the same as those identified in the legend of Fig. 3.7)

### 3.3.4 Tools with $\kappa_r > 90^\circ$

Wide use of CNC machines and manufacturing cells, a need for versatile tools capable of turning, facing, and copying led to the development of tools having the tool cutting edge angle  $\kappa_r > 90^\circ$ . The development of  $80^\circ$ ,  $70^\circ$ , and  $35^\circ$  diamond-

shaped, and  $80^\circ$  trigon cutting inserts combined with various tool holders made it possible to obtain a wide range of such tools. Tools with  $80^\circ$  diamond-shaped inserts (CNGG, CNGA, CNMA, CNMG, CNMP) became most common. Some of the common tools and tool holders are shown in Figs. 3.9 and 3.10.



Fig. 3.9. Common tools with  $\kappa_r > 90^\circ$

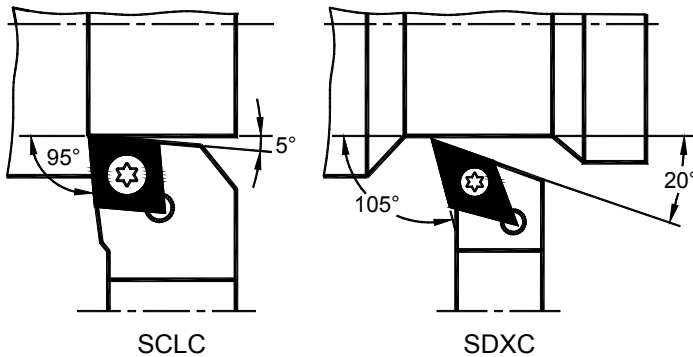
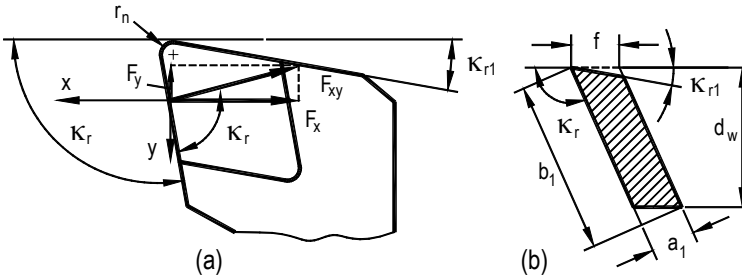


Fig. 3.10. Common tool holders for tools with  $\kappa_r > 90^\circ$

Figure 3.11 shows the changes which the discussed geometry makes to the force system and uncut chip thickness compare to the tool with  $\kappa_r \leq 90^\circ$ . As seen, the radial force  $F_y$  changes direction becoming ‘negative’, i.e., it is directed to the axis of the workpiece. If one compares two tools, one with  $\kappa_r = 85^\circ$  and another with  $\kappa_r = 95^\circ$  using the basic notions of metal cutting theory and tool geometry, one should arrive to following conclusions:

1. When depth of cut  $d_w$  is much greater than the nose radius and the theoretical depth of machined surface roughness, then:
  - The volume of the material removed is the same so that the uncut chip thickness and its width are the same for both tools.
  - Although the normal rake and flank angles are the same for both tools, the inclination angle, axial and radial rake and flank angles are not the same as discussed in Chap. 2, Sect. 2.4.2. When the inclination angle is small, the difference is negligible. This is not the case, however, when the inclination angle  $\lambda_s > 10^\circ$ .

- Because the uncut chip thickness and the volume of the work material to be removed as well as the normal rake and flank angles are the same for both tools, the power spent in cutting and thus the cutting force should be the same. The difference is in the direction of the radial force  $F_y$ , which is “negative” for the tool with  $\kappa_r = 95^\circ$ . Therefore, this tool should bend the workpiece in the opposite way to that with  $\kappa_r = 85^\circ$  with the same net result in terms of shape of the machined workpiece in the axial section plane.



**Fig. 3.11.** (a) A model of the forces in the  $xy$ -plane for a tool with  $\kappa_r > 90^\circ$  and, (b) the uncut chip cross-section

2. When depth of cut  $d_w$  is not much greater than the nose radius and the theoretical depth of machined surface roughness, then the following should be the case
  - Because the nose radius in this case adds up to 15% of the cutting power and thus cutting force [20], the radial force  $F_y$  does not become zero when  $\kappa_r = 90^\circ$  as should happen with  $r_n = 0$  according to Fig. 3.1 and Eq. 3.1. Rather, this force becomes zero when the additional radial force due to the nose radius is balanced by a certain “negative” force when the tool cutting edge angle exceeds  $90^\circ$ .
  - When  $\kappa_r = 95^\circ$ , the amount of the work material removed by the minor cutting edge increases compare to that when  $\kappa_r = 85^\circ$ . Therefore, a certain increase in the cutting force should be the case.

Figure 3.12 summarizes the results of the known studies [21–23] of tools having the tool cutting edge angle  $\kappa_r > 90^\circ$ . As seen, these results are not exactly the same as discussed using the model shown in Fig. 3.11. Therefore, the differences and similarities should be addressed:

- According to the data shown in Fig. 3.12, the tangential cutting force (the power components of the cutting force) increases with  $\kappa_r$ , which is in direct contradiction with the cutting theory [14]. This is because when  $\kappa_r$  increases and the cutting feed is kept the same, the chip compression ratio and thus the amount of plastic deformation of the layer being removed decreases which must lead to a decrease of the cutting force. The root cause



of the result shown in Fig. 3.12 was that they were not obtained in non-systemic approach to the studies. Namely, the same inserts CNMG 432 (see Appendix 2) was used to obtain different  $\kappa_r$  by placing them into different tool holders. As such, when  $\kappa_r$  was increased, the tool minor cutting edge angle  $\kappa_{r1}$  was decreased so that the amount of the work material removed by the minor cutting edge was increase. That caused an increase in the cutting force.

- The data shown in Fig. 3.12 suggest that the radial cutting force  $F_y$  does not become zero when  $\kappa_r = 90^\circ$ . Rather it becomes zero when  $\kappa_r \approx 95^\circ$  as was predicted.
- A decrease of the cutting force beyond  $\kappa_r = 95^\circ$  is not supported by the cutting theory. Rather it was caused by non-systemic approach to the studies. Namely, to obtain  $\kappa_r > 95^\circ$ , cutting insert CNMG 432 was replaced by DNMG 432 which increased the tool minor cutting edge angle  $\kappa_{r1}$ . This was the root cause of the apparent decrease in the cutting force.

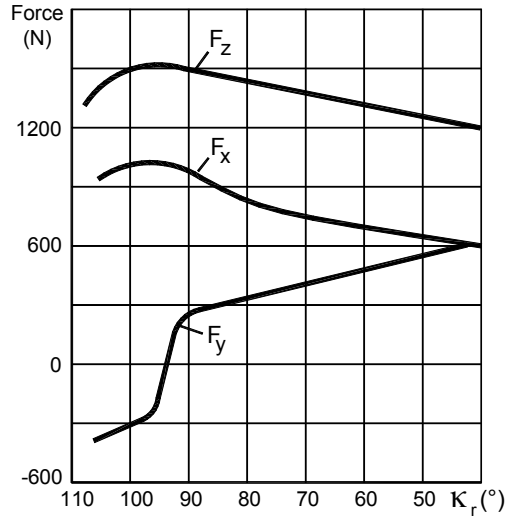


Fig. 3.12. Influence of the tool cutting edge angle on the cutting forces

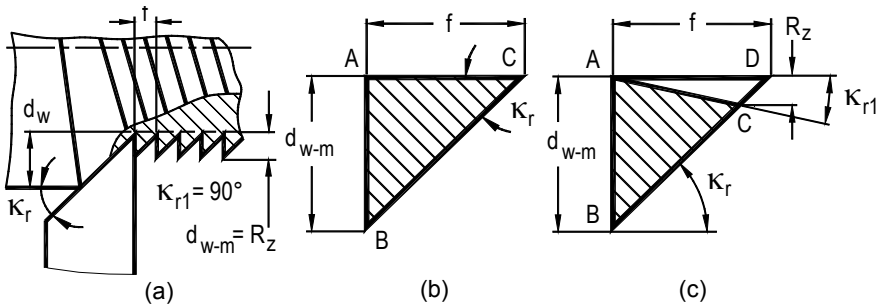
### 3.3.5 Tool Minor Cutting Edge Angle

#### 3.3.5.1 Single-point Tools

The role of the minor cutting edge and its influence on the cutting force and power consumption are seldom considered in the literature on metal cutting. At best, the influence of the tool minor cutting edge angle  $\kappa_{r1}$  is mentioned in the consideration of the theoretical roughness of the machined surface or geometric component of roughness as discussed in Sect. 3.3.3. In the author's opinion, the term "minor" probably misled many researchers in the field, causing a common perception that,

besides the microgeometry of the machined surface, this cutting edge does not affect the cutting process to any noticeable degree.

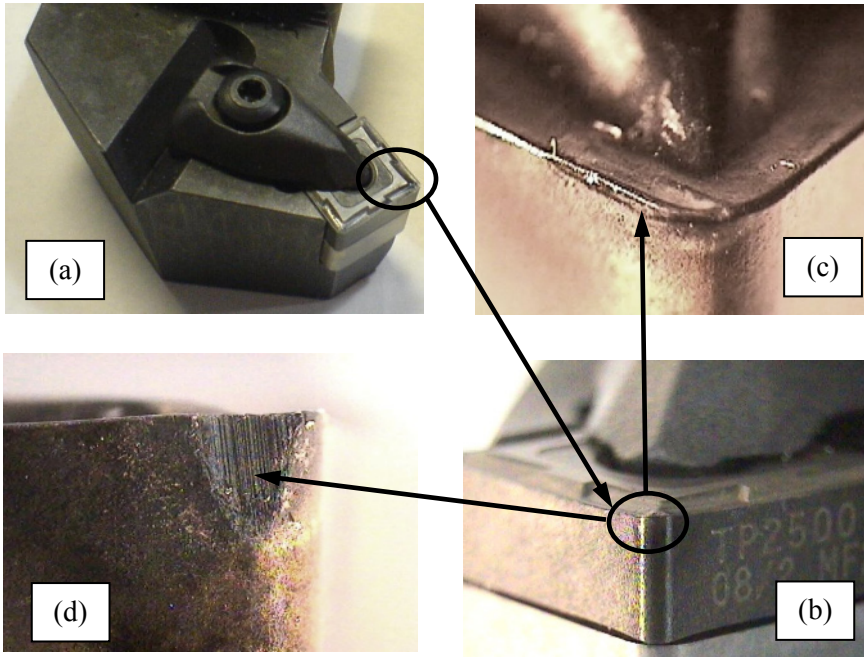
Zorev provided a detailed analysis of chip formation by the minor cutting edge [24]. He studied the velocity hodograph, associated plastic deformation, and flows in this region. Using the results of this study, one can visualize the chip cross-sectional area cut by the minor cutting edge with the aid of Fig. 3.13. Figure 3.13a shows a hypothetical single-point cutting tool having  $\kappa_{r1} = 90^\circ$  i.e. practically this tool does not have the minor cutting edge. Figure 3.13b shows the cross-sectional area  $ABC$  of ‘a tooth’ of the surface profile left after this surface was machined by this tool. Real cutting tools have the minor cutting edge with  $\kappa_{r1} \ll 90^\circ$  so that the surface profile left by the cutting tool is  $ADC$  as shown in Fig. 3.13c and its height are calculated using Eq. 3.20. Therefore, the part  $ABC$  shown in Fig. 3.13c is cut by the minor cutting edge.



**Fig. 3.13.** The cross-sectional area of the chip cut by the minor cutting edge: (a) hypothetical tool having a  $90^\circ$  tool cutting edge angle of the minor cutting edge, (b) the cross-section of the chip cut by the minor cutting edge when the tool minor cutting edge angle is  $90^\circ$ , and (c) geometrical model to calculate the cross-sectional area of the chip cut by the minor cutting edge when the tool minor cutting edge angle is less than  $90^\circ$

According to Zorev [24], the contribution of the cutting and deformation process on the minor cutting edge to the overall power spent in cutting depends on the tool minor cutting edge angle  $\kappa_{r1}$  and on the cutting feed,  $f$ . When the feed becomes significant, the minor cutting edge takes the role of the major cutting edge so that thread cutting is the case. In real cutting tools, the tool nose radius is always made to connect the major and minor cutting edges. At moderated cutting feeds, the crater tool wear combined with the wear of the major flank occur in machining a wide variety of steels in Fig. 3.14c while, when the feed rate becomes greater, wear of tool nose takes place as shown in Fig. 3.14d. This is because the energy spend due to cutting by the minor cutting edge becomes great so that the prime mode of tool wear changes shifts from crater to nose wear.

Analysis of the experimental results obtained by Zorev on the assessment of the cutting energy [24] and the comparison of the experimentally obtained powers associated with the cutting tool having various tool minor cutting edge angles suggested [20] that when the tool minor cutting edge angle  $30^\circ \leq \kappa_{r1} \leq 45^\circ$  then the



**Fig. 3.14.** Tool wear region shifts with the cutting feed: (a) a typical CNC lathe tool, (b) working part, (c) typical crater wear observed at moderated feed rates, and (d) nose wear observed at high feed rates

total power should be increased by 14%, when  $15^\circ \leq \kappa_{r1} < 30^\circ$  – by 17%, when  $10^\circ \leq \kappa_{r1} < 15^\circ$  – by 20%, and when  $\kappa_{r1} < 10^\circ$  – by 23%.

### 3.3.5.2 Drills

Although according to the author's experience the tool minor cutting edge angle is an extremely important parameter of the various drills and reamers geometry, surprisingly not many specialists in the field of metal cutting and tool design can identify this angle for these tools. Figure 3.15 shows the definition of the tool minor cutting edge angle for a straight-flute drill (in the picture,  $\kappa_{r1}$  is shown significantly exaggerated for clarity). As seen it is defined according to the standards definition provided by ISO 3002-1 standard (see Chap. 2) as the acute angle between the projection of the minor (side) cutting edge into the reference plane (a plane that contain the drill longitudinal axis) and the direction set by the vector of the cutting feed. Figure 3.15 also shows the proper definition for the tool cutting edge angle  $\kappa_r$  as it is supposed to be understood in all axial tools including drills and reamers.

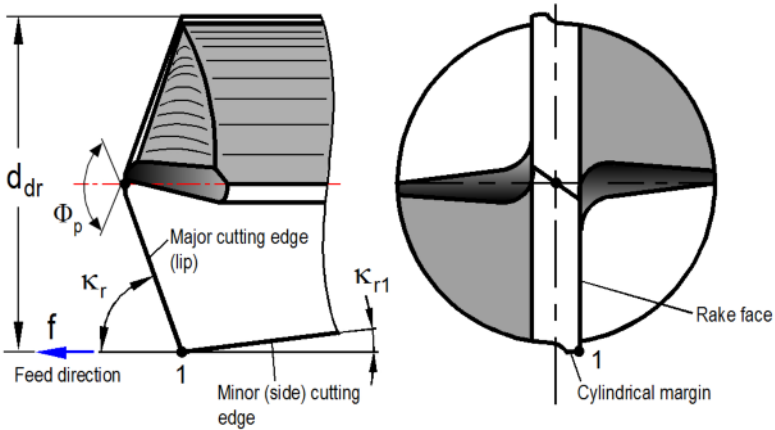


Fig. 3.15. Meaning of the tool minor cutting edge angle  $\kappa_{r1}$  for a straight-flute drill

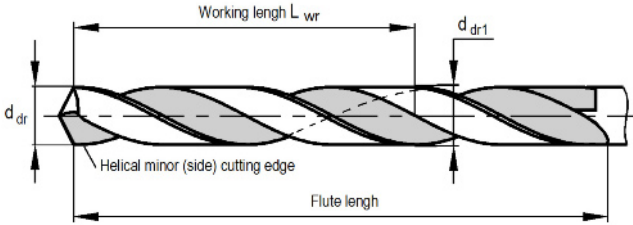
In the practice of drill design, the tool cutting edge angle and tool minor cutting edge angle are not directly shown in tool drawings. Instead the tool cutting edge angle, the so-called point angle  $\Phi_p$ , is indicated on tool drawings. The sense of this angle is shown in Fig. 3.15 As seen

$$\kappa_r = 90^\circ - \Phi_p / 2 \tag{3.24}$$

In turn, the tool minor cutting edge angle  $\kappa_{r1}$  is ‘hidden’ in the so-called backtaper. The sense of this backtaper is as follows. Normally, the drill (reamer) side cutting edges formed at the intersection line of the rake face and the cylindrical margin are not parallel to the tool longitudinal axis but rather backtapered from the front towards the tool shank. According to the accepted definition [25], the backtaper is a slight decrease in diameter from the front to back in the body of the drill. For twist drills, the backtaper  $\Delta_{bt}$  (included) is assigned on the drawing as a diameter decrease  $(d_{dr} - d_{dr1})$  per working length  $L_{wr}$  (as shown in Fig. 3.16). As such, the tool minor edge angle calculates as

$$\kappa_{r1} = \arctan \frac{\Delta_{bt}}{2L_{wr}} \tag{3.25}$$

The common perception of the role and importance of the backtaper stems from the experience with twist drills. As thought, in twist drilling, the purpose of the backtaper is to reduce the heat due to friction while the tool is engaged in the workpiece thereby preventing drill binding. Conventional drill designs have backtaper values that correspond to standards established within the industry. Most high performance drills, on the other hand, have backtaper values that are virtually double those pre-established guidelines. These higher values create more relief while the drill is in the workpiece, minimizing heat. Although such binding is one



**Fig. 3.16.** Backtaper applied over the working length

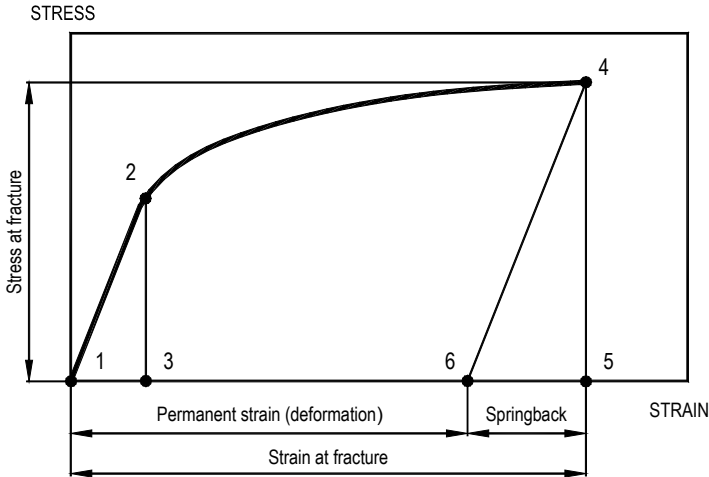
of the most common failure modes of twist drills, its cause is not well understood. Therefore, a need is felt to clarify this important issue.

When material is cut, the cutting tool deforms material elastically and then plastically to separate the stock to be removed from the rest of the workpiece. Once the working part of the drill passes a certain area of the hole being drilled, the metal will spring back as the cutting load is released so the hole diameter becomes smaller. In order to understand springback, it is necessary to consider the stress-strain diagram of the work material.

A typical diagram is shown in Fig. 3.17. Point 1 represents unstressed material. When a force is applied, the work material deforms first elastically up to point 2 on the diagram. This point represents the so-called elastic limit. Within this limit, the work material is subjected to only elastic deformation so if the applied stress is released, the material regains its initial size. The distance 1–2 on the strain axis represents the maximum elastic deformation. If the applied stress exceeds the elastic limit, the material exhibits a combination of the elastic and plastic deformations. The applied stress can grow further up to point 4 on the diagram where fracture occurs. The strain corresponding to point 4 is known as the strain at fracture. In Fig. 3.17, it is represented by distance 1–5 on the strain axis. After fracture, however, the applied stress is released and the permanent strain found in the work material (represented by distance 1–6 in Fig. 3.17) is less than that at fracture by the elastic strain represented by distance 6–5 in the stress-strain diagram. As such, the location of point 6 is readily found by drawing a line from point 4 parallel to line 1–2. As such, distance 6–5 in the stress-strain diagram is known as elastic recovery in materials testing or springback in materials processing.

As discussed in Chap. 1, when the work material is being cut, the material is deliberately over-stressed beyond the elastic limit in order to induce a permanent deformation and then separation of the stock to be removed. As such, the fracture of the chip from the wall of the hole being drilled occurs so the strain and stress at fracture are achieved at any point of separation of the work material. When the working part of the drill has passed a certain part of the machined hole, the load due to cutting is removed so that the applied stress returns to zero. As a result, the machined hole shrinks due to springback.

Moreover, the thermal energy due to plastic deformation of the work material and friction between the tool and the workpiece in their relative motion causes thermal expansion of the workpiece. When the tool periphery point (point 1 in Fig. 3.15) advances further, the work material contracts. As a result of the mentioned mechanical and thermal factors, the diameter of the hole being machined becomes



**Fig. 3.17.** A typical stress–strain diagram for the work material showing the meaning of springback

smaller than that of the diameter of the drill. Therefore, if no backtaper is made on the drill, the drill will be banded in the hole being drilled.

Several variables influence the amount of springback. Among others, the stress at fracture (defines the height of the starting point of the unloading line represented by point 4 in Fig. 3.17) and the modulus of elasticity (defines the slope of the unloading line represented by line 4-6 in Fig. 3.17). It is obvious from the diagram shown in Fig. 3.17 that the higher the strength of the work material, the greater springback; the lower the elasticity modulus, the higher springback. Therefore, the tool cutting edge angle of the minor cutting edge should be made work material specific as, on one hand, it is desirable that the diameter of drill does not change significantly with the number of re-sharpenings, but, on the other hand, the said binding should not occur either. Unfortunately, drill manufacturers do not pay much attention to this important issue.

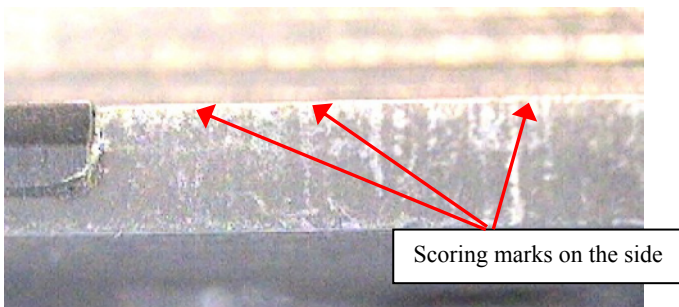
Consider few practical examples. To the first approximation, the said springback can be determined as the ratio of the ultimate strength of the work material,  $\sigma_{UTS}$  and its elasticity modulus,  $E$ , i.e.  $\text{springback} = \sigma_{UTS}/E$ . As the modulus of elasticity is almost the same for wide group of steels ( $E = 200\text{GPa}$ ), the springback is determined by the strength of the steel. For cold drawn steel AISI 1012 having  $\sigma_{UTS} = 270\text{MPa}$ ,  $\text{springback} = 0.00185$  while for annealed steel AISI 1095 having  $\sigma_{UTS} = 650\text{MPa}$   $\text{springback} = 0.00325$ . Unfortunately, the same twist drill is used for drilling these two work materials, i.e., no account is taken for the difference in springbacks of these two materials. The matter gets worse when titanium or aluminum alloys are drilled. For commonly used annealed titanium alloy Ti-Al6-4V(Grade 5)  $\sigma_{UTS} = 880\text{MPa}$ ,  $E = 113.8\text{GPa}$ ,  $\text{springback} = 0.00772$ . This explains known difficulties with drill binding in machining of titanium alloys.

As discussed above, another factor that affects the possibility of drill binding in the hole being drilled is thermal expansion. The drill margin(s) made with zero flank angles always rubs against the wall of the hole being drilled. The higher

springback, the higher the thermal energy released due to this rubbing, and the higher the temperature rises. When backtaper is sufficient, the discussed rubbing occurs only over the small portion of the margin adjacent to the drill periphery corner. If, however, the backtaper is insufficient, the discussed rubbing occurs over a great portion of the margin causing significant contact temperatures. As the contact temperature rises, the drill and the hole being drilled expand. This expansion depends on many factors primarily on the coefficient of thermal expansion (CTE), thermal conductivity, mass, etc. One should realize that for the same contact temperature and CTE for the workpiece and for the drill, the drill expands greater as its mass is much smaller so it heats up faster.

Consider a few practical examples. For tool materials: HSS M4 (common tool materials for HSS drills)  $CTE = 12.24((\mu\text{m}/\text{m})/^{\circ}\text{C})$ , for WC6Co carbide  $CTE = 6.5((\mu\text{m}/\text{m})/^{\circ}\text{C})$ . For work materials: steel AISI 1045  $CTE = 13((\mu\text{m}/\text{m})/^{\circ}\text{C})$ , steel AISI 1095  $CTE = 12.4((\mu\text{m}/\text{m})/^{\circ}\text{C})$ , Ti-alloy  $CTE = 9.2((\mu\text{m}/\text{m})/^{\circ}\text{C})$ . As seen: (1) HSS drill expands much greater than carbide drills that should be accounted for in assigning the proper backtaper for these drills, (2) Ti-alloy has much smaller coefficient of thermal expansion than HSS. As a result, backtaper on HSS drills should be made greater than on carbide drills.

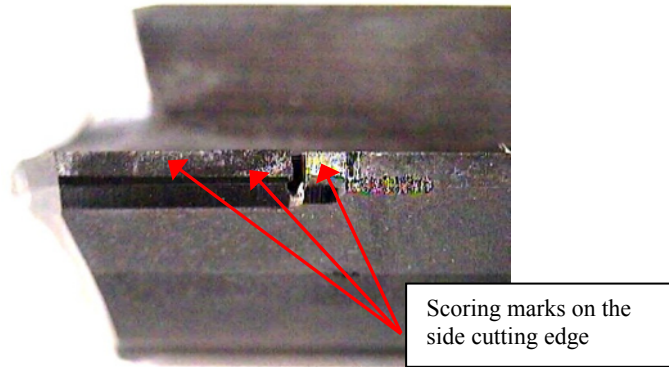
When the backtaper is insufficient, the result depends on to what extent it is insufficient and many other particularities of the hole-making operations. The simplest outcome of insufficient backtaper is the so-called scoring. Figure 3.18 shows the appearance of scoring marks on the side margin. Figure 3.19 shows the appearance of scoring marks on the side margin of a PCD insert. When the scoring happens in drilling, the surface finish of machined holes deteriorates significantly.



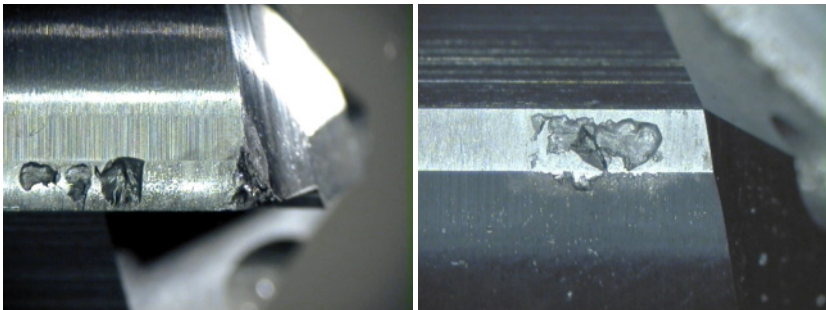
**Fig. 3.18.** Scoring marks on the side cutting edge due to insufficient backtaper

When the backtaper becomes even smaller than that causing simple scoring, the tool condition deteriorates rapidly. Figure 3.20 shows the common wear pattern that occurs on drill margins due to high contact stresses caused by insufficient backtaper. Figure 3.21a shows a comparison of new and worn detachable supporting pads of a deep-hole drill when backtaper is optimal. Figure 3.21b shows what the wear pattern is when backtaper is small. Figure 3.22 shows the working part of a drill with a severely insufficient backtaper. As can be seen, the side margin is ruined due to high contact pressure and the BUE is formed on the additional supporting pad. When this contact pressure becomes high enough, particularly for multi-edge axial tools as reamers, the tool breaks because of an excessive torque as

shown in Fig. 3.23. Often, such a breakage is wrongly attributed to a misalignment problem not noting that the tool is completely bound in the hole. Even after the tool breaks, its removal presents a significant problem. When such a failure happens, the part should be carefully sectioned to carry out the root cause analysis this failure.



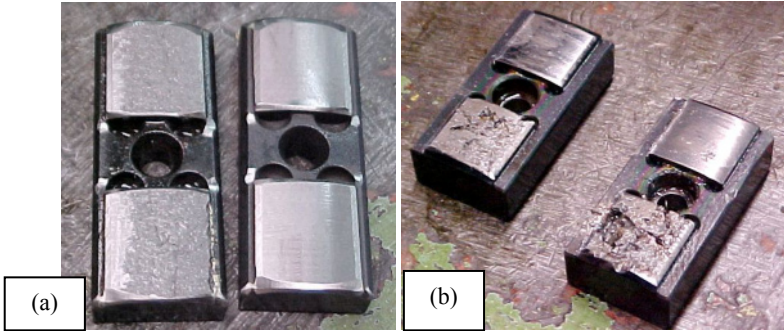
**Fig. 3.19.** Scoring marks on the side cutting edge of a PCD insert due to insufficient backtaper



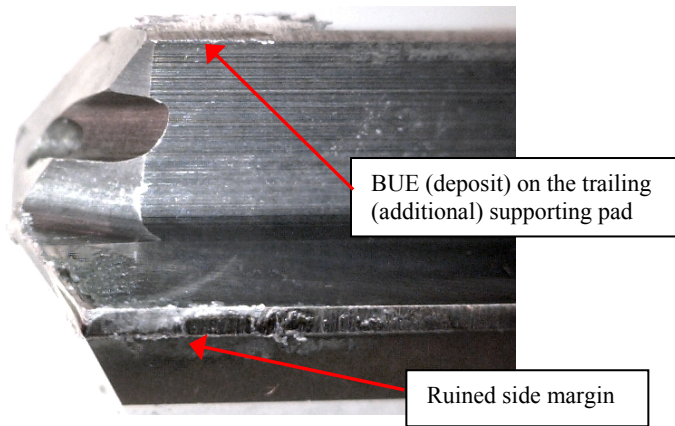
**Fig. 3.20.** Wear of the drill major and trailing margins due to high contact pressure caused by lack of backtaper

The backtaper also plays a very important role in finishing hole operations with PCD tools as reaming and boring in high-silicon automotive alloys. When the backtaper is very small, the diameter of the machined hole is smaller than that of the tool. The author observed a 7  $\mu\text{m}$  difference for a reamer of 15 mm dia. This is because such a work material having a great thermal conductivity expands significantly due to the rubbing of the side margin. When the operation is over, it rapidly contracts due to cooling by a great flow rate of MWF (coolant). When this is the case, a deep tool retraction mark can be observed on the machined surface.





**Fig. 3.21.** Wear of the detachable supporting pads of a deep-hole drill: (a) wear patten when backtaper is optimal, and (b) wear patten when backtaper is small.



**Fig. 3.22.** Consequences of a severely insufficient backtaper

To prove that this is the case, i.e., there is an optimal backtaper for given conditions, a special carefully prepared test was carried out. The workpieces (the pump cover of an automatic transmission) made of high-silicon aluminum alloy 390 containing 18%Si were selected from the same batch of die casting. The tests were carried out on a new production machining center with a high-speed ceramic-bearings spindle. All the other tools (for roughing) and work-holding fixture were the same. High-pressure MWF (of 8  $\mu\text{m}$  filtration, 9.5pH, no tramp oil, 9.5% concentration) was supplied with the same flow rate and was controlled by a digital flow valve. Three tools (Fig. 3.24) with PCD inserts were prepared for the tests. The PCD inserts made from the same PCD round blank were secured on the body with the same flax and brazing filler at the same brazing temperature. Each of the tools was ground with different backtapers. The difference in backtapers was  $0.2^\circ$ . After being machined, the workpieces were sectioned as for the inspection of the machined hole (Fig. 3.24).

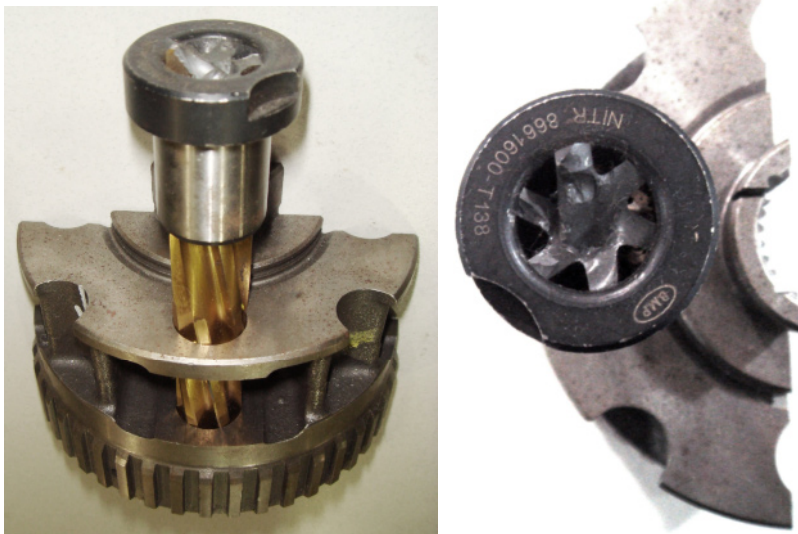
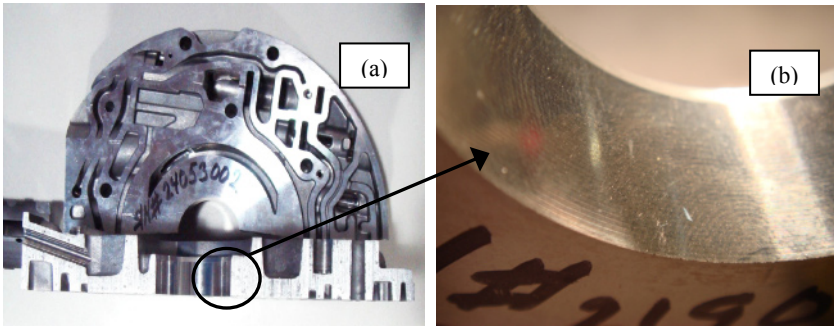


Fig. 3.23. A reamer jammed in a part (the gear carrier of an automatic transmission)

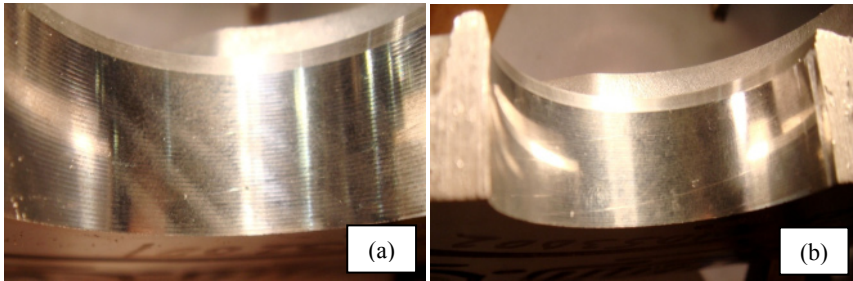


Fig. 3.24. Three tools prepared for the test

Figure 3.25a shows the sectioned hole and Fig. 3.25b the best results achieved with the optimal backtaper. As seen, the machined hole has smooth surface and no retraction marks. Figure 3.26a shows the results for the smallest backtaper. As can be seen, when the backtaper was small, the machined hole has the worst surface finish and a deep tool retraction mark. When the backtaper is slightly increased (Fig. 3.26b), the surface of the machined hole improves significantly and, although still being seen, the retraction mark does not present any problem in the mandatory transmission leakage test. The obtained results all, but conclusively prove the importance of the optimal backtaper in hole finishing operations.



**Fig. 3.25.** Sectioned workpiece (a) and the best achieved result (b)



**Fig. 3.26.** The result with (a) the smallest, and (b) intermediate backtapers

Unfortunately, this issue is not understood in the automotive industry. There are two major reasons for this. First is that the role of backtaper became significant only recently when other imperfections of the machining system (misalignment, parameters of MWF (coolant) in terms of its clearness and content, spindle runout, workholding fixture accuracy and rigidity, etc.) were improved. Moreover, new quality policies require 100% gaging of the machined part and even a CMM machine as part of the production line which measures many parameters of machined hole quality. The second issue is that PCD tipped reamers used for finishing tight-tolerance operations have relatively short PCD tips. As such, the measuring of the actual backtaper is virtually impossible even if the advanced tool pre-setting machine, such as, for example Kelch or Zoller, are used because the difference in the tool diameter due to backtaper over the actual length of an insert is beyond the recognition range of such machines.

In the author's experience, the discussed problem is one of the major issues with PCD reamers in the automotive industry as many, even the most reputable tool manufacturers, cannot produce tools with consistent backtapers. The worst scenario is when the side margins are not lapped after their EDM machining. Even the most accurate EDM machines and dividing fixtures (for multi-flute reamers) are not nearly capable of producing the backtapers with required consistency not to mention the rough surface finish of these margins and the damaged layer on their

surface. Even if the discussed margins are ground (lapped) after EDMing, there is no sound metrological procedure in place to assure the backtaper consistency.

### 3.3.5.3 Significance of the Minor Cutting Edge in Drills and Reamers

To understand the real significance of the minor cutting edge, consider a hypothetical drill as shown in Fig. 3.27. As can be seen, this drill has a single (major) cutting edge and no minor (side) cutting edge. Figure 3.28 shows the axial cross-section of the hole being drilled by this tool. For clarity, the feed per revolution is significantly exaggerated. Although this profile looks a little strange, Fig. 3.29 explains this result. Figure 3.29a shows two successive positions of the discussed drill. As seen, because there is no side cutting edge provided, a part of the work material represented by triangle  $ABC$  forms at each drill revolution that yields in the hole profile shown in Fig. 3.28. Moreover, if  $\kappa_r$  increases, as shown in Fig. 3.29b, the interference of the workpiece and the drill shank will be the case. When  $\kappa_r \rightarrow \pi/2$  (an extreme case for the considered hypothetical drill), contour  $ABB'C$  changes assuming a rectangular shape having the maximum cross-section area.

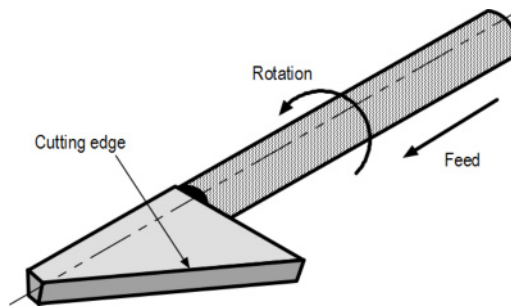


Fig. 3.27. Hypothetical drill without minor cutting edge

What happens in real drills (the foregoing analysis covers any type of drill)? A real drill is made with the minor (side) cutting edge that cuts the material left by the major cutting edge. As such, the following is true: the greater  $\kappa_r$ , the more uncut material is left for the minor (side) cutting edge. As follows from Fig. 3.29b, when  $\kappa_r = \pi/2$ , the minor (side) edge cuts the maximum amount of the work material under a given feed  $f$ . Unfortunately, this edge is not meant for cutting and thus it does not have the right clearance (flank angle) that makes drilling unstable and causes premature wear of the drill periphery corners.

Figure 3.30 exemplifies the issue. It shows a straight-flute drill (Fig. 3.30a) for high-speed machining of high-silicon aluminum alloy with a high feed. Figure 3.30b shows beginning of wear of the side cutting edge. As can be seen, excessive rubbing of the margin starts to take place because the side cutting edge is not meant to cut thus it does not have any relief (flank angle). Figure 3.30c shows the temperature profiles represented by discoloration of the carbide tool material due to high temperatures. As can be seen, the temperature increases exponentially towards the margin. As the side cutting edge is not meant to cut but is forced to

cut, such cutting unavoidably leads to the drill transverse vibrations (in the direction perpendicular to the drill's longitudinal axis). Figure 3.30d shows typical chatter marks having pitch equal to the cutting feed per revolution. Such chatter significantly reduces tool life in drilling with high feeds or in drilling of difficult-to-machine materials.

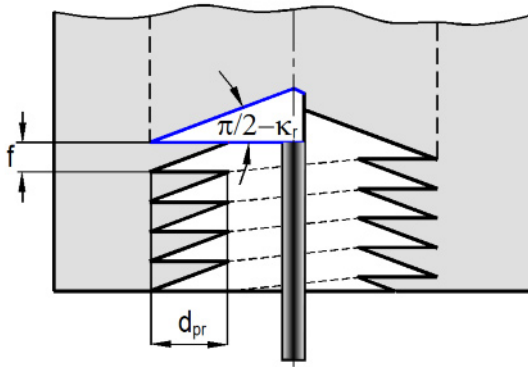


Fig. 3.28. Profile of the hole drilled by the hypothetical drill shown in Fig. 3.27

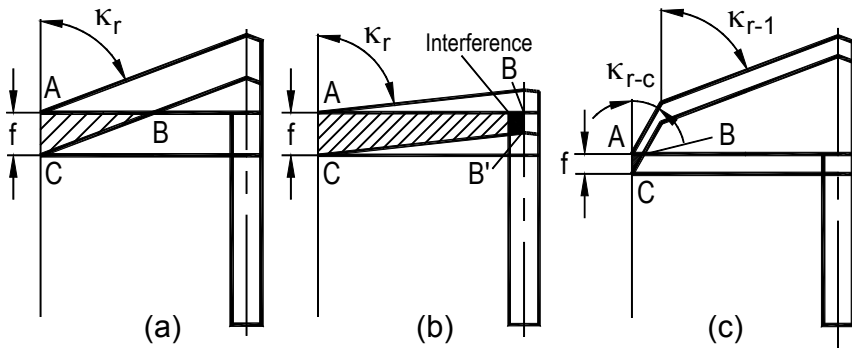
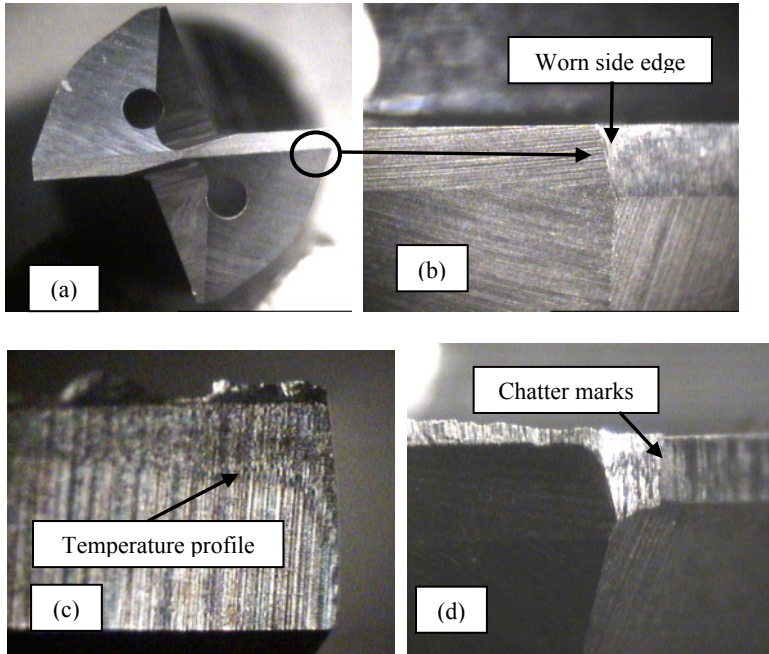


Fig. 3.29. Explanation of the profile shown in Fig. 3.28 and influence of  $\kappa_r$  on the uncut chip thickness cut by the minor (side) cutting edge

The foregoing analysis explains the significant improvement in tool life and drilled hole quality in drilling difficult-to-machine materials if the small part of the margin adjacent to the drill periphery corner is modified as shown in Fig. 3.31. The axial distance between points 1 and 2 is approximately  $0.2 \times d_{dr}$ . This great effect observed in drilling is readily explained by great tool cutting edge angles ( $\kappa_s$ ) used in the machining of difficult-to-machine materials. Moreover, great strain-hardening of these materials results in great forces if a margin with a zero flank angle tries to deform plastically the remaining of the work material left by the major cutting edge. So far, this practical finding has never been explained in the literature on metal cutting and drill design (geometry).



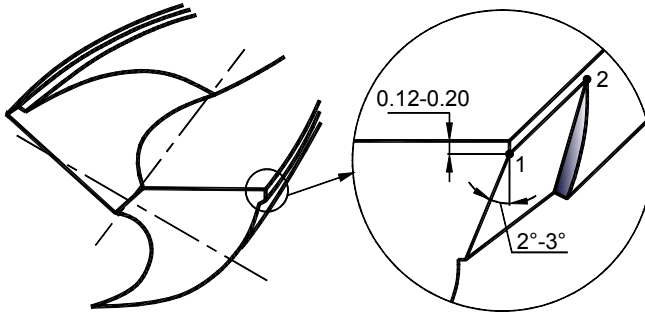
**Fig. 3.30.** Wear of the side cutting edge in machining with a high cutting feed: (a) straight-flute drill, (b) beginning of wear, (c) discoloration of the flank face due to high temperatures, and (c) chatter marks

The foregoing analysis also explains effectiveness of chamfered cutting edge (lips) in terms of reduction of drilling exit burr and improving tool life. A drill having this feature is shown in Fig. 3.32. Figure 3.29c provides the explanation. As can be seen, the cutting edge consists of the portions: the prime portion ground with  $\kappa_{r-1}$  and secondary portion ground with  $\kappa_{r-c}$ . When combined with relatively small cutting feed, such a design results in a considerably smaller portion (compare triangles  $ABC$  in Fig. 3.29a,c to be removed by the minor (side) cutting edge. Besides improving tool life, the discussed modification reduces drilling exit burr and improves surface finish of the machined holes. This explains the successful application of such a design in twist drilling and in reaming, including gunreaming.

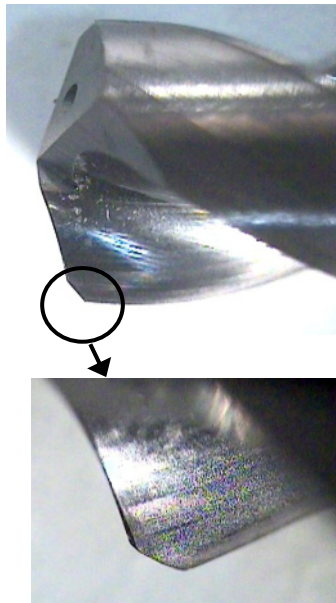
## 3.4 Edge Preparation

### 3.4.1 General

A growing number of tooling manufacturers and users have come to understand that the micro-geometry of the cutting edge itself has a more significant impact on



**Fig. 3.31.** Modification of the margin



**Fig. 3.32.** Drill with corner chamfer

performance than many specialists realize. Thus the standards to which that edge is finished – the edge prep in the jargon of the trade – should be better understood throughout the metalworking industry. Basic edge preparation shapes and dimensions are standard as shown in Table B.21. Initially, edge preparation was a matter of simple necessity as the insert manufacturing process required it. Most carbide inserts, as well as those made from other materials, are molded. The material powder is poured into a die, pressed to the basic insert form, and then sintered in a high-temperature oven. Because of the necessary clearance between the press ram and die case, this process often creates a residual flash along the insert edge which must be removed.

In some cases, other kinds of edge irregularities must be smoothed. For example, flat inserts typically undergo a double-disk grinding process which leaves an irregular edge intersection between the ground top or bottom surface and the molded side surface in between. Although on a precision insert, the side is ground as well, and small imperfections still often have to be removed.

An edge preparation is also often necessary on a sharp edge, which is highly prone to fracture due to stress concentration and microcracks left after grinding. When a radius or chamfer is applied to the edge (see Table B.21), coatings adhere properly to this transition surface between the rake and flank faces. This is particularly important for the chemical vapor deposition (CVD) process, so the edge must be rounded before this final manufacturing step.

Initially, hones were imparted manually with a honing stone – hardly a precise or consistent method. Today, they are mostly applied with an automated honing process using special machines. The T-land is a simple chamfer imparted with a conventional CNC grinding process. T-lands vary in width (typically 0.12–1.5 mm) and angle (typically 5–35°), depending on the application. For more demanding needs, two lands may be ground into an edge, or a T-land may be combined with a hone to maximize the cutting wedge's strength.

A logical question about why a sharp edge is made round, i.e., dull has to be answered. It should be clear that a sharp cutting edge is always better than a honed one in terms of metal cutting as its performance results in a lower cutting force and temperature. A problem is that it is impossible to obtain a perfectly sharp cutting edge in real tool manufacturing. Rather, a serrated cutting edge and rough (in the micro scale) tool-chip and tool-workpiece contact surface due to grinding marks are the case in practice. As a result, edge chipping and poor coating adhesion are two common features of the so-called practical sharp cutting edge. To reduce the severity of these two features, edge preparation should be used. According to Shaffer [7, 26] the tool edge preparation process, when administered properly, lengthens tool life, improves quality, and enhances surface finish of the machined parts.

In recent years, edge preparation has been universally recognized as one of the four major components required in successful design and manufacturing of the working part of any cutting tool. These four components are: (1) tool material including its composition, grade, and make, (2) tool geometry, (3) proper coating and (4) edge preparation. The first three of these four components are results of extensive research and development programs widely discussed in the literature while edge preparation needs to break away from being an “art” to join the other above-mentioned three components as a controllable manufacturing operation. To a large extent, edge preparation still remains an art. Correct honing, for the most part, is completely dependent on the best fit of part condition and is limited by machine variability and operator expertise. Most of the time, the honing process is still the best educated guess of an operator experimenting with process variables to get acceptable results.

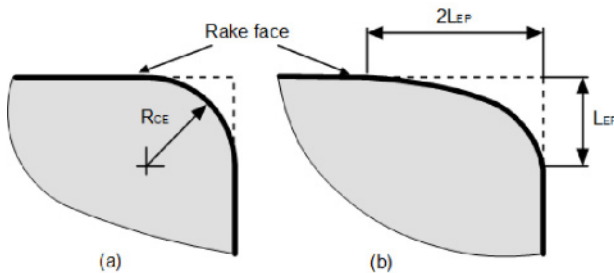


### 3.4.2 Shape and Extent

Table B.21 shows all standard shapes of edge preparation. Although all these shapes are still in use for some special application, particularly on older equipment and sub-optimal machining systems, two basic shapes of edge preparation are most common today. More than 80% of honed cutting tools receive a radius hone (Fig. 3.33a), which is centrally located on the cutting corner of the tool. Tools with this type of hone are used for general applications. A half-parabolic shape is known as a “waterfall” or “reverse waterfall”, depending on its orientation to the rake and flank surfaces. With a waterfall-shaped hone, the edge prep is skewed toward the top side of the tool as shown in Fig. 3.33b where normally for the waterfall edge preparation its size along the rake face is twice greater than that along the flank face. The main benefit of a waterfall-shaped hone is that the honing process leaves more tool material directly under the cutting edge, which further strengthens the corner [27].

The following recommended cutting edge radii have been derived from practical tests:

- Soft aluminium alloys – 1–3  $\mu\text{m}$
- High-Si aluminium alloys (automotive) – 5–10  $\mu\text{m}$
- Steel – 15–20  $\mu\text{m}$
- Titanium alloys – max. 30  $\mu\text{m}$ .



**Fig. 3.33.** Common shape of edge preparation: (a) radius hone shape, and (b) waterfall-shaped hone shape

### 3.4.3 Limitations

The majority of honed edges – perhaps 70% – are in the range of 0.08–0.025 mm [27] and that, in the author’s opinion, is excessive. Unfortunately, in the technical literature, the role of the cutting edge radius is not clearly understood. Although the definition of cutting tool edge radius is self-evident, it is more difficult to assess the influence of this parameter on the cutting process and thus to classify the tool cutting edge as being sharp or rounded.

In general, both the cutting tool edge radius  $R_{CE}$  and the uncut chip thickness  $t_l$  may vary; thus a dimensionless number termed as the Relative Tool Sharpness (hereafter, RTS) of the cutting edge was introduced as  $RTS = t_l/R_{ce}$  [28]. The maximum value of this ratio that corresponds to a negligibly small influence of the cutting edge radius on the cutting process is referred to as the critical relative tool sharpness,  $RTS_{cr}$ . Zorev [24] suggested the following empirical rule: the radius of the cutting edge does not affect the cutting process if RTS is equal to or more than 10. In many practical machining operations, however, RTS is less than 10. As a result, the radius of the cutting edge should be considered as a significant factor in modeling the cutting process. For example, if one tries to evaluate the influence of the cutting feed and the parameters of the cutting tool geometry that might affect the cutting process, the discussed  $RTS_{cr}$  should always be kept in mind.

The radius of the cutting edge and thus RTS affect both the contact stresses (force) on the tool flank and tool geometry.

#### 3.4.3.1 Influence on the Contact Processes on the Tool Flank

To estimate the forces acting on the tool flank and contact stresses, consider the model shown in Fig. 3.34. According to this model, the cutting tool has the cutting edge radius,  $R_{CE}$ . Due to this radius, the total uncut chip thickness,  $t_l$  is separated into the actual uncut chip thickness,  $t_a$  and the layer of thickness  $h_l$  to be burnished by the round part adjacent to the tool flank face. The arc distance between points  $A$  and  $D$  designated as  $\Delta$  calculates

$$\Delta = (\cup AC) + (\cup CD) = R_{CE}\psi + \frac{h_{er}}{\sin \alpha} \quad (3.26)$$

where  $\psi$  is the central angle corresponding to arc  $AC$  and  $h_{er}$  is elastic recovery (recoil) of the machined surface.

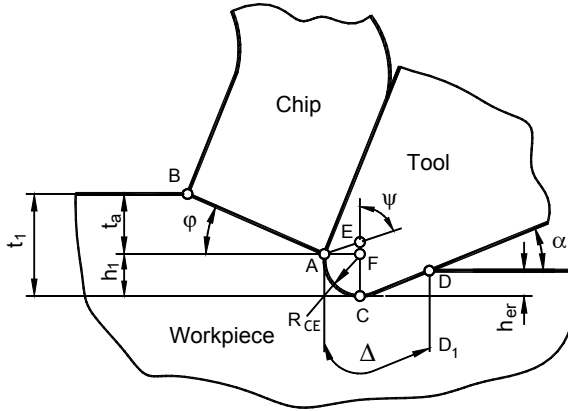
Because  $\psi = \arccos(1 - h_l/R_{CE})$  then it follows from Eq. 3.26 that

$$\Delta = R_{CE} \left( \arccos \left( 1 - \frac{h_l}{R_{CE}} \right) + \frac{h_{er}}{R_{CE} \sin \alpha} \right) \quad (3.27)$$

It is known [29] that the cutting process ceases and the layer to be removed undergoes plastic deformation similar to burnishing when

$$\frac{h_l}{\rho_{ce}} \leq 0.5 - \frac{\tau_{in}}{\sigma_y} \quad (3.28)$$

where  $\sigma_y$  is the yield strength of the work material and  $\tau_{in}$  is the strength of adhesion bonds at the tool-workpiece interface determined using results of adhesion tests [30]. As discussed above, the strength of adhesion bonds depends on mutual adhesion properties of the tool and work materials.



**Fig. 3.34.** Model of the honed cutting edge

Combining Eqs. 3.27 and 3.28 one can obtain

$$\frac{\Delta}{R_{CE}} = \arccos\left(0.5 + \frac{\tau_{in}}{\sigma_y}\right) + \frac{h_{er}\left(0.5 - \frac{\tau_{in}}{\sigma_y}\right)}{h_1 \sin \alpha} \quad (3.29)$$

The plastic deformation of the surface layer can be characterized by the burnishing factor  $m_b = h_1/h_{er}$  which according to Poletica [31] can be approximated by CCR  $\zeta$ . As a result, Eq. 3.29 becomes

$$\frac{\Delta}{R_{CE}} = \arccos\left(0.5 + \frac{\tau_{in}}{\sigma_y}\right) + \frac{\left(0.5 - \frac{\tau_{in}}{\sigma_y}\right) \sin \varphi}{\cos(\varphi - \gamma) \sin \alpha} \approx 1.25 \sqrt{\frac{Br}{\sin \alpha}} \quad (3.30)$$

where  $Br$  is a similarity criterion, referred as the Briks criterion [29, 32],

$$Br = \frac{\cos \gamma}{\zeta - \sin \gamma} \quad (3.31)$$

The experimental results showed that  $h_1 \approx 0.5\rho_{ce}$  is a good approximation when cutting ductile materials [29]. As such Eq. 3.30 becomes

$$\Delta = R_{CE} \left( \frac{\pi}{3} + \frac{0.5 \sin \varphi}{\cos(\varphi - \gamma) \sin \alpha} \right) \quad (3.32)$$

As follows from Eqs. 3.30 and 3.32, the contact length on the tool flank is a function of the tool rake angle and chip compression ratio.

Using the above considerations and the model shown in Fig. 3.34, one can obtain expressions for  $h_l$  and  $h_{er}$  as

$$h_l = R_{CE} \left( 1 - \frac{1}{\sqrt{1 + Br^2}} \right) \quad (3.33)$$

$$h_{er} = \frac{R_{CE} \left( 1 - \sqrt{\frac{1}{1 + Br^2}} \right) Br}{\cos \gamma + Br \sin \gamma} \quad (3.34)$$

According to Poletica [31], the stress distribution at the flank contact surface is as follows:

$$\tau_{c-f}(x) = \tau_y \exp \left[ -3 \left( \frac{x}{\Delta} \right)^2 \right] \quad (3.35)$$

where  $\tau_y$  is the yield shear strength of the work material and  $x$  is the distance from the cutting edge. Integrating Eq. 3.35 yields the mean shear stress at the tool flank interface

$$\tau_{c-f} = 0.505 \tau_y \quad (3.36)$$

which is an excellent agreement with experimental result obtained by Zorev [24] and Chen and Pun [33].

Foregoing analysis allows one to obtain the expression to calculate the friction force at the tool-workpiece interface as

$$F_{fF} = 0.625 \tau_y R_{CE} b_{IT} \sqrt{\frac{Br}{\sin \alpha}} \quad (3.37)$$

where  $b_{IT}$  is the true uncut chip width which calculates depending on the tool geometry (see Sect. 3.3.2).

It directly follows from Eq. 3.37 that the friction force at the tool flank is directly proportional to the radius of the cutting edge which supports the statement made earlier that cutting with the sharp edge should always be better in terms of the cutting forces and thus heat partition in the cutting system. Figure 3.35 shows an example of energy partition in the cutting system. As seen, the amount of thermal energy transported by the chip ( $Q_c$ ), conducted into the workpiece ( $Q_w$ ) and conducted into the tool ( $Q_t$ ) directly depends on RTS [28]. As RTS decreases, more heat goes into the workpiece causing machining residual stresses and into the

tool causing shorter tool life. Moreover, when machining with shallow uncut chip thicknesses, a small RTS causes a shift of the region of maximum tool temperatures from the flank face into the flank face (Fig. 3.36 [34]) that causes excessive flank wear.

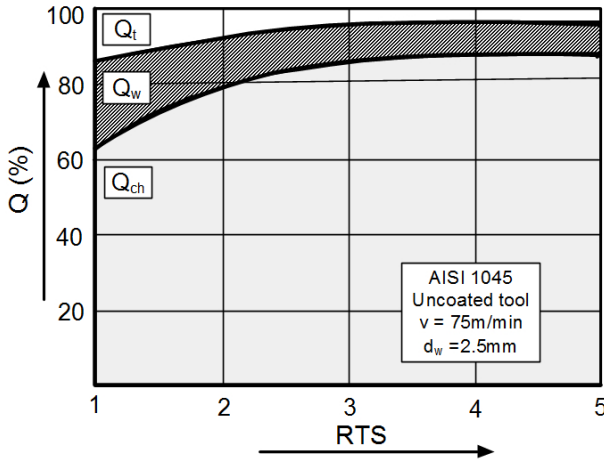


Fig. 3.35. Influence of RTS on energy balance when machining AISI 1045 steel

3.4.3.1 Influence on the Tool Geometry and Uncut Chip Thickness

Because the actual uncut chip thickness,  $t_a$ , is smaller than the apparent uncut chip thickness,  $t_l$  (see Fig. 3.34), the cutting feed  $f_T$  corresponding to the actual uncut chip thickness is smaller than the apparent cutting feed,  $f$ . As can be seen, the actual cutting feed,  $f_T$  can be calculated as

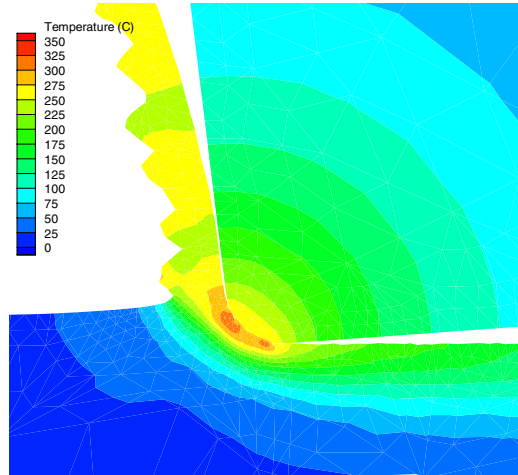
$$f_T = \frac{t_a}{\sin \kappa_r} = f - \frac{h_1}{\sin \kappa_r} \tag{3.38}$$

This equation is valid when  $t_a > h_1$  or, as it follows from Eq. 3.38, when  $f > \frac{h_1}{\sin \kappa_r}$

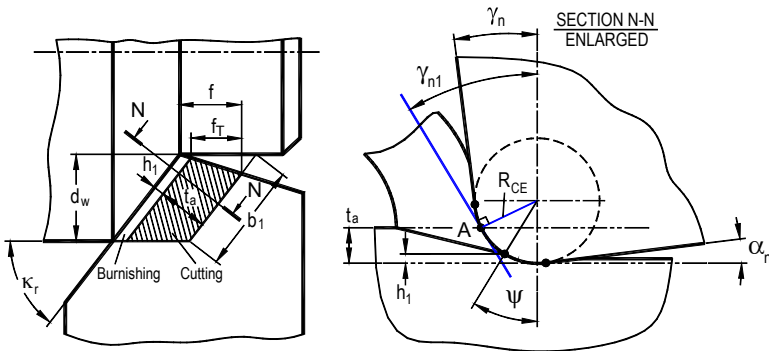
(to keep  $f_T > 0$ ).

A model shown in Fig. 3.37 reveals the difference between the apparent normal rake angle  $\gamma_n$  and actual rake angle  $\gamma_{n1}$  at point  $A$ . According to the method of tangent [28], the actual rake angle is calculated as

$$\gamma_{n1} = \begin{cases} \arcsin\left(\frac{t_l}{R_{CE}} - 1\right) & \text{if } t_l < R_{CE} \cdot (1 + \sin \gamma_n) \\ \gamma_n & \text{if } t_l \geq R_{CE} \cdot (1 + \sin \gamma_n) \end{cases} \tag{3.39}$$



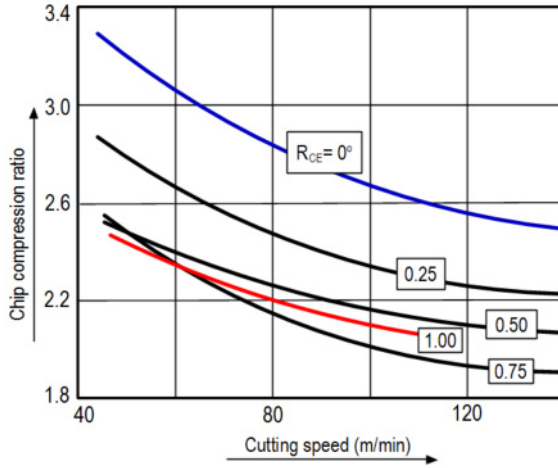
**Fig. 3.36.** Temperature distribution in the deformation zone in orthogonal cutting of the AISI 316L (courtesy of Prof. J.C. Outeiro)



**Fig. 3.37.** Schematic representation of the real cutting feed due to the cutting tool edge radius effect and a model for determination of the true tool rake angle

It is understood, that the rake angle represented by Eq. 3.39 varies along the rounded part of the tool rake face.

The importance of the introduced model (Fig. 3.37) in the experimental studies can be exemplified as follows. Figure 3.38 shows experimental results obtained by Zorev [24]. As seen, the best results were obtained with  $R_{CE} = 0.75\text{mm}$  which exceeds the uncut chip thickness. If, however, the developed model is used and thus the actual uncut (undeformed) chip thickness is used while the cutting force and tool life are also considered, the smallest deformation occurs when  $R_{CE} = 0.25\text{mm}$ . It exemplifies one more time the importance of the system consideration of the metal cutting process where one component and its individual influence cannot be considered in isolation from other components.



**Fig. 3.38.** Influence of the cutting edge radius on the CCR (work material – steel AISI 1020, tool material – P20, tool cutting edge angle –  $60^\circ$ , inclination angle –  $0^\circ$  normal rake angle –  $10^\circ$ , normal flank angle –  $6^\circ$ , depth of cut – 4 mm, cutting feed 0.5 mm/rev)

### 3.4.4 What Edge Preparation Actually Does

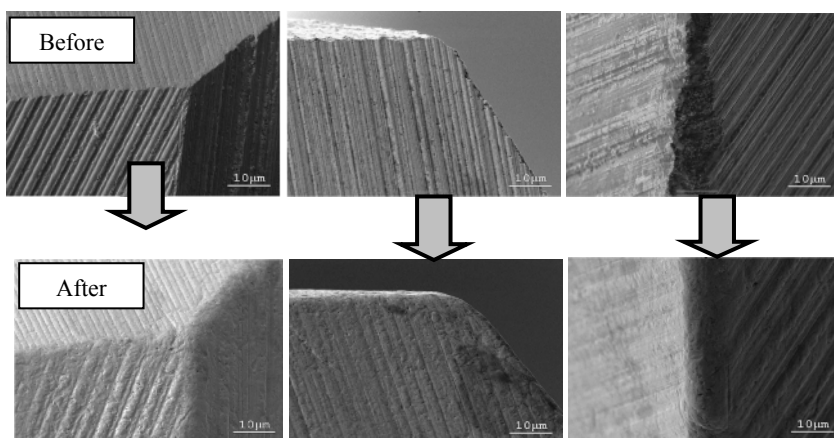
Foregoing analyses reveal that a honed edge is always worse than a sharp one in terms of cutting forces and temperatures, particularly for small RTS which is confirmed by experimental results [35, 36]. However, multiple experimental studies and author's experience reveal the following:

- Tool life of high speed steel, carbide, PCD, and PCBN tools (single point, twist and straight-flute drills, reamers, milling tools, etc.) increases when the proper (optimal hone radius) edge preparation is used [6, 37–40].
- The size and surface finish as well as the process stability (spiraling, chatter marks) in machining of aluminum alloys are much better when a suitable edge preparation is used. Even small hand honing by a diamond file increase these parameters noticeably

In the author's opinion, the explanation to the above contradiction is simple. Edge preparation does the following:

- Significantly improves the microfinish on the tool-chip and tool-workpiece contact interfaces that reduces adhesion forces over these interfaces [14].
- Heals surface micro defects as crack and voids in the vicinity of the cutting edge left by the grinding wheel. These defects are critical because they cause micro- and then macro-chipping of the cutting edge. Edge preparation just 'heals' these defects [41] as ductile micro-cutting takes place even on super hard tool materials [42–44].

Figure 3.39 exemplifies the conclusions made. The hone obtained as a result of edge preparation is just a ‘byproduct’ of this manufacturing operation, not its objective as considered in the literature. It needs to be said, however, that the above conclusions are valid only when the machining system is rigid and the allowable runouts in the relative tool-workpiece motions are small. When even one of these conditions is not the case, the cutting edge radius formed in edge preparation adds strength to the working part of the cutting wedge (the small wedge between the rake and the flank surfaces limited by the lengths of the tool-chip and tool-workpiece interfaces). This explains why a wide range of hone radius or even the waterfall edge preparation (Fig. 3.33b) recommended in the literature for the same tool and work materials. As stated by Shaffer [7], the hone radius for carbide inserts may range from 0.013 to 0.2 mm depending on particular cutting conditions.



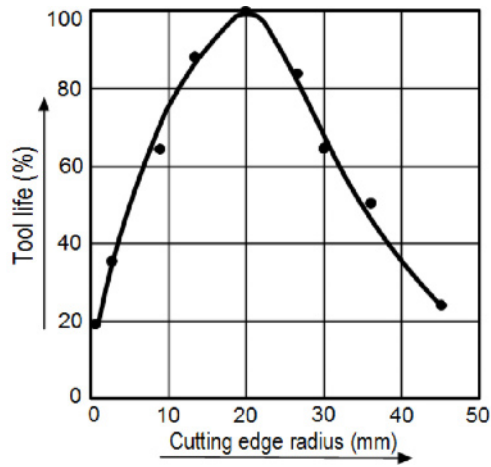
**Fig. 3.39.** Effect of edge preparation on the conditions of the tool contact surfaces (courtesy of OTEC Präzisionsfinish Co. (Germany))

Yet another important advantage of edge preparation is to assure proper coating application. When a PVD coating is applied directly on the sharp cutting edge, it results in high internal stresses in the coated layer over the cutting edge. This causes the coating to break away and thus to peel off. It does not happen, however, if edge preparation with a suitable hone made on the cutting edge is used.

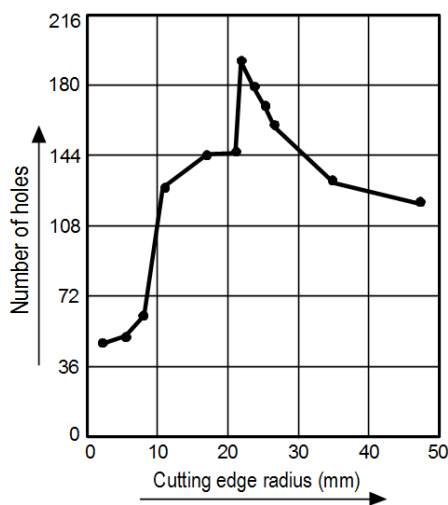
The foregoing analysis suggests that there is always a trade-off between the factors that cause an increase in tool life and better microfinish of the contact surfaces (less adhesion between the tool and work materials), better coating and strength of the cutting wedge, and those that cause a decrease in tool life because of higher friction forces and temperatures on the contact surfaces. As a result, there should be an optimal, in terms of tool life, the radius of the cutting edge. The available experimental results completely support the latter conclusion. Moreover, these results show that the optimum radius of the cutting edge varies significantly depending upon a particular machining system, cutting tool, tool and work materials, etc. What is most important, however, is that this optimum lies



within a rather narrow range as seen in Figs. 3.40 and 3.41 [37]. Unfortunately, this important issue is not well understood in industry where many practitioners are rather reluctant to use edge preparation because of the great variation in the application results present even for the same tool. To improve consistency, tool drawings should indicate not only the cutting edge radius and hone shape but also the method of edge preparation which has to be used. It may ensure to a certain extent the micro geometry of the tool contact surfaces, thus improving consistency of edge preparation results. As such, a tool designer should be well aware of at least basic methods of edge preparation listed in Fig. 3.42.



**Fig. 3.40.** Effect of the hone radius on the tool life of end mills according to Platit Advanced Coating System Co.



**Fig. 3.41.** Influence of the cutting edge radius on the tool life of twist drills

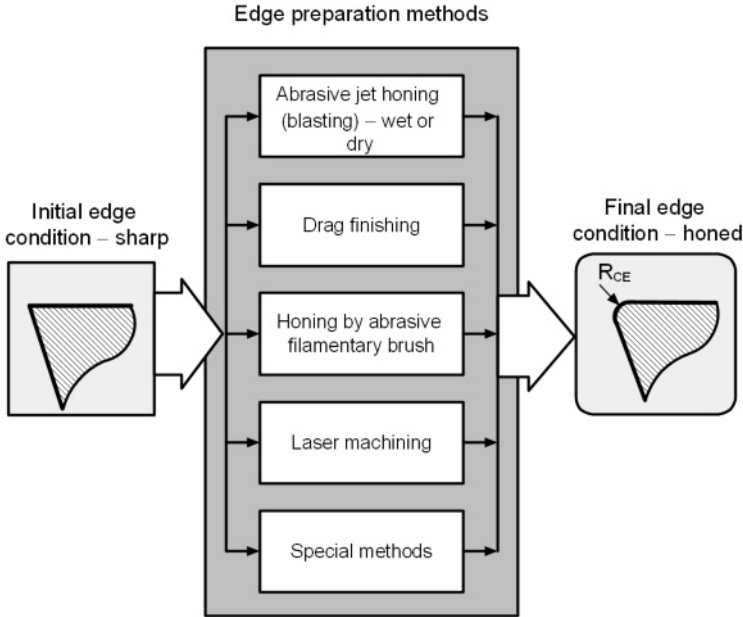


Fig. 3.42. Edge preparation methods

## 3.5 Rake Angle

### 3.5.1 Introduction

As discussed in Chap. 2, the tool rake face is the surface over which the chip formed in the cutting process slides. The rake angle is the angle between the reference plane (the trace of which in the considered plane of measurement appears as the normal to the direction of primary motion) and the intersection line formed by the considered plane of measurement and the tool rake plane. This angle may be linked to the corresponding angle in raking soil (Fig. 3.43).

The rake angle comes in three varieties, positive, zero (sometimes is referred to as neutral), and negative as shown in Fig. 3.44a–c, respectively. There is a great body of experimental and numerical modeling results dealing with the influence of the value and sign of the rake angle on the machining process. In the author's opinion, the role and importance of the rake angle in metal cutting is not well understood because these available data are contradictory and often misleading. Moreover, the available studies were not concerned with the system consideration of the influence of the rake angle on the various outcomes of the cutting process. Rather, one outcome parameter is normally considered, for example the cutting force, while others, for example tool life, are ignored. Using these data, a practical tool/process designer cannot make an intelligent selection of the proper rake angle for a given application.

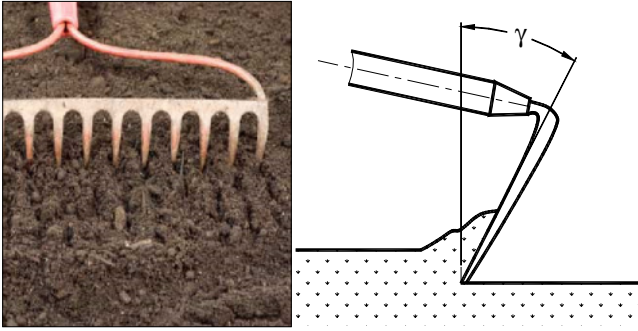


Fig. 3.43. Origin of the term “rake angle”

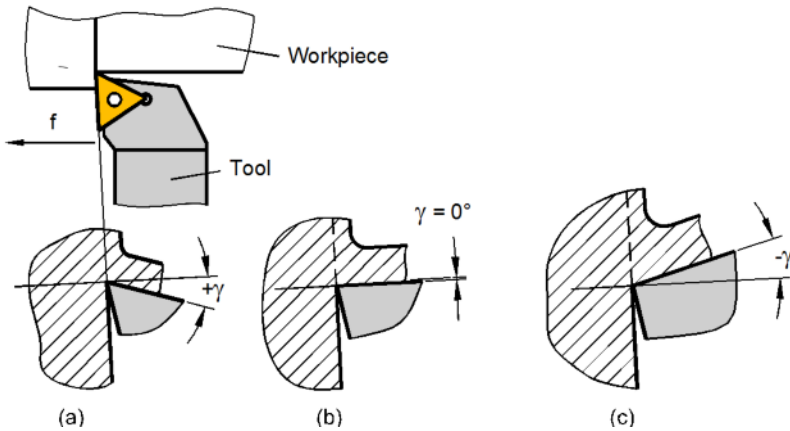


Fig. 3.44. The sense of the (a) positive, (b) neutral, and (c) negative rake angles

As mentioned earlier, Shaw [2] argues that the specific cutting energy (and thus the cutting force) decreases about 1% per degree increase in rake angle while Dahlman et al. [45] showed that, by controlling the rake angle, it is possible to generate tailor-made machining residual stresses in the product. Günay et al. [3] in their experimental study found that a change in the rake angle from  $0^\circ$  to  $+2.5^\circ$  resulted in a 2% reduction of the cutting force while a change from  $-2.5^\circ$  to  $0^\circ$  resulted in a 3.4% reduction. Tetsuji et al. [46] in their test on rock cutting found that the cutting force of the bit with a  $20^\circ$  rake angle decreased about 30–80% (depending upon other machining parameters), compared to that of the bit with a  $-20^\circ$  rake angle. Moreover an increase in cutting force with the cutting depth became lower with increase in rake angle. Gunay et al. [4] carried out a detailed experimental study of the influence of the rake angle in machining of AISI 1040 steel. They found a very small influence which diminishes at high cutting speed. Figure 3.45 shows an example of their results.

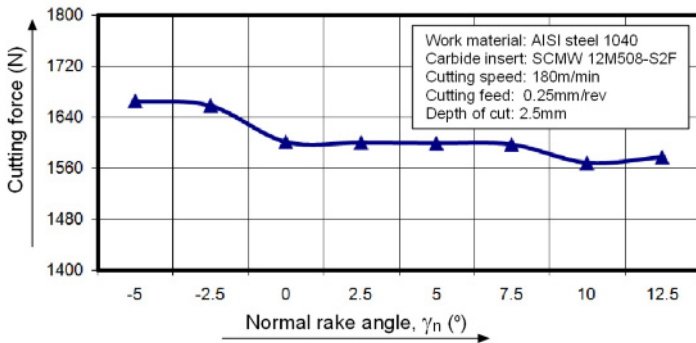


Fig. 3.45. Example of the experimental results obtained by Gunay et al. [4]

Saglam et al. carried out an extensive research program on machining of AISI 1040 steel bars hardened to HRC 40 [47] in order to reveal of the effect of tool geometry. A system consideration of the major geometry parameter was attempted as the inter-influence of these parameters was considered. An example of their results is shown in Fig. 3.46. As can be seen, an increase in the rake angle noticeably reduces the cutting force while the cutting temperature increases. It was also found that the influence of the rake angle depends on the tool cutting edge angle. More dramatic influences of the rake angle on the cutting force and temperature were found for high cutting speeds.

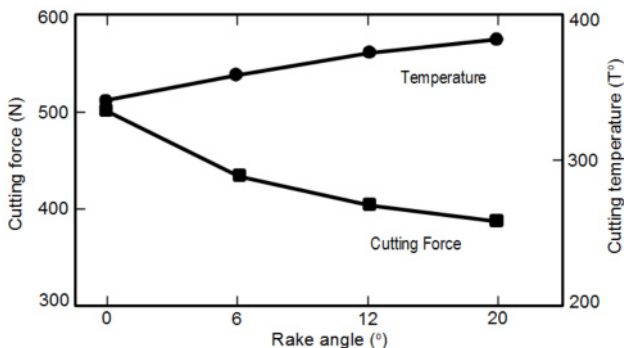


Fig. 3.46. Influence of the rake angle on the cutting force and temperature

The available data from FEM are even more contradictory than those obtained in tests. Shih [48] trying to reveal the influence of the rake angle carried out an FEA of the cutting process under rather exotic cutting conditions: work material – AISI 1020 annealed steel, tool material – high speed steel, depth of cut – 101.6 micrometers, cutting speed – 584.2 mm/s. The simulated results show that when the rake angle changes from  $-2^\circ$  to  $+15^\circ$  the cutting force and the cutting temperature noticeably decrease. Dechjarern [49] presented results of a 3D FEA of machining of AISI 1030 steel with a carbide tool under the following conditions:

depth of cut – 1 mm, cutting feed – 0.3 mm/rev, cutting edge radius – 0.8mm for cutting speeds 100–250m/min. According to his results, the cutting force decrease by 4–8% (depending on the cutting speed) when the rake angle changes from  $-16^\circ$  to  $-2^\circ$  while the cutting temperature has its minimum at  $-10^\circ \dots -8^\circ$  (depending on the cutting speed) and this temperature increases significantly when the rake angle changes in the positive or negative direction.

### 3.5.2 Influence on Plastic Deformation and Generalisations

The true influence of the rake angle can be revealed in test if:

- Other parameters of the tool geometry are suitable for the application. For example, RTS should be more than 5, the flank angle is great enough to prevent excessive friction on the tool flank, tool wear is not excessive, tool material combined with the selected machining regime do not cause excessive adhesion.
- Other parameters of the machining system, for example excessive runout of the spindle, improper or insufficiently clean MWF, variations in property of the work material due to improper heat treatment, excessive amount of inclusions (common for die casted aluminum alloys), do not overshadow this influence.

To reveal the real influence of the rake angle on the cutting process, a series of free cutting tests was carried out [24]. Figure 3.47 shows a generalization of the obtained results. The influence of the rake angle on CCR (see Sect. 3.2.3) shows that:

- Rake angle has a significant effect on the amount of work of plastic deformation in metal cutting.
- The effect of the rake angle is more profound at low cutting speeds although it is still significant at moderate and high cutting speeds.

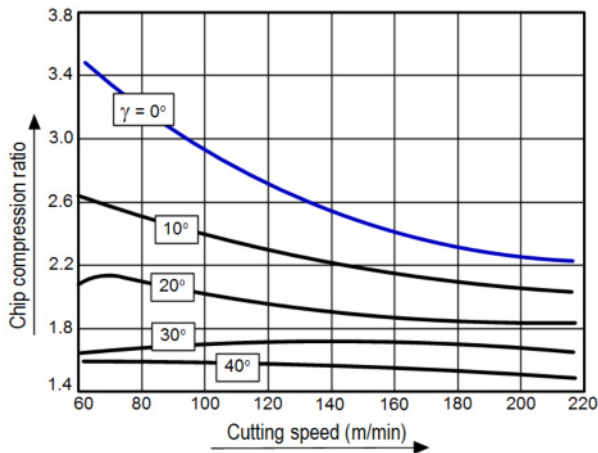
The available information on the influence of the rake angle allows one to make some important generalizations to be considered in the practice of tool design.

#### 3.5.2.1 Rake Angle and Tool–chip Contact Length

In metal cutting, the tool–chip contact length known as the length of the tool–chip interface determines major tribological conditions at this interface such as temperatures, stresses, tool wear, etc. [14]. Moreover, all the energy required by the cutting system for chip removal passes through this interface. Therefore, it is of great interest to find a way to assess this length.

To deal with the problem, the Poletica criterion (Po-criterion) was introduced [50] as the ratio of the contact length,  $l_c$  to the uncut chip thickness,  $t_1$

$$Po = \frac{l_c}{t_1} \quad (3.40)$$



**Fig. 3.47.** Influence the rake angle on CCR for the range of the cutting speed used for carbide tools. Free cutting with  $d_w = 6$  mm,  $t_1 = 0.15$ mm. Work material 2 AISI steel 4130

It was found that for a wide variety of work materials this criterion can be calculated through CCR  $\zeta$  as

$$Po = \zeta^{k_r} \tag{3.41}$$

where  $k_r = 1.5$  when  $\zeta < 4$  and  $k_r = 1.3$  when  $\zeta \geq 4$ .

Because CCR reduces with an increase in rake angle as shown in Fig. 3.47, the rake angle affects the tool chip contact length. Although this effect may vary for practical combinations of the work and tool materials, machining regimes, and many other particularities of the machining system, the general trend is still the same, i.e., the greater the rake angle, the shorter the length of the tool-chip contact. Reductions of CCR and tool-chip contact length with the rake angle have opposite effects on the outcomes of the cutting process.

Reduction of CCR reduces the work of plastic deformation, which is the major contributor to the energy spent in metal cutting (see Chap. 1 and Appendix A). Therefore, less energy should pass through the tool-chip interface that reduces the normal stress and thus normal force on this interface. In turn, this reduces tool chipping due to high normal stresses in the region of the rake face adjacent to the cutting edge.

Reduction of the tool-chip contact length increases the tool-chip normal stresses. The total effect (the reduction of the normal stresses due to reduction of plastic deformation of the work material and increase of these stresses due to reduction of the tool-chip contact length) depends on many particularities of a given machining operation.

Reduction of the tool-chip contact length may also affect the friction conditions at the tool-chip interface. However, this is not normally the case in metal cutting as far as this length is the full or natural length. Analyzing numerous experimental results, Poletica concluded [31] that, although the mean shear stress at the tool-

chip interface can be correlated with many mechanical properties of the work material, the best fit seems to be achieved with the ultimate tensile strength,  $\sigma_{UTS}$  [14]. The following empirical relation shows good correlation with available experimental data:

$$\tau_c = 0.28\sigma_{UTS} \quad (3.42)$$

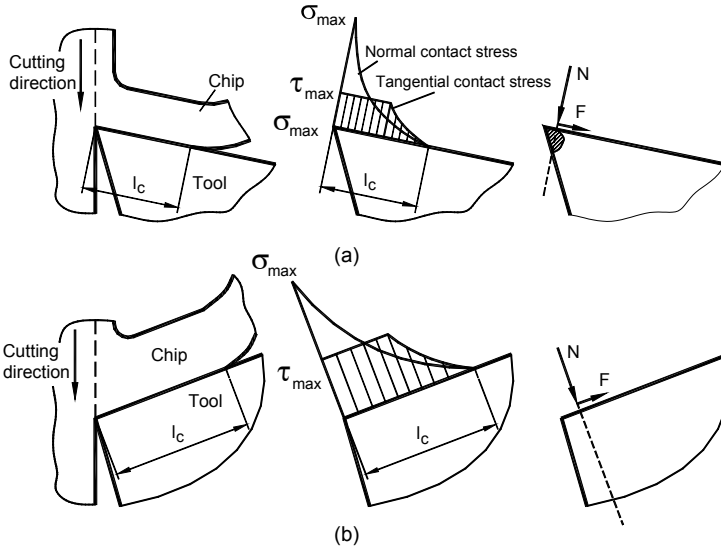
Therefore, as the shear stresses at the tool–chip interface remain the same, the reduction of the contact length reduces the friction force at the tool–chip interface, i.e. smaller amount of heat is generated due to the friction at this interface that, in turn, should result in lower contact temperatures. Although this is true, the location of the maximum temperature at this interface shifts towards the cutting edge as the contact length decreases. As cross-sectional area of the cutting wedge becomes smaller, higher temperatures occur. The total effect, i.e., the reduction of the thermal energy generated due to friction and reduction of the cross-sectional area of the cutting wedge as a heat sink, is an increase of these stresses due to reduction of the tool–chip contact length) depends on many particularities of a given machining operation.

### 3.5.2.2 Fear of Positive Rake Angles

In the professional literature for practical tool designers, a notion “positive/negative rake angle” (sometimes referred to as positive/negative tool geometry) is widely debated [51]. In the author’s opinion, the notion “positive/negative tool geometry” is an atavism that came from “ancient” times when carbide, as a tool material, was rather brittle, especially when used on the old non-rigid underpowered machines with excessive spindle runout. As such, brittle carbides chipped when positive rake angles were used. The reason for that is as follows. When cutting with a positive rake angle as shown in Fig. 3.48a, the interaction of the tool rake face with the moving chip results in certain distributions of the normal and tangential stresses over the contact length  $l_c$  [52]. These distributions can be represented in terms of the corresponding resultant normal  $N$  and tangential  $F$  forces acting on the cutting wedge. As seen, the normal force  $N$  causes bending of the tip of the cutting wedge. The presence of the bending reduces significantly the strength of the cutting wedge, causing its chipping. Moreover, the tool–chip contact area reduces with the rake angle so the point of application of the normal force shifts closer to the cutting edge. In contrast, when cutting with a tool having a negative rake angle (Fig. 3.48b), the normal force  $N$  acting on the tool rake face does not cause the mentioned bending. Instead, it results in compression of the tool material. Because tool materials have very high compressive strength, the strength of the cutting edge in this case is much higher although the normal force  $N$  is greater than that for tool with positive rake angles.

Nowadays, however, with the introduction of micro- and sub-micrograins carbides, the toughness of carbide tool materials is much greater than it used to be decades ago. The rigidity of machine structures and tool holders as well as spindle runout are dramatically improved. As a result, carbide indexable insert manufacturers introduced chipbreakers with high-positive rake angles. Figure 3.49

shows basic chipbreakers used by Seco Tools. As can be seen, highly positive rake angles are the case. As such, even tilting of such inserts to achieve relatively small flank angles (normally up to  $8^\circ$ ) does not change positive rake angles. Therefore, the outdated notion “positive/negative tool geometry” should not be used when one tries to assign the parameters of tool geometry because it does not conform to the real sign of the rake angle.



**Fig. 3.48.** Forces of the rake angle: (a) positive, and (b) negative (after Astakhov [14])

Moreover, as can be clearly seen in Fig. 3.49, the configuration of the rake face and thus the rake angle depend on the direction of chip flow which changes with the depth of cut, feed per revolution, and other parameters of machining. In other words, the real rake angle is not known even to the first approximation.

### 3.5.2.3 Tools with a Restricted Tool-chip Contact Length

The majority of studies on metal cutting concerns cutting tools having the full rake face, i.e., when the length of the rake face in the direction of chip flow is equal to or greater than that defined by Eq. 3.41. Although it is true for many drills and reamers, this is not normally the case when one uses indexable inserts having chip breakers similar to those shown in Fig. 3.49. In such tools, the length of the tool–chip contact is deliberately restricted to be smaller than the so-called “natural” contact length defined by Eq. 3.41.

According to Zhang [53], Klopstock in 1926 was the first to show that tool life and cutting forces could be favorably altered by restricting the tool–chip contact length. This was done using a composite rake face tool made of high speed steel.

Klopstock found that the presence of the stable BUE results in a better surface finish and longer tool life. Later on, it was found by multiple researchers that the use of tools with the restricted contact length may result in up to a 30% reduction in the cutting force although the real reason for that is not clearly revealed.



Limited-contact cutting has been studied by Takeyama and Usui [54], Chao and Trigger [55], Usui and Shaw [56], Hoshi and Usui [57], and Usui et al. [58]. A detailed bibliography and analysis of the studies of this kind of tool were presented by Jawahir and Lutervelt [59], Lutervelt, Childs et al. [60], Zhang [53], Karpat and Ozel [61], and many others. The cutting mechanics for such tools was discussed by the author in [14].

Two logical questions to be answered when one tries to design/select a tool with restricted contact length are: (1) what is the rake angle for a tool with the restricted contact length? and (2) how does the restricted contact length affect tool life or to what extent can this length be restricted to maximize tool performance? Unfortunately, only a few known publications are concerned with answering these practical questions.

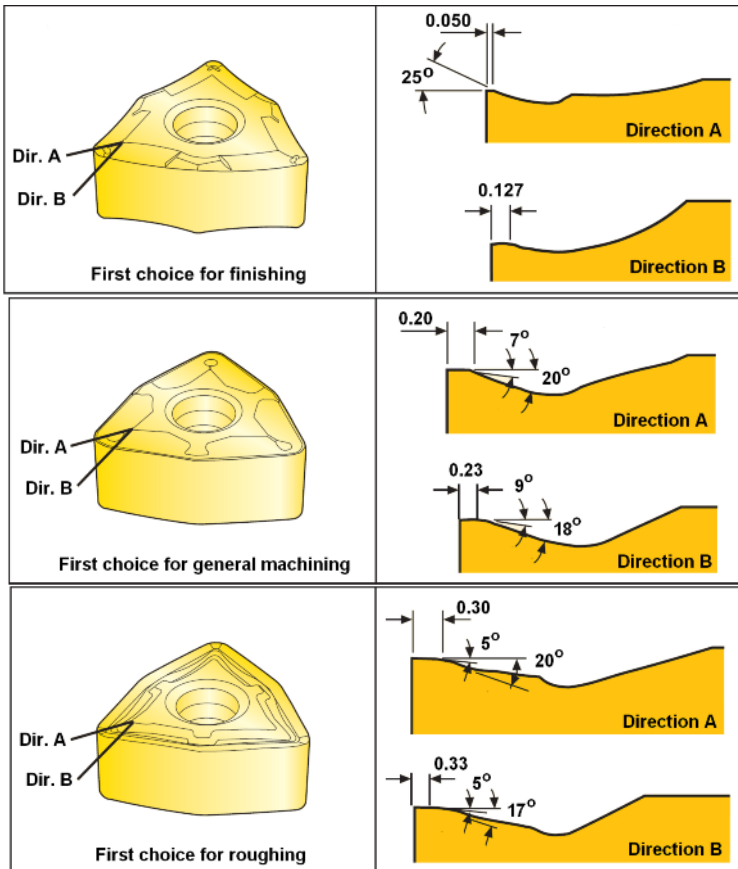
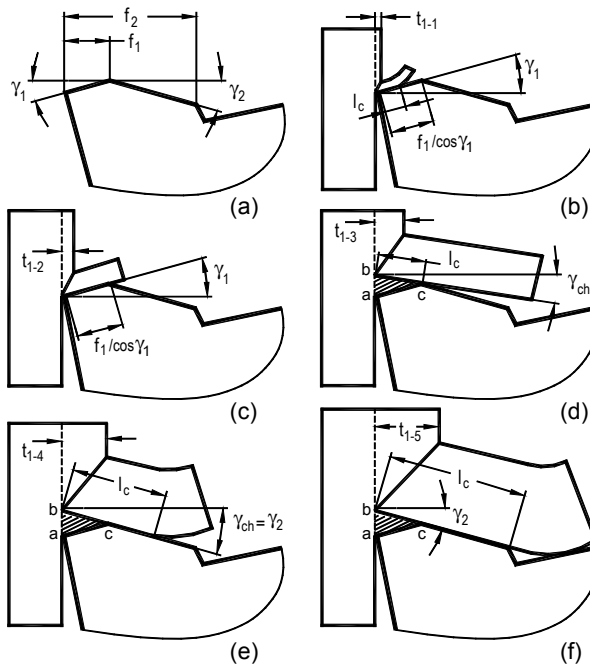


Fig. 3.49. Basic chipbreakers by Seco Tools

To answer the first question, consider a general case of rake face design with a chip breaker consisting of two chamfers as shown in Fig. 3.50a [62]. The first chamfer adjacent has rake angle  $\gamma_1$  while the second has rake angle  $\gamma_2$ . When the uncut (undeformed) chip thickness is small ( $t_{1-1}$ ), the natural tool-chip contact length (defined by Eq. 3.41) extends only over part of the first chamfer, thus cutting with the full rake face takes place as shown in Fig. 3.50b. As such, the rake angle is equal to  $\gamma_1$  which is also the angle of chip flow in the direction perpendicular to the cutting edge provided that the cutting edge inclination angle is zero. This is valid until the tool-chip contact length reaches the length of the first chamfer. If the uncut chip thickness is increased further ( $t_{1-2}$ ) then the first chamfer becomes the stabilizing chamfer and the tool is considered as having a restricted contact length equal to  $l_c = f_1/\cos\gamma_1$  as shown in Fig. 3.50c.

A further increase in the uncut chip thickness to a certain  $t_{1-3}$  results in a dramatic change in the chip flow direction as shown in Fig. 3.50d. This is due to the formation of the trapped zone  $abc$  of plastically deformed work material. Such a zone always forms in machining of ductile materials in each successive chip



**Fig. 3.50.** Chip flow schemes when cutting with a cutting tool with two chamfers on the rake face: (a) tool rake geometry, (b) full rake face, (c) restricted contact length, (d) restricted contact length with the directional chamfer, (e) the full rake face with the contact over the second chamfer, and (f) the restricted contact length with the additional stabilizing chamfer

formation cycle. When the rake face is flat, the material from this zone spreads easily over the chip contact layer and thus it is removed in each chip formation cycle [32]. This is not the case, however, when the tool rake face has a chamfer as shown in Fig. 3.50d where the deformed work material is trapped in zone *abc* so the chip starts to slide over this zone. As such, the chip flow angle changes from  $\gamma_1$  into  $\gamma_{ch}$  and the chip slides only over side *bc* of zone *abc*.

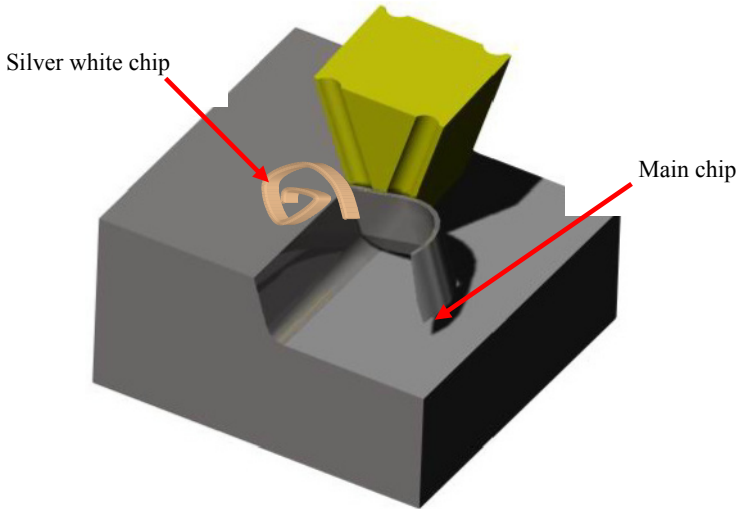
If the uncut chip thickness is increased further to certain  $t_{1-4}$  then the chip starts to make contact with the second chamfer. If the contact length does not exceed the length of the second chamfer then machining with the full contact length takes place as shown in Fig. 3.50). As such, the chip flow angle is equal to  $\gamma_2$ .

Zone *abc* of heavily deformed material is mistakenly termed as the BUE in the literature on metal cutting regardless of its existence at high cutting speeds where the BUE is not normally observed in metal cutting. The work material in this zone is heavily deformed and is under pressure of the moving chip, from one side, and the first chamfer from the other. Although it may appear that this material is stagnated in this zone, in reality this zone is filled out with new work material within each cycle of chip formation as discussed by Astakhov [32]. This explains the tool wear in this zone and high contact temperature on the first chamfer which would never occur if the work material is motionless there. It is also confirmed by chip microstructures where the heavily deformed contact layer is observed.

The discussed situation, however, may not be the case when the friction coefficients at the tool-zone *abs* and zone *abc*–chip interfaces exceed the von Mises limit [32], i.e., the internal friction in the material trapped in zone *abc* becomes less than those at the interfaces. When it happens, a thin heavily deformed continuous chip is discharged from zone *abc* in the direction parallel to the cutting edge (Fig. 3.51). The existence of such a chip was reported for the first time by Hoshi who called this chip the silver white chip [57]. The analysis of research on the subject was presented by Chang and Fuh [63].

Further increase in the contact length to certain  $t_{1-5}$  leads to the scheme shown in Fig. 3.50g when the natural contact length becomes more than the length of the second chamfer. Cutting with the restricted contact takes place. The chip flow direction does not change but the chip contacts the additional chamfer on the tool rake face.

The next question to be answered is about the extent to which the rake face can be restricted compare to the natural tool–chip contact length defined by Eq. 3.41. To answer this important question, one should understand the structure of the tool chip contact length. Zorev [24] studied the length of the plastic part using a quick-stop device and conclusively proved that the whole contact length  $l_c$  is divided into two distinctive parts: the plastic part,  $l_{c-p}$  which extends from the cutting edge and the elastic part,  $l_{c-e}$  from the plastic part to the point of tool–chip separation. Zorev showed that the contact length,  $l_c$  is a function of the cutting speed. Similar experimental results were obtained by Poletica [31] and Loladze [64]. The distribution of the tangential stress over this interface shown in Fig. 3.48 clearly distinguishes these two parts. Summarizing the results of multiple experiments,



**Fig. 3.51.** Schematic representation of the formation of the silver white chip (courtesy of Prof. J.C. Outeiro)

Abuladze [65] proposed the following expression to calculate the length of the plastic part of the tool-chip interface:

$$l_{c-p} = t_1 [\zeta (1 - \tan \gamma) + \sec \gamma] \quad (3.43)$$

For practical calculation,  $l_{c-p}$  can be taken to be 55–60% of the contact length defined by Eq. 3.41.

The most essential conclusions on the effects of the reduced contact length can be drawn from the experimental results presented by Poletica [31] and Loladze [64], Zorev [24], and Sadic and Lindstrom [66, 67]:

- Tool life normally noticeably increases and the cutting force decreases when the tool–chip contact length is reduced from its natural length to the length of the plastic part of this contact.
- The rake angle of the restricted rake face (angle  $\gamma_1$  in Fig. 3.50) is not an independent parameter. Rather, it affects the contact length through CCR  $\zeta$  (Fig. 3.47 and Eq. 3.41).
- Any further decrease of the tool–chip contact length beyond the length of the plastic contact leads to rapid reduction of tool life.
- The positive effect of the reduction of the tool–chip contact length becomes less profound for high cutting speeds.
- When tool–chip contact length reduces, the maximum cutting temperature shifts towards the cutting edge which in machining of difficult-to-machine materials leads to the plastic lowering of the cutting edge [14].

The foregoing analyses suggest that the maximum effect of the restricted tool-chip contact length is achieved when this length is equal to  $l_{c-p}$ , which, in turn, depends on the uncut chip thickness  $t_l$  and CCR  $\zeta$  (Eq. 3.43). As  $t_l$  is the direct function of the cutting feed and the tool cutting edge angle  $\kappa_r$  (see Chap. 2 and Appendix A) and CCR  $\zeta$  is a function of the tool and work materials properties as well as the cutting speed, feed, and many other parameters of the machining system, this maximum effect can be achieved only for specific applications when all these parameters are well known so that  $l_{c-p}$  can be determined with reasonable accuracy. Even small deviation from the optimal  $l_{c-p}$  may lead to significant changes in tool performance. For example, Rodrigues and Coelho found [5] that the reduction of 0.25 mm in chamfer length and increase of  $1^\circ$  in chamfer angle (from SNMG PR to SNMG PF tools) caused a reduction in the specific cutting energy of nearly 28.6% and 13.7% for conventional cutting speed and high-speed, cutting respectively.

The vast majority of practical cutting tools including those with indexable inserts, however, are meant for wide ranges of the machining regime and various machining systems. Because these inserts have a fixed restricted contact length, the performance of these inserts may vary significantly depending upon a given application. This explains great scatter in the performance of indexable carbide inserts observed in practice. By understanding the concept of CCR provided in this book and by measuring this important parameter in practical optimization of a cutting operation, any practitioner can select the proper insert for a given application.

### 3.5.3 Effective Rake Angle

#### 3.5.3.1 Methodology

The effective rake angle can be defined as the rake angle that creates the effective state of stress in the layer being removed, i.e., that state of stress under which this layer is removed with minimum possible plastic deformation. As a result, the energy spent in machining with such a rake angle is at minimum. It is understood that introduced in this manner, the effective rake angle is a function of the properties of the work material.

The development of a practical methodology to determine the effective rake angle was attempted by Mundy [68]. According to Mundy, the cutting of metal by a cutting tool is a form of failure accomplished by fracture of the work material. Unless the cutting tool can create this failure, no cutting takes place. If an excessive amount of work is required to produce the failure, significant thermal energy (heat) is released. This heat causes great process temperatures which overheat the cutting tool, lowering its tool life and inducing high machining residual stresses. If, however, the metal failure created by the cutting process can be accomplished with minimum work, there will be minimum heat and tool wear, a lower temperature and thus minimum damage created within the surface of the workpiece. The result is longer tool life and thus optimum cutting performance with high efficiency.

Tension tests are used to establish the proper rake angle because although the failure in metal cutting is in compression in the immediate vicinity of the cutting edge, the cut metal is immediately directed away from the cutting area and is therefore unrestrained, avoiding the metal interference that exists in conventional compressive loading. Accordingly, the machining of a workpiece produces the same type of granular slippage as is produced by tensile loading of a sample of the work material, and in this important respect the types of failure are the same in tensile testing and in machining.

According to the proposed approach, a tensile test of the work material is carried out. In this test, a standard specimen made of the work material is subjected to tensile loading. When the tensile forces become of sufficient magnitude to cause the metal to fail, the area of the failure is in the form of a cup cone with the peripheral surfaces of the cup cone being at a fixed angle to the longitudinal axis of the specimen. This angle is constant for a given metal and is generally accepted as being  $45^\circ$ . Due to strain hardening, the cup cone is of high hardness. Prior to failure, elongation and neck down of the specimen occur. The presence of elongation and the angle of neck down vary with different metals, generally depending on the ductility of the work material. For a given material, however, these two parameters are constants.

Because there are two physical changes in the geometry of the test specimen, elongation, and neck down, there are two forces that are considered relevant. One is the tensile force producing elongation, and the other is a force within the metal that causes neck down. These forces are at right angles to one another because the neck down occurs in direction perpendicular to elongation.

According to the principle of minimum energy, the deformation and neck down of the test specimen are at minimum to cause the failure. Therefore, the rake angle required to deform and then fail the work material is a function of the neck down angle and the elongation of the test specimen loaded under tension to failure. This rake angle is termed the effective rake angle,  $\gamma_{ef}$ .

The proposed methodology is as follows. Two marks, 3 and 4, are made on the test specimen made of the work material to define the initial length  $L_{im}$  as shown in Fig. 3.52a. Figure 3.52b shows the failed parts of this specimen after the tensile test. The surface angle of each neck down section,  $\beta_{nec}$  is measured as shown in Fig. 3.52b. Where the actual break occurs, an internal frusto-conical well is formed on the left part and a complimentary external frusto-conical section is formed on the end of the left part. Marks 3 and 4 have elongated to positions 3' and 4' on the surface of the neck down area. The axial distance between these marks is  $L_{fr}$  while the true distance is  $L_{1-fr}$  as shown in Fig. 3.52b. According to the proposed methodology, the effective rake angle is determined as

$$\gamma_{ef} = ar \cos \left( \frac{L_{im}}{L_{fr}} \cos \beta_{nec} \right) \quad (3.44)$$

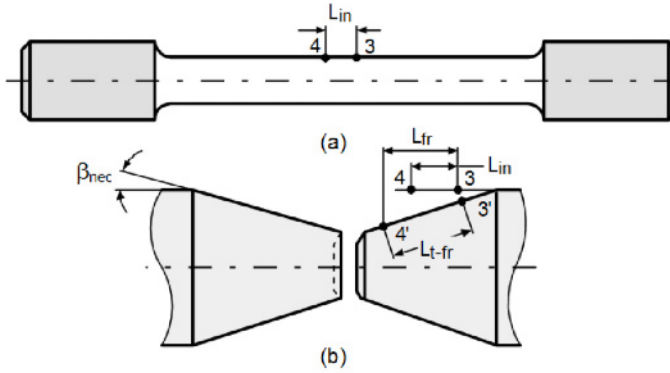


Fig. 3.52. (a) Tensile specimen, and (b) failed parts after the tensile test

Figure 3.53 is a composite drawing showing a cutting tool wedge engaged in cutting of the workpiece and the formed chip. Superimposed thereon is a portion of a tensile test specimen prior to loading and a sectional view of this specimen after having been loaded under tension to failure. The cut cone break profile is arranged so as to coincide with the chip failure line. The direction of the chip failure line and the coincidental cup failure line is designated by angle  $\phi_{fr}$ . Angle  $\phi_{fr}$  is constant for metals and generally accepted to be  $45^\circ$ , although variation in grain structure and size may make this angle appear to deviate from this value. Insofar as this explanation is concerned, it is only important that angle  $\phi_{fr}$  is a constant for a given work material.

Figure 3.53 also shows the initial distance  $L_{in}$  between points (marks) 3 and 4 made on the test specimen prior to loading. After the failure, these points deform into points 3' and 4' located in the neck-down area and the distance  $L_{t-fr}$  is the true distance between these two points. According to the described methodology, the cosine of the effective rake angle,  $\gamma_{ef}$  is equal to the ratio of  $L_{in}/L_{t-fr}$  because  $L_{t-fr}$  is the measure of the true elongation; thus the failure of the test specimen will not occur until length  $L_{in}$  has been elongated to length  $L_{t-fr}$ . When length  $L_{t-fr}$  is reached under the influence of both linear elongation and neck down under tensile loading, failure occurs. A halt in tensile forces just prior to attaining length  $L_{t-fr}$  results in an unbroken tensile specimen. Correspondingly, the instant the tensile force is great enough that length  $L_{t-fr}$  is attained, failure is irreversible and complete. The amount of work necessary to achieve length  $L_{t-fr}$  is the measure of minimum work expended to break the test specimen.

As in the test specimen, for failure to occur in the workpiece such as required in machining, the material being machined away must be moved or elongated from an initial length  $L_{in}$  to a true length  $L_{t-fr}$ . Otherwise, failure will not occur and the workpiece will not be machined. If the initial uncut chip thickness is equal to the cutting feed (length  $L_{in-c}$ ) then it is translated into the chip thickness  $L_{t-fr-c}$  under the minimum required work. The effective rake angle is then defined as that angle between  $L_{in-c}$  and  $L_{t-fr-c}$  or  $\cos\gamma_{ef} = L_{in-c}/L_{t-fr-c}$ , hence, a cutting tool having the effective rake angle so defined will require minimum work to produce the failure, resulting in greater efficiency and tool life.





The test results showed the following. Compared to the standard tool, tool life when the tool with the effective rake angle was used increased: for 303 and 4349 steels by more than 50%, for 1042 steel and titanium alloy Ti6Al4V by more than 300%.

The test results reveal that an increase in tool life is more profound for work materials of greater ductility. The reason for that is explained in Chap. 1 and Appendix 1 as more work on plastic deformation is needed for a greater strain at fracture of the work material. Therefore, it may be suggested that tools with effective rake angles should be used primarily for highly ductile work materials and materials subjected to great strain-hardening such as many titanium alloys.

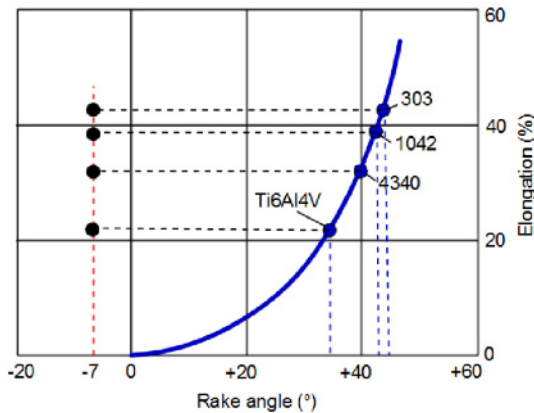


Fig. 3.54. Comparison of the standard and efficient rake angles for the tested work materials

### 3.5.3.2 Comments

When cutting with a tool with so-called an *extremely high rake angle* (an emerging term in the metalworking industry), the chip formation process is governed by a very specific model [14]. The minimum plastic deformation of the layer being removed in its separation from the rest of the workpiece is achieved. A special chip type referred to as *the continuous uniform-strength chip with wedge-shaped texture* is formed. The fluctuations of the cutting force and temperature within each cycle of chip formation are minimal.

As one might argue, however, a high positive rake angle is not very practical in cutting cast irons and similar brittle work materials due to the possible presence of a significant amount of hard inclusions. In such a case, a normal grade of tungsten carbide, as a tool material, cannot withstand peak bending loads. Modern sub-micrograin carbides possess sufficient fracture toughness to withstand the discussed inclusions successfully. The same logic is now applicable to high-speed machining of the high-silicon aluminum alloys widely used in the automotive industry. For many years, PCD brazed and indexable cutting inserts were used for this purpose with negative rake angles. Due to the recent development of ultra-micrograin PCDs, advanced cutting tools manufacturers began to offer PCD inserts with high positive (up to  $10^\circ$ ) rake angles that significantly improve machining (tool life, machined surface integrity, reduces cutting force etc) of such alloys.

Unfortunately the available recommendations for the suitable tool geometries do not reflect great advances made in the last 5–10 years in the properties of tool materials and coatings.

Gradually, many tool companies are offering tools with extremely high rake angles primarily for machining of aluminum alloys and copper. For example, Robertson Precision, Inc (Redwood City, CA) developed Shear Geometry<sup>®</sup> cutting tools with extremely high rake angles. Figure 3.55 shows an example of such tools and the chip formed in machining of an aluminum alloy. The success of this tool became possible with the development of a special submicrograin sinter-HIPed carbide tool material.



**Fig. 3.55.** Shear Geometry<sup>®</sup> cutting tool, formed chip, and high-rake insert (courtesy of Robertson Precision, Inc (Redwood City, CA))

The implementation practice of such tools reveals two problems:

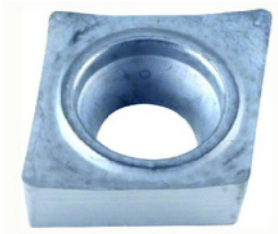
- Specialists in the field are *not psychologically ready* to use a tool with the material removal rate which five times higher than usual. They try to slow down the feed rate needed to optimal performance of such a tool that leads to its poor performance.
- As the amount of plastic deformation of the layer being removed significantly decreases with the use of this tool, CCR also decreases as a direct result. As such, a much thinner and longer chip is produced. The handling of such a coiled chip presents a serious problem. The only way to achieve its breakability is to increase the chip thickness which, under a constant CCR for a given operation, translated into increasing the feed per revolution. As mentioned in the previous bullet, there is a great psychological hurdle involved in this among many practical machinists and process engineers. In the author's opinion, a well-known Franklin D. Roosevelt quote "the only thing we have to fear is fear itself" is fully applicable in this case.

Gradually, leading tool manufactures have developed cutting tools with high rake angles. Nowadays, milling tools with high rake angles have become common. For example, Big Kaiser Precision Tooling Inc. (Elk Grove Village, IL) offers fullcut mill FCM type with a 20° rake angle. Allied Machine & Engineering Corporation (Dover OH) offers high rake geometry on its drills which is specifically designed to improve chip formation in materials with very high elasticity, extremely poor chip forming characteristics, and low material hardness recommended for use in most

soft gummy steels, steel castings, and steel forgings under a material hardness of 200 BRN.

Leading tool manufactures also offer high rake CCGT inserts (Fig. 3.56) intended for non-ferrous materials instead of CCMT inserts. Practical machinists soon found that such inserts can cut practically anything. Although regular CCMT inserts often have some positive rake angle, CCGT inserts offer much higher rake angles. The major insert manufacturers have special lines of this style insert: ISCAR CCGT-AS, Kennametal CCGT-HP, Valenite CCGT-IL, Seco CCGT21.51F-ALKX, etc. Each one has a slightly different sales pitch about why one should use the insert. ISCAR is pushing them as offering such a fine finish for aluminum that no grinding is needed, for example. The recommended materials even vary across the lines. What started out as an aluminum super finishing insert can be had in formulations that extend to high temperature alloys, stainless, and other possibilities.

It has to be pointed out, however, that the use of high-rake angle tools imposes special requirements on the components of the machining system. First and foremost, it is system static and dynamic rigidity which translates into the rigidity and accuracy of the workholding fixtures, minimum spindle runout, tool holding accuracy, etc. As the chip is normally much longer, special care should be taken to assure its reliable breakability and proper handling.



**Fig. 3.56.** A typical high rake CCGT insert

### 3.5.4 Conditions for Using High Rake Angles

A tool with a high rake angle can be deliberately made with such an angle as described in the previous section or this high rake angle is inherent for tool design and application. If the former is self-obvious, the latter is not clearly understood by many specialists in the field. For example, the T-mach-S rake angle for a standard twist drill can reach  $35^\circ$  at the drill periphery point where the major cutting edge (lip) meets the margin (Chap. 4). A similar situation is the case in many gear generating and form tools where tool-in-use rake angle can be very high. Therefore, some important conditions of using tools with high rake angle should be clearly understood.

As discussed in Chap. 4, it was noticed that while twist drilling enlarge previously-drilled holes in relatively soft work materials, such as brass, copper, Babbitt, the drill jumped ahead of the feed into the hole and caused vibration, poor quality of drilled holes, drill breakage, etc.

To understand why this happens, consider a simple model shown in Fig. 3.57. When a tool works, the normal  $N$  and friction  $F$  forces act on its rake face as discussed in Chap. 1. The radial force,  $F_y$  (the component of the cutting force in the  $y$ -direction of the tool coordinate system discussed in Chap. 2) always consists of the three components:

$$F_y = F \cos \gamma - N \sin \gamma + Q \quad (3.45)$$

where  $Q$  is the force on the tool flank land that depends on the flank angle, tool wear, MWF and other cutting parameters [14]. This force can be accounted for fairly well when its specific value of 30–60N per mm of the cutting edge length is considered.

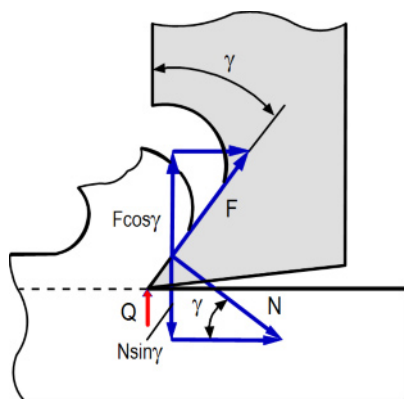


Fig. 3.57. Simplified force model

The first component,  $F \cos \gamma$ , which pushes the tool away from the workpiece, decreases with the rake angle while the second component,  $N \sin \gamma$ , which pulls the tool into the workpiece, increases. Therefore, as the rake angle increases and a sharp cutting tool is used (small  $Q$ ), the radial force can be directed into the workpiece; that is the root cause of the described phenomenon.

This phenomenon has been observed in practice. For example, it was observed that key broaches, used to make key slots in highly ductile materials, are pulled into the workpiece when the uncut chip thickness is relatively large and the rake angle is high. The same is observed when a non-rigid tool with sharp edge is used to machine a soft work material with high feeds. For example, it is the case in gundrilling of aluminum alloys with great feed. Figure 3.58 shows the bottom of the hole being drilled ‘frozen’ instantaneously by a quick-stop device. Chatter marks due to drill ‘biting’ in the feed direction can be clearly observed. The same phenomenon was noticed when a twist drill is used for enlarging previously drilled holes, i.e., when only the parts of the major cutting edges (lips) having high rake angles are engaged in cutting. Figure 3.59 shows the chatter marks on the bottom of the hole being drilled in such an application.



**Fig. 3.58.** Chatter marks on the bottom of the hole being drilled



**Fig. 3.59.** Chatter marks on the bottom of the hole being engraved with a twist drill

Besides, when a tool with a high rake angle is made (ground), the cutting edge of this tool is much sharper than that for a tool with moderated rake angle. As well known [70], they are more likely to chatter.

In any scenario, when a cutting tool with high rake angle is to be used, the first and foremost requirement is to ensure proper edge preparation. This increases the force on the tool flank land (force  $Q$ ) and thus, according to Eq. 3.45 assures a preferable force balance. This is also known from the practice of machining where freshly-ground non-rigid tools are specially dulled to prevent the discussed phenomenon from occurring. The machining system (drive, spindle, tool holder) and tool should be of high rigidity in the cutting feed direction.

### 3.6 Flank Angle

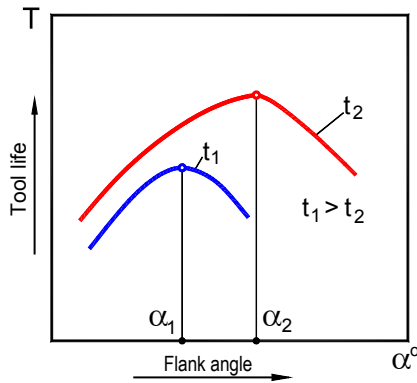
As discussed in Chap. 2 (Sect. 2.6.2), *the major distinguishing feature of the cutting tool is the flank face having flank angle  $\alpha > 0^\circ$* . If the flank angle  $\alpha = 0^\circ$  then the flank surface of the cutting tool is in full contact with the workpiece. As such, due to springback of the workpiece material, there is a significant friction force in such a contact that usually leads to tool breakage. Therefore, the flank

angle must always be  $\alpha > 0^\circ$ . A logical question to be answered is to what extent this angle should exceed the zero level.

The flank angle directly affects tool life. There are two opposite trends taking place when the flank angle increases:

- As seen in the model shown in Fig. 3.34 , when  $\alpha$  increases, the contact on the tool flank due to springback of the work material decreases. This leads to a reduction in the tool-workpiece contact area. Because the mean shear stress at the tool flank interface is constant (Eq 3.36), this leads to the corresponding reduction of heat due to friction. As a result, the flank temperature decreases which increases tool life and improves the quality of machined parts.
- When angle  $\alpha$  increases, wedge angle  $\beta$  decreases as seen in Fig. 2.13. As such, the strength of the region adjacent to the cutting edge decreases, causing possible chipping of the cutting edge. Moreover, as the wedge angle decreases, heat dissipation (heat sink) through the tool decreases, causing higher tool wedge temperatures with the maximum on the contact interfaces. These factors shorter tool life.

As a direct result of such contradictive effects, the influence of the flank angle on tool life always has a well-defined maximum as shown in Fig. 3.60. This figure also shows that the optimal (in terms of tool life) flank angle increases when the uncut chip thickness decreases. This suggests that the flank angles of the cutting tool designed for finishing operation should be increased to achieve longer tool life.



**Fig. 3.60.** General idea of the influence of the flank angle on tool life

Analysis of the great body of the available experimental data allowed [71] to introduce the following empirical formula to determine the optimal flank angle:

$$\alpha_{opt} = \frac{C_\alpha}{t_1^{0.3}} \tag{3.46}$$

where  $C_\alpha$  is a constant. For steels  $C_\alpha = 7.6$ , and for cast irons  $C_\alpha = 5.6$ . Table 3.1 shows the optimal flank angle for different uncut chip thicknesses.

Normally, the influence of the flank angle on tool life and on other outcomes of the cutting process is much stronger at low, moderate, and medium cutting speed ranges but this influence weakens at high cutting speeds. However, if the work material contains an abrasive phase (for example, the cementite phase) or abrasive particles (for example, silicon and silicon clusters in automotive aluminum alloys) then the influence of the flank angle is strong for any feasible range of cutting speeds.

### 3.7 Inclination Angle

Although the sense and sign of the inclination angle  $\lambda_s$  is clearly shown in Fig. 2.13 (VIEW S) and is defined earlier (Chap. 2) as the angle between the cutting edge and the reference plane, experience shows that there are certain difficulties and confusions in understanding this angle and its influence on the cutting process. Figure 3.61 aims to clarify the issue. The inclination angle  $\lambda_s$  is measured in the cutting edge plane  $P_s$  which is perpendicular to the reference plane  $P_r$  (Fig. 2.12) and passes through the tool tip (nose point) 1. Numbers 1 and 2 designate the ends of the cutting edge. As such, if the tool tip 1 locates below point 2, then the inclination angle  $\lambda_s$  is positive; if points 1 and 2 are at the same level, then  $\lambda_s = 0$ ; and when the tool tip 1 locates above point 2, then the inclination angle  $\lambda_s$  is negative.

**Table 3.1.** Optimal flank angles

Uncut chip thickness, $t_1$ (mm)	Optimal flank angle, $\alpha_{opt}$		Uncut chip thickness, $t_1$ (mm)	Optimal flank angle, $\alpha_{opt}$	
	Steel machining	Cast iron machining		Steel machining	Cast iron machining
0.02	24°30'	18°	0.40	10°	7°30'
0.04	20°	15°	0.80	8°	6°
0.08	16°	12°	1.20	7°15'	5°30'
0.10	15°	11°	1.50	6°40'	4°40'
0.20	12°	9°			

The sign of the inclination angle defines the chip flow direction as shown in Fig. 3.62. When  $\lambda_s$  is positive, the chip flows to the right and can potentially damage the machined surface. When  $\lambda_s$  is negative the chip flows to the left. When  $\lambda_s = 0$ , the chip flow direction in the reference plane is entirely determined by the tool cutting edge  $\kappa_r$ .

Before any discussion of the influence of the inclination angle on the cutting process, it has to be pointed out that this angle is not specified by the tool catalogs

of various tool manufactures for single point cutting tools and for drills and reamers.

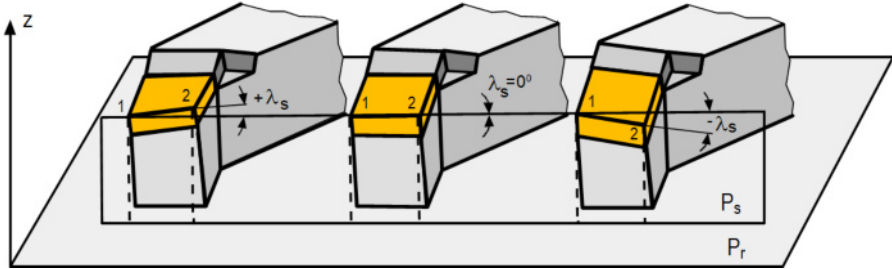


Fig. 3.61. Sense of the sign of the inclination angle (after Astakhov [14])

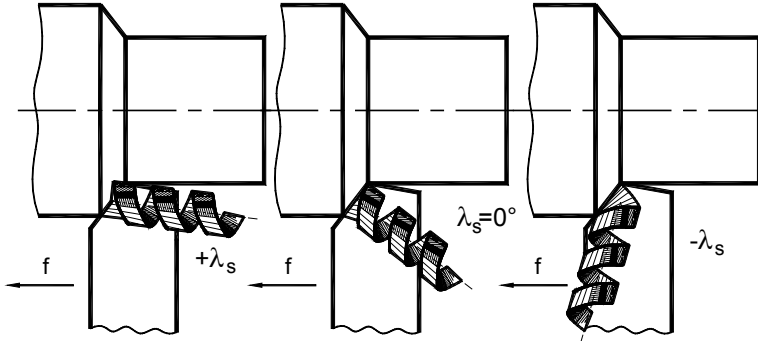
Although the influence of  $\lambda_s$  shown in Fig. 3.62 is correct, normally it cannot be readily distinguished in reality in turning because the inclination angles are rather small for standard single point tools. As most of the standard cutting are inserts made with zero inclination angle in the T-hand-S, this angle forms in the T-mach-S when the insert is placed in a tool holder and the tool holder is mounted in the machine. As such, the inclinations of the base face (Fig. 2.19) in the working plane  $\gamma_f$  and in the back plane,  $\gamma_p$  are indicated in catalogs. For a common tool holder with  $\kappa_r = 60^\circ$ ,  $\gamma_f = -6^\circ$ , and  $\gamma_p = -6^\circ$ . Using Eq. 2.20, one can calculate the most common inclination angle used in turning as

$$\lambda_s = \arctan(-\sin \kappa_r \tan \gamma_p - \cos \kappa_r \tan \gamma_f) = \arctan(-\sin 60^\circ \tan(-6^\circ) - \cos 60^\circ \tan(-6^\circ)) = 2.2^\circ \tag{3.47}$$

Therefore, the influence of the inclination angle in practical turning is small as this angle is normally small.

In the literature on metal cutting the influence of this angle is rarely discussed as this influence is complicated so the system approach is needed to reveal this influence. DeVries [72] presented an analysis of the influence of the inclination angle on the chip flow angle (direction) showing that according to previous researches this angle is close to the inclination angle. DeVries analyzed the influence of the inclination angle on the cutting force using the model of the cutting force derived using the improper Merchant’s force model modified for the case of oblique cutting (Chap. 1). He did not find any influence of the inclination angle in its range of 0–20°.





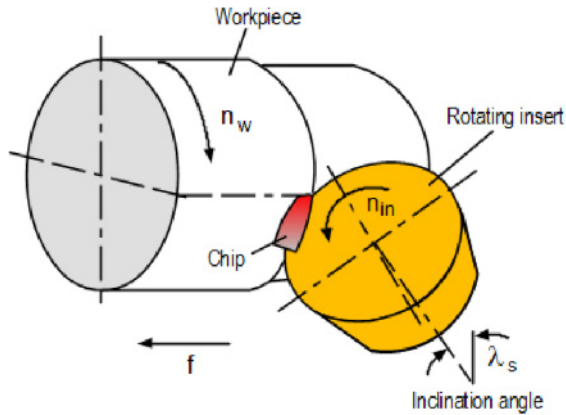
**Fig. 3.62.** Influence of the sign of the inclination angle on the direction of chip flow

In the author's opinion, the influence of the inclination angle in other practical machining operations is significant as far as the width of cut is great. In other words, the inclination angle affects the cutting process when this angle is able to change the state of stress in the deformation zone. As explained in great details by Zorev [24] and pointed out by Shaw [11], it happens when the chip flow direction changes significantly due to the inclination angle. Unfortunately, instead of being re-evaluated for new developments in tool materials and experimental techniques, these results are simply forgotten in modern theory and practice of metal cutting and tool design. Therefore, it is instructive to show the use of the inclination angle in some practical machining operations.

### 3.7.1 Turning with Rotary Tools

The continuous spinning of the cutting insert about its axis in addition to the main cutting and feed motions is the major difference between rotary cutting and conventional cutting. Figure 3.63 shows the principle of such a tool. As seen, in addition to the prime motion with rotation speed  $n_w$  and feed motion,  $f$ , the cutting insert is provided with rotation  $n_{in}$  about its axis. As a result, the cutting edge moves continuously so that fresh portions of this edge enters into the machining zone.

Initially, rotary tools were developed so that the rotating of the cutting insert was provided by the forces acting in cutting. Such tools became known as self-propelled rotary tools. The major advantage of these tools is their simple design and versatility. The major disadvantage is unstable, cutting speed and feed dependant rotation of the cutting insert due to many variables influencing the forces involved. The optimal cutting geometry has to be sacrificed for adjusting the proper direction of the forces to assure the rotation of the cutting insert. Although many years of research efforts have been undertaken in many countries, this tool concept has never found its way into practical production besides a few isolated cases as the balance between the conditions of reliable cutting insert rotation and the tool geometry (to gain advantages of such a design) exists only in a rather



**Fig. 3.63.** Kinematics of rotary turning

narrow range of process parameters so that it cannot be assured in practical applications.

To overcome the listed problems in self-propelled rotary tools, spinning tools have been developed where the insert is rotated by an independent external source, e.g., an electrical motor. In such tools, the rotation of the cutting insert is stable and it does not depend on the machining regime, properties of work and tool materials, and other variable of a particular machining operation. Moreover, with the development of the spinning tool design, the tool geometry can be set to achieve the optimal tool performance. Figure 3.64 shows the spinning tool jointly developed by the companies Mori Seiki and Kennametal.



**Fig. 3.64.** Spinning tool jointly developed by Mori Seiki and Kennametal

In rotary tools, the rotation of the cutting insert allows the continuous changing of the cutting edge so that each portion of the circumference of the insert is engaged

in cutting for a very short period. It allows one to increase the material removal rate restricted by the high cutting temperature in conventional turning single point tools. As a result, the productivity of machining and tool life are increased. This was the rationale behind the design of any rotary tool. What was noticed, however, is the great differences in tool geometry between self-propelled and spinning rotary tools. The major difference is in the inclination angle (Fig. 3.63) which normally reaches  $30\text{--}40^\circ$ . This creates a preferable state of stress in the deformation zone as the T-use-S rake angle becomes close to the effective rake angle (See Sect. 3.5.2) and the chip removal model resembles that shown in Fig. 3.53. As such, the chip deformation is the little due to small work of plastic deformation of the work material.

The discussed example reveals that, although important, the major role of the inclination angle is not to alter the direction of chip flow but rather to create a high T-use-S rake angle without compromising the strength of the cutting wedge.

### 3.7.2 Helical Treading Taps and Broaches

Another example of significant influence of the cutting edge inclination angle is shown in Fig. 3.65, where two basic threading tap designs with inclination angle were developed to enhance chip removal. The spiral point tap (Fig. 3.65a) was developed for through holes to force chip forward while the spiral flute tap (Fig. 3.65b) was developed primarily for blind hole to force chip back out of the hole. However, it was soon found that the treating torque decreases significantly while surface finish and tool life improves with these taps even when relatively short holes where chip removal does not present any problems were machined. Such observations led to the recent development of double helix thread cutting tap (US Patent Application Publication US 2008/0075550 A1) which, as claimed by the inventor, is capable of cutting a great variety of work material with great tool life and good surface finish of machined threads.



**Fig. 3.65.** Two basic threading tap designs with the cutting edge inclination angle

Yet another example of the use of the cutting tool inclination angle in tool design are various broaching tools. For years [73], broaching tools (round, flat, special-shaped) were designed with straight chip flutes to simplify re-grinding procedures performed with simple grinding fixtures on manual machines. Figure 3.66 shows an example of conventional (straight flutes) spline broaching tool. When such a tool works, unavoidable vibration due to periodic engagement/disengagement of the cutting teeth is a nuisance of the broaching process.

When more sophisticated grinding machines become available, helical broaching tools were introduced. In industry, when this principle is used for the surface or other outside broaching, this design is known as a broach with shear cutting teeth. Figure 3.67 shows an example of helical spline broaches. Helical cutting edges provide a smooth cutting action with reduced chatter and improved workpiece surface finishes while allowing users to take heavier cuts. The same as for threading taps, it was soon found that the axial force decreases while surface finish and tool life improve significantly.



**Fig. 3.66.** Conventional spline broaching tool



**Fig. 3.67.** Helical spline broaching tool

### 3.7.3 Milling Tools

The greatest influence of the inclination angle is observed in milling, particularly in end and face milling. In these operations, the so-called helical geometry results in a lower cutting force combined with better chip evacuation provided that the inclination (helix) angle is selected properly according to the work material and the amount of chip generated.

Rotary cutting end-mill tools are used for various machining operations. Such machine operations are generically referred to as milling operations and include the forming of slots, keyways, pockets, and the like. Several considerations related to

end-mill tool design include time for completing a machining operation, amount of material removed in a cut, quality of the cut, and wear on the tool itself during the milling operation.

End-mill tools are normally made of high speed steels and tungsten carbides, although other advanced materials such as ceramic, PCD, and other gradually become common. A typical tool includes a shank portion, a body portion, and a point. The body portion of the end-mill tool is located between the shank and the point. The point is formed at the opposite end of the tool from the shank portion, and typically includes one or more cutting edges. The body portion of end-mills is typically made as continuous helical flutes with continuous cutting edges helically extending from the inception location to the point (or *vice-versa*). The flutes of a milling cutter are almost always helical as shown in Fig. 3.68. If the flutes were straight, the whole tooth would impact the material at once, causing vibration and reducing accuracy and surface quality. Setting the flutes at an angle allows the tooth to enter the material gradually, reducing vibration.

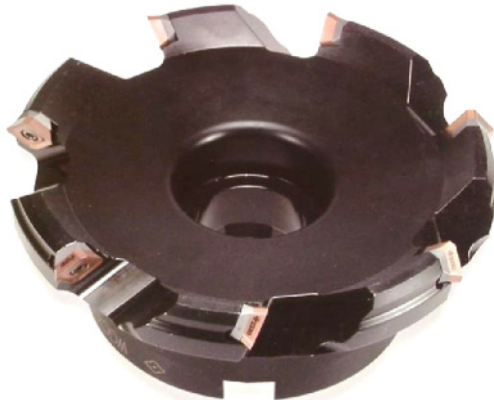
According to a common perception, the flutes function primarily for chip removal, in a manner similar to the helical flutes found on an ordinary twist drill. If it is the case, the helix angle of the flute should be selected based upon the best conditions for chip removal in the same manner as in twist drills. The practice, however, completely discards this perception as the helical (inclination) angles of a twist drill and an end milling tool made to machine the same work material are not the same. The common helical angle of the chip flute intended to machine medium carbon steels is normally  $35^\circ$  while this angle is  $60^\circ$  for tools intended to machine titanium alloys, and difficult to machine materials. This is because in an end milling tool, the cutting edge formed by the flute and the side relief surface performs cutting while the same edge in a twist drill does not participate in cutting.



**Fig. 3.68.** Helical end mills

For face milling cutters, the helical (inclination) angle is not normally specified. Instead, the rake angle is considered. Rake angles for face milling cutters are specified in two directions, axial and radial. The axial rake is the cutting insert's

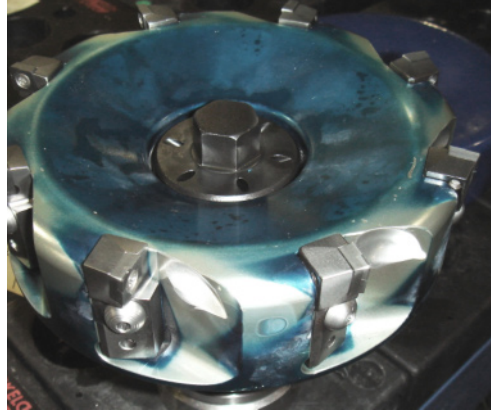
angle with respect to the central axis of the cutter/spindle assembly. The radial rake is the cutting insert's angle with respect to the periphery of the cutter. Common configurations include (1) positive in both directions (2) negative in both directions, and (3) positive in one direction and negative in the other. In any of these common cases, an inclination angle which may reach  $45^\circ$  is formed. Experience shows that when other components of the machining system support a given milling operation, a high inclination angle (Fig. 3.69) reduces the cutting force, improves the quality of milling, and increases tool life.



**Fig. 3.69.** WGC high performance face milling cutter having  $45^\circ$  inclination angle

ISCAR introduces H600 WXCUC HELIDO/FEEDMILL trigon double-sided, six-edged insert which combines strength and helical geometry to facilitate milling at very high feed rates. This insert is provided with a  $17^\circ$  lead angle cutting edge configuration. The resultant cutting forces are directed axially towards the spindle. This design provides high stability and enables machining at high feed rates even in long overhang applications.

The axial and radial rake angles combined with the geometry of the cutting insert selected for a given operation affect the direction of chip flow by means of the inclination angle formed as a direct result of these parameters. This inclination angle is important as the formed chip may interfere with the tool body. When the tool body is made of soft material (for tool weight reduction), this chip leaves distinctive marks on this body or even wears out deep craters as shown in Fig. 3.70. When one tries to use the so-called chip deflectors to prevent wear of the tool body, the matter gets worse, resulting in decreased tool life and even tool chipping with no apparent reason. Only a proper analysis of the resultant inclination angle can help solve the problem which is common for high-speed machining of automotive aluminum alloys.



**Fig. 3.70.** Improper selection of the inclination (helix) angle caused wear of the face mill body

## References

- [1] Kaldor S, Venuvinod PK (1997) Macro-level optimization of cutting tool geometry. *J. of Manufact. Science and Eng.* 119:1–9
- [2] Shaw MC (1988) Metal removal, in *CRC handbook of lubrication: theory and practice of tribology, Volume II: Theory and Design*, E.R. Booser, Editor. CRC Press: Boca Raton. p. 335–356
- [3] Gunay M, Korkut I, Aslan E, Seker U (2005) Experimental investigation of the effect of cutting tool rake angle on main cutting force. *J. of Mat. Proc. Tech.* 166:44–49
- [4] Gunay M, Seker U, Sur G (2006) Design and construction of a dynamometer to evaluate the influence of cutting tool rake angle on cutting forces. *Materials and Design* 27:1097–1101
- [5] Rodrigues AR, Coelho RT (2007) Influence of the tool edge geometry on specific cutting energy at high-speed cutting. *Journal of the Braz. Soc. of Mech. Sci. & Eng.* XXIX(3):279–283
- [6] Agnew J (1973) The importance and methods of carbide edge preparation. *SME paper MR73–905*
- [7] Shaffer WR (1999) Cutting tool edge preparation. *SME paper MR99-235*.
- [8] Kaldor S (1986) A common denominator for optimal cutting tool geometry. *Annals of the CIRP* 35:41–44
- [9] Kaldor S, Ber A (1990) A criterion to optimize cutting tool geometry. *Annals of the CIRP* 39(1):53–56
- [10] *Cemented carbide as tool and design material* (1967) Sandvik Coromont, Sweden, publication E–5758
- [11] Shaw MC (1984) *Metal cutting principles*. Science Publications, Oxford
- [12] Boothroyd G, Knight WA (2006) *Fundamentals of machining and machine tools*, Third ed. CRC, Boca Raton
- [13] Griffin RD, Li HJ, Elftheriou E, Bates CE (2002) Machinability of gray cast iron. *AFS Transactions* 01-159:1–17

- [14] Astakhov, VP (2006) Tribology of metal cutting. Elsevier, London
- [15] Oxley PLB (1989) Mechanics of machining: an analytical approach to assessing machinability. Wiley, New York
- [16] Klushin MI (1958) Metal cutting: basics of plastic deformation of the layer being removed, Mashgiz, Moscow
- [17] Stabler GV (1964) The Chip Flow Law and its Consequences. in Proc. 5th Int. MTDR Conf.
- [18] Colwell LV (1954) Predicting the angle of chip flow for single point cutting tools. Transaction ASME 76:199–202
- [19] Astakhov VP, Shvets S (2004) The assessment of plastic deformation in metal cutting. Journal of Materials Processing Technology 146:193–202
- [20] Astakhov VP, Xiao X (2008) A methodology for practical cutting force evaluation based on the energy spent in the cutting system Machining Science and Technology 12:325–347
- [21] Kattan IA, Venkates VC, Currie KR (1998) A comparative study of the effect of tool geometry with negative SCEAs on machining parameters. Int. J. of Mach. Tools and Manufact., 36(4):909–938
- [22] Kattan IA, Currie KR (1996) Developing new trends of cutting tool geometry. J. of Mat. Proc. Tech. 61:231–237
- [23] Venkatesh VC, Kattan IA, Hoy D, Ye CT, Vankirk JS (1996) An analysis of cutting tools with negative side cutting edge angles. J. of Mat. Proc. Tech. 58:351–361
- [24] Zorev NN (1966) Metal cutting mechanics. Pergamon Press, Oxford
- [25] Metal cutting tool handbook (1989), 7th ed. The Metal Cutting Tool Institute by Industrial Press, New York
- [26] Shaffer WR (2000) Cutting tool edge preparation. SME Paper TP99PUD68
- [27] Shaffer W (2000) Getting a Better Edge. Cutting Tool Engineering 52(3): 44–48
- [28] Outeiro JC, Astakhov VP (2005) The role of the relative tool sharpness in modelling of the cutting process. In: 8th CIRP international workshop on modeling of machining operations. Chemnitz University of Technology, Chemnitz, Germany, 517–523
- [29] Silin SS (1979) Similarity methods in metal cutting (in Russian). Mashinostroenie, Moscow
- [30] Shuster LSH (1988) Adhesion processes at the tool–work material interface (in Russian). Mashinostroenie, Moscow
- [31] Poletica MF (1969) Contact loads on tool interfaces (in Russian). Mashinostroenie, Moscow
- [32] Astakhov VP (1998/1999) Metal cutting mechanics. CRC, Boca Raton
- [33] Chen NNS, Pun WK (1988) Stresses at the cutting tool wear land. International J. of Mach. Tools and Manuf. 28:79–92
- [34] Outeiro JC (2003) Application of recent metal cutting approaches to the study of the machining residual stresses, Dissertation, University of Coimbra
- [35] Özel T, Hsu T-K, Zeren E (2005) Effects of cutting edge geometry, workpiece hardness, feed rate and cutting speed on surface roughness and forces in finish turning of hardened AISI H13 steel. Int. J. of Adv. Manuf. Tech. 25(3–2):262–269
- [36] Thiele JD, Melkote SN, Peascoe RA, Watkins TR (2000) Effect of cutting-edge geometry and workpiece hardness on surface residual stresses in finish hard turning of AISI 52100 steel. J. of Manuf. Science and Eng. 122(4):642–649
- [37] Cheung FYZ, Zhoua ZF, Geddam A, Li KY (2008) Cutting edge preparation using magnetic polishing and its influence on the performance of high-speed steel drills. J. of Mat. Proc. Tech. 208:196–204
- [38] Rech J (2006) Influence of cutting edge preparation on the wear resistance in high speed dry gear hobbing. Wear 261:505–512



- [39] Biermann D, Terwey I (2008) Cutting edge preparation to improve drilling tools for HPC processes. *CIRP Journal of Manufacturing Science and Technology* 1:76–80
- [40] Mayer JEJ, Stauffer DG (1973) Effects of tool hone and chamfer on wear life. ASME Technical paper MR73–907
- [41] Komarovskiy AA, Astakhov VP (2002) *Physics of strength and fracture control: fundamentals of the adaptation of engineering materials and structures*, CRC, Boca Raton
- [42] Zhong ZW (2003) Ductile or Partial Ductile Mode Machining of Brittle Materials. *Int. J. of Adv. Manuf. Tech.* 21(8):579–585
- [43] Kang X, Junichi T, Akihiko T (2006) Effect of cutting edge truncation on ductile-regime grinding of hard and brittle materials. *International Journal of Manufacturing Technology and Management* 9(1-2): 183–200.
- [44] Jahanmir S, Ramulu M, Koshy P (ed.) (1999) *Machining of Ceramics and Composites Manufacturing Engineering and Materials Processing*. CRC, Boca Raton
- [45] Dahlman P, Gunnberg F, Jacobson M (2004) The influence of rake angle, cutting feed and cutting depth on residual stresses in hard turning. *J. of Mat. Proc. Tech.* 47(2):181–184
- [46] Tetsuji O, Hirokazu K, Shigeo M (1999) Influence of clearance and rake angles on the cutting force of rock. *Journal of NIRE (National Institute for Resources and Environment)* 2(3):73–80
- [47] Saglam H, Yaldiz S, Unsacar F (2007) The effect of tool geometry and cutting speed on main cutting force and tool tip temperature. *Materials and Design* 29:101–111
- [48] Shih A (1996) Finite element analysis of the rake angle effects in orthogonal metal cutting. *International Journal of Mechanical Science* 38(1):1–17
- [49] Dechjarern S (2008) 3D finite element investigations of the influence of tool rake angle on cutting performance. *Asian International Journal of Science and Technology in Production and Manufacturing* 1(2):149–158
- [50] Poletica MF (1969) Contact loads on cutting tool interface surfaces (in Russian). *Mashinostroenie, Moscow*
- [51] Destefani J (2002) Cutting tools 101: geometries. *Manufacturing Engineering* 129(10):25–42
- [52] Astakhov VP (2004) Tribology of metal cutting. In: Totten G, Liang H (ed) *Mechanical tribology. material characterization and application*. Marcel Dekker, New York.
- [53] Zhang J-H (1991) *Theory and technique of precision cutting*, Pergamon Press, Oxford
- [54] Takeyama H, Usui H (1958) The effect of tool–chip contact area in metal cutting. *ASME Journal of Engineering for Industry* 79:1089–1096
- [55] Chao BT, Trigger KJ (1959) Controlled contact cutting tools. *Transactions of the ASME* 81:139–151
- [56] Usui E, Shaw MC (1962) Free machining steel – IV: Tools with reduced contact length. *Transactions of the ASME* B84:89–101
- [57] Hoshi K, Usui E (1962) Wear characteristics of carbide tools with artificially controlled tool-chip contact length. In: *Proceedings of the Third International MTDR Conference*. New York: Pergamon Press
- [58] Usui E, Kikuchi K, Hoshi K (1964) The theory of plasticity applied to machining with cut-away tools. *Transactions of the ASME* B86:95–104
- [59] Jawahir IS, Van Luttervelt CA (1993) Recent developments in chip control research and applications. *Annals of the CIRP* 42(2):659–693
- [60] Luttervelt CA, Childs THC, Jawahir IS, Klocke F, Venuvinod PK (1998) Present situation and future trends in modelling of machining operations. Progress report of

- the CIRP Working Group 'Modelling of Machining Operations'. *Annals of the CIRP* 74(2):587–626
- [61] Karpat Y, Ozel T (2008) Analytical and thermal modeling of high-speed machining with chamfered tools. *Journal of Manufacturing Science and Engineering* 130(1):1-15
  - [62] Vasin SA, Vereshaka AS, Kusher VS (2001) Metal cutting: termomechanical approach to inter-correlated phenomena in cutting (in Russian). MGTU Baumana, Moscow
  - [63] Chang, C-S, Fuh K-H (1998) An experimental study of the chip flow of chamfered main cutting edge tool. *J. of Mat. Proc. Tech.* 73:167–178
  - [64] Loladze TN (1958) Strength and wear of cutting tools (in Russian). Mashgiz, Moscow
  - [65] Abuladze NG (1962), The tool–chip interface: determination of the contact length and properties (in Russian). In: *Machinability of Heat Resistant and Titanium Alloys*. Kyibashev Regionsl Publ. House: Kyibashev (Russia). 87–96
  - [66] Sadic MI, Lindstrom B (1993) The role of tool-chip contact length in metal cutting. *J. of Mat. Proc. Tech.* 37:613–627
  - [67] Sadic MI, Lindstrom B (1995) The effect of restricted contact length on tool performance. *J. of Mat. Proc. Tech.* 48:275–282
  - [68] Mundy WL (1976) Cutting tool for continuous machining of metals and the method of making same, USA Patent No.3,955,448
  - [69] *Machining Data Handbook*. 2nd ed. (1972). Machinability Data Center, Cincinnati
  - [70] Stenphenson DA, Agapiou JS (2006) *Metal cutting theory and practice* 2nd ed. CRC, Boca Raton
  - [71] Larin MT (1953) *Optimal geometrical parameters of cutting tools* (in Russian). Oborongiz, Moscow:
  - [72] DeVries WR (1992) *Analysis of material removal processes*. Springer-Verlag, New York
  - [73] Viall E (1918) *Broaches and broaching* McGraw-Hill, New York

## Straight Flute and Twist Drills

*Make everything as simple as possible, but not simpler.*

Albert Einstein (1879–1955)

**Abstract.** This chapter discusses classification, geometry, and design of straight flute and twist drills. It argues that the design, manufacturing, and implementation practices of drills are lagging behind the achievements in the tool materials, powerful high-speed-spindles rigid machines, and high-pressure MWF (coolant) supply. Although the wide availability CAD design tool and CNC precision grinding machines make it possible to reproduce any drill geometry, have not many new drill designs become available recently. The chapter points out that the prime objective of the drilling system is an increase in the drill penetration rate, i.e., in drilling productivity as the prime source for potential cost savings. As the major problem is in understanding particularities of drill geometry and its components, this chapter walks the reader from simple concepts starting from the basic terminology in drill design and geometry to the most complicated concepts in the field, keeping the context to the simplest possible fashion and providing practical examples. It provides an overview of important results concerning drill geometry and synthesizes the most relevant findings in the field with the practice of tool design.

### 4.1 Introduction

Various studies and surveys indicate that holemaking (drilling) is one of the most time-consuming metal cutting operations in the typical shop. It is estimated that 36% of all machine hours (40% of CNC) are spent performing holemaking operations, as opposed to 25% for turning and 26% for milling, producing 60% of the resultant chips. Therefore, the use of high-performance drills and reamers could significantly reduce the time required for drilling operations, and thus reduce holemaking costs.

Over the past decade, the tool materials and coatings used for drills have improved dramatically. Combined with new powerful, high-speed-spindles rigid machines and high-pressure MWF (coolant) supply, these allowed a significant increase in the cutting speeds and penetration rates in drilling and reaming.

Although the wide availability CAD design tool and CNC precision grinding machines make it possible to reproduce any drill geometry, not many new drill designs have become available recently. It is known that drill geometry and topography must be optimized to utilize fully the power of modern tool materials and coatings. Points, point angles, margin geometry and topography, edge preparation, flute profile, and the number of flutes and margins must be properly adjusted for the application. The problem is in understanding particularities of drill geometry and its components.

This chapter aims at providing an overview of important results concerning drill geometry and to generalize the most relevant findings in the field with the practice of tool design. It also aims to familiarize the reader with the basic terminology, and conventional and factorial methods of drill geometry assessment.

## 4.2 Classification

A drill is an end cutting tool for machining holes having one or more cutting lips (major cutting edges), and having one or more helical or straight chip removal flutes. The prime cutting motion is rotation applied to the drill or to the workpiece or to both and the feed motion is applied along the longitudinal axis of the drill to the drill or to the workpiece.

There are a great variety of drills used in industry. They can be classified as follows:

### *Classification based on construction*

- Homogeneous drills – those made of one piece of tool material such as carbide or high speed steel.
- Tipped drills – those having a body of one material with cutting lips (or their parts as the periphery corners) made of another materials brazed or otherwise bonded in place.
- Insert drills – those having cutting portions or indexable cutting inserts (cartridges) held in place.

### *Classification based on shank configuration*

- Straight shank drills – those having cylindrical shanks which may be the same or different diameter than the body of the drill. The shank can be made with or without driving flats, tang, neck, grooves, or threads.
- Taper shank drills – those having conical shanks suitable for direct fitting into tapered holes in machine spindles, driving sleeves, or sockets. Tapered drills generally have a tang.

### *Classification based on the length-to-diameter ratio*

- Stub drills – those having very short body length.
- Regular length drills – drills having length-to-diameter ratio not exceeding 10. Jobber-length drills are the most common type of such drills. The length of the flutes is 10 times the diameter of the drill.

- Long drills – drills having length-to-diameter ratio exceeds 10.

*Classification based on number of flutes*

- Single-flute drills – those having only one flute, e.g., gundrills.
- Two-flute drills – those having two chip removal flutes, e.g., the conventional type of twist drill.
- Multiple-flute drills – those having more than two flutes. This drill type commonly used for enlarging and finishing, drilled or cast, or punched holes.

*Classification based on the helix angle of flutes*

- Twist drills – those having helical chip removal flutes.
- Straight flute drills – those having straight flutes.

*Classification based on coolant supply*

- Drills with external coolant supply – those having no special means for coolant supply.
- Drills with internal coolant supply – those having internal coolant supply holes or passages and those having coolant supply passages separated from the chip removal passages.

*Classification based on assumed force balance*

- Transiently-balanced drills – those having only margins as supporting means in the radial direction and thus relying on the complete force balance in drilling.
- Transiently-balanced drills with additional supports – those relying on the complete force balance in drilling while having additional supporting margins normally located on the hills to improve drilling stability.
- Self-piloting drills – those drills designed so that the unbalanced radial force rising in drilling acts on the supporting elements in contact with the walls of the hole being drilled. As a result, a self-piloting drill guides or steers itself during a drilling operation using the walls of the hole being drilled as the pilot surface.

*Classification based on functions and applications*

- Solid drills – those making holes in solid workpieces without previously made holes.
- Core drills – those having no center point cutting but used for enlarging or finishing previously made holes.
- Center drills – those for making center holes in workpieces to provide a starting hole for a larger sized drill, or a conical indentation in the end of a workpiece to mount it between centers for subsequent machining operations.
- Pivot drills – those having a shank diameter different to the diameter of the drill body.

- Micro drills – drills used for small holes mainly to drill circuit boards for electronic equipment.
- Spade drills – straight fluted drills having a plate-like working part with two cutting lips, usually mechanically clamped into the slot made in the shank.

### 4.3 Basic Terms

The basic terms used for straight-flute and for twist drills are the same so the basic terms related to the twist drill are considered in this section. The particularities of straight-flute drills are considered in the next section.

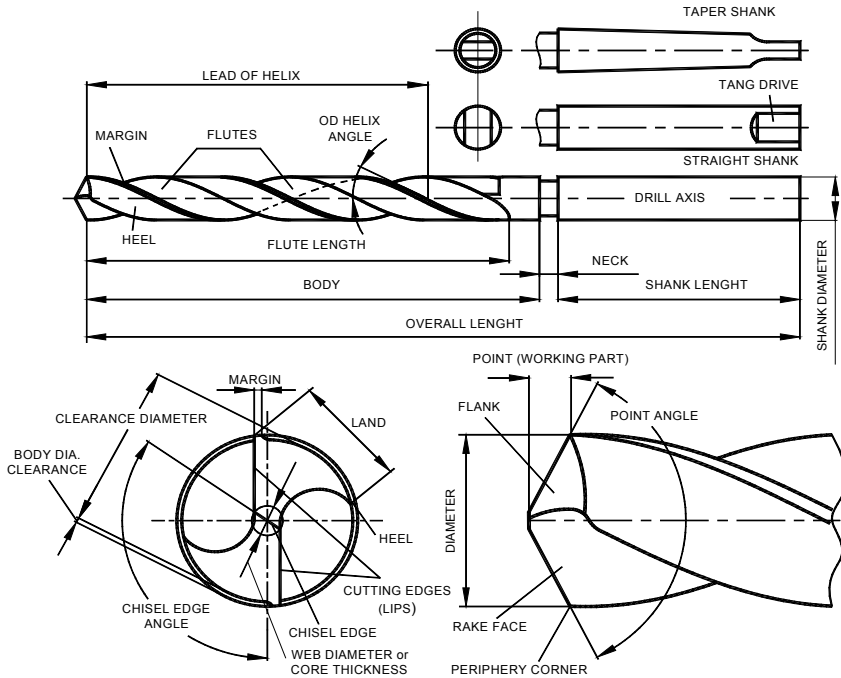
The twist drill bit was invented by Steven A. Morse who received U.S. Patent 38119 for his invention ‘Improvements of Drill-Bits’ in 1863. The original method of manufacture was to cut two grooves in opposite sides of a round bar, then to twist the bar to produce the helical flutes. This gave the tool its name. Nowadays, a flute is usually made by rotating the bar while moving it past a grinding wheel with its axis inclined by the helix angle to the axis of the bar and the profile of which corresponds to the flute profile in the normal section.

A twist drill is defined as an end cutting tool having one or more cutting teeth with cutting lips formed by the corresponding number of helical chip-removal flutes. A common twist drill is shown in Fig. 4.1. It consists of the body, neck (optional), and shank.

The working part has at least two helical flutes called the chip removal flutes. The lead of helix of the flute depends on many factors including the properties of the work material so it varies from 10–15°; standard angles are about 22–30°; and up to 45° for high-helix twist drills. The flute profile and its location with respect to the drill longitudinal axis determine many facets of twist drill performance because:

- Flute profile determines the geometry of the drill rake face: the shape of the cutting edge (lip); the rake angle and its variation along this edge; the cutting edge inclination angle and its variation along this edge; the rake angle of the side cutting edge defined as the line of intersection of the drill margin; and the flute over the length that slightly exceeds the feed per revolution. As a result, a great number of various flute profiles have been developed and many of them are available as applied to twist drills produced by various drill manufacturers.
- Flute profile parameters determine the diameters of the web (the core thickness), i.e., directly affect buckling stability of the drill.
- Flute profile together with the flute helix angle determine the torsional stability of the drill.
- Flute profile determines the reliability of chip removal, i.e., chip breakage into pieces (sections) suitable for transportation and easiness of such transportation.

Therefore, the flute profile is one of the major design features of a twist drill.



**Fig. 4.1.** Illustration of terms applying to twist drills

The chip removal flutes intersecting the flanks and the lines of intersection form the major cutting edges often called the lips. Drill manufacturers often contrived that the flute profile, flank shape, and the point angle chosen produce a straight cutting edge as shown in Fig. 4.1 although a number of recent twist drill designs feature a curved shape for these edges. The major cutting edge of a twist drill does not pass through the center of rotation as seen in Fig. 4.1 so the inclination angle of the cutting edge to the drill radius varies as the radius changes. The internal ends of the lips (sometimes called chisel edge corners) are connected by the chisel edge as shown in Fig. 4.1.

Some important terms related to the twist drill design and geometry are defined as follows:

*Axis* – the imaginary straight line which forms the longitudinal center line of the drill.

*Back Taper* – a slight decrease in diameter from front to back in the body of the drill.

*Body* – the portion of the drill extending from the shank or neck to the periphery corners of the cutting lips.

*Body diameter clearance* – that portion of the land that has been cut away to prevent its rubbing against the walls of the hole being drilled.

*Chip packing* – the failure of chips to pass through the flute during the cutting action.

*Chisel edge* – the edge at the end of the web that connects the cutting lips.

*Chisel edge angle* – the angle included between the chisel edge and the cutting lip, as viewed from the end of the drill.

*Clearance* – the space provided to eliminate undesirable contact (interference) between the drill and the workpiece.

*Cutter sweep* – the section formed by the tool used to generate the flute in leaving the flute.

*Cutting tooth* – a part of the body bounded by the rake and flank surfaces and by the land.

*Double margin drill* – a drill whose body diameter clearance is produced to leave two margins on each land and is normally made with margins on the leading edge and on the heel of the land.

*Drill diameter* – The diameter over the margins of the drill measured at the periphery corners.

*Flute length* – the length from the periphery corner of the lips to the extreme back end of the flutes. It includes the sweep of the tool used to generate the flutes and, therefore, does not indicate the usable length of flutes.

*Flutes* – helical or straight grooves cut or formed in the body of the drill to provide cutting lips, to permit removal of chips, and to allow cutting fluid to reach the cutting lips.

*Galling* – an adhering deposit of nascent work material on the margin adjacent to the periphery corner of the cutting edge.

*Hill* – the trailing edge of the land.

*Helix angle* – the angle made by the leading edge of the land with the plane containing the axis of the drill.

*Land* – the peripheral portion of the cutting tooth and drill body between adjacent flutes.

*Land clearance* – see preferred term body diameter clearance.

*Land width* – the distance between the leading edge and the heel of the land measured at right angles to the leading edge.

*Lead* – the axial advance of a helix for one complete turn or the distance between two consecutive points at which the helix is tangent to a line parallel to the drill axis.

*Lip (major cutting edge)* – a cutting edge that extends from the drill periphery corner to the vicinity of the drill center. The cutting edges of a two flute drill extending from the chisel edge to the periphery.

*Lip relief* – the relief made to form flank surface. There can be several consecutive reliefs as the prime relief, secondary relief, etc., made to clear the lip as well as to prevent interference between the flank surface and the bottom of the hole being drilled.

*Lip relief angle* – obsolete term for the lip flank angle. Normally defined as the normal flank angle at the periphery corner of the lip. Although this angle is often shown in twist drill drawings, it does not make much sense as the lip flank angle normally varies over the lip.

*Margin* – the cylindrical portion of the land which is not cut away to provide clearance.

*Neck* – the section of reduced diameter between the body and the shank of a drill.



*Overall Length* – the length from the extreme end of the shank to the outer corners of the cutting lips. It does not include the conical shank end often used on straight shank drills and taper shank drills.

*Periphery* – the outside circumference of a drill.

*Periphery corner* – the point of intersection of the lip and the margin. In a two-flute drill, the drill diameter is measured as the radial distance between two periphery corners.

*Peripheral rake angle* – the angle between the leading edge of the land and an axial plane at the drill point.

*Relative lip height* – the difference in indicator reading between the cutting lips. Lips runout is another commonly used term.

*Relief* – the result of the removal of tool material behind or adjacent to the cutting lip and leading edge of the land to provide clearance and prevent interference (commonly called rubbing or heel drag) between the cutting tooth and the bottom of the hole being.

*Shank* – the part of the drill by which it is held and driven.

*Web* – the central portion of the body that joins the lands. The extreme end of the web forms the chisel edge on a two-flute drill.

*Web thickness* – the thickness of the web at the point, unless another specific location is indicated. Measured as the web diameter as shown in Fig. 4.1.

*Web-modification* – modification of the web from its ordinary thickness, shape and/or location to reduce drilling thrust, enhance chip splitting, and change chip flow direction. The simplest modification is web thinning.

## 4.4 System Approach

The basics of the system approach to tool design are discussed in Chap. 5 where deep-hole tools are discussed. Although they are fully applicable for straight-flute and twist drills, the severity of the system influence is much greater for these drills than for deep-hole drills. This is because most deep-hole drills are intended for finishing hole operations so that somehow greater care of the machining system and its components is normally taken. In contrast, straight-flute and twist drills are used in a great variety of machining systems starting with a bench drill press used for home improvement and finishing with the most advanced manufacturing systems in the automotive industry. The great variety of applications causes a great range of the requirements for drilling operations and thus an enormous number of drill designs. Unfortunately, most academic research work does not account for these systemic issues while practical recommendations for the drill design and applications are particular to given application conditions. All this makes the analysis of straight-flute and twist drills geometry, design and application virtually impossible. As a result, no one known to the author has attempted such an analysis. Rather, general considerations, basic terms, pictures of variety point grinds are provided which are of little help to a tool/process designer to select (or design) the right drill for a given application from the great variety of drills available in the market.

#### 4.4.1 System Objective

As pointed out by Fiesselmann [1], the prime system objective is an increase in the drill penetration rate, i.e., in drilling productivity. In all industries, as an average, perishable cutting tools seldom represent more than 8% of the total direct/indirect product manufacturing costs. For CNC machining centers and manufacturing cells where \$1.00 is the benchmark; for 2,200 operating hours per year, \$1.00 minute means an operating cost of \$132,000 per year for just one machine (cell). Even factoring in 75% efficiency for loading/unloading, changing tools, and setup, an increase in the penetration rate by 50% amounts to a potential yearly savings of \$24,750 per CNC machining center per year. Often, doubling drilling productivity can be accomplished with a simple change in drill point geometry.

For many manufacturers, drilling is the only option to produce a hole because of workpiece size, workpiece shape, workpiece handling, or the hole length-to-diameter ratio, hole size, and location represent tolerances not possible with other processes. When this is the case, the systemic optimization of the whole drilling operation is important.

#### 4.4.2 Understanding the Drilling System

In a drilling operation, an overwhelming number of variables affect the hole quality and productivity. The system approach allows one to adjust these variables for the drilling system coherency, i.e., to the condition when the penetration rate is the highest for given requirements of the machined hole quality. As the number of holes drilled and the time it takes to drill a hole increase, the variables involved in each drilling operation become even more important. In high-volume operations, seconds and fractions of a second saved per hole produce significant savings in manufacturing costs and cycle time.

Books, manuals, reports, and manufacturers' drilling guides on holmaking can answer most questions on speeds, feeds, and other items related to actual drilling of a hole. Obtaining an answer to a question about a specific drilling-related problem proves tougher because these resources vary considerably with respect to type of work material, machine type, and particular situation in the drilling system.

#### 4.4.3 Understanding the Tool

In high-volume operations, the drill is application specific. Different tool manufacturers might offer a dozen of more recommended "best" drills for a particular job. Literature resources and patents also offer a great number of drill designs. As a result, a tool designer/process engineer is overwhelmed with the variety of available design/ design features so that some methodological help is needed to help him to steer clearly though this ocean of information. The first and foremost step in such a methodology is understanding the most important correlations between drill design and geometry with its performance and drilling system requirements to assure this performance.

Each drill has features designed to eliminate specific problems – to extend tool life, to improve chip evacuation, to reduce drilling force thereby increasing the

allowable penetration rate, to improve surface finish or drill a straighter hole, etc. Therefore, a clear system objective should be established before considering the design/purchase of a new drill for a given application. As mentioned above, achieving the maximum drill penetration rate while holding the required quality of machined holes is the most common objective in high-volume production because it results in much greater manufacturing cost saving compared to other objectives such as, for example, improving tool life. Therefore, a clear understanding of the correlation between the drill/drilling system features and the allowable drill penetration rate is important.

## 4.5 Force System Constrains on the Drill Penetration Rate

### 4.5.1 Force-balance Problem in Conventional Drills

A simplified free body diagram for a twist drill is shown in Fig. 4.2. In this diagram,  $F_{x1}$  and  $F_{x2}$  are resultant power components;  $F_{y1}$  and  $F_{y2}$  are the radial components;  $F_{z1}$  and  $F_{z2}$  are the axial components of the cutting forces acting on the first and the second major cutting edges (lips), respectively. The power and radial components of the cutting forces that act on the two parts of the chisel edge are not shown as these are small while the axial components  $F_{z-cl1}$  and  $F_{z-cl2}$  shown in Fig. 4.2 are significant. The tangential  $F_{f-t1}$  and  $F_{f-t2}$  and axial  $F_{f-a1}$  and  $F_{f-a2}$  are components of the friction forces on the margins. The normal components of these forces are not shown.

The drilling torque applied through the spindle of the machine calculates as

$$M_{dr} = F_{x1}r_{x1} + F_{x2}r_{x2} + F_{y1}(c_{ct-1}/2) + F_{y2}(c_{ct-2}/2) + F_{f-t1}(d_{dr}/2) + F_{f-t2}(d_{dr}/2) \quad (4.1)$$

and the axial force applied by the spindle is

$$F_{z-s} = F_{z1} + F_{z2} + F_{z-cz1} + F_{z-cz2} + F_{f-a1} + F_{f-a2} \quad (4.2)$$

The shown drill is in the static equilibrium in the  $x_0y_0$  and  $z_0y_0$  planes if and only if the following two equilibrium conditions are justified:

In the  $x_0y_0$  plane

$$F_{x1}r_{x1} + F_{y1}(c_{ct-1}/2) = F_{x2}r_{x2} + F_{y2}(c_{ct-2}/2) \quad (4.3)$$

and in the  $z_0y_0$  plane

$$F_{z1}r_{z1} + F_{f-a1}r_{dr} = F_{z2}r_{z2} + F_{f-a2}r_{dr} \quad (4.4)$$

In practice, however, the above-mentioned conditions are rarely justified. For example, the major cutting edges (lips) may have so-called runout which stands for their inequality in terms of length. Moreover, these lips may have different elevation over the  $y_0$ -axis (distances  $c_{ct-1}$  and  $c_{ct-2}$  are not equal). The radial forces, for example, may not share the same line of action. Rather, these forces can be shifter by certain distance  $\Delta F_y$  as shown in Fig. 4.2. The same can be said about all the above-listed conditions of equilibrium. Moreover, runout is an inherent feature of any real drill due to drill manufacturing tolerances, mounting accuracy in the drill holder (chuck), spindle runout etc. As a result, there are always unbalanced moments in the  $x_0y_0$  and  $z_0y_0$  planes.

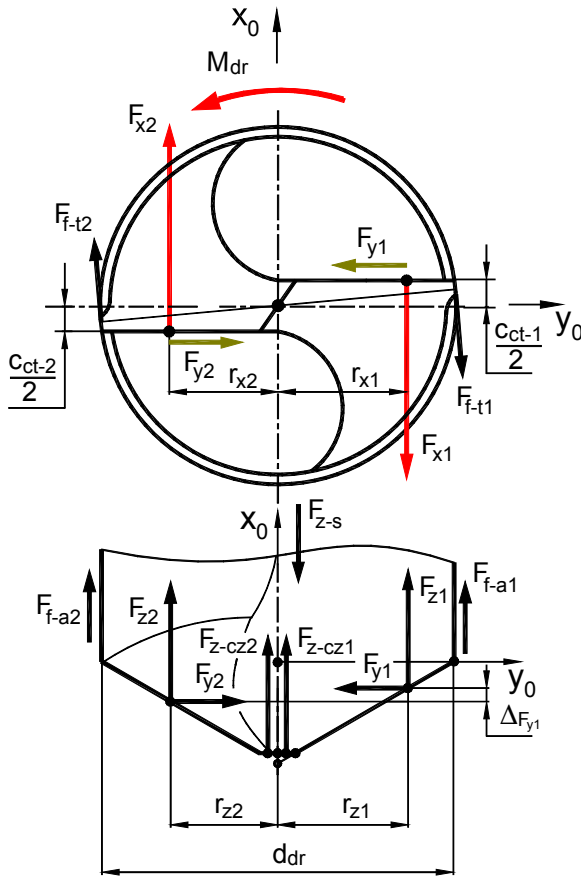
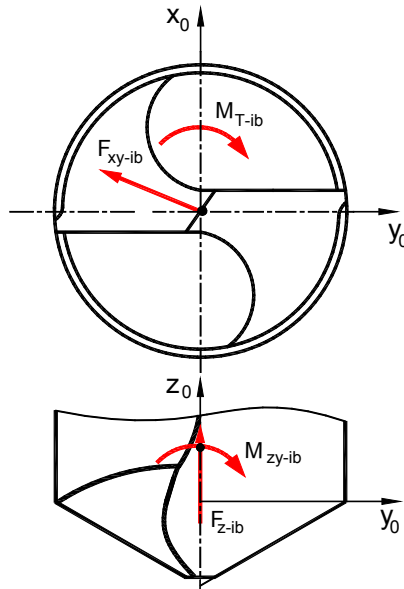


Fig. 4.2. A simplified free-body diagram of a twist drill

These moments result in an imbalanced radial force  $F_{xy-ib}$  and additional torque  $M_{T-ib}$  acting in the  $x_0y_0$  plane and an imbalanced bending moment  $M_{zy-im}$  and an additional axial force  $F_{z-im}$  in the  $z_0y_0$  plane as shown in Fig. 4.3. The imbalanced radial force  $F_{xy-ib}$  and bending moment  $M_{zy-im}$  cause a number of problems in

drilling such as the deviation of the longitudinal axis, shape distortions, and diametric deviations of the hole being drilled. The lower the strength of the work material and the greater length-to diameter ratio, the greater the deviations. As a result, additional hole-making operations such as, for example, reaming and boring, are used if precision holes are to be manufactured.



**Fig. 4.3.** System of imbalanced loads

As an important example, consider defects of holes drilled in a turbine shaft of an automatic six speed rear-wheel drive transmission. The shaft is shown in Fig. 4.4. A solid carbide drill is used. The worst drilling conditions are for the holes of 5.5/5.3 mm diameter as a long drill is required because these holes locate close to the flange. Figure 4.5 shows hole defects due to drill instability such as excessive bell-mouths, deviation of the longitudinal axis, diametric inaccuracies, etc.

It is worth mentioning that the drilling was performed on a CNC fully automated manufacturing cell widely used in the automotive industry so the defects shown are not related to excessive inaccuracies of the machine, fixture, or drill holder. Moreover, CNC sharpened drills having proper geometry and suitable coatings made by one of the most reputable tool company were used. In other words, the defects shown are inherent for drills without the self-piloting capability.

It has to be pointed out here that the design, tool materials, and manufacturing quality of conventional (straight-flute and twist) drills have been dramatically improved over the last decade:

- In terms of drill design, additional supporting areas (pads) are introduced on the top of the hills as shown in Fig. 4.6. Sometimes, bore scraper are used on the side of the supporting pads to improve surface finish of machined holes. When the parameters and geometry of these additional

design features are selected properly, they help to improve drill stability and quality of the machined holes. However, the improvement is not dramatic because the imbalanced radial force is commonly insufficient to assure proper functioning of these design features.

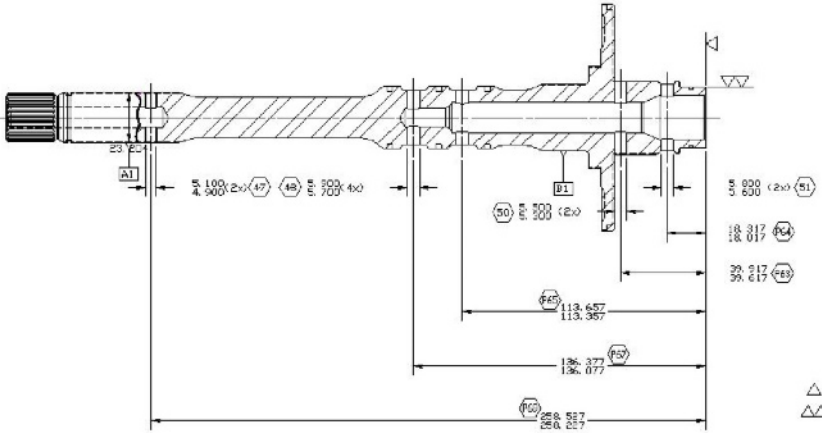


Fig. 4.4. Turbine shaft with cross-holes

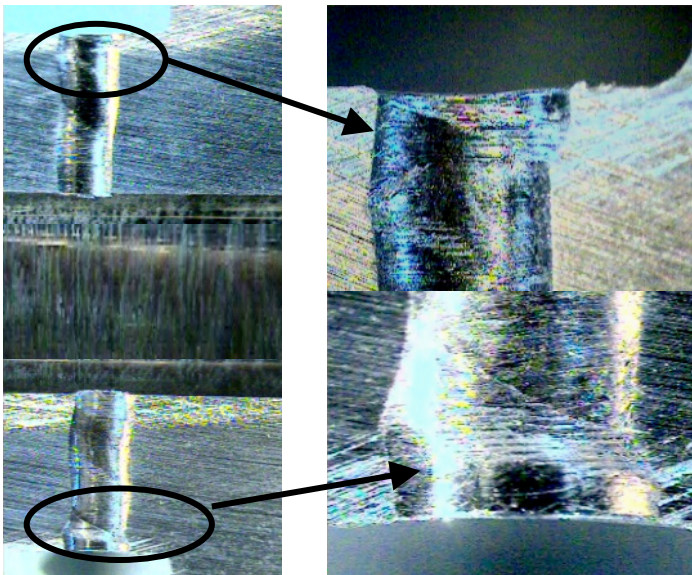


Fig. 4.5. Defects of the drilled holes

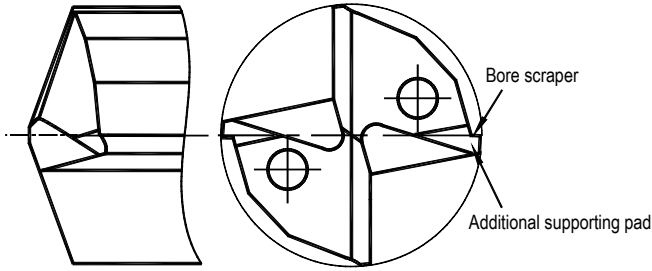


Fig. 4.6. Common design features to improve stability of drills

- In terms of tool materials, solid carbide drills application specific coatings became common, improving drill rigidity and tool life.
- In terms of manufacturing quality, CNC grinding machines used for grinding and re-sharpening of drills became common, assuring greater symmetry of drills' design and geometry features.

In further discussion, the drilling torque  $M_{dr}$  and the axial (often referred as the thrust) force applied through the spindle are two factors to be considered in the analysis of the allowable penetration rate, i.e., in maximizing the objective function. To analyze the constraints (meeting the quality requirements) in such optimization, one should consider the system of imbalanced loads shown in Fig. 4.3 and conditions of drill static equilibrium set by Eqs. 4.3 and 4.4. Although these conditions are written for a generic drill and thus can be corrected for a particular tool design, the necessity of the force balance in the  $x_0y_0$  and  $z_0y_0$  planes expressed by these conditions should be of prime concern in drill design, manufacturing and sharpening.

Figure 4.7 shows the resultant force factors model used in further consideration. The drilling torque,  $M_{dr}$  tries to unwind (twist) the drill, creating the angle of twist, while the resultant axial force,  $F_z$  compresses the drill.

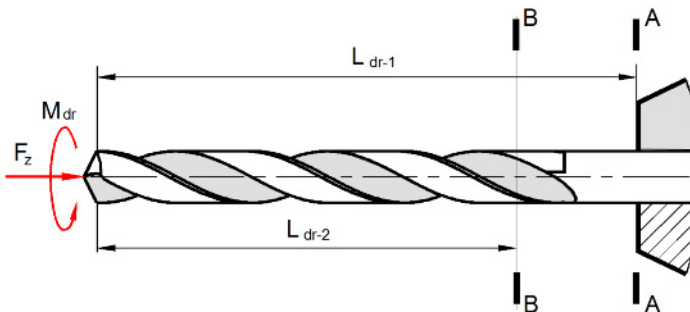


Fig. 4.7. Model of the resultant force system

#### 4.5.2 Constraints on the Drill Penetration Rate

It is discussed in Appendix A that the feed rate (which is called the penetration rate in drilling) calculates as the product of the cutting feed (mm/rev or ipr), and the spindle rotational speed (rpm) (Eq. A.4). Therefore, this rate can be increased either by increasing the rotational speed or by increasing the cutting feed. There are some constraints on each of these ways which should be understood.

The major constraint on the rotational speed is the cutting temperature primarily at drill corners as these have the highest linear (cutting) speed. The maximum allowable temperature is a sole property of the tool material (including its coating) while the maximum allowable rotational speed that causes this temperature is a function of many variables. Among them, the following are of prime importance:

- *Work material.* The stress and strain at fracture of the work material define the work spent on plastic deformation of this material in cutting which is the greatest portion of the cutting energy and thus is the major contributor to the cutting temperature [2].
- *Tool design and geometry.* This is because they define the state of stress in the deformation zone (the work of plastic deformation), chip formation, and its sliding direction, as well as the sliding conditions on the tool margins and working conditions of the side cutting edges. Moreover, tool design and geometry define to a large extent self-centering of the drill and thus affect drill transverse vibration which is the prime cause of drill failures.
- *MWF.* MWF supply (flow rate) and access to the drill corners (drill flanks design) as well as the MWF composition, concentration, clearness, tramp oil, etc.
- *Design and conditions of the drilling system.* This includes drill holder (eccentricity), starting bushing (alignment), system rigidity and many others.

Unfortunately, the listed factors and their inter-correlations are not well understood in the practice of drill design and implementation where the rotational speed for a given tool material is selected based upon the work material (type and hardness).

Compared to the drill rotational speed, there are many more constraints on the allowable cutting feed (feed per revolution). These constraints can be broadly divided into three categories: (1) constraints due to the quality requirements to machined holes (diametric, position, shape, location accuracies), (2) constraints due to the drill (buckling stability, excessive deformation, wear, breakage), and (3) constraints due to the machine (allowable axial force, power, structural rigidity). Although these listed categories relate to different phases of drilling operation planning, they have a common basis. The force factors (drilling torque, axial force, and imbalanced forces (see Sect. 4.5.1)) constitute this basis. Therefore, it is of importance to understand these force factors as drill geometry is one of the major contributors to their values.



### 4.5.3 Drilling Torque

The drilling torque is a function of the work material properties, drill diameter and geometry, and the drilling regime. Among these factors, the drill geometry and drilling regime can be varied to achieve optimal drill performance. As the cutting speed has a weak influence on the cutting force, it also has little influence on the drilling torque so that the cutting feed is the only factor to be considered.

While for modern production CNC machines the drilling torque is not a limiting factor as these machines are equipped with powerful motors to deliver high torques, for relatively small machines the drilling torque can be a constraint limited by the power of the drive motor. When the latter is the case, the feed per revolution is lowered or the hole is drilled in two consecutive drilling operations using first a smaller drill and then a drill to the required hole size.

The length of a drill imposes another important limitation. The problem is that the so-called angle of twist increases proportionally to the drill length under the same drilling torque. As known [3], this angle calculates as

$$\phi_{tw} = \frac{M_{dr} L_{dr-1}}{JG} \quad (4.5)$$

where  $L_{dr-1}$  is the length from the drill corner to the SECTION A–A (Fig. 4.7),  $J$  is the polar moment of inertia of the drill cross-section, and  $G$  is the shear modulus of the drill (tool) material. In reality, however, length  $L_{dr-2}$  is considered in Eq. 4.5 as the polar moment is much smaller in the cross-section B–B.

When angle of twist achieves a certain critical value (particular to the drill material and some other factors), the drill breaks. As follows from Eq. 4.5, there are two principle way to prevent this from happening (for a given drill material). The first is to decrease drilling torque that, in turn, reduces the penetration rate. Another way is to increase the polar moment of inertia of the drill cross section. The later is used in the practice of drill design.

The flutes are made so that the web thickness increases along the length of the drill from the tip to the shank as shown in Fig. 4.8. This is because the angle of twist increases proportionally to the drill length. Normally, a relatively shallow web taper rate is used in a drill so that the flute depth along the length of the flute is as great as possible. This should provide the maximum amount of volume to convey chips, swarf, or sawdust back from the tip and out of the hole being drilled. The American Society of Mechanical Engineers (ASME B94.11M-1993) and the Aerospace Industries Association of America, Inc. (NAS 907) standards define the conventional web thickness taper rate between 0.60mm and 0.76mm.

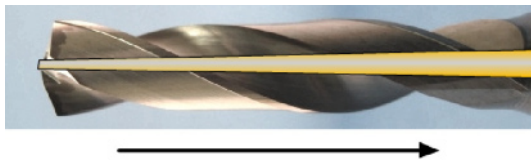
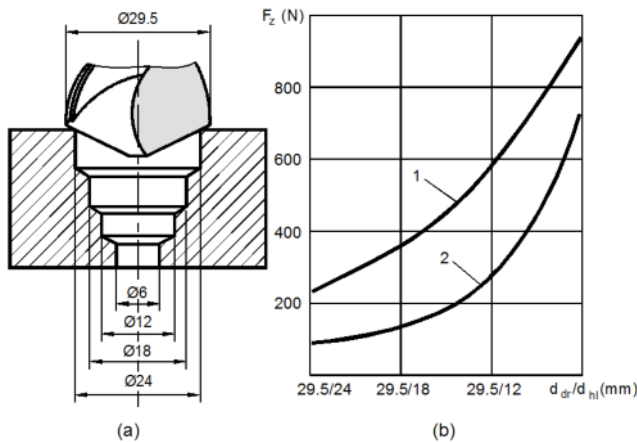


Fig. 4.8. Web thickness increases from the tip towards the shank

### 4.5.4 Axial Force

According to Eq. 4.2, the resultant axial force in drilling shown in Fig. 4.7 is the sum of the axial forces on the major cutting edges (lips), chisel edge, and due to friction on the margins. The latter is small compare to the first two terms so that the contribution of the major cutting edges (lips) and the chisel edge are considered. It is very important to realize that the axial force produced by the unit length of the cutting edge is not a linear function of the location radius of this unit length. Rather, the contributions of the portions of the cutting edge located closer to the drill center are much greater than the periphery regions. The greatest contribution to the resultant axial force is the chisel edge which is responsible for up to 60% of the total value of this force.

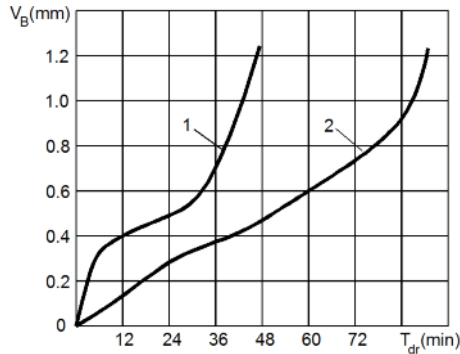
To illustrate this statement, Fig. 4.9a shows the principle and results of a simple axial force test. A predrilled test specimen made of gray cast iron (HB 200) is placed on a table dynamometer. An HSS twist drill of 29.5mm diameter was used. As the drill progressed in the pre-drilled hole, the contributions of different portions of the cutting edge into the resultant axial force can be assessed. Subtracting the axial force measured when drilled hole of 6mm diameter from the resultant axial force measured when a solid specimen was drilled, one can obtain the contribution of the chisel edge into the resultant axial force. Figure 4.9b shows the obtained result for a conventional (DIN1412) twist drill (curve 1) and for a radius-shaped major cutting edges (the radius of the cutting edge was  $0.8d_{dr}$  and shift of the radius center from the drill longitudinal axis was  $0.25d_{dr}$ ) (curve 2). As can be seen, although the lower axial forces due to modification of the cutting edge are observed when the second twist drill was used, the difference becomes smaller in the regions adjacent to the chisel edge. The test results showed that although the tool life of the second drill was nearly double compared to the standard twist drill (Fig. 4.10), the difference between the resultant axial forces for the first and second drills is negligible when the contribution of the chisel edge was considered.



**Fig. 4.9.** (a) Principle, and (b) results of a simple axial force test. Cutting speed  $v = 59\text{m/min}$ , feed  $f = 0.32\text{mm/rev}$

A significant axial force in drilling restricts the penetration rate because:

- It affects the buckling stability of drill. The compromising of this stability causes a number of hole quality problems. Figure 4.5 illustrates what happens when a twist drill loses its buckling stability. It also significantly reduces tool life causing excessive drill corner or even margin wear.
- Many machines used for drilling have insufficient thrust capacity that limits any increase in the penetration rate with standard drills.



**Fig. 4.10.** Comparison of the wear curve ( $V_B$  is the flank wear in the region adjacent to the drill corners;  $T_{dr}$  is the drilling time) for the standard and radius-shaped edges twist drills

Therefore, the reduction of the resultant axial force is vitally important when one tries to increase the allowable penetration rate of the drill. As the chisel edge is the major contributor to this axial force, one should: (1) to reduce the length of this edge and (2) to improve the geometry of this edge. These two objectives can be fulfilled simultaneously.

Figure 4.11 illustrates how differences in drill web thickness affect the axial (thrust) force requirements of drills. According to Fiesselmann [1], it is seldom understood that a drill with 30% web requires almost twice the axial force of the 20% web drill. Further, the 40% web drill found in drills recommended for harder, tougher alloys, or which result from using parabolic flute drills for holes deeper than five or six times the drill diameter in depth, have an axial force requirement almost four times that of the 20% web drill.

#### 4.5.5 Axial Force (Thrust)-Torque Coupling

Observations and tests that compare straight-flute and twist drills showed that the latter allow greater critical axial force and torques. This result can easily be explained by the so-called torque-thrust coupling effect in twist drills which should really be discussed in the literature on drilling. This effect can be explained as follows. The body of a twist drill contains two helical flutes. If a torque is applied as shown in Fig. 4.7, this torque tends to ‘unwind’ the helix and thus increase the drill length. Conversely, if an axial force is applied to the end of the drill as shown in Fig. 4.7, this force shortens the drill thus causes it to ‘wind.’ Therefore, the

effects of the drilling torque and the axial force (thrust) on drill static stability partially compensate each other. This explains the results of observations. It is important to a drill designer/user to understand to what extent this compensation takes place and how the design parameters of a twist drill affect this compensation.

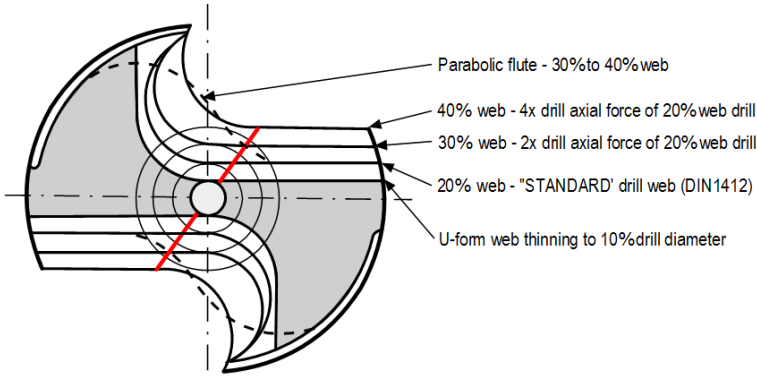


Fig. 4.11. Comparison of drill web cross sections

Narasimha et al. [4] proposed to assess torque/thrust coupling using the following coupling matrix:

$$\begin{Bmatrix} F_z \\ M_{dr} \end{Bmatrix} = \begin{bmatrix} K_{FF} & K_{MF} \\ K_{FM} & K_{MM} \end{bmatrix} \begin{Bmatrix} \epsilon_{td} \\ \theta_{td} \end{Bmatrix} \tag{4.6}$$

where  $K_{MM}$  is the axial stiffness under torsional restraint,  $K_{MF}$  is the torque-on-thrust coupling stiffness coefficient,  $K_{FM}$  is the thrust-on-torque coupling stiffness coefficient, and  $K_{FF}$  is the torsional stiffness under axial restraint.

Table 4.1 shows the values of the stiffness coefficients obtained experimentally [4]. Although unconventional, the units of the coefficient are meant for an easy quantitative comprehension of the results, i.e., the coupling effect.

The experimental results of several studies [4–6] reveal the following:

- The flute helix angle, flute profile, and web thickness significantly affect the axial and torsional stiffness of drills.
- The pure torsional stiffness of drills is maximized for a helix angle of around 28°. Departure from this angle to either side lowers this stiffness significantly (see Table 4.1).
- The torque-thrust interaction (measured by  $K_{FM}$  and  $K_{MF}$ ) has a distinct maximum at a helix angle of about 28°. As the same value of helix angle results in the largest increase in torsional stiffness, this explains a much higher allowable torque and axial force (thrust) for twist drills compared to straight-flute drills. This provides an explanation for the fact that general purpose drills are made with helix angles of a 28° to 30°.
- An increase in web thickness decreases the torque-thrust interaction, which means the benefit of the stiffening action of the axial force reduces.

**Table 4.1.** Stiffness coefficients

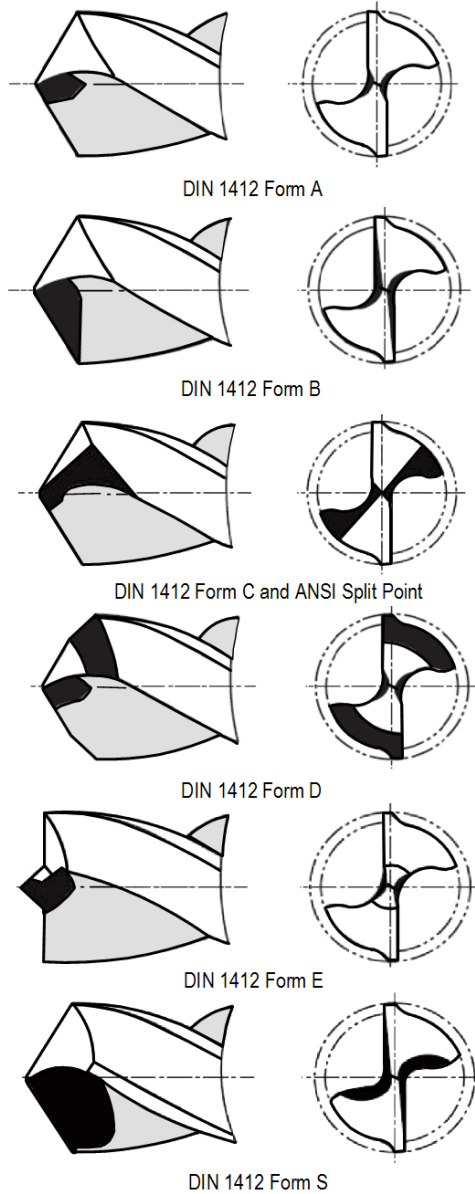
Drill dia (mm)	Helix angle (deg)	Web thickness (mm)	$K_{FF}$ (N)	$K_{MF}$ (Nm/rad)	$K_{FM}$ (Nm)	$K_{MM}$ (Nm <sup>2</sup> /rad)
12.7	32.76	1.905	$2.47 \times 10^6$	$1.91 \times 10^3$	$2.00 \times 10^3$	0.599
	51.42	1.905	$2.04 \times 10^6$	$1.68 \times 10^3$	$1.56 \times 10^3$	0.433
10.3	14.00	1.549	$2.22 \times 10^6$	514.2	658.4	0.131
	31.94	1.549	$2.41 \times 10^6$	$1.18 \times 10^3$	$1.42 \times 10^3$	0.229
	37.65	1.549	$1.88 \times 10^6$	978.8	1359.1	0.165
9.5	12.96	1.473	$2.09 \times 10^6$	437.9	535.0	0.100
	32.49	1.473	$2.47 \times 10^6$	959.9	$1.29 \times 10^3$	0.180
	36.80	1.473	$2.47 \times 10^6$	765.1	800.8	0.146
6.4	13.67	1.219	$2.47 \times 10^6$	185.9	151.7	0.019
	31.94	1.219	$2.47 \times 10^6$	399.5	321.6	0.038
	35.48	1.219	$2.47 \times 10^6$	339.7	187.8	0.032

## 4.6 Drill Point

### 4.6.1 Basic Classifications

Standard DIN 1412 defines the point grinds shown in Fig. 4.12. Type A point was initially intended for use on drills of over 20mm, to reduce the pressure on the web. Normally the chisel edge is thinned up to 8% of diameter. Nowadays, with CNC grinding machines, this becomes the most popular point for general applications. Type B point allows cutting edge runout correction and improving rake angle in the regions adjacent to the chisel edge. It was initially developed for brittle and difficult-to-machine work materials. Type C or widely-known Split Point was intended to use on drills with a heavy web to give better starting and thus producing more accurate holes. Type D is known as Cast Iron Point as its outer corners prevent frittering of the iron on breakthrough. Soon, it was found that this point grind is very useful for a wide variety of work materials, particularly when the exit burr is of concern (Fig. 3.30). Type E was developed for use on sheet metal. It was soon found that various modifications of this grind are also useful for many applications. Point S is normally used on parabolic flute drills.

Although this DIN classification gives initial ideas for available point grinds and it is used for many modern CNC multi-axis grinders, it does not compare drills in terms of the axial force that determines the penetration rate.



**Fig. 4.12.** Drill point grinds defined by DIN 1412 standard

#### 4.6.2 Tool Geometry Measures to Increase the Allowable Penetration Rate

There are four principle directions in increasing the allowable penetration rate, namely: (1) decreasing the axial force due to proper drill geometry, (2) increasing the torsional and buckling rigidities of the drill, (3) improving drill self-centering

ability, and (4) improving the shape of formed chips and their evacuation from the machining zone. Therefore, in the author's opinion, any drill design should be analyzed by its contribution to one (or more) of the listed direction. Such an approach significantly simplify any analysis of the drill design and geometry as it provides clear understanding of an improvement made by any new design compares to the known ones. In this section, some important known designs are analyzed using the proposed approach.

#### 4.6.2.1 *Decreasing the Axial Force*

This can be achieved by:

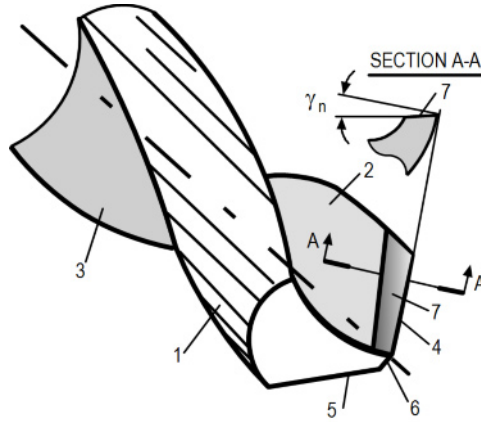
- Improving the tool rake geometry which normally decreases the total drilling force and thus the axial force as its part
- Decreasing the length of the chisel edge
- Improving the geometry of the chisel edge
- Eliminating the chisel edge

#### *Improving Tool Rake Geometry*

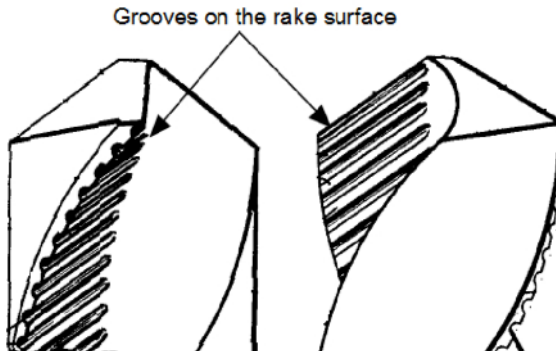
One of the inherent features of a common twist drill is variation of the tool geometry parameters over the major cutting edges (lips). It is further shown in this chapter that the normal rake angle on the lips of a conventional twist drill varies from up to  $30^\circ$  at the drill's periphery corner to  $-30^\circ$  in the region adjacent to the chisel edge. As a result, the cutting force and thus its axial component are great due to highly negative rake angles over a significant portion of the lip. To reduce the drilling torque and power as well as the axial (thrust) force, modifications to the rake face (or flute surface) just behind the cutting edge of the lips can be beneficial. Another obvious benefit that can be achieved at the same time is improved chip shape and breakability which both contribute to torque and thrust reduction.

The era of twist drill cutting edge modification began almost at the same time as wide use of these tools. Having solved the problem with chip transportation due to helical chip flute, twist drills brought another challenge to drilling which is high rake angle at the drill periphery while that close to the drill center is low. It was noticed that while a twist drill used for enlarging previously-drilled holes in relatively soft work materials, as brass, copper, Babbitt, the drill jumped ahead of the feed into the hole causing vibration, poor quality of drilled holes, drill breakage, etc. The reason for this is high rake angles in the regions adjacent to drill periphery (Sect. 3.5.4). The simplest solution for this problem was to provide a flat rake face along the cutting edge as shown in Fig. 4.13 (US Patent No. 452,896 (1891)).

As early as 1943, Stevens patented (US Patent No. 2,322,894, 1943) a drill with its rake face modified by a groove (Fig. 4.14) which, according to the inventor, improves cutting action thus reduces the cutting force. To simplify drill re-sharpening, the rake surface of the flute is made with a series of grooves so each successive re-sharpening shifts each cutting edge (lip) to the edge of the next available groove. The improved tool life and reduced thrust are attributed to lower chip deformation and better chip breaking. This invention, however, was much ahead of its time so it was not used in practice.



**Fig. 4.13.** Twist drill geometry according to US Patent No. 452,896 (1891)



**Fig. 4.14.** Twist drill with the grooved rake surface

The modification of the drill rake face by providing it with a groove adjacent to the cutting edge was attempted by Mackey (US Patent No. 3,199,381 (1965)). The patented drill shown in Fig. 4.15 consists of a shank 1 (drill body) provided with spiral flute(s) 2. A tip 3 made of tool material (carbide, ceramic, etc.) is affixed to the forward end of the shank 1 by brazing. The tip 3 is provided with a pair of major cutting edges (lips) 4 and 5 connected by the chisel edge 6. Grooves 7 and 8 are provided on opposite faces of the tip adjacent to and parallel with cutting edges 4 and 5. As claimed by the author, the grooves enhance the cutting action particularly important in drilling difficult-to-machine materials, by reducing the required power and by providing broken chips. Such a design was widely used in the 1960s when drills with the brazed carbide tip became popular. Nowadays, the same design is common for spade-drill cutting inserts as shown in Fig. 4.16.



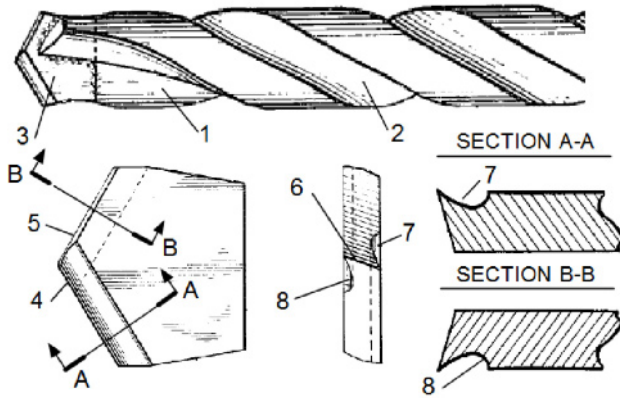


Fig. 4.15. Twist drill with a grooved insert



Fig. 4.16. Typical cutting insert used in spade drills

To solve the problem with cutting edge chipping in drilling titanium and other difficult-to-machine alloys, Ackart and Barish develop a drill with a rake face modified in the manner shown in Fig. 4.17 (US Patent No. 3,387,511 (1966)). According to this design, the cutting lip 1 is divided into two sections, a primary section 2 towards the margin, and a secondary section 3 towards the center. These two sections are of approximately the same length. They are ground with slightly different location angles – the primary lip is ground with location angle  $115\text{--}125^\circ$  while the secondary – with  $125\text{--}135^\circ$  as show in Fig. 4.17. The secondary section 3 is provided with the T-hand-S rake angle of  $4\text{--}6^\circ$  while the primary section is provided with the T-hand-S rake angle of  $12\text{--}16^\circ$ . As the secondary section passes the intersection with the chisel edge 4, and a third section 5 is formed behind the chisel edge. This third section provides relief to the hill to eliminate heeling and a path for MWF (coolant) to the chisel edge.

The values of the location and rake angles are found experimentally with no rationale to justify these values. The analysis of the rake geometry also presented in this chapter shows that such geometry provides a more uniform distribution of the rake angles along the entire cutting lip while keeping sufficient strength of the cutting wedge in the region adjacent to the drill periphery.

A similar solution to improve the geometry of the outer part of the cutting edge with the same objective according to US Patent No. 6,315,504 (2001) is shown in Fig. 4.18. It consists of a drill body 1, tip 2, and a pair of chip flutes 3 and 4 made in this body. Chisel edges 5 and 6 are formed on the tip end of the drill body, and two major edges 7 and 8 extend from each outer end of the chisel edges. Two outer cutting edges 9 and 10 extend from each outer end of the major cutting edges to the drill corners. These are inclined at angle  $\psi_{out}$  as shown in Fig. 4.18.

The plane rake faced (PRF) twist drill point geometry design shown in Fig. 4.19 developed by Armarego and Cheng [7] has been shown to yield positive normal rake angle on the entire lips while the chisel edge is point relieved. The cutting mechanics analysis and experimental studies have confirmed the

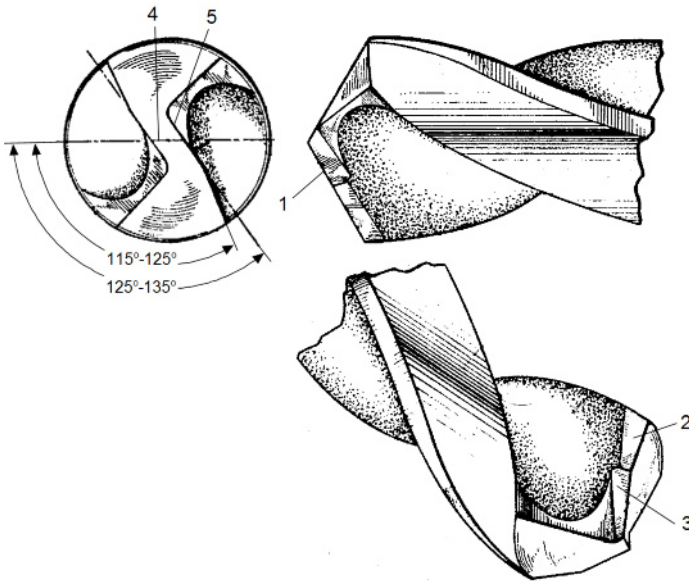


Fig. 4.17. Drill geometry according to US Patent No. 3,387,511 (1966)

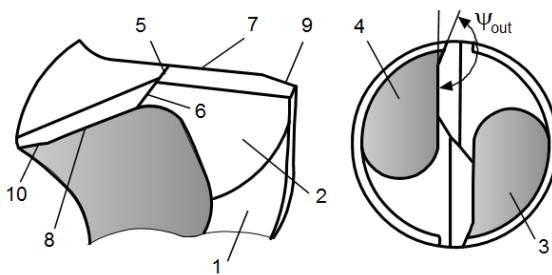
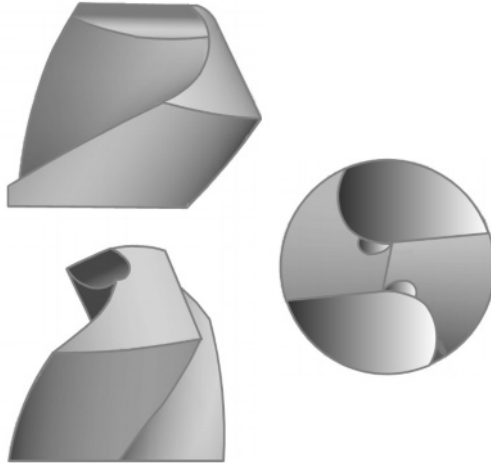


Fig. 4.18. Drill geometry according to US Patent No. 6,315,504 (2001)

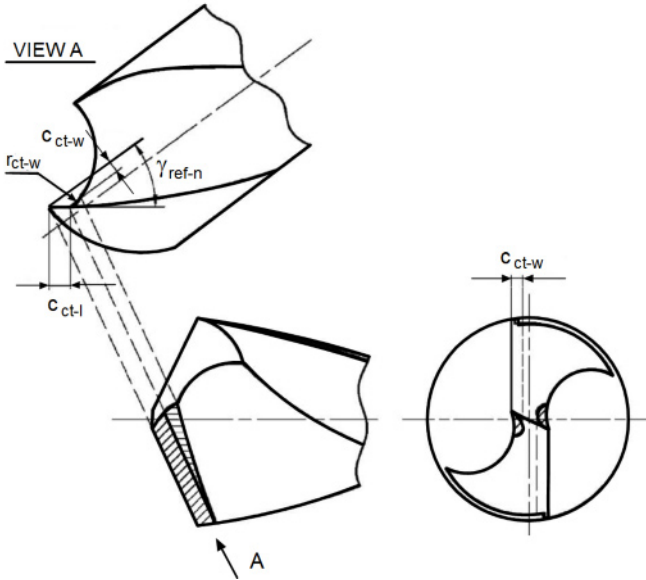
superiority of this drill point design over conventional twist drills with significant reduction in the axial force (thrust) and drilling torque and an increase in tool life for both aluminum alloys and difficult-to-machine materials [8, 9].



**Fig. 4.19.** Plane rake faced twist drill point design

An analysis of such modification has been presented by Wang and Zhang [9]. One such modification to the general purpose drills was attempted by grinding a plane rake face about each lip using a narrow disc shaped grinding wheel [7]. The essence of the geometry of the PRF drill point design is shown in Fig. 4.20. As can be seen, to achieve such geometry, a conventional twist drill is modified by grinding a plane rake face about each lip using a disk shaped grinding wheel. According to the proposed geometry, a constant reference rake angle  $\gamma_{\text{ref-n}}$  (the T-hand-S normal rake angle) is applied along each lip without changing the lips. According to Wang and Zhang [9], to achieve best performance, three geometry parameters of PRF drill should be selected as:

- Depth  $c_{ct-w}$  should be equal to 20% of the web thickness.
- Size  $c_{ct-l}$  for drill diameters of 5–30mm is determined as  $c_{ct-l} = 0.04267d_{dr} + 0.00364f + 0.00970$  (mm) where  $d_{dr}$  is the drill diameter (mm) and  $f$  is the cutting feed (mm/rev).
- Corner radius  $r_{ct-w}$  is to be determined experimentally for the best drill performance. Tool large a corner radius may reduce the drill strength, while too small  $r_{ct-w}$  may cause sudden change in chip flow direction and thus may trap the formed chip from flowing smoothly into the flutes. A corner radius around 1mm is considered reasonable for 7– to 13–mm drills.



**Fig. 4.20.** Plane rake faced drill point geometry

The reference rake angle at each lip has been selected to be equal to the reference rake angle at the outer corner of each lip and remains constant along each lip, such that the normal rake angle will remain positive along the whole lip although its value decreases as the radius decreases. Furthermore, in grinding the plane rake face, the chisel edge is “point relieved” where each flank in the vicinity of the chisel edge corner is affected by the grinding wheel.

An experimental study [15,16] on drilling an aluminum alloy showed that the reductions in the thrust forces and torque were about 50% and 15%, respectively. From the above analysis, the modified plane rake faced drill design is clearly very promising in reducing the thrust force, torque, and power in drilling. It is most desirable to use such a drill design in drilling difficult-to-machine materials such as mold steels for the manufacturing of molds for injection molded plastic part production where a large number of holes need to be produced and drilling cost and drill breakage inside a mold are important concerns for the tooling industry [17].

#### *Decreasing the Length of the Chisel Edge*

One of the most common ways to reduce the length of the chisel edge is so-called web thinning. There are several variations of web thinning such as that defined by DIN Standard 1412 Form A and Form B (Fig. 4.12). According to Form A, the chisel edge is thinned by grinding two notches at the ends of the chisel edge adjacent to the lips (Fig. 4.21).

To simplify grinding, a drill can be provided with a built-in notch according to US Patent No. 4,756,650 (1988) as shown in Fig. 4.22. According to this geometry, the standard cross-sectional profile 1 is altered by providing a subflute 2 having a U-shaped cross section (as viewed in the enlarged cross-sectional VIEW A-A)

which is formed in the central portion of the hill along the main flute 3 in a predetermined axial range from the tip of twist drill. As a result, the cross-sectional area of the flute is increased. Because the subflute 1 is formed in the top of the drill, the size of the chisel edge 4 is reduced that obviates so-called walking and the thrust is reduced. Chips broken by the chisel edge are removed through the subflutes and the main flutes. The experimental results presented by the inventors show that in drilling a medium carbon steel (0.5%C, HB 220-240) with the proposed tool, the axial force (thrust) is reduced (by 50% at feed of 0.2mm/rev and by 250% at feed of 0.5mm/rev) up to four times, the diametric accuracy increases three times and the tool life increases up to six times compare to a standard twist drill.

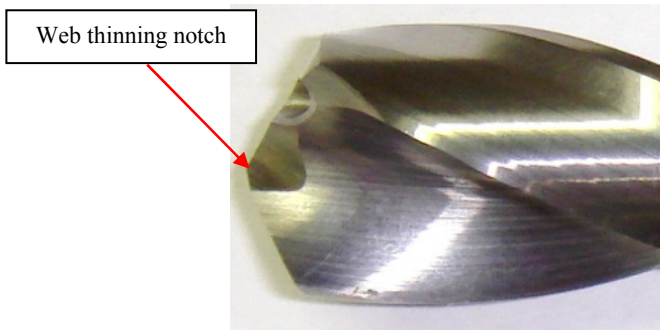


Fig. 4.21. Web thinning by notches

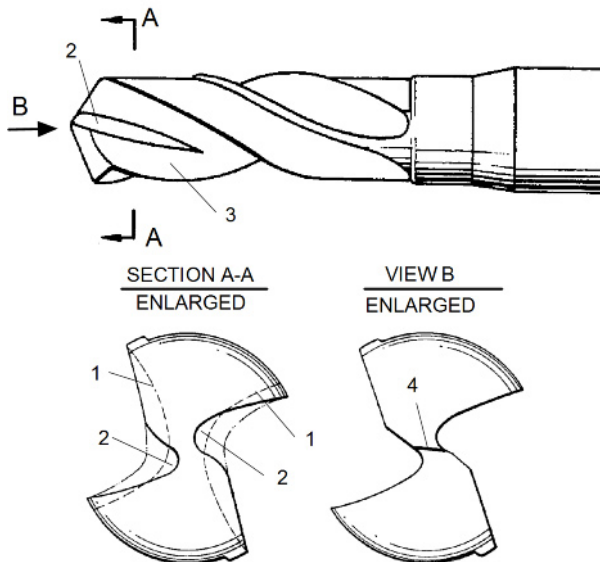
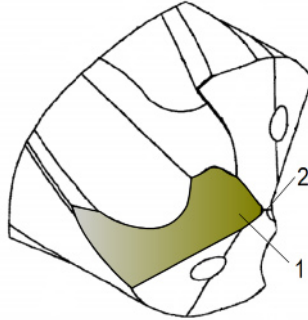


Fig. 4.22. Drill geometry according to US Patent No. 4,756,650 (1988)

The disadvantage of this geometry is that the web thinning notch can be provided only with zero or negative rake angle. A notch with positive rake angle is proposed in US Patent No. 6,676,342 (2004) as shown in Fig. 4.23. According to this patent, a notch 1 is ground with positive T-hand-S rake angle to reduce the length of the chisel edge 2. Although such geometry improves cutting conditions and thus allows higher penetration rate, the notch should be reapplied every time the drill is re-sharpened.



**Fig. 4.23.** Drill geometry according to US Patent No. 6,676,342 (2004)

A much more intelligent way of web thinning is by providing gashes that divide the lips into two logical parts as according to US Patent 2,939,658 (1960). Such geometry is shown in Fig. 4.24. As seen, each major cutting edge is divided into two parts, namely: (1) the outer part 1 that extends from the drill's periphery point to a certain radius  $r_{tn}$  and, (2) the inner part 2 (called the gash) that connect the end of the outer part and the end of the chisel edge 3. Although the outer part can be located at certain angle  $\psi_{out}$  to the drill transverse axis as shown in Fig. 4.24 and this might be needed for better separation of the chip flow into two, it is really used so that commonly  $\psi_{out} = 0$ . The distinctive feature of this design is the inclination of the inner part 2 at angle  $\psi_{in}$  which depends on the radius  $r_{tn}$  and the intended value of the web thinning. The latter is normally is in the range of 8–12% [10] and  $r_{tn}$  is equal to  $d_{dr}/4$ . The thinning or gashing may extend over the entire length of the lip. Moreover, the rake face 4 created due to web thinning may have positive normal rake angle (in the T-hand-S) in the range of 4–6° that further improves chip formation and reduces drilling force and torque. Figure 4.25 shows an example of web thinning applied to a twist drill for optimum performance in stainless steels and high-temperature alloys.

A comparison of the notched and gashed web thinning shows that the latter is much more effective even though the length of the chisel edge is the same. This fact will be explained later in this chapter in the analysis of the tool geometry. However, in the author's experience, two common flaws often reduce or even nullify the advantages of web thinning. The first one is the non-symmetrical grind of the gashes that disturb drill force balance. This sets the drill out of center and thus reduces its life and the quality of the machined surfaces. The second is the poor surface finish of the rake face (the gashes) shown in Fig. 4.26 even when CNC grinding machines are used.

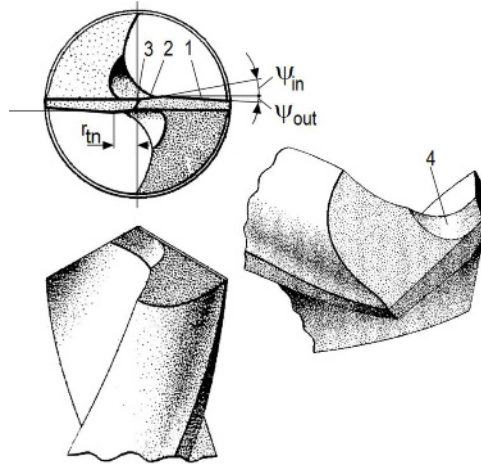


Fig. 4.24. Drill geometry according to US Patent 2,939,658 (1960)



Fig. 4.25. Mapal MEGA-Drill-Inox

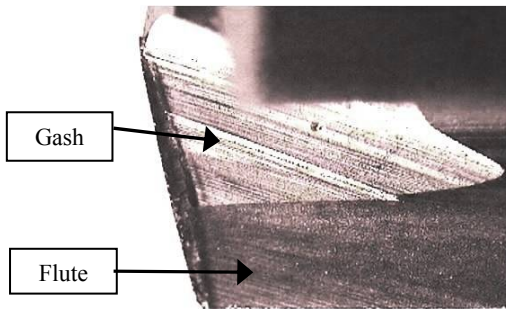


Fig. 4.26. Showing the difference in surface finish on the flute and the gash

*Improving the Geometry of the Chisel Edge*

The standard drill nomenclature always presents the chisel edge as a single design component of a drill as shown in Fig. 4.1. In reality it is not so, as if the chisel edge passes through the axis of rotation, then there are two chisel edges – each one starts from the inner end of the major cutting edges (lips) and extend to the center of rotation. Therefore, the tool geometry definitions discussed in Chap. 2 are fully applicable to these two parts of the chisel edge, i.e., each part has the rake and flank faces.

As discussed in Sect. 4.5.3, the chisel edge is responsible for up to 60% of the total value of this force. Although a common perception is that the prime cause is low cutting speeds along the chisel edge that diminish to zero at the drill axis, in reality it is not quite so. It will be discussed later in this chapter that highly-negative rake angles on both parts of the chisel edge cause excessive deformation of the metal being removed in its transformation into the chip while flank angles are high and do not present any problems in drilling. Therefore, increasing the rake angle while keeping sufficient strength of the drill tip is what should be understood to improve the geometry of the chisel edge.

There are two principle directions in increasing the rake angle:

- Extensive when an improvement in the rake angle of the chisel edge is achieved by applying a suitable shape of the tool flank that may simultaneously results in proper distribution of the flank angle along the lip. The top of this direction is multiple variations of the so-called S-shaped chisel edge.
- Intensive when the rake angle of the chisel edge is altered directly. The top of this direction is multiple known variations of the so-called split point grind.

Historically, the extensive direction was developed first. As early as 1923, Oliver patented (US Patent No. 1,467,491 (1923)) a very distinctive drill with a split point shown in Fig. 4.27. The drill has two major cutting edges, 1 and 2 and two chisel edges 3 and 4. The rake faces of these edges are provided with two depressions 5 and 6. As a result, the rake face 7 obtains the rake angle which can be varied according to the particular work material.

As claimed in the patent description, such geometry allows at least 50% higher penetration rate compared to a drill with standard geometry. Moreover, an increase in tool life and improved chip removal are also observed.

A special drill point design with split-point geometry shown in Fig. 4.28 was developed by Hallden (US Patent No. 2,334,089 (1939)). Each major cutting edge of this drill has two portions, namely, the outer 1 and the inner 2 cutting edges and corresponding flank surfaces 3 and 4. Flank surface 4 is shaped as an invert conical surface as seen in Fig. 4.28. Rake face 5 of the region of inner cutting edge 2 adjacent to the drill center is formed by providing (grinding) gash 6.

There are a number of advantages of the proposed design not realized by the inventor and apparently by the subsequent specialists who did not notice such a great advance in the design of drills:



- Because the cutting edges locate on the axis of the drill, there are no variations of the rake and flank angles along these edges over the drill radius as in traditional drill design.
- While drilling, inner cutting edge 2 (with other inner cutting edges of the drill) forms a conical surface on the drill bottom which definitely stabilizes the drill, preventing its wandering and thus improving drilling stability and quality of the hole being drilled. As such, however, additional supporting lands 7 and 8 shown in the patent would interfere with drill stability as any redundant supports in mechanical systems.

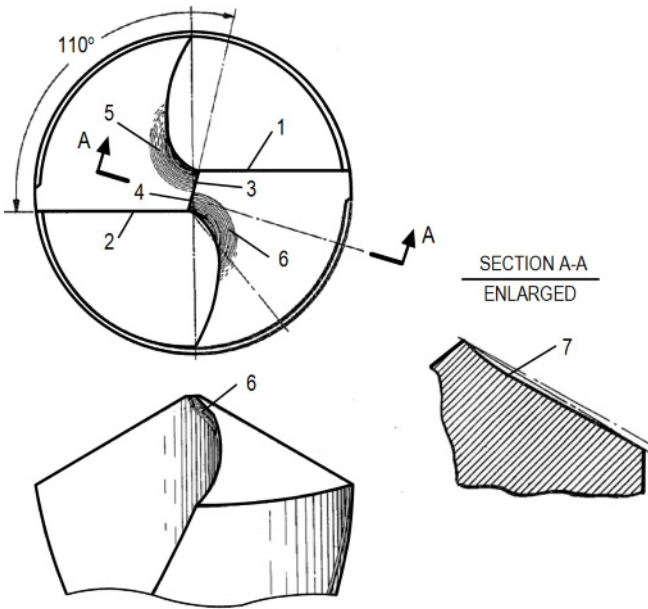


Fig. 4.27. Drill geometry according to US Patent No. 1,467,491 (1923)

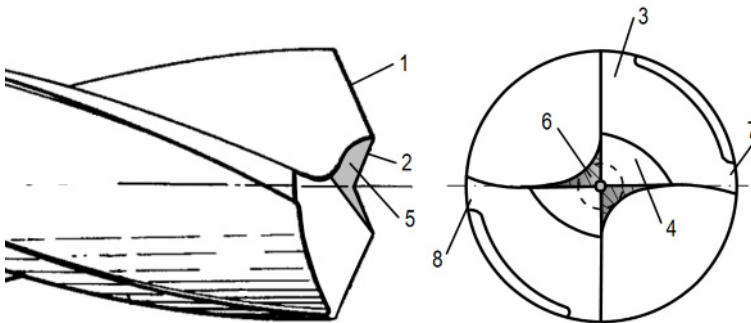
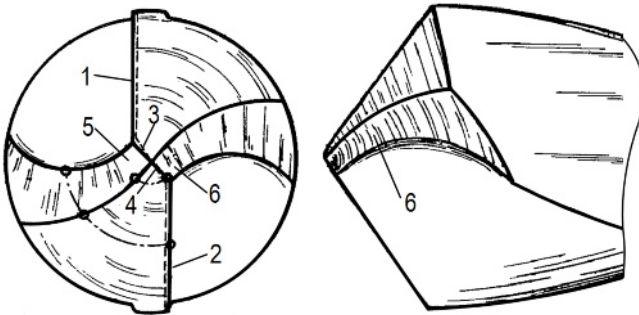
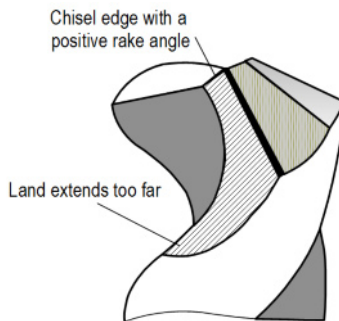


Fig. 4.28. Drill geometry according to US Patent No. 2,334,089 (1939)

The further development of the drill geometry shown in Fig. 4.27 is shown in Fig. 4.29. This drill has two major cutting edges 1 and 2 and two chisel edges 3 and 4. Instead of relatively shallow depressions, the chisel edges are provided with fully developed lands 5 and 6 that extend to the hills that improve the geometry of the chisel edges and provide better conditions for the removal of the chip formed by the chisel edge. The disadvantage of this geometry is that lands 5 and 6 should be ground too far back to achieve the desired geometry of the twist drill as shown in Fig. 4.30. This weakens the drill tip and worsens conditions of internal MWF supply and chip removal.

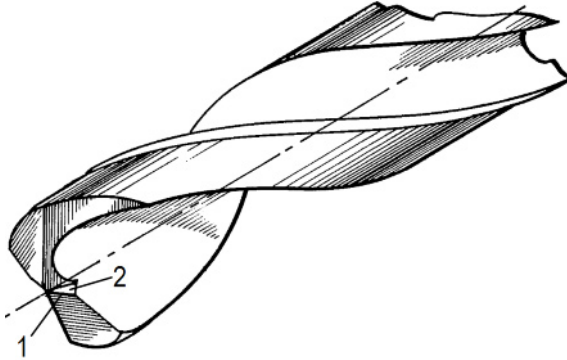


**Fig. 4.29.** Drill geometry according to US Patent No. 3,564,947 (1964)



**Fig. 4.30.** Land that forms the rake face of the chisel edge

The latter problem can be solved if the tip geometry offered by US Patents No. 4,556,347 (1985) and 4,898,503 (1990) is used. Such geometry is shown in Fig. 4.31. According to these patents, the chisel edge 1 is provided with the rake face (notch) 2 having a rake angle of between  $5^\circ$  and  $10^\circ$  while the angle of the notch to the drill axis is selected to be between  $32^\circ$  and  $38^\circ$ . As claimed by US Patents No. 4,556,347 (1985), comparison of a drill with a commercially available precision twist drill conforming to NAS 907 standard showed significant improvement in tool life when drilling difficult to machine materials. For example, a 5.8 times increase in tool life was achieved in drilling Inconel 718 of 44 HRC.



**Fig. 4.31.** Drill geometry according to US Patents No. 4,556,347 (1985) and 4,898,503 (1990)

The best application results with the discussed split point geometries are achieved when the rake angles of the chisel edge are selected properly, the rake faces of the chisel edges are ground symmetrically, the proper carbide grade combined with rigid systems and internal MWF supply are used. Figure 4.32 shows WSTAR solid carbide drills for machining of aluminum developed and manufactured by Mitsubishi Materials Corporation.



**Fig. 4.32.** WSTAR drill by Mitsubishi Materials Corporation

Although modern machines, tool holders, tool materials, and many other components of the drilling system as well as CNC drill re-sharpening practice fully support various split point geometries, historically it was not always so. To deal with a reduced strength of the drill tip when using split point geometries, partial split geometries were developed. The essence of these geometries is that not the entire length of each chisel edge is provided with the rake face having neutral or positive rake angle (in the T-hand-S), but rather just part.

Figure 4.33 shows a drill with the simplest partial split geometry. As can be seen the drill has two major cutting edges 1 and 2 and the chisel edge 3. Two pits 4

and 5 are ground as shown to provide rake faces to the corresponding parts of the chisel edge. Angle  $\tau_{pt}$  is adjusted to provide the intended rake angle to the parts of the chisel edge and facilitate chip removal [11].

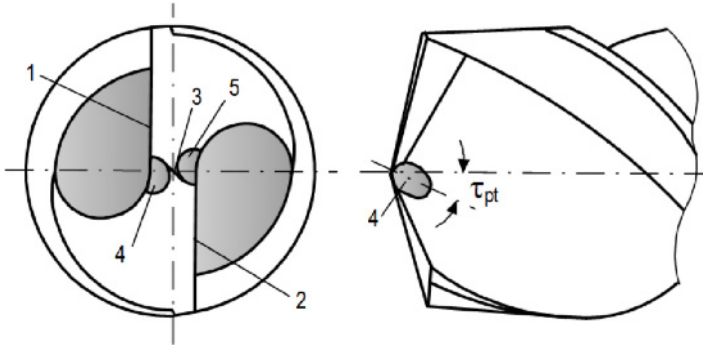


Fig. 4.33. Drill geometry according to US Patent No. 5,590,987 (1997)

Figure 4.34 shows a drill with another version of the partially split point geometry. As can be seen, the drill has two major cutting edges 1 and 2 and two chisel edges  $a\theta$  and  $d\theta$ . Two U-shaped grooves 3 and 4 provide partial splits  $ab$  and  $cd$  of the chisel edge. Each groove has a dedicated flute 5 to transport the chip. The sharp corners  $a$  and  $d$  can be chamfered or provided with radii, giving an ‘S’ shape to the chisel edge. This geometry and design resembles those shown in Fig. 4.22.

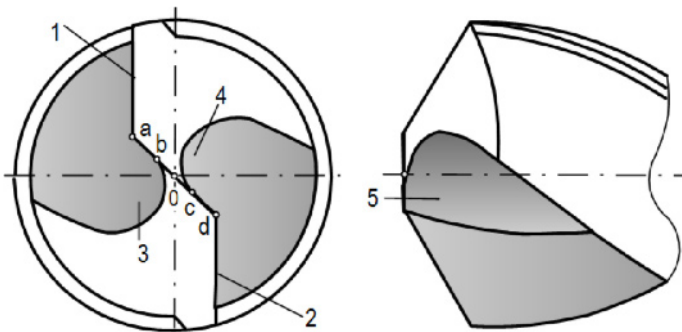
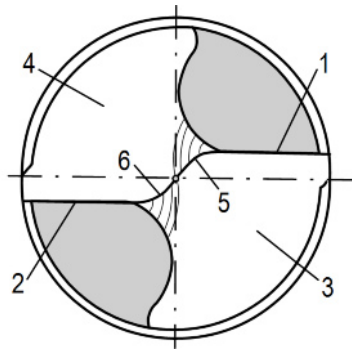


Fig. 4.34. Drill geometry according to US Patent No. 4,688,972 (1987)

Even though the achievable reduction of the axial force (the thrust) and thus allowable penetration rate when using drills having various partial split geometries are lower than those with drills having split geometries, these drills are still in use today because a lot of old machines, ancient tool holders, and obsolete tool materials are used in many shops.

Helical grind of the drill flank surface was considered an effective improvement and valuable alternative to the widely used conical flanks. Helical grind is applied by simultaneous rotation and translation of the drill blank. As a result, drill flanks are generated to complex helical surfaces. As the helical angle

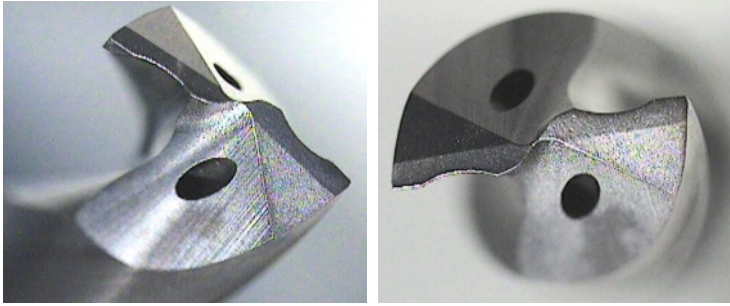
increases while approaching the chisel edge, more preferable rake angles of the chisel edges are achieved. Under certain combinations of parameters of rotation and translation motions, the chisel edge becomes 'S' shaped as shown in Fig. 4.35. This figure shows a drill having two major cutting edges 1 and 2 and helically ground flank surfaces 3 and 4. Two chisel edges 5 and 6 are provided with the rake angles that are much greater than those found in a conventional twist drill. Properly designed and applied S-shaped chisels provide a continuous cutting edge that starts at the center of the drill and blends with the cutting lip so the drill point cuts along the entire length of its cutting edge. Such geometry provides an increased rake angle along the chisel edge that allows drilling feed rates increasing by 10% to 20%, improving chip formation and force distribution (even tool wear) over the cutting edge.



**Fig. 4.35.** 'S' shaped chisel edge

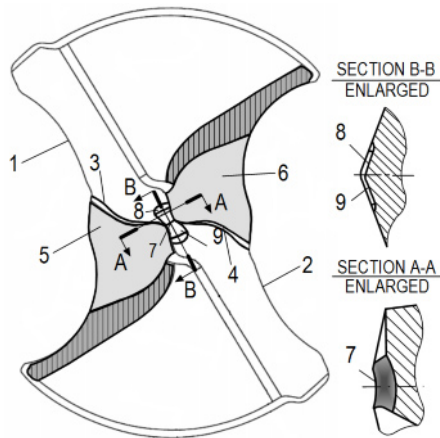
The obvious disadvantages of the increased length of the chisel edge is restricted self centering. Another disadvantage is that in improving the rake angle of the chisel edges, the 'S' shaped helical grind decreases the strength of the region adjacent to the chisel edge because the flank angles of the chisel edge are also increased thus the wedge angle of the chisel edge becomes smaller. This is favorable for self centering ability but not favorable for high feed rates since it weakens the drill point. US Patent No. 4,826,368 (1987) offers a possible solution by modifying motions of the grinding wheel. Although the proposed solution is reasonable and feasible, a re-sharpening of such a drill should be carried out only on a CNC sharpener that has such a modified program.

There are a number of improvements made to the discussed 'S' chisel edge which became known as "S' helical relieved point grind or just 'S' point grind. These improvements aimed to increase the allowable penetration rate and are related mainly to improvements in the geometry of the chisel edge and to improvements in chip shape and its transportation over the flutes. Although 'S' shaped helical grind nowadays is often combined with the split geometry as shown in Fig. 4.36, such a combination does not possess the advantages either of the 'S' helical or split geometries.



**Fig. 4.36.** ‘S’ shaped grind combined with split geometry

Figure 4.37 shows a drill design according to US Patent No. 6,071,046 (2000) that combines several above-described modifications to the chisel edge geometry. It has an “S” helical relived point grind, partial split geometry, and the further modification of the remaining sections of the chisel edge. The drill has two major cutting edges 1 and 2, two portions 3 and 4 of the chisel edge provided with the rake surfaces 5 and 6. The remaining part 7 of this chisel edge having a concave shape is provided with recesses 8 and 9 formed in the front flank faces, each recess providing one chisel edge cutting section with the rake surface and the other with the flank surface. The portion of each recess which constitutes the rake surface merges with an adjacent web-thinning recess surface. Thereby, improved chip evacuation from the major cutting edges and, particularly, from the chisel edge cutting section may be effectively obtained as claimed by the patent. Self-centering ability is another advantage of this geometry. A complicated point grind and its metrology as well as sensitivity to the drill runout (sets the middle of the chisel edge out of the center of rotation) are shortcomings of this geometry.

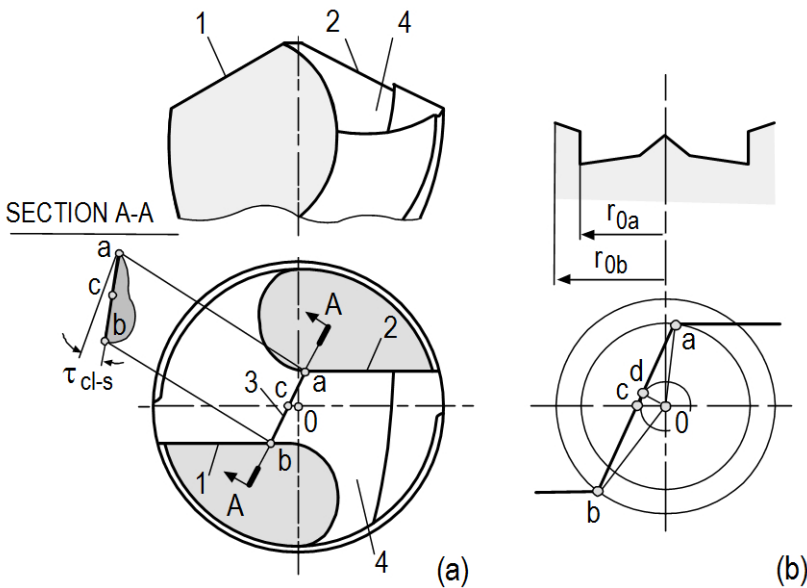


**Fig. 4.37.** Drill design according to US Patent No. 6,071,046 (2000)

So far, the traditional methods of improving chisel edge geometry have been considered. These methods originate from the conventional wisdom that a drill

must have two (or more) major cutting edges (lips) connected by the chisel edge passing through the theoretical axis of rotation. This perception is based on an incorrect notion of the force balance in drilling (Chap. 3, Sect. 4.3.1) can only be achieved through geometrical similarity of the major cutting edge and parts of the chisel edge. To assure this similarity, the chisel edge must cross the axis of rotation. Although this perception is correct, it is not the only possibility to achieve the force balance in drilling. In the author's opinion, once scientific and engineering communities realize this simple rule, entirely new designs and geometries of drills will appear that fully utilize the capability of multi-axis CNC drill grinders.

As an example, consider the geometry of a drill with a non-central chisel edge developed, studied, and successfully implemented by Vinogradov [12] which can be referred to as the Vinogradov's drill with shifter chisel edge or *VDSCE*. The basic geometry of *VDSCE* is shown in Fig. 4.38a. As can be seen, the drill has two major cutting edges 1 and 2 and the chisel edge 3. This chisel edge is shifted by distance  $0c$  from the axis of rotation 0 by grinding an additional flank surface 4 adjacent to the inner part of the major cutting edge 2. This additional surface alters the cutting edge 2 in such a way that the drill force balance disturbed by the shift of the chisel edge is restored.



**Fig. 4.38.** Vinogradov's drill with shifter chisel edge (VDSCE)

The results of multiple tests and implementation practice proved that the drill geometry shown in Fig. 4.38a has the following advantages:

- No one point of the chisel edge has zero cutting speed, i.e., cutting instead of indentation as is the case in traditional drills.

- Self-centering ability without compromising the strength of the drill tip that important in machining difficult-to-machine heat treated work materials. This self-centering ability is explained in SECTION A–A in Fig. 4.38a,b. As can be seen, the point  $a$  of the chisel edge is the first point of the drill that touches the workpiece due to angle  $\tau_{cl-s}$  which is formed as a result of the discussed shift. As shown in Fig. 4.38b, the chisel edge forms the complicated shape of the bottom of the hole being drilled with stabilizing cylinder of  $r_{0a}$  radius and conical surface having the radius of the base equal to distance  $0d$ .
- Positive rake angles (higher than normally achieved even with the best split point geometry) over the chisel edge with the maximum at point  $d$  that reduce the cutting force and drilling torque.
- Extremely high inclination angles over the chisel edge with the maximum of  $90^\circ$  at point  $d$ . Because the BUE does not form under any cutting conditions when the cutting edge inclination angle is high, the stability of drilling, quality of machined holes, and tool life of  $VDSCE$  are much superior over the known drill point geometries.

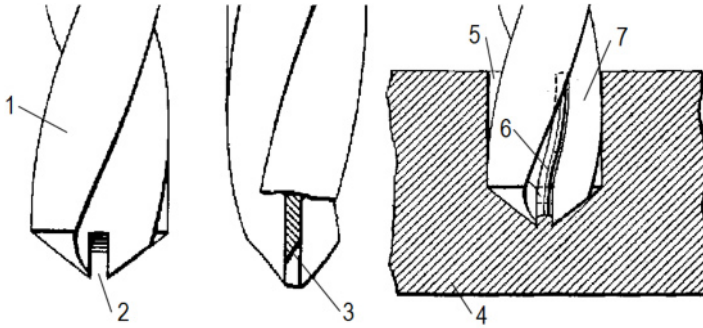
Naturally, many particular design and drill geometries can be developed using the idea of shifting the chisel edge from the drill axis. However, knowledge of tool geometry, particularly T-use-S geometry combined with mechanics and tribology of metal cutting is a prerequisite for such development.

#### *Eliminating the Chisel Edge*

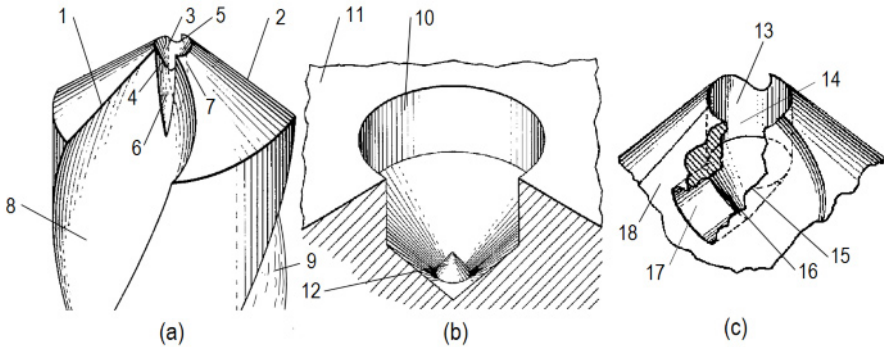
The problems created by the chisel edge were always at the center of attention in drill design [13]. The most radical solution to these problems is the total elimination of this edge from the drill point design. As early as 1911, Mather patented a drill with no chisel edge (US Patent No. 989,379 (1911)). In the proposed drill shown in Fig. 4.39, a common twist drill 1 is provided at the apex of the web with the slot 2. This slot having a width equal to the web diameter extends upward into the drill body and terminates at the upper end in the inclined surface 3. When drill 1 penetrates into the workpiece 4 drilling hole 5, core 6 forms. This core either breaks due to bending when its front end comes into contact with inclined surface 7 or, when the work material is ductile, bends into the chip flute 7 and thus is removed at the end of drilling.

The next basic solution of the chisel edge problems shown in Fig. 4.40a is described in US Patent No. 3,028,773 (1962). As seen, a drill has two major cutting edges 1 and 2. Conical surface 3 is formed instead of the chisel edge. This surface 3 has cutting edges 4 and 5 and two secondary flutes 6 and 7 which communicate with the flutes 8 and 9 of the major cutting edges 1 and 2. When such a drill works, i.e., drills a hole 10 in workpiece 11, protuberance 12 of conical shape is formed by the cutting edges 4 and 5. As claimed by the inventor, protuberance 12 acts as a journal for the drill as it progresses through the workpiece. This journal and bearing arrangement supports the drill at a point adjacent to the drill center, thereby assuring that the hole being drilled and the drill remain concentric.





**Fig. 4.39.** Drill design according to US Patent No. 989,379 (1911)



**Fig. 4.40.** Drill design according to US Patent No. 3,028,773 (1962)

Figure 4.40c shows a portion of another embodiment of the twist drill shown in Fig. 4.40a. As can be seen, the opening 13, concentric with the drill axis, comprises a cylindrical portion 14 and conical portion 15. According to the patent, the major portion of the bearing load is sustained by surface 14. Cutting edge 16, which maintains the maximum length of the protuberance, acts along conical surface 15 which has hole 17. Hole 17 is in communication with the front part 18 of flute 8.

Although the idea of self-support of the discussed drill in the central is valuable and can be successfully implemented, obvious drawbacks of the proposed design and geometry should be noted:

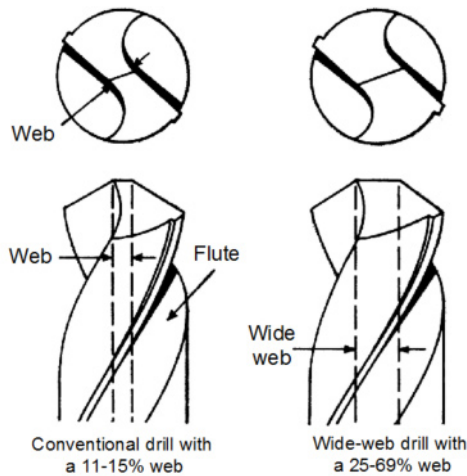
- It is rather difficult to grind the proposed drill, as a specially designed and dressed grinding wheel together with grinding fixture and metrological equipment are needed. Re-sharpening of this drill presents an even greater challenge.
- The internal cutting edges, e.g., 4 and 5, actually shave the work material so that they should be made sharp to perform the shaving action. Smallest BUE due to low speed and high contact pressure can easily disable these edges.

- The bending of the protuberance into hole 17 may actually disturb rather than improve self-support.

The subsequent developments, for example, described in US Patents No. 4,143,723 (1979), 4,342,368 (1982), and well summarised in US Patent No. 4,373,839 (1983) did not offer new ideas. Rather, various design applications of the ideas described above, particular to various drill configurations, were attempted.

#### 4.6.2.2 Increase the Torsional and Buckling Rigidities of the Drill

The drill penetration rate can be increased if the drill can withstand the corresponding increase in the axial force and drilling torque, i.e., if its buckling and torsional rigidities are high enough to bear these loads. The so-called wide-web drills are more rigid and stronger than conventional drills thus higher penetration rates (up to 20%), greater length-to-diameter ratios, and better accuracy of machined holes are achieved with these drills. These drills are normally used to produce holes in difficult-to-machine and heat treated work materials. Figure 4.41 shows the comparison of a conventional and a wide-web drill. Naturally, all the methods described above for the chisel edge modification such as, for example, web thinning, split point, or even special shape of the cutting edges [14], are used for these drills.



**Fig. 4.41** Conventional and wide-web drills

There has been, however, a significant drawback to wide-web drills in the reduced cross-sectional area of the chip flutes. However, the penetration rate in drilling of difficult-to-machine and heat treated work materials is rather low that results in much smaller amounts of chip produced that needed to be transported from the machining zone through these flutes.

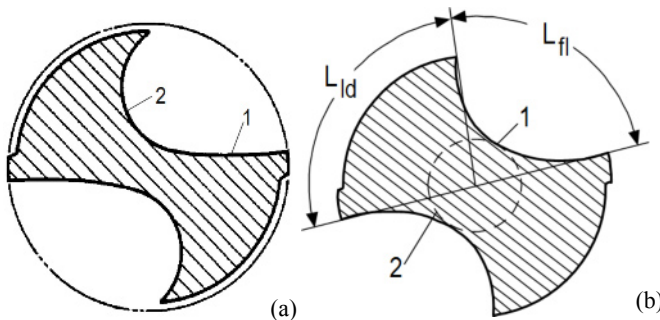
Another feasible way to increase drill rigidity is to optimize the cross-sectional profile (area, polar moment of inertia, and other cross-sectional characteristics) of the drill shank. Besides increasing drill rigidity, this optimization also aims to

improve chip transportation in the flutes. The profile of a drill should be designed in such a way that the flutes provide the maximum space for the chip and facilitate chip removal while ensuring that the drill is capable to withstand adequately the drilling torque and axial force. These are two major requirements.

The known theoretical and numerical studies on the matter [15–17] are of little help as they: (1) do not consider thrust-torque coupling (Sect. 4.5.4) which is actually one of the major advantage and reserves in increasing the drill penetration rate, (2) do not consider particular drill geometry and thus cutting force distribution over the drill diameter, and (3) do not include the formed chip in terms of the additional force imposed by the chip, its breakability and transportation conditions over the flute.

Figure 4.42a shows a profile of a standard twist drill. As seen, the flute has two distinctive parts, namely the so-called straight part 1 which in its intersection with the flank surface forms the major cutting edge (lip) and concavely-curved surface 2 having a relatively large radius of curvature. Figure 4.42b shows the flute profile 1 of a wide web drill. As the diameter of web 3 is great, the profile 4 is normally made as a single curve to enhance drill rigidity.

According to US Patents No. 4,744,705 (1988) and 5,230,593 (1993), the profile of a drill made of high speed steel (HSS) and that made of a sintered carbide are not the same, particularly for heavy-duty drilling operations. The profile is usually characterized by the so-called flute-width ratio (FWR) which is the ratio of ark length  $L_{fl}$  of the flute to ark length  $L_{ld}$  of the lend (Fig. 4.42b). For HSS drills having a profile shown in Fig. 4.42a, FWR is 0.7 at the forward end of the drill. To increase drill rigidity, FWR can be equal to 1.16 away from the forward end. For carbide drills, FWR is in the range of 0.4–0.8.



**Fig. 4.42.** Profile of the standard drill (a) and that of a wide-web drill (b)

Figure 4.43 shows the relationships between the drill torsional rigidity and web thickness ratio for two different FWR according to the data presented in US Patent No. 4,583,888 (1988). According to this patent, simply increasing the web thickness ratio and decreasing FWR increases the cutting resistance and makes the chip injection difficult. Thus, the web thickness ratio and FWR have their limits; generally, the web thickness ratio is set in the range 15–23% and FWR is in the range of 1.0–0.76.

The quest for a better shape of a chip flute and thus for more rigid profile of the drill body started a long time ago. As early as 1882, Hartshorn had proposed a profile (US Patent No. 262,588 (1882)) shown in Fig. 4.44 which became popular over a century later. This drill has a drill body 1 and two straight or helical flutes 1 and 2 situated opposite to each other (Fig. 4.44a. As seen in Fig. 4.44b, the side of each flute gives the cutting edge a convex curvature along its entire length, so that when the forward end of the drill is ground away to form the point by providing the flank surfaces 4 and 5, the corresponding lips or the major cutting edges 6 and 7 (which form as the intersection lines between the flutes and the flank surfaces as shown in Fig. 4.44c), of convex shape are produced. According to the patent, such lips' shape results in significant reduction of the drilling torque.

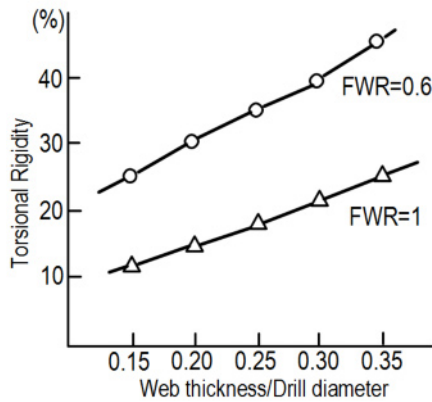


Fig. 4.43. Drill torsional rigidity as a function of the web thickness ratio

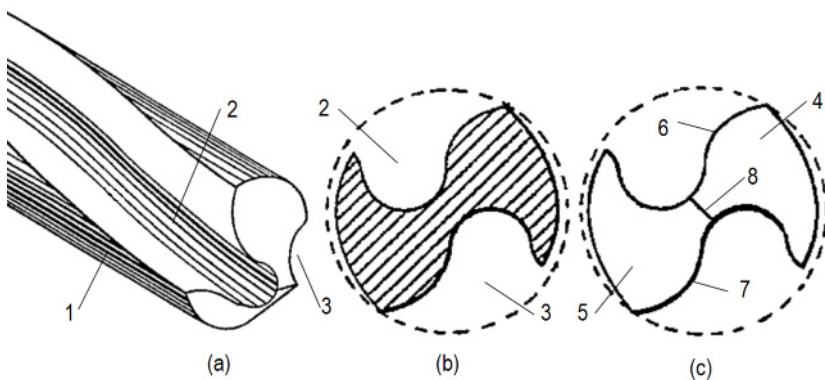
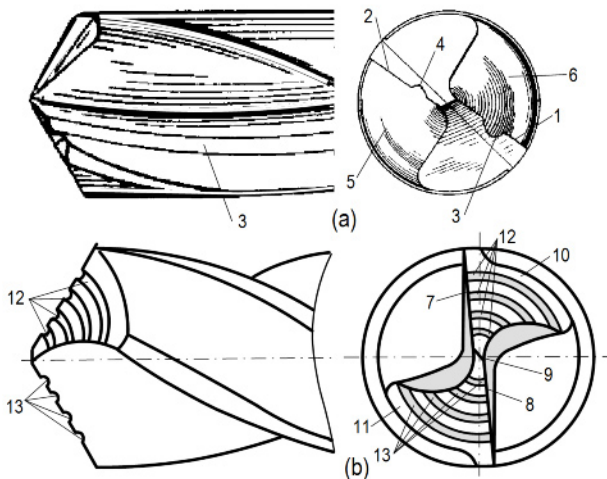


Fig. 4.44. Drill design according to US Patent No. 262,588 (1882)

As a modification of this flute profile, US Patent No. 4,065,224 (1976) claims that the shape of the concave cutting edges 6 and 7 shown in Fig. 4.44c can be made so

the constant rake angle along these edges is achieved for any desired combination of helix angle, point angle, and lip rake required. Although it is not mentioned in the patent description and in the literature on drill design, a concave as shown in Fig. 4.44 or the popular today convex cutting (as shown in Fig. 4.36) edge forms a much more rigid chip (compare a sheet of metal and a car hood made of this sheet) which is much easier to break due to bending. These are the simplest types of the flute profile to enhance chip breakage while improving tool life simultaneously.

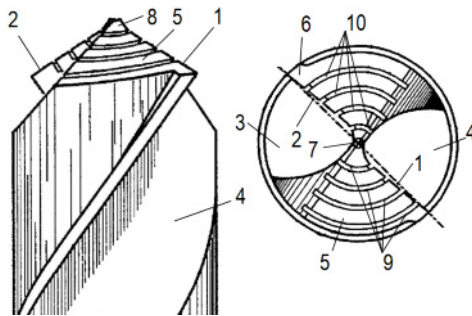
The chip breakability can be enhanced if a cutting edge is provided with chip splitting grooves often called nicks. Initially developed for spade drills (Fig. 4.16) and evolved into ANSI Standard B94.49-1975, such nicks have also been used for twist drills since the eighteenth century [18]. Figure 4.45a shows a drill design according to US Patent No. 1,383,733 (1921). The drill has the major cutting edges 1 and 2 provided with chip splitting grooves 3 and 4 extending over the length of flutes 5 and 6. A number of various drill designs with chip splitting nicks were introduced. A detailed analysis of their effect on drill performance was presented by Nakayama and Ogawa [19]. The design of a twist drill having multiple nicks ground as radial grooves on its flank shown in Fig. 4.45b in was described as early as 1940 by Veremachuck (Fig. 244 in [20]) who also extensively studied the application specifics of this design in its comparison with the standard twist drill. In this drill, the major cutting edges (lips) 7 and 8 are located so that preferable distributions of the rake and flank angles along these edges are achieved as well as thinning of the chisel edge 9. Flank surfaces 10 and 11 are provided with radial grooves 12 and 13 respectively that aim to separate the forming chip into rather narrow strips.



**Fig. 4.45.** Drills with radial chip splitting grooves: (a) made on the rake face, (b) made on the flank surface

Figure 4.46 shows a drill design according to US Patent No. 5,452,971 (1994). According to Neville, the inventor, it is a completely new concept in twist-drill

theory, design, and method of construction which will revolutionize the rotary end cutting tool systems. The drill has two curved major cutting edges 1 and 2 formed as intersection lines of flutes 3 and 4 and flank surfaces 5 and 6. These edges are connected by the chisel edge 7. Two series of offset volumetric grooves 9 and 10 (deep nicks ground as radial grooves) are ground on each flank surface as shown in Fig. 4.46. The patent claims that such a drill produces precise, near mirror-like well-finished holes in various work materials. Besides, its penetration rate nearly four times faster and tool life seven times longer in comparison to a comparable-sized standard twist drill.



**Fig. 4.46.** Drill design according to US Patent No. 5,452,971 (1994)

A number of concerns about a drill having radial chip splitting grooves can be identified. The major design concern is a difficulty to assure the flank angle on the sides of the grooves to prevent friction of these sides in drilling. According to the design shown in Fig. 4.45b, these grooves are rather shallow and have round cross section, and thus severity of the problem is low. In the design shown in Fig. 4.46, these grooves are deep and, having a rectangular cross-section, the problem becomes of real concern. To apply the flank angle on the groove sides, their profile should be of fish-tail cross section which is virtually impossible to apply using standard machines and grinding wheels. The application problem is that the radial grooves should be re-applied with relatively high accuracy on each successive re-sharpening. In the author's opinion, these two prime problems prevent practical applications of the discussed designs.

The chip rigidity and thus breakability can be achieved if a drill has a means to increase the rigidity of the forming chip. US Patent No. 2,204,030 (1940) offers a drill design where the major cutting edges 1 and 2 are made with ribs (projections) 3 and 4 as shown in Fig. 4.47. The formed chip would have a rib of rigidity so its breakability would be much greater. To achieve the same objective, US Patents No. 867,639 (1907) and 1,404,546 (1922) offer various combinations of the above described means located asymmetrically about the axis of rotation. Although the described ideas of chip rigidity enhancement are widely used in modern designs of cutting inserts, including those for drills, the formation of additional rigidity is always accompanied by increased drilling torque and force.

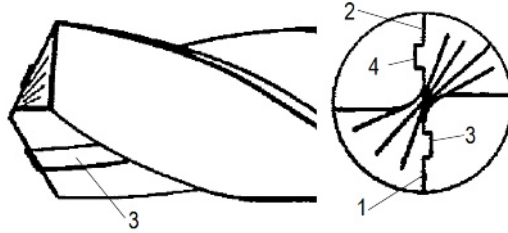


Fig. 4.47. Enhancing chip rigidity by providing ribs on the drill rake faces

However, it is often not sufficient to obtain the desirable chip shape and to avoid significant force due to chip interaction with the side wall of the flute and with the walls of the machined hole. The latter should be particularly avoided as it results in damage to hole quality and significant friction. Therefore, the chip flute profile should be made so that it helps to curl the chip into an easier transportable shape and then transport this chip away from the machining zone out of the hole being drilled.

To understand a need for more sophisticated shapes of the chip flute, consider a simple model of chip flow shown in Fig. 4.48. One should realize that in any drill, the length of the chip produced by the periphery point  $A$  (its nearest vicinity to assume some finite chip width) over one drill revolution is much greater than that by point  $B$  which is the inner end of the major cutting edge where this edge meets with the chisel edge. This is because the path travelled by point  $A$  in one drill revolution is  $r_A/r_B$  time greater than that by point  $B$  (where  $r_A$  and  $r_B$  are radii of points  $A$  and  $B$ , respectively). For example, for a standard 20 mm diameter drill,  $r_A = 10\text{mm}$  and  $r_B = 2\text{mm}$ , i.e., the path passed by point  $A$  is fivefold greater than that by point  $B$ . The chip length is determined as the length of the path divided by chip compression ratio [21, 22]. Because this ratio is normally 50–70% higher for point  $B$  because of its much smaller cutting speed and not favorable tool geometry, the total difference in the chip length produced by point  $A$  is normally 7–8 times greater than that by point  $B$ . Because the chip is continuous along the major cutting edge  $AB$ , the discussed difference causes the deviation of the chip flow direction from the normal, defined by the cutting edge inclination angle as shown in Fig. 4.48. As a result the forming chip 1 flows along straight part 2 of the flute and then over its curved part 3 as shown in Fig. 4.48, reaching the walls of the machined hole.

To deal with the problem, various approaches are used. The first is to use groove-type and obstruction-type chip breakers like those used in single-point tool operations [23–25]. Figure 4.49a shows a drill with groove 1 placed on the rake face 2 near the major cutting edge 3 that facilitates chip breaking and prevents chip clogging [26]. Figure 4.49b shows a drill according to US Patent No. 2,966,081 (1960). In this drill, the flute profile is of a concave shape 4 and the chip breaking step (VIEW B) is provided so that the cutting edge 5 is formed.

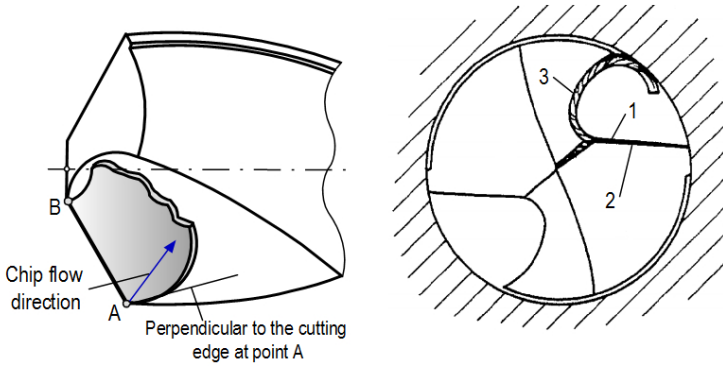


Fig. 4.48. Simple model of chip flow

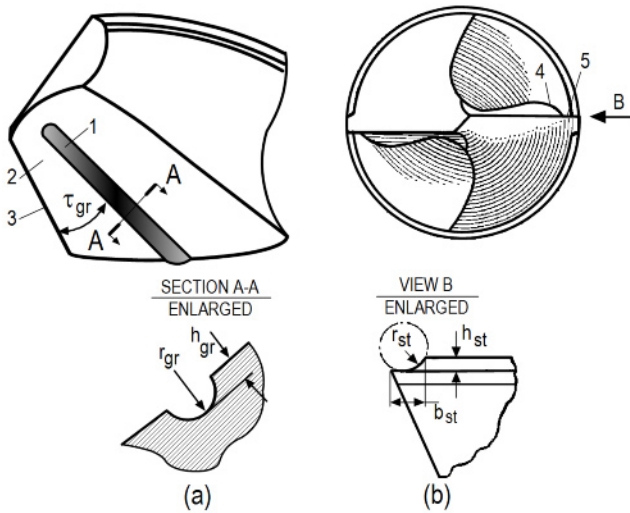


Fig. 4.49. (a) Groove-type, and (b) obstruction-type chip breakers for a drill

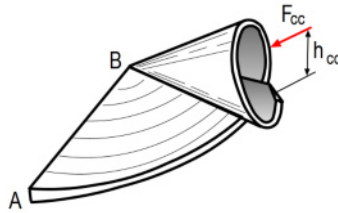
Although these chip breakers may produce broken chips suitable for evacuation from the machining zone, they are really used in drilling because:

- Groove geometry (parameters  $r_{gr}$  and  $h_{gr}$ ) and orientation (angle  $\tau_{gr}$ ) as well as chip step geometry ( $h_{st}$ ,  $b_{st}$ , and  $r_{st}$ ) are application specific, i.e. they work for a rather narrow range of the combination of the work materials properties, feed, speed, MWF, etc. A small departure from one of these parameters may ruin chip breaking.
- Groove-type and obstruction-type chip breakers increase the drilling torque and the axial force.
- The groove and chip step geometry should be reproduced with relatively high accuracy on each drill re-sharpening. Particularly with the groove shown in Fig. 4.49a, a great amount of the tool material should be removed



to restore the original shape of the drill that significantly lowers the number of possible re-sharpenings.

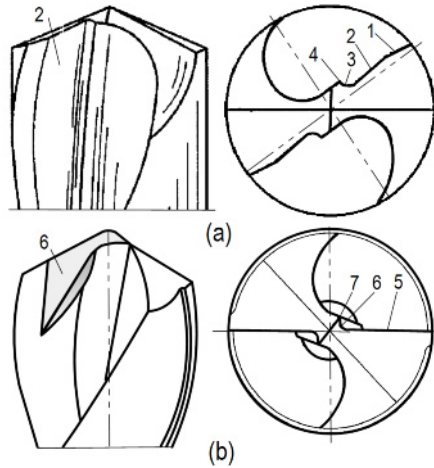
More intelligent ways to design the flute profile to achieve a suitable shape of the chip can be understood if one considers a simple model of chip shape formation (chip curling during drilling) as shown in Fig. 4.50. In this picture the letters *A* and *B* designate the corresponding ends of the cutting edge *AB* shown in Fig. 4.48. To curl such a chip into cone-like shape in order to break it when the deformation in its root reaches the strain at fracture or to form long tight curls, a certain force  $F_{cc}$  should be applied to the chip at a certain distance  $h_{cc}$ . Because the force  $F_{cc}$  is the reaction force from some obstacle made on the flute, it depends on the drilling process parameters while the direction of this force and the distance  $h_{cc}$  can be varied by flute profile parameters. This is the principle that outlines many patented drill designs which differ only by particular values of these two parameters.



**Fig. 4.50.** Model of chip curling

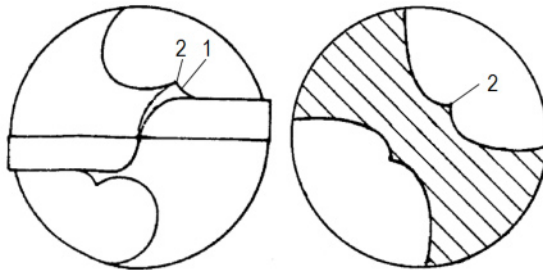
Figure 4.51a shows flute profile according to US Patent No. 5,622,462 (1997). As can be seen, each major cutting edge (lip) consist of the outer straight part 1 and inclined inner part 2 having concave portion 3. The apex 4 is formed as a meant to apply the force  $F_{cc}$  shown in Fig. 4.50. The inner part is built-in in the flute profile that assures its consistency over each successive drill re-grind. Figure 4.51b shows a similar flute profile according to US Patent No. 5,931,615 (1999). As seen, the major cutting edge 5 is located on the drill transverse axis. It has concave part 6 which ends with apex 7. The location of the major cutting edge on the drill transverse axis improve the distribution of the flank and rake angles over the straight part of the cutting edge and decrease the plastic deformation of the chip that reduces the drilling torque and force. However, complicated concave part 6 should be ground on each successive drill re-grind.

There two obvious disadvantages of the profiles shown in Fig. 4.51. the first is that the cutting geometry over the radiused parts and apexes are not favorable (this will be discussed later in this chapter). As a result, one should expect an increase in the drilling torque and force. Second, the arm ( $h_{cc}$  in Fig. 4.50) is small that may not create a sufficient bending moment to at the chip root to break the forming chip into pieces while force  $F_{cc}$  is excessive because the radius of the radiused parts is too small. However, it has been found that the breaking up of the forming chip into small pieces is not always desirable. Rather, the efficiency of drilling is improved and less down time is needed if the drill flute profile is constructed so that the chip coming out from the cutting edge is formed into long sustained curls.



**Fig. 4.51.** Two flute profiles with a mean for chip curling as a part of the major cutting edge

Figure 4.52 shows the flute profile according to US Patent No. 4,222,690 (1980) where curved part 1 and apex 2 belong to the flute. Many other known flute profiles originated from the same idea. The difference is in the location of apex and the radius of the curved part. For example, Fig. 4.53 shows a twist drill in which a concavely-shaped surface 1 extends from the inner end 2 of the major cutting edge 3 towards the outer periphery of the drill body and apex 4 is located on the side wall of flute 5.



**Fig. 4.52** Drill design according to US Patent No. 4,222,690 (1980)

As extreme cases, it is worthwhile to consider some special profiles of the chip flute and thus drill cross sections shown in Fig. 4.54. Figure 4.54a represents a limiting case of the profile shown in Fig. 4.53. An attempt was made to increase the cross-sectional area of the flute according to the profile shown in Fig. 4.53. The part of the flute located above apex 4 in Fig. 4.53 is not very useful for chip transportation. In the profile shown in Fig. 4.54a, the flute is formed by the cutting edge portion 1 which becomes concave portion 2 which extends to apex 3 located almost at the intersection of the flute and the relieved part of the drill body. According to US Patent No. 4,583,888 (1986), the positions of apex 3 is selected so the chip contact with the wall of the machined hole is prevented. It can be

accomplished by selecting the web thickness  $d_{ww} = (0.25-0.35)d_{dr}$  and FWR = 0.4–0.8. According to US Patents No. 4,983,079 (1991) and 5,088,863 (1992), a significant reduction in the axial force, drilling torque and thus drilling power as well as improvement in chip transportation from the machining zone in heavy-duty drilling operation is achieved when distance  $W_{ww}$  is selected properly from the range of  $(0.45-0.65)d_{dr}$ .

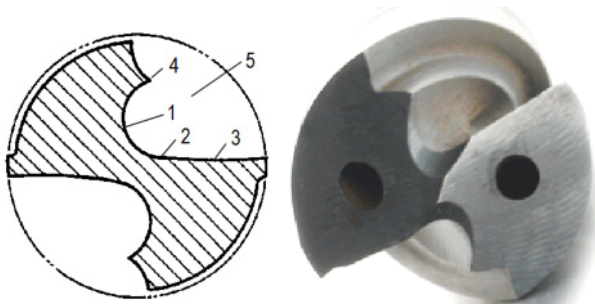


Fig. 4.53. Drill body and the chip-curling apex located on the side wall of the flute

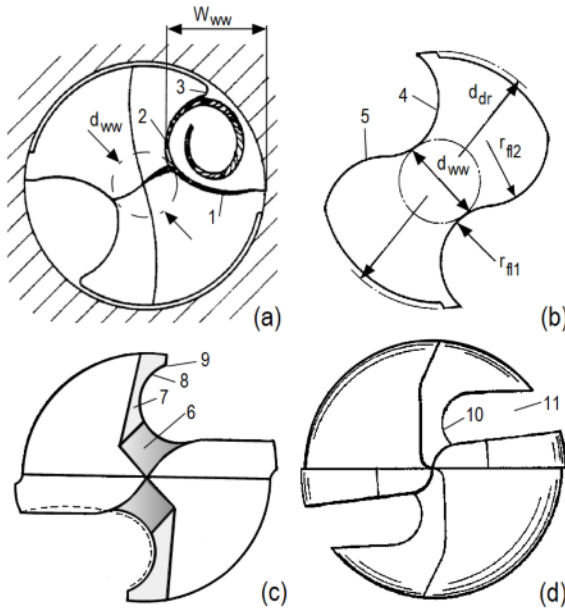


Fig. 4.54. Some other shapes of the chip flute

Figure 4.54b shows double-radius chip flute profile. According to US Patent No. 4,744,705 (1988), significant reduction in drilling power and improvement stability of drilling operations are achieved when the web thickness  $d_{ww} = (0.25-0.50)d_{dr}$ ,

$r_{f1} = (0.2-0.3)d_{dr}$  and  $r_{f2} = (0.25-0.40)d_{dr}$ . It is understood that the cutting edge formed as the line of intersection of the concave portion 4 of the flute with that flank surface would be concave. Convex part 5 of the flute profile is to curl the forming chip. US Patent No. 302,325 (1881) describes practically the same cutting edge profile with better chip curling ability and with the prime chip curling feature shown in Fig. 4.51a.

Figure 4.54c shows the flute profile according to US Patent No. 5,716,172 (1998) meant for heavy-duty drills. It has the front chip curling means consisting of two flat surfaces 7 and 8 which are made to fold and then curl the chip emerging from the cutting edges into the concave flute 8. Flute 8 is provided with apex 9 to prevent the contact of the chip and the wall of the drilled holes.

Figure 4.54d represents the generic idea of extremely heavy-duty and deep-hole drills with FWR of 0.5–0.02 to give increase torsional rigidity to the drill shank (for example, US Patents No. 4,565,473 (1986) and 4,975,003 (1990)). The concave part 10 of the chip flute 11 has a small radius to bend, curl, and break the forming chip or just direct it into the flute without breaking as a small diameter curl or a string.

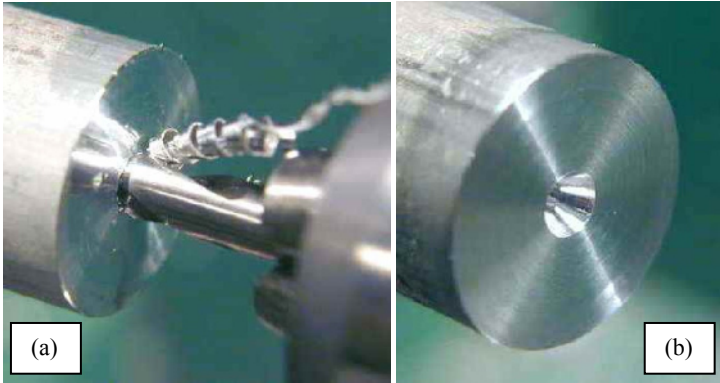
#### 4.6.2.3 Improve Drill Self-centering Ability

Center drills were initially developed to produce center holes with a chamfer to be used as manufacturing datum in parts which are machined between centers (lathe operation, milling, grinding, etc.). The part is then located on these holes using live, dead, or driven centers which locate the part about the axis of the center hole. This axis is called the manufacturing datum and used in many manufacturing operations to locate the part in various machines. This axis can also be used as the metrological datum for part inspection between the centers. Figure 4.55 shows a modern center drill. Figure 4.56a shows a center drill producing a center hole in a shaft and Fig. 4.56b shows a finished central hole.



**Fig. 4.55.** A typical modern center drill

Center drills found another wide application in machining. Traditional twist drills particularly with a wide web may tend to wander or wobble (known in industry as walking) when started on an unprepared surface. Once a drill wanders off-course it is difficult to bring it back on center. A center drill frequently provides a reasonable starting point as it is short and therefore has a reduced tendency to wander when drilling is started. This is particularly important when the surface of the part to be drilled is not flat or rough (for example, as-cast surface). Modified versions of a center drill used for this purpose became known as spot (spotting) drills.



**Fig. 4.56.** (a) Center drill producing a central hole, and (b) finished central hole in a shaft

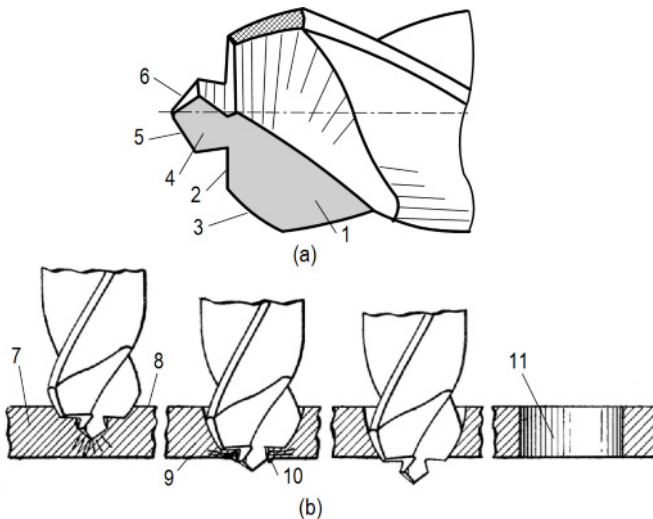
Naturally, improving the self-centering capability of twist drills came into the focus of drill designers and manufacturers when decent grinding machines and fixtures became capable of reproducing complicated point grinds. As mentioned above, ‘S’ shaped helical (particularly with its improved geometry known for example from US Patent No. 6,739,809 (2004)) and split point grinds possess some self-centering capabilities compared to a standard twist drill. However, true self-centering capability is thought of as a drill design which combines the advantages of center drills and conventional twist (straight-flute) drills. These designs became known as drills with six-facet point geometry. Such a drill is considered to be fully self-centering which is its major advantage. The axial force (thrust) requirements of this drill is equivalent to four-faced drills with the 10% web thinned chisel point or to properly designed and made ‘S’ helical relieved point geometry. The author’s experience with application this geometry shows that its self-centering advantage comes at the cost of tight tolerances on the geometry parameters and surface finish, particularly on the center part of the drill. Unfortunately, many drill manufacturers do not fully understand this important issue. As a result, the performance of such drills in general does not show great advantages over four-faced or ‘S’ helical relieved geometry drills.

A self-centering drill design according to US Patent No. 3,592,555 (1971) is shown in Fig. 4.57a. Each cutting tooth of the drill has flute 1 which ends up with two portions of the major cutting edge, namely, 2 is the straight portion and 3 is the curved portion. In the center of the drill, a center-drill-like tip 4 having cutting edges 5 and 6 is located. Such a drill will penetrate the workpiece without pre-punching or center drilling a hole at the exact center of the larger hole to be drilled thus it possesses self-centering capability. It allows drilling a hole that is round and within very close tolerance from the top to the bottom of the hole.

Figure 4.57b demonstrates the drill in use in penetrating a plate 7 made of a work material. Tip 4 penetrates first the plate’s surface 8 to form an initial small diameter hole similar to a center drill. Then the flat portion 2 of the cutting edge and eventually its curved portion 3 start to drill the hole using the small hole as a pilot surface that stabilizes the drilling process and prevents wobbling of the drill which might cause bell mouthing at the hole entrance and exit. As tip 4 reaches the

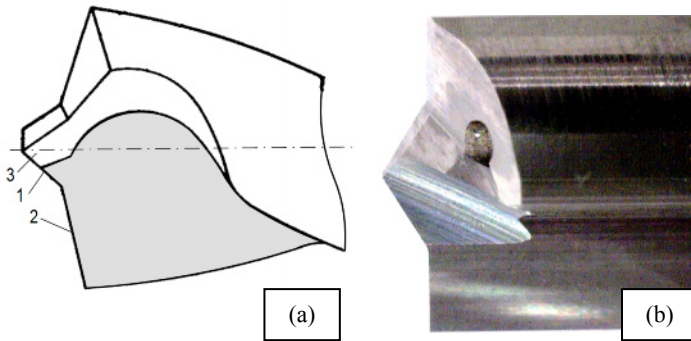
surface 9, it easily breaks through with small exit burr as the straight portion 2 of the cutting edge applies the axial force on the thin bottom 10 of the hole being drilled. Then, the curved portion smooths the hole and removes the burr. As a result, the drilled hole 10 is round, straight, and has no exit burr. As claimed by the patent, a significant reduction of the axial force (thrust) is achieved.

A self-centering drill design according to US Patent No. 4,878,788 (1989) is shown in Fig. 4.58a. The tip of this drill has a pair of major cutting edges. Each major cutting edge consists of inner major cutting edge 1 and outer major cutting edge 2. The inner cutting edges 1 extend from the corresponding outer cutting edges 2 diagonally to the front to form protrusive leading part 3. The diameter of a circle scribed by the pair of inner major cutting edges 1 is in the range of 40–50% of the drill diameter. This drill design is particularly useful for small drill diameters. Various version of this design (an example is shown in Fig. 4.58b) and its improvements (for example, US Patents No. 6,190,097 (2001) and 6,857,832 (2005)) are widely used today.

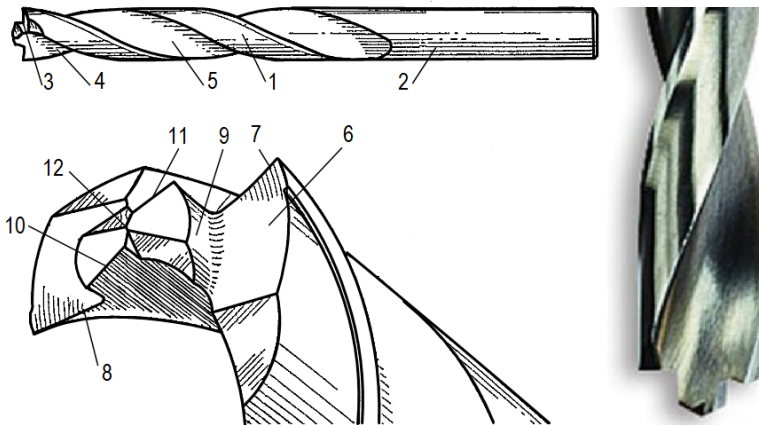


**Fig. 4.57.** (a) Self-centering drill design according to US Patent No. 3,592,555 (1971), and (b) cross-sectional views of the plane being drilled

Practically all other known designs developed the above-discussed ideas. Another design of self-centering drills developed in details in US Patents No. 4,968,193 (1990), 6,190,097 (2001), and 7,267,514 (2007) is shown in Fig. 4.59. The drill includes an elongated drill body 1 having shank 2 and a working end 3. Flutes 4 and 5 are formed in the drill body. The working end of the drill body is formed with the first section 6 of the nominal drill diameter and includes major cutting edges (lips) 7 and 8 arranged in a “fishtail” or inversely angled configuration. A second section 9 is formed with a minor drill diameter which is smaller than the nominal drill diameter. This section has its own major cutting edges 10 and 11



**Fig. 4.58.** Simple design of a self-centered drill (a) and an example its practical implementation (b)

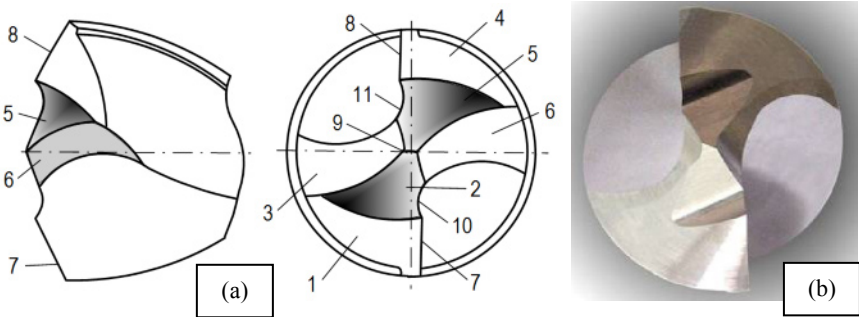


**Fig. 4.59.** Self-centering drill with inversely angled configuration

connected in their inner ends by chisel edge 12. As seen, the split-pint grind is used for further enhancement of self-centering ability.

Yet another line of self-centering drill is the so-called multifacet drills. As discussed by Wu and Shen [27], around 1953, a new type of drill points with multifacet flank shapes was successfully developed experimentally to drill a special alloy steel. Since then, a great variety of such drills has been developed for different work materials. This new drill became known as a multifacet drill or MFD for short. A typical MFD is shown in Fig. 4.60. This drill has six facets 1, 2, 3, 4, 5, and 6 in a symmetric form although not all MFD are symmetrical. Flanks 1 and 4 are ground in the same way as for a standard twist drill so that straight portions 7 and 8 of the major cutting edge are formed. Flanks 3 and 6 are ground to form other cylindrical surfaces near the center of the drill to thin the chisel edge 9, while flanks 2 and 5 are ground to form curved parts 10 and 11 of the major cutting edges.

As believed, when properly designed and manufactured, an MFD has the following advantages over a standard twist drill: (1) the axial force (thrust) is reduced up to 70%, (2) self-centering ability, (3) reduced exist burr, and (4) the chip is separated into easy-to-transport pieces and shapes. In spite of these advantages being proven experimentally, these drills did not attract much attention from drill manufacturers and users because the complicity of their geometry which should be applied on each re-grind almost manually. Although some simplified versions of MFD were patented (US Patents No. 5,011,342 (1991) and 5,422,979 (1995)), it did not help in any noticeable increase in the use of such designs.



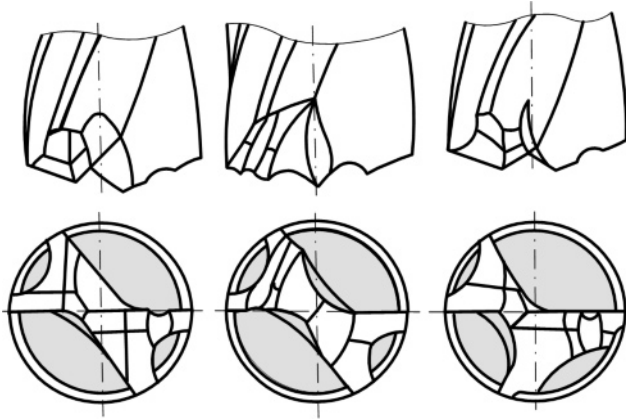
**Fig. 4.60.** (a) Generic MFD, and (b) MFD by Shenzhen Gold-Drill Tools & Manuf. Co. (China)

Modern development of MFD originated at the Xi'an Petroleum Institute [28]. Figure 4.61 shows some developed geometries known as the four-margin design. This design which can be of symmetrical or asymmetrical forms offers a number of beneficial features: (1) the major cutting edges have positive rake angles and preferable angle distribution along their length, (b) thick web that allows high penetration rate, and (c) four margins increase drill stability and provide separate channels for MWF supply into the machining zone and flutes for chip removal.

Although the developed and tested MFD offer these advantages and thus it makes good sense to produce and use such drills, drill manufacturers and users are rather reluctant to produce and implement them in industry. In the author's opinion, there are a number of reasons for that. These reasons can be broadly separated into two categories: (1) design concerns, and (2) tool manufacturing concerns.

The design concerns stem from the fact that there is no simple methodology to analyze the geometry and force balance of an MFD and its components. For example, a practical drill designer is not aware what the result would be if he locates a cutting edge in certain fashion in the tool coordinate system or if he makes it in a curved shape.





**Fig. 4.61.** MFD developed at the Xi'an Petroleum Institute [28]

The manufacturing concerns relate to the grinding the tip of an MFD and inspecting the results of this grinding (re-sharpening). To make such grinding feasible and economically efficient, a CNC grinding machine with multiple wheels equipped with controllers programmed to dress these wheels adequately and then to reproduce the intended shape of MFD should be available. Although it is possible with the latest CNC grinders (Star, ANCA, Walter CNC tool grinders), a lot of work has yet to be done to program these machines to manufacture MFD. Another aspect is MFD metrology as modern tool geometry inspection machines (as for example, Walter Helicheck and Zoller Genius 3 Pilot) are not readily programmed for such inspection.

Regardless of the listed concerns, MFD design is the right direction for development in the author's opinion. The methodology and information presented later in this chapter can help to overcome difficulties and scepticism in industry so that a new line of highly efficient drills can be developed for use in modern manufacturing facilities.

## 4.7 Common Design and Manufacturing Flaws

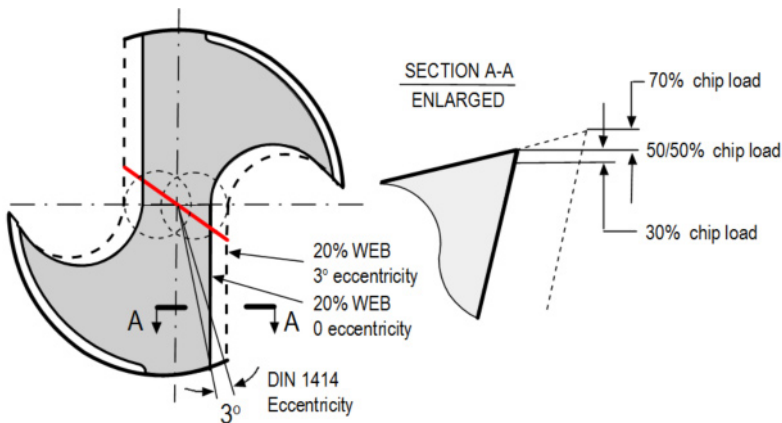
One should realize that any geometry is good as long its parameters are properly calculated, designed (properly assigned in the tool drawing), applied to a drill during its manufacturing, and then properly inspected. According to Fiesselmann [1], although most of drill tool manufacturers are members of the U.S. Cutting Tool Institute (USCTI) and thus supposed to meet the drill tolerances established by this institute or DIN tolerances that are very similar, few drill manufacturers certify/guarantee their tools to meet these published tolerances. Surprisingly, only a few high-volume drill users, or those drilling difficult-to-machine work materials either demand tool certification from their suppliers or correct/re-sharpen all new drills as received and thus pay close attention to their drilling operations.

In the author's experience, among many others, the following design and manufacturing flaws are most persistent as they affect drill performance dramatically: (1) web eccentricity/lip index error, (2) Poor surface finish, (3) Improper tool material/hardness, and (4) Coolant holes location and size.

#### 4.7.1 Web Eccentricity/ Lip Index Error

Web eccentricity/lip index error allowed by DIN 1414 or equivalent USCTI tolerance is  $3^\circ$ . Figure 4.62 illustrates how this allowed drill web eccentricity of lip/flute index affects the desired 50/50% chip load (force) balance. While USCTI and DIN standards used the lip height-to-lip height measurement to determine point eccentricity, this allowed  $3^\circ$  and equivalent USCTI decimal allowance has a direct effect on this measurement even if the point is truly concentric.

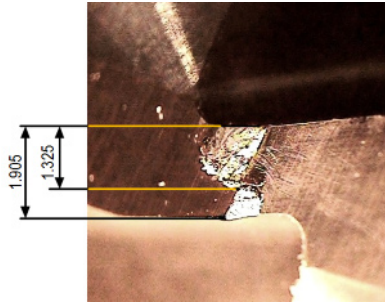
The problem with this error is that there is no adequate metrology support for the detection of this error. Common inspection equipment locates a drill in a V-block not on its rotational axis thus does not allow drill precision rotation about its true longitudinal axis. Common tool pre-setting machines allow focusing only on one lip and then rotating the drill to focus on the other. As such, the web eccentricity cannot be detected. Common tool geometry measurement machines do not include this feature in their basic programs.



**Fig. 4.62.** Effect the allowed drill web eccentricity of lip/flute index error on the chip load (force) balance

When machining aluminum and its alloys, the web eccentricity can be observed after a short time of cutting. Figure 4.63 shows an example of this concentricity error. As can be seen, the two parts of the chisel edge are not equal and that causes hole size and location problems. When machining steels, web eccentricity causes the so-called chisel edge 'walking' hindering precise location as the tool enters the workpiece. Figure 4.64 shows three hole entrances drilled by tools with excessive web eccentricity: (1) allowable web eccentricity, and (2) less than  $1^\circ$  web

eccentricity. In the practice of CNC machining, to prevent chisel edge ‘walking’ a center drill is first used to make hole starts to assure their accurate locations and improve entrance conditions for the drill. In practice of the automotive industry, a short end mill is used to start the hole (cut pilot holes) when an inclined hole entrance or uneven/out of location core hole is to be drilled.



**Fig. 4.63.** Web eccentricity marks made in drilling of aluminum alloy



**Fig. 4.64.** Hole entrances made by a drill with: 1- excessive web eccentricity, 2 – maximum allowable web eccentricity, 3- with web eccentricity less than  $1^\circ$

One of the most common and obvious indications of drill lips index error or improper (non-symmetrical) location of the lips in the axial plane is the inequality of the appearance of the chip produced by the lips as shown in Fig. 4.65. Often, this difference is not so profound as shown in this picture. To assure the equality of the working conditions of the symmetrically-placed cutting edges, including lips and chisel edges, the chip compression ratio should be measured (Chap. 1) for each cutting edge. The drill is ground properly if the chip compression ratio variation from one to similar other cutting edge does not exceed 10%.

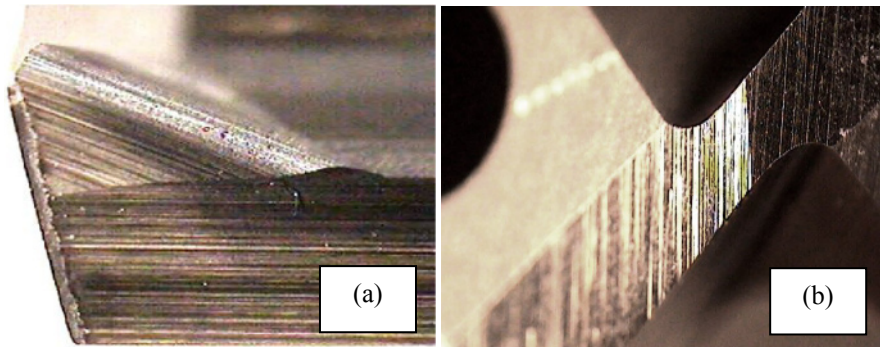
#### 4.7.2 Poor Surface Finish and Improper Tool Material/Hardness

These are two issues that are tightly intertwined in terms of their influence on tool life and quality of drilled holes. Unfortunately, this combined influence is not considered in the practice of tool design and manufacturing as well as in the use of tools. Therefore, the need is felt to clarify this important issue.



**Fig. 4.65.** Unequal chips from the lips

As an example, consider drill used in the automotive industry for drilling holes in high-silicon aluminum alloys. In such an application, a coarse grind of the tool contact surfaces combined with non-application-specific carbide grade are two prime issues. A coarse grind of drill of the drill rake (Fig. 4.66a) and flank (Fig. 4.66b) surfaces causes aluminum BUE on these surfaces that lowers tool life. Surprisingly for many, the same effect has an improper tool material. The problem is in popular sub-micrograin carbide grades. Although these grades possess a great combination of hardness and toughness, they contain 10–12% (or even more) of cobalt as the matrix material (binder) that holds the carbide particles together. In machining of common steels, it does not present any problems so the users enjoy the mentioned advantage of such carbide grades. In machining of automotive aluminum alloys, however, a high cobalt content causes BUE of aluminum on the contact surface as the aluminum matrix adheres to cobalt and not to carbide particles. Therefore, low-cobalt carbide grades should be used.



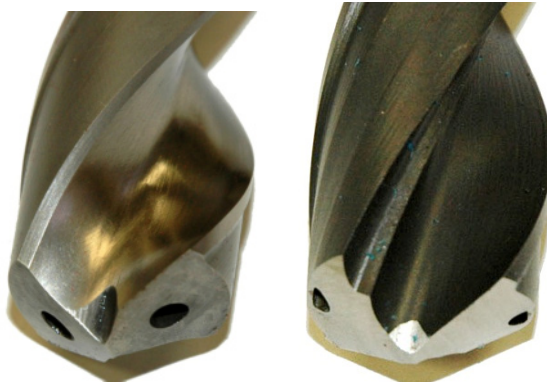
**Fig. 4.66.** Coarse grind of (a) the tool rake, and (b) flank surfaces

Two common concerns arise when a tool manufacturer is asked to apply low-cobalt carbide grades. The first and the most common is that these are hard to find nowadays as the fashion trend with sub-micrograin grades has practically extinguished them from the market although the leading carbide suppliers still

carry these grades as specials. The second is a common fear of high brittleness of these grades due to their high hardness and thus brittleness. Low cobalt grades require much more gentle grinding in drill manufacturing. It often takes a great deal of patience to convince the tool manufacturers that if a machine is running PCD tools then it definitely will run the most brittle carbide grades as the latter are still much tougher than any PCD. Moreover, high hardness of low-cobalt grades is their great asset as it allows these carbides to withstand abrasion by silicon particles in the automotive aluminum alloys.

#### 4.7.3 Coolant Hole Location and Size

There are two design features of a drill with internal coolant supply that play the same important role as in deep-hole drilling (see Appendix D). Still these two important features are not yet well-understood and thus neglected in the practice of tool design, manufacturing, and application. As a result, various drill and reamers suppliers design and manufacture drills of the same diameters with considerable different coolant hole sizes and location. Figure 4.67 shows an example. As discussed in Appendix D, under a given inlet pressure, the MWF flow rate through a hole is proportional to the hole diameter *raised to the power four*. As a result, a small change in the coolant hole size under a given MWF pressure (normally preset on the machine by the control valve) causes significant change in the MWF flow rate and thus in drill performance.



**Fig. 4.67.** Two drills of the same diameter having different sizes and locations of the coolant holes

As discussed in Chap. 5 and Appendix D, the MWF supplied to the drill through its internal holes is intended for reliable chip transportation from the machining zone and for increasing tool life. As such, the diameter of these holes as well as the location of their outlets on the tool flanks are of equal importance. A common perception implies that the location of the outlet section of the coolant holes should be positioned so that the greatest flow rate under a given inlet MWF pressure is achieved. As a result, many outlets of the coolant holes (particularly in straight flute drills) are made in the manner shown in Fig. 4.25, i.e., with at least a half

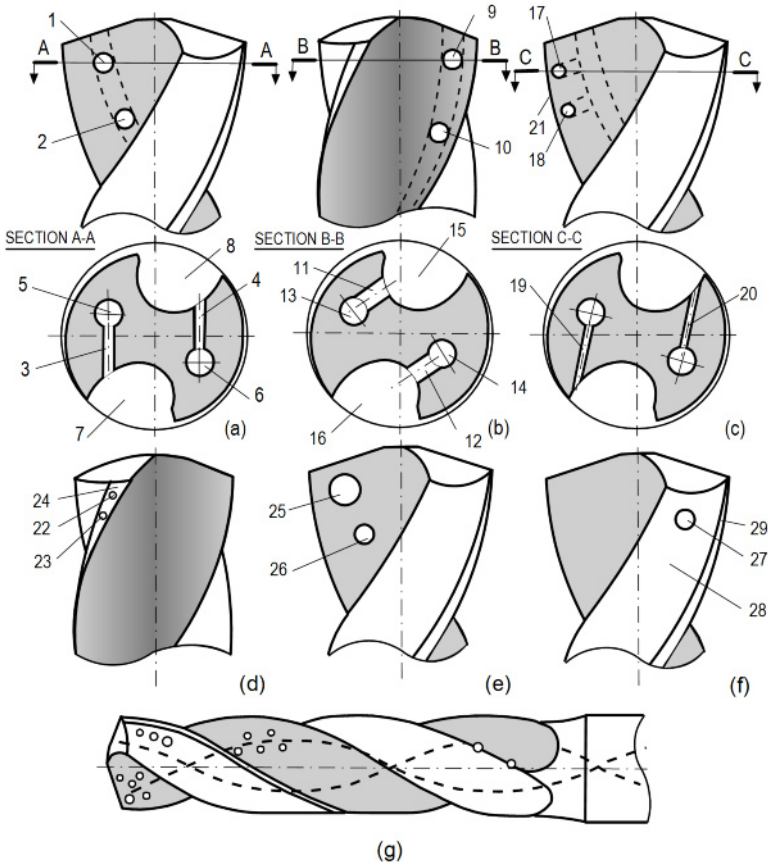
cross-section located in the flute. In full analogy with deep-hole tools (Chap. 5), it can be stated that although the intent behind these designs was to increase the MWF flow rate through drills and thus improve chip removal, the application of these designs improves only the apparent flow rate (measured by a flow meter installed on the machine) and thus creates more problems than it solves.

US Patent No. 6,045,301 (1998) covers all possible and impossible locations on the outlet orifices of the coolant channels in a drill. Some of the design solutions according to this patent are shown in Fig. 4.68. It worthwhile to discuss here some important conclusions of the analysis of the propose coolant hole locations. In the simplest case, the outlet coolant orifices 1 and 2 are located on the drill rake surface as shown in Fig. 4.68a. These are connected by holes 3, 4 with internal spiral coolant channels 5 and 6 thus these channels can supply MWF into the chip flutes 5 and 6. Although this design allows one to increase the apparent MWF flow rate (see Chap. 5), it actually worsens the cooling and lubricating conditions of the tool flanks as a greater portion of MWF flow rate goes through holes 1 and 2 due the their lower hydraulic resistance compared to the holes with outlet orifices on the tool flanks. Moreover, the position of holes 1 and 2 changes with each drill re-sharpening that also causes changes in the MWF flow rate.

Figure 4.68b shows another variation where the outlet orifices 9 and 10 of the coolant holes 11 and 12 that connect internal coolant channels 13 and 14 with the side wall of the chip flutes 15 and 16. Besides the disadvantages listed in the previous bullet, such a design may suffer chip pick up problems (Chap. 5). Most the supplied MWF does not even go to the bottom clearance space between the drill major flank faces and the bottom of the hole being drilled. Rather, this flow enters the chip flute, missing the region adjacent to the rake face where the chip is formed. The formed chip has a hard time to join this flow and a stagnation zone can form.

Figure 4.68c shows a drill design, where the outlet orifices 17 and 18 of the additional coolant channels 19 and 20 are located close to the drill margin 21. No advantages of such additional coolant channels can be pointed out while these channels definitely reduce the amount of MWF used for cooling and lubricating the flank surfaces. Figure 4.68e shows a drill design where the outlet orifices 22 and 23 of the additional coolant channels are located on the drill margin 24. As this margin is cylindrical, i.e., with a zero clearance between its surface and the walls of the hole being drilled, the MWF pressure should be unreasonably high to achieve any MWF flow rate from these channels. Figure 4.68d shows a design which is analogous to that shown in Fig. 4.68a except the outlet orifices 25 and 26 are of different diameter. Figure 4.68f shows a design where the outlet orifice 27 is located on the drill body relieve surface 28. Although such a location may improve the working conditions of the drill margin 29 and stabilize thedrill, reducing its transverse vibrations, this happens if the MWF pressure and flow rate are much higher than those normally available on drilling machines.

Figure 4.68g summarizes the essence of US Patent No. 6,045,301(1998) where the outlet orifices of the additional coolant channels are located wherever it is possible with no rationale behind such locations.

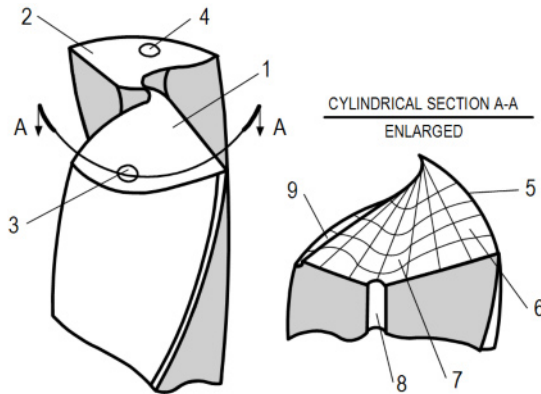


**Fig. 4.68.** Drills with internal coolant supply according to US Pat. No. 6,045,301(2000)

As discussed in Chap. 5 and Appendix D, when drilling, the drill's flank surfaces and the bottom of the hole being drilled form the bottom clearance space. The MWF (coolant) pressure and flow directions in this space define tool life. To increase tool life, the MWF pressure in the bottom clearance space should be high so that MWF can penetrate into the extremely narrow passages between the drill flank adjacent to the periphery points and the bottom of the hole being drilled (Design Rule No. 3 formulated in Chap. 5). As discussed in Chap. 5, in deep-hole drilling it can be achieved by adjusting the shoulder deb-off shape and geometry [29–31]. In straight-flute and twist drills similar solutions can be useful and feasible.

One of the feasible solutions was proposed by Colvin (US Patents 6,056,486 and 6,270,290). According to this design (US Patents 6,056,486 (2000) and 6,270,290 (2001)) called the “Pressure Tip Tool” [32] which is shown in Fig. 4.69, the flank surfaces 1 and 2 of the drill containing the outlet orifices 3 and 4 of the internal coolant passages are modified. The proposed modification can be seen in cylindrical cross-section A-A, where the contour lines have been added and

accentuated to show the topography of the flank surfaces. Each flank surface has three distinctive regions. Starting from the cutting edge 5, the first region 6 of the flank surface inclines at normal flank angles over the major cutting edge (lip) 5. The second region is a recessed surface 7 where the internal coolant passage intersects the flank surface creation its outlet orifice 8. In drilling, this recessed surface serves at the MWF reservoir together with the bottom of the hole being drilled. The third region is a trailing dam.

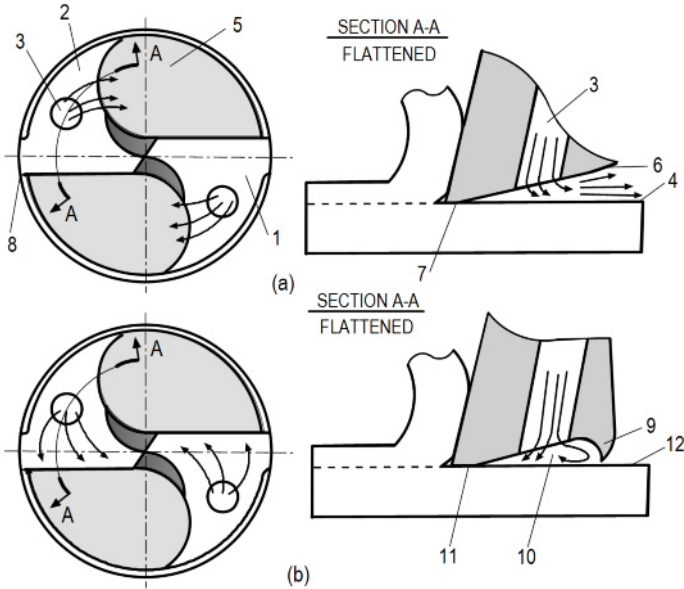


**Fig. 4.69.** The pressure tip tool according to US Patents No. 6,056,486 (2000) and 6,270,298 (2001)

Figure 4.70a, SECTION A–A shows visualization of the MWF flow in the bottom clearance space in a standard drill having curved or flat flank surfaces 1 and 2. The MWF flow supplied to this space through the internal coolant passage 3 separates into a number of elementary flows. The directions of these flows are shown by streamlines. Most of the MWF deflects from bottom of the hole being drilled 4 and flows into flute 5 as the flow goes in the direction of the least hydraulic resistance (Appendix D). Due to low MWF pressure in the bottom clearance space, MWF does not flow to the narrow passage between flank 6 and the bottom of the hole being drilled 4 to the tool flank-workpiece contact interface 7 and thus does not provide cooling and lubrication to this important interface, particularly in the regions adjacent to the drill periphery point 8 where these functions are most needed.

Figure 4.70b shows the MWF flow model in the bottom clearance space in the pressure tip drill. As seen, a trailing dam 9 is added to the flank surface that increases hydraulic resistance  $h_9$  (Appendix D, Sect. D4.2.3). As a result, MWF pressure in the bottom clearance space 10 increases and so does the penetration ability of MWF into the tool flank-workpiece contact interface 11. As explained in Appendix D, the actual pressure in the bottom clearance space 10 is determined by the maximum MWF pressure available on the machine and by the hydraulic resistance  $h_9$  (Appendix D, Sect. D4.2.3) which directly depends on the gap between the training dam 9 and the bottom of the hole being drilled 12.





**Fig. 4.70.** Visualization of the MWF flow in the bottom clearance space (a) for the common, and (b) for the pressure tip drills

Although a minimum sixfold increase in tool life with this tool is reported [32], which is consistent with the increase in tool life indicated in Chap. 5 for high bottom-clearance space MWF pressure tools, such an improvement does not fall into the category ‘No strings attached.’ The major issue is the necessity of the accurate drill geometry (flank model) as the drill performance, determined by the MWF pressure in the bottom clearance space 10 (Fig. 4.70b) is very sensitive to the gap between the trailing dam 9 and the bottom of the hole being drilled 12. If this gap is negative, the interference of the tool flank with the bottom of the hole being drilled takes place that ruins drill performance. If this gap is excessive, the MWF in the bottom clearance space 10 is insufficient to improve drill performance. The difference between these two extremes is of the order of 0.1mm. Therefore, a mathematical model of the bottom of the hole being drilled (accounting for a particular cutting feed) should be combined with that of the drill flank in order to develop a subroutine for a CNC grinding machine. The second issue is a requirement for the drilling machine to be used to deliver high pressure at the MWF flow rate needed for the drill (see Chap. 5). It is understood that other components of the drilling system should also support this drill design.

## 4.8 Tool Geometry

There are two principally different ways to present tool geometry. The descriptive approach that is commonly used in the literature explains the geometry of a particular drill design, presenting some graphs on the distributions of the cutting

angles. This approach is usually used in books on metal cutting and cutting tools where a wide range of subject matter is to be covered in a relatively limited space. Such an approach is of a descriptive nature and thus is not intended to teach particularities of tool design and geometry. Rather, it aims to familiarize the reader with the subject. The best publications additionally list important points and issues. Being useful for educational purposes, this approach sometimes does more damage than good as many statements and results presented are taken out of context. The presented information confuses tool manufacturers engineers and practitioners who might take this information as a set of general rules valid under any conditions of the law of physics without seeing specifics of a particular application. Moreover, such information is carried from one book to another for years which makes it outdated. For example, the results and pictures taken from classical papers on drilling [33–35] found their way into modern references, texts and handbooks. Being of great importance in the historical development of the drills and drilling processes, these results should be taken today with educated discretion as the conditions under which the results were obtained and the research equipment used in the tests are not even remotely resemble those used today.

As pointed out by Webb [36], although the belief that drilling is simple and well understood may have been valid in the past, i.e., the knowledge of the time satisfied the needs of the time, this belief is in need of complete revision. Emergence of new work materials to be cut by drilling, introduction of new and substantial improvement of the existing tool materials, wide use of CNC unmanned drilling machines and manufacturing cells, CNC multi-axis drill grinding machines, grinding techniques, and grinding wheel materials necessitates a complete rethink of drilling techniques. In the author's opinion, the major problem is normative information which includes that in various standards, manuals and handbooks. It includes obsolete empirical, semi-empirical, and best practice (normally of half a century ago) formulas and recommendation to select drill's design components, secondary tooling, drilling regime, grinding practices and others.

Another approach is to derive general relationships of a rather complicated nature that hold for various drill designs and geometries [37–50]. Being useful for academic and development purposes, this approach provides little help in practical drill design as a lot of work has yet to be done to bring general relationships to the level of practical calculation and analysis.

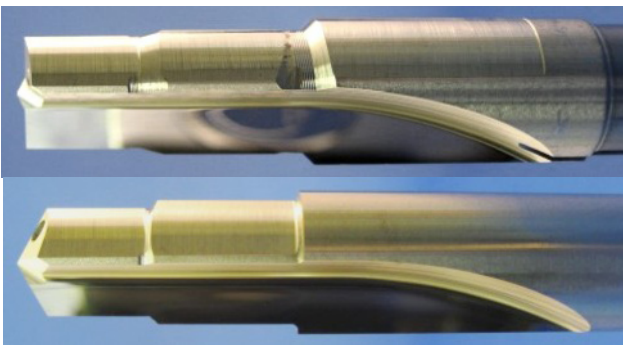
In this book, another course is taken. Rather than developing and analyzing the complete drill geometry, the geometry of essential components of this geometry will be analyzed. Therefore, a practical designer can use the analyses as 'Lego blocks' to build any drill design consisting of various components or to analyze any new and existing drill design. Knowing and understanding this methodology and design components, one should be able to design a drill of any configuration having any number of cutting edges of any shape and location with respect to the drill coordinate system to achieve any one of many common design objectives, namely, improve drilling efficiency, tool life, quality of machined surface, etc.

### 4.8.1 Straight-flute and Twist Drills Particularities

Straight-flute drills find wide application in industry. The effectiveness of today's straight-flute drills changed traditional assumptions about the indispensability of spiral-flute drills known as twist drills. In some applications, a straight-flute drill is a better choice than a twist drill. Modern straight-flute drills were preceded by die drills – short, stiff tools with beefy tips for drilling hard steels. Run at a slow spindle speed and light feed rate, the die drill's strength and rigidity enabled it to make straight, round holes [51].

Die drills worked well because the work materials they were engineered to machine typically produced short chips. Chip control is still the key issue in the application of straight-flute drills, which work best in materials that don't generate long, stringy chips. These include various grades of cast iron, powder metals, and medium- to high-silicon aluminum alloys widely used in the automotive industry. However, new machine tools with high r.p.m. spindles and high-pressure coolant-delivery technologies, as well as enhanced tool geometries and advanced tool materials, have expanded the application range of straight-flute drills. These drills are cheaper than twist drills, their manufacture and metrology are simpler, their design allows one to make multi-step designs and a one-pass tool instead of traditionally three tools to complete a precise hole (Fig. 4.71). The use of straight-flute drills increased dramatically over recent years in the automotive and aerospace industries.

Twist drills (Fig. 4.72) are still in wide use for general applications. When properly designed and made, the helical flute facilitates chip removal from the machining zone. The coupling of the axial force (thrust) and drilling torque enhance drilling stability and allowable penetration rate compared to straight-flute drills that are particularly important in drilling difficult-to-machine work materials. That is why twist drills dominate in such applications.



**Fig. 4.71.** Modern straight-flute drill used in the automotive industry by Sonic Tools



**Fig. 4.72.** A typical twist drill

Traditionally, besides helical flutes, two major differences in tool geometry (often referred as the point grind) between twist and straight-flute drills were the shape of the rake and the flank surfaces. The rake face of a straight-flute drill is planar while that of a twist drill is helical. The flank face of straight-flute drills is planar while for twist drills, hyperbolic, cylindrical, conical, and helical basic surfaces were used [37]. However, these differences have been disappearing over last 10 years with the rapid development of modern grinding fixtures and CNC grinders as well as the introduction of better tool materials. Nowadays, the rake surface of twist drills is often modified as discussed earlier in this chapter so that the geometry particularities caused by the flute helical surface do not affect the rake geometry. The flank surface is often made planar within a small margin called the primary clearance angle as shown in Fig. 4.73 on top of, for example, conical grind while many carbide twist drill are made with multi-facet planar flank surfaces. Therefore, further geometry analysis is equally applicable for straight-flute and for twist drills as their geometrical features and particularities nowadays are easily interchangeable.

#### 4.8.2 Geometry of the Typical Drill Point

Figure 4.74 shows a typical two-flute drill. The following parameters are assigned by the drill drawing:

- Drill diameter  $d_{dr}$ .
- Point angle  $\Phi_p$ . As seen in Fig. 4.74, this point angle is double the tool cutting edge angle  $\kappa_r$  defined in Chap. 2 as the angle between the projection of the major cutting edge into the reference plane and the feed direction. The approach angle  $\varphi_p$  is also used to simplify the current tool geometry analyses. It is obvious that  $\varphi_p = \pi/2 - \kappa_r = 1/2(\pi - \Phi_p)$ .
- Angle  $\psi_{cl}$  of the chisel edge in the sense show in Fig. 4.74.
- A major cutting edge (lip) is represented by the straight cutting edge 1–2. The radii of its ends are known to be  $r_1$  and  $r_2$ , correspondingly (Fig. 4.74).
- Distance between the cutting edges (lips)  $c_{cr}$ . In drill drawings and calculations, the distance  $c_{cr}/2$  between cutting edge 1–2 and the horizontal drill axis is normally considered.

- Flank face having the normal flank angle  $\alpha_n$  is applied to cutting edge 1–2. Normally, this angle varies over cutting edge 1–2.
- Normal rake angle  $\gamma_{n1-2}$  (defined in the sense shown in Fig. 4.74, SECTION A–A–1 and SECTION A–A–2) for cutting edge 1–2 in the T-hand-S. For a straight flute drill this angle is equal to zero (SECTION A–A–1) while for twist drill this angle is not normally equal to zero (SECTION A–A–2). Normally for a twist drills, this angle varies over cutting edge 1–2.



**Fig. 4.73.** Planar flank face ground on the top of a standard conical grind

For convenience and simplifications of further derivations, a right-hand  $x_0y_0z_0$  coordinate system, illustrated in Fig. 4.74 is set as follows:

1. The  $z_0$ -axis along the longitudinal axis of the drill, with sense as shown in Fig. 4.74, toward the drill holder.
2. The  $y_0$ -axis passes through periphery point 1 and is perpendicular to the  $z_0$ -axis. The intersection of these axes constitutes the coordinate origin  $0$  as shown in Fig. 4.74.
3. The  $x_0$ -axis is perpendicular to the  $y_0$ - and  $z_0$ -axes as shown in Fig. 4.74.

Throughout the further considerations this system is referred to as the original coordinate system or the T-mach-S. The original coordinate system should also be the setting system in drill manufacturing, point grinding, re-sharpening, and control. This system should also be considered as the datum system in drill and drilling machine accessories (drill holder, starting bushing, etc.) design. Any departure from this recommendation would result in the reduction of drill reliability considered as a complex parameter of its performance, including quality of machined holes, tool life, drill breakage, and chip removal problems.

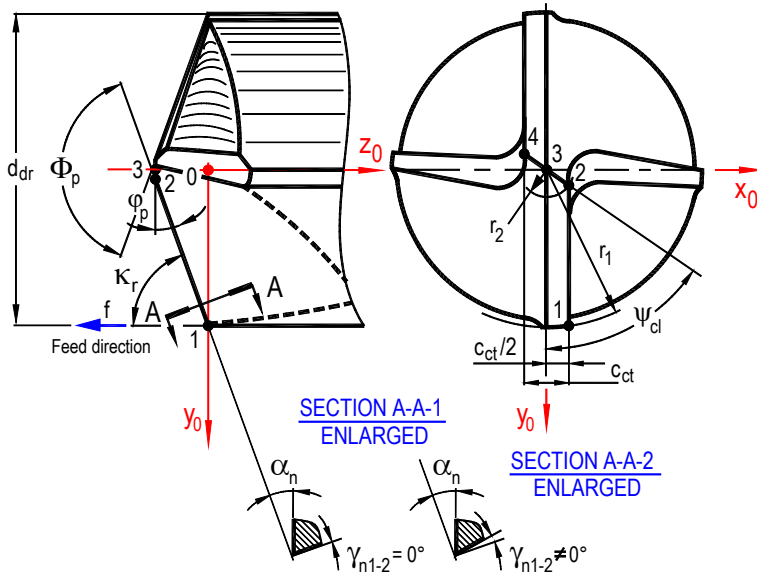


Fig. 4.74. Basic geometry parameters

### 4.8.3 Rake Angle

#### 4.8.3.1 Rake Angle of Straight Cutting Edge 1-2 Parallel to the $y_0$ -axis Plane Rake and Flank Faces

For this edge, the approach angle  $\phi_p$  is positive and shift distance  $c_{ct}/2$  is positive (the cutting edge locates above the  $y_0$ -axis. Figure 4.75 shows this cutting edge in the original coordinate system. Consider a point of interest ‘ $r$ ’ on part 1–2. The location of this point  $r$  in the  $x_0y_0$  plane of the original coordinate system is uniquely determined by distance  $c_{ct}/2$  (the excess of the cutting edge over the  $y_0$ -axis) and by the location angle  $\mu_r$  calculated as

$$\sin \mu_r = \frac{c_{ct}/2}{R_r} \quad \text{or} \quad \tan \mu_r = \frac{c_{ct}/2}{R_{pr}} \quad (4.7)$$

The senses of radial distance  $R_r$  and radius  $R_{pr}$  are shown in Fig. 4.75.

The T-hand-S right-hand xyz current coordinate system is set as follows: its origin is in point  $r$ ; the  $z$ -axis is parallel to the  $z_0$ -axis; the  $x$ - and  $y$ -axes are perpendicular to the  $z$ -axis as shown in Fig. 4.75. Let  $\mathbf{i}$ ,  $\mathbf{j}$ , and  $\mathbf{k}$  be unit vectors along the positive  $x$ -,  $y$ -, and  $z$ -axes, respectively. This system is considered as the T-hand-S for drills because the tool geometry parameters in this coordinate system are indicated on tool drawings. Therefore, the objective of this and subsequent sections is to establish the correlation between the T-hand-S parameters shown in tool drawing and those in the T-mach-S (T-use-S) that affect drill performance.

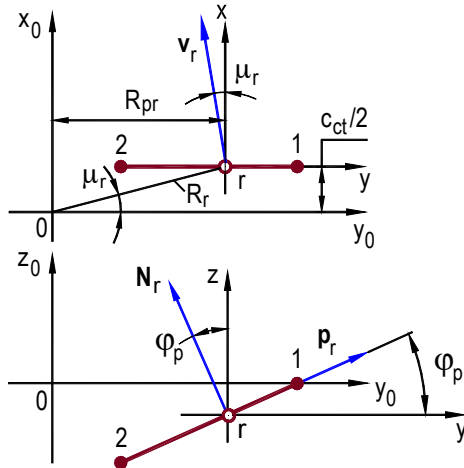


Fig. 4.75. Cutting edge 1–2

Let  $\mathbf{v}_r$  be a vector along the direction of the cutting speed. Because the cutting speed is perpendicular to the radius  $Or$ , this vector can be represented in the current coordinate system as

$$\mathbf{v}_r = \mathbf{i} - \mathbf{j} \tan \mu_r \quad (4.8)$$

Let  $\mathbf{p}_r$  be a vector along the considered cutting edge 1–2. In the current coordinate system this vector is then represented as

$$\mathbf{p}_r = \mathbf{j} + \mathbf{k} \tan \varphi_p \quad (4.9)$$

Normal  $\mathbf{N}_p$  to the T-mach-S cutting edge plane (a plane tangent to the bottom of the hole being drilled at point  $r$  as shown in Fig. 4.75), which is perpendicular to the cutting edge at point  $r$ , is determined as the vector product of  $\mathbf{v}_r$  and  $\mathbf{p}_r$  as

$$\mathbf{N}_p = (\mathbf{v}_r \times \mathbf{p}_r) = \begin{vmatrix} \mathbf{i} & \mathbf{j} & \mathbf{k} \\ 1 & -\tan \mu_r & 0 \\ 0 & 1 & \tan \varphi_p \end{vmatrix} = -\mathbf{i} \tan \mu_r \tan \varphi_p - \mathbf{j} \tan \varphi_p + \mathbf{k} \quad (4.10)$$

Normal  $\mathbf{N}_r$  is perpendicular to the cutting edge at point  $r$  (Fig. 4.75), lies in the reference plane through point  $r$  as shown in Fig. 4.75 and can be represented as

$$\mathbf{N}_r = -\mathbf{j} \tan \varphi_p + \mathbf{k} \quad (4.11)$$

Because the angle between the T-hand-S and T-mach-S cutting edge planes can be thought of as the angle between the normals to these planes,  $\xi_{ad}$  is calculated as (Appendix C)

$$\tan \xi_{ad} = \frac{\|\mathbf{N}_r \times \mathbf{N}_p\|}{\mathbf{N}_r \cdot \mathbf{N}_p} \quad (4.12)$$

The module of the vector product of  $\mathbf{N}_r$  and  $\mathbf{N}_p$  calculates as

$$\begin{aligned} \mathbf{N}_r \times \mathbf{N}_p &= \begin{vmatrix} \mathbf{i} & \mathbf{j} & \mathbf{k} \\ 0 & -\tan \varphi_p & 1 \\ -\tan \mu_r \tan \varphi_p & -\tan \varphi_p & 1 \end{vmatrix} = \\ &\mathbf{i}(-\tan \varphi_p + \tan \varphi_p) + \mathbf{j}(-\tan \mu_r \tan \varphi_p) + \mathbf{k}(-\tan \mu_r \tan^2 \varphi_p) = \\ &-\mathbf{j} \tan \mu_r \tan \varphi_p - \mathbf{k} \tan \mu_r \tan^2 \varphi_p \end{aligned} \quad (4.13)$$

$$\|\mathbf{N}_r \times \mathbf{N}_p\| = \sqrt{\tan^2 \mu_r \tan^2 \varphi_p + \tan^2 \mu_r \tan^4 \varphi_p} = \frac{\tan \mu_r \tan \varphi_p}{\cos \varphi_p} \quad (4.14)$$

The scalar product of  $\mathbf{N}_r$  and  $\mathbf{N}_p$  calculates as (see Appendix C)

$$\mathbf{N}_r \cdot \mathbf{N}_p = \tan^2 \varphi_p + 1 = 1/\cos^2 \varphi_p \quad (4.15)$$

and finally substituting Eqs. 4.14 and 4.15 into Eq. 4.12, one obtains

$$\tan \xi_{ad} = \frac{\|\mathbf{N}_r \times \mathbf{N}_p\|}{\mathbf{N}_r \cdot \mathbf{N}_p} = \tan \mu_r \sin \varphi_p = \tan \mu_r \cos \kappa_r = \tan \mu_r \cos(\Phi_p/2) \quad (4.16)$$

As discussed in Chap. 2 (Fig. 2.44), when  $\kappa_r > \pi/2$  and the cutting edge is located above the  $y$ -axis, the rake angle in the T-mach-S calculates as (Eq. 2.104)

$$\gamma_{mw}(R_r) = -\xi_{ad}(R_r) = -\tan \mu_r \sin \varphi_p = \tan \mu_r \cos \kappa_r = \tan \mu_r \cos(\Phi_p/2) \quad (4.17)$$

where  $(R_r)$  symbolizes that the rake angle depends on the location of point  $r$  on the cutting edges 1–2.

#### 4.8.3.2 Cutting Edge with Rake Face Having $\gamma_n = 0$

Because the rake angle in the T-hand-S  $\gamma_n = 0$ , Eq. 4.17 can be re-written accounting for Eqs. 4.16 and 4.7 as



$$\begin{aligned}
\gamma_{nw}(R_r) &= -\xi_{ad}(R_r) = -\arctan(\tan \mu_r \sin \varphi_p) = \\
&-\arctan \left[ \tan \left( \arcsin \frac{c_{ct}}{2R_r} \right) \sin \varphi_p \right] = -\arctan \left( \frac{c_{ct}}{2R_{pr}} \sin \varphi_p \right) = \\
&-\arctan \left( \frac{c_{ct}}{2R_{pr}} \cos \kappa_r \right) = -\arctan \left( \frac{c_{ct}}{2R_{pr}} \cos(\Phi_p/2) \right)
\end{aligned} \tag{4.18}$$

Equation 4.18 defines the distributing of rake angles along cutting edge 1–2, i.e.  $r_2 \leq R_r \leq r_1$ . Because  $r_1 > r_2$  and the approach angle  $\varphi_p$  and distance  $c_{ct}$  are the same for all points of cutting edge 1–2, the rake angle at point 2 is smaller than that at point 1.

#### 4.8.3.3 Cutting Edge with Modified Rake Surface with $\gamma_n \neq 0$

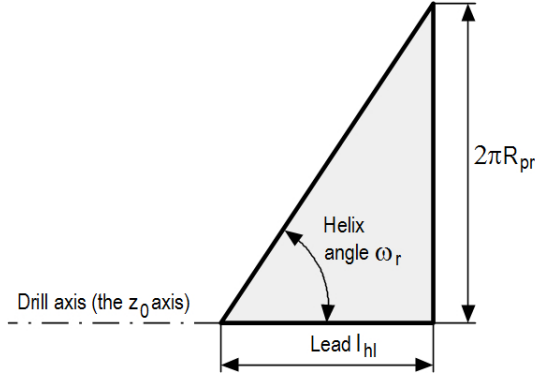
As above discussed, the rake surface of a drill can be modified by applying additional design features as plane rake face (for example shown in Figs.4.13, 4.17, 4.19 and 4.20) or grooves (for example shown in Fig. 4.14). The rake angle over cutting edge 1–2 then calculates as

$$\begin{aligned}
\gamma_{nw}(R_r) &= \gamma_n(R_r) - \xi_{ad}(R_r) = \gamma_n(R_r) - \arctan(\tan \mu_r \sin \varphi_p) = \\
&\gamma_n(R_{pr}) - \arctan \left[ \tan \left( \arcsin \frac{c_{ct}}{2R_r} \right) \sin \varphi_p \right] = \\
&\gamma_n(R_{pr}) - \arctan \left( \frac{c_{ct}}{2R_{pr}} \sin \varphi_p \right) = \\
&\gamma_n(R_{pr}) - \arctan \left( \frac{c_{ct}}{2R_{pr}} \cos \kappa_r \right) = \\
&\gamma_n(R_{pr}) - \arctan \left( \frac{c_{ct}}{2R_{pr}} \cos(\Phi_p/2) \right)
\end{aligned} \tag{4.19}$$

where  $\gamma_n(R_r)$  determines the distribution of the rake face on the modified rake surface. Often, this surface is ground with a constant rake angle in the T-hand-S so that this angle does not change over cutting edge 1–2, i.e.,  $\gamma_n(R_r) = Const$ .

#### 4.8.3.4. Helical Rake Face

The model shown in Fig. 4.75 is fully applicable to this case. In twist drills, the rake face is a helical surface normally having a constant lead,  $l_{hl}$ . This surface can be thought of as consisting of a number of helixes corresponding to points located on the cutting edge. Referring to Fig. 4.75, consider point  $r$  located at radius  $R_{pr}$ . The helix angle of the helix corresponding to this point can be found by unraveling the helix from the drill body (its helical flute) and representing the section as a right triangle as shown in Fig. 4.76.



**Fig. 4.76.** Unraveled helix corresponding to point  $r$  of the cutting edge 1-2

As follows from Fig. 4.76, the helix angle corresponding to point  $r$  calculates as

$$\omega_r = \arctan \frac{2\pi R_{pr}}{l_{hl}} \quad (4.20)$$

Normally in tool drawings, the helix angle,  $\omega_d$  corresponding to the drill outside diameter ( $d_{dr} = 2r_{dr}$ ) is indicated. Knowing this angle, one can calculate the helix angle corresponding to any point of the cutting edge 1-2 located at radius  $R_{pr}$  as

$$\omega_r = \arctan \left( \frac{R_{pr}}{r_{dr}} \tan \omega_d \right) \quad (4.21)$$

Following the same procedure used in Sect. 4.8.3.1, the normal rake angle  $\gamma_n$  is determined as the angle between the normal  $\mathbf{N}_p$  to the T-mach-S cutting edge plane (a plane tangent to the bottom of the hole being drilled at point  $r$  as shown in Fig. 4.75) and the normal  $\mathbf{N}_r$  is perpendicular to the cutting edge at point  $r$  and lies in the reference plane through point  $r$  as shown in Fig. 4.75. This angle calculates as

$$\tan \gamma_n = \frac{\|\mathbf{N}_r \times \mathbf{N}_p\|}{\mathbf{N}_r \cdot \mathbf{N}_p} \quad (4.22)$$

As the location of the cutting edge is the same as considered in Sect. 4.8.3.1, the normal  $\mathbf{N}_p$  is determined by Eq. 4.10. The normal  $\mathbf{N}_r$  can be determined as the cross product of vector  $\mathbf{p}_r$  along the cutting edge at point  $r$  and the vector  $\mathbf{p}_{tr}$  tangent to the rake face at point  $r$ .

The vector  $\mathbf{p}_r$  can be written through the tool cutting edge angle  $\kappa_r$  (equal to a half of the drill point angle  $\Phi_p$ )

$$\mathbf{p}_r = \mathbf{j} \sin \kappa_r + \mathbf{k} \cos \kappa_r \quad (4.23)$$

The vector  $\mathbf{p}_{tr}$  can be written as

$$\mathbf{p}_{tr} = -\mathbf{i} \tan \omega_r + \mathbf{j} \tan \omega_r \sin \mu_r + \mathbf{k} \quad (4.24)$$

then the normal  $\mathbf{N}_r$  is defined as

$$\mathbf{N}_r = \mathbf{p}_r \times \mathbf{r}_{tr} = \begin{vmatrix} \mathbf{i} & \mathbf{j} & \mathbf{k} \\ 0 & \sin \kappa_r & \cos \kappa_r \\ -\tan \omega_r \cos \mu_r & \tan \omega_r \cos \mu_r & 1 \end{vmatrix} = \quad (4.25)$$

$$\mathbf{i}(\sin \kappa_r - \tan \omega_r \sin \mu_r \cos \kappa_r) - \mathbf{j} \tan \omega_r \cos \mu_r \cos \kappa_r + \mathbf{k} \tan \omega_r \cos \mu_r \sin \kappa_r$$

Following the procedure described in Sect. 4.8.3.1, one can obtain [52]

$$\tan \gamma_n(R_r) = \frac{1 - \sin^2 \kappa_r \sin \mu_r}{\sin \kappa_r \cos \mu_r} \tan \omega_r - \cos \kappa_r \tan \mu_r \quad (4.26)$$

As expected, when  $\omega_r = 0$ , Eq. 4.26 coincides with Eq. 4.17 obtained for a straight flute. Substituting Eqs. 4.7 and 4.21 into Eq. 4.26, one obtains

$$\tan \gamma_n(R_{pr}) = \left( \frac{R_{pr}}{r_{dr}} \tan \omega_d \right) \frac{1 - \sin^2 \kappa_r \sin \left( \arctan \frac{c_{ct}/2}{R_{pr}} \right)}{\sin \kappa_r \cos \left( \arctan \frac{c_{ct}/2}{R_{pr}} \right)} - \cos \kappa_r \frac{c_{ct}/2}{R_{pr}} \quad (4.27)$$

An analysis of Eq. 4.27 shows that the normal rake angle of a cutting edge when the rake surface is helical depends on the point angle  $\Phi_p$  (as  $\kappa_r$  is half of the point angle), distance  $c_{ct}$  (often referred to in the literature as the web diameter  $d_{ww}$  although in general the cutting edge may consist of a number of parts with individual  $c_{ct}$ s or it can be inclined as per DIN 1214 Type B shown in Fig. 4.12), and on the helix angle  $\omega_d$ . Figure 4.77 shows the influence of the point angle for twist drill having the following parameters:  $\omega_d = 30^\circ$ ,  $d_{ww} = 0.2d_{dr}$  [52]. As can be seen, small point angles cause a significant increase of the normal rake angle in the vicinity of the periphery point 1 with a sharp decrease of this angle along the cutting edge towards the drill axis. For a drill with  $\Phi_p = 180^\circ$ , the normal rake angle varies along the cutting edge from  $30^\circ$  to  $3^\circ$ . For a drill with the standard point angle  $\Phi_p = 120^\circ$ , the normal rake angle varies from  $+30^\circ$  to  $-30^\circ$ . Therefore, an increase in the point angle reduces the spread in the normal rake angle along the cutting edge.

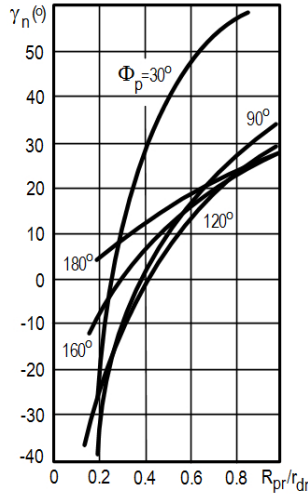


Fig. 4.77. Influence of the point angle on the normal flank angle

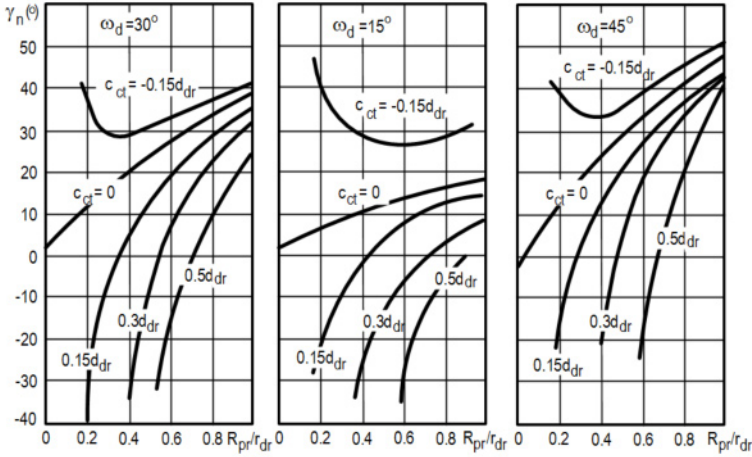
The latter occurs because the point angle affects the shape and thus curvature of the surface of cut (the bottom of the hole being drilled). In general in drilling, this surface is hyperboloid, which becomes a plane when  $\Phi_p = 180^\circ$ . When it happens, the normal to the surface of cut does not change its direction along the cutting edge remaining parallel to the  $z_0$ -axis. As such, the distance  $c_{ct}$  (the web diameter  $d_{ww}$ ) has only a weak influence on the normal rake angle. Equation 4.27 can be modified in this case as

$$\tan \gamma_n (R_{pr}) = \left( \frac{R_{pr}}{r_{dr}} \tan \omega_d \right) \cos \left( \arctan \frac{c_{ct}/2}{R_{pr}} \right) \tag{4.28}$$

The influence of the distance  $c_{ct}$  (the web diameter  $d_{ww}$ ) on the normal rake angle is shown in Fig. 4.78 for standard drills with  $\Phi_p = 120^\circ$ . As seen, an increase in  $c_{ct}$  leads to a decreasing  $\gamma_n$ . If the major cutting edge (lip) along drill radius is as in the drill design shown in Fig. 4.51b, then  $\mu_r = 0$  for any point of such a cutting edge. Equation 4.27 can be modified in this case as

$$\tan \gamma_n (R_{pr}) = \frac{R_{pr}}{r_{dr}} \frac{\tan \omega_d}{\sin \kappa_r} \tag{4.29}$$

An analysis of Eq. 4.29 shows that much smaller spread of the normal rake angle is achieved compared to standard twist drills. This is because, if the cutting edge extends along the drill radius, the surface of cut (the bottom of the hole being drilled) is a conical surface. The normal to this surface at any point of the cutting edge has the same direction that improves the distribution of the normal rake angle over the cutting edge.

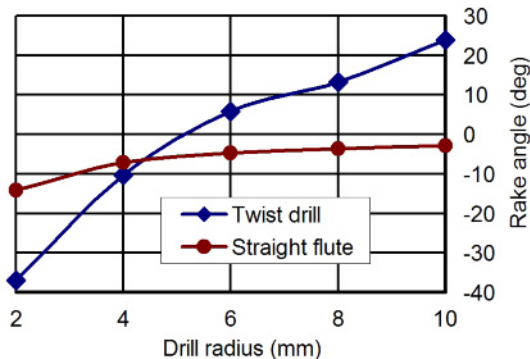


**Fig. 4.78.** Influence of the distance  $c_{ct}$  and the helix angle,  $\omega_d$  on the distribution of the normal rake angle

4.8.3.5 Example 4.1

Compare the distributions of the T-mach-S rake angle along the major cutting edge (lip) of straight flute and twist drills. Drill diameter  $d_{dr} = 20\text{mm}$ , web diameter (thickness)  $d_{ww} = c_{ct} = 4\text{mm}$ , helix angle of the drill flute  $\omega_d = 30^\circ$ .

Figure 4.79 shows the rake angle distribution along the major cutting edge (lip) for the twist and straight flute drills with the given parameters obtained using Eqs. 4.18 and 4.27, respectively. As can be seen, the rake angle for the twist drill varies from  $+24^\circ$  at the drill periphery (point 1) to  $-37^\circ$  at the inner end of the major cutting edge, while that for the straight flute drill varies from  $-3^\circ$  to  $-14^\circ$ . Therefore, in terms of cutting conditions, the straight flute drill has a much more desirable rake angle distribution.



**Fig. 4.79.** Rake angle distribution along the major cutting edge (lip) for a twist and a straight flute drills

#### 4.8.4 Inclination Angle

Cutting edge inclination angle  $\lambda_s$  is normally considered for the lip because it is zero for the chisel edge of a generic twist drill as the chisel edge of this drill is straight and passes through the origin  $0$ . Cutting edge inclination angle for the minor cutting edge is always equal to the margin helix angle.

Although this angle is not shown on twist drill drawings and its value is not set by these drawings, it has the same significance as for single-point tools. It affects chip formation and determines the direction of the chip flow. As the major cutting edge does not pass through the origin  $0$  of the  $x_0y_0z_0$  coordinate system, the cutting edge inclination angle varies along this edge according to the consideration discussed in Chap. 2, Sect. 2.7.3. The cutting edge inclination angle  $\lambda_s$  was defined as the angle between the cutting edge and the reference plane. It follows from Eq. 2.84 that the inclination angle of point  $r$  of cutting edge 1–2 in T-mach-S can be calculated as

$$\lambda_s = -\arcsin \frac{\mathbf{p}_r \cdot \mathbf{v}_r}{\|\mathbf{p}_r\| \cdot \|\mathbf{v}_r\|} \quad (4.30)$$

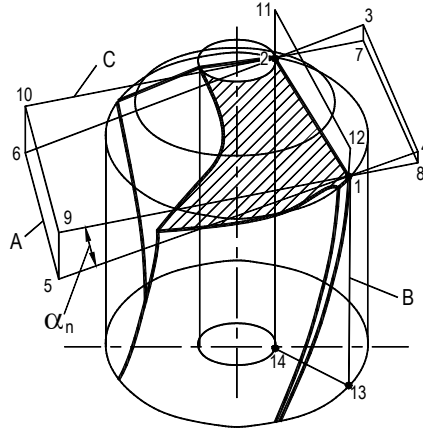
where vectors  $\mathbf{p}_r$  and  $\mathbf{v}_r$  are defined by Eqs. 4.9 and 4.8, respectively. Substituting these equations into Eq. 4.30, one can obtain

$$\lambda_{s-r} = -\arcsin \left( \frac{C_{ct}}{2R_{pr}} \sin \kappa_r \right) \quad (4.31)$$

Experience shows, however, that there are certain difficulties and confusions in understanding this angle in axial tools. VIEW A in Fig. 4.80 shows the true location of the cutting edge and sense of the cutting edge inclination angle  $\lambda_s$  for the considered point  $r$  and for the end points (1 and 2) of the major cutting edge (lip). Figure 4.80 also shows the variation of the cutting edge inclination angle  $\lambda_s$  for the drill data considered in Example 4.1. As can be seen, this angle varies along the cutting edge according to Eq. 4.31 with its minimum at point 1 (the periphery point or drill corner) and its maximum at point 2 where the major cutting edge joins the chisel edge.

As discussed in Chap. 3, Sect. 3.7, the sign of the inclination angle defines the chip flow direction, i.e., this direction deviated from the normal to the cutting edge by this angle. This allowed representing the direction of chip flows in the manner illustrated in Fig. 4.80 where this direction is shown by vectors of chip velocity for points 1,  $r$ , and 2 [52, 53]. However, such a representation of chip flow direction is incorrect as explained in the description of the simple model of chip flow shown in Fig. 4.48. In other words, the amount of chip formed in each drill revolution is much higher for point 1 than that for point  $r$  or 2. As a result, the chip flows almost perpendicular to the chip flow vectors shown in Fig. 4.80. However, the additional





**Fig. 4.81.** Visualization of the T-hand-S flank angle for planar rake face

The T-mach-S flank angle  $\alpha_{nw}$  varies along the cutting edge. As shown further in this chapter, it consists of two parts, namely the T-hand-S flank angle (which is constant for the planar flank) and the location part which depends on the coordinates of a considered point of the cutting edge in the  $x_0y_0z_0$  original (tool) coordinate system (Fig. 4.74).

*4.8.5.1 Relationships Between Flank Angles in the Standard Planes*

Figure 4.82 shows a model for analyzing the flank geometry. As before, cutting edge 1–2 is set in the original  $x_0y_0z_0$  coordinate system. Consider a point of interest ‘r’ on cutting edge 1–2. The location of this point  $r$  in the  $x_0y_0$  plane of the original coordinate system is uniquely determined by distance  $c_{cl}/2$  (the excess of the cutting edge over the  $y_0$ -axis) and by the location angle  $\mu_r$  calculated by Eq. 4.7.

The right-hand  $xyz$  current coordinate system (T-hand-S) is set as follows: its origin is in point  $r$ ; the  $z$ -axis is parallel to the  $z_0$ -axis; the  $x$ - and  $y$ -axes are perpendicular to the  $z$ -axis as shown in Fig. 4.82. Let  $\mathbf{i}$ ,  $\mathbf{j}$ , and  $\mathbf{k}$  be unit vectors along the positive  $x$ -,  $y$ -, and  $z$ -axes, respectively.

Following the result obtained for the T-mach-S normal flank angle,  $\alpha_{nw}$  in earlier consideration of the model shown in Fig. 2.44, one can apply Eq. 2.105 to the considered case. In other words, a T-mach-S flank angle for any point of the cutting edge should be considered as the sum of the T-hand-S flank angle and an additional flank angle due to location of the considered point in the T-mach-S. For example, the T-mach-S normal flank angle calculates as

$$\alpha_{nw} = \alpha_n + \xi_{ad-n} \tag{4.32}$$

where  $\alpha_n$  is the T-hand-S flank angle (as applied to the cutting edge (in the  $xyz$  coordinate system), and  $\xi_{ad-n}$  is the angle between the tool cutting edge planes in the T-hand-S and the T-mach-S.

As discussed in the analysis of the rake angle, the normal rake angle  $\alpha_n$  makes more sense in terms of understanding the physics of cutting. The same can be said



about the flank angle because the maximum flank forces act in the direction of the normal flank angle and thus the maximum flank tool wear takes place in this direction. Moreover, if the metal cutting theory is to be applied to drilling, the normal flank angle should be used in such an application.

As for the rake angle, the flank angle, in general, may differ for different points of the cutting edge. Therefore, a particular value of the flank angle should be attributed to a certain point of interest. Analyzing the flank angle at each point of the cutting edge, one should be able to obtain the distribution of the flank angle along a particular cutting edge.

By definition, the normal flank angle  $\alpha_{n-r}$  at a point of interest  $r$  in the T-hand-S is the angle between plane  $T$  tangent to the flank at point  $r$  and the cutting edge plane  $Q$  perpendicular to the assumed reference plane (plane  $yz$ ) (Chap. 2). In Fig. 4.82, planes  $T$  and  $Q$  are shown by their traces in SECTION  $n-n$ . In the T-mach-S, the vector of the cutting speed  $\mathbf{v}$  is not perpendicular to the  $yz$  plane so a new reference plane in this system should be defined as to be perpendicular to this vector. This plane  $G$  is shown by its trace in SECTION  $n-n$  in Fig. 4.82.

Figure 4.82 shows the following flank angles:

- $\alpha_{n-r}$ ,  $\xi_{ad-n-r}$ ,  $\alpha_{nw-r}$  are the flank angles in the orthogonal plane,  $P_o$ , which for the considered configuration coincides with the normal plane  $P_n$  (represented by SECTION  $n-n$  in Fig. 4.82). These angles are important to know when cutting conditions at point  $r$  of the cutting edge are of interest, including its cooling and lubricating. In other words, these angles are considered when one tries to apply the recommendations on the optimum flank angle or to optimize this angle using mechanics of cutting.
- $\alpha_{f-r}$ ,  $\xi_{ad-f-r}$ ,  $\alpha_{fw-r}$  are the flank angles in the assumed working plane,  $P_f$ . These angles define the condition of drill free penetration (without interference of the flanks and the bottom of the hole being drilled) into the workpiece in the feed direction. In any event,  $\alpha_{fw-r}$  should be positive to assure this condition.
- $\alpha_{p-r}$ ,  $\xi_{ad-p-r}$ ,  $\alpha_{pw-r}$  are the flank angles in the back plane,  $P_p$ . These angles define the condition of drill free rotation (without interference of the flanks and the bottom of the hole being drilled) about  $z_0$ -axis.

Consider first the relationships between flank angles in the T-hand-S. In the practice of drill design (with planar flanks), the T-hand-S normal flank angle  $\alpha_n$  is usually indicated on the tool drawing. Therefore, the relationship amongst the flank angles in the standard planes should be determined considering this angle as given. To do so, the following unit vectors are introduced. Still considering the same point of interest  $r$ , one can define unit vectors  $\mathbf{a}_{f-r}$ ,  $\mathbf{a}_{p-r}$ , and  $\mathbf{a}_{n-r}$  along the corresponding flank planes in the section planes  $P_f$ ,  $P_p$ , and  $P_o$ , respectively as shown in Fig. 4.82. In this figure,  $\mathbf{p}_m$  is a unit vector along the cutting edge 1-2. In the T-hand-S, these vectors can be defined through their coordinates:

$$\mathbf{p}_m = \mathbf{j} \cos \kappa_r + \mathbf{k} \sin \kappa_r \quad (4.33)$$

$$\mathbf{a}_{f-r} = -\mathbf{i} \cos \alpha_{f-r} + \mathbf{k} \sin \alpha_{f-r} \quad (4.34)$$

$$\mathbf{a}_{p-r} = -\mathbf{i} \cos \alpha_{p-r} - \mathbf{j} \sin \alpha_{p-r} \tag{4.35}$$

$$\mathbf{a}_{n-r} = -\mathbf{i} \cos \alpha_{n-r} - \mathbf{j} \cos \kappa_r \sin \alpha_{n-r} + \mathbf{k} \sin \kappa_r \sin \alpha_{n-r} \tag{4.36}$$

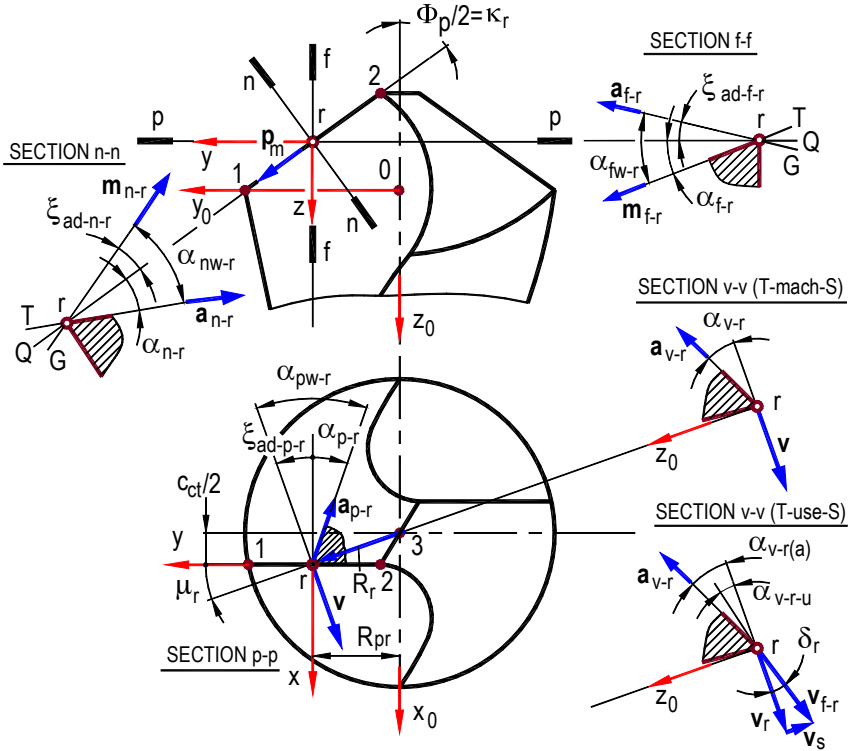


Fig. 4.82. Flank model for cutting edge 1-2

Because these four vectors belong to the same flank plane, the scalar triple product of any three of them is equal to zero. Consider the scalar triple product of vectors  $\mathbf{p}_m$ ,  $\mathbf{a}_{n-r}$ , and  $\mathbf{a}_{f-r}$ , which involves angles  $\varphi_p$ ,  $\alpha_{n-r}$  and  $\alpha_{f-r}$

$$\mathbf{p}_m \cdot (\mathbf{a}_{n-r} \times \mathbf{a}_{f-r}) = \begin{vmatrix} 0 & -\cos \varphi_p & -\sin \varphi_p \\ -\cos \alpha_{n-r} & -\sin \varphi_p \sin \alpha_{n-r} & \cos \varphi_p \sin \alpha_{n-r} \\ -\cos \alpha_{f-r} & 0 & \sin \alpha_{f-r} \end{vmatrix} = 0 \tag{4.37}$$

which yields

$$\tan \alpha_{f-r} = \frac{\tan \alpha_{n-r}}{\sin \kappa_r} \tag{4.38}$$

Equation 4.38 establish the relation between the T-hand-S flank angles in the orthogonal,  $P_o$  and the assumed working,  $P_f$  planes.

Considering the scalar products of vectors  $\mathbf{p}_m$ ,  $\mathbf{a}_{f-r}$ , and  $\mathbf{a}_{p-r}$ , which involves angles  $\varphi_p$ ,  $\alpha_{f-r}$  and  $\alpha_{p-r}$ :

$$\mathbf{p}_m \cdot (\mathbf{a}_{f-r} \times \mathbf{a}_{p-r}) = \begin{vmatrix} 0 & \sin \kappa_r & \kappa_r \\ -\cos \alpha_{f-r} & 0 & \sin \alpha_{f-r} \\ -\cos \alpha_{p-r} & -\sin \alpha_{p-r} & 0 \end{vmatrix} = 0 \quad (4.39)$$

one can obtain

$$\tan \alpha_{p-r} = \tan \alpha_{f-r} \tan \kappa_r \quad (4.40)$$

Combining Eqs. 4.38 and 4.40, one obtains relationship between  $\alpha_{p-r}$  and  $\alpha_{n-r}$  as

$$\tan \alpha_{f-r} = \frac{\tan \alpha_{n-r}}{\sin \kappa_r} \quad (4.41)$$

Combining Eqs. 4.40 and 4.41, one can obtain

$$\tan \alpha_{p-r} = \frac{\tan \alpha_{n-r}}{\cos \kappa_r} \quad (4.42)$$

Consider now the “location” part  $\xi_{ad}$  of the total flank angle  $\alpha$  (Eq. 4.32). Because all the considered flank surfaces are planes, the position of each flank plane in the  $x_0y_0z_0$  coordinate system is defined by: (1) the tool cutting edge angle equal to a half of the drill point angle, i.e.,  $\kappa_r = \Phi_p/2$ , (2) distance  $c_{ct}$ , (3) the T-hand-S flank angle  $\alpha_n$  applied on drill grinding.

The simplest determination of the angle between the tool cutting edge planes in the T-hand-S and the T-mach-S is in SECTION p-p where, as follows from Fig. 4.82, this angle calculates as

$$\xi_{ad-p-r} = \mu_r = \arctan \frac{c_{ct}}{2R_r} = \arctan \frac{c_{ct}}{2R_{pr}} \quad (4.43)$$

where  $R_{pr}$  is the radius of point  $r$  as shown in Fig. 4.82.

Thus, the T-mach-S flank angle in SECTION p-p (Fig. 4.82) calculates as

$$\alpha_{pw-r} = \alpha_{p-r} + \xi_{ad-p-r} \quad (4.44)$$

i.e., the location of the cutting edge above the  $y_0$ -axis leads to an increase in the total flank angle  $\alpha_{pw-r}$  compared to the T-hand-S flank angle  $\alpha_{p-r}$ . In Eq. 4.43,  $c_{ct}$  is

constant for cutting edge 1–2 while  $R_r$  varies and thus angle  $\xi_{ad}$  varies along cutting edge 1–2. Equation 4.44 defines the distributing of the T-mach-S flank angle along part 1–2 due to variation of  $R_r$  as angle  $\xi_{ad}$  varies because the T-hand-S flank angle  $\alpha_{p-r}$  is constant. Because  $\mu_{r1} < \mu_{r2}$ , the total flank angle,  $\alpha_{pw-r}$  at point 2 is greater than that at point 1.

To determine the relationships among angles  $\xi_{ad}$  in different section planes, consider the following unit vectors shown in Fig. 4.82:

- Vector  $\mathbf{v}_r$  in the direction of rotation velocity of point  $r$
- Vector  $\mathbf{m}_{n-r}$  in the direction of intersection of the orthogonal plane  $P_o$  and plane  $G$  with the sense as it shown in Fig. 4.82
- Vector  $\mathbf{m}_{f-r}$  in the direction of intersection of the assumed working plane  $P_f$  and plane  $G$  with the sense as it shown in Fig. 4.82

These vectors have the following coordinates:

$$\mathbf{v}_r = \mathbf{i} \cos \xi_{ad-p-r} - \mathbf{j} \sin \xi_{ad-p-r} \quad (4.45)$$

$$\mathbf{m}_{n-r} = -\mathbf{i} \cos \xi_{ad-p-r} + \mathbf{j} \sin \xi_{ad-p-r} \cos \kappa_r - \mathbf{k} \sin \xi_{ad-p-r} \sin \kappa_r \quad (4.46)$$

$$\mathbf{m}_{f-r} = -\mathbf{i} \cos \xi_{ad-f-r} - \mathbf{j} \sin \xi_{ad-f-r} \quad (4.47)$$

Because vectors  $\mathbf{p}_m$ ,  $\mathbf{v}_r$ ,  $\mathbf{m}_{n-r}$ , and  $\mathbf{m}_{f-r}$  belong to the same flank plane, the scalar triple product of any three of them is equal to zero (Appendix C). Considering the scalar triple product of vectors  $\mathbf{p}_m$ ,  $\mathbf{v}_r$ , and  $\mathbf{m}_{n-r}$

$$\mathbf{p}_m \cdot (\mathbf{v}_r \times \mathbf{m}_{n-r}) = \begin{vmatrix} 0 & \sin \kappa_r & \cos \kappa_r \\ \cos \xi_{ad-p-r} & -\sin \xi_{ad-p-r} & 0 \\ -\cos \xi_{ad-n-r} & \sin \xi_{ad-n-r} \cos \kappa_r & -\sin \xi_{ad-n-r} \sin \kappa_r \end{vmatrix} = 0 \quad (4.48)$$

one can obtain

$$\tan \xi_{ad-n-r} = \tan \xi_{ad-p-r} \cos \kappa_r \quad (4.49)$$

To derive an equation that correlates angles  $\xi_{ad-p-r}$  and  $\xi_{ad-f-r}$ , consider the scalar triple product of vectors  $\mathbf{p}_m$ ,  $\mathbf{v}_r$ , and  $\mathbf{m}_{f-r}$ :

$$\mathbf{p}_m \cdot (\mathbf{v}_r \times \mathbf{m}_{f-r}) = \begin{vmatrix} 0 & \sin \kappa_r & \cos \kappa_r \\ \cos \xi_{ad-p-r} & -\sin \xi_{ad-p-r} & 0 \\ -\cos \xi_{ad-f-r} & 0 & -\sin \xi_{ad-f-r} \end{vmatrix} = 0 \quad (4.50)$$

or

$$\tan \xi_{ad-p-r} = \tan \xi_{ad-f-r} \tan \kappa_r \quad (4.51)$$

Combining Eqs. 4.49 and 4.51, one can obtain

$$\tan \xi_{ad-n-r} = \tan \xi_{ad-f-r} \sin \kappa_r \quad (4.52)$$

Although the flank angles in the planes  $P_o(P_n)$ ,  $P_f$ , and  $P_p$  are of prime concern, one more plane should also be considered. This is the cutting speed plane,  $P_v$  which is perpendicular to the  $x_0y_0$  plane and contains the unit vector  $\mathbf{v}_r$  in the direction of the cutting velocity. This plane is represented by section plane  $v-v$  in Fig. 4.82. The sections in this plane are referred to as the cylindrical sections.

To determine the T-mach-S flank angle  $\alpha_{v-r}$ , consider a unit vector  $\mathbf{a}_{v-r}$  along the intersection of the flank plane with section plane  $v-v$  (Fig. 4.82):

$$\mathbf{a}_{v-r} = -\mathbf{i} \cos \xi_{ad-p-r} \cos \alpha_{v-r} + \mathbf{j} \sin \xi_{ad-p-r} \cos \alpha_{v-r} + \mathbf{k} \sin \alpha_{v-r} \quad (4.53)$$

Because the vectors  $\mathbf{a}_{f-r}$ ,  $\mathbf{p}_m$ , and  $\mathbf{a}_{v-r}$  belong to the same flank plane, their scalar triple product is equal to zero, i.e.,

$$\mathbf{p}_m \cdot (\mathbf{a}_{f-r} \times \mathbf{a}_{v-r}) = \begin{vmatrix} 0 & \sin \kappa_r & \cos \kappa_r \\ -\cos \alpha_{f-r} & 0 & \sin \alpha_{f-r} \\ -\cos \xi_{ad-p-r} \cos \alpha_{v-r} & \sin \xi_{ad-p-r} \cos \alpha_{v-r} & \sin \alpha_{v-r} \end{vmatrix} = 0 \quad (4.54)$$

and expanding this determinate, one obtains

$$\tan \alpha_{v-r} = \frac{\tan \alpha_{n-r} \cos \xi_{ad-p-r}}{\sin \kappa_r} + \cot \kappa_r \sin \xi_{ad-p-r} \quad (4.55)$$

This equation is used to determine the T-mach-S flank angle  $\alpha_{v-r}$  knowing the T-hand-S flank angle  $\alpha_{n-r}$  applied during drill sharpening. The inverse problem can also be solved as

$$\tan \alpha_{n-r} = \frac{\tan \alpha_{v-r} \sin \kappa_r}{\cos \xi_{ad-p-r}} - \tan \xi_{ad-p-r} \cos \kappa_r \quad (4.56)$$

The T-use-S flank angle  $\alpha_{v-r(a)}$  in a cylindrical section through point  $r$  accounts for the cutting feed velocity (the feed rate in Appendix A). This angle is smaller than  $\alpha_{v-r}$  (see SECTION  $v-v$ (T-mach-S) in Fig. 4.82) and calculates as

$$\alpha_{v-r-u} = \alpha_{v-r} - \delta_{u-r} \quad (4.57)$$

where angle  $\delta_{u-r}$  calculates as

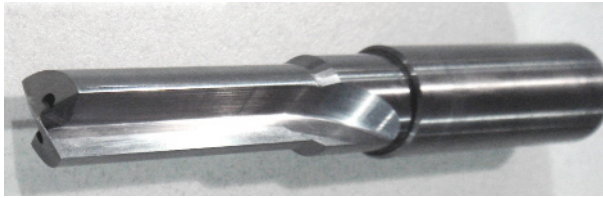
$$\delta_{u-r} = \arctan \frac{nf \cdot 10^{-3} / 60}{v_r / 60} = \arctan \frac{nf \cdot 10^{-3} / 60}{\omega R_r \cdot 10^{-3}} = \arctan \frac{0.5f}{\pi R_r} \quad (4.58)$$

where  $n$  is rotational speed (r.p.m) of the drill (spindle),  $f$  is the feed per revolution (mm/rev),  $\omega$  is angular velocity (rad/s),  $R_r$  is the radius of point  $r$  (mm).

Our calculations have shown that angle  $\delta_{u-r}$  is rather small and should be taken into consideration for points that locate close to the chisel edge when the cutting feed is more than 0.4mm/rev. For example for a point on the drill edge with  $R_r = 1.5\text{mm}$  and  $f = 0.5\text{mm/rev}$  this angle  $\delta_{u-r} = 3^\circ$ .

#### 4.8.5.2 Example 4.2

To exemplify the results obtained, the geometry of a common straight-flute drill used in the automotive industry and shown in Fig. 4.83 is considered. Figure 4.84 shows the relevant geometrical parameters.



**Fig. 4.83.** Straight-flute drill

There are a number of problems with this drill type in the automotive industry. As will be shown shortly, the root cause of all major problems is an excessive point angle  $\Phi_p$  which reaches  $160\text{--}165^\circ$ . The reason why such an excessive point angle is chosen is shown in Fig. 4.85. As can be seen, the distance between the hole exist and the next vein is small so that the choice of an excessive point angle is dictated by this distance.

Figure 4.86 shows the variations of the T-mach-S rake and flank angles with the radius of the drill under consideration. As seen, the T-mach-S rake angle decreases with the drill radius, becoming highly negative in the region close to the chisel edge. For a drill of 14% web (standard for aluminum machining) when  $c_{cl} = 0.6\text{mm}$  with point angle  $90^\circ$ , this angle reaches  $-54^\circ$  and when point angle is  $120^\circ$  (the most common case in general machining), the T-mach-S rake angle becomes  $-45^\circ$  in this region. The least variation of the rake angle has a drill with point angle  $160^\circ$  which reaches only  $-19^\circ$ . The latter is one of a very few advantages of drills with a great point angle.

It directly follows from Fig. 4.86 that the T-mach-S flank angles are greater than those in the T-hand-S. Moreover, the T-mach-S flank angle increases significantly when the radius of a considered point of the cutting edge becomes smaller. This significant variation of the T-mach-S flank angle is probably the major disadvantages of drills with planar flanks. Therefore, an  $8^\circ$  T-hand-S normal flank angle should be used for drilling steels (the low and moderated feed rate) while a  $12^\circ$  angle should be used in machining of aluminum and other light

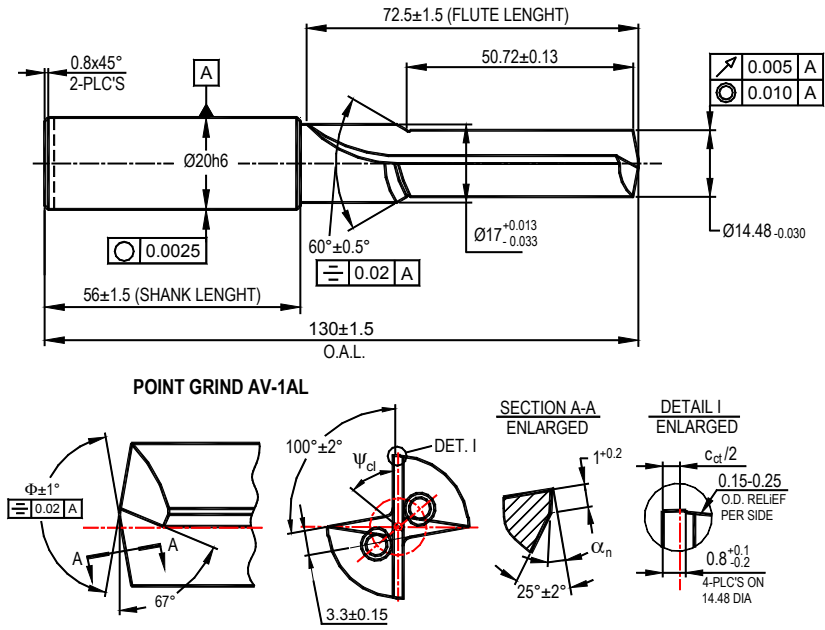


Fig. 4.84. Geometry of a straight-flute drill

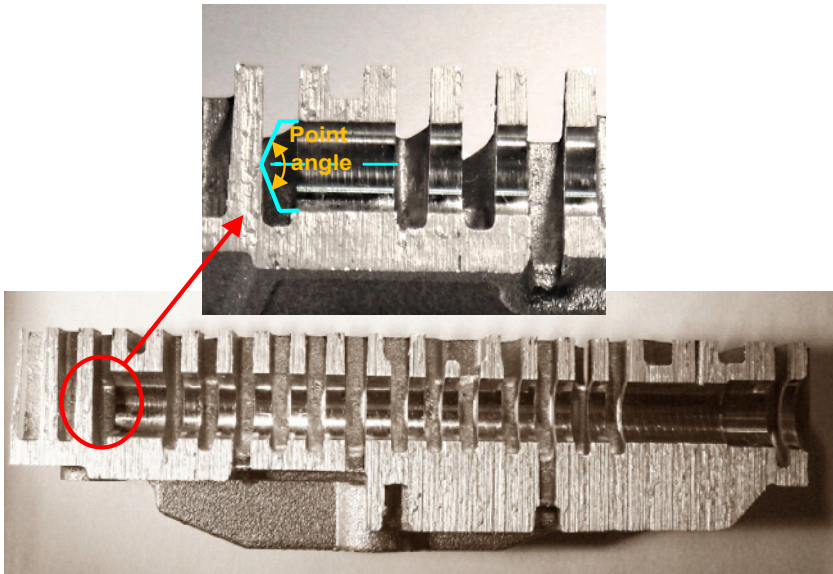
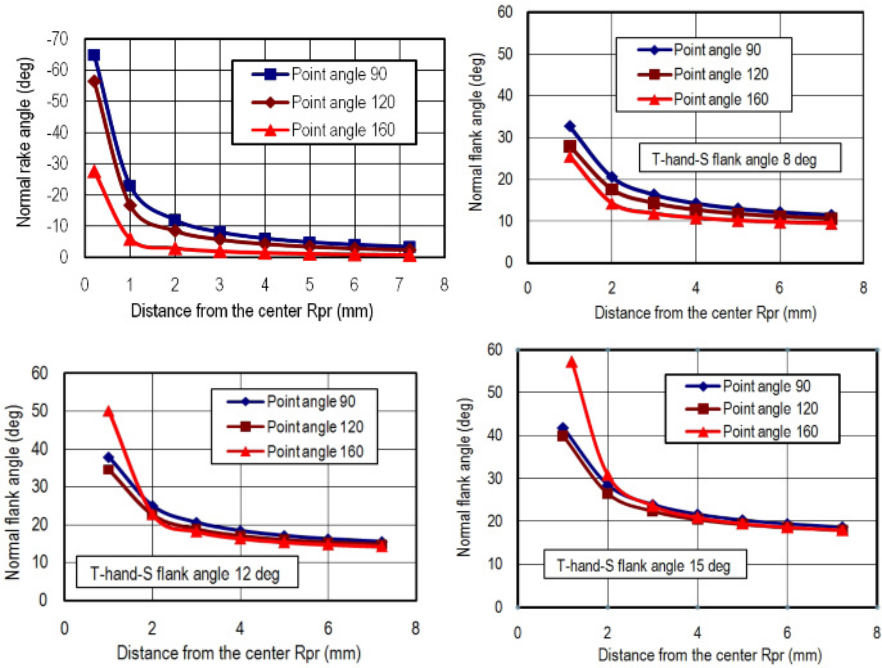


Fig. 4.85. Typical hole made in a typical automotive aluminum part (the upper valve body of a six-speed automatic transmission)



**Fig. 4.86.** Variations of the T-mach-S rake (the T-hand-S rake angle is zero) and flank (for different T-hand-S flank angles) over the major cutting edge

materials (when the feed rate is high) provided that drill and spindle runouts are small.

It also follows from Fig. 4.86 that the T-mach-S flank angle increases significantly in the region adjacent to the chisel edge for great drill point angles. This may compromise the strength of the cutting wedge in this region. To prevent this from happening, a portion of the cutting edge 1-2 adjacent to the chisel edge can be modified as discussed in the next section.

#### 4.8.5.3 Condition of Interference of a Flank Plane with the Bottom of the Hole Being Drilled

A drill works properly if and only if there is no interference of the drill flanks and the bottom of the hole being drilled, i.e., when there is some clearance between the drill flank and this bottom. Therefore, a model of interference is of importance as it helps in the proper drill design.

Consider the basic principle of such a model for a simple case when the flank surface is a single plane. To develop a condition of interference, consider an axial cross-section of the drill by the back plane  $P_p$  through the periphery point 1 as shown in Fig. 4.87. This plane intersects with the flank plane along the intersection line 1-a located at angle  $\alpha_{p-1}$  (the T-hand-S back flank angle). This plane  $P_p$  intersects with the bottom of the hole being drilled along the intersection circle having radius  $3-1$ , i.e. formed by the rotation of point 1 about drill axis. This circle crosses the flank plane at point a. As shown in Fig. 4.87, point  $b$  is located out of



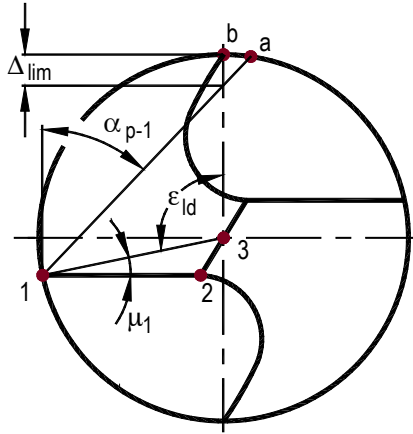


Fig. 4.87. Model of interference

the drill hill that assures drill free penetration into the hole being drilled (the absence of interference) if the feed is assumed to be zero.

Using the model shown in Fig. 4.87, one can write a condition of drill free penetration in the following form:

$$\Delta_{\text{lim}} > 0 \quad (4.59)$$

or

$$\alpha_{p-1} > \frac{\varepsilon_{ld}}{2} - \mu_1 \quad (4.60)$$

where  $\alpha_{p-1}$  is the T-hand-S back rake angle at periphery point 1, and  $\varepsilon_{ld}$  is the angle correspond to the drill lend having  $L_{ld}$  arc length as discussed in Sect. 4.6.2.2 and shown in Fig. 4.42 (for many common twist drills this angle is about  $90^\circ$ ),  $\mu_1$  being the location angle of point 1 determined from Eq. 4.7 as

$$\mu_1 = \frac{c_{ct}}{2r_{dr}} \quad (4.61)$$

In the most common case, the planar tool flank is ground with the constant T-hand-S normal flank angle,  $\alpha_n$  indicated in tool drawings. As such, the T-hand-S back rake angle at periphery point 1,  $\alpha_{p1}$  is also invariable over the cutting edge 1–2. It calculates using Eq. 4.42 as

$$\alpha_{p-1} = \alpha_p = \arctan \frac{\tan \alpha_n}{\cos \kappa_r} \quad (4.62)$$

For a common 120°-point angle twist drill,  $\mu_1=10^\circ$ ,  $\epsilon_{1d}=90^\circ$ ,  $\alpha_{p-1}$  according to Eq. 4.60 should be more than 35° and thus according to Eq. 4.62, the T-hand-S normal flank angle,  $\alpha_n$  should be more than 19° to assure the condition of drill free penetration. Obviously, it is not feasible. That is why, in the practice of drill design, at least two flank planes are used to form the drill flank surface. First one is ground to assure the proper flank angles along the cutting edge while the secondary flank plane is normally applied to clear the drill hill.

#### 4.8.6 Geometry of a Cutting Edge Located at an Angle to the $y_0$ -axis

To improve the tool geometry of drills, part of the cutting edge is ground inclined. The improvement relates to web thinning (Figs. 4.21–4.25) or to obtaining a better shape of the chip (Figs. 4.17 and 4.18). To understand what a change into geometry of a straight cutting edge brings its inclination with respect to the  $y_0$  axis, consider the drill shown in Fig. 4.88. As can be seen, the major cutting edge (lip) is represented by two parts, namely straight part 1–2 and the so-called web-thinning part 2–3. Radii of their ends are known to be  $r_1$ ,  $r_2$ , and  $r_3$ , respectively. The geometry of the straight part 1–2 calculates and other parameter of the drill are the same as considered above.

##### 4.8.6.1 Simplification Method

The analysis of the tool geometry for such a cutting edge can be significantly simplified and generalized if one realizes that the edge geometry is invariant to the rotation of the T-mach-S coordinate system about its origin  $O$  as the drill rotates about the  $z_0$ -axis and its geometry does not change in this rotation. Therefore, a simple method that utilizes this property can be used to analyze geometry of any straight cutting edge inclined with respect to the  $y_0$ -axis. Figure 4.89 exemplifies the proposed method. Figure 4.89a shows cutting edge 2–3 in its original location in the original coordinate system. The sense of invariable (along the entire edge)  $c_{pv}/2$  for cutting edge 2–3 is shown by the distance  $OA$  which is the perpendicular from the origin to the direction of cutting edge 2–3. Angle  $\psi_{12}$  is the position vector of this edge with respect to the  $y_0$ -axis.

Figure 4.89b shows what happens if the original coordinate system is rotated clockwise by this angle. In this figure, the location of cutting edge 2–3 is parallel to the  $y_0$ -axis and its geometry can be analyzed in the same way as discussed above for a cutting edge parallel to the  $y_0$ -axis with  $c_{pv}/2$  defined as the length of  $OA$ . Note that the approach angle of the cutting edge changes with rotation of the original coordinate system. Although for practical designs this change is insignificant, the exact value of this angle in general case calculates as

$$\varphi_{p23-st} = \arctan\left(\tan \varphi_{p23} \cos \psi_{23}\right) \quad (4.63)$$

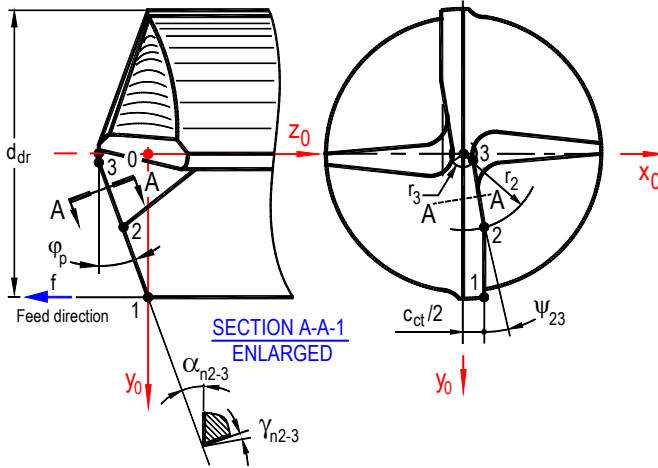


Fig. 4.88. Straight-flute drill with the inclined portion of the cutting edge

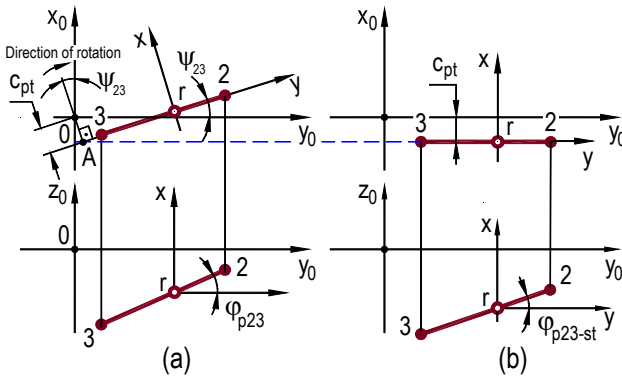


Fig. 4.89 Simplification in the analyses of drill geometry

4.8.6.2 Example 4.3

Consider the changes in the major cutting edge geometry if a portion of the major cutting edge is made as shown in Fig. 4.90. This is commonly called “web thinning” and the major advantage of this grind gained in practice is thought of as the reduction of the length of the chisel edge. This example is to show that, although this notion is correct, another attractive advantage can be gained due to web thinning.

Using the method described above,  $c_{ct}/2$  for cutting edge 2–3 is calculated to be 0.4mm compared to 0.6mm that considered for cutting edge 1–2 in Example 4.1. Variations of the T-mach-S rake (the T-hand-S rake angle is zero) and flank (for different T-hand-S flank angles) over the drill radius for the modified drill are shown in Fig. 4.91. A comparison of these results with those for cutting edge 1–2

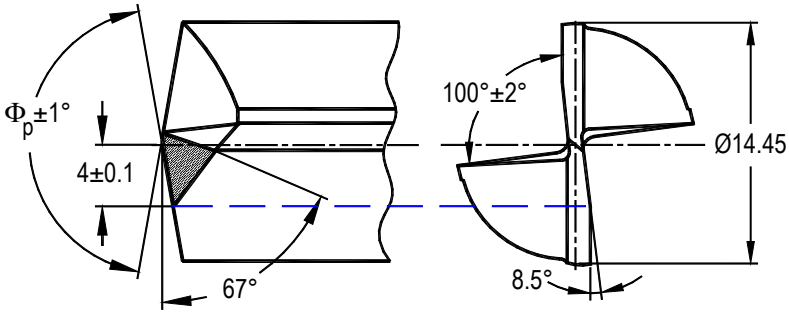


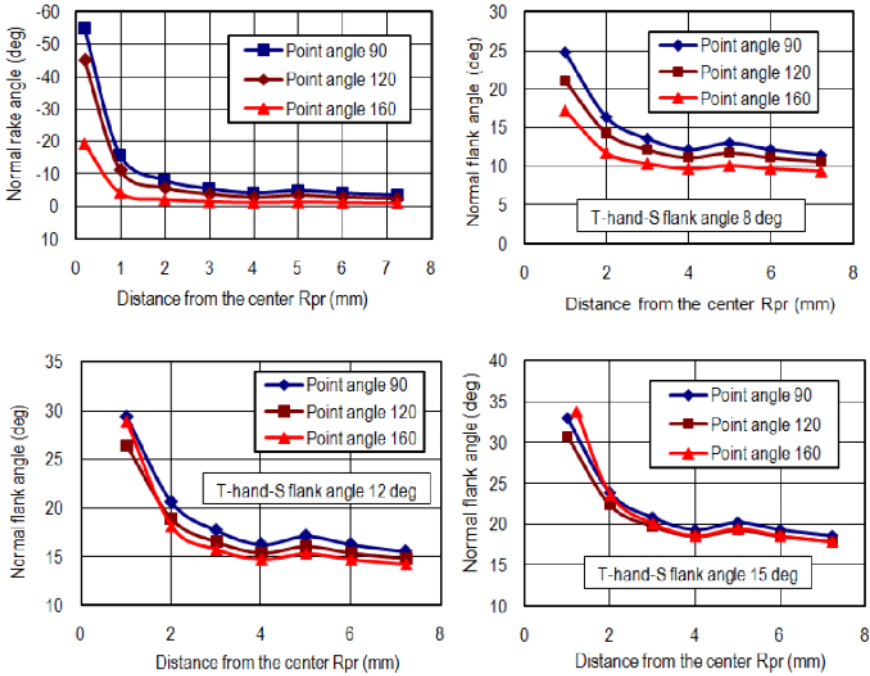
Fig. 4.90. Drill with web thinning

in Example 4.1 (shown in Fig. 4.86) shows that the modified drill is characterized by much more desirable rake and flank angles variation over the cutting edge. Particularly, the rake angle is much less negative and the flank angle does not reach unreasonable high values in the region adjacent to the chisel edge.

#### 4.8.6.3 Useful Generalizations

Examples 4.1 and 4.2 prove the known practical knowledge that even small change in the drill geometry may result in significant improvement in its geometry and thus performance. Therefore, an inclination of a cutting edge with respect to the  $y_0$ -axis is a powerful means at a tool designer's disposal to assure preferable cutting edge geometry. As such, the inclination angle of this edge to the  $y_0$ -axis and edge location in the original coordinate system (its extent) are two variables to be used in drill design. For example, a short edge with steep inclination angle can be used to assure preferable rake and flank angles in the region close to the chisel edge (Figs. 4.22 and 4.23) or a small inclination angle and a long cutting edge that can start right at the periphery point can be used to assure uniformity of these angles along edge length (Fig. 4.12, DIN 1412 Form S). The discussed model provides the rationale to both the mentioned empirical findings.

The directly opposite effects are achieved if the cutting edge is inclined in the direction opposite to that shown in Fig. 4.88. An inclination in this direction increases  $c_{cr}$ . As a result, the rake angle decreases according to Eqs. 4.7, 4.17, and 4.18 while the flank angle increases according to Eqs. 4.32, 4.43 and 4.44. These effects are very useful to improve geometry of twist drills. As mentioned above and will be discussed later, one of the inherent problems of twist drills is a high rake angle at the periphery region of the major cutting edges due to helical shape of the chip flute. On the other hand, the flank angle at the periphery cannot be selected to be optimal for a given work material because, as is clearly seen in Fig. 4.86, this angle significantly increases for the point of the major cutting edge (lip) located closer to the drill longitudinal axis. As seen, the selection of the optimum flank angle to be  $12^\circ$  at drill periphery point for a standard  $120^\circ$ -point-angle drill results in an unreasonable  $35^\circ$  flank angle at the inner end of this edge.



**Fig. 4.91.** Variations of the tool-in-machine rake (the tool-in-hand rake angle is zero) and flank (for different tool-in-hand flank angles) over the drill radius for the drill show in Fig. 4.90

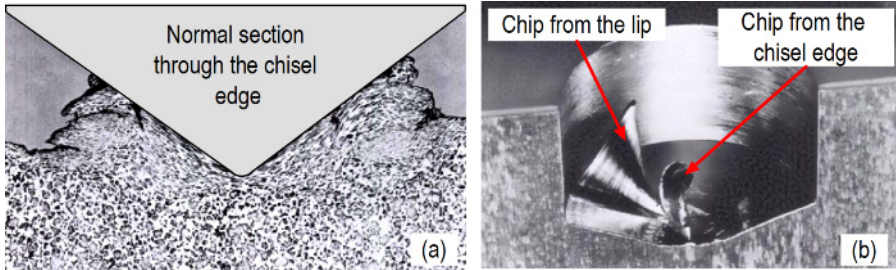
To solve these two problems simultaneously, a certain periphery portion of the major cutting edge can be inclined to the direction opposite to that shown in Fig. 4.88 and a small T-hand-S flank angle can be provided. Such an inclination results in a decrease in the rake angle with simultaneous increase in the flank angle that solves the discussed problems. Such a solution discovered empirically is incorporated in the patented drills shown in Figs. 4.17 and 4.18. The model developed in the above sections provides a clear rationale for such designs and means for a tool designer to select the optimal parameters of these drills.

## 4.8.7 Chisel Edge

### 4.8.7.1 Proper Representation of the Chisel Edge

As pointed out earlier, the chisel edge length (distance 2–4 in Fig. 4.74), its location angle known as the chisel angle,  $\psi_{cl}$ , and geometry (the rake and flank angles) of this edge define to a large extent the performance of the drill. The standard drill nomenclature always presents the chisel edge as a single design component of a drill as shown in Fig. 4.1. Moreover, a picture of the chisel edge that acts as an indenter penetrating into the workpiece (Fig. 4.92a) taken out of the context from a classical paper by Galloway [33] is presented in many manufacturing books while a picture of partially formed chips Fig. 4.92b by the

same author did not attract the same attention. A thoughtful reader going to Galloway’s paper [33] understands that the image shown in Fig. 4.92a is not taken in the cross-section not through point  $o$  (Fig. 4.74) which is the point where two chisel edges meet each other as claimed by Galloway [33]. Rather, it was taken in a cross section which is shifted from point 3. As a result, the chip seemingly formed on both sides of the chisel wedge is an optical illusion.



**Fig. 4.92.** Images of the chisel edge penetration into the workpiece commonly presented by manufacturing books: (a) normal section through the chisel edge, and (b) partially formed chips obtained using a quick-stop device

As pointed out in Sect. 4.6.2.1, if the chisel edge passes through the axis of rotation then there are two chisel edges – each one starts from the inner end of the major cutting edges (lips) and extends to the center of rotation. Each part has its rake and flank angles and the two chips form on each part as shown in Fig. 4.92b that flow in the opposite directions. Therefore, the tool geometry definitions discussed in Chap. 2 are fully applicable to these two parts of the chisel edge, i.e. each part has the rake and flank faces.

*4.8.7.2 Chisel Edge Formed by Two Flank Planes Having the Same T-hand-S Flank Angles*

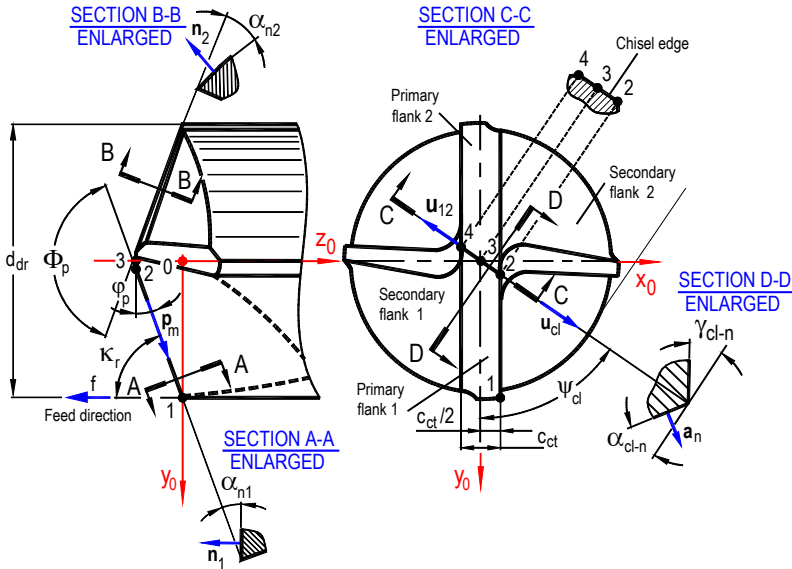
Figure 4.93 shows a model to determine geometry of the chisel edge. This figure shows the chisel edge 2–4 (its two parts 2–3 and 4–3) as formed by two flank planes 1 and 2 having flank angles  $\alpha_{n1}$  and  $\alpha_{n2}$ . All other parameters shown in this figure have been defined earlier. As can be seen in Fig. 4.93, the chisel edge is a line of intersection of two flank planes. Therefore, its orientation can be determined using the cross product of the normal vectors to these planes (Appendix C). To do that, two normal vectors  $\mathbf{n}_1$  and  $\mathbf{n}_2$  for the flank planes 1 and 2 (shown in Fig. 4.93) are defined as

$$\mathbf{n}_1 = -\mathbf{i} \sin \alpha_{n1} + \mathbf{j} \cos \alpha_{n1} \sin \varphi_p - \mathbf{k} \cos \alpha_{n1} \cos \varphi_p \tag{4.64}$$

$$\mathbf{n}_2 = \mathbf{i} \sin \alpha_{n2} - \mathbf{j} \cos \alpha_{n2} \sin \varphi_p - \mathbf{k} \cos \alpha_{n2} \cos \varphi_p \tag{4.65}$$

The position of their intersection line defined by directional vector is determined using Eq. C.16 (Appendix C) as

$$\begin{aligned}
 \mathbf{u}_{12} &= \mathbf{n}_1 \times \mathbf{n}_2 = \\
 & (n_{1y}n_{2z} - n_{1z}n_{2y})\mathbf{i} + (n_{1x}n_{2z} - n_{1z}n_{2x})\mathbf{j} + (n_{1x}n_{2y} - n_{1y}n_{2x})\mathbf{k} = \\
 & \mathbf{i} \left[ (\cos \alpha_{n1} \sin \varphi_p) (-\cos \alpha_{n2} \cos \varphi_p) - (-\cos \alpha_{n1} \cos \varphi_p) (-\cos \alpha_{n2} \sin \varphi_p) \right] + \quad (4.66) \\
 & \mathbf{j} \left[ (-\cos \alpha_{n1} \cos \varphi_p) \sin \alpha_{n2} - (-\sin \alpha_{n1}) (-\cos \alpha_{n2} \cos \varphi_p) \right] + \\
 & \mathbf{k} \left[ (-\sin \alpha_{n1}) (-\cos \alpha_{n2} \sin \varphi_p) - (\cos \alpha_{n1} \sin \varphi_p) \sin \alpha_{n2} \right]
 \end{aligned}$$



**Fig. 4.93.** Model for the chisel edge formed by two flank planes having the same flank angles

In a particular practical case when flank planes 1 and 2 are ground with the same flank angles, i.e., when  $\alpha_{n1} = \alpha_{n2} = \alpha_n$ , Eq. 4.66 simplifies to

$$\mathbf{u}_{12} = \mathbf{n}_1 \times \mathbf{n}_2 = -\mathbf{i} \cos^2 \alpha_n 2 \sin \varphi_p \cos \varphi_p - \mathbf{j} \cos \varphi_p 2 \cos \alpha_n \sin \alpha_n \quad (4.67)$$

and thus the chisel angle calculates as

$$\begin{aligned}
 \psi_{cl} &= \arctan \frac{\cos^2 \alpha_n 2 \sin \varphi_p \cos \varphi_p}{\cos \varphi_p 2 \cos \alpha_n \sin \alpha_n} = \arctan \frac{\sin \varphi_p}{\tan \alpha_n} = \\
 \arctan \frac{\cos \kappa_r}{\tan \alpha_n} &= \arctan \frac{\cos(\Phi_p/2)}{\tan \alpha_n} \quad (4.68)
 \end{aligned}$$

where  $\kappa_r$  is the tool cutting edge angle and  $\Phi_p$  is the point angle as shown in Fig. 4.93.

One important conclusion immediately follows from Eq. 4.67, namely, the both chisel edges 2–3 and 4–3 lay in a plane parallel to the  $x_0y_0$  plane as there is no projections of these edges on the  $z_0$  axis. They appear as a single edge as shown in SECTION C–C in Fig. 4.93. Because the flank angles in common drills are ground with the same flank angles (regardless the shape of the flank face), this creates an impression of the single chisel edge.

The normal T-hand-S flank angle of the chisel edge,  $\alpha_{cl-n}$  is the same as the T-mach-S chisel edge because it is considered in the  $x_0y_0z_0$  coordinate system. To determine this angle, consider three vectors in the flank plane, namely  $\mathbf{p}_m$  along the cutting edge 1–2,  $\mathbf{a}_n$  which is normal to the chisel flank face (Fig. 4.93), thus determined the  $x_0y_0z_0$  coordinate system as

$$\mathbf{a}_n = -\mathbf{i} \cos \alpha_{cl} \cos \psi_{cl} + \mathbf{j} \cos \alpha_{cl} \sin \psi_{cl} + \mathbf{k} \sin \alpha_{cl} \quad (4.69)$$

and the directional vector of the chisel edge  $\mathbf{u}_{cl}$  (shown in Fig. 4.93) defined as

$$\mathbf{u}_{cl} = \mathbf{i} \sin \psi_{cl} + \mathbf{j} \cos \psi_{cl} \quad (4.70)$$

As these three vectors belong to the same flank plane, their scalar triple product is equal to zero, i.e.,

$$\mathbf{p}_m \cdot (\mathbf{u}_{cl} \times \mathbf{a}_n) = \begin{vmatrix} 0 & -\sin \varphi_p & -\cos \varphi_p \\ \sin \psi_{cl} & \cos \psi_{cl} & 0 \\ -\cos \alpha_{cl} \cos \psi_{cl} & \cos \alpha_{cl} \sin \psi_{cl} & \sin \alpha_{cl} \end{vmatrix} = \quad (4.71)$$

$$\sin \alpha_{cl} \sin \psi_{cl} \sin \varphi_p + \cos \alpha_{cl} \cos \varphi_p = 0$$

Therefore, the normal T-hand-S (T-mach-S) flank angle of the chisel edge,  $\alpha_{cl-n}$  calculates as

$$\alpha_{cl-n} = \arctan \frac{\tan \varphi_p}{\sin \psi_{cl}} = \arctan \frac{1}{\tan \kappa_r \sin \psi_{cl}} = \arctan \frac{1}{\tan(\Phi_p/2) \sin \psi_{cl}} \quad (4.72)$$

Similar consideration for the normal T-hand-S (T-mach-S) rake angle of the chisel edge,  $\gamma_{cl-n}$  yields

$$\gamma_{cl-n} = \alpha_{cl-n} - 90^\circ \quad (4.73)$$



The total length of the chisel edge  $l_{2-4}$  (distance 2–4), which is actually is the sum of two chisel edges, i.e.  $l_{2-3} + l_{4-3}$ , calculates as

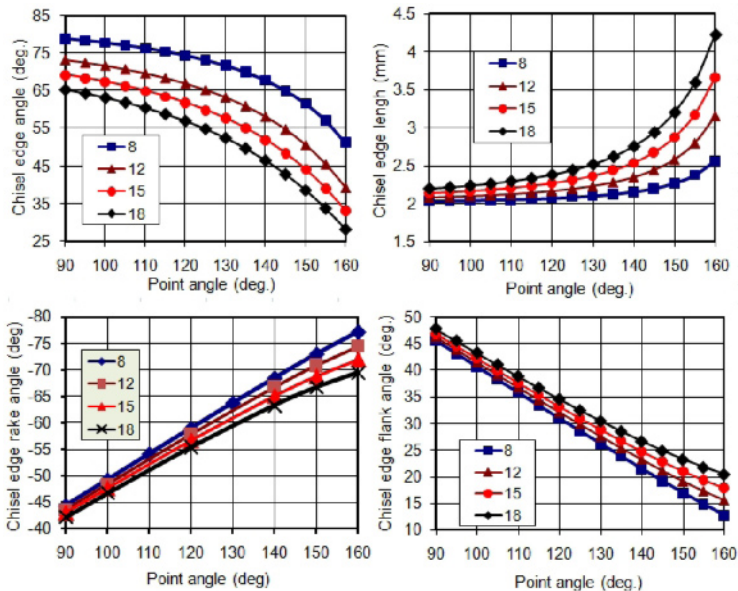
$$l_{cl} = l_{2-4} = \frac{c_{ct}}{\sin \psi_{cl}} \quad (4.74)$$

#### 4.8.7.3 Example 4.4

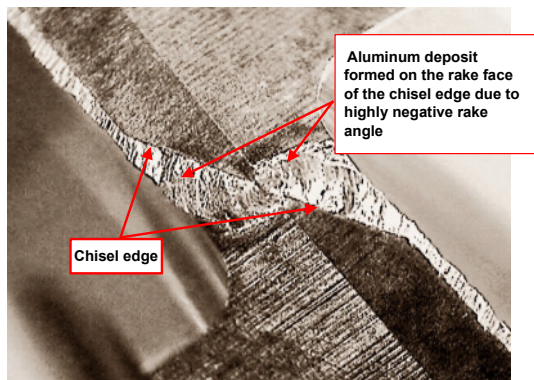
To exemplify the results obtained, consider the geometry of the chisel edge for a drill shown in Fig. 4.84 where the chisel edge is formed by two primary flank planes and  $c_{ct} = 1.2\text{mm}$ . Figure 4.94 presents the results of calculations. As seen, the angle of the chisel edge becomes smaller and its length becomes greater with increasing point angle. It is also seen that the variation is much more profound for large T-hand-S normal flank angles of the cutting edge. To increase the chisel angle and thus to reduce the length of the chisel edge, the T-hand-S flank angle should be chosen as small as it possible for a given work material. No more than an  $8^\circ$  T-hand-S flank angle should be selected in machining of steels and cast irons while that of  $12^\circ$  is the maximum that can be recommender for drilling aluminum alloys.

Probably the most important issue directly follows from the data shown in Fig. 4.94, namely the variation of the chisel edge rake angle with the point angle. When the point angle is  $160^\circ$  as in the considered case of valve body drilling (Fig. 4.84), the rake angle of the chisel edge exceeds  $-70^\circ$  that makes machining virtually impossible. When an aluminum alloy is drilled with this drill, the aluminum deposit (BUE) forms on the rake face of the chisel edge as shown in Fig. 4.95. This deposit destabilizes the drilling process causing a number of problems. The major problem is an increased cutting force, particularly its axial component (thrust). When a drill with the mentioned deposit drills through the veins, the increased axial force at the exit of each vein causes fracture of the thin wall having the shape of the bottom of the hole being drilled as shown in Fig. 4.96.

The fractured pieces shown in Fig. 4.96 are known in the automotive industry as the “sludge.” The sludge itself may cause significant problems when it stacks in the veins causing malfunction of automatic transmissions. Although it happens relatively rarely, the total liability cost associated with defective transmissions can be significant. Yet another significant problem with the formation of the sludge is faulty hole exits at the end of each vein. This includes fractured surface and feed marks as shown in Fig. 4.97. This fractured surface forms when the drill pushes out a sludge due to excessive axial force caused by the deposit on the rake faces of the chisel edge. When a sludge fractures out, the axial load on the drill is released so the drill moves fast forward leaving distinctive feed marks as seen in Fig. 4.97. These defects may cause malfunctions of the valves of automatic transmissions, resulting in a high rejection rate of the valve body assemblies in their testing.



**Fig. 4.94.** Chisel edge geometry parameters for the drill shown in Fig. 4.84 when its flank faces are having the same T-hand-S flank angles as shown in Fig. 4.93



**Fig. 4.95.** Aluminum deposit (BUE) formed on the rake faces of the chisel edge due to highly negative rake angle of this edge

*4.8.7.4 Chisel Edge Formed by Two Flank Planes Having Different T-hand-S Flank Angles*

Consider the next common case where the flank surface of each major cutting edge (lip) consists of two planes as shown in Fig. 4.98. As can be seen the so-called primary flank plane adjacent to the cutting edge 1–2 is applied with the normal T-hand-S flank angle  $\alpha_{n1-1}$  and extends from this cutting edge to the drill transverse axis so that this plane is the flank plane for the chisel edge 2–3. The secondary flank plane is then applied with the normal T-hand-S flank angle  $\alpha_{n1-2}$  as shown in

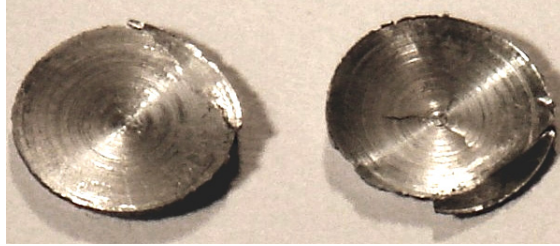


Fig. 4.96. Fractured walls at the exit of the veins

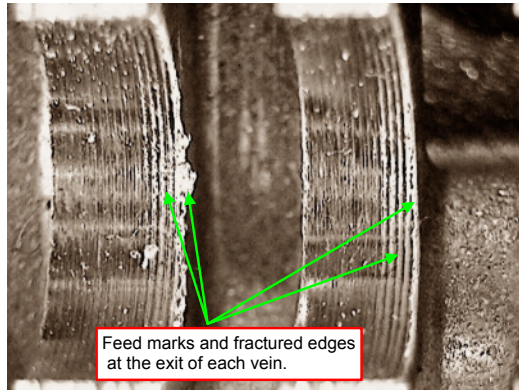


Fig. 4.97. Faulty hole exits

Figure 4.98 so that this plane serves as the rake plane for the chisel edge 4–3. Symmetrically, the primary and secondary flank planes are applied to the major cutting edge 4–5.

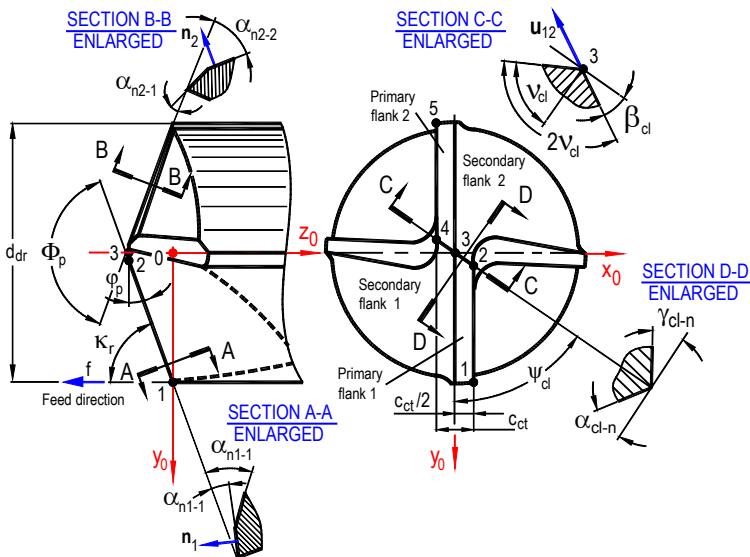
The directional vector of the chisel edge,  $\mathbf{u}_{12}$  is defined by Eq. 4.66. The ratio of its projections on the  $x_0$ -axis,  $p_x$  and on the  $y_0$ -axis,  $p_y$  defines the tangent of the inclination angle  $\psi_{cl}$ . Therefore, the latter calculates as

$$\psi_{cl} = \arctan \frac{2 \cos \alpha_{n1-1} \cos \alpha_{n2-2} \sin \varphi_p \cos \varphi_p}{\cos \varphi_p (\cos \alpha_{n1-2} \sin \alpha_{n2-2} + \sin \alpha_{n1-1} \cos \alpha_{n2-2})} =$$

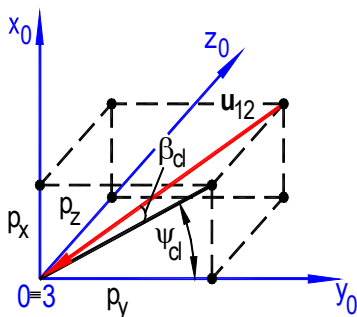
$$\arctan \frac{2 \sin \varphi_p}{\tan \alpha_{n2-2} + \tan \alpha_{n1-1}} = \arctan \frac{2 \cos \kappa_r}{\tan \alpha_{n2-2} + \tan \alpha_{n1-1}} = \tag{4.75}$$

$$\arctan \frac{2 \sin (\Phi_p / 2)}{\tan \alpha_{n2-2} + \tan \alpha_{n1-1}}$$

It also follows from Eq. 4.66 that the two chisel edges 2–3 and 3–4 are no more lines laying in a plane parallel to the  $x_0y_0$  plane as it was in the previous case. Rather, this edge makes an angle  $\beta_{cl}$  with such a plane as shown in Fig. 4.98. Figure 4.99 shows a simple model to determine this angle. As can be seen



**Fig. 4.98.** Model to determine parameters of the chisel edge when it formed by two flank planes having different flank angles



**Fig. 4.99.** Model to determine  $\beta_{cl}$

substituting projections on the  $x_0$  axis,  $p_x$  and on the  $z_0$ -axis,  $p_z$  taken from Eq. 4.66, one can obtain

$$\begin{aligned} \tan \beta_{cl} &= \frac{(\sin \alpha_{n1-1} \cos \alpha_{n2-2} - \cos \alpha_{n1-1} \sin \alpha_{n2-2}) \sin \varphi_p \sin \psi_{cl}}{-\cos \alpha_{n1-1} \cos \alpha_{n2-2} 2 \sin \varphi_p \cos \varphi_p} = \\ \frac{(\tan \alpha_{n2-2} - \tan \alpha_{n1-1}) \sin \psi_{cl}}{2 \cos \varphi_p} &= \frac{(\tan \alpha_{n2-2} - \tan \alpha_{n1-1}) \sin \psi_{cl}}{2 \sin \kappa_r} = \\ \frac{(\tan \alpha_{n2-2} - \tan \alpha_{n1-1}) \sin \psi_{cl}}{2 \sin (\Phi_p / 2)} & \end{aligned} \quad (4.76)$$

In tool drawings, the half chisel wedge angle,  $v_{cl}$  or chisel wedge angle  $2v_{cl}$  is normally indicated as shown in Fig. 4.98. The chisel wedge angle  $2v_{cl}$  calculates as

$$\begin{aligned}
 2v_{cl} &= 180^\circ - 2 \arctan \frac{(\tan \alpha_{n2-2} - \tan \alpha_{n1-1}) \sin \psi_{cl}}{2 \cos \varphi_p} = \\
 180^\circ - 2 \arctan \frac{(\tan \alpha_{n2-2} - \tan \alpha_{n1-1}) \sin \psi_{cl}}{2 \sin \kappa_r} &= \\
 180^\circ - 2 \arctan \frac{(\tan \alpha_{n2-2} - \tan \alpha_{n1-1}) \sin \psi_{cl}}{2 \sin (\Phi_p / 2)} &=
 \end{aligned} \tag{4.77}$$

The apex 3 formed at the intersection of chisel edges 2–3 and 4–3 (Fig. 4.98) can be regarded as the centering point of the drill. As this apex first touches the workpiece at the beginning of drilling, it helps to reduce drill wandering and thus reduces drill transverse vibrations at the hole entrance, i.e. a drill with such a point gains some self-centering ability. It was also found that this shape of the chisel edge makes the chisel wedge stronger and less susceptible to chipping.

Due to the fact that the chisel edge is not a line laying in a plane parallel to the  $x_0y_0$  plane, but rather is inclined to this plane by angle  $\beta_{cl}$ , the expression for its flank angle can be obtained combining Eqs. 4.72 and 2.12:

$$\begin{aligned}
 \alpha_{cl-n} &= \arctan \left( \frac{\tan \varphi_p}{\sin \psi_{cl}} \cos \beta_{cl} \right) = \arctan \left( \frac{1}{\tan \kappa_r \sin \psi_{cl}} \cos \beta_{cl} \right) = \\
 \arctan \left( \frac{1}{\tan (\Phi_p / 2) \sin \psi_{cl}} \cos \beta_{cl} \right) &=
 \end{aligned} \tag{4.78}$$

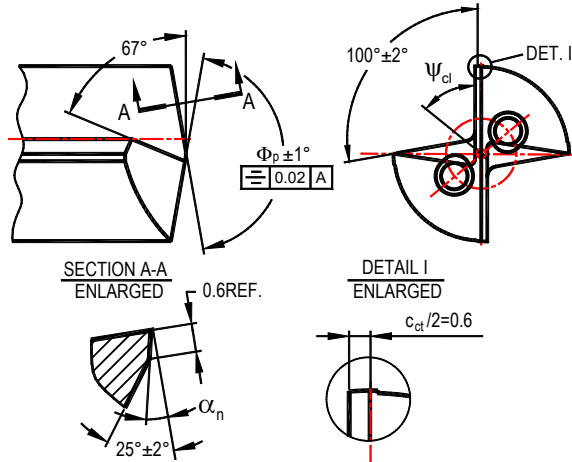
while the rake angle can be calculated using Eq. 4.73.

The length of each chisel edge  $l_{2-3}$  (distance 2–3) which is equal to  $l_{4-3}$  (distance 4–3) calculates accounting  $\beta_{cl}$  as

$$l_{2-3} = l_{4-3} = \frac{c_{cl}}{2 \sin \psi_{cl} \cos \beta_{cl}} \tag{4.79}$$

#### 4.8.7.5 Example 4.5

Consider the changes in the chisel edge geometry, if the flanks of the drill shown in Fig. 4.84 are ground so that the chisel edge is formed by the primary and the secondary flank planes as shown in Fig. 4.98. The changes in the point geometry are shown in Fig. 4.100. Figure 4.101 shows the geometry parameters for this case.



**Fig. 4.100.** The chisel edge of the drill formed by the primary and secondary flank planes

A simple comparison of Figs. 4.94 and 4.101 shows that in the case when the chisel edge is formed by the primary and secondary flanks, the chisel edge rake angle decreases while the length of the chisel edge increases. For example, for the drill with the chisel edge formed by two primary flank planes when the drill point angle is  $\Phi=120^\circ$ , T-hand-S flank angle  $\alpha_n = 8^\circ$ , the chisel edge rake angle  $\gamma_{cl-n} = -60^\circ$ , chisel edge angle  $\psi_{cl} = 75^\circ$ , and its length  $l_{cl} = 2.1\text{mm}$ , while for the drill shown in Fig. 4.100, when the drill point angle is  $\Phi = 120^\circ$ , T-hand-S flank angle  $\alpha_n = 8^\circ$ , the chisel edge rake angle  $\gamma_{cl-n} = -57^\circ$ , chisel edge angle  $\psi_{cl} = 59^\circ$ , and its length  $l_{cl} = 2.3\text{mm}$ . The difference in the drill geometry becomes more profound for great point angles. When  $\Phi=120^\circ$  and T-hand-S flank angle  $\alpha_n = 8^\circ$ , the chisel edge rake angle  $\gamma_{cl-n} = -78^\circ$ , chisel edge angle  $\psi_{cl} = 52^\circ$ , its length  $l_{cl} = 2.6\text{mm}$  for the first drill while the chisel edge rake angle  $\gamma_{cl-n} = -70^\circ$ , chisel edge angle  $\psi_{cl} = 30^\circ$ , and its length  $l_{cl} = 4\text{mm}$  for the second drill. The results obtained reveal the options in the selecting particular drill geometry. Namely, when the chisel edge is formed by two primary flank planes, its rake angle is more negative but its length is shorter while when this edge is formed by the primary and secondary flank planes, its rake angle is less negative but its length is greater. The differences are more profound in the case of great point angles.

The importance of the obtained results is fully appreciated if one recalls that cutting is ceased at a certain negative rake angle depending upon a particular work material. Therefore, the final choice of the first or second grind should be base on the workpiece material properties.

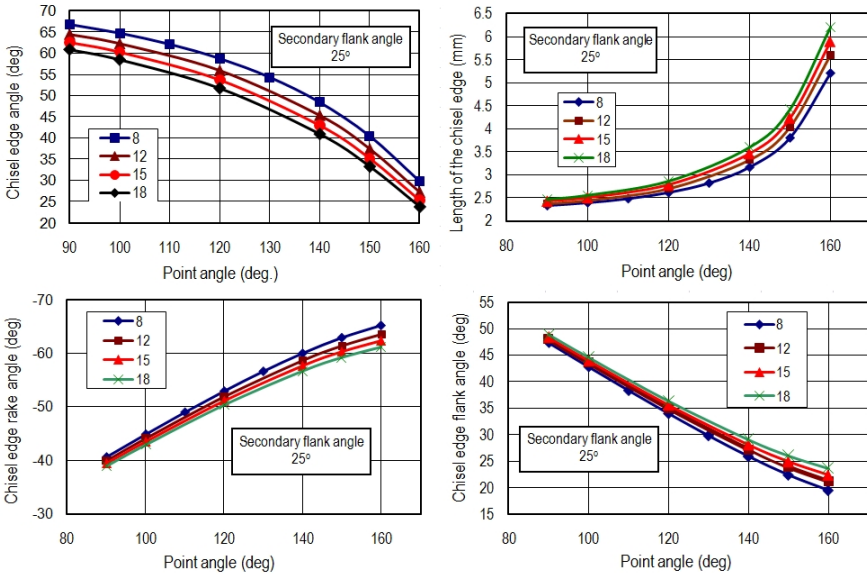


Fig. 4.101. Chisel edge geometry parameters for the grind shown in Fig. 4.100

Figure 4.102 shows a drill ground with the geometry parameters shown in Fig. 4.100. As can be seen, the chisel edge is formed by two adjacent edges meeting together to form the centering point as was predicted by the developed model.

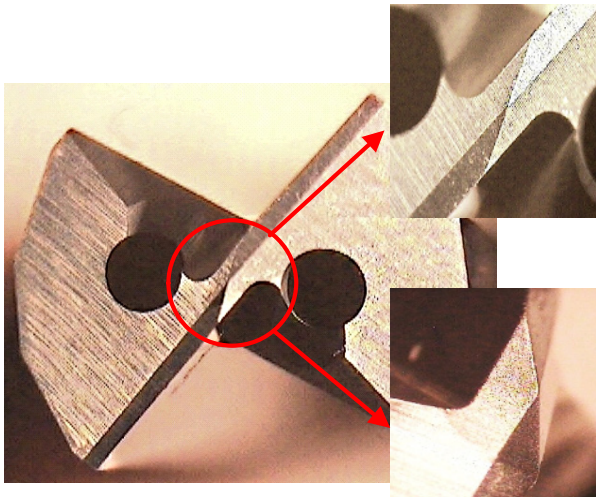


Fig. 4.102. Drill ground according to the geometry show in Fig. 4.100

Calculations showed that if the secondary flank is ground with T-hand-S flank angle  $\alpha_{n2} = 35^\circ$  instead of  $25^\circ$ , the chisel edge rake angle decreases further while the length of the chisel edge becomes greater. The chisel wedge angle decreases, resulting in some improvements in drill entrance conditions. However, a significant increase in the length of the chisel edge increases the axial force. Therefore, this kind of grind is suitable for small ( $90\text{--}100^\circ$ ) and normal ( $120^\circ$ ) point angles while it is completely unsuitable for great point angles ( $>140^\circ$ ).

#### 4.8.8 Drill Flank is Formed by Two Planes: Generalization

A general objective in forming a two-plane flank can be thought of as follows [52]: find the positions of the flank planes, primary  $R$  and secondary  $F$  (Fig. 4.103) that assures the following given drill geometry parameters: (1) flank angle of the periphery point 1  $\alpha_{v-1}$  in the cylindrical section  $v\text{--}v$  (Fig. 4.82), (2) point angle  $\Phi_p$  ( $=2\kappa_r$ ), and (3) chisel edge angle,  $\psi_{cl}$  (to maintain a certain length of chisel edge). The location of plane  $R$  is uniquely defined by the point angle and the flank angle at point 1. Therefore, the problem reduces to finding the location of plane  $F$  that assures the desired  $\psi_{cl}$ .

In the considered flank face design, the chisel edge is formed as an intersection line or rib of plane  $F$  for the current flank and plane  $R$  of the second lip. As the position of plane  $R$  is uniquely defined, the chisel edge can be found as a line belonging to this plane and having desirable chisel angle. Plane  $F$  should include this line. To define the location of plane  $F$ , a second line belonging to this plane is to be found. The line of intersection of planes  $R$  and  $F$  can be such a line. For simplicity, it can be assumed that a line of intersection of planes  $R$  and  $F$  passes through the drill axis as shown in Fig. 4.103 and thus its projection on the back plane (the plane face plane perpendicular to the drill longitudinal axis that coincides with the  $x_0y_0$  plane) makes an angle  $\psi_F$  with the  $y_0$ -axis. As this angle can be varied, the location of the plane  $F$  is not uniquely defined as the same chisel edge angle can be obtained under various combinations of angles  $\psi_F$  and inclination angles of plane  $F$ .

The analysis of this problem is carried out using the same methodology as that been used for single-plane flank. The purpose of this analysis is to establish geometrical relationships between angles  $\alpha_{v-1}$ ,  $\Phi_p$  ( $=2\kappa_r$ ),  $\psi_{cl}$  and  $\psi_F$ . To do that, the following unit vectors are introduced in the  $x_0y_0z_0$  coordinate system (Fig. 4.103):

$\mathbf{p}_m$  along the cutting edge 1–2

$$\mathbf{p}_m = \mathbf{j} \sin \kappa_r + \mathbf{k} \cos \kappa_r \quad (4.80)$$

$\mathbf{a}_{p-1}$  along the intersection line of plane  $F$  and section plane  $p\text{--}p$  (the back plane)

$$\mathbf{a}_{p-1} = -\mathbf{i} \cos \alpha_{p-1} - \mathbf{j} \sin \alpha_{p-1} \quad (4.81)$$



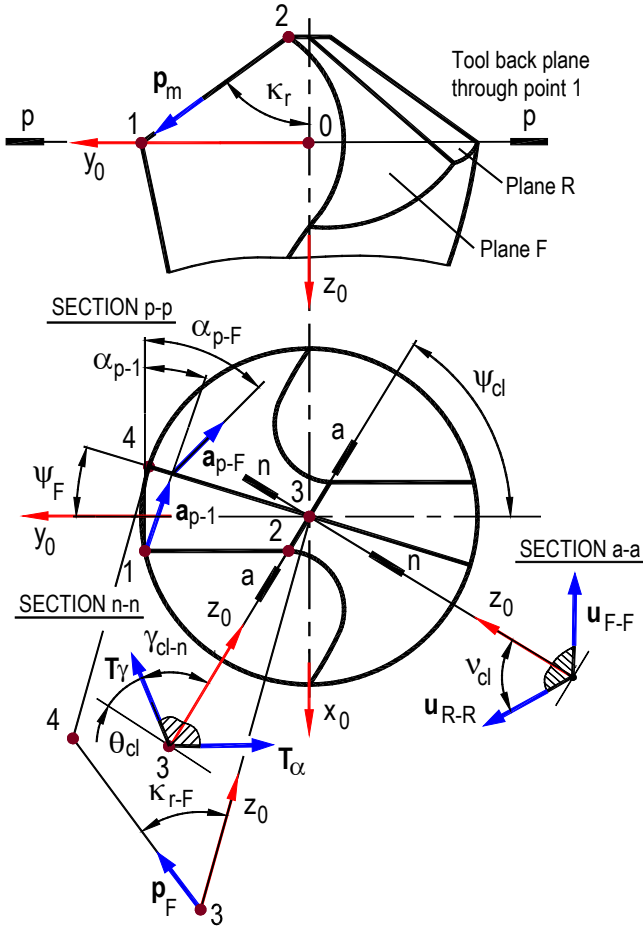


Fig. 4.103. Flank model for a two-plane flank

and along the chisel edge (SECTION a-a)

$$\mathbf{u}_{R-R} = \mathbf{i} \sin v_{cl} \sin \psi_{cl} + \mathbf{j} \sin v_{cl} \cos \psi_{cl} + \mathbf{k} \cos v_{cl} \quad (4.82)$$

Because these vectors belong to the same plane  $F$ , their scalar triple product is equal to zero, i.e.,

$$\mathbf{p}_m \cdot (\mathbf{a}_{p-1} \times \mathbf{u}_{R-R}) = \begin{vmatrix} 0 & \sin \kappa_r & \cos \kappa_r \\ -\cos \alpha_{p-1} & -\sin \alpha_{p-1} & 0 \\ \sin v_{cl} \sin \psi_{cl} & \sin v_{cl} \cos \psi_{cl} & \cos v_{cl} \end{vmatrix} = 0 \quad (4.83)$$

and expanding this determinant, one can obtain

$$\tan \nu_{cl} = \frac{\tan \kappa_r \cos \alpha_{p-1}}{\cos(\alpha_{p-1} + \psi_{cl})} \quad (4.84)$$

To determine angle  $\kappa_{r-F}$  which intersection line 3–4 makes with the  $x_0y_0$  plane (SECTION n–n), direct vector  $\mathbf{p}_F$  along this line. In the  $x_0y_0z_0$  coordinate system, this vector can be represented through its coordinates as

$$\mathbf{p}_F = -\mathbf{i} \sin \kappa_{r-F} \sin \psi_F + \mathbf{j} \sin \kappa_{r-F} \cos \psi_F + \mathbf{k} \cos \kappa_{r-F} \quad (4.85)$$

Because vectors  $\mathbf{p}_m$ ,  $\mathbf{a}_{p-1}$ , and  $\mathbf{p}_F$  belong to the same plane  $R$ , their scalar triple product is equal to zero, i.e.,

$$\begin{vmatrix} 0 & \sin \kappa_r & \cos \kappa_r \\ -\cos \alpha_{p-1} & -\sin \alpha_{p-1} & 0 \\ -\sin \kappa_{r-F} \sin \psi_F & \sin \kappa_{r-F} \cos \psi_F & \cos \kappa_{r-F} \end{vmatrix} = 0 \quad (4.86)$$

and expanding this determinant, one can obtain

$$\tan \kappa_{r-F} = \frac{\tan \kappa_r \cos \alpha_{p-1}}{\cos(\alpha_{p-1} - \psi_F)} \quad (4.87)$$

When  $\psi_F = 0$  then  $\kappa_{r-F} = \kappa_r$  and the intersection line of planes  $R$  and  $F$  is parallel to the cutting edge. When  $\psi_F = \alpha_{p-1}$ , angle  $\kappa_{r-F}$  is calculated calculates as

$$\tan \kappa_{r-F} = \tan \kappa_r \cos \alpha_{p-1} \quad (4.88)$$

To determine angle  $\alpha_{p-F}$  between the  $x_0z_0$  plane and the intersection line that plane  $F$  make with the back plane  $p$ – $p$ , a unit vector  $\mathbf{a}_{p-F}$  is directed along this line. In the  $x_0y_0z_0$  coordinate system, this vector can be represented through its coordinates as

$$\mathbf{a}_{p-F} = -\mathbf{i} \cos \alpha_{p-F} - \mathbf{j} \sin \alpha_{p-F} \quad (4.89)$$

Vector  $\mathbf{u}_{F-F}$  is along the chisel edge (Fig. 4.103) and is symmetrical to  $\mathbf{u}_{R-R}$ . Because vectors  $\mathbf{p}_F$ ,  $\mathbf{a}_{p-F}$ , and  $\mathbf{u}_{F-F}$  belong to the same plane  $F$ , their scalar triple product is equal to zero, i.e.,

$$\begin{vmatrix} -\cos \alpha_{p-F} & -\sin \alpha_{p-F} & 0 \\ -\sin \kappa_{r-F} \sin \psi_F & \sin \kappa_{r-F} \cos \psi_F & \cos \kappa_{r-F} \\ -\sin \nu_{cl} \sin \psi_{cl} & -\sin \nu_{cl} \cos \psi_{cl} & \cos \nu_{cl} \end{vmatrix} = 0 \quad (4.90)$$

and expanding this determinant, one can obtain

$$\tan \alpha_{p-F} = \frac{\tan \kappa_{r-F} \cos \psi_F + \tan \nu_{cl} \cos \psi_{cl}}{\tan \nu_{cl} \sin \psi_{cl} - \tan \kappa_{r-F} \sin \psi_F} \quad (4.91)$$

When  $\psi_F = 0$  then  $\kappa_{r-F} = \kappa_r$  then Eq. 4.92 becomes

$$\tan \alpha_{p-F} = \frac{\tan \kappa_r + \tan \nu_{cl} \cos \psi_{cl}}{\tan \nu_{cl} \sin \psi_{cl}} \quad (4.92)$$

The normal rake angle of the chisel edge is determined in SECTION n-n (Fig. 4.103) which is normal to the projection of the chisel edge into the  $x_0y_0$  plane (the back plane through point 1). A unit vector  $\mathbf{T}_\gamma$  (Fig. 4.103) is introduced along the line of intersection of plane  $F$  and SECTION n-n. In the  $x_0y_0z_0$  coordinate system, this vector can be represented through its coordinates as

$$\mathbf{T}_\gamma = -\mathbf{i} \cos \theta_{cl} \sin \psi_{cl} + \mathbf{j} \sin \theta_{cl} \cos \psi_{cl} + \mathbf{k} \sin \theta_{cl} \quad (4.93)$$

Because vectors  $\mathbf{T}_\gamma$ ,  $\mathbf{a}_{p-F}$ , and  $\mathbf{p}_F$  belong to the same plane  $F$ , their scalar triple product is equal to zero, i.e.,

$$\begin{vmatrix} -\cos \alpha_{p-F} & -\sin \alpha_{p-F} & 0 \\ -\sin \kappa_{r-F} \sin \psi_F & \sin \kappa_{r-F} \cos \psi_F & \cos \kappa_{r-F} \\ -\cos \theta_{cl} \sin \psi_{cl} & \sin \theta_{cl} \cos \psi_{cl} & \sin \theta_{cl} \end{vmatrix} = 0 \quad (4.94)$$

and expanding this determinant, one can obtain

$$\tan \theta_{cl} = \frac{\sin(\alpha_{p-F} + \psi_F)}{\tan \kappa_{r-F} \cos(\alpha_{p-F} - \psi_F)} \quad (4.95)$$

When  $\psi_F = 0$ , Eq. 4.96 becomes

$$\tan \theta_{cl} = \frac{\sin(\alpha_{p-F} + \psi_F)}{\tan \kappa_r \cos \alpha_{p-F}} \quad (4.96)$$

Assuming that the feed does not the rake angle of the chisel edge,  $\gamma_{cl-n}$ , this angle calculates as

$$\gamma_{cl-n} = 90^\circ - \theta_{cl} \quad (4.97)$$

The normal flank angle of the chisel edge is determines in SECTION n-n (Fig. 4.103) which is normal to the projection of the chisel edge into the  $x_0y_0$  plane (the back plane through point 1). A unit vector  $\mathbf{T}_\alpha$  (Fig. 4.103) is introduced along the

line of intersection of plane R and SECTION n–n. In the  $x_0y_0z_0$  coordinate system, this vector can be represented through its coordinates as

$$\mathbf{T}_\alpha = -\mathbf{i} \cos \alpha_{cl-n} \cos \psi_{cl} + \mathbf{j} \cos \alpha_{cl-n} \sin \psi_{cl} + \mathbf{k} \sin \alpha_{cl-n} \quad (4.98)$$

The flank angle of the chisel edge,  $\alpha_{cl-n}$  can be determined considering unit vectors  $\mathbf{T}_\alpha$ ,  $\mathbf{a}_{p-1}$ ,  $\mathbf{p}_m$  which belong to the same plane  $R$ . Therefore, their scalar triple product is equal to zero, i.e.,

$$\begin{vmatrix} 0 & \sin \kappa_r & \cos \kappa_r \\ -\cos \alpha_{p-1} & -\sin \alpha_{p-1} & 0 \\ -\cos \alpha_{cl-n} \cos \psi_{cl} & \cos \alpha_{cl-n} \cos \psi_{cl} & \sin \alpha_{cl-n} \end{vmatrix} = 0 \quad (4.99)$$

and expanding this determinant, one can obtain

$$\tan \alpha_{cl-n} = \frac{\sin(\psi_{cl} - \alpha_{p-1})}{\tan \kappa_r \cos \alpha_{p-1}} \quad (4.100)$$

#### 4.8.9 Drill Flank Angle Formed by Three Planes

The flank surface of each major cutting edge can be formed by three planes as shown in Figs. 4.30 and 4.32. A model for such a three-plane surface is shown in Fig. 4.104 where plane  $R$  is directly forms the cutting edge 1–2. This plane followed by planes  $F$  and  $Q$ . The location of plane  $R$  is fixed by the drill point angle and the rake angle  $\alpha_{p-1}$  of the periphery point 1. The location of plane  $Q$  can be defined by two angles: the chisel edge angle  $\psi_{cl}$  and the normal rake angle of the chisel edge,  $\gamma_{cl-n}$ . The plane  $R$  can have various positions. Its position can be defined either by the intersection lines that this plane makes with planes  $F$  and  $Q$  or by the intersection line between planes  $F$  and  $R$  and the angle between planes  $Q$  and  $F$ . Assuming the angle  $\psi_{1F}$  and half-point angle  $\kappa_{r-Q}$  intersection line 3–5 between planes  $F$  and  $Q$  to be given. Angle  $\psi_{1F}$  is selected to assure the sufficient strength of the cutting wedge of the major cutting edge and condition of drill free penetration into the hole being drilled (no interference between drill flank and the bottom of the hole being drilled). Angle  $\kappa_{r-Q}$  is selected to be less than  $\kappa_r$  to assure sufficient space for the flow of the chip formed by the chisel edge. If angles  $\Phi_p (=2\kappa_r)$ ,  $\psi_{cl}$ ,  $\alpha_{p-1}$ , and  $\psi_F$  are known then the half point angle  $\kappa_{r-F}$  of the intersection line 3–4 of plane  $R$  and  $F$  can be calculated using Eq. 4.88, the half point angle of the chisel edge,  $\nu_{cl}$  calculates using Eq. 4.85, and the flank angle of the chisel edge calculates using Eq. 4.101.

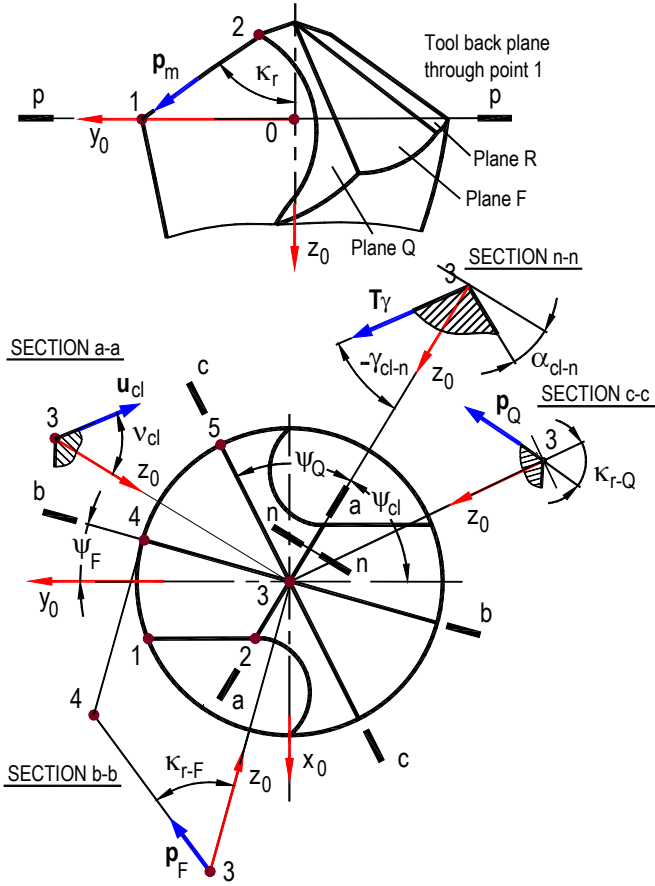


Fig. 4.104. Flank model for a three-plane flank

The relationship between the rake angle of the chisel edge  $\gamma_{cl-n}$  and angle  $\psi_Q$  (the angle between projections of the chisel edge and intersection line 3–5 into the  $x_0y_0$  plane as shown in Fig. 4.104. To do that, the following unit vectors are introduced:  $\mathbf{u}_{cl}$  along the chisel edge:

$$\mathbf{u}_{cl} = \mathbf{i} \sin \nu_{cl} \sin \psi_{cl} + \mathbf{j} \sin \nu_{cl} \cos \psi_{cl} - \mathbf{k} \cos \nu_{cl} \quad (4.101)$$

$\mathbf{p}_Q$  along intersection line 3–5

$$\mathbf{p}_Q = \mathbf{i} \sin \kappa_{r-Q} \sin (\psi_{cl} - \psi_Q) + \mathbf{j} \sin \kappa_{r-Q} \cos (\psi_{cl} - \psi_Q) - \mathbf{k} \cos \kappa_{r-Q} \quad (4.102)$$

$\mathbf{T}_\gamma$  in the plane  $Q$  at angle  $\gamma_{cl-n}$  to the  $z_0$ -axis

$$\mathbf{T}_\gamma = \mathbf{i} \sin \gamma_{cl-n} \cos \psi_{cl} - \mathbf{j} \sin \gamma_{cl-n} \sin \psi_{cl} + \mathbf{k} \cos \gamma_{cl-n} \quad (4.103)$$

Vectors  $\mathbf{u}_{cl}$ ,  $\mathbf{p}_Q$ , and  $\mathbf{T}_\gamma$  belong to the same plane  $Q$ . Therefore, their scalar triple product is equal to zero, i.e.,

$$\begin{vmatrix} \sin v_{cl} \sin \psi_{cl} & \sin v_{cl} \cos \psi_{cl} & -\cos v_{cl} \\ \sin \kappa_{r-Q} \sin(\psi_{cl} - \psi_Q) & \sin \kappa_{r-Q} \cos(\psi_{cl} - \psi_Q) & -\cos \kappa_{r-Q} \\ \sin \gamma_{cl-n} \cos \psi_{cl} & -\sin \gamma_{cl-n} \sin \psi_{cl} & \cos \gamma_{cl-n} \end{vmatrix} = 0 \quad (4.104)$$

and expanding this determinant, one can obtain

$$\tan \gamma_{cl-n} = \frac{\sin \kappa_{r-Q}}{\cot \kappa_{r-Q} - \cot v_{cl} \cos \psi_Q} \quad (4.105)$$

When  $\gamma_{cl-n} = 0$ , angle  $\psi_Q = 0$ .

To determine the position of plane  $F$ , angle  $\alpha_{p-F}$  should be known. To determine angle  $\alpha_{p-F}$  between the  $x_0z_0$  plane and the intersection line that plane  $F$  makes with the back plane  $p-p$ , consider unit vector  $\mathbf{a}_{p-F}$  defined by Eq. 4.90, vector  $\mathbf{p}_F$  defined by Eq. 4.86 and vector  $\mathbf{p}_Q$  defined by Eq. 4.103. Because these vectors all belong to plane  $F$ , their scalar triple product is equal to zero, i.e.,

$$\begin{vmatrix} -\cos \alpha_{p-F} & -\sin \alpha_{p-F} & 0 \\ -\sin \kappa_{r-F} \sin \psi_F & \sin \kappa_{r-F} \cos \psi_F & \cos \kappa_{r-F} \\ \sin \kappa_{r-Q} \sin(\psi_{cl} - \psi_Q) & \sin \kappa_{r-Q} \cos(\psi_{cl} - \psi_Q) & -\cos \kappa_{r-Q} \end{vmatrix} = 0 \quad (4.106)$$

and expanding this determinant one can obtain

$$\tan \alpha_{p-F} = \frac{\tan \kappa_{r-F} \cos \psi_F + \tan \kappa_{r-Q} \cos(\psi_{cl} - \psi_Q)}{\tan \kappa_{r-Q} \sin(\psi_{cl} - \psi_Q) - \tan \kappa_{r-F} \sin \psi_F} \quad (4.107)$$

The discussed model and methods of determination of the locations of flank planes can be used to design any drill, including the whole variety of split-point drills. An important consideration in such a designing is to assure the proper grinding of the designed drill point which might have multiple planes. To deal with this issue and to simplify programming of the controllers of multi-axis CNC drill grinders, the normal to each plane of the flank face should be determined. Programming of a CNC controller to grind a particular flank plane, one has to assure that the normal to this plane is perpendicular to the working surface of the grinding wheel. Normally, the angular position of the drill (rotation and translation about the  $z_0$  axis) is accomplished by the spindle that holds the drill, while the grinding wheel spindle handles other positional motions.

The normal to each flank plane can be determined using the cross product of two known vectors belonging to this plane (Fig. C.7, Appendix C). In the considered case, the normal to plane  $R$  is defined as cross product of the known vectors of  $\mathbf{p}_m$  and  $\mathbf{a}_{p-1}$ , the normal to plane  $Q$  is defined using the known vectors  $\mathbf{T}_\gamma$  and  $\mathbf{p}_Q$ , and the normal to plane  $F$  is determined using the known vectors  $\mathbf{p}_F$  and  $\mathbf{p}_Q$ . For example, the normal to plane  $F$  is determined as

$$\mathbf{N}_F = \mathbf{p}_F \times \mathbf{p}_Q = \begin{vmatrix} \mathbf{i} & \mathbf{j} & \mathbf{k} \\ -\sin \kappa_{r-F} \sin \psi_F & \sin \kappa_{r-F} \cos \psi_F & \cos \kappa_{r-F} \\ \sin \kappa_{r-Q} \sin(\psi_{cl} - \psi_Q) & \sin \kappa_{r-Q} \cos(\psi_{cl} - \psi_Q) & -\cos \kappa_{r-Q} \end{vmatrix} \quad (4.108)$$

and expanding this determinant, one can obtain

$$\begin{aligned} \mathbf{N}_F = & \mathbf{i} \left[ -\sin \kappa_{r-F} \cos \psi_F \cos \kappa_{r-Q} - \sin \kappa_{r-Q} \cos(\psi_{cl} - \psi_Q) \cos \kappa_{r-F} \right] - \\ & \mathbf{j} \left[ \sin \kappa_{r-F} \sin \psi_F \cos \kappa_{r-Q} - \sin \kappa_{r-Q} \sin(\psi_{cl} - \psi_Q) \cos \kappa_{r-F} \right] + \\ & \mathbf{k} \left[ -\sin \kappa_{r-F} \sin \kappa_{r-Q} \sin(\psi_F + \psi_{cl} - \psi_Q) \right] \end{aligned} \quad (4.109)$$

#### 4.8.10 Flank Formed by Quadratic Surfaces

Besides the facet grind of the drill flank faces discussed above, quadratic surfaces can also be used as the tool flank surface. Examples of quadratic surfaces include the cone, cylinder, ellipsoid, elliptic cone, elliptic cylinder, elliptic hyperboloid, elliptic paraboloid, hyperbolic cylinder, hyperbolic paraboloid, paraboloid, sphere, and spheroid. The geometry of these surfaces is well-known [54, 55] and can be utilized to achieve the preferred cutting geometry of drills. Among these surfaces, the following shown in Fig. 4.105 have been used in the practice of drill design and manufacturing: (1) conical, (2) hyperboloidal, (3) cylindrical, and (4) ellipsoidal. Figure 4.105 also shows the relevant geometrical parameters that can be used to determine the grinding geometry knowing the desired geometry of the drill to be ground.

Although in the professional literature it has long been decided that a drill having a four and six faced planar flank face normally outperform a drill having quadratic surfaces, the author is not familiar with any relevant study where a fair comparison of the planar and quadratic flanks drills were carried out. Although the latter requires knowledge of drill geometry, experience, and CNC grind to manufacture, they put many more control parameters at the tool designer's disposal to optimize drill performance.

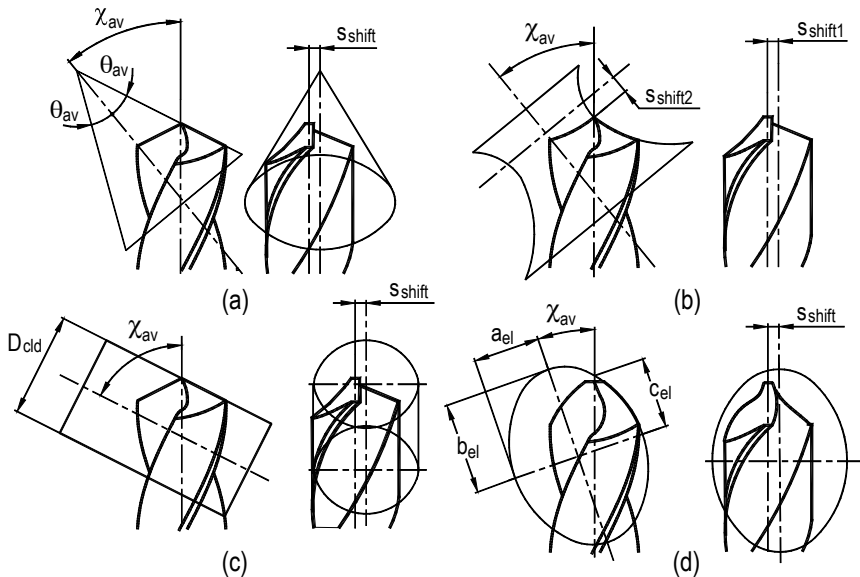


Fig. 4.105. Simplified models for quadratic drill points

Before starting the drill pointing process, the drill is positioned to a known orientation with respect to a grinding wheel. Initially positioning the drill is commonly known as timing the drill. Normally, the drill is gripped in a holder and the holder and drill are positioned as a unit to time the drill.

Machine grinding of the various drill points requires complex three-dimensional relative motion between the drill and the grinding wheel. Normally, the grinding wheel rotates about a stationary axis and the drill is cylindrically fed against the wheel while the drill undergoes at least three components of motion during each cycle. The first component of motion is a constant velocity rotation of the drill about its longitudinal axis. The second component of motion is a linear reciprocation of the drill in the direction perpendicular to the drill longitudinal axis. This motion is commonly referred to as the lift motion. The third motion is movement of the drill nominally along its longitudinal axis. This motion is known as feed motion.

Lift and feed motions occur in timed relation to the rotation of the drill. Lift and feed motions also occur in cycles that correspond to the number of cutting edges on the drill point, with a cycle being repeated for each cutting edge during one revolution of the drill. Although the drill rotates about its longitudinal axis at a constant angular velocity, neither the lift nor the feed motions need to be of constant velocity.

For some of the drill points, a fourth motion is required. This motion is rotation of the drill about an axis that is perpendicular to but does not intersect the drill longitudinal axis. That motion is frequently referred to as a rock motion. Like the lift and feed motions, the rock motion is cyclically repeated for each cutting edge during a drill revolution about its longitudinal axis.



In many commercially available drill grinding machines, the lift, feed, and rock motions are imparted to the drill being ground by a series of cams, cam followers, links, and levers. The cams are rotated at a constant speed. The links and levers convert cam rotational motion into the appropriate list, feed, and rock motions at the drill point. Different cams are used for different types of drill points and for different drill diameters. In addition, many of various components, such as links and levers, are adjustable to suit drill points and diameters. Examples of drill grinding machines are their kinematics to achieve various drill point which are given in US Patent No. 4,364,444 (1982).

In this section, the conical and helical drill flank grinds will be considered. The former is still in wide use because many old fixture and grinding machine accessories are used in the industry while the later is in wide use because it is reproduced by specialized drill grinding machines including those used in small shops or even at home (for example, Drill Doctor).

#### 4.8.10.1 Conical Flank Face

Two principal arrangements in grinding the flank face as part of a conical surface are shown in Fig. 4.106. In Fig. 4.106a the radius of the cone increases from the drill center towards its periphery while in Fig. 4.106b it *vice versa*. In practice, the first arrangement is used so that the T-hand-S flank angle increases towards the drill center. This arrangement is considered in this section.

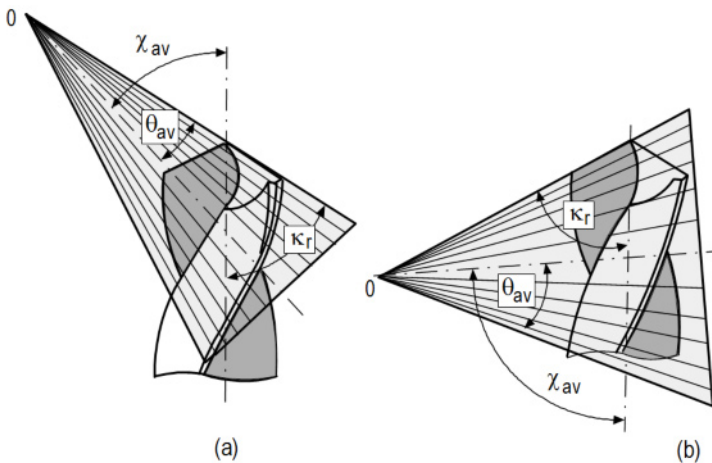


Fig. 4.106. Two principal arrangement in conical grind

The tool cutting edge angle (the drill half-point angle)  $\kappa_r$  is determined knowing the grinding cone half angle  $\theta_{av}$  and the angle between drill axis and the cone,  $\chi_{av}$  as

$$\kappa_r = \theta_{av} + \chi_{av} \quad (4.110)$$

It follows from this equation that the desired tool cutting edge angle (the drill half-point angle)  $\kappa_r$  can be obtained under various combination of angles  $\theta_{av}$  and  $\chi_{av}$ .

The model to determine flank angles in standard cross-sectional planes at point  $r$  of the cutting edge 1–2 for the conical point grind for the arrangement shown in Fig. 4.106a is shown in Fig. 4.107. As before, the location of point  $r$  is defined by its radius  $R_{pr}$  and angle  $\mu_r$  (Fig. 4.75). The right-hand coordinate system  $x_1y_1z_1$  is introduced as shown with the  $z_1$ -axis being perpendicular to the cutting edge and  $y_1$ -axis along this edge.

The following parameters  $s_{shift}$ ,  $l_{av}$ ,  $\theta_{av}$ , and  $\kappa_r$  are considered to be known. SECTION A–A is drawn through point  $r$  perpendicular to the axis of the grinding cone. This section plane crosses the conical flank surface over a circle which at point  $r$  determines flank angle  $\alpha_A$ . It follows from Fig. 4.107 that

$$\tan \alpha_A = \frac{s_{shift} - c_{ct}/2}{q_r} \tag{4.111}$$

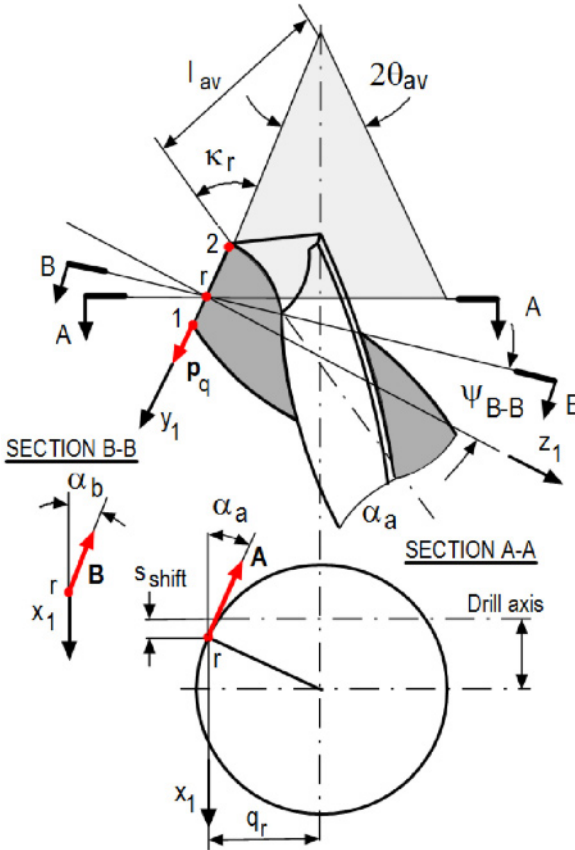


Fig. 4.107. Model for determining drill geometry parameters for conical grind

Distance  $q_r$  can be approximately determined as

$$q_r = \frac{(l_{av} + R_{pr} \cos \mu_r) \sin \theta_{av}}{\sin \kappa_r} \quad (4.112)$$

and

$$\tan \alpha_A = \frac{(s_{shift} - c_{cl}/2) \sin \kappa_r}{(l_{av} + R_r \cos \mu_r) \sin \theta_{av}} \quad (4.113)$$

To find T-hand-S flank angles in the standard section planes, three unit vectors belonging to the flank face are introduced as:

$\mathbf{p}_q$  is along the cutting edge

$$\mathbf{p}_q = \mathbf{j}_1 \quad (4.114)$$

$\mathbf{A}$  is along the tangent to the conical flank surface at point  $r$  in SECTION A–A. In coordinate system  $x_1y_1z_1$

$$\mathbf{A} = -\mathbf{i}_1 \cos \alpha_A - \mathbf{j}_1 \sin \alpha_A \sin \theta_{av} + \mathbf{k}_1 \sin \alpha_A \cos \theta_{av} \quad (4.115)$$

$\mathbf{B}$  is along the tangent to the conical flank surface at point  $r$  in some section plane B–B which makes angle  $\psi_{B-B}$  with the  $z_1$ -axis

$$\mathbf{B} = -\mathbf{i}_1 \cos \alpha_B - \mathbf{j}_1 \sin \alpha_B \sin \psi_{B-B} + \mathbf{k}_1 \sin \alpha_B \cos \psi_{B-B} \quad (4.116)$$

where  $\alpha_B$  is the flank angle in SECTION B–B (Fig. 4.107).

Because the introduced vectors belong to the same plane tangent to the flank surface at point  $r$ , their scalar triple product is equal to zero, i.e.,

$$\begin{vmatrix} 0 & 1 & 0 \\ -\cos \alpha_A & -\sin \alpha_A \sin \theta_{av} & \sin \alpha_A \cos \theta_{av} \\ -\cos \alpha_B & -\sin \alpha_B \sin \psi_{B-B} & \sin \alpha_B \cos \psi_{B-B} \end{vmatrix} = 0 \quad (4.117)$$

and expanding this determinant, one can obtain

$$\tan \alpha_B = \frac{\tan \alpha_A \cos \theta_{av}}{\cos \psi_{B-B}} \quad (4.118)$$

For the section plane normal to the cutting edge  $\psi_{B-B} = 0$  and thus Eq. 4.119 yields

$$\tan \alpha_N = \tan \alpha_A \cos \theta_{av} = \frac{(s_{shift} - c_{ct}/2) \sin \kappa_r}{(l_{av} + R_{pr} \cos \mu_r) \tan \theta_{av}} \quad (4.119)$$

In full analogy with point  $r$ , consider the imaginary apex point of the drill conical flank where the drill axes crosses the surface of the grinding cone. For this point, the flank angle in the section perpendicular to the axis of the grinding cone calculates as

$$\tan \alpha_{ap-A} = \frac{s_{shift} \sin \kappa_r}{l_{av} \sin \theta_{av}} \quad (4.120)$$

and in the section perpendicular to the drill axis the flank angle calculates as

$$\tan \alpha_{ap-B} = 90^\circ - \psi_{cl} \quad (4.121)$$

so that

$$\psi_{cl} = 90^\circ - \tan \alpha_{ap-B} \quad (4.122)$$

For the section perpendicular to the drill axis, angle  $\psi_{B-B} = \kappa_r$ , therefore

$$\tan \alpha_{ap-B} = \cot \psi_{cl} = \frac{\tan \alpha_{ap-A} \cos \theta_{av}}{\cos \kappa_r} \quad (4.123)$$

Combining Eqs. 4.121 and 4.124, one can obtain

$$\tan \psi_{cl} = \frac{l_{av} \tan \theta_v}{s_{shift} \sin \kappa_r} \quad (4.124)$$

This equation determines the chisel angle when the location of the drill relative to the grinding cone is known.

To summarize the results obtained, consider the practical application of a conical grind on a drill sharpening machine. In conical grinding, the point angle,  $\Phi_p (=2\kappa_r)$ , normal T-hand-S flank angle at the periphery point of the major cutting edge,  $\alpha_{n-1}$ , and chisel edge angle  $\psi_{cl}$  should be obtained. The point angle,  $\Phi_p (=2\kappa_r)$  depends on the grinding cone angle  $\theta_{av}$  and the angle between the axis of the grinding cone and the drill,  $\chi_{av}$ . For a given machine, these two angles are known so that the relative location of the grinding cone and the drill is determined by two parameters, namely shift  $s_{shift}$  and distance  $l_{av}$  which should be determined knowing the chisel edge angle  $\psi_{cl}$  and normal T-hand-S flank angle at the periphery point of the major cutting edge,  $\alpha_{n-1}$ . Equation 4.120 establishes relationship  $\alpha_{n-1}$  with the

shift,  $s_{shift}$  and distance  $l_{av}$ . Referring to this equation, for periphery point 1 of the major cutting edge

$$R_r \cos \mu_r = \frac{d_{dr}}{2} \quad (4.125)$$

then

$$\tan \alpha_{n-1} = \frac{(s_{shift} - c_{ct}/2) \sin \kappa_r}{(l_{av} + d_{dr}/2) \tan \theta_{av}} \quad (4.126)$$

from where the shift  $s_{shift}$  is calculated as

$$s_{shift} = \frac{\tan \alpha_{n-1} \tan \theta_{av}}{\sin \kappa_r} (l_{av} + d_{dr}/2) + c_{ct}/2 \quad (4.127)$$

For the fixed values of  $\alpha_{n-1}$ ,  $\Phi_p (=2\kappa_r)$  and angle  $\theta_{av}$ , the part

$$c_\alpha = \frac{\tan \alpha_{n-1} \tan \theta_{av}}{\sin \kappa_r} \quad (4.128)$$

is a constant. Therefore, values of the shift  $s_{shift}$  and distance  $l_{av}$  that assure the obtaining the desired flank angle at the periphery point 1 correlate as

$$s_{shift} = c_\alpha l_{av} + \frac{c_\alpha d_{dr}}{2} + \frac{c_{ct}}{2} \quad (4.129)$$

Equation 4.125 establishes relationship  $\psi_{cl}$  with the shift  $s_{shift}$  and distance  $l_{av}$ . From this equation

$$s_{shift} = l_{av} \frac{\tan \theta_{av}}{\tan \kappa_r \tan \psi_{cl}} = c_{sh} l_{av} \quad (4.130)$$

Solving two simultaneous Eqs. 4.130 and 4.131, one can find the shift  $s_{shift}$  and distance  $l_{av}$  for any particular case of grinding.

#### Example 4.6.

Assume drill diameter,  $d_{dr}$ , distance  $c_{ct} = 0.143d_{dr}$ , point angle  $\Phi_p (=2\kappa_r) = 120^\circ$ , grinding cone angle  $\chi_{av} = 26^\circ$  be known. Find the shift  $s_{shift}$  and distance  $l_{av}$  to obtain the chisel edge angle  $\psi_{cl} = 55^\circ$  and the T-mach-S flank angle in the cylindrical cross-section at the periphery point 1  $\alpha_{v-1} = 10^\circ$  (normally found to prevent the interference of the tool flank and the bottom of the hole being drilled; see Sect. 4.8.5.1).

According to Eq. 4.43, angle  $\xi_{ad-p-r}$  for the periphery point 1 calculates as

$$\tan \xi_{ad-p-1} = \frac{c_{ct}}{d_{dr}} = 0.143 \quad \text{so that} \quad \xi_{ad-p-1} = 8.14^\circ \quad (4.131)$$

Then the T-hand-S flank angle at the periphery point calculates using Eq. 4.56 as

$$\alpha_{n-1} = \arctan \left( \frac{\tan 10^\circ \sin 60^\circ}{\cos 8.14^\circ} - \tan 8.14^\circ \cos 60^\circ \right) = 4.73^\circ \quad (4.132)$$

For simplicity  $\alpha_{n-1} = 5^\circ$  is adopted.

The condition of obtaining the T-hand-S flank angle at the periphery point  $\alpha_{n-1} = 5^\circ$  becomes

$$s_{shift} = 0.0233l_{av} + \frac{0.0233d_{dr}}{2} + \frac{0.143d_{dr}}{2} \quad (4.133)$$

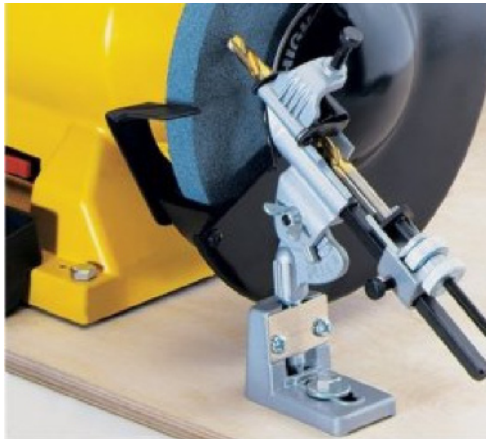
The condition of obtaining  $\psi_{cl} = 55^\circ$  is

$$s_{shift} = 0.094l_{av} \quad (4.134)$$

Solving two simultaneous Eqs. 4.134 and 4.135, one obtains

$$s_{shift} = 0.11d_{dr} \quad \text{and} \quad l_{av} = 1.17d_{dr} \quad (4.135)$$

Figure 4.108 shows a drill set in the machine for conical point grind. End of Example 4.6.



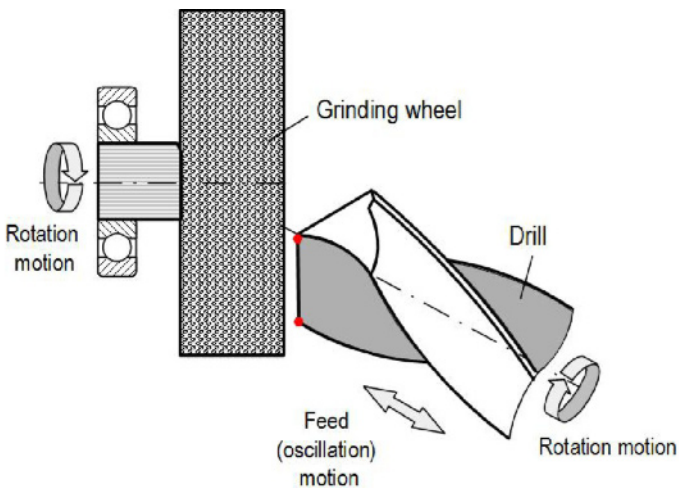
**Fig. 4.108.** Drill set in the fixture for conical point grind

The foregoing analysis reveals that the distribution of the flank angle along the cutting edge 1–2 in cone grinding depends on the grinding parameters so that it is insufficient to indicate the T-hand-S flank angle at the periphery point  $\alpha_{n-1}$  and simple ‘conical grind’ to know this distribution. This explains great scatter in the performance of the so-called ‘standard twist drill with conical point.’ It also explains the popularity of the planar drill point where the tool geometry normally indicated in the drill drawing assures the same distribution of the flank angles along the major cutting edge (lip) and the chisel edge from one drill manufacture to another. Unfortunately, this issue is not understood in industry.

#### 4.8.10.2 Helical Flank Surface

The above-described conical or ‘conventional’ drill point has a conical configuration with the straight chisel edge at its forward end. As discussed, such a chisel edge contributes to walking of the drill point, and this, often requires prior use of a center drill. The helical drill point, on the other hand, generally has ‘S’ or helical shaped crowned chisel edge which provides some self-centering ability.

In the simplest case of helical flank grinding, the drill is gripped in a holder (for example, collet chuck) which simultaneously rotates about the drill longitudinal axis, oscillated toward and away from a grinding wheel and reciprocated along the axis of oscillation as shown in Fig. 4.109. The described combined motion is cyclic as it is repeated for each flank face of the drill in succession until a finished point is obtained. This grinding combined motion generates a flank surface which is part of the helicoid coaxial to the drill longitudinal axis as shown in Fig. 4.110. The resulting drill point is commonly referred to as a helical drill point.



**Fig. 4.109.** Kinematics of grinding a helical drill point

As known, a helicoid is a warped surface which may be generated by a straight line moving in such a manner that every point of the line shall have a uniform motion in the direction of another fixed straight line, and at the same time a uniform angular motion about it. As a result, the exact geometry of the helical drill point is

rather complicated. However, with some simplification which do not affect the accuracy of the obtained result, this geometry can be analyzed in a much simple fashion [52].

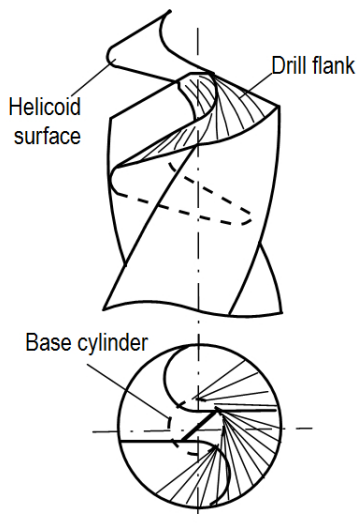


Fig. 4.110. Helical grinding surface generates drill flank

For simplicity, the axial motion of the grinding surface towards the drill flank and rotation of this flank is considered. A surface generated in the result of these two motions is a helical surface generated by a straight line. A normal to this surface makes an angle  $\epsilon_{hl}$  with the axis of instantaneous motion that calculates as

$$\tan \epsilon_{hl} = \frac{p_{hl}}{r_o} \tag{4.136}$$

where  $p_{hl}$  is the parameter of helical motion,  $p_{hl} = p_h / 2\pi$ , where  $p_h$  is the pitch of the helical surface, and  $r_o$  is the radial distance between the normal at a considered point and the axis of helical motion which is the radius of the base cylinder of the helicoid.

In the considered case of drill sharpening, the axis of the helical surface is the drill longitudinal axis which makes angle  $\kappa_r$  with the generation straight line. Therefore, any normal to the helicoidal surfaces makes angle  $90^\circ - \kappa_r$  with the axis of this surface. Therefore

$$\tan (90^\circ - \kappa_r) = \frac{p_{hl}}{r_o} \text{ or } r_o = p_{hl} \tan \kappa_r \tag{4.137}$$



The result of such helical motion is the helical surface (helicoid) having the radius of the base cylinder  $r_o$  and parameter  $p_{pl}$ . The flank face is generated as a part of the helical surface.

When the diameter of the base cylinder is greater than the web diameter  $d_{ww}$ , then the flank face consists of helical and planar parts. As such, a straight chisel edge is formed as the result of intersection of two planar surfaces. When this is not the case, the chisel edge is formed as a line of intersection of two helical surfaces. As a result, an S-shaped chisel edge is formed. Moreover, the longitudinal axis of the helicoid used for form each drill flank may not coincide with the longitudinal axis of the drill but be parallel to this axis.

Under the adopted simplifications, the flank angle in the cylindrical section (see Sect. 4.8.5.1) for the periphery point 1 of the cutting edge calculates as

$$\tan \alpha_{v-1} = \frac{p_{hl}}{r_{dr}} \quad (4.138)$$

For any other point  $r$  of the cutting edge having the radius  $R_r$ , less than that of the base cylinder, the flank angle in the cylindrical section can be determined knowing  $\alpha_{v-1}$  as

$$\tan \alpha_{v-r} = \frac{r_{dr}}{R_r} \tan \alpha_{v-1} \quad (4.139)$$

When the radius of the considered point is equal to the base radius of the helicoid  $r_o$ , the flank angle in the cylindrical section becomes

$$\tan \alpha_{v-r_o} = 1/\tan \kappa_r \quad \text{or} \quad \alpha_{v-r_o} = 90^\circ - \kappa_r \quad (4.140)$$

i.e., this angle is constant and does not depend on the flank angle in the cylindrical section for the periphery point 1.

Therefore, the grinding parameters  $p_{hl}$  and  $r_o$  can be determined knowing the flank angle in the cylindrical section for point 1 as

$$p_{hl} = r_r \tan \alpha_{v-1} \quad (4.141)$$

$$r_o = r_r \tan \alpha_{v-1} \tan \kappa_r \quad (4.142)$$

#### Example 4.7.

Let drill diameter,  $d_{dr}$ , distance  $c_{ct} = 0.143d_{dr}$ , point angle  $\Phi_p (=2\kappa_r) = 120^\circ$ , the T-mach-S flank angle in the cylindrical cross-section at the periphery point 1  $\alpha_{v-1} = 10^\circ$  (normally found to prevent the interference of the tool flank and the bottom of the hole being drilled; see Sect. 4.8.5.1).

The radius of the base cylinder calculates as

$$r_o = \frac{d_{dr}}{2} \tan 10^\circ \tan 60^\circ = 0.15d_{dr}$$

As can be seen, when helical point grind is used, the T-mach-S flank angle in the cylindrical cross-section from point 1 to the cylinder having radius  $0.15d_{dr}$  varies from  $10^\circ$  to  $30^\circ$ . When conical grind with  $\psi_{cl} = 55^\circ$  is applied, this flank angle varies over the same length of the cutting edge from  $10^\circ$  to  $21^\circ$ . When planar flank is used, the T-mach-S flank angle in the cylindrical cross-section varies from  $10^\circ$  to  $20^\circ$ . Higher T-mach-S flank angle in the cylindrical cross-section in the region adjacent to the chisel edge improves the rake angle of this edge.

## 4.9 Load Over the Drill Cutting Edge

The degree of optimality of the geometry of any cutting tool can be assessed through optimality of the geometry of the cutting edge, on one hand, and by uniformity of the load over this edge. The latter is particularly true for cutting tools with long cutting edges over which the cutting conditions change substantially as in the case of drills. For given work material and tool design, the load at point  $r$  of the cutting edge is characterized by the cutting speed,  $v_r$ , uncut (undeformed) chip thickness,  $t_{l-r}$ , and time of cutting. This load determines the tool wear rate [56] and thus tool life.

Often for tools with long cutting edges, the cutting speed and uncut chip thickness as well as the time of cutting may vary over the cutting edge. Therefore, accounting for these variations, one should establish a criterion of the load on a given part of the cutting edge to be able to determine the most loaded portions of the cutting edge. As pointed out by Rodin [52], to make load odds even is one of the prime requirements in cutting tool improvements. The wear rate can be in the sense as it was introduced by the author [56] or tool life (if the tool life of the considered portion of the cutting edge is greater compared to other parts) can be used as such a criterion.

In the simplest case, the following empirical formula is used to correlate the cutting speed with tool life and cutting parameters:

$$v = \frac{C_T C_w C_{cc}}{T^{m_T} t_1^{m_t} b_1^{m_b}} \quad (4.143)$$

where  $C_T$ ,  $C_w$ , and  $C_{cc}$  are constant depending upon the tool material, work material and cutting conditions, respectively,  $T$  is tool life,  $t_1$  and  $b_1$  uncut chip thickness and its width, respectively, and  $m_T$ ,  $m_t$ , and  $m_b$  are powers to be determined experimentally using cutting tests (for example as discussed by Astakhov (Chap. 5 in [22])).

To analyze the distribution of load over a given cutting edge, a point  $r$  on this edge is selected to be the base point, where cutting speed is  $v_r$ , uncut chip thickness is  $t_{l-r}$ , and tool life is  $T_r$ . For any other point of the cutting edge, for example point  $p$ , tool life can be calculated using Eq. 4.144. Let it be  $T_p$ . The load coefficient at

this point can be calculated as  $k_{N-p} = T_r/T_p$ . If  $k_{N-p} > 1$  then this point is loaded more than the base point  $r$ .

The load coefficient  $k_N$  can also be determined as the ratio of the uncut (undeformed) chip thickness  $t_{1-p}$  at the considered point to that at  $t_{1-T}$  corresponding to tool life T determined using Eq. 4.144, i.e.,

$$k_{N-p} = \frac{t_{1-p}}{t_{1-T}} \tag{4.144}$$

If  $k_N$ s for various point of the cutting edge are known, then the uniformity of the load over this edge can be assessed.

### 4.9.1 Uncut Chip Thickness in Drilling

Although the uncut (undeformed) chip thickness can be easily determined using vector analysis, it was found instructive to visualize this important characteristic of the cutting process graphically to develop its material sense. Figure 4.111 shows a graphical model to visualize the uncut chip thickness. In this model, a drill having two lips is shown. There are two surfaces of cut in the axial (the  $y_0z_0$  plane) section. The surface of cut is a surface of revolution formed by each cutting edge so the axis distance between these surfaces of cut is equal to a half of the cutting feed  $f$  ( $f/2$  as shown in Fig. 4.111).

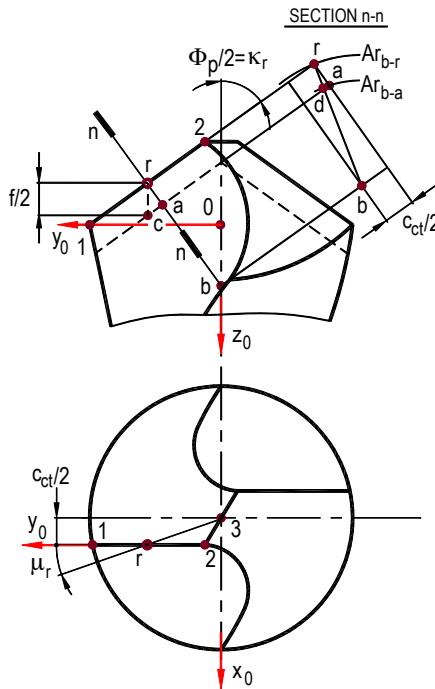


Fig. 4.111. Model for graphical determination of the uncut chip thickness

In the model shown in Fig. 4.111, the uncut chip thickness  $t_1$  is determined for point  $r$  of the cutting edge. The normal to the surface of cut lays in the plane  $n-n$  which is normal to the cutting edge at point  $r$ . This plane crosses the  $z_0$ -axis (the longitudinal axis of the drill) at point  $b$ . Therefore, line  $rb$  is the normal to the surface of cut at point  $r$ .

As the normal section plane  $n-n$  crosses the two surfaces of cut, curves  $Ar_{b-r}$  and  $Ar_{b-a}$  are intersection lines. For the sake of simplicity, these curves can be replaced by circular arcs having point  $b$  as their center. Segment  $rd$  of the normal to the point of cut is between point  $r$  and point  $d$  formed at the intersection of arc  $Ar_{b-a}$  with this normal (line  $rb$ ). This segment  $rd$  is graphical interpretation of the uncut (undeformed) chip thickness.

To determine the uncut chip thickness analytically, consider a vector  $\mathbf{F}$  along the direction of the cutting feed  $f$  and the normal to the surface of cut  $\mathbf{N}_p$ . If the angle between these two vectors is designated as  $\varepsilon_{NF}$  then the uncut chip thickness can be represented as

$$t_1 = \frac{1}{2} f \cos \varepsilon_{NF} \quad (4.145)$$

Using Eq. C.3 (Appendix C) one can calculate the angle between two vectors  $\mathbf{F}$  along the direction of the cutting feed  $f$  and the normal to the surface of cut  $\mathbf{N}_p$  as

$$\cos \varepsilon_{NF} = \frac{\mathbf{N}_p \cdot \mathbf{F}}{\|\mathbf{N}_p\| \|\mathbf{F}\|} \quad (4.146)$$

A unit vector of the normal to the surface of cut in the  $x_0y_0z_0$  coordinate system is

$$\mathbf{N}_p = -\mathbf{i} \sin \mu_r \cos \kappa_r + \mathbf{j} \cos \mu_r \cos \kappa_r - \mathbf{k} \cos \mu_r \sin \kappa_r \quad (4.147)$$

so its modulus is

$$\|\mathbf{N}_p\| = \sqrt{\sin^2 \mu_r \cos^2 \kappa_r + \cos^2 \mu_r \cos^2 \kappa_r + \cos^2 \mu_r \sin^2 \kappa_r} = \sqrt{\cos^2 \mu_r + \sin^2 \mu_r \cos^2 \kappa_r} \quad (4.148)$$

Unit vector  $\mathbf{F}$  in the feed direction is

$$\mathbf{F} = -\mathbf{k}f \quad (4.149)$$

Substituting Eqs. 4.148, 4.149 and 4.150 into 4.147, one can obtain

$$t_1 = \frac{f}{2} \frac{1}{\sqrt{1 + \left( \frac{\cot \kappa_r}{\cos \mu_r} \right)^2}} \quad (4.150)$$

This equation can be used to determine the uncut (undeformed) chip thickness for any point of the cutting edge 1–2.

#### 4.9.2 Load Distribution Over the Cutting Edge

Load distribution over the drill cutting edge is determined for a drill which rotates with the angular velocity  $\omega$  and fed with the feed  $f$ . As discussed in Appendix C (Sect. C.4.1), the cutting speed at point  $r$  of the cutting edge located at radius  $R_r$  calculates as

$$v_r = R_r \omega \quad (4.151)$$

Thus the cutting speed changes over the cutting edge 1–2 in proportion to the radius from the inner point 2 to the periphery point 1.

It follows from Eq. 4.151

$$t_1 = \frac{f}{2} \frac{1}{\sqrt{1 + \tan^2 \kappa_r \cos^2 \mu_r}} \quad (4.152)$$

that the uncut chip thickness also varies over cutting edge 1–2 as angle  $\mu_r$  depends on the location of a considered point on this edge.

Calculations showed [52] that for standard twist drills with web diameter  $d_{ww} = 0.15d_{dr}$  having the point angle  $\Phi_p = 120^\circ$  and chisel edge angle  $\psi_{cl} = 55^\circ$ , the uncut chip thickness  $t_1$  changes from  $0.43f$  at the periphery point 1 to  $0.35f$  at point 2 where the major cutting edge intersects the chisel edge. Thus,  $t_1$  at point 2 is 18% lower than that at point 1.

Accounting only for the influence of the uncut chip thickness and cutting speed on tool life, the condition when tool life is constant ( $T = Const$ ) can be represented as

$$v = \frac{C_{vt}}{t_1^{m_{vt}}} \quad (4.153)$$

Substituting Eq. 4.152 into Eq. 4.154 and accounting for the fact that the angular velocity is constant, one can obtain

$$R_r = \frac{C_{vt-\omega}}{t_{1-r}^{m_{vt}}} \quad (4.154)$$

where  $c_{vt-\omega} = c_{vt}/\omega$ .

If the uncut chip thickness corresponding to constant tool life for point  $r$  is  $t_{1-r}$  then that for point  $p$  it can be represented as

$$\frac{R_p}{R_r} = \left( \frac{t_{1-r}}{t_{1-p}} \right)^{m_{vt}} \quad (4.155)$$

Experiments showed [52] that for medium-carbon steels  $m_{vt} \cong 0.5$ . If it is assumed that the uncut chip thickness is equal to 1 at the periphery point 1 then the theoretical uncut chip thickness assuring the equality of tool life for other points of the cutting edge 1–2 can be determined by the following formula:

$$t_{1-i} = \left( \frac{r_{dr}}{R_i} \right)^2 \quad (4.156)$$

Table 4.2 shows theoretical and real (for a drill having point angle  $\Phi_p = 120^\circ$  and the web diameter  $d_{ww} = 0.15d_{dr}$ ) uncut chip thicknesses calculated for various points of the cutting edge 1–2. The load coefficients  $k_N$  for the same points are also shown. As seen, the load coefficient for the periphery point 1 is manytimes greater than for the central part of the cutting edge 1–2. This is the prime cause for drill non-uniform wear observed in practice. Observations show that tool wear at the drill corner is normally much greater than that of central parts of the cutting edge.

**Table 4.2.** Theoretical and real uncut chip thicknesses and load coefficients for points of cutting edge 1–2

$R_i/r_{dr}$	Theoretical uncut chip thickness	Real uncut chip thickness	Load coefficient
1	1	0.43f	1
0.6	2.8	0.43f	0.36
0.2	25	0.38f	0.035
0.183	30		

## 4.10 Drills with Curved and Segmented Cutting Edges

The twist drill used in industry for more than 140 years for the most widely employed metalworking operation (drilling) can be regarded as an unperfected cutting tool. Severe problems associated with this cutting tool are great variation of the load coefficient and tool geometry parameters over the cutting edge. Over the major cutting edge (lip), the normal rake angle varies from  $+30^\circ$  at drill periphery part of the cutting edge (point 1) to  $-30^\circ$  at the inner end of this edge (point 2), the

load coefficient varies from 1 at point 1 to 0.035 at point 2. These are the greatest variations among general purpose cutting tools used in industry.

Although researchers, tool engineers, and professionals in the field are well aware about importance of the region of the major cutting edge adjacent to periphery point 1 in tool life consideration, the influence of other parts of the major cutting edge (lip) as well as the chisel edge on tool life is not well understood. For example, improving conditions of the chisel edge (web thinning or splitting) cause not only improvement in self centering ability but also in tool life defined by the wear of the drill corners (point 1). This influence also follows from the results of the tests carried out with standard drill of 30 mm diameter used for enlarging pre-drilled holes in gray cast iron [52]. Series of tests with pre-drilled holes of 26, 17.5, and 11.5mm were carried out. It was found that tool life in machining of pre-drilled hole of 26mm diameter was 29.5 min while that in machining pre-drilled holes of 11.5mm diameter was threetime less. This result exemplifies the inter-influence of various parts of the cutting edge on tool life. Unfortunately this inter-influence was not a subject of extensive research activities.

#### 4.10.1 Load of the Cutting Part of a Drill with Curved Cutting Edges

For simplicity of consideration, consider a drill with so-called diametral cutting edges, i.e., the major cutting edge (lip) along drill radius is as in the drill design shown in Fig. 4.51b, then  $\mu_r=0$  for any point of such a cutting edge. As follows from Eq. 4.153, the uncut (undeformed) chip thickness is constant along this cutting edge while the cutting speed significantly changes, causing non-uniform wear of the drill along the cutting edge. The objective of the further considerations is to alter the shape of the cutting edge to achieve uniform drill wear.

According to Eq. 4.154, the cutting speed and the uncut chip thickness under  $T = const$  for any point  $r$  of the cutting edge 1–2 correlate as

$$v_r = \frac{c_{vt}}{t_{1-r}^{m_{vt}}} \quad (4.157)$$

For diametral cutting edge, the uncut chip thickness for a point  $r$  of this edge calculates according to Eq. 4.153 as

$$t_{1-r} = \frac{f}{2} \sin \kappa_{r-r} \quad (4.158)$$

The cutting speed at point  $r$  is calculated (see Appendix C, Sect. C4.1) as

$$v_r = \frac{2\pi n}{1000} R_r \quad (4.159)$$

where where  $\pi = 3.141$ ,  $R_r$  is in millimeters, and  $n$  is the rotational speed in r.p.m. or rev/min.

Substituting Eqs. 4.159 and 4.160 into Eq. 4.158, and after some rearrangements, one can obtain

$$\tan \kappa_{r-r} = \frac{(A_r/R_r)^{1/m_r}}{\sqrt{1-(A_r/R_r)^{2/m_r}}} = \frac{dR_r}{dz_0} \quad (4.160)$$

The differential Eq. 4.161 defines the shape of the uniformly loaded cutting edge in the  $y_0z_0$  plane. Its numerical differentiation, however, shows that the length of the drill point under the accepted conditions is way too long for practical applications. The closest known shape of the cutting edge to the obtained result is the ellipsoidal drill point shown in Fig. 4.105d. The result obtained shows why, even though complicated and difficult to grind as the grinding accessories and programs are not fully developed, this drill point is still in use showing remarkable results when applied properly.

So far, the attempt has been made in this section to adjust drill geometry to obtain more uniform load distribution by varying the tool cutting edge angle  $\kappa_r$ . Another reserve in this way is angle  $\mu_r$ , i.e., the cutting edge can be curved not only in the  $y_0z_0$  plane but also in the  $x_0y_0$  plane. The advantages of such geometry were found out by the try and error method as early as at the beginning of the twentieth century. For example, US Patent No. 1,309,706 (1917) describes a drill design shown in Fig. 4.112 where the major cutting edges (lips) 1 and 2 are curved in both the  $y_0z_0$  and  $x_0y_0$  planes. The advantages as a remarkable increase of tool life and drilling ‘smoothness’ are explained using an intuitive but very precise perception as “By this constriction the work of removing metal, that is, the cutting, is distributed in such a manner that a unit of length of edge at the periphery does no more work than a unit of length of edge nearer the axis and therefore that the amount of heat produced in removing the metal is more nearly uniform for each unit length of the cutting edge.” If this heat results in the uniform temperatures equal to the optimal cutting temperature (see Sect. 1.4.2.1) along this edge then the maximum tool life and uniform tool wear along the cutting edge can be achieved.

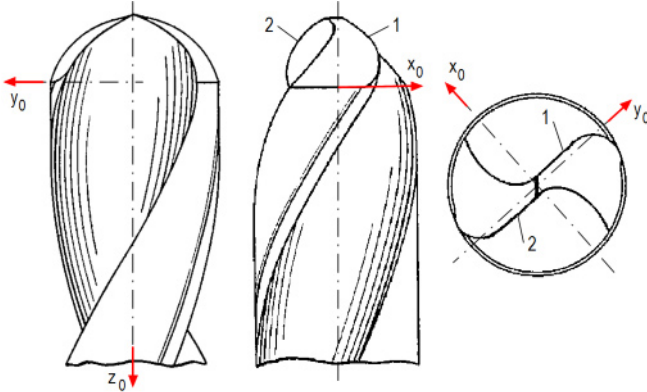
To model the major cutting edge of a standard twist drill, let direct vector  $\mathbf{p}_b$  along its cutting edge 1–2. The location of this vector is characterized by angles  $\kappa_{r-in}$  and  $\mu_{r-in}$  where subscripts ‘in’ is used to emphasis that these are initial parameters at some point  $r$ . In the current  $xyz$  coordinate system this vector can be written through its coordinates as

$$\mathbf{p}_b = \mathbf{i} \cos \mu_{r-in} - \mathbf{j} \cot \kappa_{r-in} + \mathbf{k} \sin \mu_{r-in} \quad (4.161)$$

Vector  $\mathbf{p}_a$  is drawn along the tangent to the rake surface in the  $zy$  plane. It makes an angle  $\omega_r$  defined by Eq. 4.21. This vector can be represented as

$$\mathbf{p}_a = \mathbf{j} - \mathbf{k} \tan \omega_r \quad (4.162)$$





**Fig. 4.112.** Drill geometry according to US Patent No. 1,309,706 (1917)

Consider the case when the drill is ground with curved cutting edges each point of which is characterized by its own angles  $\kappa_{r-q}$  and  $\mu_i$  which can be quite different from angles  $\kappa_{r-in}$  and  $\mu_{r-in}$ . Then in the  $xyz$  coordinate system, a vector  $\mathbf{p}_c$  tangent to the cutting edge at certain point I of the cutting edge can be introduced. This vector can be represented through its coordinates as

$$\mathbf{p}_c = \mathbf{i} \cos \mu_i - \mathbf{j} \cot \kappa_{r-i} + \mathbf{k} \sin \mu_i \quad (4.163)$$

Because the introduced vectors all belong to the same plane tangent to the rake face in the considered point, their scalar triple product is equal to zero, i.e.,

$$\begin{vmatrix} 0 & 1 & -\tan \omega_r \\ \cos \mu_{r-in} & -\cot \kappa_{r-in} & \sin \mu_{r-in} \\ \cos \mu_i & -\cot \kappa_{r-i} & \sin \mu_i \end{vmatrix} = 0 \quad (4.164)$$

Expanding this determinant, one obtains

$$\cot \kappa_{r-i} = \frac{\tan \omega_r \cos \mu_i \cot \kappa_{r-in} + \sin(\mu_i - \mu_{r-in})}{\tan \omega_r \cos \mu_{r-in}} \quad (4.165)$$

This equation correlates  $\mu_i$  and  $\kappa_{r-i}$  for a curved cutting edge.

Solving simultaneous Eqs. 4.153, 4.156, and 4.166, one can determine the geometrical parameters of the curved cutting edge. Calculations showed [52] that when  $m_{vt} = 0.5$ , the uncut chip thickness at the drill periphery point 1 should be 25 times smaller than at inner point 2 located on the radius  $R_2 = 0.2r_{dr}$ . In this case, if the tool cutting edge angle (the half point angle) on the radius  $R_2 = 0.2r_{dr}$  is  $\kappa_{r-2} = 60^\circ$ , then that at point 1 should be  $\kappa_{r-1} = 30^\circ$  while  $\mu_1 = 87^\circ$ .

It is rather difficult (but not impossible) to assure the conditions  $T = Const$  along the entire cutting edge 1–2 due to excessive length of the drill working part. However, it is feasible to assure this condition in some important point of this edge, for example at points 1 and 2 of the major cutting edge.

For the sake of simplicity, consider a drill with the major cutting edge which has  $\mu_1 = \mu_2 = 0$ . Lets assume that the curvilinear major cutting edge forms a the line of intersection of the helical surface of a drill flute and spherical flank surface of a  $\rho_{fl}$  radius. This radius can be roughly determined as

$$\rho_{fl} = \frac{R_1 - R_2}{\cos \kappa_{r-1} - \cos \kappa_{r-2}} \quad (4.166)$$

Experimental studies showed that tool life of twist drill increase three to five times in drilling of steels and cast irons (compare to the standard twist drills) if this radius is selected to be in the range of  $(0.5-1.2)d_{dr}$  [52].

Because the uncut chip thickness varies over the cutting edge due to variation of angle  $\mu_i$ , using Eq. 4.150 one can express this angle as

$$\cos \mu_r = \frac{f}{2} \frac{\cot \kappa_r}{\sqrt{\frac{f^2}{4R_r^2} - 1}} \quad (4.167)$$

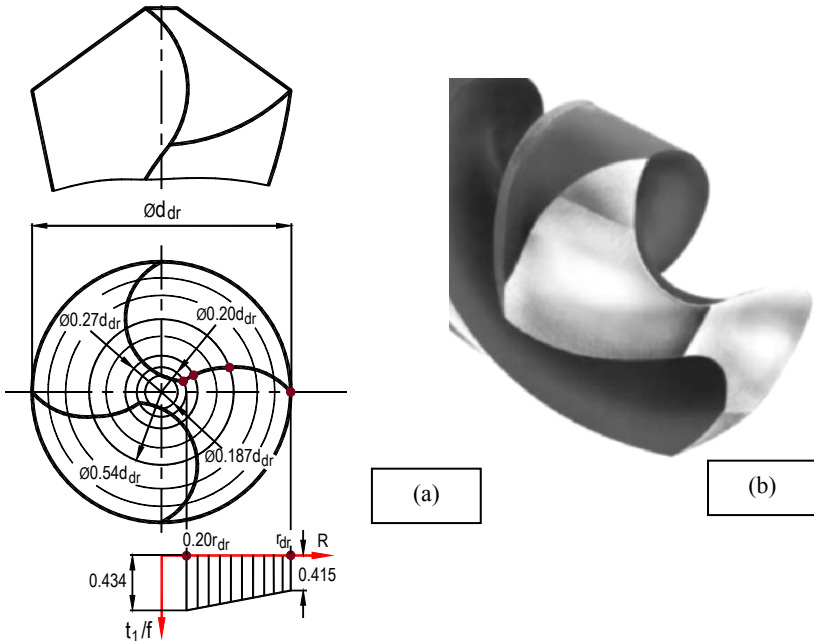
Figure 4.113a shows a drill geometry where the cutting edge is constructed using with angles  $\mu_i$  calculated by Eq. 4.168. As seen from the graph below the picture, the uncut chip thickness varies along the cutting edge following a linear fashion with the minimum at the drill periphery. The results obtained constitute the background for a drill with curved cutting edge, for example for the so-called radiused conventional point known in industry as Racon<sup>®</sup> point grind shown in Fig. 4.113b.

## 4.10.2 Rake Angle

### 4.10.2.1 Segmetal Cutting Edge in the Plane Parallel to the $y_0z_0$ Plane

It follows from Fig. 4.77 for a twist drill having  $\omega_d = 30^\circ$ ,  $d_{ww} = 0.2d_{dr}$ , with increasing point angle, the normal rake angle increases at drill periphery while sharply decreases along the major cutting edge. When  $\Phi_p=180^\circ$ , the normal rake angle varies from  $+30^\circ$  at periphery point 1 to  $3^\circ$  at the inner end of this edge while when  $\Phi_p=120^\circ$ , the normal rake angle varies from  $+30^\circ$  to  $-30^\circ$ . This is readily explained by the change of the shape of the surface of cut (the bottom of the hole being drilled). When drilling with a drill with  $\Phi_p=120^\circ$ , this surface is hyperboloid while when  $\Phi_p$  becomes  $180^\circ$  this surface is a plane.

The foregoing analysis suggests that to increase the normal rake angle in the central region of a twist drill, greater point angles can be used. However, as shown above, if the point angle is increased, the length of the chisel edge increases with



**Fig. 4.113.** Calculated curvilinear cutting edge (a) and Racon<sup>®</sup> drill supplied by Winslow Engineering Inc. (b)

simultaneous decrease of the rake angle of this edge. Therefore, to solve this problem, a slot similar to that shown in Fig. 4.39 can be made instead of the chisel edge.

Figure 4.114 shows a practical drill design that includes the above-mentioned features. For this drill, the rake and flank angles along the cutting edge do not experience sharp variations compare to a standard twist drill. Practical testing of such drill showed a 2–3 increase in tool life and a 2.5–3.5 reduction in the axial force (thrust). The tests also showed that these drill work well only when the drilling system including drill holder, spindle and fixture are rigid. Otherwise, frequent drill breakages were observed.

This problem can be resolved if the major cutting edge is partitioned in the manner shown in Fig. 4.28, i.e., when a part of the lip is provided with a reverse point angle as shown in Fig. 4.115. Practical application of this design clearly demonstrated the listed advantages in the description given to Fig. 4.28. It was found that, when applied this point grind under the conditions considered in Example 4.4, the axial force (thrust) and the drilling power reduce by 25–30% in high-penetration rate drilling of automotive aluminum alloys. The fractured pieces known in the automotive industry as the “sludge” become smaller and thinner as shown in Fig. 4.116 compared to those shown in Fig. 4.96. As such, the fracture originated at the point where the outer and inner parts of the cutting edge meet that reduces the extent of faulty hole exits at the end of each vein shown in Fig. 4.97.

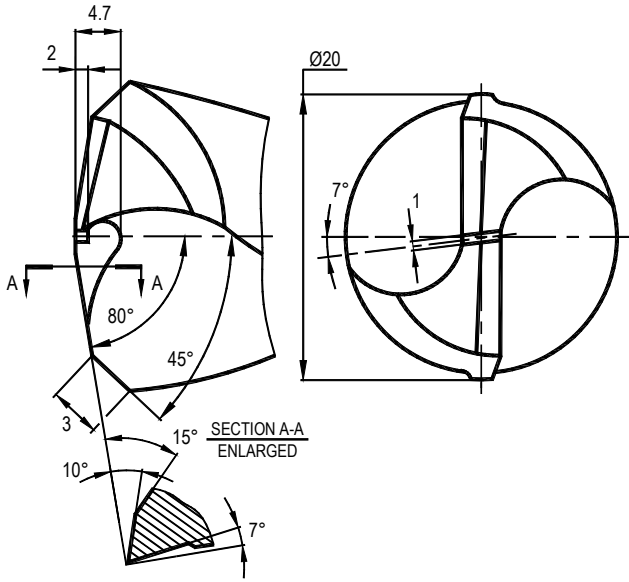


Fig. 4.114. Drill with an increase point angle at its central portion

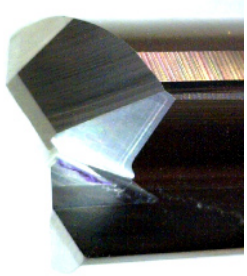
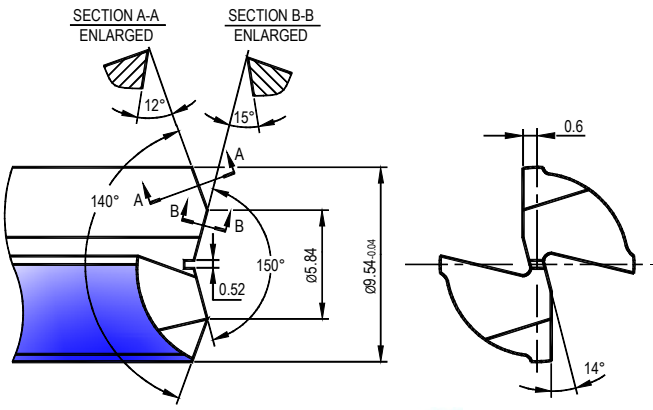
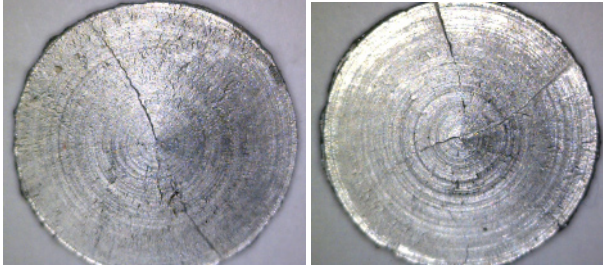


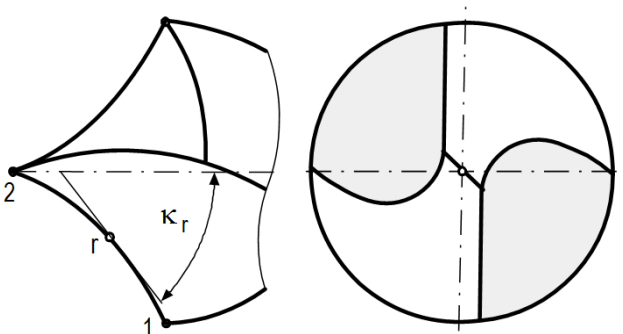
Fig. 4.115. Drill design with partitioned cutting edge



**Fig. 4.116.** Fractured walls at the exit of the veins (slage) obtained with drill shown in Fig. 4.115

#### 4.10.2.2 Curved Cutting Edge in the Plane Parallel to the $y_0z_0$ Plane

It follows from Fig. 4.77 that the suitable distribution of the normal flank angle along the cutting edge can also be achieved by curving the cutting edge in the plane parallel to the  $y_0x_0$  plane that leads to continuous variation of the tool cutting edge angle (the half-point angle)  $\kappa_r$  along this cutting edge. This also causes change in the rake angles in points of this edge. Schematically, such a twist drill is shown in Fig. 4.117. Each point of the cutting edge, for example point  $r$ , is characterized by its own point angle  $\kappa_r$  which is the angle between the tangent to the cutting edge at  $r$  and the drill longitudinal axis.



**Fig. 4.117.** Twist with curved cutting edge in the  $y_0x_0$  plane

To determine the shape of the cutting edge 1–2 that results in a constant rake angle along this edge, the graph similar to that shown in Fig. 4.77 is used. For a given rake angle, say  $29^\circ$ , one may draw a horizontal line in Fig. 4.77 that corresponds to this angle. Points of intersection of this line with corresponding curves define point angles  $\Phi_p (= 2\kappa_r)$ . Table 4.3 shows the calculated the tool cutting edge angles for the considered case.

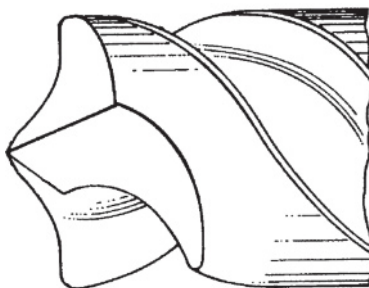
A drill shown in Fig. 4.118 is described in US Patent No. 5,273,380 (1993). As seen, it is similar to that shown in Fig. 4.117. According to this patent, the drill shown in Fig. 4.118 is provided with a novel drill point that includes the concave

cutting edges. As claimed, this drill is characterized by a much longer tool life due to improved heat dissipation along the concave cutting edge.

**Table 4.3.** Tool cutting tool angles for the curved cutting edge 1–2

$R/r_{dr}$	0.40	0.69	0.84	0.95	1.00
$\kappa_r$	15°	30°	45°	60°	90°

A great disadvantage of this drill is that the uncut chip thickness is greatest at the drill periphery and that shortens tool life.



**Fig. 4.118.** Drill design according to US Patent No. 5,273,380 (1993)

*4.10.2.3 Curved Cutting Edge in the Plane Parallel to the  $x_0y_0$  Plane*

If the cutting edge is curved in the  $x_0y_0$  plane, then each point of this edge would have its own  $c_{ct}$ . According to Fig. 4.78, the distance  $c_{ct}$  directly affects the rake angle. Therefore, the curvature of the cutting edge can be selected so that a uniform rake angle along the cutting edge 1–2 is achieved. If the tool designer knows what rake angle is to be achieved, then he can draw a horizontal line on a corresponding graph similar to those shown in Fig. 4.78. The intersection points of this line with corresponding curves indicate  $c_{ct}$ s along the cutting edge to achieve the objective.

For example, for a twist drill having point angle  $\Phi_p = 120^\circ$  and helix angle of the drill flute  $\omega_d = 30^\circ$  when a  $20^\circ$  invariable rake angle is to be achieved along the major cutting edge if  $c_{ct}$ s in points of the major cutting edge are as shown in Table 4.4. Figure 4.119 shows a graphical representation of these results. Experimental study of a drill with this geometry showed that tool life increases while the drilling torque decreases.

**Table 4.4.** Distances  $c_{ct}$ s along the cutting edge to achieve a  $20^\circ$  invariable rake angle

$R/r_{dr}$	0.43	0.50	0.73	0.85	0.95
$c_{ct}$	$-0.07d_{dr}$	0	$0.15d_{dr}$	$0.30d_{dr}$	$0.50d_{dr}$

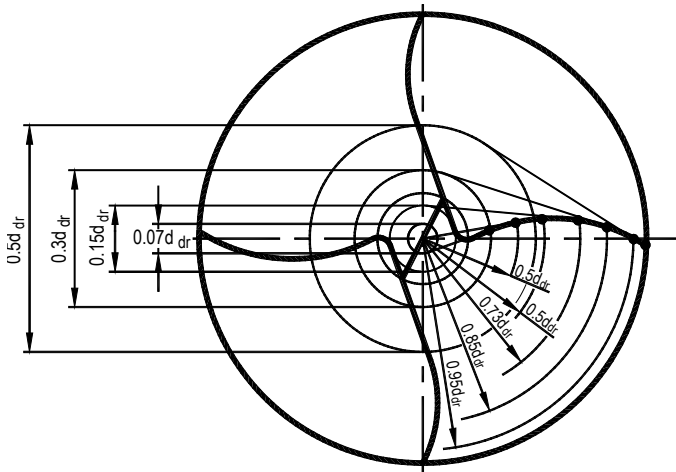


Fig. 4.119. The curved cutting edge constructed using the data of Table 4.4

## References

- [1] Fiesselmann F (1993) An option for doubling drilling productivity. *The Fabricator* 23(4):36–38
- [2] Astakhov VP, Xiao X (2008) A methodology for practical cutting force evaluation based on the energy spent in the cutting system. *Machining Science and Technology* 12:325–347
- [3] Beer FP, Johnston ER Jr, DeWolf JT (2006) *Mechanics of materials*, 4th ed. McGraw Hall, Boston
- [4] Narasimha K, Osman MOM, Chandrashekhar S, Frazao J (1987) An investigation into the influence of helix angle on the torque-thrust coupling effect in twist drills. *The Int J. of Adv. Manuf. Tech.* 2(4):91–105
- [5] De Beer C (1970) The web thickness of twist drills. *Annals of the CIRP* 18:81–85
- [6] Lorenz G (1979) Helix angle and drill performance. *Annals of the CIRP* 28:83–86
- [7] Armarego EJA, Cheng CY (1972) Drilling with flat rake face and conventional twist drills—Part I: Theoretical investigation. *Int. J. of Mach. Tool Des. and Res.* 12:7–35
- [8] Armarego EJA, Cheng CY (1972) Drilling with flat rake face and conventional twist drills. Part II: Experimental investigation. *Int. J. of Mach. Tool Des. and Res.* 12:37–54
- [9] Wang J, Zhang Q (2008) A study of high-performance plane rake faced twist drills. Part I: Geometrical analysis and experimental investigation. *Int. J. of Mach. Tools & Manufact.* 48:1276–1285
- [10] Stenphenson DA, Agapiou JS (1996) *Metal cutting theory and practice*. Marcel Dekker, New York
- [11] Bhattacharyya A, Bhattacharya A, Chatterjee AB, Ham I (1971) Modification of drill point reducing thrust. *ASME J. of Eng. for Ind.* 93:1073–1078
- [12] Vinogradov AA (1985) Physical foundation of the drilling of difficult-to-machine materials with carbide drills (in Russian). *Naukova Dumka*, Kyiv

- [13] Thornley RH, Wahab ABI, Maiden JD (1987) A new approach to eliminate twist drill chisel edge. Part 1. Asymmetrical configuration. *Int. J. of Prod. Res.* 25(4):589–602
- [14] Fuh K-H, Chen, W-C. (1995) Cutting performance of thick web drills with curved primary cutting edges. *Int. J. of Mach. Tools & Manufact.* 35(7):975–991
- [15] Chen W-C (1997) Applying the finite element method to drill design based on drill deformations. *Finite Elements in Analysis and Design* 26(1):57–81
- [16] Chen YR, Ni J (1999) Analysis and optimization of drill cross-sectional geometry. *SME Paper MR99–162*
- [17] Selvam SVM, Sujatha C (1995) Twist drill deformation and optimum drill geometry *Computers & Structures* 57(5):903–914
- [18] French LG, Goodrich CI (1910/2001) Principles of deep hole drilling, in *Deep Hole Drilling*. Machinery's Reference Series No. 25. 1910 (reprinted in 2001).: Lindsay Publication, Bradley, IL
- [19] Nakayama K, Ogawa M (1985) Effect of chip splitting nicks in drilling. *Annals of the CIRP* 34(1):101–104
- [20] Veremachuk ES (1940) Deep hole drilling (in Russian). State Publishing House of Defence Industry, Moscow
- [21] Astakhov VP, Shvets S (2004) The assessment of plastic deformation in metal cutting. *J. of Mat. Proc. Tech.* 146:193–202
- [22] Astakhov VP (2006) *Tribology of metal cutting*. Elsevier, London
- [23] Jawahir IS, Van Luttervelt CA (1993) Recent developments in chip control research and applications. *Annals of the CIRP* 42(2):659–693
- [24] Jawahir IS, Zhang JP (1995) An analysis of chip curl development, chip deformation and chip breaking in orthogonal machining. *Transactions of NAMRI/SME XXIII*:109–114
- [25] Jawahir IS, Balaji AK, Stevenson R, van Luttervelt CA (1997) Towards predictive modeling and optimization of machining operations. in *Manufacturing Science and Engineering*. In: Proc. 1997 ASME International Mechanical Engineering Congress and Exposition. Dallas, TX: ASME, 3–12
- [26] Sahu SK, Ozdoganlar OB, DeVor RE, Kapoor SG (2003) Effect of groove-type chip breakers on twist drill performance. *Int. J. of Mach. Tools & Manufact.* 43:617–627
- [27] Wu SM, Shen JM (1983) Mathematical model for multifacet drills. *ASME J. of Eng. for Ind.* 105:177–182
- [28] Wang S, Shu L, Xiao Z (1993) A new twist drill. *Cutting Tool Engineering* (2):32–35
- [29] Astakhov VP, Frazao J, Osman MOM (1994) On the experimental optimization of tool geometry for uniform pressure distribution in single edge gundrilling. *ASME J. of Eng. for Ind.* 118:449–456
- [30] Astakhov VP, Galitsky VV, Osman MOM (1995) A novel approach to the design of self-piloting drills. Part 1. Geometry of the cutting tip and grinding process. *ASME J. of Eng. for Ind.* 117:453–463
- [31] Astakhov VP, Galitsky VV, Osman MOM (1995) A novel approach to the design of self-piloting drills with external chip removal, Part 2: Bottom clearance topology and experimental results. *ASME J. of Eng. for Ind.* 117:464–474
- [32] Editorial (2001) Farewell to BUE. *Cutting Tool Engineering* 53(2):43–47
- [33] Galloway DF (1957) Some experiments on the influence of various factors on drill performance. *ASME Transactions* 79:191–231
- [34] Oxford CJ Jr (1955) On the drilling of metals—I. Basic mechanics of the process. *Transactions of the ASME* 77:103–114
- [35] Ernst H, Haggerty WA (1958) The spiral point drill—a new concept in drill point geometry. *Transactions of the ASME* 80:1059–1072



- [36] Webb PM (1993) The three-dimensional problem of twist drilling. *Int. J. of Prod. Res.* 31(5):1247–1254
- [37] Fujii S, DeVries MF, Wu, SM (1970) An analysis of drill geometry for optimum drill design by computer-I: Drill geometry analysis. *ASME J. of Eng. for Ind.* 92:647–656
- [38] Fujii S, DeVries MF, Wu SM (1970) An analysis of drill geometry for optimum drill design by computer-II: Computer aided design. *ASME Journal of Engineering for Industry* 92:657–666
- [39] Fujii S, DeVries MF, Wu SM (1971) An analysis of the chisel edge and the effect of the  $d$ - $\theta$  relationship on drill point geometry. *ASME J. of Eng. for Ind.* 93:1093–1105
- [40] Fujii S, DeVries MF, Wu SM (1972) Analysis and design of a drill grinder and evaluation of grinding parameter. *ASME J. of Eng. for Ind.* 94:1157–1163
- [41] Tsai WD, Wu SM (1979) A mathematical model for drill point design and grinding. *ASME J. of Eng. for Ind.* 101:333–340
- [42] Tsai WD, Wu SM (1979) Computer analysis of drill point geometry. *Int. J. of Mach. Tool Des. and Res.* 19:95–108
- [43] Tasi WD, Wu SM (1979) Measure and control of the drill point grinding process. *Int. J. of Mach. Tool Des. and Res.* 19:109–120
- [44] Kaldor S, Moore K (1983) Drill point designing by computer. *Annals of the CIRP* 32:27–31
- [45] Watson AR (1985) Geometry of drill elements. *Int. J. of Mach. Tool Des. and Res.* 25:209–227
- [46] Salama AS, Elsayw AH (1996) The dynamic geometry of a twist drill point. *J. of Mat. Proc. Tech.* 56:45–53
- [47] Billau, D.J., McGoldrick, P. F. (1979) An analysis of the geometry of the periphery of the flank face of twist drills ground with cylindrical and conical forms. *Int. J. of Mach. Tool Des. and Res.* 19:69–86
- [48] Kaldor S, Lenz E (1982) Drill point geometry and optimization. *ASME J. of Eng. for Ind.* 104:84–90
- [49] Hsiau JS (1985) Computer aided design of multifacet drills. *Transactions of NAMRI/SME* 13:490–496
- [50] Hsieh J-F, Lin PL (2002) Mathematical model of multi-flute drill point. *Int. J. of Mach. Tools & Manufact.* 42:1181–1193
- [51] Kennedy B (2006) The straight story. *Cutting Tool Engineering* 58(1):58-64
- [52] Rodin PR (1971) *Cutting Geometry of Twist Drills* (in Russian). Technika, Kyiv
- [53] Granovsky GE, Granovsky VG (1985) *Metal cutting* (in Russian). Vishaya Shkola, Moscow
- [54] Beyer WH (1987) *CRC standard mathematical tables*. 28th ed. CRC, Boca Raton
- [55] Mollin RA (1995) *Quadrics*. CRC, Boca Raton
- [56] Astakhov VP (2004) The assessment of cutting tool wear. *Int. J. of Mach. Tools & Manufact.* 44:637–647

## Deep-hole Tools

*You can avoid reality, but you cannot avoid  
the consequences of avoiding reality.*

Ayn Rand (1905–1982)

**Abstract.** This chapter discusses classification, geometry, and design of deep-hole drills. The concept of self-piloting is explained. The system approach to deep-hole machining is introduced and common system issues are discussed with examples. The major emphasis is placed on gundrills. A number of simple design rules are proposed and explained with examples. The conditions of free penetration of the drill into the hole being drilled are explained. The geometry consideration is systemically related to MWF flow and thus the concept of the optimum MWF flow rate is explained. A number of novel design concepts are revealed. This chapter also discusses system consideration in experimental study of gundrill parameters. It is demonstrated that tool life is a complex function not only of geometry parameters and machining regime alone but also of their combination. Tool geometry optimization using the Hooke and Jeeves method is also discussed.

### 5.1 Introduction

The term deep hole machining (DHM) relates to a machining operation of a hole with an excessive depth-to-diameter ratio (known as  $L/D$ ). For many years it was considered that if an  $L/D$  is 3–5, one enters the realm of DHM that implies the use of special tools and machines. With the introduction of some modern machinery and tooling including high-pressure solid carbide straight-flute and twist drills, this range is considered to be too conservative. Nowadays, an  $L/D$  greater than 8 can be accepted as a reasonable indicator.

However, the  $L/D$  criterion is not sufficient to make the proper decision in a consideration of hole manufacturing where there are high requirements of diametric accuracy, hole longitudinal axis, straightness, surface finish, etc. This is because, when properly used, DHM tools produce superior holes with close

tolerances. It is possible due to the fact that a group of special tools, called self-piloting tools (hereafter SPT), are normally used in deep hole machining when the quality requirements are high and when L/Ds are excessive.

The techniques of self-piloted drilling began developing in the late eighteenth century with the growing need for more accurate bores in rifle barrels and cannons. While self-piloting drills (hereafter SPD) are still used for this purpose, their use has been extended to an increasingly wider variety of applications. Today SPDs are the most efficient tools, if not the only tools, for producing extremely deep holes, regardless of the precision required.

While most applications involve hole depths varying from 10 to 30 diameters, it is common to encounter drills with depth-to-diameter ratios of 100 to 1. Furthermore, holes with depth-to-diameter ratios of 300 to 1 have been successfully drilled [1]. While such features may be accomplished with a twist drill, the extra problems involved in getting MWF (coolant) in and the chips out of the hole makes it quite difficult to drill beyond an L/D of about 20 to 1, and completely impractical for an L/D beyond 50 to 1.

Besides high L/Ds, SPDs are also capable of drilling very straight deep holes. The hole that the tool has machined is actually a continuation to the guide bushing so that the tool will continue to machine a straight hole along the same initial direction. Although the SPT were developed primarily for producing deep holes, their ability to produce holes of good surface finish and close size control is often attractive to engineers requiring close tolerance holes of much shorter lengths. SPDs can even be economical for holes as short as one diameter, under certain conditions.

Usually in order to produce a finished hole, two to five operations are required: drilling, boring, rough and finish reaming, and finally honing. Not only are these operations costly by themselves, but each carries many other hidden costs that may not be so obvious. These include the cost of multiple handling and transporting of the parts between several machines; making extra setups; carrying more sizes and kinds of tools; and, under critical conditions, they can require extra inspections which involve the procuring and maintaining of gages and allied equipment.

SPDs can eliminate such subsequent operations if one or more of the following conditions exist: (1) the precision requirements for the drilled hole (either size, finish, straightness, location, or all four) are such that they are difficult to attain by the more conventional methods, (2) the material is one in which a self-piloting drill can readily produce the degree of precision required, (3) the configuration of the part is such that it would be difficult to index from one station to another, (4) the location of the hole must be held accurately with respect to other holes or surfaces, and (5) the size of the hole or the configuration of the part and/or machine would require special tooling and/or fixture.

However, SPDs also have their limitations in deep hole applications. A tool as long as 100 diameters or more is rather flimsy and obviously cannot withstand as much torque or thrust as a shorter tool. Not only will the torque cause torsional deflection or twisting, but the axial force can cause axial deflection or buckling of the tool. Due to this fact, SPDs are very sensitive to even small changes in their geometric parameters and require both a proper design and a skillful regrinding procedure. Unfortunately to date, little is known of the choice of the SPD

geometric parameters and their influence on tool life, quality of the machined holes, and stability of the drilling process, etc. Because of this, the choice of the SPD parameters is based on the experimental data and there are no sufficient explanations of the inter-influence of the drill parameters, specific drill's angles, and drill geometry.

## 5.2 Generic Classification of Deep-hole Machining Operations

In general, deep-hole machining operations are classified by the method of MWF supply and chip removal. It can be gundrill (gun-)type machining, BTA-type (known also as the single-tube system or STS) machining, and Ejector-type machining.

The principle of gundrilling is shown in Fig. 5.1. MWF is supplied under high pressure through the tool holder to the drill shank. Then the supplied MWF flows through a kidney-shaped internal passage made in the shank and then through the coolant passage made in the tip. After cooling and lubrication the machining zone, MWF carries away the formed chips in the mixture (often referred to as the swarf) over the external V-shaped flute made on the shank. The swarf ends up in the chip box from where it goes into the chip separator.

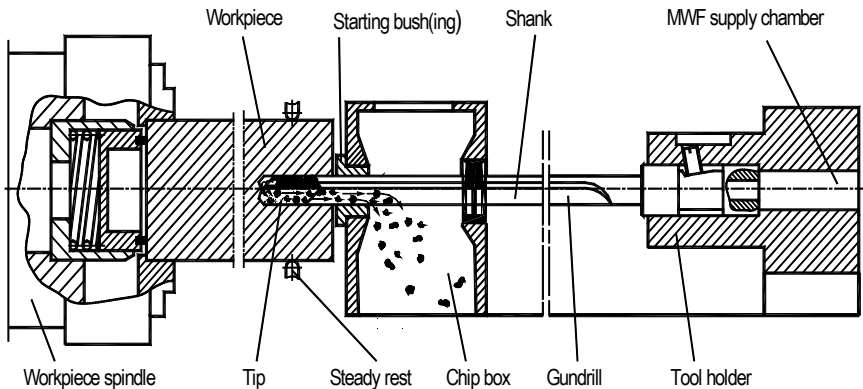
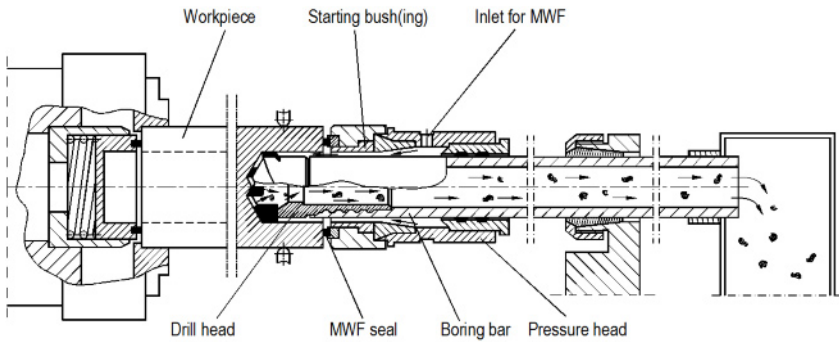


Fig. 5.1. Gundrilling

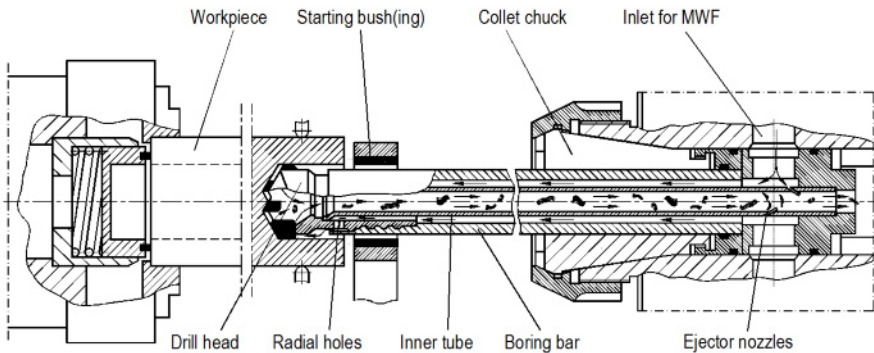
Figure 5.2 shows the principle of BTA drilling. The BTA tool consists of a boring bar and a single or a multi-edged drill head secured at its terminal end. MWF is supplied under high pressure through the inlet of the pressure head and flows through the annular channel between the boring bar and the bore wall towards the drill head. After cooling and lubricating the machining zone, MWF carries away the chips through the interior of the drill head and boring bar. In contrast to gundrilling, the returning chips do not come in contact with the bore wall and thus a better surface finish can be achieved.

The tubular cross-section of the boring bar possesses greater buckling stability compared to the gundrill's shank and thus the greater feed rates can be achieved in BTA drilling. As such, the annular chip removal channel is of much greater cross section compare to the V-flute of the gundrill and thus more chip per unit time can be transported without clogging. Moreover, even when chip clogging occurs due to poor chip breaking, the inlet pressure increases helping to push forward the chip cluster that clogs the chip removal channel. A requirement for reliable sealing between the face of the workpiece and the pressure head is a price to pay for this advantage.



**Fig. 5.2.** BTA drilling

Figure 5.3 shows the principle of ejector drilling. MWF is supplied to the inlet of the collet chuck. Then this fluid separates into two parts. The first part flows in the annular channel formed by the boring bar, called the outer tube and the inner tube. In the drill head, MWF flows outside through the radial holes made in the drill head and thus this reaches the machining zone where it cools and lubricates the cutting elements and the bearing areas. Then the MWF-chip mixture (the swarf) goes into the inner tube. The second part flows through the ejector nozzle(s) on the inner tube. As a result, this flow creates a partial vacuum (the ejector effect) in the inner tube which sucks the swarf into the inner tube like a vacuum cleaner.



**Fig. 5.3.** Ejector drilling

The great advantages of ejector drilling are: (1) there is no need for a non-reliable seal between the face of the workpiece and the starting bushing, (2) much lower inlet MWF pressure is needed. As a result, ejector drilling does not always require a special drilling machine as it can be used in many general purpose machines or even machining centers as one of common drilling operations.

However, this versatility comes at certain costs. First, it is not available for hole diameters below 20 mm. Second, it is suitable only for the work materials that generate easy-to-control chips. That eliminates most nickel-based and many non-ferrous alloys. This is because if the chip even slightly clogs the chip removal channels including the inner tube, there is no pressure available to push the formed chip cluster through as the maximum pressure created by the ejector is much less than 0.1MPa. As a result, MWF that leaves the radial coolant holes then flows between the boring bar and the bore outside the drilling coolant circuit. When this happens, the drill normally breaks.

## 5.3 What does ‘Self-piloting Tool’ Mean?

### 5.3.1 Force Balance in Self-piloting Tools

To comprehend the concept of SPT, one should first consider the force balance of multi-edge drilling tools discussed in Chap. 4, Sect. 4.5.

Figure 5.4 shows a simple drill head of an SPT. It has the cutting insert and two supporting pads located on the tool body. Figure 5.5 shows the force balance for such a tool in the T-mach-S  $x_0y_0z_0$  coordinate system. When an SPT works, the cutting force generated is due to the resistance of the workpiece material to cutting. This force is a 3D vector which can be thought of as applied at a certain point of the drill rake face. The cutting force  $\mathbf{R}$  (or the resultant cutting force for multi-edge tools) can be resolved into three components, namely: the power (tangential)  $\mathbf{F}_x$ , axial,  $\mathbf{F}_{z_s}$ , and radial,  $\mathbf{F}_y$  components, respectively, commonly referred to as the tangential, radial, and axial forces [2]. The axial force is balanced (equal in magnitude and opposite direction) by the axial force  $\mathbf{F}_{z-s}$  of the feed mechanism of the deep-hole machine while the tangential and radial forces sum to create force  $\mathbf{F}_{zy}$  (acts in the  $z_0y_0$  plane) which (in contrast to other axial tools such as twist drills, reamers, milling tools) is generally not balanced, regardless of the number of cutting edges used. To prevent drill bending due to this unbalanced force, some special measures are taken. The term ‘deep-hole drilling’ has grown to mean that the unbalanced cutting force generated in the cutting process is balanced by the equal and opposite force due to supporting pads, which bear against the walls of the hole being drilled.

Due to the action of the mentioned forces on the supporting pads, these pads ensure balancing of the tool in the  $x_0y_0$  plane simultaneously providing for a unique additional machining operation known today as burnishing. The fact that the pads bear against the walls of the hole being drilled behind the side cutting edge effectively means that the tool machines its own bushing. The concept of self-piloting (sometimes referred to as self-guidance), meaning the tool guiding or

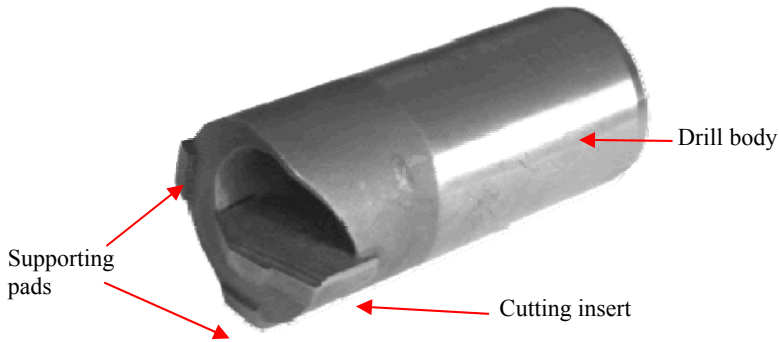


Fig. 5.4. Simple self-piloting drill head

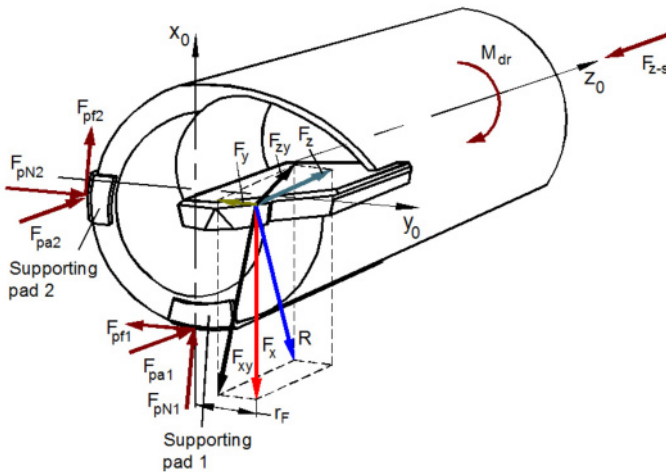


Fig. 5.5. Force balance for a typical self-piloting tool

steering itself along the bore, has been recognized as the major underlying principle of the design of STDs [3, 4].

Not only does the self-piloting design make it possible to machine deep holes but it also provides stable cutting conditions for the cutting insert or cutting portion of the tool through elimination of the radial vibrations that often cause drill failure in ordinary drills [5]. When machining conditions are selected properly, a machining operation with SPT is very stable and consistently produces holes of high quality. Although the use of SPTs requires a number of additional accessories such as starting bushings, high-pressure coolant system, etc., the benefits gained with the use of these tools are greater as SPTs proved capable of maintaining close size control and producing holes of good surface finish that met the output requirements of honing. The elimination of the whole sequence of standard hole-making operations makes the use of SPTs appealing even for machining shallow

holes. Thus, the use of SPTs is considered whenever one or more of the following conditions exist:

- $L/D > 8$
- Precision requirements – size, surface finish, and straightness – difficult to attain by conventional hole machining operations
- Tight position tolerance on the longitudinal axis of the machined hole
- Tight shape tolerance on the machined hole

One important feature of the force balance shown in Fig. 5.5 is that the tangential and radial forces (or their resultant  $\mathbf{F}_{xy}$ ) are normally fully balanced by the normal,  $\mathbf{F}_{pN1}$  and  $\mathbf{F}_{pN2}$  and tangential  $\mathbf{F}_{pf1}$  and  $\mathbf{F}_{pf2}$  reactions acting on the supporting pads [3, 6]. The axial force  $\mathbf{F}_z$  is balance by the  $\mathbf{F}_{z-s}$ . The problem with the drill head shown in Figs. 5.4 and 5.5 is additional bending moment. The equilibrium condition in the  $x_0y_0$  plane

$$F_z r_F = F_{pa1} (d_{dr}/2) + F_{pa2} (d_{dr}/2) \quad (5.1)$$

Because the friction forces  $\mathbf{F}_{pa1}$  and  $\mathbf{F}_{pa2}$  are low compared to the axial force  $\mathbf{F}_z$ , this causes the additional bending moment

$$M_{b-Fz} = F_z r_F - (F_{pa1} (d_{dr}/2) + F_{pa2} (d_{dr}/2)) \quad (5.2)$$

which tends to bend the drill in the counterclockwise direction in the  $z_0y_0$  plane.

A number of measures have been undertaken to reduce harmful consequences of this moment. The most common is to use very shallow feed rates to reduce the axial force. This measure, however, results in low productivity in SPT machining. Another common measure is to introduce additional array of the supporting pads at the rear end of the drill head.

The problem with the above-mentioned force balance was solved when STPs with the partitioned cutting edge were introduced. In such drills, the cutting inserts are located on the both sides of the  $x_0$ -axis. Figure 5.6a shows a traditional SPT and Fig. 5.6b shows a tool with the partitioned cutting edge. A simplified force model in the  $y_0z_0$  plane for a drill with the partitioned cutting edge is shown in Fig. 5.7. A simple condition of equilibrium, where there is no bending moment is this plane directly follows from Fig. 5.7

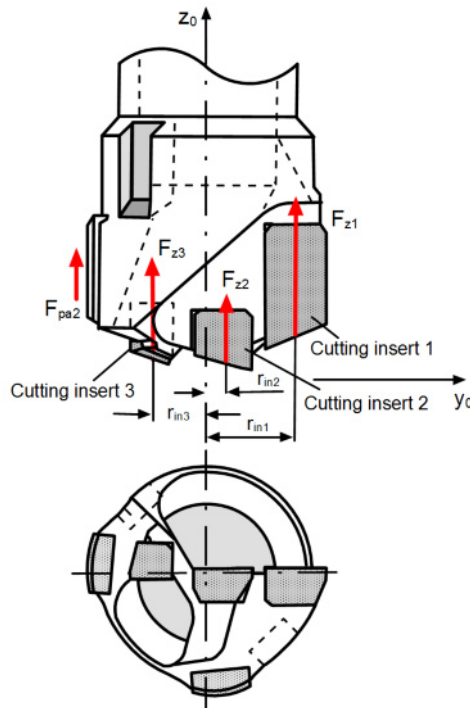
$$F_{z1} r_{in1} + F_{z2} r_{in2} = F_{z3} r_{in3} + F_{pa2} r_{dr} \quad (5.3)$$

Although, such a design was apparently introduced to improve the chip removal as the chip flow is separated into two portions that flow in two chip mouths, it was soon found that such drills allow much greater feeds measurable with those found in conventional twist drilling. This advantage of such drills has never been explained in the manner offered here.





**Fig. 5.6.** Drill design: (a) with single cutting insert, and (b) with partitioned cutting edge made by three cutting inserts



**Fig. 5.7.** Simplified force balance in the  $y_0z_0$  plane

Nowadays, multi-edge and multi-supporting pad SPT tools are used thus the described self-piloting feature may not be obvious. Figure 5.8 shows a model for such a SPT. Referring to Fig. 5.8,  $F_{xy1}$ ,  $F_{xy2}$ ,  $\dots$ ,  $F_{xyn}$  are the cutting forces acting on the cutting inserts (it is assumed that the tool has  $n$  cutting inserts) in the  $x_0y_0$  plane then the cutting moment  $\mathbf{M}$  and the unbalanced force resultant  $\mathbf{R}_s$  in the  $x_0y_0$  plane are calculated from the equilibrium conditions as follows [7]

$$\mathbf{M} = -\sum_{i=1}^n (\mathbf{r}_i \times \mathbf{F}_{xyi}) \quad (5.4)$$

and

$$\mathbf{R}_s = \sum_{i=1}^n \mathbf{F}_{xyi} \quad (5.5)$$

Expressing Eq. 5.5 in complex form, one obtains

$$\mathbf{R}_s = |\mathbf{R}_s| \exp(j\lambda) = \sum_{i=1}^n |\mathbf{F}_{xyi}| \exp j(\psi_i + \phi_i) \quad (5.6)$$

where  $\lambda$  is the angle of vector  $\mathbf{R}_s$  with respect to the  $y_0$ -axis.

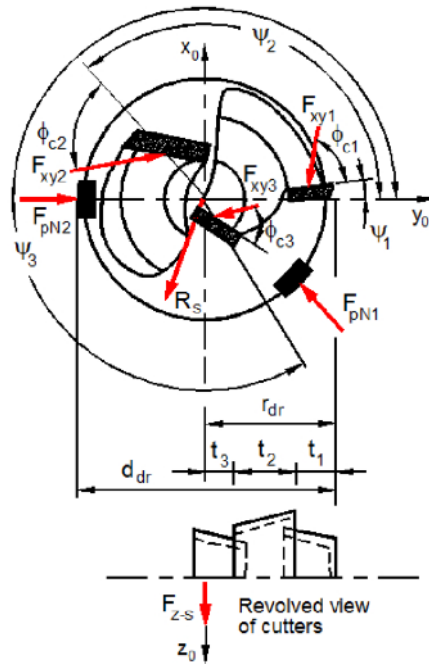


Fig. 5.8. Model of an asymmetrical multi-edge SPT

Equation 5.6, written in the trigonometric form, gives the magnitude  $R_s$  and the directional angle  $\lambda$  of the resultant  $\mathbf{R}_s$ :

$$R_s = \left[ \left( \sum_{i=1}^n |F_{xyi}| \cos(\psi_i + \phi_i) \right)^2 + \left( \sum_{i=1}^n |F_{xyi}| \sin(\psi_i + \phi_i) \right)^2 \right]^{1/2} \quad (5.7)$$

$$\lambda = \arctan \left( \frac{\sum_{i=1}^n |F_{zyi}| \sin(\psi_i + \phi_i)}{\sum_{i=1}^n |F_{xyi}| \cos(\psi_i + \phi_i)} \right) \quad (5.8)$$

Angles  $\psi_i$  are the location angles of SPT cutting inserts with respect to the  $y_0$  axis as seen in Fig. 5.8.

Equations 5.4 through 5.8 can be used for direct computation and optimization of the supporting pad reactions for given tool diameter, number, location, and geometry of the cutting inserts, machining regime and work materials properties.

The foregoing analysis suggests that the terms 'self-piloting tools' (SPTs) and 'self-piloting drills' (SPDs) which convey the idea of the drill guiding or steering itself during a drilling operation due to the inventively imbalanced radial force should replace the widely used terms as 'gundrill', 'BTA', or 'ejector drill' which reflect, as mentioned above, methods of MWF supply only. It is clear that according to the introduced principle the term 'gundrill' means a self-piloting drill with internal MWF supply and external chip removal, which may have one or more cutting elements. The term 'two-flute gundrills', which is currently widely used in practice to describe a deep-hole drill with two identical cutting elements symmetrically located with respect to the drill longitudinal axis, should not be used. This is because as there is no (at least, theoretically) unbalanced radial force, it is simply wrong to regard such a tool as a gundrill. It is not self-piloted although it is a drill with internal coolant supply and external chip removal along straight V-flutes.

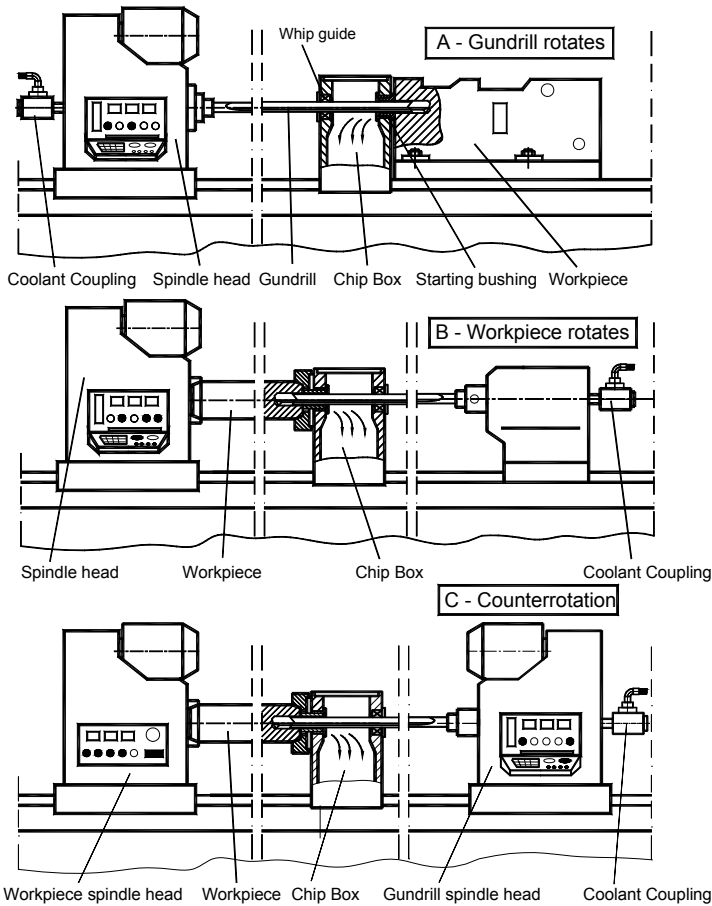
## 5.4 Three Basic Kinematic Schemes of Drilling

A particular kinematic scheme of drilling is defined by what component of the SPT rotates. In terms of relative rotation, there are three possible kinematic schemes of SPT drilling shown in Fig. 5.9. In this figure, gundrilling is used for the sake of explanations which are valid for any kind of drill.

When there are no installation errors, no misalignment between the axis of the drill and that of the hole to be drilled, no clearance in the starting bushing, etc., the results obtained using these three scheme are exactly the same in terms of quality of machined holes. It is understood, however, that this is not the case in practice. In the real world, the mentioned inaccuracies affect the various parameters of quality of machined hole differently depending upon the particular scheme used.

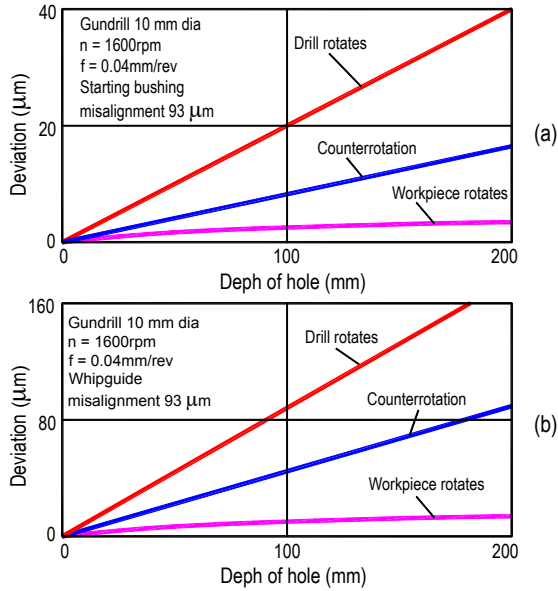
### 5.4.1 Gundrill Rotates and the Workpiece is Stationary

This scheme is used when the workpiece has a shape that not suitable for its rotation. The use of this method imposes special requirements on the accuracy of the gundrill used and gundrilling installation. The alignment of the gundrill components should be next to perfect when drilling holes of relatively small diameter (less than 10mm) in light materials such as aluminum alloys, i.e., when the rotational speed (6,000–15,000 rpm) and the feed rate (600–1400 mm/min) are high.



**Fig. 5.9.** Three basic kinematic schemes of drilling

Compared to the other kinematic schemes shown in Fig. 5.9, the best diametral accuracy and surface finish and the worse deviation of the hole axis hole (Fig. 5.10) are common features of this method. The clearance in the starting bushing, drill holder-starting bushing, and whipguide alignments, and the accuracy of the feed motion are the key factors in using this method when the deviation of the hole



**Fig. 5.10.** Deviation of the hole axis (position error) for different gundrilling methods: (a) influence of the misalignment of the starting bushing, and (b) influence of the misalignment of the whip guide

axis is also important. Extremely important and unknown to end users fact follows from the comparison of Fig. 5.10a,b: the whipguide alignment affects the deviation of the hole axis much more than that of the starting bushing [8].

A high speed coolant coupling should be used to introduce high-pressure MWF to the rotating spindle which normally limits the higher allowable MFW pressure and spindle speed. A balanced collet chuck or shrink fit holder should also be used to reduce “whipping” on longer drill applications.

#### 5.4.2 Workpiece Rotates and the Gundrill is Stationary

This method is used when the workpiece has a suitable shape allowing its accurate clamping and high-speed rotation. The drill monitoring, MWF supply, and chip evacuation are easier compared to the first method. The minimum deviation of the hole axis (Fig. 5.10) and the worse diametral accuracy are common features of this method.

#### 5.4.3 Counterrotation

This method is used when both the diametral accuracy and position of the axis of drilled holes are important. Both the workpiece and the gundrill rotate. Normally, rotations of the drill and the workpiece are opposite so that this method is also known as the counterrotation drilling method. Traditionally it was used when the

speed of one rotation is not sufficient to achieve the required cutting speed particularly for gundrills of small diameters. As can be seen in Fig. 5.10, the use of this method requires special machines having two spindle heads. As a result, such machines are much longer than those used in the first method and more expensive than those used in the first and the second methods.

## 5.5 System Approach

### 5.5.1 Handling Tool Failure

Although the general intent of a tool manufacturing company is to supply the right tool at the right time and at the right cost, no definition(s) of the word “right” is normally provided. Presumably, one can define that the “right time” is when the customer needs the tool to keep its production running; the right cost can be justified by calculating tooling cost per unit (CPU) for a given application, showing that it is lower than that for similar applications. The term “the right tool,” however, is totally illusive.

The “right tool” can be thought of as one made to the print (drawing) approved by the customer (for example, an automotive company) and thus posted in the corresponding tooling database system. However, if this tool does not work properly, the blame goes to the tool supplier. Moreover, this supplier becomes responsible for the investigation of the tool failure. Normally, a sales representative of the tool supplier picks up the failed tool, asking some question surrounding the failure, and the failed tool is sent back to the tool supplier with minimum info on this failure. The tool supplier should complete a 5Why form so that the root cause of the problem can presumably be found and thus corrected. In reality, however, it is not the case as most of the filled 5Why forms do not even tackle the root cause of the problem unless there is manufacturing flaw(s) obvious to everyone found in the failed tool. This is because:

- The information provided to the tool manufacturer to carry out a failure analysis is normally incomplete and often misleading.
- Many tool manufacturers do not have sufficiently educated and trained personnel and equipment to do such an analysis. Moreover, the top research and technical personnel of the overseas tool companies are located far away so they cannot see the “crime scene” and question the people involved is the case. As a result, a root cause analysis is based on second or even third hand information about the failure. Moreover, such analyses cannot be completed in a timely manner.

That is why many completed 5Why analyses failed to find the root cause of the problem. Rather, a bandage is offered, which lasts to the next tool failure. When the number of such bandages exceeds a certain critical level, fire-fighting tool management becomes a way of life. It is not uncommon that a site tool manager lives on a 24/7 schedule to receive a call for the next tool failure. To prevent this scenario from happening, system engineering should be an inherent part of tool and application specialists’ training curricula.

## 5.5.2 System Considerations

### 5.5.2.1 Gundrilling System

Although the following section discusses the system approach to gundrilling, its main ideas are fully applicable to any cutting tool and tooling. In the author's opinion, such an approach should be used in machining system design, retrofitting, components and tool selection, i.e., in any aspect of manufacturing.

Many tool manufacturers do not have adequate technical support as they rely on the experience and expertise of their sales force. Although sales specialists can suggest the best product they have, it may not be suitable for a given application which they are not trained to understand fully. For example, if one buys and installs advanced sidewall design tires specially designed for use at the Indianapolis 500 with the Speedway's distinctive "Wing and Wheel" official logo in full color on an old car, the performance of the car will be worse than with its old "native" tires. Although these tires are probably the best that the tire manufacturers can offer (not to mention their cost), they are not suitable for this old car. The same analogy can be made for cutting tools – the best and most expensive tool will not perform well if the machining system does not support its performance. In other words, a tool may have the best geometry, tool materials, and can be perfectly designed, but it may not perform well for a given application.

Significant progress in gundrilling has been achieved that resulted in introduction of high penetration rate gundrilling [9]. It has emerged during the last 10 years as the process that allows the penetration rate of more than 1,000 mm/min for aluminum alloys, more than 250 mm/min for cast irons, and more than 180 mm/min for alloyed steels. It became possible due to significant improvements in the manufacturing quality of gundrills including the quality of their components, implementation of better gundrilling machines equipped with advanced controllers as well as their proper maintenance, application of better MWFs, better training of engineers and operators, and many other factors. However, the actual penetration rate and drilling process efficiency (the cost per unit length of drilled holes) vary significantly from one application to another, from one manufacturing plant to the next, depending on an overwhelming number of variables. Optimum drill performance in gundrilling is achieved when the combination of the cutting speed (rpm), feed, tool geometry, carbide grade, and MWF parameters is selected properly depending upon the work material (its hardness, composition, and structure), deep-hole machine conditions, and the quality requirements of the drilled holes [10]. To get the most out of a gundrilling job, one must consider the complete gundrilling system, which includes everything related to the operation (Fig. 5.11). Such a consideration is known as the system engineering approach according to which the gundrilling system should be distinguished and analyzed for coherency of its components.

According to system engineering theory, it is improper to consider any component of machining operation separately, thereby ignoring system properties. The so-called "component approach" is a common manufacturing practice in today's environment, where different manufacturers produce the various components of the machining system but no one seems to be responsible for system coherency. Tool failure is a direct result of such an approach because the





its control unit, MWF (coolant) parameters and coolant delivery unit, fixture and accessories, workpiece, operator, and maintenance. One can appreciate the system properties of the gundrilling system if he realizes that the same gundrill used in different gundrilling machines shows a wide range of outcomes from breakage to excellent performance; the same gundrill used on the same machine exhibits different results for different work materials; the same gundrill used on the same machine for drilling the same work material performs differently depending upon a particular brand of coolant used for the operation, the coolant flow rate, filtration and temperature; the performance of the same gundrill used on the same machine for drilling the same work material using the same coolant parameters would depend largely on the extent of the operator's experience and training. The latter is particularly true if the control system provides relevant information to the operator. As seen, each system component can affect system performance dramatically. The key here is to assure system coherency, i.e., the condition when all system components work as a 'team' to achieve the ultimate system's objective.

Unfortunately, the tool manufacturer is often unfairly blamed as the lone culprit because the gundrill, as the weakest link, fails as a result of improper performance of various components of the gundrilling system. For example, one manufacturer of gundrills for the automotive industry was blamed for gundrill breakage occurring at the tip-shank brazed joint. For over 5 years this manufacturer tried to improve the strength of this joint. When this strength became sufficiently great, breakage of gundrill carbide tips began to occur. An analysis of the root cause of this problem showed that the lack of the MWF flow rate supplied to the drilling zone caused drill breakage. Because the root cause was not properly determined, the increased strength of the discussed brazed joint shifted the breakage to the carbide tip as a new weakest link. Yet another common case is insufficient quality of the MWF in terms of its concentration and purity. When this MWF is used, gundrills' tool life deteriorates dramatically. Again, gundrill manufacturers are unfairly blamed for poor tool life.

#### *5.5.2.2 Common System Issues*

Although the complete description of the coherency of the gundrilling systems is a separate subject, some very important features of the components of such a system will be discussed in this section. One should realize that gundrilling is not always a precise science or art that can be defined in exact formulas. The design of gundrilling systems also requires experience to develop skill, methods, and 'know how' accumulated over the years. That is why the hands-on approach [11], combined with the theory of gundrilling, can help solve a variety of design and application problems.

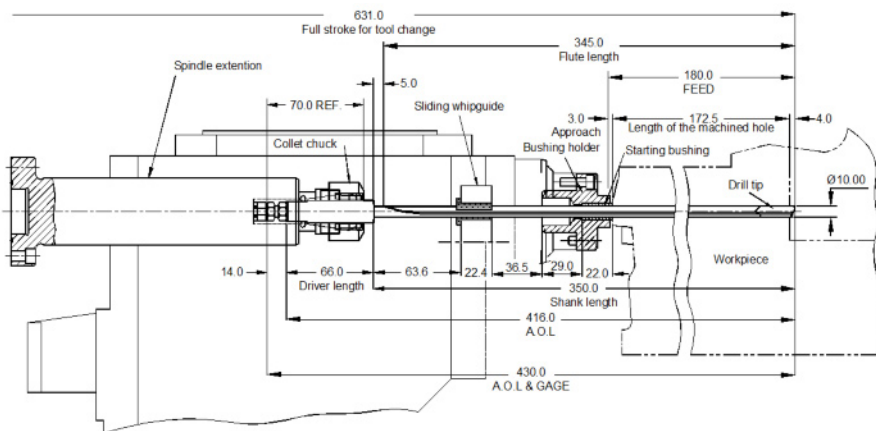
#### *Alignment*

The most common method of gundrilling in the automotive industry is one where the gundrill rotates and the workpiece is stationary. As discussed above, this method imposes special requirements on the accuracy of gundrilling machines and their components [12]. The alignment of the gundrill components should be next to perfect when drilling holes having diameters less than 10mm in light materials such as aluminum alloys, i.e., when the rotational speed (6,000–15,000 rpm) and

the feed rate (600–1,200 mm/min) are high. The clearance in the starting bushing, drill holder-starting bushing, and whipguide alignments, and the accuracy of the feed motion are key factors in using this method.

Although the importance of machine alignment is well known [13, 14], and its awareness grows in the automotive industry, there are at least three important issues that remain. First, there is no simple way to check the discussed alignment in many gundrilling machines built in production lines. Normally, it takes many hours to clean up the space for such an inspection. Second, the discussed gundrilling machines do not have any means to correct alignment when needed. Commonly, shims are used to adjust this alignment that reduces the machines dynamic stability. Third, the alignment is normally checked between the starting bushing holder and the spindle of the machine. Although it is an important parameter, it is not nearly sufficient. It should be clearly understood that the alignment in the system ‘actual gundrill holder – actual starting bushing’ should be examined although it is not that easy accounting for the current method and accessories used for misalignment checking.

The drill length  $L_{dr}$  is one of the most important system parameters. Needless to say, this length should be as short as possible. The proper way to determine this length is to design the so-called tool layout. An example of the tool layout is shown in Fig. 5.12. The following sequence is recommended for determining the drill length: start with the length of the machined hole then add the approach and overshoot distances, then the length of the bushing including bushing holder, chip box, etc.



**Fig. 5.12.** A typical tool layout to determine the drill length

At this point an important decision is to be made about the use of steady rest(s) and their number to restrict whipping of the shank. Figure 5.13 helps to make such a decision. For example, if the shank length of an 8 mm drill rotating at 3,000 rpm is 400mm, then a whip guide is needed because the maximum allowable distance

between supports for these conditions is 350mm. Information similar to shown in Fig. 5.13 should always be requested from gundrill manufactures.

It is worthwhile to point out that gundrills can also be classified according to drill length-to-diameter ratio. When this ratio is less than 10, gundrills are called short; when it is between 11 and 50, gundrills are called normal; when it is between 51 and 100 and they are called long; and when this ratio exceeds 100, gundrills are called extra long. The properties of the gundrill system must be adjusted depending on the category a particular gundrill falls in to.

For short gundrills, the alignments ‘tip–shank’ and ‘drill holder–starting bushing’ are key factors. This is because the shank of short gundrills is rigid so a significant additional force directly proportional to the misalignment acts on the gundrill. This force, which may well exceed the cutting force, causes multiple problems in drilling such as chipping of the cutting edge, poor surface finish, inadequate diametric accuracy, and low tool life. Therefore, the discussed alignment should not exceed 2 microns. When this alignment cannot be adjusted to this accuracy (for example, when the gundrill is to be used on a versatile CNC machining center or on a gundrilling machine which does not have suitable alignment adjustments), the length of the gundrill must be deliberately increased to allow the gundrill to be truly self-piloting and thus to reduce the consequences of shank high rigidity.

Gundrills of normal length require that the alignment ‘drill holder–starting bushing’ is adjusted to be no worse then 4–6 microns. This is particularly important when the drill rotates because the addition force due to misalignment caused shank failure due to accumulated fatigue. As such, a fatigue crack develops in the shank as shown in Fig. 5.14a. The worse case scenario occurs when the additional forces due to misalignment act in the direction of the side cutting edge.

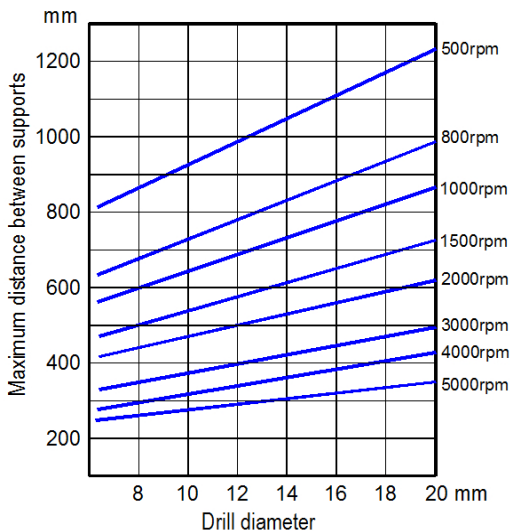
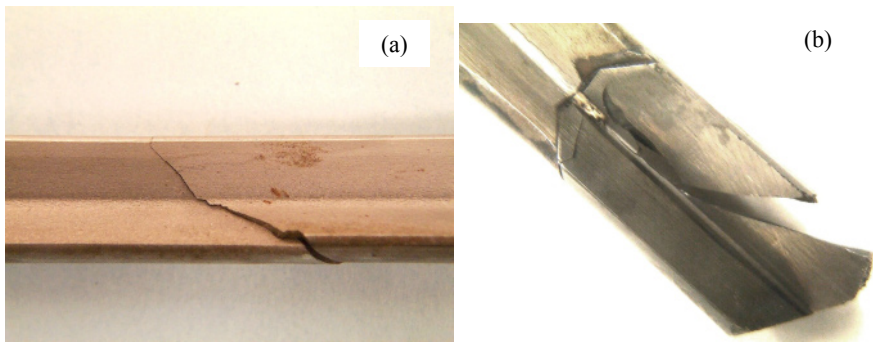


Fig. 5.13. Maximum allowable distance between supports

This normally leads to the fracture of this edge (as shown in Fig. 5.14) because its geometry is not designed to cut the work material in the transverse direction.

Long and especially extremely long gundrills suffer low torsion strength. The alignment ‘drill holder-starting bushing’ becomes not that important and should be not worse than 15–20 microns. For a given drilling torque, the angle of twist of the shank is proportional to its length and thus the maximum angle of twist is at the shank-driver connection. When this angle exceeds its critical value, the shank fails. When it happens, the failed gundrill looks like a twist drill having a helical V-flute.



**Fig. 5.14.** Gundrill failures due to excessive misalignment: (a) shank fatigue crack, and (b) fracture of the side cutting edge

### *MWF Issues*

High-pressure MWF delivery is necessary to cool the workpiece and the tool, to provide lubrication between tool and workpiece, as well as to carry away chips from the machining zone along the flute to the chip box. Cooling action dissipates both the external heat of friction and the internal heat of plastic deformation due to cutting and burnishing. Lubrication between the workpiece and the drill contact areas reduces contact stresses and the amount of the thermal energy generated in these areas so it reduces adhesion and/or diffusion wear of the gundrills. To move chips away effectively, the MWF should possess a sufficient combination of viscosity and velocity. Improper selection of this combination causes chip clogging in the flute that lead to an increase in torque and probable drill breakage in the manner shown in Fig. 5.15. As insufficient MWF flow rate in drilling is one of the most common and, at the same time, least understood issues, and it is discussed in this chapter in detail.

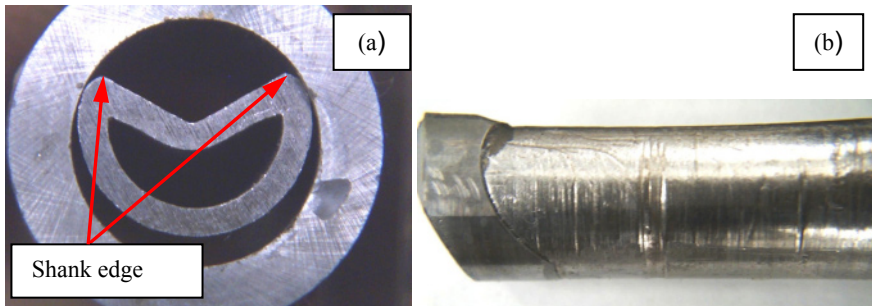
### *Shank*

The shank must be designed and made properly. Although there are a number of issues that affect shank performance, the excessive corner radii and shank material related considerations are of prime concern in high penetration rate gundrilling. Figure 5.16a shows corner radii as they appear on a shank cross-section. Such

excessive corner radii trap chips transported along the V-flute because the shank rotates at high speed in high penetration rate gundrilling. As a result, chips are trapped in the space between the wall of the hole being drilled and the shank side surface damaging the shank (as shown in Fig. 5.16b) and the walls of the drilled hole causing increased drilling torque that limits penetration rate.



**Fig. 5.15.** Gundrill failure due to chip clogging

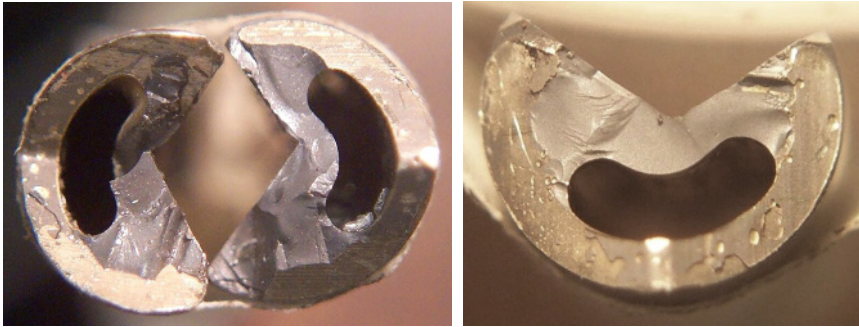


**Fig. 5.16.** Shank corner radii: (a) as it appears on a shank cross-section, and (b) shank damaged by chips penetrating between the shank and the wall of the hole being drilled due to excessive corner radii

Gundrill shanks must be made of a high yield strength material and properly heat treated. Unfortunately, these issues are not always followed by gundrill manufacturers. First, high yield strength materials present problems (such as excessive warping, wrinkling, cracking) when the V-flute is formed (crimped) using old tube crimping technology. As a result, tubular products made of 4130 and 34Cr6Mo steels having moderate strength are common in the gundrilling industry. Second, very few gundrill manufacturers understand the proper heat treatment procedure for shanks and thus fact that it must include a thermo-mechanical rather than pure thermal relief of the stresses formed on producing the V-flute. The best structure of the shank for short gundrills is a tempered martensitic structure while for normal and long gundrills the upper bainitic structure is the best choice. This is the only structure that possesses the very unique combination of

high hardness, large toughness, and great wear resistance suitable for gundrill shanks. Unfortunately, not one shank produced today has this structure.

When the shank is brazed to the tip and to the driver, the excessive heat from this brazing often ruins the results of the heat treatment at the brazed joints. Often this heat causes high residual thermal stresses hidden in the tip. When an increased drilling torque occurs due to, for example, chip blockage or tool wear, the tip fails as shown in Fig. 5.17. Therefore, the use of low temperature, high-strength brazing filler materials (known as BFM) combined with infrared in-process temperature control followed by a 100% torque test are mandatory for gundrill brazing operations.



**Fig. 5.17.** Failure of the drill tip due to the residual stresses formed on brazing

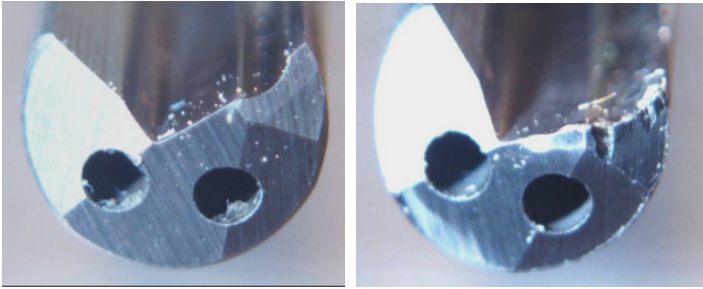
Experience shows that when the shank is made of high yield strength material, properly heat treated to achieve small grain size binate structure, and properly connected to the driver (using a low-temperature brazing filler metal), the increase in the gundrill penetration rate can be as high as twice that of gundrills commonly used today.

#### *Tool Material*

Hundreds of different tool material types and grades are used in metal cutting depending on the work material, coolant, cutting operations, required quality of the machined part, and so on. Surprisingly, only very few carbide grades are used to make gundrill tips.

There was a time not long ago when only two grades of carbide were used to produce gundrills for the automotive industry, namely C2 and C3. It is still believed that C2 grade containing 8% of cobalt is a 'forgiving' carbide and thus can be used on any drilling machine with much less than perfect working conditions. A 'small' price to pay includes relatively short tool life and poor surface finish. The other is C3, proving to be much harder and thus more wear-resistant. Unfortunately, it is also more brittle and therefore cannot be used in gundrilling systems having excessive misalignment and/or runout. Recent advancements in the development of carbide materials and their technology resulted in the appearance of new micro- and sub-micro grain carbides. The use of such carbides for gundrill tips significantly enhances the tip strength and its wear

resistance. Another problem, however, has emerged: how to select the proper grade for the given application from the great variety of available grades? Experience shows that the improper selection of even sub-micro-grain good quality carbide leads to premature tool failure. In other words, the margin for errors in carbide selecting becomes significantly smaller with the discussed variety of different carbide grades. Figure 5.18 shows an example of a new and worn drill tip chipping due to improper carbide grade selection for crankshaft gundrilling.



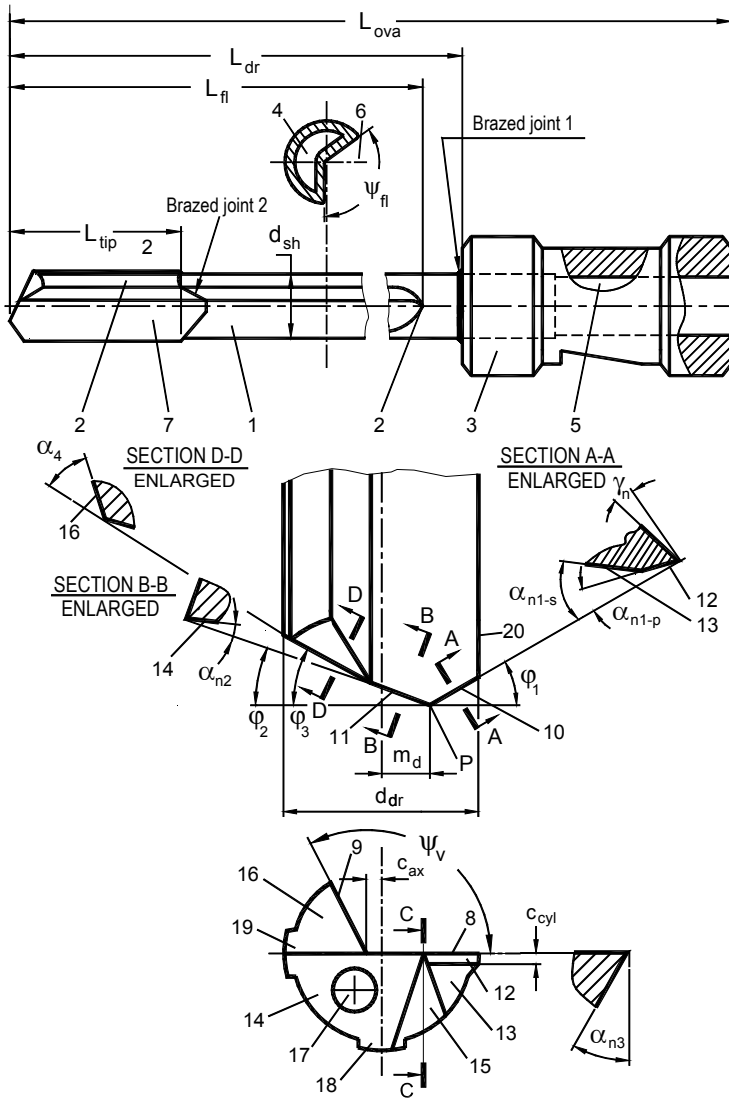
**Fig. 5.18.** Tip chipping due to improper carbide grade selection for crankshaft gundrilling

## 5.6 Gundrills

### 5.6.1 Basic Geometry

The basic design and geometry parameters of a commonly used gundrill are shown in Fig. 5.19. The gundrill consists of a drill body having a shank 1 and a tip 2. The tip is made up of a hard wear-resistant material such as tungsten carbide. The other end of the shank incorporates an enlarged driver 3 having the machine-specific design. The shank is of tubular shape having an elongated passage 4 extending over its entire length and connects to the MWF supply passage 5 in the driver. The shank has a V-shaped flute 6 on its surface which serves as the chip removal passage. The shank length depends mainly on the depth of the drilled hole as well as on the lengths of the bushing and its holder, chip box, etc.

The tip is larger in diameter than the shank which prevents the shank from coming into contact with the walls of the hole being drilled. Flute 7 on the tip, which is similar in shape to flute 6, extends along the full length of the tip. This flute is bounded by side faces 8 and 9 known as the cutting face and side face, respectively. The depth of this flute is such that the cutting face 8 extends past the axis (distance  $F_{pl}$ ) of the tip, which is also the axis of the drill body. The angle  $\psi_v$  between the side and cutting faces is known as the profile angle of the tip, which is usually equal or close to the V-flute profile of the shank.



**Fig. 5.19.** Geometry of a common gundrill

The terminal end of the tip is formed with the approach cutting edge angles  $\phi_1$  and  $\phi_2$  of the outer 10 and inner 11 cutting edges, respectively. These cutting edges meet at the drill point. The location of the drill point (defined by the distance  $m_d$  in Fig. 5.19) can be varied for optimum performance depending on the work material and the finished hole specifications. One common point grind calls for the outer angle, ( $\phi_1$ ), to be  $30^\circ$  and the inner angle ( $\phi_2$ ), to be  $20^\circ$ . The geometry of the terminal end largely determines the shape of the chips and the effectiveness of the cutting fluid, the lubrication of the tool, and removal of the chips. The process of



chip formation is also governed by other cutting parameters such as the cutting speed, feed rate, work material, etc.

The prime flank surface 12 having normal primary flank angle  $\alpha_{n1-p}$  of  $7-10^\circ$  is applied to the other cutting edge 10. To assure drill free penetration, the secondary flank surface 13 having normal flank angle  $\alpha_{n1-s}$  of  $12-20^\circ$  is applied as shown in Fig. 5.19. Flank surface 14 having normal flank angle  $\alpha_{n2}$  of  $8-12^\circ$  is applied to the inner cutting edge 11. To assure drill-free penetration, i.e., to prevent the interference of the drill's flanks with the bottom of the hole being drilled, the auxiliary flank 15 (normal flank angle  $\alpha_{n3}$ ) and shoulder dub-off 16 (flank angle  $\phi_4$ ) are provided. Their location and geometry are uniquely defined for a given gundrill.

Another common shape of the flank surface is a helical surface rather than a planar surface. The helical flank surface is normally applied to the flank of the outer cutting edge. Different manufacturers have different standards on the lead and generating diameter of the helical flank surface, depending upon drill diameter and design of the grinding fixture. Modern designs use great lead and generating diameters so that the flank surface of the outer cutting edge does not affect the shape of the flank plane of the inner cutting edge, or the shoulder dub-off as shown in Fig. 5.20a [15]. The lead and generating diameter of this surface are relatively large so the line, or rib of intersection 1 of outer 2 and inner 3 flank surfaces does not extend too far from the vertical axis. Therefore, shoulder dub-off 4 is not affected by the helical surface. In older designs, for example US Patent No. 2,325,535, which are still in use, a relatively small lead and generating diameter of the helix surface is used so that this surface passes through the outer flank and shoulder dub-off as shown in Fig. 5.20b. In this figure, a helical convex surface 5 is applied to an outer cutting edge. This helical convex surface has a small lead and generating diameter so that it passes through a flank surface of the inner cutting edge.

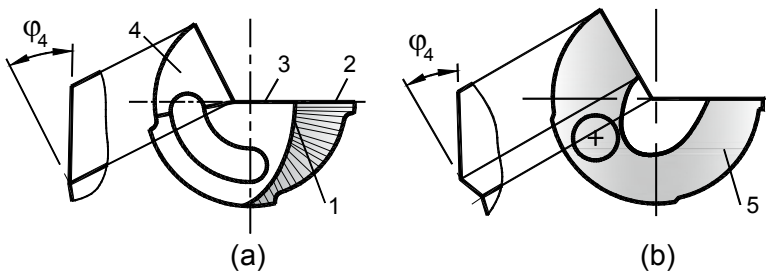


Fig. 5.20. Helical point grinds

A most common question asked by users is about which point grind is better. Some time ago, the answer to this question was determined by the design of manual grinding fixtures available. Although various grinding fixture are still in use in industry, particularly in small shops, CNC point grind becomes more common. When the latter is used, virtually any known point grind can be applied. For example, Fig. 5.21 shows a combined grind where the primary flank surface is

ground flat followed by a helical secondary flank surface. Therefore, another rationale should be used to select a particular point grind for a given application. As such, the whole gundrilling system should be considered including the MWF flow and its access to the flank surfaces, entrance, static and dynamic stability, chip removal, quality requirements, machine alignment, clearance in the starting bushing, and many others. This is because a particular point grind is system-dependant so it should not be considered independently as is the case today.



**Fig. 5.21.** Combined point grind

### 5.6.2 Rake Surface

The rake face geometry of a typical gundrill is the same as that considered in Chap. 4, Sect. 4.8.3. This geometry considered in a right-hand  $x_0y_0z_0$  coordinate system (the tool-in-machine (T-mach-S) system), illustrated in Fig. 5.22 is set as follows:

- The  $z_0$ -axis along the longitudinal axis of the drill, with sense as shown in Fig. 5.22, toward the drill holder.
- The  $y_0$ -axis passes through periphery point 1 and is perpendicular to the  $z_0$ -axis. The intersection of these axes constitutes the coordinate origin  $0$  as shown in Fig. 5.22.
- The  $x_0$ -axis is perpendicular to the  $y_0$ - and  $z_0$ - axes.

Throughout further considerations this system is referred to as the original coordinate system. As pointed out in Chap. 4, Sect. 4.8.2, the original coordinate system should also be the setting system in drill manufacturing, point grinding, re-sharpening, and control. This system should also be considered as the datum system in drill and drilling machine accessories (drill holder, starting bushing, etc.) design. Any departure from this recommendation would result in the reduction of drill reliability considered as a complex parameter of its performance including quality of machined holes, tool life, drill breakage, chip removal problems.

Figure 5.22 shows the terminal end of a conventional gundrill having the rake surface as a plane, which coincides with the  $y_0$ -axis and passes through the origin  $0$ . Today, this design of the rake face is used in approximately 99% of gundrills due to its apparent simplicity. As such, the T-hand-S rake angle of any point of a gundrill is considered to be zero and does not change with re-sharpening.

Moreover, because the shift of the outer and inner cutting edges with respect to the  $y_0$  axis is small, these angles are considered to be diametral, i.e., the rake angles in T-hand-S and T-mach-S are the same because, as discussed in Chap. 4 and shown in Fig. 5.22, the vector of the cutting speed does not change its direction along the cutting edge as the directions of the cutting speed vectors are parallel. Therefore, no geometry model for the rake angles will be considered.

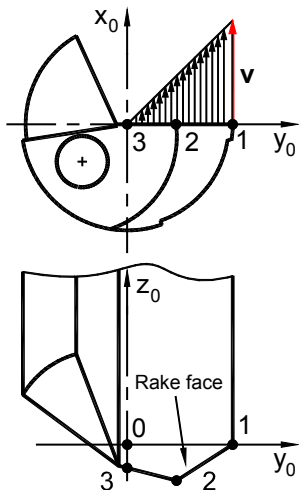
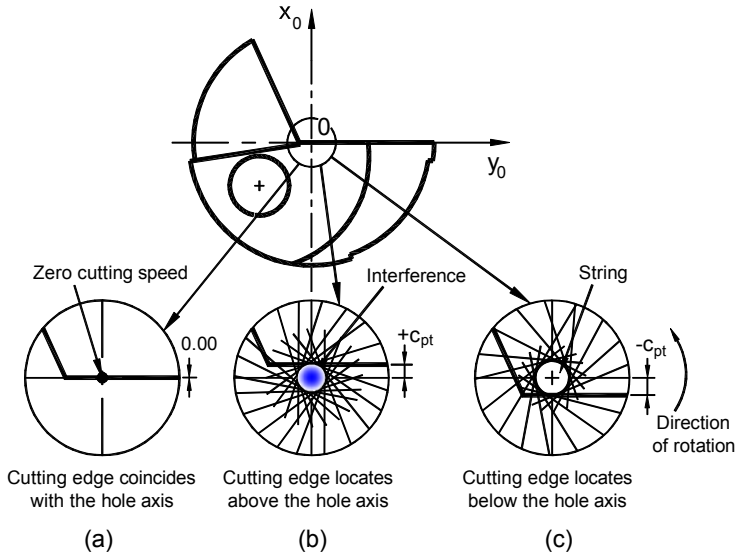


Fig. 5.22. The original coordinate system

A special issue with the rake face to be discussed is the actual location of the cutting edge with respect to the  $y_0$ -axis. It is obvious that the maximum cutting speed is at point 1 while this speed is zero at point 3 as shown in Fig. 5.22. One should realize that a certain tolerance on the cutting edge location should be allowed. Figure 5.23a shows the theoretical location of the cutting edge where its projection into the  $x_0y_0$  plane coincides with the projection of the  $y_0$ -axis. In reality, a certain shift from its ideal location is the case. The rake face can be made so that the location of the cutting edge is as shown in Fig. 5.23b. This is the worst case scenario because of interference between the flank surface of the drill and the bottom of the hole being drilled as clearly seen in this figure. In other words, when the cutting edge is shifted up by a certain distance  $c_{pt}$  with respect to the  $y_0$ -axis, the drill cannot remove the cylindrical core having the radius equal to  $c_{pt}$  as shown in Fig. 5.23b. When this distance is relatively small, the drill bends to compensate for this core. When  $c_{pt}$  exceeds a certain threshold (depending upon particular drill design and parameters of the gundrilling system), the tip breaks.

To avoid the interference, the rake face should always be located so that the projection of the cutting edge into the  $x_0y_0$  plane occupies position right on or slightly below the projection of the  $y_0$ -axis as shown in Fig. 5.23c. When the latter is the case, the string is formed as the result of such a location. The theoretical string diameter would be equal to  $2(-c_{pt})$ . The string will be attached to the bottom of the hole being drilled as shown in Fig. 5.24. It is clear that this string is

undesirable particularly when blind holes are drilled. In practice, however, the string presents some problems only when blind holes are being drilled in special high alloys steels. Otherwise, the string usually breaks into relatively small portions and does not create any problems. Moreover, multiple testings of gundrills have shown that proper selection of distance  $c_{pt}$  results in lower cutting forces and greater drill stability. The author's application experience shows that this distance should be assigned within the range of 0 to  $-c_{pt} = 0.02d_{dr}$ . This should be included in an inspection report and clearly indicated on any gundrill drawing.



**Fig. 5.23.** Location of the cutting edge with respect to the  $y_0$  axis

It is also worthwhile to explain the role of  $c_{pt}$  at the entrance of the hole being drilled. Figure 5.25a shows the ideal location of a drill tip in a starting bushing (no misalignment). In this figure,  $\Delta_{sb}$  is the radial clearance between the tip and the bushing. When drilling begins, the cutting force applied to the cutting edge shifts the tip toward the bushing walls. As such, when the drill rotates, the string changes its location at the entrance with respect to the center of the would be drilled hole (Fig. 5.25b). Eventually, when the supporting part enters the hole, the drill occupies a new location and its longitudinal axis coincides with the axis of rotation. The string, however, does not change its diameter. It shifts together with the tip after the full tip entrance into the hole being drilled. A small additional force due to this shift does not normally present any problem. This is not the case, however, when the workpiece rotates and the gundrill is stationary. The situation may change dramatically when the workpiece rotates. This case is shown in Fig. 5.25c. As such, the diameter of the string increases, becoming equal to  $2(\Delta_{sb} + c_{pt})$ . If  $\Delta_{pt}$  is significant (due to improper diameter of the starting bushing or due to bushing wear), the large additional force acts on the rake face that often causes tip breakage. Besides, interference between the string and the sidewall of the V-flute

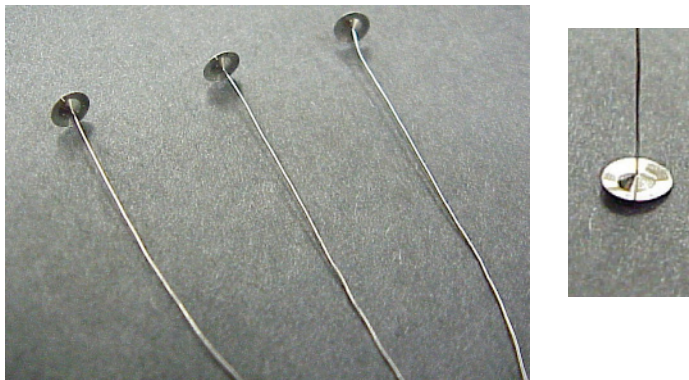


Fig. 5.24. Strings

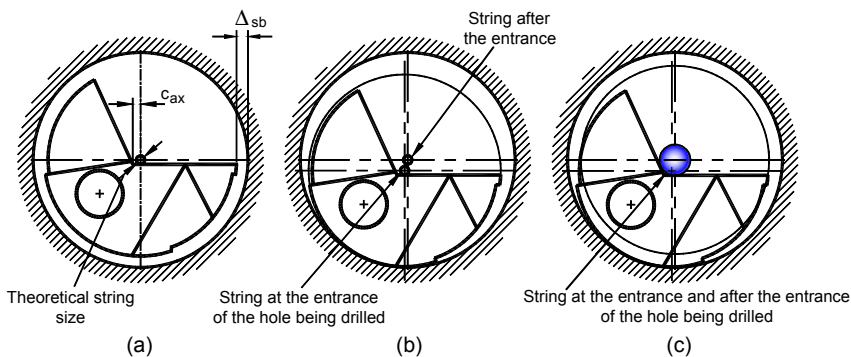
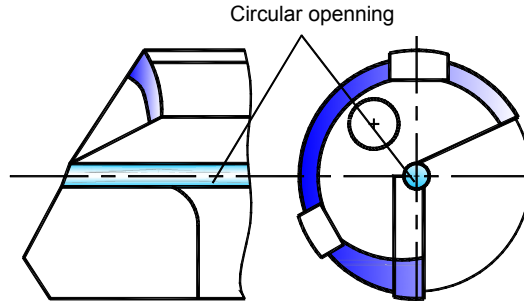


Fig. 5.25. Affect of the kinematics of drilling on the string formation

may take place that affects the position of the gundrill with respect to the axis of rotation. To avoid this, the extension of the inner cutting edge past the  $y_0$ -axis,  $F_{pl}$  (Fig. 5.25a) should not be less that  $F_{pl} = 0.05d_{dr}$ .

The discussed string can provide some useful benefits in gundrilling if its diameter is deliberately increased as shown in Fig. 5.26. In such a design (US Patent 2,418, 021(1944)), the gundrill is made with a circular opening and thus a rod forms in drilling. This rod extends from the bottom of the hole being drilled throughout the length of the workpiece, thus forming a kind of support around which the drill rotates. The rode is removed after the drilling operation is over. Technically, the discussed drill is a trepanning tool as it does not drill the entire work material. Such a drill can be used only for through holes as it was intended for rifle barrels, cam shafts, etc.

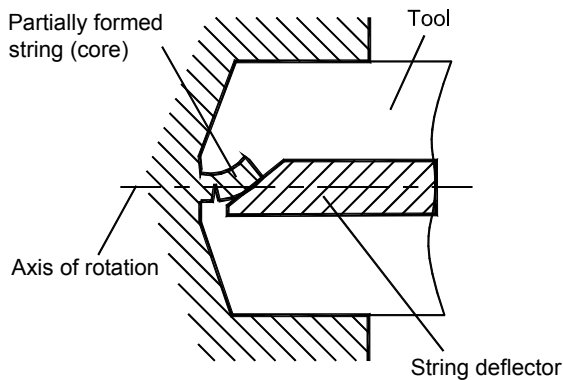


**Fig. 5.26.** Design with a circular opening(US Patent 2,418,021(1944))

The following advantages of the drill design shown in Fig. 5.26 are:

- It improves accuracy of the drilled hole as the rod formed in drilling provides a reliable guide for the drill
- It removes less work material
- The problem with low cutting speeds in the region adjacent to the axis of rotations is eliminated

A universal means to deal with a partially formed string is shown in Fig. 5.27 where a general string deflector is part of the drill design (US Patent No. 4,565,471 (1986)). As can be seen, when a partially formed string contacts the deflector, it bends and then fractures from the bottom of the hole being drilled. The design and location of the chip deflector depends on the type and design of a particular drill and thus can be used with any type of drill when one tries to solve the problems that unavoidably occur for any drill in the region adjacent to the axis of rotation.



**Fig. 5.27.** Sting deflector as a part of the drill design (US Patent No. 4,565,471 (1986))

### 5.6.3 Geometry of Major Flanks

The flank angle affects many facets of drilling and drill working conditions starting from the interference of the drill's flank surfaces with the bottom of the hole being drilled and finishing with the contact conditions at the flank-workpiece interface.

In general, the cutting edge of a gundrill may consist of a number of segments having different orientations with respect to the  $x_0y_0z_0$  drill coordinate system as shown in Fig. 5.22. In other words, it may consist of a number of sequentially adjusted segments that may have any shape and orientation with respect to the drill coordinate system. Therefore, an individual geometry analysis for each particular part of the cutting edge should be performed using the geometrical parameters (in the T-hand-S) assigned for the considered segment of the cutting edge. In the simplest case shown in Fig. 5.22, the cutting edge can consist of two segments (1–2 and 2–3) that simplifies the analysis.

#### 5.6.3.1 Segment 1–2

For this segment which represents the outer cutting edge, the approach angle  $\phi_{p12}$  and shift distance  $c_{pt}$  are as shown in Fig. 5.28. Consider a point of interest 'r' on the cutting edge 1–2. The location of this point  $r$  in the  $x_0y_0$  plane of the original coordinate system is uniquely determined by distance  $c_{pt}$  and by the location angle  $\mu_r$  calculated as

$$\sin \mu_r = \frac{c_{pt}}{R_r} \quad \text{or} \quad \tan \mu_r = \frac{c_{pt}}{R_{pr}} \quad (5.9)$$

The right-hand xyz current coordinate system (T-hand-S) is set as follows: its origin is in point  $r$ ; the z-axis is parallel to the  $z_0$ -axis; x- and y-axes are perpendicular to the z-axis as shown in Fig. 5.28. Let  $\mathbf{i}$ ,  $\mathbf{j}$ , and  $\mathbf{k}$  be unit vectors along the positive x-, y-, and z- axes, respectively.

Following the result obtained for the T-mach-S flank angle,  $\alpha_w$  in earlier considerations of the model shown in Fig. 2.46, one can apply Eq. 2.80 to the considered case as

$$\alpha_w = \alpha + \xi_{ad}^{\prime} \quad (5.10)$$

where  $\alpha_n$  is the T-hand-S flank angle (as applied to the cutting edge in the xyz coordinate system and shown in tool drawings) which depends on the shape of the flank only,  $\xi_{ad-n}$  is the angle between the tool cutting edge planes in the T-hand-S and the T-mach-S, i.e., it depends on the position of the considered flank with respect to the original coordinate system.

As discussed in the analysis of the rake angle (Chap. 2), the normal rake angle  $\alpha_n$  makes more sense because it is measured in the direction which is fairly close to that of chip motion (Chap. 3). The same can be said about the flank angle because the maximum flank forces act in the direction of the normal flank angle and thus the maximum flank tool wear takes place in this direction. Moreover, if the metal

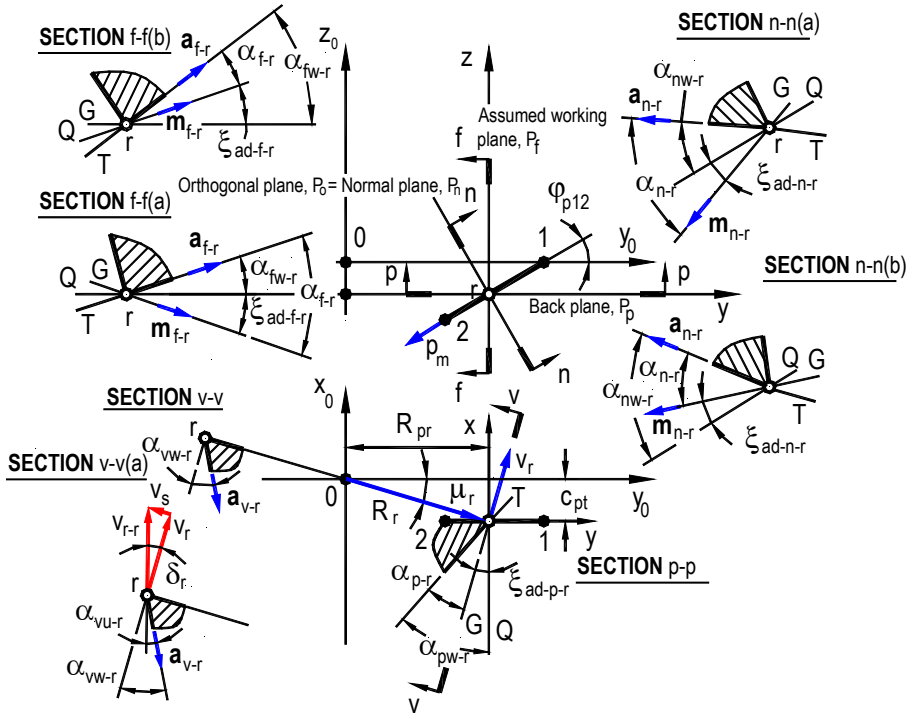


Fig. 5.28. Flank geometry parameters for segment 1–2

cutting theory is to be applied to drilling, the normal flank angle should be used in such an application.

By definition, the normal flank angle  $\alpha_{n-r}$  at a point of interest  $r$  in the T-hand-S is the angle between plane  $T$  tangent to the flank at point  $r$  and the cutting edge plane  $Q$  perpendicular to the assumed reference plane (plane  $yz$ ) (Chapter 2). In Fig. 5.28, planes  $T$  and  $Q$  are shown by their traces in SECTION  $n-n$ . In the T-mach-S, the vector of the cutting speed  $v$  is not perpendicular to the  $yz$  plane so a new reference plane in this system should be defined as to be perpendicular to this vector. This plane  $G$  is shown by its trace in SECTION  $n-n$  in Fig. 5.28.

Figure 5.28 shows the following flank angles:

- $\alpha_{n-r}$ ,  $\xi_{ad-n-r}$ ,  $\alpha_{nw-r}$  are the flank angles in the orthogonal plane,  $P_o$ , which for the considered configuration coincides with the normal plane  $P_n$  (represented by SECTION  $n-n$  in Fig. 5.28). These angles are important to know when cutting conditions at point  $r$  of the cutting edge are of interest, including its cooling and lubricating. In other words, these angles are considered when one tries to apply the recommendations on the optimum flank angle or to optimize this angle using mechanics of cutting.
- $\alpha_{f-r}$ ,  $\xi_{ad-f-r}$ ,  $\alpha_{fw-r}$  are the flank angles in the assumed working plane,  $P_f$ . These angles define the condition of drill free penetration (without interference of the flanks and the bottom of the hole being drilled) into the



workpiece in the feed direction. In any event,  $\alpha_{fw-r}$  should be positive to assure this condition.

- $\alpha_{p-r}$ ,  $\xi_{ad-p-r}$ ,  $\alpha_{pw-r}$  are the flank angles in the back plane,  $P_p$ . These angles define the condition of drill free rotation (without interference of the flanks and the bottom of the hole being drilled) about the  $z_0$ -axis.

Because all the considered flank surfaces are planes, the position of each flank plane in the  $x_0y_0z_0$  coordinate system (T-mach-S) is defined by the approach angle,  $\varphi_{p12}$ , distance  $c_{pl}$ , and the flank angle  $\alpha_n$  applied on drill grinding. Still considering the same point of interest  $r$ , one can define unit vectors  $\mathbf{a}_{f-r}$ ,  $\mathbf{a}_{p-r}$ , and  $\mathbf{a}_{n-r}$  along the corresponding flank planes in the section planes  $P_f$ ,  $P_p$ , and  $P_o$ , respectively as it shown in Fig. 5.28. In this figure,  $\mathbf{p}_m$  is a unit vector along the cutting edge 1–2. The relationship among these vectors in the  $xyz$  current coordinate system can be written as

$$\mathbf{p}_m = -\mathbf{j} \cos \varphi_{p12} - \mathbf{k} \sin \varphi_{p12} \quad (5.11)$$

$$\mathbf{a}_{f-r} = -\mathbf{i} \cos \alpha_{f-r} + \mathbf{k} \sin \alpha_{f-r} \quad (5.12)$$

$$\mathbf{a}_{p-r} = -\mathbf{i} \cos \alpha_{p-r} - \mathbf{j} \sin \alpha_{p-r} \quad (5.13)$$

$$\mathbf{a}_{n-r} = -\mathbf{i} \cos \alpha_{n-r} - \mathbf{j} \sin \varphi_{p12} \sin \alpha_{n-r} + \mathbf{k} \cos \varphi_{p12} \sin \alpha_{n-r} \quad (5.14)$$

Because these four vectors belong to the same flank plane, the scalar triple product of any three of them is equal to zero (Appendix C). Consider the scalar triple product of vectors  $\mathbf{p}_m$ ,  $\mathbf{a}_{n-r}$ , and  $\mathbf{a}_{f-r}$ , which involves angles  $\varphi_p$ ,  $\alpha_{n-r}$  and  $\alpha_{f-r}$ :

$$\mathbf{p}_m \cdot (\mathbf{a}_{n-r} \times \mathbf{a}_{f-r}) = \begin{vmatrix} 0 & -\cos \varphi_{p12} & -\sin \varphi_{p12} \\ -\cos \alpha_{n-r} & -\sin \varphi_{p12} \sin \alpha_{n-r} & \cos \varphi_{p12} \sin \alpha_{n-r} \\ -\cos \alpha_{f-r} & 0 & \sin \alpha_{f-r} \end{vmatrix} =$$

$$\cos \varphi_{p12} \cos \varphi_{p12} \sin \alpha_{n-r} \cos \alpha_{f-r} - \cos \varphi_{p12} \sin \alpha_{f-r} \cos \alpha_{n-r} +$$

$$\sin \varphi_{p12} \sin \varphi_{p12} \sin \alpha_{n-r} \cos \alpha_{f-r} = 0 \quad (5.15)$$

or

$$\tan \alpha_{f-r} = \frac{\tan \alpha_{n-r}}{\cos \varphi_{p12}} \quad (5.16)$$

Equation 5.16 establishes the relation between the T-hand-S flank angles in the orthogonal,  $P_o$  and the assumed working,  $P_f$  planes.

Considering the scalar products of vectors  $\mathbf{p}_m$ ,  $\mathbf{a}_{f-r}$ , and  $\mathbf{a}_{p-r}$ , which involves angles  $\varphi_p$ ,  $\alpha_{f-r}$  and  $\alpha_{p-r}$ :

$$\mathbf{p}_m \cdot (\mathbf{a}_{f-r} \times \mathbf{a}_{p-r}) = \begin{vmatrix} 0 & -\cos \varphi_{p12} & -\sin \varphi_{p12} \\ -\cos \alpha_{f-r} & 0 & \sin \alpha_{f-r} \\ -\cos \alpha_{p-r} & -\sin \alpha_{p-r} & 0 \end{vmatrix} = \quad (5.17)$$

$$\cos \varphi_{p12} \sin \alpha_{f-r} \cos \alpha_{p-r} - \sin \varphi_{p12} \sin \alpha_{p-r} \cos \alpha_{f-r} = 0$$

one can obtain

$$\tan \alpha_{f-r} = \tan \alpha_{p-r} \tan \varphi_{p12} \quad (5.18)$$

Thus the flank angles in the back,  $P_p$  the assumed working,  $P_f$  planes correlate as

$$\tan \alpha_{p-r} = \frac{\tan \alpha_{f-r}}{\tan \varphi_{p12}} \quad (5.19)$$

Consider now the “location” part  $\xi_{ad}$  of the total flank angle  $\alpha$  (Eq. 5.10). As seen from SECTION p-p (Fig. 5.28) the following is valid:

$$\alpha_{pw-r} = \alpha_{p-r} - \xi_{ad-p-r} \quad (5.20)$$

i.e., the location of the cutting edge below the  $y_0$  axis leads to reduction of the total flank angle  $\alpha_{pw-r}$  compared to the T-hand-S flank angle  $\alpha_{p-r}$ . It is also seen in Fig. 5.28 that  $\xi_{ad-p-r}$  calculates as

$$\xi_{ad-p-r} = \mu_r = \arcsin \frac{c_{pt}}{R_r} = \arctan \frac{c_{pt}}{R_{pr}} \quad (5.21)$$

where  $R_{pr}$  is the radial distance of point  $r$  as shown in Fig. 5.28.

In Eq. 5.21,  $c_{pt}$  is constant for cutting edge 1–2 while  $R_r$  varies thus angle  $\xi_{ad}$  varies along cutting edge 1–2. Equation 5.20 defines the distributing of flank angles along part 1–2 due to variation of  $R_r$  as angle  $\xi_{ad-p-r}$  varies because the T-hand-S flank angle  $\alpha_{p-r}$  is constant. Because  $\mu_{r1} < \mu_{r2}$ , the total flank angle,  $\alpha_{pw-r}$  at point 2 is smaller than that at point 1.

To understand the limits in gundrill geometry, consider the extreme cases of Eq. 5.20 when cutting edge 1–2 extends for the complete drill radius  $R_{dr}$ . As such,  $\max R_r = R_{dr}$  and  $\min R_r = c_{pt}$ . It follows from Eq. 5.21 that when  $R_r \rightarrow c_{pt}$ ,  $\mu_r \rightarrow \pi/2$ , and thus  $\xi_{ad-p-r} \rightarrow \pi/2$ . Because  $\alpha_{p-r}$  for any given point of the cutting edge is much less than  $\pi/2$ , there is unavoidable interference of the flank and the bottom of the hole being drilled in SECTION p-p when the approach angle  $\varphi_p$  is positive and shift distance  $c_{pt}$  is negative as shown in Fig. 5.28. The next section where the flank geometry of cutting edge 2–3 is analysed discusses how to avoid this interference.

To determine the relationships among angles  $\xi_{ad}$  in different section planes, consider the following unit vectors are shown in Fig. 5.28:

- Vector  $\mathbf{v}_r$  in the direction of rotation velocity of point  $r$
- Vector  $\mathbf{m}_{n-r}$  in the direction of intersection of the orthogonal plane  $P_o$  and plane  $G$  with the sense as it shown in Fig. 5.28
- Vector  $\mathbf{m}_{f-r}$  in the direction of intersection of the assumed plane  $P_f$  and plane  $G$  with the sense as it shown in Fig. 5.28

These vectors have the following coordinates

$$\mathbf{v}_r = \mathbf{i} \cos \xi_{ad-p-r} + \mathbf{j} \sin \xi_{ad-p-r} \quad (5.22)$$

$$\mathbf{m}_{n-r} = -\mathbf{i} \cos \xi_{ad-p-r} - \mathbf{j} \sin \xi_{ad-p-r} \sin \varphi_{p12} + \mathbf{k} \sin \xi_{ad-p-r} \cos \varphi_{p12} \quad (5.23)$$

$$\mathbf{m}_{f-r} = -\mathbf{i} \cos \xi_{ad-f-r} - \mathbf{j} \sin \xi_{ad-f-r} \quad (5.24)$$

Because vectors  $\mathbf{p}_m$ ,  $\mathbf{v}_r$ ,  $\mathbf{m}_{n-r}$ , and  $\mathbf{m}_{f-r}$  belong to the same flank plane, the scalar triple product of any three of them is equal zero (Appendix C). Considering the scalar triple product of vectors  $\mathbf{p}_m$ ,  $\mathbf{v}_r$ , and  $\mathbf{m}_{n-r}$ :

$$\mathbf{p}_m \cdot (\mathbf{v}_r \times \mathbf{m}_{n-r}) = \begin{vmatrix} 0 & -\cos \varphi_{p12} & -\sin \varphi_{p12} \\ \cos \xi_{ad-p-r} & -\sin \xi_{ad-p-r} & 0 \\ -\cos \xi_{ad-n-r} & \sin \xi_{ad-n-r} \sin \varphi_{p12} & -\sin \xi_{ad-n-r} \cos \varphi_{p12} \end{vmatrix} =$$

$$-\cos^2 \varphi_{p12} \cos \xi_{ad-p-r} \sin \xi_{ad-n-r} - \sin^2 \varphi_{p12} \cos \xi_{ad-p-r} \sin \xi_{ad-n-r} +$$

$$\sin \varphi_{p12} \sin \xi_{ad-p-r} \cos \xi_{ad-n-r} = 0 \quad (5.25)$$

one can obtain

$$\tan \xi_{ad-n-r} = -\tan \xi_{ad-p-r} \sin \varphi_{p12} \quad (5.26)$$

As can be seen from this equation, the “location” part  $\xi_{ad-p-r}$  of the total rake angle  $\alpha_{wp-r}$  (defined by Eq. 5.10) is negative. It means that the SECTION n–n(a) shown in Fig. 5.28 is incorrect in terms of location of planes  $G$  and  $Q$ . In other words, the “location” part  $\xi_{ad-n-r}$  should reduce the total flank angle  $\alpha_{wn-r}$  compared to the tool-in-hand flank angle  $\alpha_{n-r}$  as shown in SECTION n–n(b). As such, the scalar triple product of vectors  $\mathbf{p}_m$ ,  $\mathbf{v}_r$ , and  $\mathbf{m}_{n-r}$  calculates as

$$\mathbf{p}_m \cdot (\mathbf{v}_r \times \mathbf{m}_{n-r}) = \begin{vmatrix} 0 & -\cos \varphi_{p12} & -\sin \varphi_{p12} \\ \cos \xi_{ad-p-r} & -\sin \xi_{ad-p-r} & 0 \\ -\cos \xi_{ad-n-r} & -\sin \xi_{ad-n-r} \sin \varphi_{p12} & -\sin \xi_{ad-n-r} \cos \varphi_{p12} \end{vmatrix} =$$

$$-\cos^2 \varphi_{p12} \cos \xi_{ad-p-r} \sin \xi_{ad-n-r} + \sin^2 \varphi_{p12} \cos \xi_{ad-p-r} \sin \xi_{ad-n-r} -$$

$$\sin \varphi_{p12} \sin \xi_{ad-p-r} \cos \xi_{ad-n-r} = 0 \quad (5.27)$$

which yields

$$\tan \xi_{ad-n-r} = \tan \xi_{ad-p-r} \sin \varphi_{p12} \quad (5.28)$$

To derive an equation that correlates angles  $\xi_{ad-p-r}$  and  $\xi_{ad-f-r}$ , consider the scalar triple product of vectors  $\mathbf{p}_m$ ,  $\mathbf{v}_r$ , and  $\mathbf{m}_{f-r}$ :

$$\mathbf{p}_m \cdot (\mathbf{v}_r \times \mathbf{m}_{f-r}) = \begin{vmatrix} 0 & -\cos \varphi_{p12} & -\sin \varphi_{p12} \\ \cos \xi_{ad-p-r} & \sin \xi_{ad-p-r} & 0 \\ -\cos \xi_{ad-f-r} & 0 & -\sin \xi_{ad-f-r} \end{vmatrix} = 0 \quad (5.29)$$

which gives

$$\tan \xi_{ad-f-r} = \tan \xi_{ad-p-r} \tan \varphi_{p12} \quad (5.30)$$

Combining Eqs. 5.26 and 5.30, one can obtain

$$\tan \xi_{ad-n-r} = \tan \xi_{ad-f-r} \cos \varphi_{p12} \quad (5.31)$$

Although the flank angles in the planes  $P_o(P_n)$ ,  $P_f$ , and  $P_p$  are of prime concern, one more plane in the T-use-S should also be considered. This is the cutting speed plane,  $P_v$  which is perpendicular to the  $x_0y_0$  plane and contains the unit vector  $\mathbf{v}_r$  in the direction of the cutting velocity (the cylindrical section as defined in Chap. 4). This plane is represented by section plane v-v in Fig. 5.28.

To determine the T-mach-S flank angle  $\alpha_{vw-r}$ , consider a unit vector  $\mathbf{a}_{v-r}$  along the intersection of the flank plane with SECTION v-v (Fig. 5.28):

$$\mathbf{a}_{vw-r} = -\mathbf{i} \cos \xi_{ad-p-r} \cos \alpha_{v-r} - \mathbf{j} \sin \xi_{ad-p-r} \cos \alpha_{v-r} + \mathbf{k} \sin \alpha_{v-r} \quad (5.32)$$

Because vectors  $\mathbf{a}_{f-r}$ ,  $\mathbf{p}_m$ , and  $\mathbf{a}_{v-r}$  belong to the same flank plane, their scalar triple product is equal zero (Appendix C), i.e.,

$$\mathbf{a}_{f-r} \cdot (\mathbf{p}_m \times \mathbf{a}_{v-r}) = \begin{vmatrix} -\cos \alpha_{f-r} & 0 & \sin \alpha_{f-r} \\ 0 & -\cos \varphi_{p12} & -\sin \varphi_{p12} \\ -\cos \xi_{ad-p-r} \cos \alpha_{vw-r} & -\sin \xi_{ad-p-r} \cos \alpha_{v-r} & \sin \alpha_{vw-r} \end{vmatrix} = 0 \quad (5.33)$$

or

$$\tan \alpha_{vw-r} = \tan \alpha_{f-r} \cos \xi_{ad-p-r} - \tan \varphi_{p12} \sin \xi_{ad-p-r} \quad (5.34)$$

The T-use-S flank angle  $\alpha_{vu-r}$  accounts for the cutting feed velocity (the feed rate). This angle is smaller than  $\alpha_{v-r}$  (see SECTION v-v(a) in Fig. 5.28) and calculates as

$$\alpha_{vu-r} = \alpha_{vw-r} - \delta_{u-r} \quad (5.35)$$

where angle  $\delta_{u-r}$  calculates as

$$\delta_{u-r} = \arctan \frac{v_s}{v_r} = \arctan \frac{nf}{\pi 2R_r n} = \arctan \frac{0.5f}{(\pi R_r) / \cos \mu_r} \quad (5.36)$$

where  $n$  is the rotational speed (r.p.m) of the drill (spindle),  $f$  is the feed per revolution (mm/rev),  $\omega$  is angular velocity (rad/s), and  $R_r$  is the radius of point  $r$  (mm).

Our calculations have shown that angle  $\delta_{u-r}$  is rather small and should be taken into consideration for points that locate close to the chisel edge when the cutting feed is more than 0.4mm/rev. For example for a point on the drill edge with  $R_r = 1.5\text{mm}$  and  $f = 0.5\text{mm/rev}$  this angle  $\delta_{u-r} = 3^\circ$ .

### 5.6.3.2 Segment 2–3

For this segment which represents the inner cutting edge, the approach angle  $\varphi_{p23}$  and shift distance  $c_{pr}$  are as shown in Fig. 5.29. As before, consider a point of interest ‘ $r$ ’ on the cutting edge 2–3. The location of this point  $r$  in the  $x_0y_0$  plane of the original coordinate system is uniquely determined by distance  $c_{pr}$  and by the location angle  $\mu_r$  calculated using Eq. 5.9. The set of unit vectors is the same as use in the analysis of cutting edge 1–2.

Considering the same point of interest  $r$ , one can define unit vectors  $\mathbf{a}_{f-r}$ ,  $\mathbf{a}_{p-r}$ , and  $\mathbf{a}_{n-r}$  along the corresponding flank planes in the section planes  $P_f$ ,  $P_p$ , and  $P_o$ , respectively as is shown in Fig. 5.29. In this figure,  $\mathbf{p}_m$  is a unit vector along the cutting edge 1–2. The relationship among these vectors in the  $xyz$  current coordinate system can be written as

$$\mathbf{p}_m = -\mathbf{j} \cos \varphi_{p23} + \mathbf{k} \sin \varphi_{p23} \quad (5.37)$$

$$\mathbf{a}_{f-r} = -\mathbf{i} \cos \alpha_{f-r} + \mathbf{k} \sin \alpha_{f-r} \quad (5.38)$$

$$\mathbf{a}_{p-r} = -\mathbf{i} \cos \alpha_{p-r} + \mathbf{j} \sin \alpha_{p-r} \quad (5.39)$$

$$\mathbf{a}_{n-r} = -\mathbf{i} \cos \alpha_{n-r} + \mathbf{j} \sin \varphi_{p23} \sin \alpha_{n-r} + \mathbf{k} \cos \varphi_{p23} \sin \alpha_{n-r} \quad (5.40)$$

Because these four vectors belong to the same flank plane, the scalar triple product of any three of them is equal to zero (Appendix C). Consider the scalar triple product of vectors  $\mathbf{p}_m$ ,  $\mathbf{a}_{n-r}$ , and  $\mathbf{a}_{f-r}$ , which involves angles  $\varphi_{p23}$ ,  $\alpha_{n-r}$  and  $\alpha_{f-r}$ :

$$\mathbf{p}_m \cdot (\mathbf{a}_{n-r} \times \mathbf{a}_{f-r}) = \begin{vmatrix} 0 & -\cos \varphi_{p23} & \sin \varphi_{p23} \\ -\cos \alpha_{n-r} & \sin \varphi_{p23} \sin \alpha_{n-r} & \cos \varphi_{p23} \sin \alpha_{n-r} \\ -\cos \alpha_{f-r} & 0 & \sin \alpha_{f-r} \end{vmatrix} =$$

$$\cos \varphi_{p23} \cos \varphi_{p23} \sin \alpha_{n-r} \cos \alpha_{f-r} - \cos \varphi_{p23} \sin \alpha_{f-r} \cos \alpha_{n-r} +$$

$$\sin \varphi_{p23} \sin \varphi_{p23} \sin \alpha_{n-r} \cos \alpha_{f-r} = 0 \quad (5.41)$$

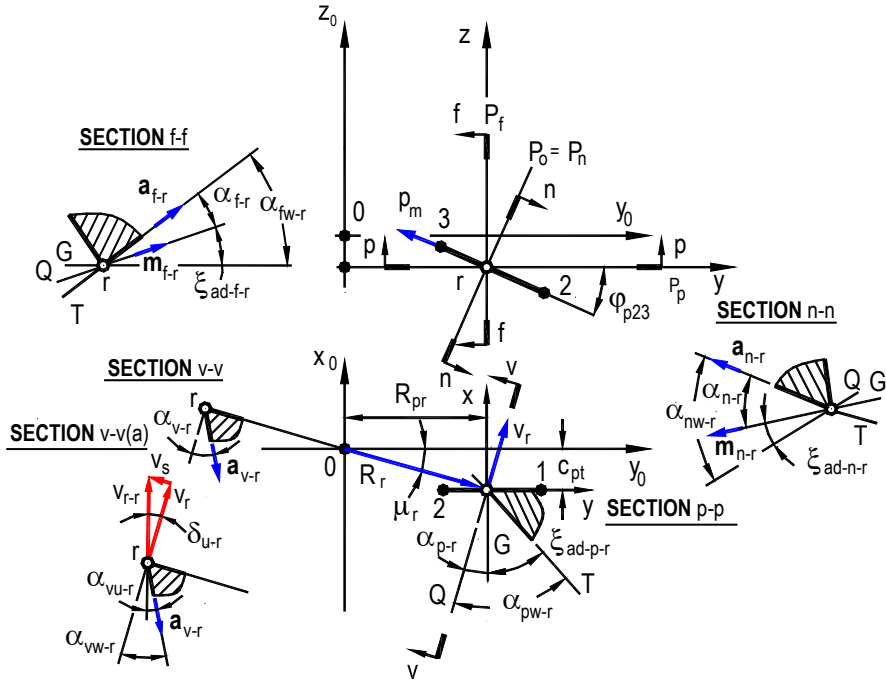


Fig. 5.29. Flank geometry parameters for segment 2-3

or

$$\tan \alpha_{f-r} = \frac{\tan \alpha_{n-r}}{\cos \varphi_{p23}} \tag{5.42}$$

Equation 5.42 establishes the relation between the T-hand-S flank angles in the orthogonal,  $P_o$  and the assumed working,  $P_f$  planes.

Considering the scalar products of vectors  $\mathbf{p}_m$ ,  $\mathbf{a}_{f-r}$ , and  $\mathbf{a}_{p-r}$ , which involves angles  $\varphi_{p23}$ ,  $\alpha_{f-r}$  and  $\alpha_{p-r}$ :

$$\mathbf{p}_m \cdot (\mathbf{a}_{f-r} \times \mathbf{a}_{p-r}) = \begin{vmatrix} 0 & -\cos \varphi_{p23} & \sin \varphi_{p23} \\ -\cos \alpha_{f-r} & 0 & \sin \alpha_{f-r} \\ -\cos \alpha_{p-r} & \sin \alpha_{p-r} & 0 \end{vmatrix} = 0 \tag{5.43}$$

one can obtain

$$\tan \alpha_{f-r} = \tan \alpha_{p-r} \tan \varphi_{p23} \tag{5.44}$$

Thus the flank angles in the back,  $P_p$  the assumed working,  $P_f$  planes correlate as

$$\tan \alpha_{p-r} = \frac{\tan \alpha_{f-r}}{\tan \varphi_{p23}} \quad (5.45)$$

Consider now the “location” part  $\xi_{ad}$  of the total flank angle  $\alpha$ . As seen from SECTION p-p (Fig. 5.29) the following is valid:

$$\alpha_{pw-r} = \alpha_{p-r} + \xi_{ad-p-r} \quad (5.46)$$

i.e., the location of the cutting edge below the  $y_0$ -axis leads to reduction of the total flank angle  $\alpha_{pw-r}$  compared to the T-hand-S flank angle  $\alpha_{p-r}$ . It is also seen in Fig. 5.29 that  $\xi_{ad-p-r}$  calculates as

$$\xi_{ad-p-r} = \mu_r = \arctan \frac{c_{pt}}{R_r} = \arctan \frac{c_{pt}}{R_{pr}} \quad (5.47)$$

In Eq. 5.47,  $c_{pt}$  is constant for cutting edge 2–3 while  $R_r$  varies and thus angle  $\xi_{ad-p-r}$  varies along this edge. Therefore, Eq. 5.46 defines the distributing of flank angles along edge 2–3 due to variation of  $R_r$  as angle  $\xi_{ad-p-r}$  varies because the T-hand-S flank angle  $\alpha_{p-r}$  is constant. Because  $\mu_{r2} < \mu_{r3}$ , the total flank angle,  $\alpha_{pw-r}$  at point 3 is smaller than that at point 3.

To understand the limits in gundrill geometry, consider the extreme cases of Eq. 5.46 when cutting edge 2–3 extends for the complete drill radius  $R_{dr}$ . As such,  $\max R_r = R_{dr}$  and  $\min R_r = c_{pt}$ . It follows from Eq. 5.47 that when  $R_r \rightarrow c_{pt}$ ,  $\mu_r \rightarrow \pi/2$ , and thus  $\xi_{ad-p-r} \rightarrow \pi/2$ . Because  $\alpha_{p-r}$  for any given point of the cutting edge is constant, the flank angle becomes very large at point  $R_r = c_{pt}$  so there is no interference as in the case of positive  $\varphi_p$  as considered in the analysis of cutting edge 1–2. Therefore, to avoid interference, the approach angle in the region adjacent to the center should be made negative as shown in Fig. 5.29.

To determine the relationships among angles  $\xi_{ad}$  in different section planes, consider the following unit vectors shown in Fig. 5.29:

- Vector  $\mathbf{v}_r$  in the direction of rotation velocity of point  $r$
- Vector  $\mathbf{m}_{n-r}$  in the direction of intersection of the orthogonal plane  $P_o$  and plane  $G$  with the sense as it shown in Fig. 5.29
- Vector  $\mathbf{m}_{f-r}$  in the direction of intersection of the assumed plane  $P_f$  and plane  $G$  with the sense as it shown in Fig. 5.29

These vectors have the following coordinates:

$$\mathbf{v}_r = \mathbf{i} \cos \xi_{ad-p-r} + \mathbf{j} \sin \xi_{ad-p-r} \quad (5.48)$$

$$\mathbf{m}_{n-r} = -\mathbf{i} \cos \xi_{ad-p-r} - \mathbf{j} \sin \xi_{ad-p-r} \sin \varphi_{p23} - \mathbf{k} \sin \xi_{ad-p-r} \cos \varphi_{p23} \quad (5.49)$$

$$\mathbf{m}_{f-r} = -\mathbf{i} \cos \xi_{ad-f-r} - \mathbf{j} \sin \xi_{ad-f-r} \quad (5.50)$$

Because vectors  $\mathbf{p}_m$ ,  $\mathbf{v}_r$ ,  $\mathbf{m}_{n-r}$ , and  $\mathbf{m}_{f-r}$  belong to the same flank plane, the scalar triple product of any three of them is equal to zero (Appendix C). Considering the scalar triple product of vectors  $\mathbf{p}_m$ ,  $\mathbf{v}_r$ , and  $\mathbf{m}_{n-r}$ :

$$\mathbf{p}_m \cdot (\mathbf{v}_r \times \mathbf{m}_{n-r}) = \begin{vmatrix} 0 & -\cos \varphi_{p23} & \sin \varphi_{p23} \\ \cos \xi_{ad-p-r} & \sin \xi_{ad-p-r} & 0 \\ -\cos \xi_{ad-n-r} & \sin \xi_{ad-n-r} \sin \varphi_p & -\sin \xi_{ad-n-r} \cos \varphi_p \end{vmatrix} = 0 \quad (5.51)$$

one can obtain

$$\tan \xi_{ad-n-r} = \tan \xi_{ad-p-r} \sin \varphi_{p23} \quad (5.52)$$

To derive an equation that correlates angles  $\xi_{ad-p-r}$  and  $\xi_{ad-f-r}$ , consider the scalar triple product of vectors  $\mathbf{p}_m$ ,  $\mathbf{v}_r$ , and  $\mathbf{m}_{f-r}$ :

$$\mathbf{p}_m \cdot (\mathbf{v}_r \times \mathbf{m}_{f-r}) = \begin{vmatrix} 0 & -\cos \varphi_{p23} & \sin \varphi_{p23} \\ \cos \xi_{ad-p-r} & \sin \xi_{ad-p-r} & 0 \\ -\cos \xi_{ad-f-r} & 0 & -\sin \xi_{ad-f-r} \end{vmatrix} = 0 \quad (5.53)$$

which gives

$$\tan \xi_{ad-f-r} = \tan \xi_{ad-p-r} \tan \varphi_{p23} \quad (5.54)$$

Combining Eqs. 5.52 and 5.54, one can obtain

$$\tan \xi_{ad-n-r} = \tan \xi_{ad-f-r} \cos \varphi_{p23} \quad (5.55)$$

As discussed earlier, besides planes  $P_o(P_n)$ ,  $P_f$ , and  $P_p$ , one more plane in the T-use-S should also be considered. This is the cutting speed plane,  $P_v$  which is perpendicular to the  $x_0y_0$  plane and contains the unit vector  $\mathbf{v}_r$  in the direction of the cutting velocity. This plane is represented by SECTION v-v in Fig. 5.29.

To determine the T-mach-S flank angle  $\alpha_{v-t}$ , consider a unit vector  $\mathbf{a}_{v-r}$  along the intersection of the flank plane with section plane v-v (Fig. 5.28):

$$\mathbf{a}_{v-r} = -\mathbf{i} \cos \xi_{ad-p-r} \cos \alpha_{v-r} - \mathbf{j} \sin \xi_{ad-p-r} \cos \alpha_{v-r} + \mathbf{k} \sin \alpha_{v-r} \quad (5.56)$$



Because vectors  $\mathbf{a}_{f-r}$ ,  $\mathbf{p}_m$ , and  $\mathbf{a}_{v-r}$  belong to the same flank plane, their scalar triple product is equal to zero (Appendix C), i.e.,

$$\mathbf{a}_{f-r} \cdot (\mathbf{p}_m \times \mathbf{a}_{v-r}) = \begin{vmatrix} -\cos \alpha_{f-r} & 0 & \sin \alpha_{f-r} \\ 0 & -\cos \varphi_{p23} & \sin \varphi_{p23} \\ -\cos \xi_{ad-p-r} \cos \alpha_{v-r} & -\sin \xi_{ad-p-r} \cos \alpha_{v-r} & \sin \alpha_{v-r} \end{vmatrix} = 0 \quad (5.57)$$

or

$$\tan \alpha_{v-r} = \tan \alpha_{f-r} \cos \xi_{ad-p-r} + \tan \varphi_{p23} \sin \xi_{ad-p-r} \quad (5.58)$$

As earlier, the T-mach-S flank angle  $\alpha_{v-r(a)}$  accounts for the cutting feed velocity (the feed rate). This angle is smaller than  $\alpha_{v-r}$  (see SECTION v-v(a) in Fig. 5.29) and calculates as

$$\alpha_{v-r-u} = \alpha_{v-r} - \delta_{u-r} \quad (5.59)$$

where angle  $\delta_{u-r}$  calculates using Eq 5.36.

As discussed later in this chapter, regardless of the number of straight parts of the cutting edge, each part can be analyzed separately as the line parallel to the  $y_0$ -axis and having two geometrical parameters: the approach angle  $\varphi$  and distance  $c_{pt}$ .

### 5.6.3.3 Example 5.1

To exemplify the results obtained, the geometry of a common gundrill is considered. Figure 5.30 shows the geometrical parameters. Work material – aluminum alloy 319, rotational speed = 8,000.0 r.p.m., cutting feed = 0.12 mm/rev.

Part 1–2 of the cutting edge (the outer cutting edge)

As can be seen this part falls in the considerations of Case 1. As seen in Fig. 5.30,  $\alpha_{n-r} = 15^\circ$  is constant over entire length of cutting edge 1–2. The approach angle for this edge is  $\varphi_{p12} = 35^\circ$ . Therefore, the following sequence is used to determine its geometry:

- The T-hand-S flank angle in the assumed working plane

$$\alpha_{f-r} = \arctan \left( \frac{\tan \alpha_{n-r}}{\cos \varphi_{p12}} \right) = \arctan \left( \frac{\tan 15^\circ}{\cos 35^\circ} \right) = 18.1^\circ$$

- The T-hand-S flank angle in the back plane

$$\tan \alpha_{p-r} = \arctan \left( \frac{\tan \alpha_{f-r}}{\tan \varphi_{p12}} \right) = \arctan \left( \frac{\tan 18.1^\circ}{\tan 35^\circ} \right) = 25.0^\circ$$

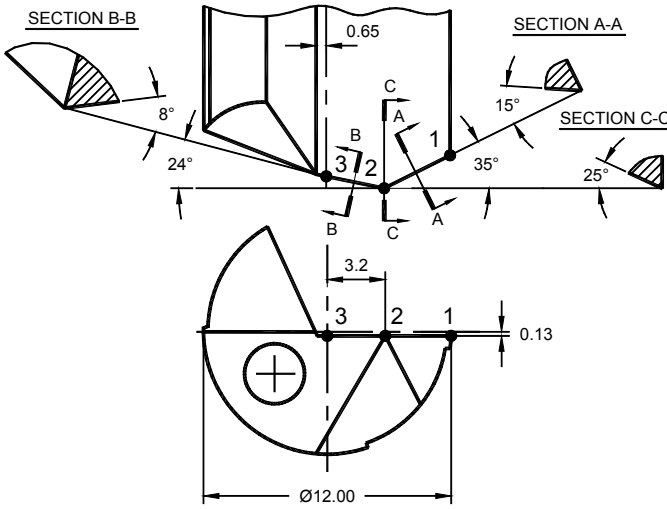


Fig. 5.30. Geometry of tool used in Example 5.1

- The “location” part  $\xi_{ad-p-r}$  in the back plane

$$\xi_{ad-p}(R_{pr}) = \arctan \frac{C_{pt}}{R_{pr}} \text{ where } m_d \leq R_{pr} \leq R_{dr}$$

- The “location” part  $\xi_{ad-n-r}$  in the normal plane

$$\xi_{ad-n}(R_{pr}) = \arctan \left( \tan \left[ \xi_{ad-p}(R_{pr}) \right] \sin \varphi_{p12} \right) \text{ where } m_d \leq R_{pr} \leq R_{dr}$$

- The “location” part  $\xi_{ad-f-r}$  in the assumed working plane

$$\xi_{ad-f}(R_{pr}) = \arctan \left( \tan \left[ \xi_{ad-p}(R_{pr}) \right] \cos \varphi_{p12} \right) \text{ where } m_d \leq R_{pr} \leq R_{dr}$$

- Distribution of the T-mach-S flank angle in the back plane

$$\alpha_{pw}(R_{pr}) = \alpha_{p-r} - \xi_{ad-p}(R_{pr}) \text{ where } m_d \leq R_{pr} \leq R_{dr}$$

- Distribution of the T-mach-S flank angle in the back plane

$$\alpha_{pw}(R_{pr}) = \alpha_{p-r} - \xi_{ad-p}(R_{pr}) \text{ where } m_d \leq R_{pr} \leq R_{dr}$$

- Distribution of the T-mach-S flank angle in the back plane

$$\alpha_{pw}(R_{pr}) = \alpha_{p-r} - \xi_{ad-p}(R_{pr}) \text{ where } m_d \leq R_{pr} \leq R_{dr}$$

- The T-mach-S flank angle  $\alpha_{vw-t}$

$$\alpha_{vw}(R_{pr}) = \arctan\left(\tan \alpha_{f-r} \cos \xi_{ad-p}(R_{pr}) + \tan \varphi_{p12} \sin \xi_{ad-p}(R_{pr})\right)$$

$$\text{where } m_d \leq R_{pr} \leq R_{dr}$$

- Angle  $\delta_{u-t}$  calculates as

$$\delta_u(R_{rp}) = \arctan \frac{v_s}{v_r} = \arctan \frac{nf}{\pi 2 R_r n} = \arctan \frac{0.5f}{(\pi R_{rp}) / \cos \mu_r} \text{ where } m_d \leq R_{pr} \leq R_{dr}$$

- The T-use-S flank angle  $\alpha_{vu-t}$

$$\alpha_{vu}(R_{pr}) = \alpha_{vw}(R_{pr}) - \delta_u(R_{pr}) \text{ where } m_d \leq R_{pr} \leq R_{dr}$$

Figure 5.31 shows the distributing of the flank angles over the cutting edge 1–2. As seen, there is not significant differences between the flank angles in the T-mach-S (T-use-S) and those in the T-hand-S. This is one of the major advantages of gundrill geometry. It will be shown later in the next chapter that this is not the case for common straight flute and twist drills.

Part 2–3 of the cutting edge(the inner cutting edge)

As seen this part falls in the considerations of Case 2. As can be seen in Fig. 5.30,  $\alpha_{n-r} = 8^\circ$  is constant over entire length of cutting edge 2–3. The approach angle for this edge is  $\varphi_{p23} = 24^\circ$ . Therefore, the following sequence is used to determine its geometry:

- The T-hand-S flank angle in the assumed working plane

$$\alpha_{f-r} = \arctan\left(\frac{\tan \alpha_{n-r}}{\cos \varphi_{p23}}\right) = \arctan\left(\frac{\tan 9^\circ}{\cos 24^\circ}\right) = 9.8^\circ$$

- The T-hand-S flank angle in the back plane

$$\tan \alpha_{p-r} = \arctan\left(\frac{\tan \alpha_{f-r}}{\tan \varphi_{p23}}\right) = \arctan\left(\frac{\tan 9.8^\circ}{\tan 24^\circ}\right) = 21.2^\circ$$

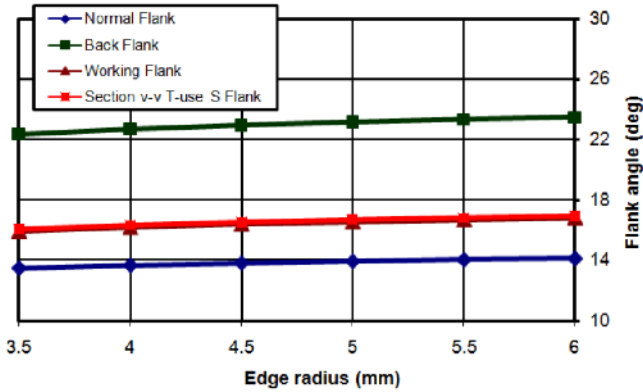


Fig. 5.31. Distribution of the flank angles over the outer cutting edge 1–2

- The “location” parts  $\xi_{ad-p-r}$  in the back plane

$$\xi_{ad-p}(R_{pr}) = \arctan \frac{C_{pr}}{R_{pr}} \text{ where } 0.05 \leq R_{pr} \leq m_d$$

- The “location” part  $\xi_{ad-n-r}$  in the normal plane

$$\xi_{ad-n}(R_{pr}) = \arctan \left( \tan \left[ \xi_{ad-p}(R_{pr}) \right] \sin \varphi_{p12} \right) \text{ where } 0.05 \leq R_{pr} \leq m_d$$

- The “location” part  $\xi_{ad-f-r}$  in the assumed working plane

$$\xi_{ad-f}(R_{pr}) = \arctan \left( \tan \left[ \xi_{ad-p}(R_{pr}) \right] \cos \varphi_{p12} \right) \text{ where } 0.05 \leq R_{pr} \leq m_d$$

- Distribution of the T-mach-S flank angle in the back plane

$$\alpha_{pw}(R_{pr}) = \alpha_{p-r} + \xi_{ad-p}(R_{pr}) \text{ where } m_d \leq R_{pr} \leq R_{dr}$$

- Distribution of the T-mach-S flank angle in the back plane

$$\alpha_{pw}(R_{pr}) = \alpha_{p-r} + \xi_{ad-p}(R_{pr}) \text{ where } 0.05 \leq R_{pr} \leq m_d$$

- Distribution of the T-mach-S flank angle in the back plane

$$\alpha_{pw}(R_{pr}) = \alpha_{p-r} + \xi_{ad-p}(R_{pr}) \text{ where } 0.05 \leq R_{pr} \leq m_d$$

- The T-mach-S flank angle  $\alpha_{vw-r}$

$$\alpha_{vw}(R_{pr}) = \arctan\left(\tan \alpha_{f-r} \cos \xi_{ad-p}(R_{pr}) + \tan \varphi_{p23} \sin \xi_{ad-p}(R_{pr})\right)$$

where  $0.05 \leq R_{pr} \leq m_d$

- angle  $\delta_{u-r}$  calculates as

$$\delta_u(R_{pr}) = \arctan \frac{v_s}{v_r} = \arctan \frac{nf}{\pi 2 R_r n} = \arctan \frac{0.5f}{(\pi R_{rp}) / \cos \mu_r} \text{ where } 0.05 \leq R_{pr} \leq m_d$$

- The T-use-S flank angle  $\alpha_{vu-r}$

$$\alpha_{vu}(R_{pr}) = \alpha_{vw}(R_{pr}) - \delta_u(R_{pr}) \text{ where } 0.05 \leq R_{pr} \leq m_d$$

Figure 5.32 shows the distributing of the flank angles over the cutting edge 2–3. As can be seen, there is no significant differences between the flank angles in the T-mach-S (T-use-S) and those in the T-hand-S over the major part of this edge. Seemingly great increases in flank angles in the region adjacent to the  $x_0$  axis do not affect the drill performance. However, the T-use-S flank angle  $\alpha_{vu}$  becomes zero at a radius of 0.5mm and then for smaller radii becomes negative. This definitely causes interference of the flank of the bottom of the hole being drilled in this region that leads to an increase in the axial force and to the drill bending to accommodate this interference. In drilling relatively soft materials such as, for example, automotive aluminum, this interference does not cause any problems while in machining high-strength alloys this may cause chipping of the cutting edge in this region.

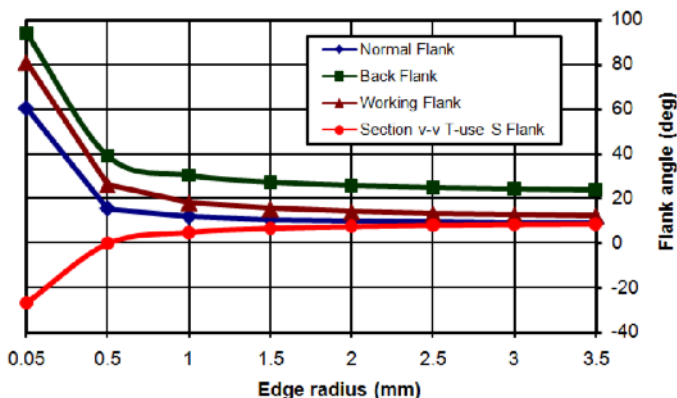
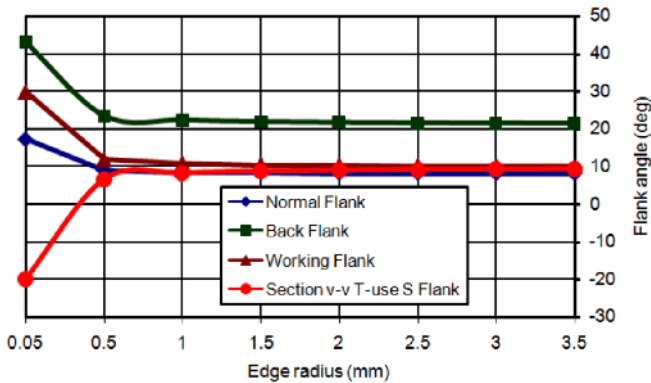


Fig. 5.32. Distribution of the flank angles over the outer cutting edge 2–3

In the latter case, to cure the problem, distance  $c_{pt}$  should be decreased. Figure 5.33 shows what happens when  $c_{pt}=0.02\text{mm}$ . Although the T-use-S flank angle  $\alpha_{vu}$  is still negative in the region adjacent to the axis of rotation, it does not present any problems due to the geometry of the string that forms in this region. Therefore, distance  $c_{pt}$  should be small at least in the region adjacent to the axis of rotation.



**Fig. 5.33.** Distribution of the flank angles over the outer cutting edge 2–3 when  $c_{pt}=0.02$  mm

#### 5.6.3.4 General Location of a Cutting Edge

In general, a part of the cutting edge of a gundrill may not be parallel to the  $y_0$ -axis. Figure 5.34 shows examples of such designs. Although these designs look rather exotic, they can be easily reproduced using modern CNC tool grinders. In the author's opinion, the only obstacle in the development of many new designs of gun- and many other drills (as these designs can be used for any drill type) is physiological. Because tool designers do not have information on the geometry of such tools and thus guidelines for their design, they use traditional designs. The following section provides a methodology for the assessment of the geometry of drills (gundrills, straight-flute drills, twist drills, etc.) with general location of cutting edges.

For the analysis of the tool geometry of such a cutting edge, a simplification method discussed in Chap. 4, Sect. 4.8.6.1 can be used. According to this method, the edge geometry is invariant to the rotation of the original coordinate system about its origin  $O$  as the drill rotates about the  $z_0$ -axis and its geometry does not change in this rotation. Figure 5.35 exemplifies the method for gundrilling applications. Figure 5.35a shows cutting edge 1–2 in its original location in the original coordinate system. The sense of invariable (along the entire edge)  $c_{pt}$  is shown by the distance between the direction of cutting edge 1–2 and the  $z_0$ -axis. Angle  $\psi_{12}$  is the position vector of this edge with respect to the  $y_0$ -axis.

Figure 5.35b shows what happens if the original coordinate system is rotated clockwise by this angle. In this figure, the location of cutting edge 1–2 is parallel to the  $y_0$ -axis and its geometry can be analyzed in the same way in the Case 1 in the previous section. Note that the approach angle of the cutting edge changes with

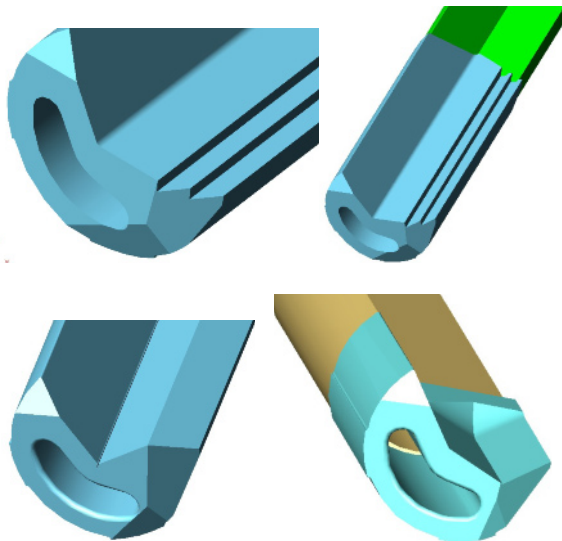


Fig. 5.34. Examples of gundrill designs where cutting edges are not parallel to the  $y_0$ -axis

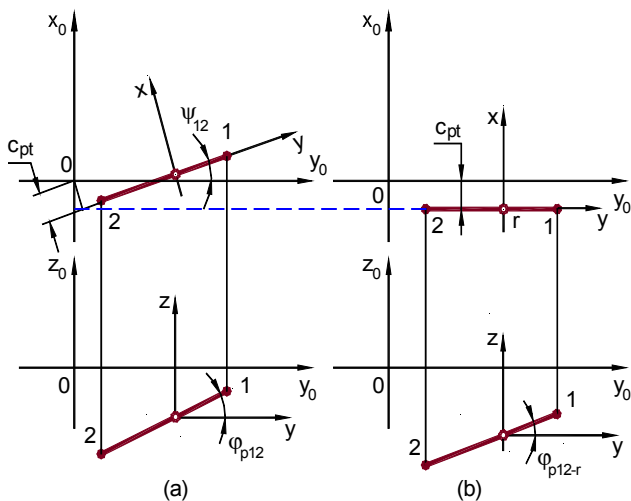


Fig. 5.35. Simplification in the analyses of drill geometry

rotation of the original coordinate system. Although for practical designs this change is insignificant, the exact value of this angle in general case calculates as

$$\varphi_{p12-r} = \arctan(\tan \varphi_{p12} \cos \psi_{12}) \tag{5.60}$$

### 5.6.3.5 Example 5.2

To exemplify the consideration of the previous section, the geometry of a special gundrill is considered. Figure 5.36a shows the geometrical parameters. Work material – aluminum alloy 319, rotational speed = 8,000 r.p.m., cutting feed = 0.12 mm/rev.

Figure 5.36b shows a model where the real geometry of cutting edges 1–2, 2–3, and 3–4 can be analyzed as discussed in the previous section. As such, the approach angles calculate using Eq. 5.60:

$$\varphi_{p12-r} = \arctan(\tan \varphi_{p12} \cos \psi_{12}) = \arctan(\tan 36^\circ \cos 25^\circ) = 33.4^\circ$$

$$\varphi_{p23-r} = \arctan(\tan \varphi_{p23} \cos \psi_{23}) = \arctan(\tan 20^\circ \cos 25^\circ) = 18.3^\circ$$

$$\varphi_{p24-r} = \arctan(\tan \varphi_{p34} \cos \psi_{34}) = \arctan(\tan 20^\circ \cos 15^\circ) = 19.4^\circ$$

#### Cutting edge 1–2

As can be seen, this part falls in the considerations of Case 1 and thus procedure used in Example 5.1 (Sect. 5.6.3.3) for cutting edge 1–2 should be followed. As can be seen in Fig. 5.36a,  $\alpha_{n-r} = 18^\circ$  is constant over entire length of cutting edge 1–2. The approach angle for this edge is  $\varphi_{p12} = 33.4^\circ$ .

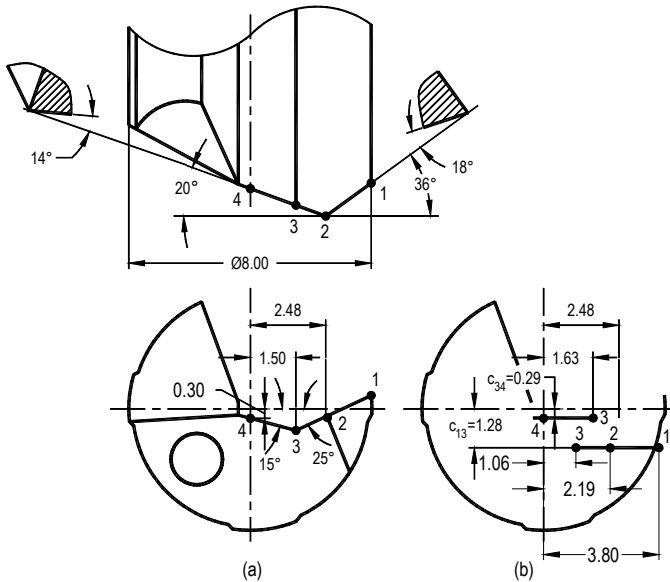
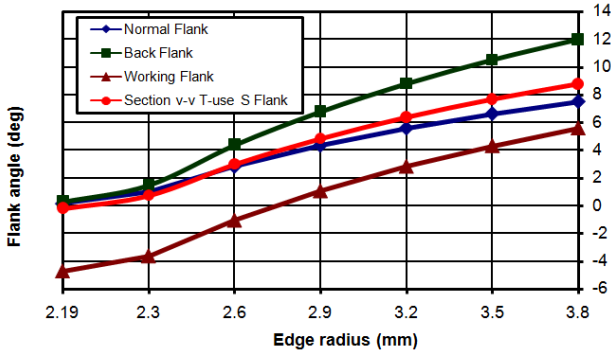


Fig. 5.36. Geometry of the gundrill used in Example 5.2

Following the procedure described in Example 5.1 for cutting edge 1–2, Fig. 5.37 shows the distribution of flank angle along cutting edge 1–2. As can be seen, T-mach-S and T-use-S flank angles tends to zero at point 2 and the T-mach-S

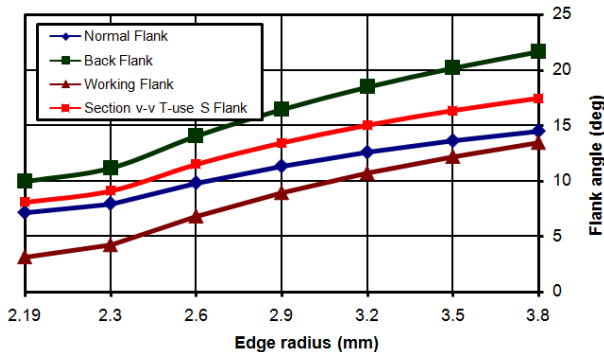




**Fig. 5.37.** Distribution of the flank angles over the outer cutting edge 1–2 of the drill shown in Fig. 5.36a

working plane flank angle  $\alpha_{fw}$  is negative at point 2 of cutting edge 1–2. Obviously, such geometry is not suitable for any practical use as the interference of the tool flank and the bottom of the hole being drilled will take place.

To solve the problem, the T-hand-S normal flank angle should be increased. Figure 5.38 shows the distribution of flank angle along cutting edge 1–2 when this angle is increased to  $25^\circ$ . As seen, all the flank angles are positive thus such geometry can be used in practice.

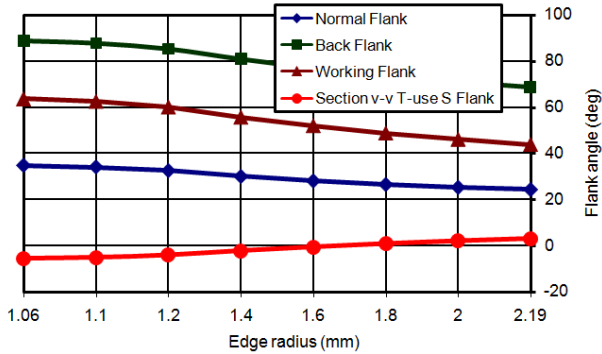


**Fig. 5.38.** Distribution of the flank angles over the outer cutting edge 1–2 of the drill shown in Fig. 5.36a with the increased T-hand-S normal flank angle

Cutting edge 2–3

As can be seen, this part falls in the considerations of Case 2 and thus procedure used in Example 5.1 (Sect. 5.6.3.3) for cutting edge 2–3 should be followed. As can be seen in Fig. 5.36a,  $\alpha_{n-r} = 14^\circ$  is constant over entire length of cutting edge 2–3. The approach angle for this edge is  $\varphi_{p23} = 18.3^\circ$ .

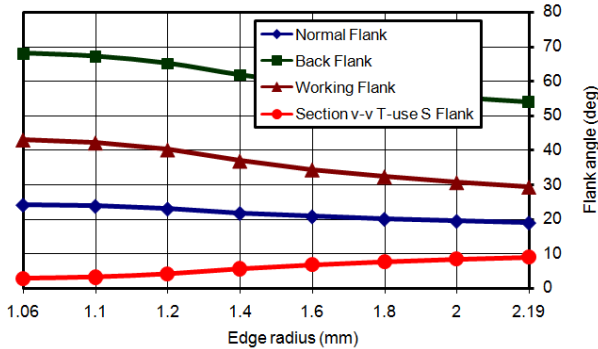
Following the procedure described in Example 5.1 for cutting edge 3–2, Fig. 5.39 shows the distribution of flank angle along cutting edge 2–3. As can be seen, T-mach-S flank angles are unreasonable high while the T-use-S flank angle  $\alpha_{vu}$



**Fig. 5.39.** Distribution of the flank angles over the outer cutting edge 2–3 of the drill shown in Fig. 5.36a

becomes negative. Obviously, such geometry is not suitable for any practical use as strength of the cutting wedge is low and interference between the tool flank and the bottom of the hole being drilled will take place.

To solve the problem, distance  $c_{pt}$  can be decreased. Figure 5.40 shows the distribution of the flank angles along cutting edge 1–2 when  $c_{pt} = 0.6\text{mm}$ . Although the T-mach-S flank angles are still high, there is not interference due to a negative flank angle  $\alpha_{vu}$ .



**Fig. 5.40.** Distribution of the flank angles over the outer cutting edge 2–3 of the drill shown in Fig. 5.36a with  $c_{pt} = 0.6\text{mm}$

#### Cutting edge 3–4

As can be seen, this part falls in the considerations of Case 2 and thus procedure used in Example 5.1 (Sect. 5.6.3.3) for cutting edge 2–3 should be followed. As can be seen in Fig. 5.36a,  $\alpha_{n-r} = 14^\circ$  is constant over entire length of cutting edge 3–4. The approach angle for this edge is  $\varphi_{p23} = 19.4^\circ$ .

Following the procedure described in Example 5.1 for cutting edge 2–3, Fig. 5.41 shows the distribution of flank angle along cutting edge 3–4. As can be seen,

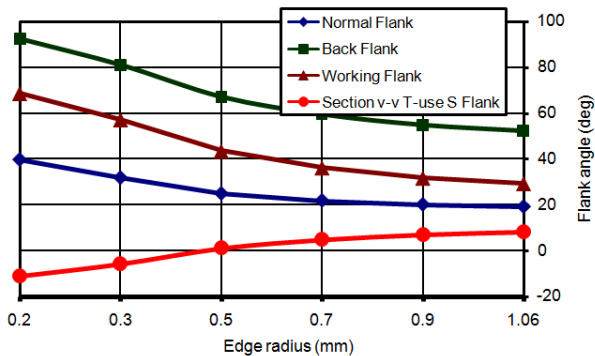


Fig. 5.41. Distribution of the flank angles over the outer cutting edge 3–4 of the drill shown in Fig. 5.36(a)

T-mach-S flank angles are unreasonably high while the T-use-S flank angle  $\alpha_{vu}$  becomes negative. Obviously, such geometry is not suitable for any practical use as strength of the cutting wedge is low and the interference of the tool flank and the bottom of the hole being drilled will take place.

To solve the problem, distance  $c_{pt}$  can be decreased. Figure 5.42 shows the distribution of the flank angles along cutting edge 1–2 when  $c_{pt} = 0.09\text{mm}$ . As can be seen, the T-mach-S flank angles are normal for the application. Although a small interference is still present due to a negative flank angle  $\alpha_{vu}$  adjacent to the axis of rotation, it can be tolerated in many practical applications.

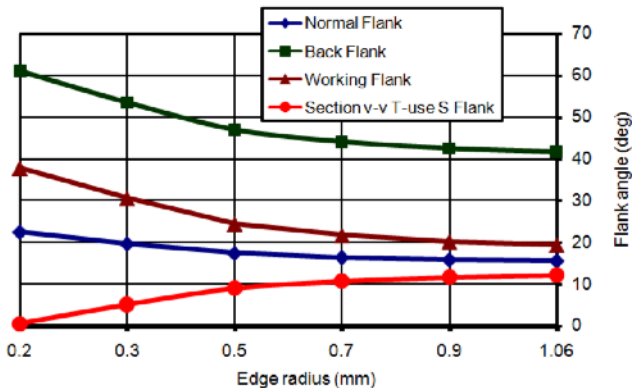


Fig. 5.42. Distribution of the flank angles over the outer cutting edge 3–4 of the drill shown in Fig. 5.36a with  $c_{pt} = 0.09\text{mm}$

### 5.6.4 System Considerations in Gundrill Design

The following section is probably the most important in terms of comprehending systemic design considerations for any kind of drills. Although the understanding

of the rake and flank geometries and their adjustments for a particular work material are important stages in the design of any drill including gundrills, it is only the tip of the iceberg. Ultimately, any serious tool designer pursuing the best tool design should consider a reasonable balance in justifying a number of objective functions of the tool design. This section for the first time presents a short analysis of these functions and provides distinctive strategies for their balancing. The proposed strategies are of methodological significance as they can be used for any kind of drills or even cutting tools.

The following objective functions must be considered in the gundrill design:

- Meeting hole quality requirements
- Achieving maximum tool life under the desirable productivity (the penetration rate)
- Producing chip shapes suitable for reliable removal
- Assuring stability at the entrance to the hole being drilled (preventing an excessive bell-mouth)

Although these objective functions seem to be independent, this section aims to show that they are just different facets of the proper tool design developed using these functions at various design stages. In other words, one can start the design with practically any feature and then develop others using iteration procedures to balance the final design. In the author's opinion, however, it is easy and more logical to start with the consideration of the influence of the cutting force components.

Following the introduced cutting force and its components in SPT (Fig. 5.5), one can represent the components of the cutting force as the projections of this force on the axes of the original (T-mach-S) coordinate system for cutting edges 1–2 and 2–3 as shown in Fig. 5.43. Besides the above discussed bending moments due to the axial components of the cutting force, the following bending moments act:

in the  $y_0z_0$  plane

$$M_{y_0z_0} = F_{y12}z_{b12} - F_{y23}z_{b23} \quad (5.61)$$

and in the  $x_0z_0$  plane

$$M_{x_0z_0} = F_{x12}z_{a12} + F_{x23}z_{a23} \quad (5.62)$$

#### 5.6.4.1 Bending Moment in the $x_0z_0$ Plane

Because the power components of the cutting force,  $F_x$  is normally (besides some special cases) much greater than the radial component  $F_y$ , and because the bending moment in the  $x_0z_0$  plane calculates at the sum of the moments due to  $F_{x12}$  and  $F_{x23}$ , the bending of the gundrill in this plane by angle  $\theta_{xz}$  (Fig. 5.44) is normally of prime concern. The greater angle  $\theta_{xz}$ , the lower the quality (surface finish and diametric accuracy) of the machined holes. Moreover, the greater angle  $\theta_{xz}$ , the

lower the contact area of the leading supporting pad. As a result, the contact stress on the tip of this pad increases which often causes its fracture as shown in Fig. 5.45. Although the bending moment in the  $x_0z_0$  plane is the “Achilles' heel” of any STP, but it is more profound in gundrilling due to small drill diameters and thus weak shanks.

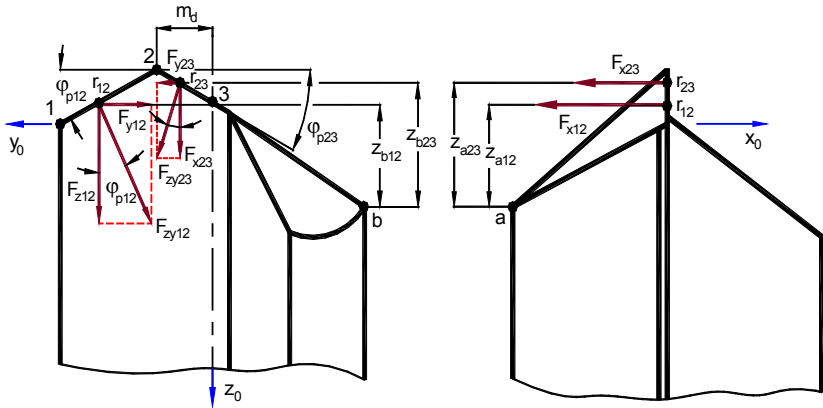


Fig. 5.43. Components of the cutting force causing additional bending moments

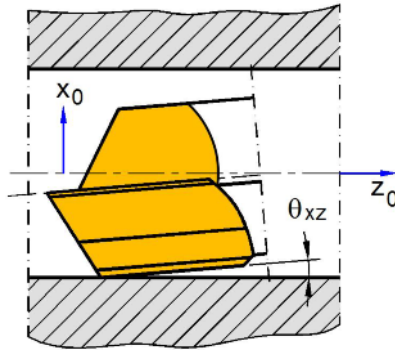
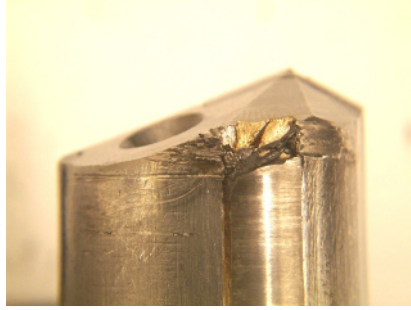


Fig. 5.44. Bending of the gundrill in the  $x_0z_0$  plane

It follows from Eq. 5.61 that this bending moment depends on the properties of the work material and drilling regime (forces  $F_{x12}$  and  $F_{x23}$ ) and on the location of the pad's front point a with respect to the cutting edges. The latter is determined by the approach angles (outer angle  $\phi_{p12}$  and inner angle  $\phi_{p23}$ ) as well as by the flank angles of cutting edges 1–2 and 2–3. Therefore, these parameters should be optimized to minimize the bending moment in the  $x_0z_0$  plane – this constitutes *Rule No.1 in drill design*.



**Fig. 5.45.** Fracture of the tip of the leading supporting pad due to excessive contact stress

#### 5.6.4.2 Bending Moment in the $x_0z_0$ Plane

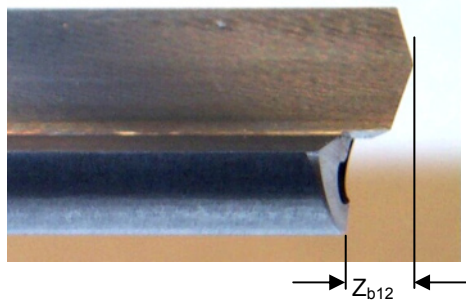
As seen in Fig. 5.43, for a particular cutting edge, the approach angles of the outer,  $\phi_{p12}$  and inner  $\phi_{p23}$  cutting edges determine the ratio of axial  $F_z$  and radial  $F_y$  forces as parts of  $F_{zy}$ . It follows from Eq. 5.61 and Fig. 5.43 that the additional bending moment in the  $y_0z_0$  plane can be eliminated if the approach angles and distance  $m_d$  are selected so that

$$F_{y12}z_{b12} = F_{y23}z_{b23} \quad (5.63)$$

However, this scenario is highly undesirable by any means. First, the trailing supporting pad has to be firmly pressed to the wall of the hole being drilled to assure the static stability in drilling and to take its share in burnishing of the hole being drilled. Second, if the conditions defined by Eq. 5.63 is justified then the length of outer cutting edge and its angle  $\phi_{p12}$  should be rather small compare to that of the inner cutting edge. If this is the case then the formed chip is directed into the machined surface, ruining its surface finish. Third, as discussed later, there will be a number of problems with the direction of MWF flow in the machining zone. Therefore, force component  $F_{y1}$  should be significant.

The arm of this component (with respect to point  $b$  in Fig. 5.43) can also be significant when the so-called stepped-slash point grind common in the automotive industry is used as seen in Fig. 5.46.

Obviously, the bending moment in the  $y_0z_0$  plane affects the drill deflection, particularly for small drill diameters and for long gundrills where the shank is not rigid enough to withstand the additional bending moment in this plane [16]. Therefore, the tool geometry parameters should be optimized to minimize the bending moment in the  $y_0z_0$  plane – this constitutes *Rule No.2 in drill design*.



**Fig. 5.46.** Arm of  $F_{y12}$  in the stepped-slash point grind

#### 5.6.4.3 Tool Wear Patterns

As well known, after a cutting operation has progressed for some time, wear takes place in two different regions on the cutting tool [17]. Wear appears on the flanks of the tool below the cutting edge(s) forming a wear land, and also appears on the tool face forming a characteristic cavity at a certain distance from the cutting edge on the rake face.

Like any other cutting tool, tool wear is of prime concern in gundrilling as it defines tool life. In gundrilling, two characteristics of tool life should always be considered:

- *Tool Life* is that time over which a tool performs cutting between two successive re-sharpenings. It can also be measured by a number of drilled holes per one re-sharpening providing that these holes are the same. It can also be measured by the overall length of the drilled holes produced by the drill between two re-sharpenings. Therefore, tool life can be measured in the units of time and length or by non-dimension numbers of the holes. To measure tool life properly, a clear and accurate criterion of tool life should be established.
- *Overall Tool Life* calculates as tool life times the number of re-sharpenings. This number varies depending upon the wear pattern achieved within tool life. Unfortunately, this is seldom understood in gundrilling where the topography of the wear pattern has never been considered as a factor limiting overall tool life. Normally, a gundrill is ground back on a re-sharpening by 0.4–0.6 mm to remove visible wear marks. As such, an average gundrill can normally allows 8–10 re-sharpenings.

To establish clear criteria of tool life, the regions of wear on a gundrill and wear patterns should be known. Figure 5.47 shows regions of wear on a gundrill which are:

- *Wear on the flank surface of the inner and outer cutting edges.* This is known as flank wear. The first essential feature of gundrilling is the variation in cutting speed along the cutting edges with the maximum at the

periphery point of the drill. The second essential feature is that the amount of material removed by the part of the cutting edge adjacent to the drill periphery point is much greater than that by the regions of the inner cutting edge. The third feature is that the distance passed by the periphery point of a gundrill per one drill revolution is greater than that by other points of the cutting edge. As a result, the wear pattern on the flank faces is not uniform as seen in Fig. 5.47, the flank wear being maximum in the region of the drill periphery point.

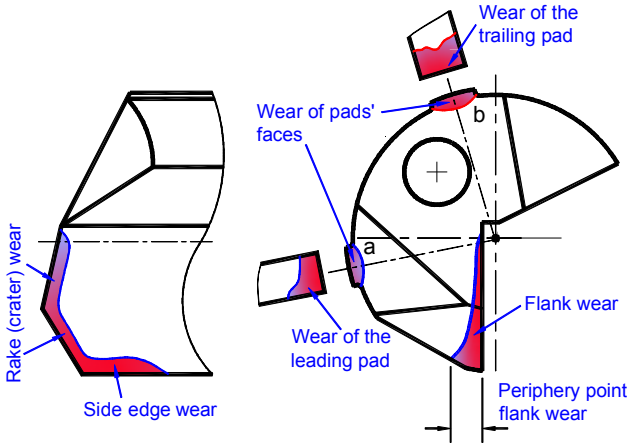


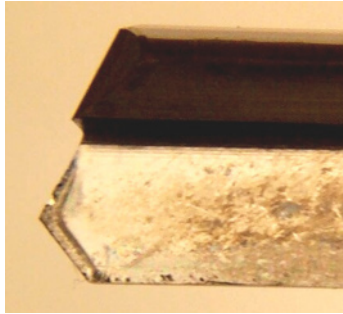
Fig. 5.47. Typical regions of wear on a gundrill

- *Wear on the rake face.* This wear is due to high temperature conditions and high contact pressures at the tool-chip interface. Normally, it appears as a groove (called the crater) along the cutting edges. Figure 5.48 shows normal wear pattern on the rake face while Fig. 5.49 shows excessive wear on the rake face and side cutting edge.
- *Wear of the side cutting edge.* It was discussed in Chap. 3 that this cutting edge actually cuts in any kind of drilling even if all the parameters of the machining system are perfect. Another common cause of premature wear of the side cutting edge is a lack of backtaper. This can be caused by insufficient backtaper applied during drill manufacturing and/or due to inaccuracies in the gundrilling system. Moreover, when static or entrance stability of the tool is insufficient [4, 18, 19], this edge experiences additional side cutting that leads to its rapid deterioration. This type of wear is the least desirable because a substantial amount of tool material should be ground on re-sharpening to restore the drill. As a drill is provided with a backtaper, its diameter decreases on drill sharpening so that the total tool life reduces significantly. The wear of the side edge due to lack of backtaper may also lead to bulk fracture of the side cutting edge as shown in Fig. 5.50.
- *Wear of the supporting pad and their faces.* Normally in gundrilling, the leading supporting pad is loaded much more than the trailing supporting

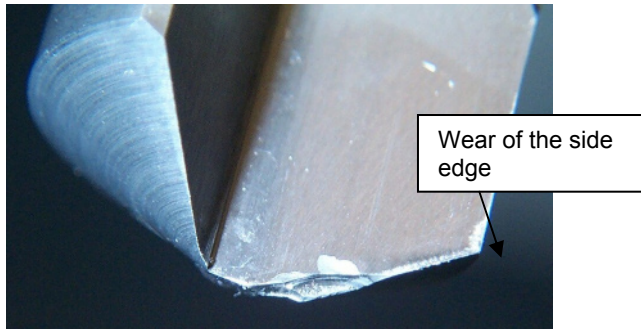


pad. This is due to higher force, acting on this part causing higher plastic deformation of the work material due to burnishing compared to the trailing pad. As a result, the severity of wear of this pad is much higher and may lead to the fracture of the front end of the leading supporting pad.

The amount of wear and wear rate in the discussed zones depends on many parameters of the gundrilling system such as the tool and work materials, machining regime, etc. It is important to note, however, that besides the rake face, the



**Fig. 5.48.** Normal wear pattern of the rake face



**Fig. 5.49.** Wear pattern of the rake face and side cutting edge



**Fig. 5.50.** Bulk fracture of the side cutting edge

discussed regions of wear are parts of the tool flank surfaces or close to these surfaces. Therefore, for the given conditions, the wear of the discussed regions depends directly on cooling and lubrication conditions of the tool flanks. To understand these conditions and thus to improve tool life, one should consider MWF flow in the space enclosed between the bottom of the hole being drilled and tool flank termed the bottom clearance space.

#### 5.6.4.4 Bottom Clearance Space Definition

While drilling, the gundrill geometry results in the formation of the sculptured surface 1 known as the bottom of the hole being drilled (Fig. 5.51). This bottom, from one side, with the drill's flanks 2, 3 and 4, from the other side, form a limited space 5 named as the bottom clearance space. The topology of the bottom clearance space can be appreciated in different cross-sections as shown in Fig. 5.51.

MWF (the coolant) is supplied into the bottom clearance space 5 under pressure through the internal passage 6 of the shank and coolant passage 8 made in the tip 7. The MWF pressure in the bottom clearance space directly affects tool life as it has a major influence on the cooling and lubrication conditions on the tool flank (of the

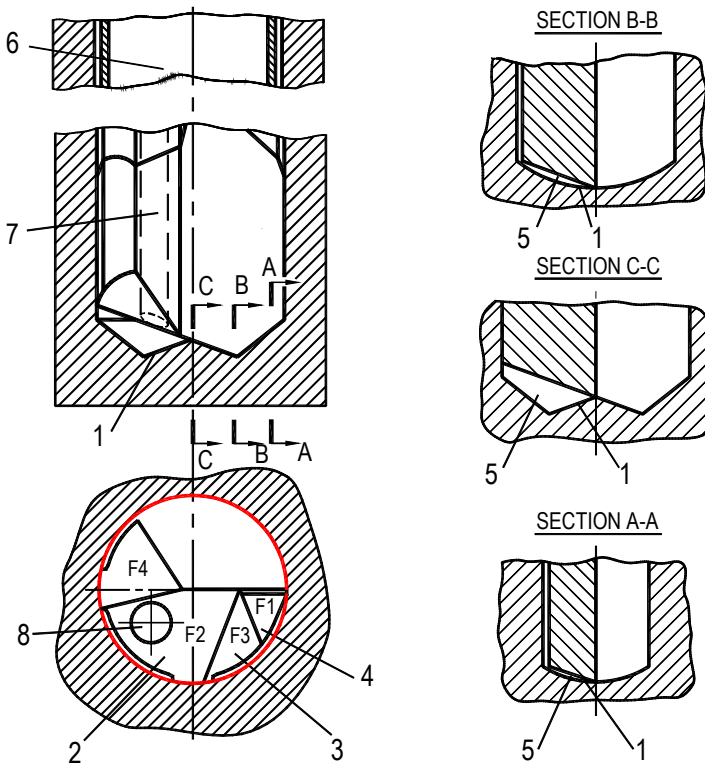
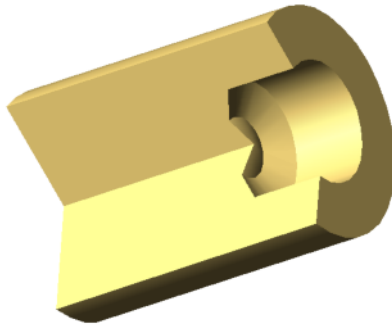


Fig. 5.51. Concept of the bottom clearance space

inner, outer, and side cutting edges) surfaces as well as on the supporting pads. The higher the MWF pressure, the higher tool life. This constitutes *Rule No.3 in drill design*. High MWF pressure in the bottom clearance space provides a better penetration of the MWF into the extremely narrow passages (see SECTION A–A in Fig. 5.51) between the tool flanks and the bottom of the hole being drilled, that is better conditions for lubricating and cooling of the flank contact areas. This is particularly important for MWF penetration in the regions adjacent to the drill periphery point where this MWF is most needed. Unfortunately, it is not achieved in standard gundrills and thus the tool wear in this zone is much higher than in any other.

The topology of the bottom clearance is rather complicated as it is formed by two sculptured surfaces: the bottom of the hole being drilled and the flank surfaces of the gundrill. The bottom of the hole being drilled in general is formed by two adjacent hyperboloids of revolution. If the cutting edges are not straight, this bottom has an even more complicated shape. In the particular case, however, when the cutting edges are straight, horizontal (as in the T-mach-S) and located on the  $y_0$  axes (the distance  $c_{pt}$  is small thus can be neglected in considerations of the geometry of the bottom of the hole being drilled), the bottom 1 (Fig. 5.51) consist of two adjacent conical surface (one reversed due to the outer cutting edge and the other is direct as formed by the inner cutting edge). A section of the bottom of the hole being drilled is shown in Fig. 5.52.

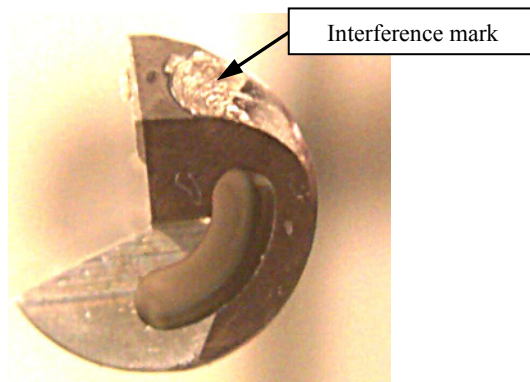


**Fig. 5.52.** Section of the bottom of the hole being drilled

The complicated shapes of the drill flanks and the bottom make the shape of the bottom clearance very irregular and complex. One may ask a logical question: why is it important to know the topology of this space? There are two prime reasons for that. First is to assure drill free penetration into the hole being drilled with no interference. Second is to assure the preferable MWF flows in this space. The latter is important in order to reduce wear in the places indicated in Fig. 5.47.

The condition of the drill free penetration into the hole being drilled is justified if there is no interference between the drill flanks and the bottom of the hole being drilled. The term “interference” is commonly associated with the interaction of coherent waves. In tool design, this term describes the hypothetical overlapping or even contact of any surfaces or points of the cutting tools which are not supposed

to overlap or to be in contact with the workpiece. It should be clear that, when interference takes place, free penetration is theoretically impossible. In reality, it is not always so because a gundrill is not a rigid body so, when ‘light’ interference occurs, the drill usually bends (of course, to a certain extent) so that its cutting edges come into contact at the surfaces of interference and just rub against the workpiece. As such, the interference mark(s) are left on the tip as shown in Fig. 5.53. This surface is definitely, not meant to make contact with the bottom of the hole being drilled. Such interference leads to additional forces on the tip, elevated temperatures due to rubbing and to drill vibration. It ruins the quality of the drilled holes and reduces tool life. Therefore, any interference in any kind of drilling should be prevented – this constitutes *Rule No.4 in drill design*.



**Fig. 5.53.** Interference mark on the flank surface of the outer cutting edge

Because the bottom clearance space has very a complicated shape, it is very difficult to assure the absence of interference in the 2D design by taking cross sections as shown in Fig. 5.51. A possible way to analyze interference is 3D modeling where a section of the hole being drilled is considered in its contact with the cutting edges. Rotating this tool with respect to the workpiece, one can visualize the clearances and interferences in the bottom clearance space. A few frames in such a modeling are shown in Fig. 5.54. This method, however, is not yet common in gundrill design because it requires real understanding of tool geometry and profile generating mathematics. As a result, interference in the design gundrill is assured ‘by eye’ that causes a common interference problem. Because ASTM did not adopt (at least that far) any standard procedure for human eye evaluation and certification, such ‘assurance’ cannot be considered to be accurate and objective.

At best, the condition of drill free penetration is verified by a few 2D cross-sections. The tip point grind design of many modern gundrills has remained the same over last 50+ years when CAD systems were not available so the tip was designed so that interference is avoided “for sure” by grinding tool secondary tool flanks. As such, other parameters such as drill bending (Rules No. 1 and 2) and the MWF pressure in the bottom clearance space (Rule No.3) are neglected.

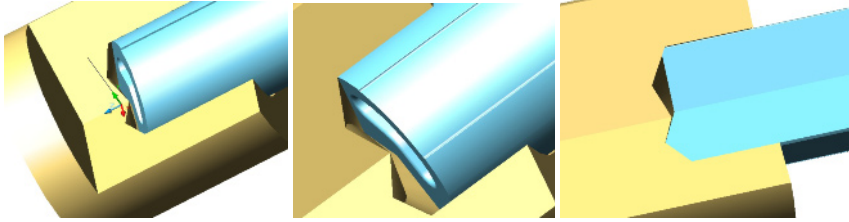


Fig. 5.54. Graphic modeling of the conditions of drill free penetration

5.6.4.5 Conditions of Free Penetration

To understand these conditions, one should ask a logical question: How many flank planes are really needed for free penetration of a gundrill? Normally, four flank surfaces (planes) are provided. Figure 5.52 shows  $F1$ ,  $F2$ ,  $F3$ , and  $F4$  flank planes. Planes  $F1$  and  $F2$  are flank planes of the outer and inner cutting edges while planes  $F3$  and  $F4$  are meant to assure drill free penetration into the hole being drilled. Because there are no recommendations on the selection of the location of planes  $F3$  and  $F4$ , most of gundrill manufacturers and users follow the common pattern established more than 50 year ago (Fig. 5.19).

This section aims to resolve this long-standing issue. Figure 5.55 shows a gundrill made with only two flank planes. The free penetration of the drill's flank can be verified by the set of the clearances  $\delta_{cl}$  between the flank points and the bottom of the hole being drilled. The drill's flank touches the bottom when the value of this clearance is equal to zero. The value of  $\delta_{cl}$  varies continuously along the flank and the graphical analysis shows that the most “dangerous” points of the drill flank (the possibility of interference with the bottom) are located at the periphery points “a” and “b” shown in Fig. 5.55.

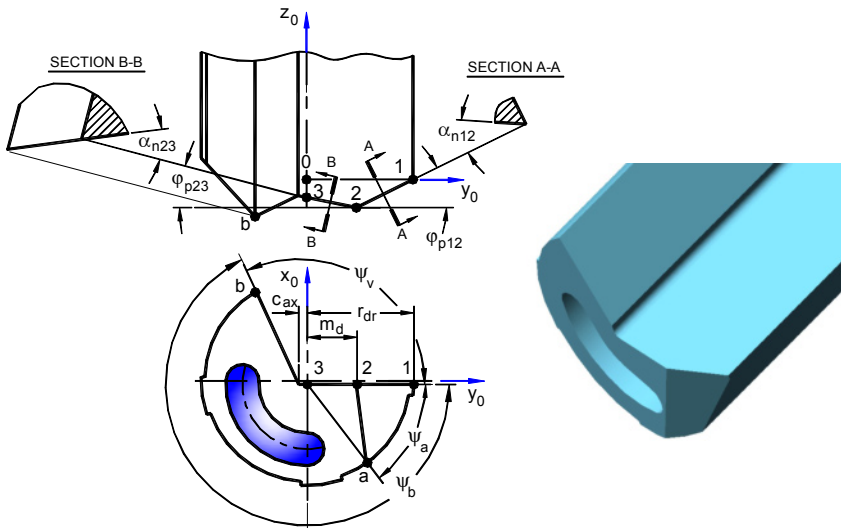


Fig. 5.55. Gundrill with two flanks

The angular location of points  $a$  and  $b$  in the  $x_0y_0$  plane are [20]

$$\psi_a = 180^\circ - \nu_{a12} - \arcsin\left(\frac{m_d}{r_{dr}} \sin \nu_{a12}\right) \quad (5.64)$$

$$\psi_b = \psi_{1b} + \arcsin\left(\frac{c_{ax}}{r_{dr}} \sin \psi_{1b}\right) \quad (5.65)$$

where  $\psi_{1b}$  ( $= 360^\circ - \psi_v$ ) is the angle of the sector the  $x_0y_0$  plane corresponding to the drill body, and

$$\nu_{a12} = \arctan\left(\frac{\sin(\varphi_{p12} - \varphi_{p23})}{\tan \alpha_{n1} \cos \varphi_{p23} - \tan \alpha_{n2} \cos \varphi_{p12}}\right) \quad (5.66)$$

The foregoing analysis suggests that two conditions of drill free penetrations, one for point  $a$  and another for point  $b$ , should be established. In other words, it should be established if flanks  $F3$  and  $F4$  (Fig. 5.52) are needed and if needed, what should be the geometry of these flanks.

The design of the cutting edges fully determines the shape of the bottom of the hole being drilled. In general, the static shape (when the feed is not considered) of the bottom of the hole being drilled consists of a number of connected hyperboloids of revolution and this number is equal to the number of the cutting edges of the drill. Figure 5.56 shows a general case where a gundrill having two cutting edges, 1–2 and 2–3, drills a hole. In drilling, these two cutting edges form the bottom of the hole being drilled which counter  $1_w 2_w 3_w 2'_w 1'_w$  appears in SECTION N2–N2. As seen, the shape of this bottom consists of two connected hyperboloids of revolution,  $1_w 2_w$  and  $2_w 3_w$ , due to the shape and location of the corresponding cutting edges 1–2 and 2–3, which form these hyperboloids.

In the original  $x_0y_0z_0$  coordinate system, the connected hyperboloids of revolution can be represented by the following equation, which relates their shape with corresponding points of the cutting edge:

$$H = -\mathbf{i}r_i \sin \psi_{ib} + \mathbf{j}r_i \cos \psi - \mathbf{k}r_i \cos \mu_i \tan \varepsilon_i \quad (5.67)$$

Here,  $r_i$  is the radius of the considered point of the cutting edge  $i$ ,  $\psi_{bi}$  is the location angle of the radius-vector  $\rho_i$  of the considered point of the cutting edge in the  $x_0y_0$  plane,  $\mu_i$  is the angle between the normal to the cutting edge in the considered point  $i$  and the vector of the cutting velocity  $v$  at this point,  $\varepsilon_i$  is the angle between radius-vector  $\rho_i$  and the  $y_0$ -axis.

It follows from the model shown in Fig. 5.56 that angle  $\mu_i$  calculates as follows

For  $e_d < r_i \leq r_{dr}$

$$\mu_i = -\arcsin \frac{r_{dr} \sin \beta_1 + c \cos \beta_1}{r_i} \tag{5.68}$$

For  $0 \leq r_i \leq e_d$

$$\mu_i = -\arcsin \frac{c_{pt} \cos \beta_2}{r_i} \tag{5.69}$$

where  $r_{dr}$  is the drill radius.

Angle  $\varepsilon_i$  calculates as

For  $m_d < r_i \leq r_{dr}$

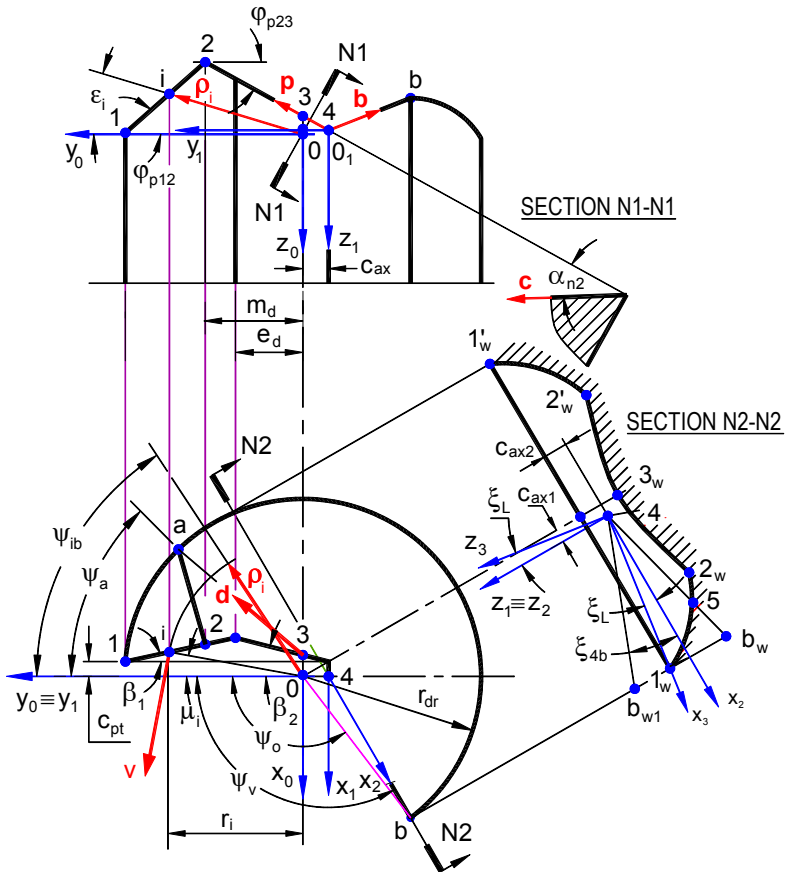


Fig. 5.56. Representation of the formation of the bottom of the hole being drilled and location of point  $b$

$$\tan \varepsilon_i = \left(1 - \frac{r_{dr}}{r_i}\right) \tan \varphi_{p12} \quad (5.70)$$

For  $0 \leq r_i \leq m_d$

$$\tan \varepsilon_i = \left(\frac{r_{dr}}{r_i} - 1\right) \tan \varphi_{p12} - \left(\frac{m_d}{r_i} - 1\right) \tan \varphi_{p23} \quad (5.71)$$

For the further analysis, a new coordinate system  $x_1y_1z_1$  having the origin at point 4 and the axes parallel to the original coordinate system  $x_0y_0z_0$  is introduced as shown in Fig. 5.56. In this new coordinate system, consider three vectors:  $\mathbf{p}$  which originates from point 4 and is in the direction of the inner cutting edge with its positive sense as shown in Fig. 5.56;  $\mathbf{b}$  which originates from point 4 and is in the direction of side 4b;  $\mathbf{c}$  which originates from point 4 and in the direction of the line of intersection of normal plane N1–N1 to the inner cutting edge and the flank plane of the inner cutting edge with its positive sense as shown in Fig. 5.56. Let,  $\mathbf{i}$ ,  $\mathbf{j}$ , and  $\mathbf{k}$  be unit vectors along the positive directions of the  $x_1$ -,  $y_1$ -, and  $z_1$ - axes, respectively. Then the introduced vectors  $\mathbf{p}$ ,  $\mathbf{b}$ , and  $\mathbf{c}$  can be represented as

$$\mathbf{p} = -\mathbf{i} \sin \beta_2 + \mathbf{j} \cos \beta_2 \cos \varphi_{p23} - \mathbf{k} \cos \beta_2 \sin \varphi_{p23} \quad (5.72)$$

$$\mathbf{b} = \mathbf{i} \sin \psi_v \cos \xi_{4b} + \mathbf{j} \cos \psi_v \cos \xi_{4b} + \mathbf{k} \sin \xi_{4b} \quad (5.73)$$

$$\mathbf{c} = -\mathbf{i} \cos \alpha_{n2} + \mathbf{j} \sin \varphi_{p23} \sin \alpha_{n2} + \mathbf{k} \cos \varphi_{p23} \sin \alpha_{n2} \quad (5.74)$$

Because these vectors belong to the same plane, their triple product is equal to zero (Appendix C), i.e.,

$$\mathbf{b} \cdot (\mathbf{p} \times \mathbf{c}) = 0 \quad (5.75)$$

or

$$\begin{vmatrix} \sin \psi_v \cos \xi_{4b} & \cos \psi_v \cos \xi_{4b} & \sin \xi_{4b} \\ -\sin \beta_2 & \cos \beta_2 \cos \varphi_{p23} & -\cos \beta_2 \sin \varphi_{p23} \\ -\cos \alpha_{n2} & \sin \varphi_{p23} \sin \alpha_{n2} & \cos \varphi_{p23} \sin \alpha_{n2} \end{vmatrix} = 0 \quad (5.76)$$

Solving this equation with respect to  $\xi_{4b}$ , one obtains

$$\xi_{4b} = \arctan \left[ \frac{\frac{\sin \psi_v}{\cos \varphi_{p23}} \tan \alpha_{n2} - \cos \psi_v (\tan \beta_2 \tan \alpha_{n2} + \tan \varphi_{p23})}{\tan \beta_2 \tan \alpha_{n2} \tan \varphi_{p23} - 1} \right] \quad (5.77)$$



A particular yet common case in the design of gundrills takes place when angle  $\beta_2 = 0$ . As such the corresponding projection of vectors  $\mathbf{p}$ ,  $\mathbf{b}$  and  $\mathbf{c}$  are

$$\mathbf{p} = \mathbf{j} \cos \varphi_{p23} - \mathbf{k} \sin \varphi_{p23} \quad (5.78)$$

$$\mathbf{b} = \mathbf{i} \sin \psi_v \cos \xi_{4b} + \mathbf{j} \cos \psi_v \cos \xi_{4b} + \mathbf{k} \sin \xi_{4b} \quad (5.79)$$

$$\mathbf{c} = -\mathbf{i} \cos \alpha_{n2} + \mathbf{j} \sin \varphi_{p23} \sin \alpha_{n2} + \mathbf{k} \cos \varphi_{p23} \sin \alpha_{n2} \quad (5.80)$$

Because these vectors belong to the same plane, their triple product is equal to zero, i.e.,

$$\mathbf{b} \cdot (\mathbf{p} \times \mathbf{c}) = 0 \quad (5.81)$$

or

$$\begin{vmatrix} \sin \psi_v \cos \xi_{4b} & \cos \psi_v \cos \xi_{4b} & \sin \xi_{4b} \\ 0 & \cos \varphi_{p23} & -\sin \varphi_{p23} \\ -\cos \alpha_{n2} & \sin \varphi_{p23} \sin \alpha_{n2} & \cos \varphi_{p23} \sin \alpha_{n2} \end{vmatrix} = 0 \quad (5.82)$$

Solving this equation with respect to  $\xi_{4b}$ , one obtains

$$\xi_{4b} = -\arctan \left[ \cos \varphi_{p23} \left( \tan \alpha_{n2} \sin \psi_v + \sin \varphi_{p23} \cos \psi_v \right) \right] \quad (5.83)$$

Equation 5.77 as well as its particular case represented by Eq. 5.83 define the actual angle  $\xi_{4b}$  in cross-section plane N2–N2. As seen, it depends on the special location of the inner cutting edge (angles  $\varphi_{p23}$  and  $\beta_2$ ), the normal flank angle of this edge ( $\alpha_{n2}$ ), and the shift  $c_{ax}$  (Fig. 5.56). The later should always be considered the profile angle,  $\psi_v$  and the actual angle of profile,  $\psi_o$  (Fig. 5.56) are related as

$$\psi_o = \psi_v + \arcsin \left( \frac{c_{ax}}{r_{dr}} \sin \psi_v \right) \quad (5.84)$$

This actual angle is important in the selection of the V-flute profile angle of the shank and in point grinding because the gundrill rotates with respect to the center 0 in actual drilling and is positioned in the grinding fixture with respect to this center.

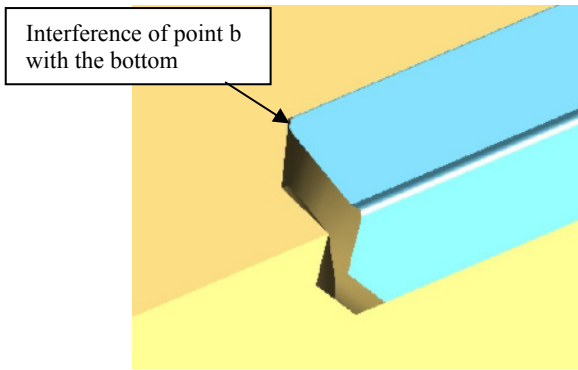
To clarify the significance of the inclination angle  $\xi_{4b}$ , one should consider cross-section N2–N2 in Fig. 5.56. To simplify further considerations, a new coordinate system  $x_2y_2z_2$  has the origin at point 4. The  $z_2$ -axis of this system coincides with the  $z_1$ -axis, the  $y_2$ - and  $x_2$ - axes are rotated by angle  $\psi_v - \pi/2$  counterclockwise with respect to the corresponding axes of the  $x_1y_1z_1$  coordinate system. Note that the coordinate of the origin (point 4) with respect to the origin 0 of the original coordinate system are

$$c_{ax1} = -c_{ax} \cos \psi_v \quad (5.85)$$

$$c_{ax2} = (r_{dr} - m_d) \tan \varphi_{p12} - (m_d + c_{ax}) \tan \varphi_{p23} \quad (5.86)$$

As shown in Fig. 5.56 (cross-section N2–N2), point b may occupy positions:

- Within the workpiece shown by point  $b_w$  and thus interferes with the bottom of the hole being drilled as shown in Fig. 5.59. In this case, flank  $F4$  (Fig. 5.52) is required.
- Outside as shown by point  $b_w$ . In this case, there is no need to make flank  $F4$  in order to avoid interference.



**Fig. 5.57.** Interference of point  $b$  with the bottom of the hole being drilled. As can be seen, point  $b$  makes contact with the bottom before the cutting edges do

It is important to comprehend the concept of the limiting position of side 4b. This limiting position occurs when point  $b$  touches the bottom of the hole being drilled, i.e., this point  $b$  coincides with point  $1_w$  of the bottom. Such a position is characterized by the limiting angle  $\xi_L$  (Fig. 5.52, section N2–N2). Therefore, the condition of free penetration of point  $b$  can be written as

$$\xi_{4b} \geq \xi_L \quad (5.87)$$

The sign of  $\xi_{4b}$  in its calculation using Eqs. 5.77 and 5.83 is as follows: if  $\xi_{4b} > 0$  then side 4b is rotated clockwise with respect to the  $x_2$ -axis and if  $\xi_{4b} < 0$  then side 4b is rotated counterclockwise.

The limiting angle  $\xi_L$  (Fig. 5.52, section N2–N2) calculates as

$$\xi_L = \arctan \frac{(r_{dr} - m_d) \tan \varphi_{p12} - (m_d + c_{ax}) \tan \varphi_{p23}}{c_{ax} \cos \psi_v + \sqrt{r_{dr}^2 - c_{ax}^2 \sin^2 \psi_v}} \quad (5.88)$$

It is clear that  $\xi_L$  is the same for any point of the drill's flank. Therefore, the condition of free penetration for point a can be written as

$$\xi_{3a} \geq \xi_L \tag{5.89}$$

Because point a belongs to the same flank plane  $F2$ , one can find  $\xi_{3a}$  by considering the triple product of vectors  $\mathbf{d}$ ,  $\mathbf{p}$ , and  $\mathbf{c}$ . Here, vector  $\mathbf{d}$  originates from point 3 and is in the direction of line 3a. For a particular yet common case in the design of gundrills shown in Fig. 5.55, simplified conditions can be used [20]:

$$\xi_L = \arctan \left( \tan \varphi_{p12} - \frac{m_d}{r_{dr}} (\tan \varphi_{p12} - \tan \varphi_{p23}) \right) \tag{5.90}$$

$$\xi_{3a} = \arctan \left[ \left( \cos \psi_a + \tan \alpha_{2n} \frac{\sin \psi_a}{\sin \varphi_{p23}} \right) \tan \varphi_{p23} \right] \tag{5.91}$$

$$\xi_{4b} = \arctan \left[ \left( \cos \psi_b + \tan \alpha_{2n} \frac{\sin \psi_b}{\sin \varphi_{p23}} \right) \tan \varphi_{p23} \right] \tag{5.92}$$

where

$$\psi_b = \psi_{1b} + \arcsin \left( \frac{c_{ax}}{r_{dr}} \sin \psi_{1b} \right) \tag{5.93}$$

$$\psi_a = 180 - \alpha_a - \arcsin \left( \frac{m_d}{r_{dr}} \sin \alpha_a \right) \tag{5.94}$$

where  $\psi_{1b}$  ( $= 360^\circ - \psi_v$ ) as before is the angle of the sector the  $x_0y_0$  plane corresponding to the drill body and

$$\alpha_a = \frac{\sin(\varphi_{p12} - \varphi_{p23})}{\tan \alpha_{n1} \cos \varphi_{p23} - \tan \alpha_{n2} \cos \varphi_{p12}} \tag{5.95}$$

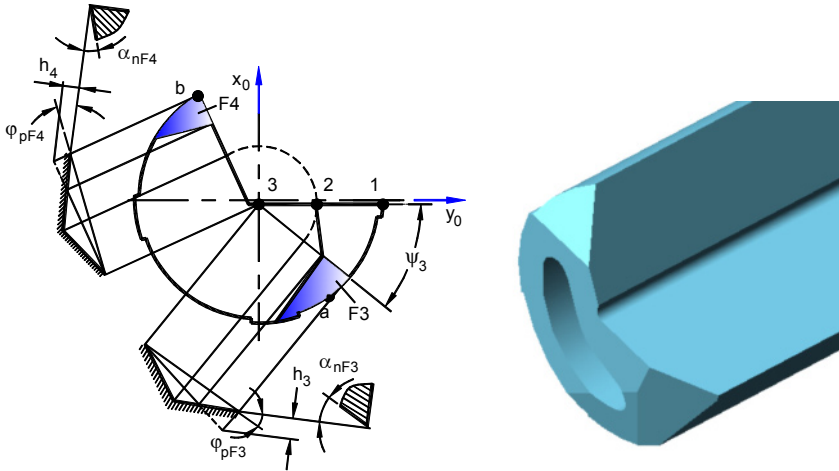
If  $\alpha_a > 0$  then its value calculated by Eq. 5.95 is substituted into Eq. 5.94, otherwise

$$\psi_a = \alpha_a - \arcsin \left( \frac{m_d}{r_{dr}} \sin(180 - \alpha_a) \right) \tag{5.96}$$

When conditions set by Eqs. 5.87 and 5.89 are justified, there is no need to make flank surfaces  $F3$  and  $F4$  (Fig. 5.52) to assure drill free penetration thus the drill can be as that shown in Fig. 5.55. However, practical parameters of the tool geometry flank surfaces  $F3$  and/or  $F4$  are often needed when one of these or both

conditions are not valid. Therefore, the next question to be answered is about what the geometry of these flanks  $F3$  and  $F4$  should be.

Figure 5.58 shows the limiting positions of flanks  $F3$  and  $F4$  when these flanks touch the bottom of the hole being drilled, i.e., when the bending moments at  $x_0z_0$  and  $y_0z_0$  planes are at possible minimum. There are four geometry parameters needed to make these flanks, namely, the location angle, the approach angle, the depth, and the flank angle. These can be determined graphically or analytically using the model shown in Fig. 5.56.



**Fig. 5.58.** Model for flank surfaces  $F3$  and  $F4$

Analytical determination of the introduced geometrical parameters of flanks  $F3$  and  $F4$  resulted in the followings. It is obvious as it directly follows from Figs. 5.56 and 5.58 that  $\varphi_{pF3} = \varphi_{pF4} = \varphi_{pF1}$  ( $\varphi_3 = \varphi_4 = \varphi_1$ ) as the considered part of the bottom of the hole being drilled is formed by the outer cutting edge 1–2. The location angle  $\psi_3$  of the flank  $F3$  calculates as [20]

$$\psi_3 = 2 \arctan \frac{\tan \alpha_{n1}}{\sin \varphi_{p23}} \tag{5.97}$$

The flank angle of flank  $F3$  calculates as

$$\alpha_{n3} = \arctan \left( \sin \varphi_{pF3} \tan (\psi_m - \psi_3) \right) \tag{5.98}$$

where

$$\psi_m = \arcsin \frac{\cos \psi_3 + \sin (\tau_{13} + \alpha_{p2})}{2 \sin \frac{c_m}{2}} \tag{5.99}$$

$$c_m = 90 + \tau_{13} + \alpha_{p2} - \psi_3 \quad (5.100)$$

$$\tau_{13} = -\arcsin \left( \frac{(r_{dr} - m_d) \tan \varphi_{p12} + m_d \tan \varphi_{p12}}{r_{dr}} \right) \frac{\cos \alpha_{p2}}{\tan \varphi_{p23}} \quad (5.101)$$

$$\alpha_{p2} = \arctan \frac{\tan \alpha_{2n}}{\sin \varphi_{p23}} \quad (5.102)$$

and the depth  $h_3$  calculates as

$$h_3 = r_{dr} \sin \theta_{\psi 2} \tan(\alpha_{n3} + \theta_{\psi 3}) + \frac{f}{360} (90 + \tau_{13} + \theta_{2b}) \frac{\cos \alpha_{n3}}{\cos \varphi_{pF3}} \quad (5.103)$$

where

$$\theta_{\psi 3} = \arctan \frac{\tan \alpha_{n1} \cos \psi_3}{\tan \varphi_{pF3} \sin \psi_3 + 1} \quad (5.104)$$

$$\theta_{\psi 2} = \arccos \left( \frac{m_d \frac{1 - \frac{\tan \varphi_{p12}}{\tan \varphi_{p23}}}{r_{dr} \left( 1 - \frac{\tan \varphi_{p12}}{\tan \varphi_{p23}} - 2 \sin^2 \alpha_{p1} \left( 1 + \tan \alpha_{p1} \tan \left( \frac{\tan \alpha_{p2}}{\tan \alpha_{p1}} \right) \right) \right)}}{r_{dr} \frac{1 - \frac{\tan \varphi_{p12}}{\tan \varphi_{p23}}}{r_{dr} \left( 1 - \frac{\tan \varphi_{p12}}{\tan \varphi_{p23}} - 2 \sin^2 \alpha_{p1} \left( 1 + \tan \alpha_{p1} \tan \left( \frac{\tan \alpha_{p2}}{\tan \alpha_{p1}} \right) \right) \right)}}} \right) \quad (5.105)$$

$$\alpha_{p1} = \arctan \frac{\tan \alpha_{n1}}{\sin \varphi_{p12}} \quad (5.106)$$

The flank angle of flank  $F4$  calculates as

$$\alpha_{n4} = \arcsin \frac{1 - \cos(\theta_{\psi 4} - \psi_v)}{r_{dr} \sin(\theta_{\psi 4} - \psi_v) - c_{ax} \sin \psi_v} r_{dr} \sin \varphi_{p12} \quad (5.107)$$

where

$$\theta_{\psi 4} = \arccos \left( \frac{\tan \xi_L \tan \xi_L \sin \varphi_{p23} - \tan \alpha_{2n} \sqrt{\tan^2 \alpha_{n2} + \sin^2 \varphi_{p23} - \tan^2 \xi_L \tan^2 \xi_L}}{\sin^2 \varphi_{p23} + \tan^2 \alpha_{2n}} \right) \quad (5.108)$$

and the depth  $h_4$  calculates as

$$h_4 = \cos \varphi_{p12} \left[ \begin{array}{l} r_{dr} (\tan \varphi_{p12} - \tan \xi_{4b}) - c_{ax} \cos \psi_a (\tan \varphi_{p23} - \tan \xi_{4b}) \\ -m_d (\tan \varphi_{p12} - \tan \varphi_{p23}) \end{array} \right] + \frac{f \psi_v \cos \alpha_{n4}}{360 \cos \varphi_{pF4}} \quad (5.109)$$

#### 5.6.4.6 Example 5.3

Problem: Let the following parameters of the self-piloting drill with external chip removal be given as:

Drill diameter	$2r_{dr}$	31.75 mm
Approach cutting edge angle of the outer cutting edge	$\varphi_1(\varphi_{p12})$	$25^\circ$
Main cutting angle of the inner cutting edge	$\varphi_2(\varphi_{p23})$	$-15^\circ$
Normal flank angle of the outer cutting edge	$\alpha_{n1}$	$20^\circ$
Normal flank angle of the inner cutting edge	$\alpha_{n2}$	$8^\circ$
Size of V-shaped flute extension	$c_{ax}$	1.8 mm
Angle of the sector corresponding to the V-shaped flute	$\psi_v$	$116^\circ$
Angle of the sector corresponding to the drill body	$\psi_c$	$244^\circ$
Offset of the point P of the cutting edge	$m_d$	7.94 mm.
Maximum cutting feed	$f$	0.2 mm/rev.

Determine if flank planes  $F3$  and  $F4$  are needed.

*Solution:* The calculated grinding parameters for this case are shown in Table 5.1. Because  $\xi_{3a} \geq \xi_L$  (Eq. 5.89), flank plane  $F3$  is not needed. Taking into account the grinding, measurements, and installation tolerances,  $\alpha_{n4} = 7^\circ$ ,  $h_4 = 1.2$  mm were accepted. A gundrill with these parameters is shown in Fig. 5.59.

**Table 5.1.** The grinding parameters of the drill ( Example 5.3)

$\xi_L$	$\xi_a$	$\xi_b$	$\varphi_4$	$\alpha_{n4}$	$h_4$ mm
$5.65^\circ$	$5.84^\circ$	$1.01^\circ$	$25^\circ$	$6.37^\circ$	1.065

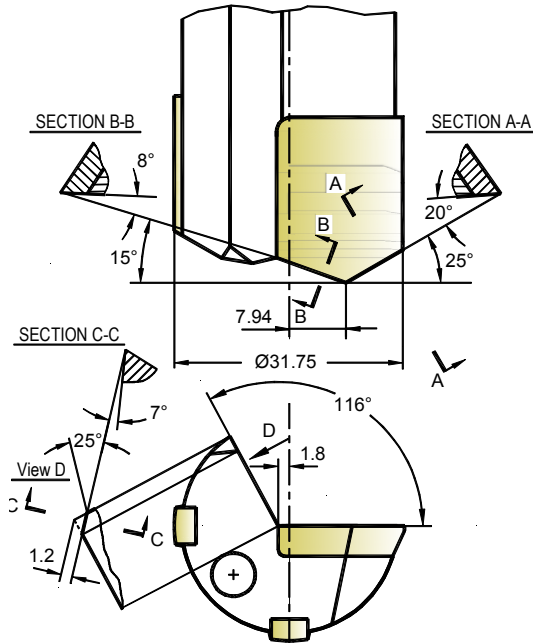


Fig. 5.59. Gundrill with parameters calculated in Example 5.3

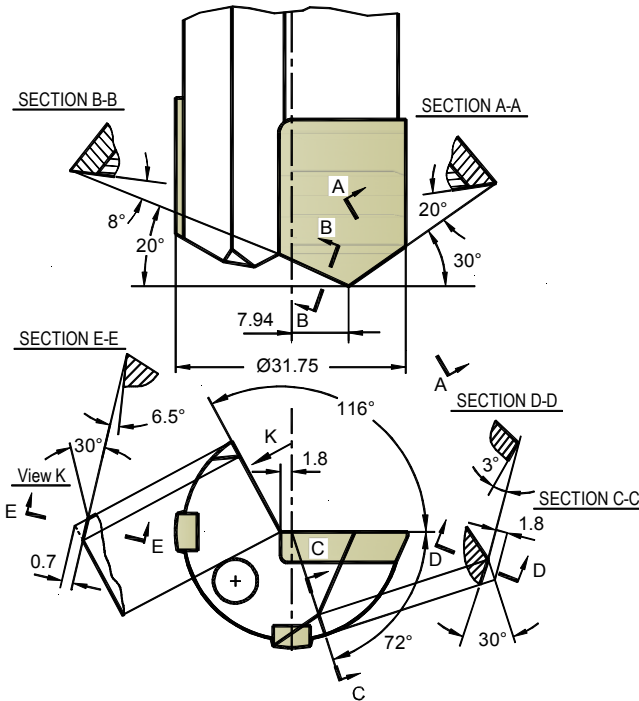
5.6.4.7 Example 5.4

Problem: Let the given parameters of the self-piloting drill with external chip removal be the same as in Example 5.3 except  $\varphi_1 = 30^\circ$  and  $\varphi_2 = -20^\circ$ . Determine if flank planes  $F3$  and  $F4$  are needed.

Solution: The calculated grinding parameters are shown in Table 5.2. As seen in this table, both conditions of free penetration (Eqs.5.87 and 5.89) are not justified. Therefore, to assure gundrill free penetration into the workpiece, flanks  $F3$  and  $F4$  are needed. As before, considering the tolerances, parameters  $\psi_3 = 72^\circ$ ,  $\alpha_{n3} = 3^\circ$ ,  $h_3 = 1.8$  mm,  $\alpha_{n4} = 6.5^\circ$ ,  $h_4 = 0.7$  mm. were accepted. A drill with these parameters is shown in Fig. 5.60.

Table 5.2. The grinding parameters of the drill (Example 5.4)

$\xi_L$	$\xi_3$	$\xi_9$	$\varphi_3$	$\psi_3$	$\alpha_{n3}$	$h_3$ mm	$\varphi_4$	$\alpha_{n4}$	$h_4$ mm
6.09°	3.78°	3.71°	30°	72.1°	2.45°	1.43	30°	6.15°	0.44



**Fig. 5.60.** Gundrill with parameters calculated in Example 5.4

#### 5.6.4.8 Test Results

To show the discussed advantages of the proposed designs (US Patent No. 7,147,411 (2006)) in terms of improving the quality of the machined holes, several tests using both the ordinary and the newly designed gundrill as per Example 5.4 were performed. The tests were carried out under the following conditions: cutting speed  $v = 70\text{m/min}$ , feed  $f = 0.08 - 0.17\text{mm/rev}$ , workpiece material ANSI 1045 steel of HB = 220 hardness. The depth of 300mm of drilled holes was kept the same for all the tests. The influence of the clearance (between the gundrill and the starting bushing) on the diametric accuracy of drilled hole was investigated. The critical clearance is chosen as corresponding to the maximum clearance required to obtain a hole-tolerance of IT9 according to ISO standards.

The experimental results are shown in Fig. 5.61. As can be seen, the critical clearance is 30 micrometers which was found to be the case for the ordinary gundrill while, for the newly designed drill, the critical clearance is found to be as great as 100 micrometers. This result is of a particular practical importance because little attention is paid to the wear of starting bushings. Figure 5.62 shows a typical carbide starting bushing used in the automotive industry. Inferior drill design, alignment problems, and improper selection of the optimal bushing diameter causes drill entrance instability and thus bushing excessive wear, particularly in the region adjacent to the hole entrance.



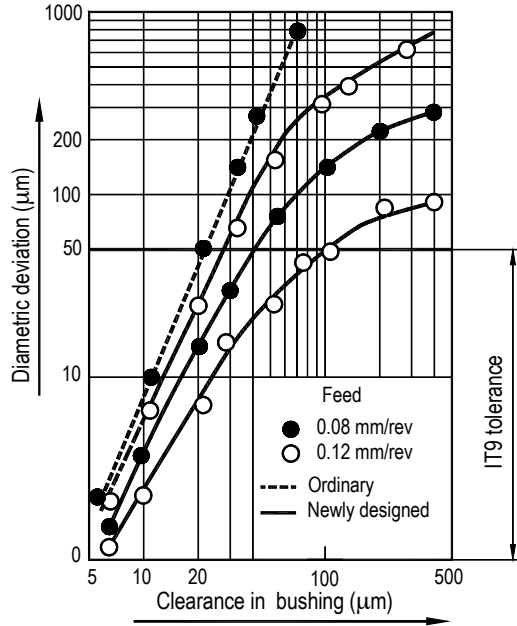


Fig. 5.61. Effect of the clearance between the starting bushing and the drill on the diametric error of drilled holes

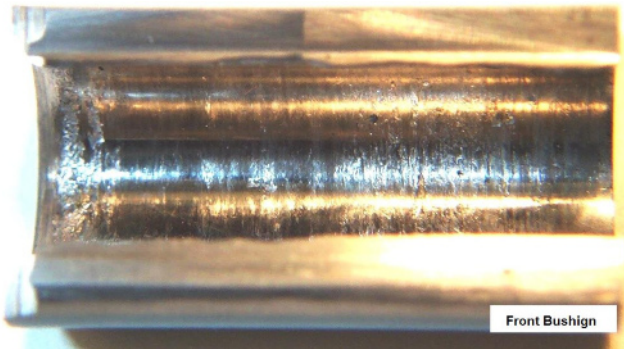


Fig. 5.62. Typical carbide starting bushing used in the automotive industry

Moreover, it is found that, under the same feed, the length of the bell mouth (the tapered entrance part of drilled holes) is three to five times shorter and the diameter error is four to eight times smaller when using the newly-designed drills compare to the ordinary drill [18, 19, 21]. The level of vibrations during the tool entrance was estimated by the effective acceleration, which is measured using accelerometers installed on the workpiece. Also, under the same clearance between the pilot bushing and the drill tip and with increasing feed, the effective acceleration came to be approximately five to six times smaller than that of the ordinary drill [19].

#### 5.6.4.9 MWF Pressure Management in the Bottom Clearance Space

The MWF pressure in the bottom clearance space defines tool life, drill stability, and quality of drilled holes. As discussed in Appendix E, it is determined by hydraulic resistance of the outlet section of the shoulder dub-off  $h_9$ . To acquire full control of this pressure, one needs to know the answers to the following questions: (1) What is the shoulder dub-off?, (2) How to arrange the contour of the its outlet cross section in order to achieve maximum efficiency?, (3) Is there limitations on reducing the length of the shoulder dub-off?, and (4) How this length correlates with the actual cross-sectional area of the outlet section of the side passage? This sections aims to provide the answers to these questions.

Figure 5.63 shows the real outlet cross-sectional area of the side passage for the standard gundrill geometry shown in Fig. 5.19. It appears in the cross-section plane  $Q-Q$ , which is perpendicular to the  $x_0y_0$  plane and inclined at angle  $\psi_v$  (the profile angle of the V-flute) to the  $y_0$  axis. In the cross-section plane  $Q-Q$ , this area is enclosed by the polygon  $C_1C_2C_3C_4C_5$ . Figure 5.64 presents a 3D visualization of the outlet cross section of the side passage.

As seen in Fig. 5.63, side  $C_1C_5$  of the polygon  $C_1C_2C_3C_4C_5$  belongs to the drill. It is a line of intersection the sidewall of the V-flute and the shoulder dub-off. The sidewall of the V-flute is always a plane – otherwise it is not possible to keep the same profile of the V-flute having profile angle  $\psi_v$ . Therefore, side  $C_1C_5$  is always a flat (2D) line, i.e., always lies in plane  $Q-Q$ . This fact significantly simplifies the analysis of the outlet cross-sectional area of the side passage.

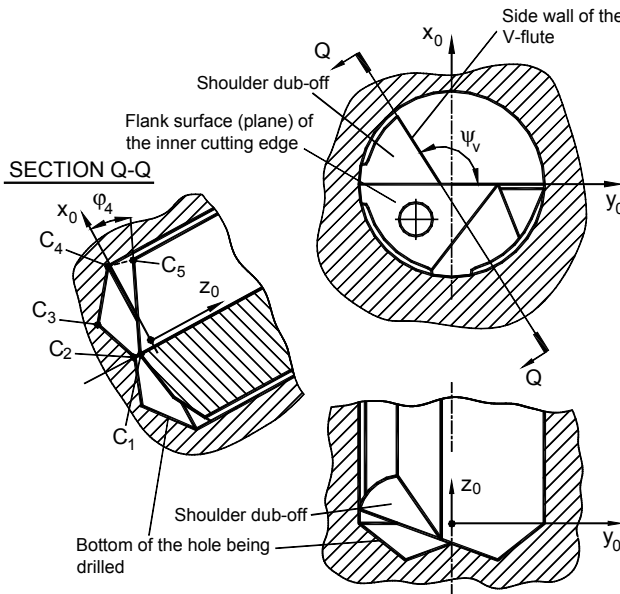
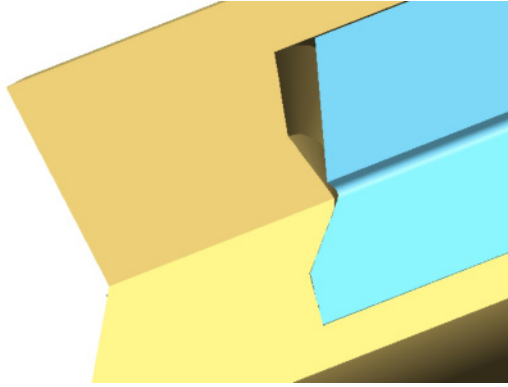


Fig. 5.63. Representation of the real outlet cross-sectional area of the side passage



**Fig. 5.64.** Visualization of the outlet section of the side passage

### *Known Designs*

The flank (clearance) surfaces should assure drill free penetration into the workpiece. In other words, there should be no interference between the drill's flanks and the bottom of the hole being drilled. Because there is no model for the flank geometry available, these flanks are ground down with great angles to avoid interference and thus the above-described additional bending moments are introduced.

Although shoulder deb-off surface (in most known designs it is a plane as shown in Fig. 5.19) does not participate directly in cutting, it is one of the most important design components of a gundrill. Unfortunately, specialists in the field do not yet understand its role and thus it was thought of as a design component that can be of any shape convenient in grinding.

There are several widely recognized designs of the shoulder deb-off surfaces (Fig. 5.65). The slash or general purpose shown in Fig. 5.65a is the most common for European made drills (Botek, TBT, Gildemaster, Heller) although some Japanese (Toshiba) and North American (Drill Masters) companies also use such a design. In the author's opinion, this is still the best design although it has been used for more than 100 years (with small modifications). When gundrills were used on old or retrofitted machines which were not able to deliver high MWF (coolant) pressure, a notch was added on the shoulder deb-off surface as shown in Fig. 5.65b to increase the MWF flow rate and thus to assure reliable chip removal. A drawback of this design is that the notch should be ground every time when the drill is re-sharpened. Because the notch is ground manually, it was found difficult to keep its dimensions the same from one re-grind to another. To solve this problem and to achieve even greater flow rate under a given pressure, the stepped (square) shown in Fig. 5.65c and the stepped-slash shown in Fig. 5.65d designs (known as point grinds) were introduced. Although modern gundrilling machines are able to deliver high coolant pressure, the stepped-slash design is still in wide use today, particularly in the automotive industry where inferior designs of gundrilling machine are widely used.

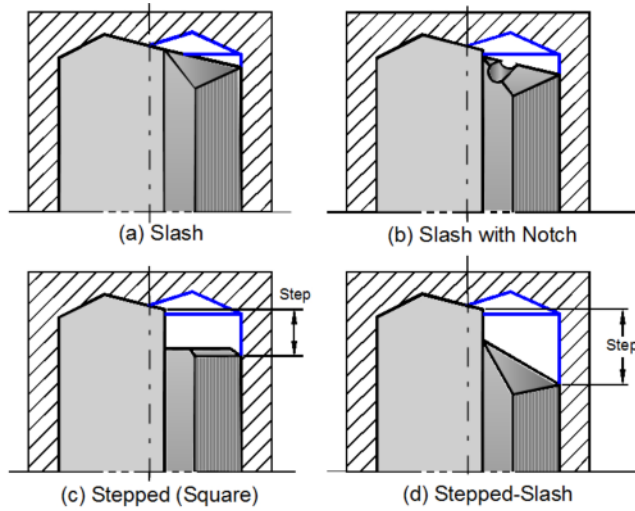


Fig. 5.65. Different designs of the shoulder dub-off

In the author's opinion, the stepped (square) and the stepped-slash designs were introduced by the gundrill manufactures that had shallow knowledge of gundrilling. Although the intent behind these designs was to increase the MWF flow rate through gundrills and thus improve chip removal, the application of these designs only improves the apparent flow rate (measured by a flow meter installed on the machine) and thus creates more problems than it solves.

The known designs shown in Fig. 5.65 differ significantly in the outlet cross-sectional area of the side passage. In the simplest common case slash design (Fig. 5.65a) when the outer and inner cutting edges are straight, this area calculates as

$$A_{ot-sl} = 0.5 \left\{ A_{BS} + \left( \sqrt{R_d^2 - c_{ax}^2 \sin^2 \psi_v} + c_{ax} \cos \psi_v \right)^2 (\tan \varphi_4 - 2 \tan \xi_L) \right\} \quad (5.110)$$

wherein  $\varphi_4$  is the shoulder dub-off angle (Fig. 5.19).

To increase the MWF flow rate under a given pressure, a notch was added on the shoulder dub-off surface as shown in Fig. 5.65b. The MWF pressure in the bottom clearance space, however, becomes lower because the cross-sectional area of the side passage increases. In the notched design when the outer and inner cutting edges are straight, the area of the side passage calculates as

$$A_{ot-sl-n} = A_{ot-sl} + A_n \quad (5.111)$$

where  $A_n$  is the cross-sectional area of the notch.

The stepped (square) (Fig. 5.65c) and the stepped-slash (Fig. 5.65d) designs provide a cross-sectional area of the outlet section of the side passage that is relatively large. In the stepped (square) design, a side passage is formed without a shoulder dub-off surface. Instead, a drill flat flank face is spaced from the distal

end in the axial direction. This flank and the bottom of the hole being drilled form the step shown in Fig. 5.65c. In the simplified stepped (square) gundrill when the outer and inner cutting edges are straight, the cross-sectional area of the side passage is calculated as

$$A_{ot-st} = R_d S_t + 0.5 A_{BS} \quad (5.112)$$

where  $S_t$  is the length of the step, and  $A_{BS}$  is the axial cross-sectional area of the bottom space

$$A_{BS} = \left[ (r_{dr} - m_d)^2 \tan \varphi_1 + m_d^2 \tan \varphi_2 \right] + 2m_d \left[ (r_{dr} - m_d) \tan \varphi_1 + m_d \tan \varphi_2 \right] \quad (5.113)$$

In the stepped-slash design, a shoulder dub-off is added to the flat flank face of the stepped (square) design. In the most common case when the outer and inner cutting edges are straight, the cross-sectional area of the side passage is calculated as

$$A_{ot-st} = r_{dr} S_t + 0.5 (A_{BS} + r_{rd}^2 \tan \varphi_4) \quad (5.114)$$

With the stepped (square) and the stepped-slash designs, the MWF static pressure in the bottom clearance space is very low. As a result, the MWF does not have sufficient static pressure to flow in the narrow passages adjacent to the flank of the outer cutting edge. Insufficient static pressure results in reduced tool life.

Another important parameter is the ratio of the cross-sectional area of the outlet of the side passage to the bottom space area. This parameter is referred to as the bottom space ratio.

Table 5.3 summarizes the comparison of the various tip designs for an 8mm diameter gundrill. The various designs are ranked by the cross-sectional area of the outlet section in an effort to develop design parameters that are useful. Table 5.3 also presents a comparison of static MWF pressure in the bottom space for the discussed designs. Controlling the area of the outlet passage by careful tip design enables one to improve greatly chip removal and tip cooling. Traditionally, large outlet passage areas are used in practice as it is believed that they allowed for a greater MWF flow rate for a given inlet MWF pressure. However, it has been determined that the apparent MWF flow rate is unimportant if this MWF does not adequately cool and lubricate the tip or if stagnation pockets form in the region of the drill point.

Another drawback of the discussed designs is not readily apparent to gundrill manufacturers and users. The chip transportation from the machining zone can be thought of as consisting of two stages, namely, chip pick up and chip transportation along the V-flute. As discussed in Appendix E, the latter requires at least critical MWF velocity and thus its flow rate. The former, however, has to be explained. The author proposed to define the chip pick up as the initial MWF – chip interaction which should result in picking up the chip (formed at the cutting edges) by the MWF flow from the outlet cross section of the side passage. As such, the MWF is considered as just left the outlet cross-section of the side passage and the

chip is considered as just formed on the rake face adjacent to the outer and inner cutting edges. As a result of proper pick up, the chip should be found in the MWF flow so that its normal transportation over the V-flute is possible.

**Table 5.3.** Comparison of the cross-sectional area of the outlet passage of the side passages and MWF pressure in the bottom clearance space for the known designs shown in Fig. 5.65

Gundrill parameters: diameter $D = 8\text{mm}$ , $r_{dr} = 5\text{mm}$ , $m_d = 2\text{mm}$ , $c_{ax} = 0.5\text{mm}$ , $\phi_1 = 30^\circ$ , $\phi_2 = 20^\circ$ , $\alpha_{n2} = 12^\circ$ , $\psi_v = 120^\circ$ , $\phi_4 = 30^\circ$ . For slash design with a notch: $A_n = 2.5\text{mm}^2$ . For the stepped design: $S_r = 3\text{mm}$ , $\phi_4 = 0^\circ$ . For the stepped-slash design: $S_r = 3\text{mm}$ , $\phi_4 = 30^\circ$ . Drilling fluid flow rate is 18.74 L/min				
Design	Cross-sectional area of the outlet section of the side passage, $A_{ot}$ ( $\text{mm}^2$ )	Axial cross-sectional area of the bottom space, $A_{BS}$ ( $\text{mm}^2$ )	Bottom Space Ratio $A_{ot}/A_{BS}$	Static Drilling fluid pressure in the bottom clearance space (MPa)
Slash	6.32	5.64	112%	0.15
Slash with a notch	8.82	5.64	156%	0.10
Stepped	14.82	5.64	263%	0.04
Stepped-slash	24.06	5.64	423%	0.01

When a gundrill having stepped-slash design is used, the following happens. The MWF supplied in the bottom clearance space hits the bottom of the hole being drilled and then is deflected by this bottom into the V-flute (Fig. 5.66a). Most of the deflected MWF does not even go to the bottom clearance space between the drill major flank faces and the bottom of the hole being drilled. When the deflected MWF flow enters the V-flute, it ‘misses’ the region adjacent to the rake face where the chip is formed as shown in Fig. 5.66a. The formed chip has a hard time joining this flow and a stagnation zone is formed. A special experimental study conducted using a transparent workpiece and high-speed camera allowed one to visualize the discussed stagnation zone (Fig. 5.66b).

The author’s showed [21] that the chip pick up depends on the angle  $\beta_{cp}$ , which the MWF flow (entering the V-flute) makes with the  $z_0$ -axis (Fig. 5.67). This angle depends on practically all parameters of gundrill geometry as well as the location of the outlet of the coolant passage in the tip (shown in Fig. 5.67 by angle  $\psi_{cp}$ ). A rule of thumb here is “the greater  $\beta_{cp}$ , the better chip pick up.” It was also observed that when this angle is less than  $40^\circ$ , a stagnation zone forms on the tool rake face and the chips experience difficulties joining the MWF flow. For the standard stepped-slash design shown in Fig. 5.46, angle  $\beta_{cp}$  is less than  $40^\circ$  that explains why chip clogging happens the V-flute in the proximity of the cutting edges,

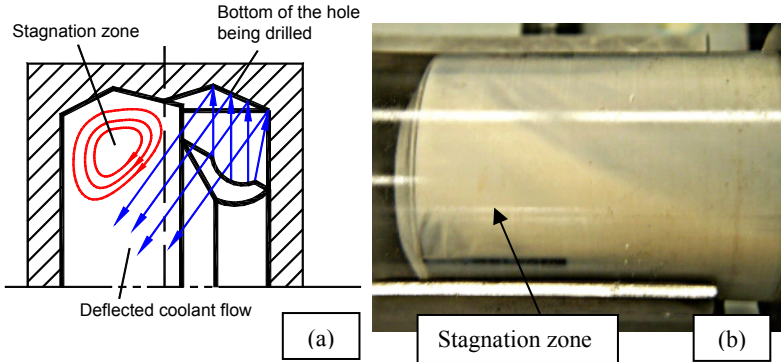


Fig. 5.66. Stagnation zone: (a) model, and (b) visualization

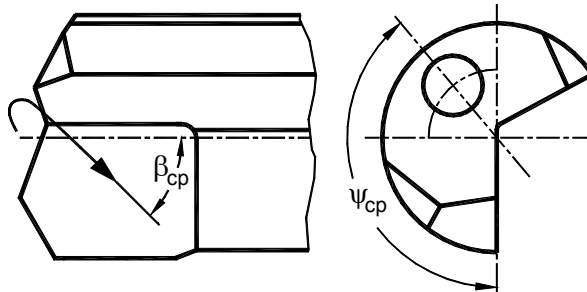


Fig. 5.67. Sense of angle  $\beta_{cp}$

although the overall MWF flow rate is very high. As a result, drill breakages are often observed due to chip clogging at the drill tip (Fig. 5.68).

*What is the Length of the Shoulder Dub-off?*

The length of the shoulder dub-off is the length which the shoulder dub-off makes in its intersection with the side wall of the V-flute. For a common gundrill (Fig. 5.19), this length  $C_1C_5$  coincides with that of the side wall of the V-flute as shown in Fig. 5.63. The sense of the length of the shoulder dub-off for the drills shown in Figs. 5.59 and 5.60 is shown in Fig. 5.69 by the length  $C_6C_5$ . Note that the counter of the outlet cross-section of the side passage is flat (2D). Moreover, it should always be considered in the section plane  $Q-Q$ .

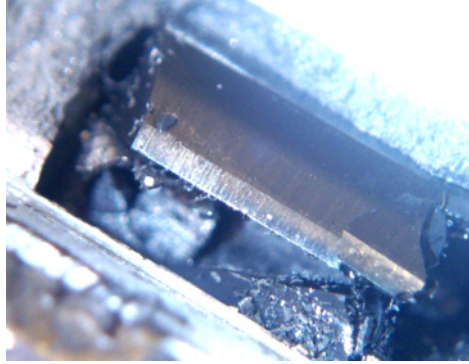


Fig. 5.68. Drill failure due to chip clogging in the stagnation zone

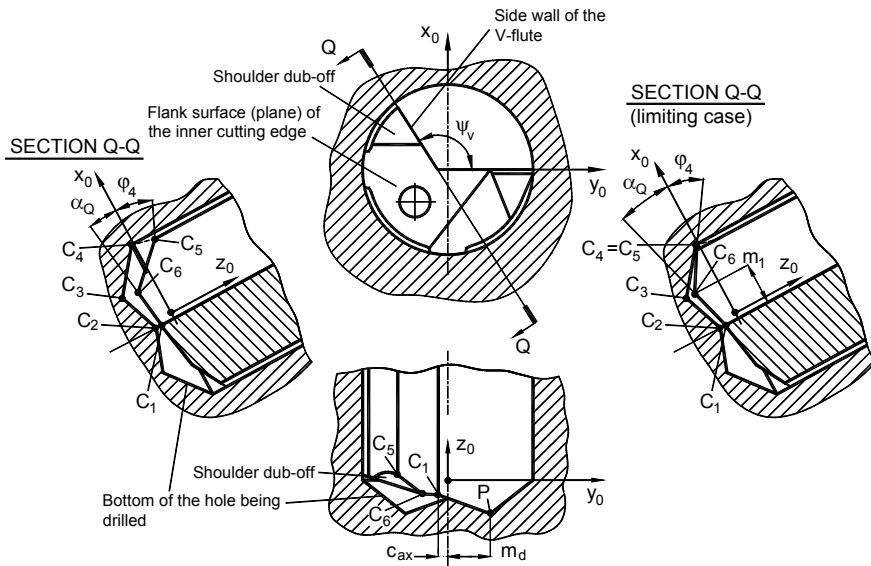


Fig. 5.69. Graphical representation of the length of the shoulder dub-off

*How to Arrange the Contour of the Outlet Cross Section in Order to Achieve Maximum Efficiency?*

As follows from the gundrill geometry, side  $C_1C_2$  entirely depends on  $c_{ax}$  which is a design parameters of a gundrill. Side  $C_2C_3$  is the trace made by the inner cutting edge so that its inclination and length are uniquely defined by the geometry of the inner cutting edge. Side  $C_3C_4$  is the trace made by the outer cutting edge so its inclination and length are uniquely defined by the geometry of the outer cutting edge. Side  $C_4C_5$  is uniquely defined by the location of point  $C_5$  with respect to the bottom of the hole being drilled. Therefore, as follows from Fig. 5.69, the cross-section area of the outlet section of the side passage can only be altered by varying



the length and inclination of sides  $C_5C_6$  and  $C_6C_1$ . Consider the position and the length of these segments separately.

Side  $C_6C_1$ . This side is uniquely defined by its inclination angle  $\alpha_Q$  and position of point  $C_6$ . Figure 5.69 also shows the limiting case where the cross-section area of the outlet section of the side passage is at minimum. To achieve this minimum, a tool design requires to meet three conditions: (1)  $m_l = m_d$  ( $m_d$  is the location distance of point  $P$ ), (2) sides  $C_1C_6$  and  $C_2C_3$  should be parallel, and (3) side  $C_6C_5$  and side  $C_3C_4$  should also be parallel.

Because the inclination angle  $\alpha_Q$  calculates as

$$\alpha_Q = \arctan \left( \frac{\tan \alpha_{n2} \sin \psi_b + \tan \varphi_2 \cos \psi_b}{\cos \varphi_2} \right) \quad (5.115)$$

where  $\psi_b$  is the location angle of point  $C_5$  (Eq. 5.65) and the inclination angle of side  $C_2C_3$  is equal to  $\varphi_2$  then sides  $C_6C_1$  and  $C_2C_3$  are parallel when

$$\alpha_Q = \varphi_2 \quad (5.116)$$

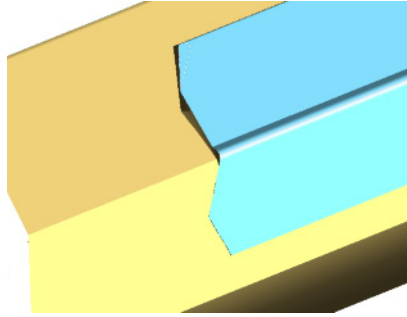
Substituting Eq. 5.116 into 5.115, one obtains the condition of parallelism of sides  $C_1C_6$  and  $C_2C_3$  as

$$\alpha_{n2} = \arctan \left[ \frac{\sin \varphi_2 (1 - \cos \psi_b)}{\tan \psi_v} \right] \quad (5.117)$$

As it follows from Fig. 5.69, sides  $C_6C_5$  and  $C_3C_4$  are parallel when  $\varphi_4 = \varphi_1$ . If  $\varphi_4 > \varphi_1$  then an excessive gap between the shoulder deb-off and the bottom of the hole being drilled is the case. If  $\varphi_4 < \varphi_1$  then interference between the shoulder deb-off and the bottom takes place.

In the limiting case when  $c_{ax} = 0$ , then  $\psi_b = \psi_v$ , and the cross-sectional area of the outlet section of the side passage is equal zero. This is the limiting case where the pressure in the bottom clearance space could be made very high. The maximum pressure, however, may be restricted by the maximum MWF pressure available in the machine. Therefore, in real-world situations, the cross-sectional area of the outlet section of the side passage is selected using this and other restrictions. Figure 5.70 shows an example of an optimized cross-sectional area of the outlet section of the side passage.

Characterizing the cooling action of MWF, the author showed that the velocity of the MWF affects its cooling ability almost as much as its thermal conductivity and much more than its specific heat [22, 23]. Although, high MWF static pressures in the bottom clearance space allows MWF penetration in the narrow coolant passages in the bottom clearance, sufficient cooling ability of MWF flow is achieved only when the MWF flow has high velocity around the places where the cooling action is needed.

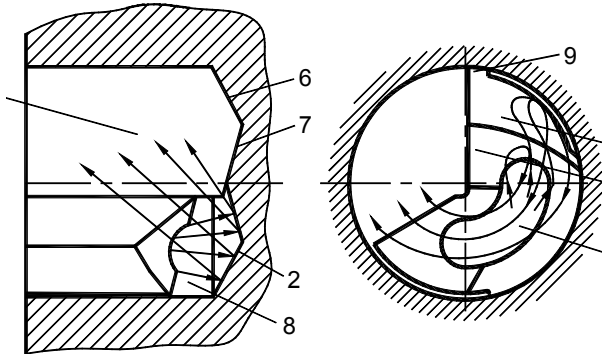


**Fig. 5.70.** An example of the optimized cross-sectional area of the outlet section of the side passage

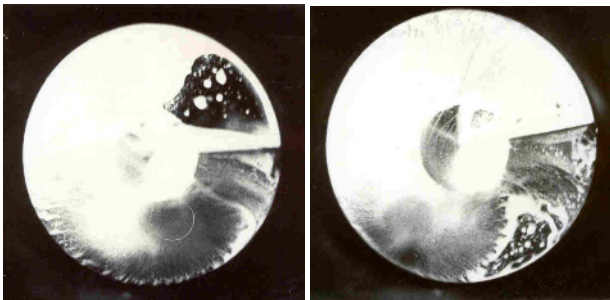
Figure 5.71 shows the MWF flow model in the bottom clearance space in a standard gundrill having the stepped-slash design (Fig. 5.65d). The MWF flow supplied to this space through kidney-shaped orifice 1 separates into a number of elementary flows. The directions of these flows are shown by streamlines. Most of the MWF deflects from bottom of the hole being drilled 2 and flows into chip removal passage 3. The streamlines of the rest of the MWF flow shown in Fig. 5.71 indicate that MWF elementary flows directed towards the flanks 4 and 5 of the outer 6 and inner 7 cutting edges, respectively. As can be seen, these elementary flows should make loops to come back as these should pass through to the side passage 8 in order to exit the bottom clearance space. These loops result in the formation of multiple vortexes in the bottom clearance space [24] that significantly reduces the MWF velocity and thus its cooling ability. Moreover, MWF does not flow to the narrow passage between flank 4 and the bottom of the hole being drilled and thus does not provide cooling and lubrication to the region adjacent to the drill periphery point 9 where they mostly needed.

The experiments carried out using a transparent workpiece and a stroboscopic light having variable flashing frequency allowed observation of the drilling fluid flow distribution in the bottom clearance space. Figure 5.72 shows examples of the observation taken at two different rotational frequencies of the gundrill. As can be seen, the distributions of the MWF flow corresponds to that qualitatively described in Fig. 5.71. The region of the outer flank surface adjacent to the drill periphery point has the poorest cooling and lubricating conditions. This explains why a common gundrill has the greatest wear in this region.

To solve the problem by assuring an MWF flow around the periphery region and the working part of the side cutting edge, a gundrill design should be modified in the manner shown in Fig. 5.73 (US Patent No. 7,195,428 (2007)). In this modified drill, a part of the periphery of the tip 1 adjacent to the side cutting edge 2 is removed to form an auxiliary side 3 MWF passage extending longitudinally over the whole length of the tip and over a certain length  $L_{sh-ax}$  of the shank. The outlet of this passage is formed on the shank connecting the auxiliary side MWF passage with the chip removal groove of the shank. For small gundrills, a radial relief having radius  $r_{sh-ax}$  can be made to increase MWF flow rate as shown in Fig. 5.73 VIEW A2.



**Fig. 5.71.** Model of MWF elementary flows in the bottom clearance space



**Fig. 5.72.** Visualization of the MWF elementary flows in the bottom clearance space when a common gundrill is used

When such a gundrill works, the MWF is supplied through the outlet orifice 1 of the tip coolant passage into the bottom clearance space 2 as shown in Fig. 5.74. In this space, the MWF separates into a number of elementary flows. The directions of these flows are shown in by streamlines. A greater part of the MWF deflects from the bottom of the hole being drilled 3, cools and lubricates the region adjacent to the inner cutting edge 4 and the drill point  $P$ , and then flows through the side passage 5 formed between the shoulder dub-off surface 6 and the bottom of the hole being drilled 3 into chip removal passage 7 where it cools and lubricates the rake faces of the inner 4 and outer 8 cutting edges. This flow picks up the formed chip for transportation along the chip removal passages (V-flutes) 9 and 10 of the tip and that of the shank respectively as shown in Fig. 5.74 by the streamlines of MWF flow.

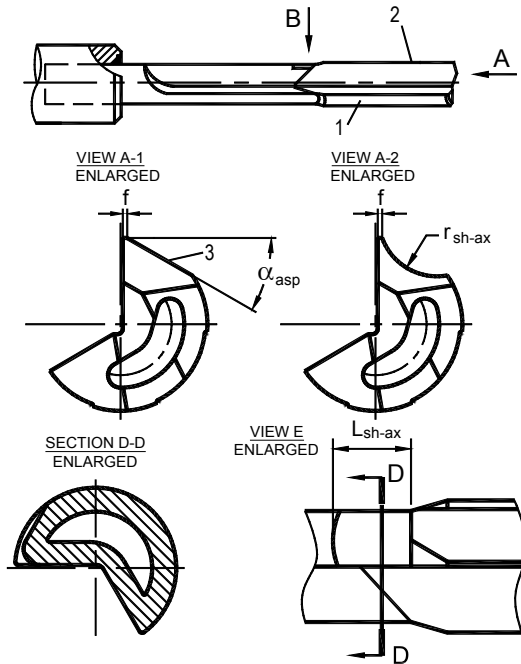
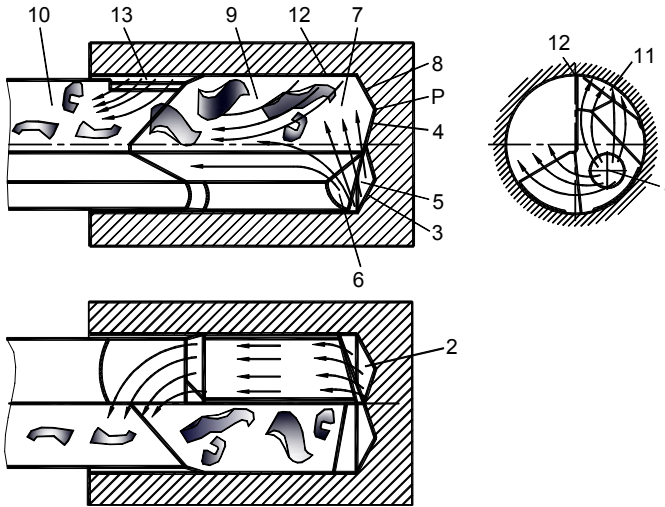


Fig. 5.73. A gundrill design with the auxiliary side passage

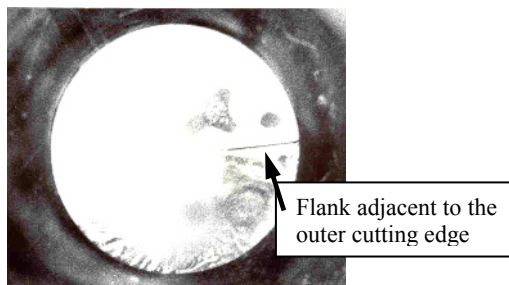
Because part of the tip periphery surface is removed, an auxiliary passage 11 is formed between the periphery surface of the tip portion adjacent to the side cutting edge 12. This passage continues over the entire length of the tip and then eventually meets with the chip removal passage 10 of the shank through passage 13 made on the shank. As a result, a part of the MWF supplied to the bottom clearance space 2, flows through passages 11 and 13 and then joins the rest of the MWF flow with the chip as shown in Fig. 5.74. The separation on the MWF supplied into the bottom clearance space 2 into two flows prevents the formation of vortices (Fig. 5.72). Figure 5.75, which is a picture taken when a transparent workpiece was used, shows that no vortices form when a gundrill with an auxiliary side passage is used. As shown by the experiments, the MWF flow with high velocity around the drill periphery portion leads to reduction of the cutting temperature and thus increases tool life two- to fivefold depending on the other parameters of the gundrilling system. Moreover, this auxiliary flow prevents the formation of the BUE on the side cutting edge 12 that improves the surface integrity of drilled holes and improves chip removal.

### 5.6.5 Exemplification of Significance of the High MWF Pressure in the Bottom Clearance Space

Earlier in this chapter, the advantages which may be gained by complying with the introduced Rules No. 1 and 2 were discussed. This section exemplifies the advantages of a high MWF pressure in the bottom clearance space (Rule No. 3).



**Fig. 5.74.** Model of MWF flow in a gundrill with the auxiliary side passage



**Fig. 5.75.** Uniform MWF elementary flows in the bottom clearance space when a drill with the auxiliary side passage is used

Figure 5.76 compares tool life of the ordinary and newly designed gundrills (see geometry in Sect. 5.6.4.7). Two important conclusions follow from the shown data:

- Complying with Rule 3 (maximum MWF pressure in the bottom clearance space) results in a threefold increase in tool life. The multiple tests preferment by the author in various manufacturing facilities show that this tool life can be increased up to five times when other conditions of the gundrilling system properly support a gundrill designed with compliance to Rule 3.

There is an optimum MWF flow rate in terms of tool life. If a flow rate greater than the optimum one is applied then tool life is decreased. The ordinary gundrill is much more sensitive to any departure from the optimum flow rate.

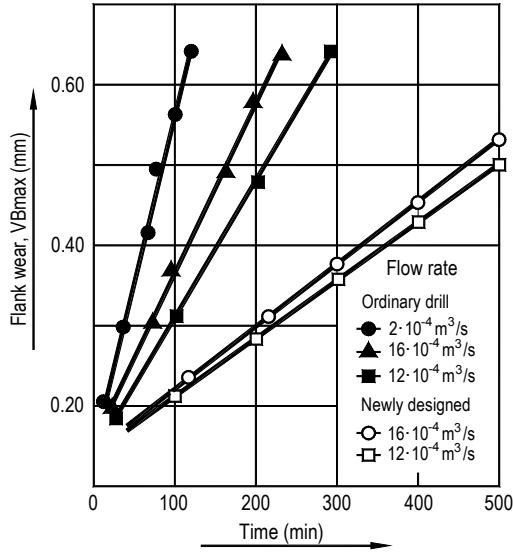


Fig. 5.76. Comparison of tool life of the ordinary and newly-designed gundrills

### 5.6.6 Example of Experimental Study

Any gundrill includes many design variables which may affect each other. Unfortunately, in today's practice of gundrill testing at the design, research, and implementation stages, it is common to consider one variable at a time while keeping all other invariants. In the author's opinion, this is the major drawback in such testings as it does not allow the proper optimization of the gundrill design. As a result, there have been no new gundrill designs introduced over the last 30 years due to the lack of understanding of the geometry and basic principles of this tool as well as non-system considerations in its implementations.

To deal with these numerous gundrill design variables, Astakhov and Galitsky used the group method of data handling [25] and obtained the following correlation equation for gundrill tool life:

$$T = 6.7020 - 0.6518 \frac{\alpha_{n1}}{\varphi_2 c_{pt2}} - 0.0354 \frac{\alpha_{n2} \ln c_{pt2}}{m_d} - 0.0005 \frac{\varphi_1^2}{c_{pt2}} + 0.0168 \frac{\ln c_{pt2}}{\varphi_1} - 2.8350 \frac{vf}{\varphi_1} - 0.5743 \frac{c_{pt2} m_d}{\ln \alpha_1 \varphi_1} \quad (5.118)$$

where  $v$  is the cutting speed (m/min),  $f$  is the feed (mm/rev),  $c_{pt1}$  and  $c_{pt2}$  are the shift distances of the outer and inner cutting edges, respectively (mm) (see Sect. 5.6.3).

The mathematical model of tool life defined by Eq. 5.118 indicates that tool life in gundrilling is a complex function not only of design and process variables but also of their interactions. Although the including of these interactions in the model brings a new level of understanding of their influence on tool life and quality of the machined surface [26, 27], specialists in the field argue that this is a particular case so more experimental evidences are needed to prove the significance of revealed interactions.

The objective of this section is to present the results of an extensive experimental program on the mutual influence of the process and design parameters on tool life in gundrilling cast iron.

#### 5.6.6.1 Experimental Conditions

The schematic of the experimental setup is shown in Fig. 5.77. It is mainly composed of the deep hole drilling machine, a Kistler six-component dynamometer, charge amplifiers, and Kistler signal analyzer [19]. The system details are as follows:

- Machine – a special TBT gundrilling machine was used. The drive unit was equipped with a programmable AC converter to offer variable speed and feed rate control. The machine included a high pressure MWF delivery system capable of delivering a flow rate up to 120 L/min and generating a pressure of 12 MPa. The stationary tool-rotating workpiece working method was used in the tests. The feed motion was applied to the gundrill.
- Work material – because special parts, calender bowls, were drilled, the work material was malleable iron casting, Class 80002 having the following properties: Hardness, Brinell HB 241 – 285 Tensile Strength, Ultimate (Rm) 655 MPa Tensile Strength, Yield (Rp0.2) 552 MPa, Elongation at Break – 2 %.
- Gundrills – specially designed gundrills of 35 mm diameter were used. The material of their tips was carbide K30. The parameters of drill geometry were kept within a close tolerance of  $\pm 0.2^\circ$ . The surface roughness  $R_a$  of the rake and flank faces did not exceed  $0.25\mu\text{m}$ . Each gundrill used in the tests was examined using a vision system at a magnification of  $\times 25$  for visual defects such as chipping, burns and microcracks. When re-sharpening, the tips were ground back at least 2mm beyond the wear marks.
- MWF (coolant) – a water soluble coolant having 7% concentration, filtration – 10 microns.
- Tool life criteria – the average width of the flank wear land  $VB_{B(cr)}=1.0$  mm was selected as the prime criterion and was measured in the tool cutting edge plane containing the cutting edge and the directional vector of prime motion according to the methodology suggested in [28]. However, excessive tool vibration and/or squeal were also used in some extreme cases as a criterion of tool life.

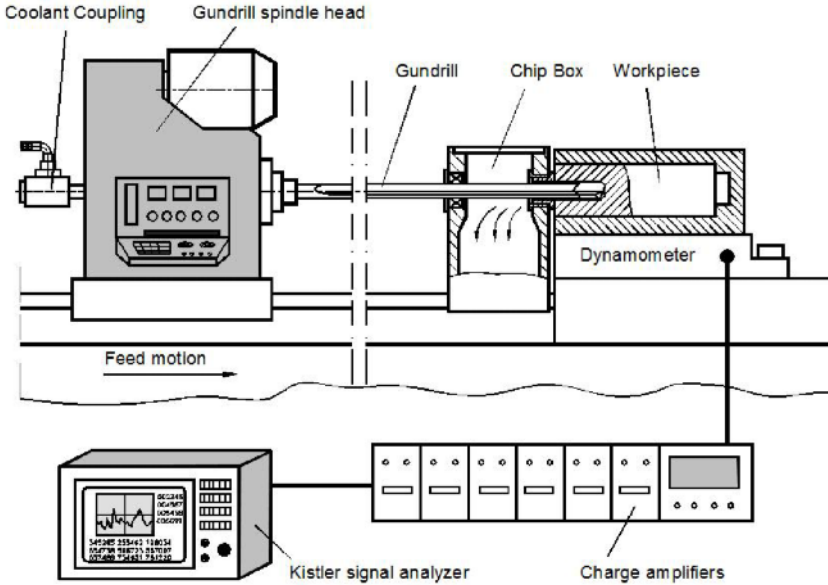


Fig. 5.77. Experimental setup

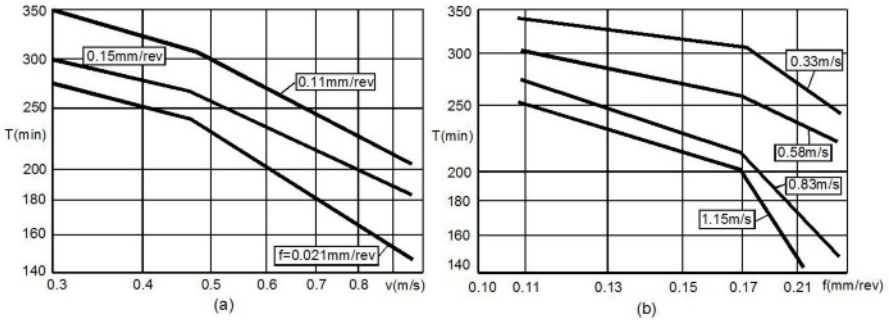
#### 5.6.6.2 Influence of the Cutting Speed and Feed

The influence of the cutting speed for different feeds on tool life is shown in Fig. 5.78a. The appearance of the tool life curves is similar to the known results [29] in the range of cutting speed from 0.33m/s to 1.15m/s. When the cutting speed is about 0.37–0.40m/s, the wear rate is higher due to high contact stresses at the tool chip–interface. Increasing the cutting speed to about 0.40–0.45m/s leads to a reduction of both the cutting force and the chip compression ratio. As such, the maximum dimension of the deformation zone in front of the cutting edge was observed. As a result, the tool-chip contact length reduces as well as the maximum contact stress and thus the temperature. The presence of the plastically deformed zone distributes the contact stress almost evenly over the tool-chip interface. The wear rate (calculated using proper metric [28]) in this range of the cutting speed is at minimum. The further increase in the cutting speed leads to a decrease in the dimensions of the deformation zone and the length of the tool-chip interface. The latter causes an increase in the contact stress at the tool-chip interface that, in turn, increases wear rate and thus reduces tool life.

Because the cutting feed also affects the cutting temperature, it affects tool life in the manner shown in Fig. 5.78b. It was noticed that the topography of tool wear changes with the cutting feed. When the cutting feed increases alone, the maximum wear occurs at the drill corner. As such, this wear begins from the rake face where the contact temperature and stresses are at maximum due to chip sliding. Increasing the cutting feed leads to the corresponding increase in the uncut chip thickness and thus the chip thickness. This reduces the severity of the contact process at the tool rake face and reduces the influence of the cutting edge radius on the cutting process. The conditional center of tool wear shifts into the flank surface



of the outer cutting edge so that the geometry of this surface and its cooling and lubrication conditions start to play the most important role in tool life considerations. As such, any small change in the geometry and/or design of the flank surface of the outer cutting edge may affect tool life dramatically [24]. Although obtained for gundrills, this conclusion is valid for the whole class of carbide-tipped drills with straight flutes.



**Fig. 5.78.** (a) Tool life vs the cutting speed for different feeds, and (b) tool life vs the cutting feed for different cutting feeds

5.6.6.3 Approach Angles  $\varphi_1$  and  $\varphi_2$

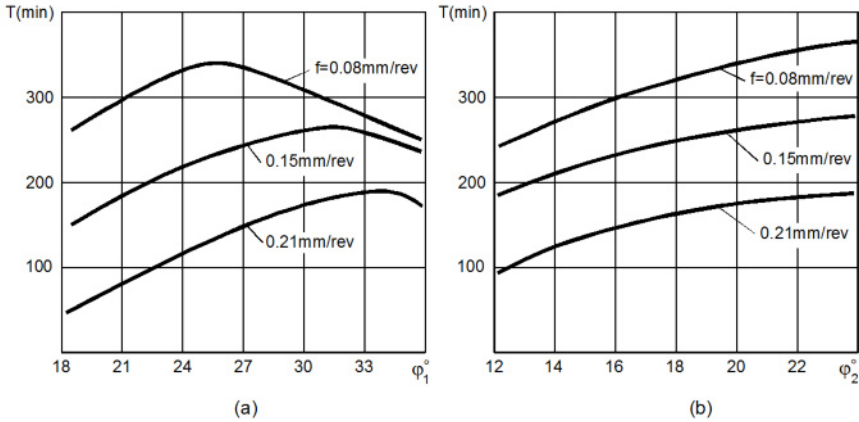
According to gundrilling practice [1], the approach angles of the outer  $\varphi_1$  and inner  $\varphi_2$  cutting edges are selected in pairs (for example,  $(25^\circ/15^\circ, 30^\circ/20^\circ, 45^\circ/30^\circ)$ ) depending on the work material and its hardness. These angles are also included in the consideration of the force balance and static stability of gundrills [30–32]. However, no one study discussed the influence of these angles on tool life.

The influences of the approach angles on tool life are shown in Fig. 5.79. As can be seen, tool life increases with increasing approach angle of the outer cutting edge,  $\varphi_1$  to a certain extent. It can be readily explained by the reduction of the uncut chip thickness,  $t_1$  (sometimes referred to as the chip load as discussed in Chap.)

$$t_1 = f \cos \varphi_1 \tag{5.119}$$

Therefore, the greater the approach angle, the smaller the uncut chip thickness. The reduction of the uncut chip thickness results in the ‘spread’ of the cutting force over the wider contact surface so that, the contact stress and contact temperatures reduce. As a result, tool life increases.

Such a trend continues, however, until the uncut chip thickness becomes small enough that the radius of the cutting edge, RCE (Chap. 3) starts to play a significant role. In gundrilling, it happens when  $RCE \geq 0.3t_1$ . When this is the case, cutting with highly negative rake angle and with significant burnished layer takes place so that the contact temperatures increase dramatically and thus tool life decreases with any further increase in  $\varphi_1$ . Because the uncut chip thickness,  $t_1$  depends on the feed,  $f$  and  $\varphi_1$  (Eq. 5.119), there is the optimal (by the tool life criterion) value of  $\varphi_1$  for each  $f$ . For the considered case, it clearly seen in



**Fig. 5.79.** Tool life  $T$  vs (a) the approach angles of outer cutting edge,  $\varphi_1$ , and (b) the approach angle of the inner cutting edge,  $\varphi_2$  for different feeds

Fig. 5.79a that:  $\varphi_{1-\text{opt}} = 26^\circ$  for  $f = 0.08$  mm/rev;  $\varphi_{1-\text{opt}} = 31.5^\circ$  for  $f = 0.15$  mm/rev;  $\varphi_{1-\text{opt}} = 34^\circ$  for  $f = 0.21$  mm/rev.

Increasing  $\varphi_1$  beyond a certain limit has its negative consequences. It was noticed in the tests that the amplitude of the drill transverse vibration increases with  $\varphi_1$  may lead to the reduction of tool life for long gundrills ( $L/D > 50$ ) and not very rigid gundrilling systems. Moreover, when  $\varphi_1$  becomes more than  $30^\circ$ , the drill static stability suffers which leads to an increase in the drilling torque and deterioration of the quality (diametric accuracy and axis deviation) of the drilled holes. Therefore, the selection of the optimum value of this angle should be based on the consideration of the whole gundrilling system combined with the requirements of quality of the drilled holes.

It follows from Fig. 5.79b that increasing  $\varphi_2$  leads to increasing tool life. This is because the uncut chip thickness on the inner cutting edge decreases. As such, the axial force reduces. However, an increase of  $\varphi_2$  is restricted by the strength of the drill point and by drill stability determined by the force balance. Any increase in  $\varphi_2$  leads to a corresponding increase in the radial force acting towards the periphery cutting edge. When this force exceeds that generated by the outer cutting edge, drill balance is disturbed and the side cutting edge may be forced into the surface of the hole being drilled [19]. This is particularly noticeable when drill enters the hole being machined from the starting bushing [19, 21, 32].

#### 5.6.6.4 Normal Flank Angles

As discussed in Chap. 3, the flank angle directly affects tool life. When angle  $\alpha_{n1}$  increases, wedge angle  $\beta$  decreases (Chap. 2). As such, the strength of the region adjacent to the cutting edge decreases as well as heat dissipation through the tool. This factor shortens tool life. On the other hand, the following advantages may be gained by increasing the flank angle (1) The cutting edge radius  $R_{CE}$  decreases with the flank angle that leads to corresponding lowering in the frictional and deformation components of the flank force. As a result, less heat generates that leads to an increase in tool life, and (2) As the flank angle becomes larger, more

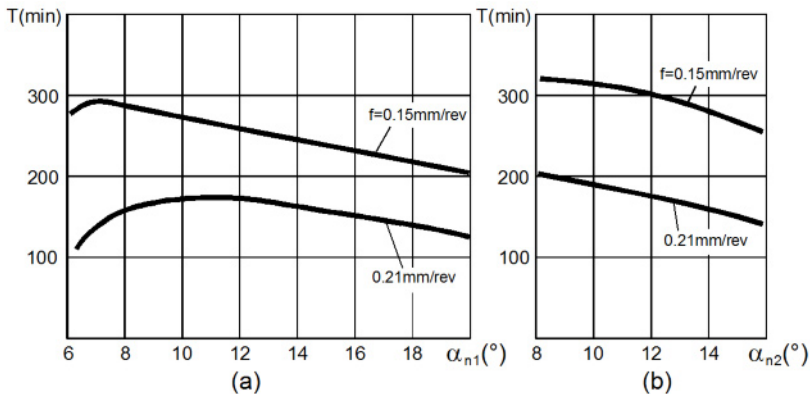
tool material should be removed (worn out) to reach the same flank wear [28]. As a result, tool life increases. As a direct result of such contradictive influences of the flank angle on tool life, the influence of this angle on tool life always has a maximum. In other words, there is always the optimal (tool life) flank angle for a given combination of the other geometry and process parameters.

Figure 5.80a,b shows the influences of the normal flank angles of the outer,  $\alpha_{n1}$  and inner,  $\alpha_{n2}$  cutting edges on tool life for the considered case of gundrilling. As can be seen, angle  $\alpha_{n1}$  has its optimum value for each particular cutting feed as discussed earlier. When this angle is small, the cutting wedge (a part of the cutting tool between the rake and flank contact surfaces) has the maximum strength and the maximum heat can be transferred into the tool from the rake and flank contact surfaces. As such, however, MWF cannot access this contact surface because the clearance between the flank surface and the bottom of the hole being drilled is very small in the vicinity of the flank contact surface. Moreover, the elastic recovery (springback) of the work material causes the significant initial area of the flank contact surface. Under these conditions, an increase in  $\alpha_{n1}$  provides better access of MWF to the flank contact area. This results in an increase in tool life. The maximum tool life is achieved when the maximum heat is removed from the flank contact surface by MWF (forced convection) and by transferring heat into the tool body.

The further increase in  $\alpha_{n1}$  leads to reduced tool life although the access of the MWF to the flank contact surfaces improves. This is because much less thermal energy can be transferred into the tool due to a reduction of the mass of the cutting wedge. This decrease cannot be compensated by the increase portion of the thermal energy that is transferred into MWF. As a result, the contact flank temperature increases that reduces tool life. As pointed out by Astakhov [22], the thermal energy transferred into MWF depends on its thermal properties (its cooling ability), its physical and chemical properties (reduction of the amount of the thermal energy generated at the flank contact surface), and on the MWF velocity. Therefore, the optimum value of this angle is not only a function of the tool design parameters (primary approach angles of the other and inner cutting edges) of the tool and work materials but it also depends on the properties of the MWF and elementary MWF flows in the bottom clearance space [24].

The position of the flank surface of the inner cutting edge depends upon angle  $\alpha_{n2}$  and thus this angle determines not only the contact processes on the flank contact surface but also the cooling and lubricating conditions of the flank contact surface of the outer cutting edge as well as drill stability [24]. When  $\alpha_{n2}$  is in the range of  $6^\circ$ – $8^\circ$ , greater drill tool life is due to the fact that drill static stability is at its maximum due to location of the leading supporting pad and due to high MWF velocity in the vicinity of the flank contact surface. Because it was found that the wear rate of the flank surface of the inner cutting edge is 1.8–2.2 times smaller than that of the flank surface of the outer cutting edge (Fig. 5.81), one should realize that the influence of  $\alpha_{n2}$  in the tool life model reflects a combined influence of this angle. In other words, it does not represent dynamics of wear of the flank surface of the inner cutting edge but rather reflects the influence of the position of the flank face adjacent to the inner cutting edge. This location is one of the most important design parameters of any gundrill because it determines the location of

the outlet orifice of the tip coolant passage and the distance of the center of this orifice from the bottom of the hole being drilled. In other words, it determines to a large extent the MWF flow parameters in the bottom space. This is why the flank angle  $\alpha_{n2}$  should be considered not only as a parameter of the gundrill geometry where it plays an insignificant role (Fig. 5.81), but as one of the most important design parameters.



**Fig. 5.80.** Influence of the flank angles of: (a) the outer,  $\alpha_{n1}$ , and (b) inner,  $\alpha_{n2}$  cutting edges on tool life

#### 5.6.6.5 Location Distances $c_{pt1}$ , $c_{pt2}$ , and $m_d$

The location distance of the cutting edge with respect to the  $y_0$ -axis of the tool coordinate system defines the distribution of the rake angles along the cutting edge [20]. Therefore, the influence of this parameter on tool life should be considered from this viewpoint. As known [33], a relatively small change in the rake angle may affect the cutting force significantly and thus it should have the same influence on tool life because it directly depends on this force. The rake angle plays an entirely different role in the machining of brittle and ductile materials. In the former, a small change of the rake angle may change the mechanism of chip formation while in the latter it just result in gradual change of the cutting force and tool wear [33]. Therefore, it should be expected that the location distance could affect tool life significantly in the considered case even though the resultant changes in the rake angle can be relatively small.

Figure 5.82a,b shows the influence of location distances of the outer,  $c_{pt1}$  and the inner,  $c_{pt2}$  cutting edges. As can be seen in Fig. 5.82a, the positive rake angles along the outer cutting edge which are the result of “negative”  $c_{pt1}$ s improve tool life dramatically (the sense of the “negative” and “positive” sign of  $c_{pt}$ s are show in Fig. 5.23). As such, a greater influence is observed at smaller cutting feeds. As can be seen in Fig. 5.82b, the negative rake angles along the inner cutting edge increase tool life because cutting takes place at low cutting speeds. As such, to achieve positive  $c_{pt2}$ s and thus negative rake angles, a special chamfer on the inner cutting edge can be provided.

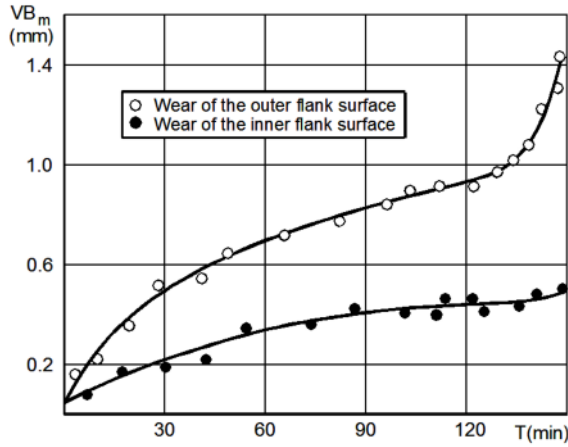


Fig. 5.81. Wear curves for the outer and inner cutting edges

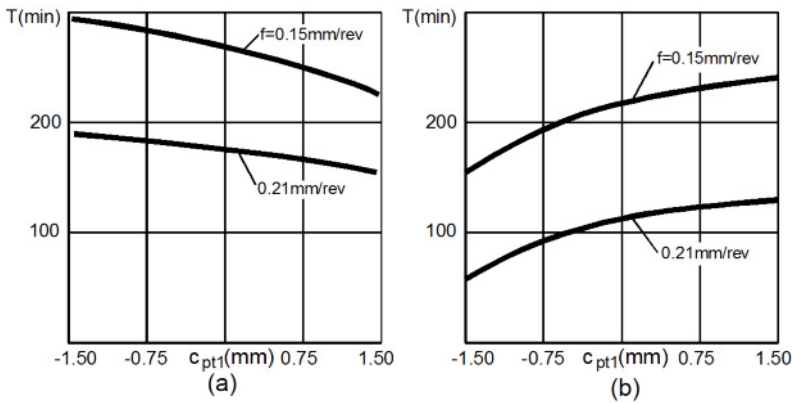


Fig. 5.82. Influence of the location distances of: (a) the outer,  $c_{pt1}$ , and (b) the inner,  $c_{pt2}$  cutting edges on tool life

Location distance  $m_d$  determines the length of the inner and outer cutting edges and thus affects tool life. Relation  $T=f(m_d)$  is shown in Fig. 5.83 for different cutting feeds have their maxima for certain  $m_d$ 's. It was shown [32] that this maximum corresponds to the preferable force balance. In the test, it was found that if  $m_d$  is too large, the radial force pushes the side cutting edge into the wall of the hole being drilled which leads to drill vibrations and, sometimes, to the breakage of the drill corner and/or side cutting edge. When  $m_d$  is too small, the trailing supporting pad was found to be overloaded which resulted in a significant increase in the drilling torque. This torque may deform and even break the shank. The latter is particularly true when the shank already experiences the working load (including torque) close to the limit it can sustain.

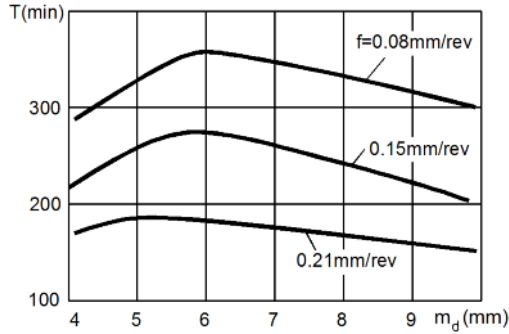


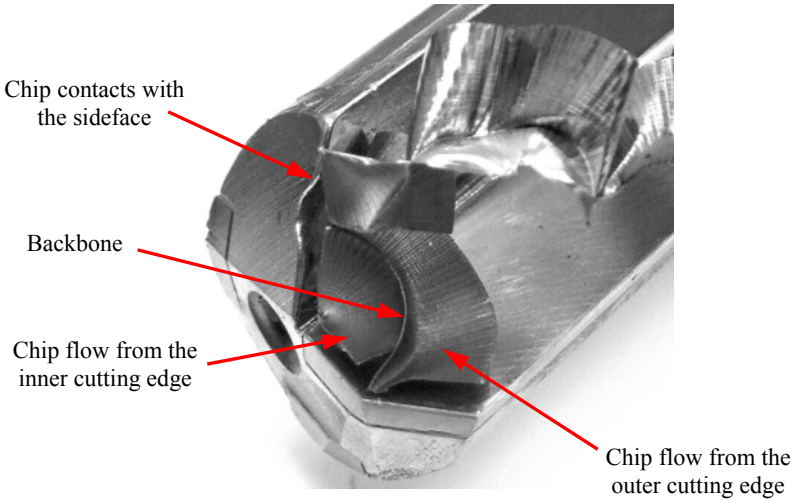
Fig. 5.83. Influence of the location distance of the drill point,  $m_d$  on tool life

It is also seen in Fig. 5.83 that the optimum  $m_d$  depends on the cutting feed. This is because the cutting feed has direct influence on the cutting force and thus on its radial and tangential components [19]. The influence of  $m_d$  becomes less noticeable at higher feeds.

Another important consideration in the selection of the optimum value for  $m_d$  is chip breakage. Although known studies (for example [34]) discuss the influence of the approach angles and  $m_d$  on the shape of the chip formed by the outer and inner cutting edges, an important issue, which is chip breaking in gundrilling, has been overlooked. Among deep-hole drills, gundrills are only drills without chip-breaking steps ground on the rake face. This makes re-sharpening of gundrills much simpler and faster using standard grinding wheels and fixtures. This is possible because gundrills are drill with external chip removal, i.e., these drills have the outside chip removal flute.

In gundrilling, the chip formed at the inner cutting edge should impinge on the chip formed by the outer cutting edge and thus should serve as an obstacle chip breaker. In other words, the collision of these two chip flows should result in the formation of the so-called backbone at their interface which, colliding with the rotating bottom of the hole being drilled (or, at worse, the side walls of the hole being drilled), causes the breakage of such a combined chip. This point is illustrated in Fig. 5.84.

The problem is in the direction of motion of this backbone. It is understood that the discussed direction is a function of the cutting edge approach angles as well as of  $m_d$ . Therefore, the optimum value of  $m_d$  should be selected not only as that resulting in the maximum tool life but also as that which improves chip breakability, avoiding its collisions with the side wall of the gundrill. If the discussed collision takes place, it results in the wear of the side wall of the gundrill. The discussed collision results in a significant force acting on the side wall of the gundrill that may seriously violate the tool static stability. Unfortunately, such a force has never been included in the analysis of drill stability.



**Fig. 5.84.** Interaction of the chip flows from the outer and inner cutting edges

#### 5.6.6.6 Interrelations of Different Gundrilling Parameters

Productivity in gundrilling is defined as the drill penetration rate known as the feed rate,  $v_f$ . It follows from Eq. A.4 (Appendix A) that this rate can be calculated as

$$v_f = nf = \frac{vf}{\pi d_{dr}} \quad (5.120)$$

where  $n$  is the drill (workpiece) rotational speed (r.p.m.) and  $f$  is the cutting feed (mm/rev). Thus, the productivity of gundrilling can be increased either through increasing the cutting speed or by increasing the cutting feed per revolution. The experimental results presented in Fig. 5.85 show that, if the tool geometry (the uncut chip thickness) is kept unchanged, a 1.62-fold increase in the penetration rate (productivity) due to increasing the cutting speed from 0.42 m/s to 0.83 m/s results in a 1.3-fold decrease in tool life. However, if the same increase in productivity is achieved by increasing the feed from 0.11mm/rev to 0.17mm/rev, this would result in only a 1.14-fold decrease in tool life. Therefore, the feed is a better choice to achieve greater productivity. Moreover, increasing the feed normally results in decreasing deviation of the axis of the drilled hole and reduced tool vibration. The drilling system becomes more rigid and less susceptible to self-exciting vibrations due to various factors of the drilling process as cross-holes, inclusions in the work material, variation of machinability along the hole being drilled, etc.

The maximum effect, however, is achieved when it is possible to control the contact process affected by the contact temperature to keep the cutting temperature close to the optimal cutting temperature [22, 33]. This is impossible to achieve under a constant cutting speed. If tool life is kept constant, an increase in the feed leads to a corresponding decrease in the cutting speed to keep the optimum cutting

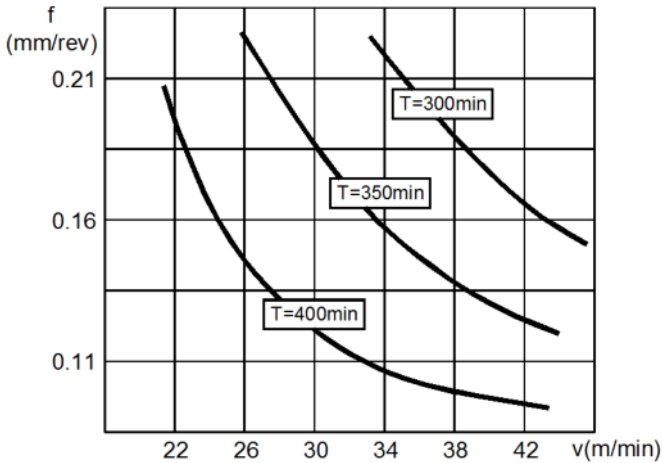


Fig. 5.85. Relationship between the cutting speed and feed for invariable tool life

temperature invariable. It can be achieved if the cutting speed and feed are selected using data presented in Fig. 5.85.

More uniform distribution of the thermal and mechanical loads over the tool-chip contact surfaces can be achieved by varying the uncut chip thickness on the outer cutting edge. The easiest way to do so is by varying the approach angle of the outer cutting edge,  $\varphi_1$ . Figure 5.86 shows the influence of  $\varphi_1$  on the optimal cutting speed. As seen, this speed first increases with  $\varphi_1$  for different feeds and then decreases. When  $\varphi_1$  is small and thus the uncut chip thickness is great, an increase in the cutting feed affects the optimum cutting speed much less than for large  $\varphi_1$ .

It was found experimentally that the optimum values of the approach angles of the outer  $\varphi_1$  and inner  $\varphi_2$  cutting edges do not depend on the cutting regime (feed and speed) under given geometry parameters of the cutting wedge (the rake, flank and inclination angles), design of the shank, and work material. As illustrated in Fig. 5.87, for the considered case of tool life testing, the optimum (criterion – tool life) inner and outer approach angles are still the same when the cutting speed is increased from 0.42m/s to 0.83m/s. They are  $\varphi_1 = 31.5^\circ$  and  $\varphi_2 = 18.8^\circ$ , respectively.

The experimental results also show that the approach angle  $\varphi_1$  significantly affects the optimal cutting feed when the cutting speed is relatively low and this influence becomes rather weak at high cutting speeds. It can be explained by the prevailing influence of the temperature factor over the deformation one at high cutting speeds and by changes of the load of the periphery cutting edge that indirectly follows from the relationship  $T=f(m_d)$  shown in Fig. 5.83. The compensation of the load of the periphery part of the drill is possible by changing  $\varphi_2$ . Figure 5.88 shows that as  $\varphi_1$  increases, the optimal  $\varphi_2$  decreases.



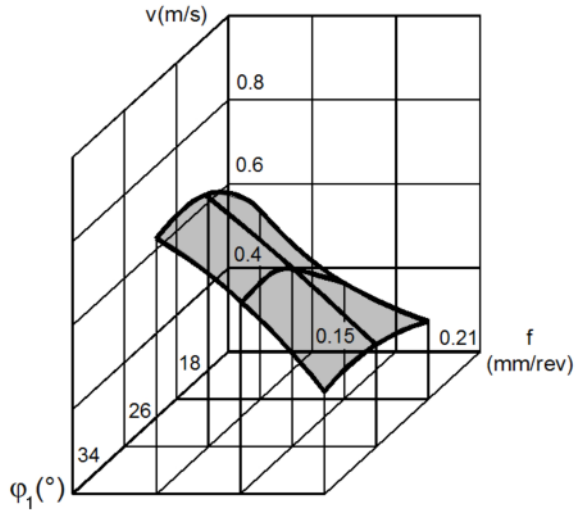


Fig. 5.86. Relationship  $v_{opt} = f(f, \phi_1)$

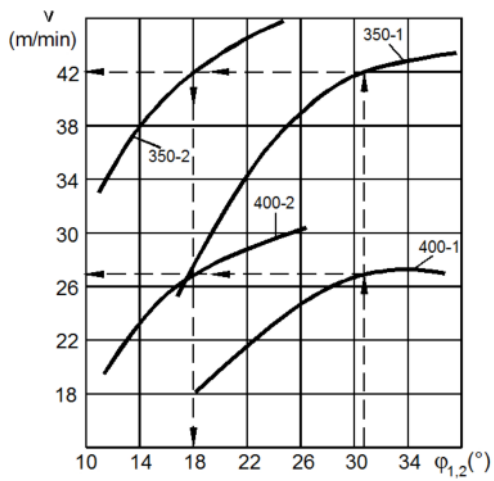
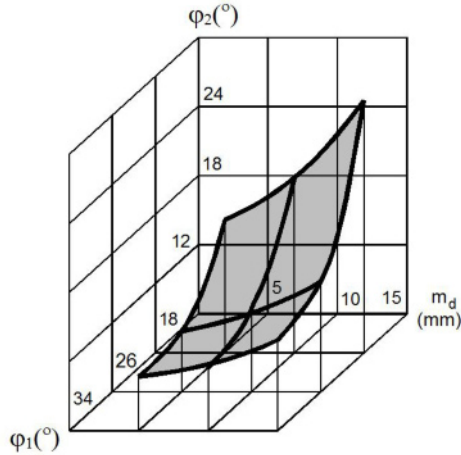


Fig. 5.87. Relationships showing that optimum approach angles do not depend on the cutting regime

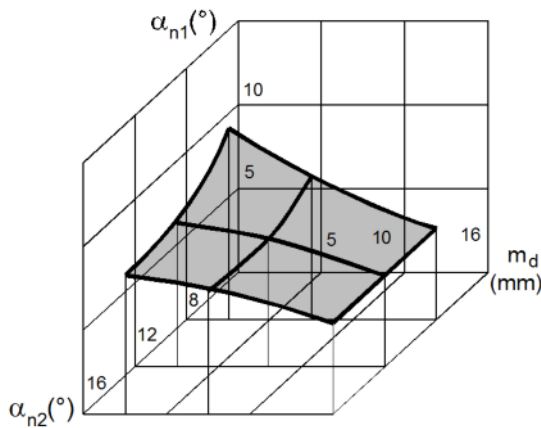
As seen in Fig. 5.88, the correlation between  $\phi_1$  and optimal  $\phi_2$  strongly depends on  $\phi_2$ . However, the final selection of  $\phi_1$  and  $m_d$  should be made also accounting for other parameters of the drill and drilling process and thus selection of optimal  $\phi_2$  in terms of tool life may violate force balance in gundrilling [19]. When this happens in gundrilling of homogeneous materials, it leads to a reduction of diametric accuracy of drilled holes when  $m_d$  and  $\phi_2$  are selected to be too great while  $\phi_2$  is relatively small. In drilling work materials having non-uniform machinability over the diameter being drilled (as in the considered case), the drill unavoidably breaks



**Fig. 5.88.** Correlation between  $\phi_1$  and optimal  $\phi_2$  strongly depends on  $m_d$

when  $\phi_1/\phi_2 = 1.81$  and  $m_d \leq 0.2d_{dr}$ . The optimal  $\phi_1/\phi_2 = 1.47-1.70$  and  $m_d = (0.22-0.33)d_{dr}$ .

The experimental correlation between the optimal flank angles  $\alpha_{n1}$  and  $\alpha_{n2}$  with  $m_d$  is shown in Fig. 5.89. This correlation is weak because  $m_d$  does not affect the uncut chip thickness having the strongest effect on the flank angles.



**Fig. 5.89.** Correlation of the flank angles  $\alpha_{n1}$  and  $\alpha_{n2}$  with the point location  $m_d$

The cutting feed directly defines the uncut chip thickness and thus it has a strong correlation with the flank angles of the outer and inner cutting edges as shown in Fig. 5.90. When the cutting feed increases, the optimal flank angles  $\alpha_{n1}$  and  $\alpha_{n2}$  decrease. Inter-influence of  $\alpha_{n1}$  and  $\alpha_{n2}$  decreases when the drill point shifts further from the axis of rotation (distance  $m_d$  increases). The latter is explained by changing the contact conditions in the region adjacent to the drill point. As distance

$m_d$  increases, the cutting speed of this point increases which leads to an increase in the temperatures around the drill point. To keep the optimal cutting temperature, the approach angle  $\phi_1$  and the cutting feed can be changed correspondingly as seen in Fig. 5.91. This conclusion is of particular importance in gundrilling where the reliable chip breaking is normally achieved by adjusting the approach angles and by varying  $m_d$ . The data presented in Fig. 5.91 show that such an adjustment may affect tool life (optimum condition) and thus cannot be accomplished accounting only for the shape of the produced chip. Rather, the optimal correlations should be established and then any adjustments can be made to achieve the desirable chip shape while keeping optimal drill performance in terms of tool life.

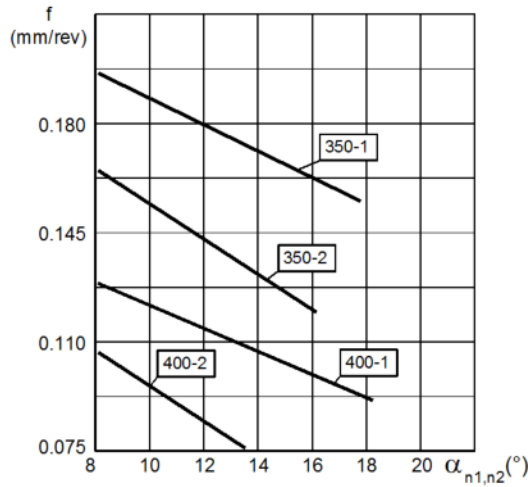
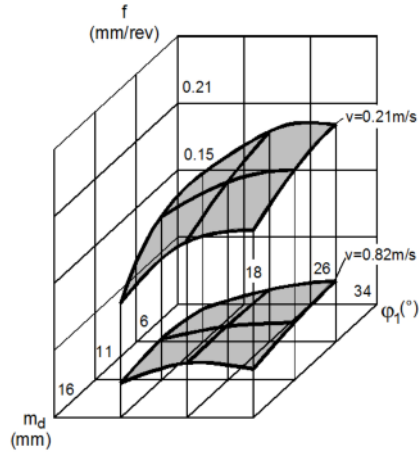


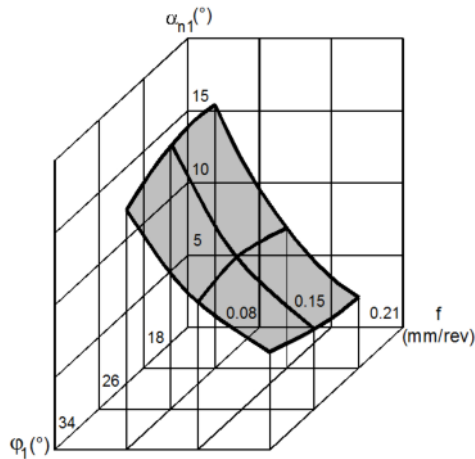
Fig. 5.90. Influence of the cutting feed on the flank angles  $\alpha_{n1}$  and  $\alpha_{n2}$

As the experimental results show, an increase in  $m_d$  can be compensated by decreasing flank angles  $\alpha_{n1}$  and  $\alpha_{n2}$ . As such, angle  $\alpha_{n1}$  plays a more important role. The optimal value of this angle depends on the uncut chip thickness, which in turn, is a function of two parameters – the cutting feed and approach angle  $\phi_1$ . Figure 5.92 shows that, keeping the same optimal flank angle  $\alpha_{n1}$ , gundrilling productivity can be increased (under the same tool life) by increasing the cutting feed and the corresponding increase of approach angle  $\phi_1$ .

One should remember, however, that if the flow of the MWF in the bottom clearance are not optimized and thus the static pressure of the cutting fluid is low, the MWF will not flow through the narrow clearances between the bottom of the hole being drilled and the flank surface when flank angles  $\alpha_{n1}$  and  $\alpha_{n2}$  become too small [21, 24].



**Fig. 5.91.** Optimal relation  $m_d = f(f, \phi_1)$  for different cutting speeds



**Fig. 5.92.** Optimal relation  $\alpha_{n1} = f(f, \phi_1)$

### 5.6.7 Optimization of Tool Geometry

Problems that involve the operation or the design of systems are generally of the type to which optimization principles can be beneficially applied. Unfortunately, there are no fundamental studies on the optimization of the tool geometry so that the tool geometry given by the tool manufacturer is considered the best. Whenever one uses “best” or “optimal” to describe a technical system including the cutting tool, an immediate question to be asked is: “The best with respect to what criteria and subject to what limitations?” Given a specific measure of performance and a specific set of constraints, one can designate a system as optimal (with respect to the performance measure and constraints) if it performs as well as, if not better

than, any other system which satisfies the given constraints. The term suboptimal is used to describe any system, which is not optimal (with respect to the given performance measure and constraints). The problem of optimization of tool geometry can be thought of as: For a given cutting regime and process constraints, and for the selected performance measure(s) (tool life, production rate, cost per drilled hole, for example), find a combination of the parameters of the cutting tool geometry that maximizes (minimizes when necessary) the chosen performance measure(s). In practical terms, the problem is reduced to the finding of the extreme of the objective function

$$\bar{A} = F(x, \bar{B}) \quad (5.121)$$

which is continuous with respect to the vector of arguments  $\bar{x} = (\bar{x}_1, \bar{x}_2, \dots, \bar{x}_n)$  each of which can be varied independently in the range  $[\bar{x}_{\min}, \bar{x}_{\max}]$ . In Eq. 5.121,  $\bar{B} = (\bar{b}_1, \bar{b}_2, \dots, \bar{b}_n)$  is the vector of the estimates for the model's coefficients.

The input variables vector contains nine variables ( $n = 9$ ) which are:  $x_1$  is the approach angle of the outer cutting edge,  $\varphi_1$ ;  $x_2$  is the approach angle of the inner cutting edge,  $\varphi_2$ ;  $x_3$  is the normal flank angle of the outer cutting edge,  $\alpha_{n1}$ ;  $x_4$  is the normal flank angle of the inner cutting edge,  $\alpha_{n2}$ ;  $x_5$  is distance  $c_{pl1}$ ;  $x_6$  is distance  $c_{pl2}$ ;  $x_7$  is the location distance of the drill point with respect to the  $x_0$ -axis of the tool coordinate system,  $m_d$ ;  $x_8$  is the cutting speed,  $v$ ;  $x_9$  is the cutting feed,  $f$ .

A primary goal for the selection of an optimization method is to find a method which is adequate to the problem and its constraints and that, given good starting points, requires only a few iterations for finding a solution. The comparison of different optimization techniques showed that the Hook and Jeeves method [35] is the most suitable for the considered problem. The advantages of this method are: (1) the quality of solutions improves at each successive step on the response surface, (2) it is suitable for the response surface which may have deep narrow "cavities/craters" (thus the gradient methods are not suitable), (3) self-acceleration.

The essence of this method can be described as follows. First, the initial or starting point of vector  $\bar{x} = (\bar{x}_1, \dots, \bar{x}_9)$  is selected ( $\bar{x}[0]$ ) using the experimental results obtained. By changing the components of this vector, the vicinities of the starting point are investigated and, as a result, the direction of increasing (decreasing) of the objective function  $\bar{A}$  is found. The climb (or descent) takes place until  $\bar{A}$  increases (decreases). When there is no greater (smaller) value of  $\bar{A}$  in this direction, the step of climb (or descent) is reduced. If it does not help, this direction is abandoned and a new search in the vicinity of the current point takes place. After a few changes of the search direction, the method allows one to reach the optimal point. A step of 3% of the initial value of each parameter involved in the study was used.

The optimal parameters of the tool geometry corresponding to tool life of 497 min, obtained using the Hook and Jeeves method, are: approach angle of the outer cutting edge,  $\varphi_1 = 31.5^\circ$ ; approach angle of the inner cutting edge,  $\varphi_2 = 18.0^\circ$ ; normal flank angle of the outer cutting edge,  $\alpha_{n1} = 14.5^\circ$ ; normal flank angle of the

outer cutting edge,  $\alpha_{r2} = 9.0^\circ$ ; location distances  $c_{pt1} = 1.36\text{mm}$ ,  $c_{pt2} = 0.9\text{mm}$ ; location distance of the drill point  $m_d = 10.4\text{mm}$  for cutting speed  $v = 0.43\text{m/min}$  and feed  $f = 0.11\text{mm/rev}$ .

## References

- [1] Swinehart HJ (ed) (1967) *Gundrilling, trepanning, and deep hole machining*. SME Dearborn, MI
- [2] Sakuma K, Taguchi K, Katsuki A (1980) Study on deep-hole-drilling with solid-boring tool: the burnishing action of guide pads and their influence on hole accuracies. *Bulletin of the JSME* 23(185):1921–1928
- [3] Griffiths BJ (1993) Modeling complex force system, Part 1: The cutting and pad forces in deep drilling. *ASME J. of Eng. for Ind.* 115:169–176
- [4] Astakhov VP, Galitsky VV, Osman MOM (1995) An investigation of the static stability in self piloting drilling. *Int. J. of Prod. Res.* 33(6):1617–1634
- [5] Sakuma K, Taguchi K, Katsuki A, Takeyama H (1981) Self-guiding action of deep hole drilling tools. *Annals of the CIRP* 30(1):311–315
- [6] Richardson R, Bhatti R (2001) A review of research into the role of guide pads in BTA deep-hole machining. *J. of Mat. Proc. Tech.* 110(1):61–69
- [7] Latinovic V, Osman MOM (1989) Optimal design of BTA deep-hole cutting tools with staggered cutters. *Int. J. of Prod. Res.* 27(1):153–173
- [8] Katsuki A, Sakuma K, Onikura H (1988) Axial hole deviation in deep drilling - the influence of the shape of the shape of the cutting edge. *Transactions of the Japan Society of Mechanical Engineers, Part C* 54(502):1350–1356
- [9] Astakhov VP (2004) High-penetration rate gundrilling for the automotive industry: system outlook. *SME Paper TPO4PUB249:1–20*
- [10] Astakhov VP (2002) Instead of Introduction: Metal Cutting: Missed Chances or a Science Without History. Introduction to book- in-preparation "Physical Fundamentals of Metal Cutting" (Part 1 and Part 2). <http://viktorastakhov.tripod.com/>
- [11] Astakhov VP (2002) A primer on gundrilling. *F&M Magazine* (11):32–41
- [12] Deng C-S, Huang J-C, Chin J-H (2001) Effects of support misalignments in deep-hole drill shafts on hole straightness. *Int. J. of Mach. Tools and Manuf.* 41:1165–1188
- [13] Katsuki A, Onikura H, Sajimi T, Rikimaru M, Kudo H (1997) Development of a high-performance deep hole laser-guided boring tool: guiding characteristics. *Annals of the CIRP* 46(1):319–323
- [14] Katsuki A, Onikura H, Sajima T, Akashi T (1992) Development of deep-hole boring tool guided by laser. *Annals of the CIRP* 41(1):83–87
- [15] Zhang W, He F, Xiong D (2004) Gundrill life improvement for deep-hole drilling on manganese steel. *Int. J. of Mach. Tools and Manuf.* 44(2–3):237–331
- [16] Hasegawa X, Horiuchi G (1975) On the motion of drill tip and accuracy of the hole in gundrilling. *Annals of the CIRP* 24:53–58
- [17] [Ramakrishana RK, Shunmugam MS (1988) Wear studies in boring trepanning association drilling. *Wear* 124:33–43
- [18] Astakhov VP (2002) The mechanisms of bell mouth formation in gundrilling when the drill rotates and the workpiece is stationary. Part 2: The second stage of drill entrance. *Int. J. of Mach. Tools and Manuf.* 42:145–152
- [19] Astakhov VP (2002) The mechanisms of bell mouth formation in gundrilling when the drill rotates and the workpiece is stationary. Part 1: The first stage of drill entrance. *Int. J. of Mach. Tools and Manuf.* 42:1135–1144

- [20] Astakhov VP, Galitsky VV, Osman MOM (1995) A novel approach to the design of self-piloting drills. Part 1. Geometry of the cutting tip and grinding process. *ASME J. of Eng. for Ind.* 117:453–463
- [21] Astakhov VP, Galitsky VV, Osman MOM (1995) A novel approach to the design of self-piloting drills with external chip removal, Part 2: Bottom clearance topology and experimental results. *ASME J. of Eng. for Ind.* 117:464–474
- [22] Astakhov VP (2006) *Tribology of metal cutting*. Elsevier, London
- [23] Astakhov VP (2008) *Ecological machining: near-dry machining*. In Davim PJ(ed) *Machining: fundamentals and recent advances*, Springer: London
- [24] Astakhov VP, Frazao J, Osman MOM (1994) On the experimental optimization of tool geometry for uniform pressure distribution in single edge gundrilling. *ASME J. of Eng. for Ind.* 118:449–456
- [25] Astakhov VP, Galitsky V (2005) Tool life testing in gundrilling: an application of the group method of data handling (GMDH). *Int. J. of Mach. Tools and Manuf.* 45:509–517
- [26] Astakhov VP, Osman MOM, Al-Ata M (1997) Statistical design of experiments in metal cutting – Part 1: Methodology. *Journal of Testing and Evaluation* 25(3):322–327
- [27] Astakhov VP, Al-Ata M, Osman MOM (1997) Statistical design of experiments in metal cutting. Part 2: Application. *Journal of Testing and Evaluation* 25(3):328–336
- [28] Astakhov VP (2004) The assessment of cutting tool wear. *Int. J. of Mach. Tools and Manuf.* 44:637–647
- [29] Astakhov VP (2004) *Tribology of metal cutting*, In: Totten G, Liang H (ed) *Mechanical tribology. material characterization and application*. Marcel Dekker, New York
- [30] Pfler F (1977) Aspekte zur konstruktiven gestolrung von tiefbohrwerkseugen (in German). *Werkstattstechnik* 67:211–218
- [31] Sakuma K, Taguchi K, Katsuki A (1981) Self-guiding action of deep-hole-drilling tools. *Annals of the CRIP* 30:311–315
- [32] Astakhov VP, Galitsky VV, Osman MOM (1995) An investigation of the static stability in self-piloting drilling. *Int. J. of Prod. Res.* 33:1617–1634
- [33] Astakhov VP (1998/1999) *Metal cutting mechanics*. CRC, Boca Raton
- [34] Fink P (1979) Achneidkeilgeometrie von einlippenbohrern and bohrungsgute (In German). *Technisches Zentralblatt für praktische Metallbearbeitung* 73(5):16–22
- [35] Kelley CT (1999) *Iterative methods for optimization*. The Society for Industrial and Applied Mathematics (SIAM), Philadelphia, PA

# Appendix A

---

## Basic Kinematics of Turning and Drilling

*Science is simply common sense at its best.*  
Thomas H. Huxley (1825–1895)

**Abstract.** This Appendix discusses basic turning and drilling operation and presents the definitions of the basic terms used in kinematics of turning, boring, and drilling. The cutting speed, cutting feed, feed rate, depth of cut, and material removal rate are considered with practical examples of calculations. Based on the chip compression ratio (CCR) discussed in Chap. 1, a simple practical methodology to calculate the cutting power (force) and its partition in the cutting system is considered with examples. It is shown that the greatest part of the energy needed for cutting is spent in plastic deformation of the layer being removed.

### A.1 Introduction

The term “Machining” covers a group of machining operations. The three principal machining processes are classified as turning, drilling, and milling. Other operations falling into miscellaneous categories include shaping, planing, boring, broaching, and sawing. The common feature of all machining operations is the use of the cutting tool that removes a certain layer from the workpiece in the form of the chip. As discussed in Chap. 1, the tool, the workpiece, and the chip constitute the machining system.

To perform machining operations, relative motion is required between the tool and workpiece. This relative motion is achieved in most machining operation is a combined motion consisting of several elementary motions as the primary motion, called the cutting speed and the secondary motion called the cutting feed. The tool geometry and tool setting relative to the workpiece, combined with these motions, produce the desired shape of the machined surface.



While performing the basic motions to shape the workpiece, the tool requires energy which is normally represented by the cutting forces and velocities in the corresponding directions. This energy determines tool life, integrity of the machined surface and accuracy of machining. Therefore, a simple and reliable method to determine this energy has to be developed to improve cutting tools and the machining operation as the whole.

## A.2 Turning and Boring

### A.2.1 Basic Motions in Turning

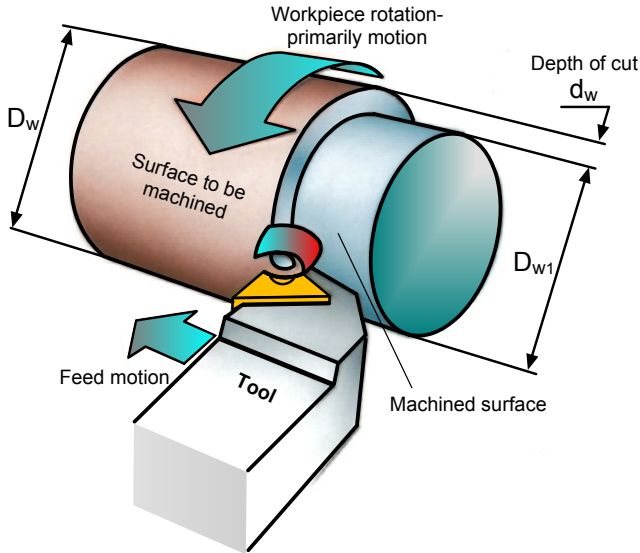
Turning is a general term for a group of machining operations in which the workpiece carries out the prime rotary motion while the tool performs feed motion. These are used for the external and internal turning of surfaces. Figure A.1 shows a common turning arrangement. The workpiece is clamped in a self-centering three-jaw lathe chuck installed on the machine spindle that provides rotation and the tool installed on the tool post which is a part of a lathe carriage that provides the feed motion.

Turning is used for machining cylindrical surfaces. The basic motions of turning are shown in Fig. A.2. They are:

- The primary motion is the rotary motion of the workpiece around the turning axis
- The secondary motion is the translational motion of the tool, known as the feed motion



Fig. A.1. Generic turning



**Fig. A.2.** Turning motions and parameters

Basic external turning operations are classified according to the direction of the feed motion with respect to the turning axis (Fig. A.3):

- Straight turning occurs when the direction of the feed motion is kept parallel to the turning axis
- Transverse turning when the direction of the feed motion is perpendicular to the feed motion
- Profiling turning occurs when the direction of feed motion changes according to the profile (contour) of the machined part due to coordinated feed motions along the coordinate axes

Internal turning known as boring is used to increase the inside diameter of an existent hole made with a drill, or it may be a cored hole in a casting. Figure A.4 shows a common boring arrangement. The workpiece with a hole is clamped in a self-centering three-jaw lathe chuck installed on the machine spindle that provides rotation and the boring tool installed on the tool post which is a part of a lathe carriage that provides the feed motion.

The basic motions of boring are the same as in turning as shown in Fig. A.5. They are:

- The primary motion is the rotary motion of the workpiece about the boring axis
- The secondary motion is the translational motion of the tool, known as the feed motion

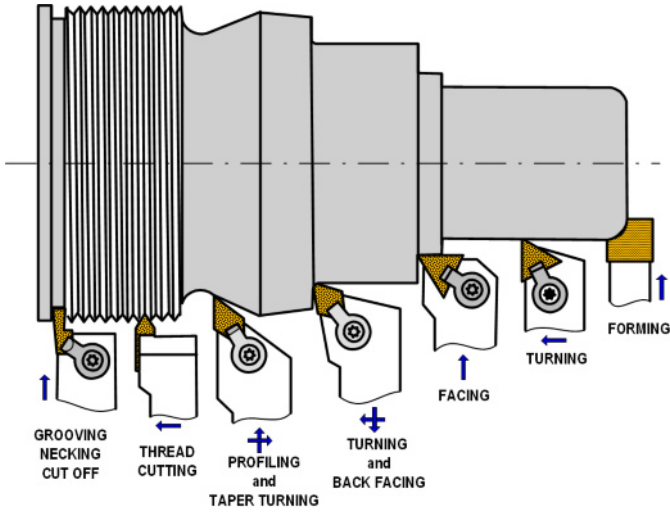


Fig. A.3. External turning operations

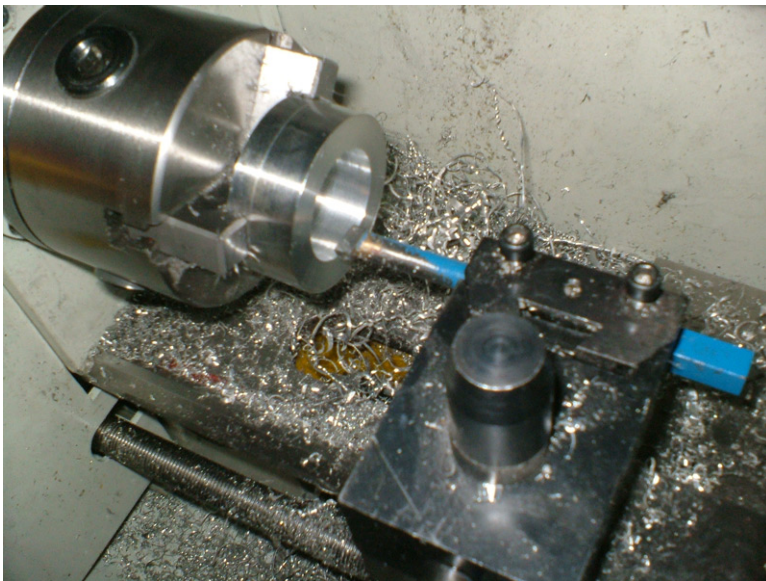


Fig. A.4. Generic boring

Boring achieves three basic objectives:

- Sizing: boring brings the hole to the proper size and surface finish
- Straightness: boring straightens the original drilled or cast (core) hole
- Concentricity: boring makes the hole concentric with the axis of rotation

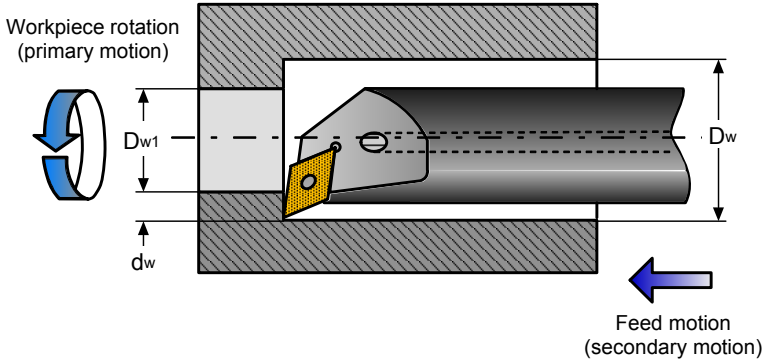


Fig. A.5. Boring motions and parameters

Most of the turning operations that occur with external turning are also to be found in boring as shown in Fig. A.6. With external turning, the length of the workpiece does not affect the tool overhang and the size of the toolholder. However, with internal turning, or boring, the choice of tool is very much restricted by the workpiece's hole diameter and length.

A general rule, which applies to all machining, is to minimize the tool overhang to obtain the best possible stability and thereby accuracy. With boring, the depth of the hole determines the overhang. The stability is increased when a larger tool diameter is used, but even then the possibilities are limited since the space allowed by the diameter of the hole in the workpiece must be taken into consideration for chip evacuation and radial movements.

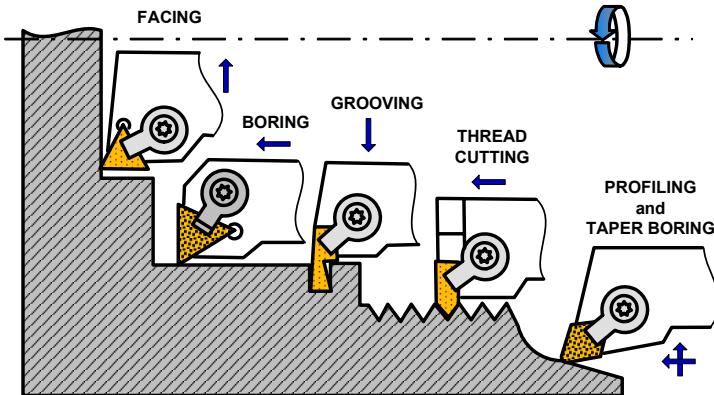


Fig. A.6. Internal turning (boring) operations

### A.2.2 Cutting Speed in Turning and Boring

In any machining operation, the cutting speed is the rate at which the workpiece surface is passed by the cutting edge. It is measured in meters per minute, or feet per minute (often referred to as surface feet per minutes or sfm). This definition is UNIVERSAL and holds no matter what are the arrangements (spatial location, motions, velocities, etc.) of the components of a particular cutting system. Note that when both the tool and the workpiece move (rotate, for example), the cutting speed is the relative speed of the tool and the workpiece according to this definition.

In metric units of measure (the SI system), the cutting speed calculates as

$$v = \frac{\pi D_w n}{1000} \text{ (m/min)} \quad (\text{A.1})$$

where  $\pi = 3.141$ ,  $D_w$  is diameter of the workpiece in millimeters, and  $n$  is the rotational speed in r.p.m or rev/min.

For example, if  $D_w = 76.2\text{mm}$  and  $n = 670\text{rpm}$ , then  $v = \pi D n / 1000 = 3.141 \times 76.2 \times 670 / 1000 = 160.4 \text{ m/min}$ .

In the Imperial units of measure, the cutting speed calculates as

$$v = \frac{\pi D_w n}{12} \text{ (sfm or ft/min)} \quad (\text{A.2})$$

where  $\pi = 3.141$ ,  $D_w$  is diameter of the workpiece in inches, and  $n$  is the rotational speed in r.p.m or rev/min.

For example, if  $D_w = 3\text{in}$  (76.2mm) and  $n=670\text{rpm}$ , then  $v = \pi D n / 12 = 3.141 \times 3 \times 670 / 12 = 526.1 \text{ sfm}$ .

Normally in practice of machining, the cutting speed  $v$  is selected for given tool design, tool material, work material, and particularities of a given operation. Then the spindle rotational speed should be calculated using Eq. A.1 and the given diameter of the workpiece as

$$n = \frac{1000v}{\pi D_w} \quad (\text{A.3})$$

### A.2.3 Feed and Feed Rate

The feed motion is provided to the tool or the workpiece, and when added to the primary motion leads to a repeated or continuous chip removal and the formation of the desired machined surface. The cutting feed,  $f$  is the distance in the direction of feed motion at which the cutting tool advanced into the workpiece per one revolution and thus the feed is measured in millimeters per revolution (inches per revolution). The feed rate,  $v_f$  is the velocity of the tool in the feed direction. It

measures in millimeters per minute (mm/min) or inches per minute (ipm) and calculates as

$$v_f = f \cdot n \quad (\text{A.4})$$

where  $f$  is the feed (mm/rev or ipm), and  $n$  is the spindle rotational speed (rpm).

*Example A.1.*

*Problem:* Determine the spindle rotational speed and feed rate for a turning operation if the selected cutting speed  $v=200$  m/min, diameter of workpiece is  $D_w=50$ mm, feed  $f=0.35$ mm/rev.

*Solution:* The spindle rotational speed calculates using Eq. A.3 as  $n = \frac{1000v}{\pi D_w} = \frac{1000 \cdot 200}{3.141 \cdot 50} = 1273.48$ rpm. For practical input in the CNC controller,  $n = 1273$ rpm.

The feed rate calculates using Eq. A.4  $v_f = f \times n = 0.35 \times 1273 = 445.55$  mm/min.

End of Example A.1.

### A.2.4 Depth of Cut

In turning and boring, the depth of cut (sometimes called back engagement) calculates as

$$d_w = \frac{D_w - D_{w1}}{2} \quad (\text{A.5})$$

where  $D_{w1}$  is the diameter of the machined surface as shown in Figs. A.2 and A.5.

### A.2.5 Material Removal Rate

The material removal rate is known as MRR, in mm<sup>3</sup>/min in turning and boring is given by

$$MRR = 1000 f v d_w \quad (\text{A.6})$$

where  $v$  is in m/min,  $f$  is in mm/rev,  $d_w$  is in mm.

Equation A.6 shows that to increase MRR, one has to increase the cutting speed, feed and depth of cut under given constraints on tool life, surface finish, dimensional accuracy, available power of the machine tool, efficiency of machining, etc.

### A.2.6 Resultant Motion

Because the cutting speed and feed rate are velocities, they can be characterized by their magnitudes and directions, i.e., by vectors. Summation of these vectors gives the direction and magnitude of the so-called resultant motion,  $v_e$  in the sense shown in Fig. A.7. Although pictures similar to that shown in Fig. A.7 appear in many metal cutting books and student's texts on the subject (for example Fig. 1.5, page 8 in [1]), some explanation to this picture should be given.

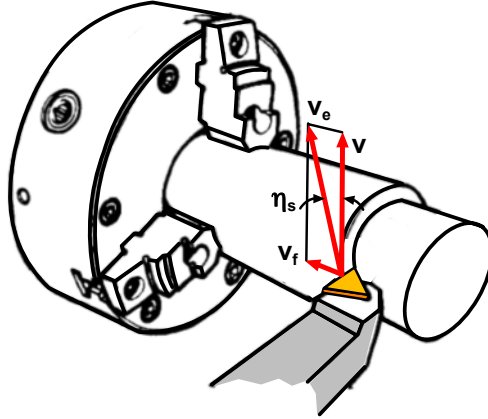


Fig. A.7. Sense of the resultant motion.

The problem is that the vector summation shown in Fig. A.7 is dramatization of reality due to great exaggeration of angle  $\eta_s$ . As follows from Fig. A.7, this angle calculates as

$$\tan \eta_s = \frac{v}{v_f} = \frac{f}{\pi D_w} \quad (\text{A.7})$$

For example, in machining of a workpiece having diameter  $D_w = 50\text{mm}$  with feed  $f = 0.5\text{mm/rev}$ , this angle is  $0.18^\circ$ , i.e., it is much less than the accuracy of tool mounting in the tool post of many machines in practice. Therefore, beside few special cases discussed in Chap. 2, this angle can be safely neglected in kinematic considerations of metal cutting.

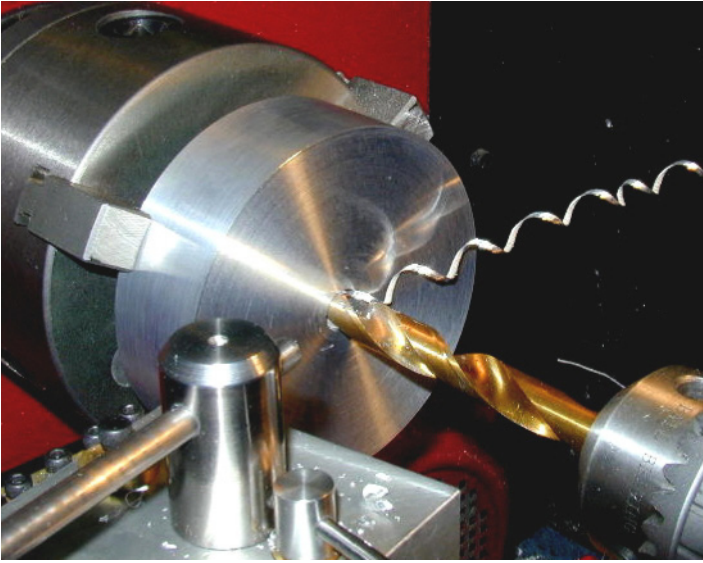
## A.3 Drilling and Reaming

### A.3.1 Basic Motions in Drilling

Drilling is a holemaking machining operation where the tool called a drill is used. Figure A.8 shows a common drilling arrangement on a lathe. The workpiece is clamped in a self-centering three-jaw lathe chuck installed on the machine spindle

that provides rotation and the tool is installed on the tailstock engaged with the lathe carriage that provides the feed motion.

In drilling operations, the primary motion is rotation of the workpiece or the tool or both (counter-rotation drilling) and translational feed motion which can be applied to the tool or the workpiece depending on the particular design of the machined tool used as shown in Fig. A.9. Basic drilling operations are shown in Fig. A.10.



**Fig. A.8.** Generic drilling

### A.3.2 Machining Regime

The cutting speed in drilling is calculated using Eq. A.1. The sense of  $D_w$  is shown in Fig. A.9. Normally in the practice of drilling and reaming, the cutting speed  $v$  is selected for given tool design, tool material, work material, and particularities of a given operation. Then the spindle rotational speed calculates using Eq. A.3.

The feed motion is provided to the tool or the workpiece, and when added to the primary motion leads to a repeated or continuous chip removal and the formation of the desired machined surface. The cutting feed,  $f$  is the distance in the direction of feed motion at which the cutting tool advanced into the workpiece per one revolution and thus the feed is measured in millimeters per revolution (inches per revolution). The feed rate,  $v_f$  is the velocity of the tool in the feed direction. It is often called the penetration rate and measures in millimeters per minute (mm/min) or inches per minute (ipm). The penetration rate calculates using Eq. A.4.

In drilling, the depth of cut is equal to  $D_w/2$ . In reaming, it calculates using Eq. A.5 where the sense of  $D_w$  is shown in Fig. A.9.



MRR in drilling calculates by substituting  $d_w = D_w/2$  in Eq. A.6

$$MRR = 500 f v D_w \tag{A.8}$$

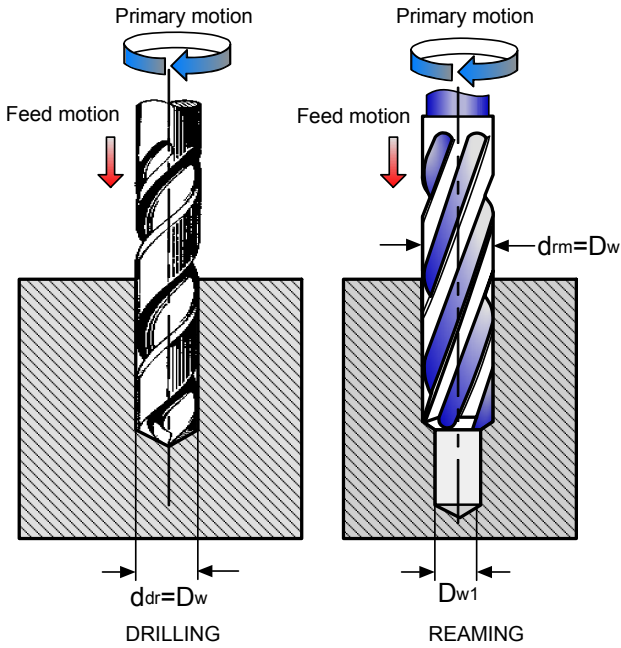


Fig. A.9. Motions in drilling and reaming

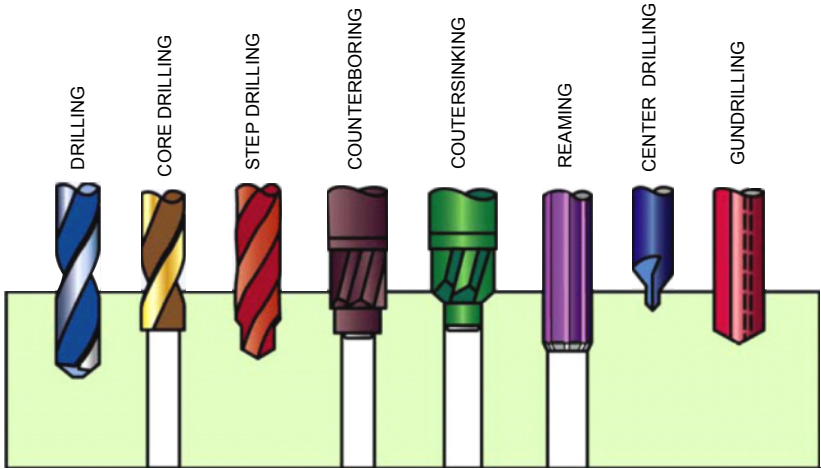


Fig. A.10. Basic drilling operations

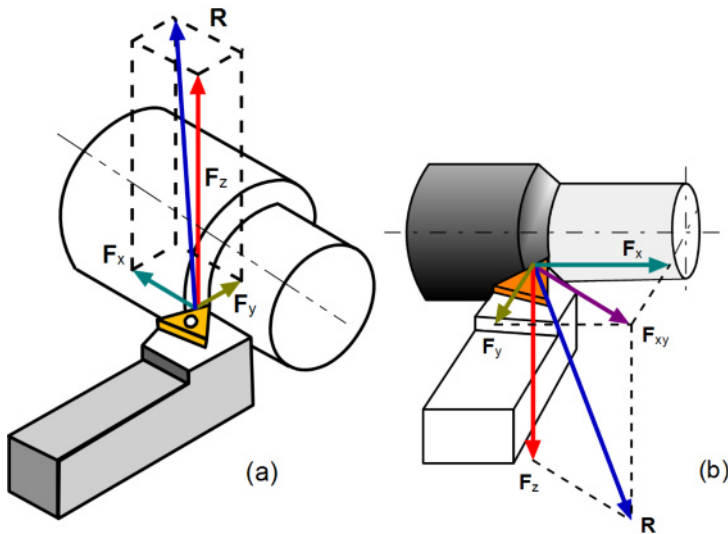
where  $v$  is in m/min,  $f$  is in mm/rev, and  $D_w$  is in mm.

In reaming, MMR calculates using Eq. A.6.

## A.4 Cutting Force and Power

### A.4.1 Force System in Metal Cutting

While cutting, the tool applies a certain force to the layer being removed through the tool-chip interface as discussed in Chap. 1. This force, known as the resultant cutting force  $R$ , is a 3D vector in the T-hand-S as shown in Fig. A.11a. For convenience, this force is normally resolved into three components. The main or power component of the resultant force,  $F_z$  (known also as the tangential force) is along the  $z$ -axis. It is normally the greatest component. The force in the feed direction which is the  $x$ -direction is known as the feed or axial force  $F_x$ . The component along the  $y$ -axis  $F_y$  is known as the radial component as it acts along the radial direction of the workpiece.



**Fig. A.11.** Cutting force and its components: (a) as applied to the workpiece, and (b) as applied to the tool

The equal and opposite force  $R$  is applied to the cutting tool as a reaction force of the workpiece as shown in Fig. A.11b. This force is also resolved into three orthogonal components along the coordinate axis of the T-hand-S. Additional component  $F_{xy}$  that acts in the  $xy$  coordinate plane is also considered. Its significance is discussed in Chap. 3 in the consideration of the tool cutting edge angle  $\kappa_r$ .

### A.4.2 Cutting Power

As known [2–4], power calculates as the product of the resultant force and the velocity in the direction of this force. In metal cutting, however, the force components and the corresponding velocities can be considered. As the velocity in the direction of the radial force  $F_y$  is zero, this component does not participate in power considerations. The axial force  $F_x$  is normally much smaller than the tangential force  $F_z$ . As discussed above, the velocity in the axial direction (the speed of feed) is negligibly smaller than the cutting speed. As a result, the contribution of the power due to the axial force  $F_x$  to the total cutting power is small. The greatest force component that acts in the direction of the cutting speed is  $F_z$ . Therefore, the cutting power calculates as

$$P_c = F_z \times v \quad (W) \quad (A.9)$$

where  $F_z$  is in newtons (N), and  $v$  is in m/s.

That is why  $F_z$  is often referred to as the power component or the cutting force.

If the  $P_c$  is divided by the volume of material removed per unit time, i.e., by MMR, then the power required to remove a unit volume per unit time (e.g.,  $\text{mm}^3/\text{s}$ ) is obtained. This is termed as the specific cutting power,  $P_{c-c}$ :

$$P_{c-c} = \frac{F_z v}{MMR} \quad (A.10)$$

Substituting Eq. A.6 into Eq. A.10 and converting units, one can obtain

$$P_{c-c} = \frac{F_z v}{f v d_w} = \frac{F_z}{f d_w} \left( W / \text{mm}^3 \right) \quad (A.11)$$

where the cutting feed,  $f$  is in mm/rev and the depth of cut,  $d_w$  is in mm.

It is important to discuss here the common misconceptions associated with Eq. A.11. As can be seen, the proper dimension of  $P_{c-c}$  is  $\text{W}/\text{mm}^3$ . Unfortunately, many specialists in the field do not realize the physical essence of this equation so they see only its second part where its formal dimension can be thought of as  $\text{N}/\text{mm}^2$ . As a result,  $P_{c-c}$  is often called specific cutting pressure [1, 5–8] or even specific cutting force (symbol  $k_c$ ) [9–11]. In reality, it is not a true pressure or stress item.

Moreover, it is claimed that it is a kind of property of the work material that may characterize its machinability [12] and can be used to calculate the cutting force. The whole idea of the so-called mechanistic approach in metal cutting is based on this false perception. The role of tool geometry as the major contributor to the state of stress in the machining zone is totally ignored. As discussed in Chap. 1, the strain at fracture strongly depends on this state of stress. This strain defines the energy needed for fracture of the layer being removed and thus directly affects the cutting force.

### A.4.3 Practical Assessment of the Cutting Force

Astakhov showed that the existing notions of the theoretical determination of the cutting force are fruitless as they cannot pass a simple reality check [13]. When it comes to experimental determination of the cutting force, there are at least two problems:

- The first and foremost is that the cutting force cannot be measured with reasonable accuracy. Even if extreme care is taken, a 50% variation is the case [14].
- Second, many tool and cutting inserts manufacturers (not to mention manufacturing companies) do not have adequate dynamometric equipment to measure the cutting force. Many dynamometers used in the field are not properly calibrated because the known literature sources did not provide proper experimental methodology for cutting force measurements using piezoelectric dynamometers [15].

Therefore, to make practical calculations of the cutting force and thus energy spent in machining, another approach has to be found.

The advanced methodology [16] is based on the definition of the metal cutting process proposed by Astakhov [17] and on the model of energy partition in the metal cutting system developed using this definition (Fig. 2.1 in [13]). According to this model, the power balance in the cutting system can be written as

$$P_c = F_c v = P_{pd} + P_{fR} + P_{fF} + P_{ch} \quad (\text{A.12})$$

from where the cutting force calculates as

$$F_c = \frac{P_{pd} + P_{fR} + P_{fF} + P_{ch}}{v} \quad (\text{A.13})$$

where  $P_{pd}$  is the power spent on the plastic deformation of the layer being removed,  $P_{fR}$  is the power spent at the tool-chip interface,  $P_{fF}$  is the power spent at the tool-workpiece interface, and  $P_{ch}$  is the power spent in the formation of new surfaces.

The power spent on the plastic deformation of the layer being removed,  $P_{pd}$  can be calculated knowing the chip compression ratio (see Chap. 1) and parameters of the deformation curve of the work material as follows [13, 18]:

$$P_{pd} = \frac{K(1.15 \ln \zeta)^{n+1}}{n+1} v A_w \quad (\text{A.14})$$

where  $K$  is the strength coefficient ( $\text{N/m}^2$ ) and  $n$  is the hardening exponent of the work material,  $\zeta$  is the chip compression ratio [13, 18], and  $A_w$  is uncut chip cross-sectional area ( $\text{m}^2$ ):

$$A_w = d_w f \quad (\text{A.15})$$

where  $d_w$  is the depth of cut (m), and  $f$  is the cutting feed per revolution (m/rev).

Power spent due to friction at the tool-chip interface calculates as

$$P_{fR} = \tau_c l_c b_{1T} \frac{v}{\zeta} \quad (\text{A.16})$$

where  $\tau_c = 0.28\sigma_{UTS}$  is the average shear stress at the tool-chip contact ( $\text{N/m}^2$ ) [13],  $\sigma_{ut}$  is the ultimate tensile strength of the work material ( $\text{N/m}^2$ ),  $l_c$  is the tool-chip contact length (m),  $b_{1T}$  is the true chip width (m) (Chap. 3).

The tool-chip contact length calculates as [13]

$$l_c = t_{1T} \zeta^{1.5} \quad (\text{A.17})$$

where  $t_{1T}$  is the true uncut chip thickness (m) [7] (Chap. 3).

The true uncut chip thickness and the true chip width depend on the configuration of the projection of the cutting edge into the main reference plain (Chapter 2). Formulae to calculate  $t_{1T}$  and  $b_{1T}$  for various configuration are presented in Chapter 3 [13, 17].

Power spent due to friction at the tool-workpiece interface calculates as

$$P_{fF} = F_{fF} v \quad (\text{A.18})$$

where  $F_{fF}$  is the friction force on the tool—workpiece interface

$$F_{fF} = 0.625 \tau_y \rho_{ce} l_{ac} \sqrt{\frac{Br}{\sin \alpha^*}} \quad (\text{A.19})$$

where  $\tau_y$  is the shear strength of the tool material ( $\text{N/m}^2$ ),  $\rho_{ce}$  is the radius of the cutting edge (m),  $\alpha^*$  is the normal flank angle ( $^\circ$ ), and  $l_{ac}$  is the length of the active part of the cutting edge (the length of the cutting edge engaged in cutting) (m).

The most common case of machining is when the cutting insert has the tool cutting edge angle  $\kappa_r$  and the tool minor cutting edge angle  $\kappa_{r1}$  and is made with a

nose radius  $r_n$  and set so that the depth of cut  $d_w$  is greater than the nose radius. If the following relationships are justified:

$$d_w \geq r_n (1 - \cos \kappa_r), \quad f \leq 2r_n \sin \kappa_{r1} \quad (\text{A.20})$$

then

$$l_{ac} = r_n \left( 0.018 \kappa_r + \frac{r_n + \cos \kappa_r}{\sin \kappa_r} \right) \quad (\text{A.21})$$

$Br$  is the Briks similarity criterion [13, 17],

$$Br = \frac{\cos \gamma_n}{\zeta - \sin \gamma_n} \quad (\text{A.22})$$

where  $\gamma_n$  is the normal rake angle ( $^\circ$ ).

The power spent in the formation of new surfaces  $P_{ch}$  calculates as the product of the energy required for the formation of one shear plane and the number of shear planes formed per second, i.e.,

$$P_{ch} = E_{fr} \cdot f_{cf} \quad (\text{A.23})$$

where  $f_{cf}$  is the frequency of chip formation, i.e. the number of shear planes formed per second, and  $E_{fr}$  is the energy of fracture per one shear plane.

The frequency of chip formation determines how many shear planes form per one second of machining time. This frequency depends primarily on the work material and on the cutting speed as discussed by Astakhov [17]. Figure A.12 provides some data for common work materials.

The work of fracture per a shear plane is

$$E_{fr} = E_{fr-u} \cdot A_{fr} \quad (\text{A.24})$$

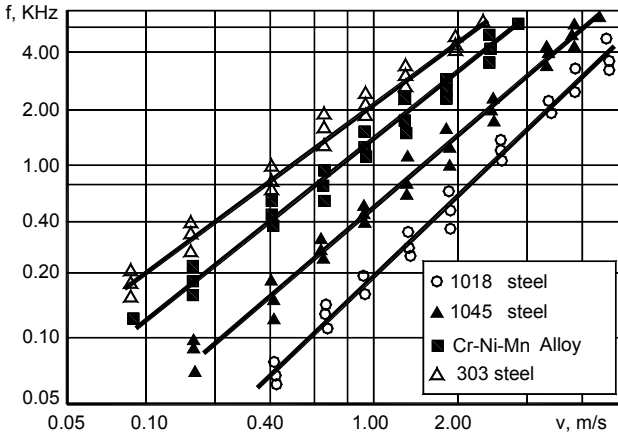
where  $E_{ch}$  the cohesive energy ( $\text{J}/\text{m}^2$ ) [19], and  $A_{ch}$  is the area of fracture ( $\text{m}^2$ ).

The area of fracture is the area of the shear plane determined as

$$A_{fr} = L_{sh} \cdot b_{1T} \quad (\text{A.25})$$

where the length of the shear plane  $L_{sh}$  is calculated as

$$L_{sh} = \frac{t_{1T}}{\sin \text{arc tan } Br} \quad (\text{A.26})$$



**Fig. A.12.** Effect of the cutting speed on the frequency of chip formation (after Atakhov [17])

Equations A.12 and A.13 do not account for the influence of the minor cutting edge. An analysis of a great body of the experimental results and the results obtained by Zorev [3] and Astakhov [7,10] showed [20] that when the tool minor cutting edge angle  $30^\circ \leq \kappa_{r1} \leq 45^\circ$  then the total power should be increased by 14%, when  $15^\circ \leq \kappa_{r1} < 30^\circ$  – by 17%, when  $10^\circ \leq \kappa_{r1} < 15^\circ$  – by 20%, and when  $\kappa_{r1} < 10^\circ$  – by 23%.

Table A.1 shows an example of the results of calculations using the proposed practical methodology as well as the total power required by the cutting system  $P_{Tot}$ .

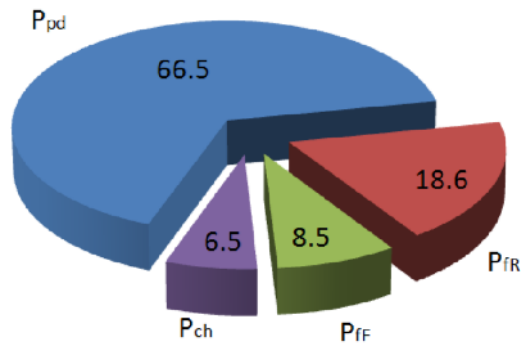
Figures A.13 and A14 show the relative impact of the discussed energies on the cutting force in the machining of steel 5210 and aluminum 2420 obtained using the discussed methodology of the cutting force assessment. Table A.2 shows the data used in the calculations. The major advantage of the proposed methodology is that it allows not only calculating the total power and thus the cutting force, but also provides a valuable possibility to analyze the energy partition in the cutting system.

The results obtained using the discussed methodology are valid for new tools (a fresh cutting edge of a cutting insert). Tool wear significantly increases the cutting force. For steel E52100,  $VB_B=0.45$  mm causes 2.0–2.5 times increase in the cutting force when no plastic lowering of the cutting edge [21] occurs (for cutting speeds 1 and 1.5 m/s) and 3.0–3.5 increase when plastic lowering is the case (for cutting speeds 3 and 4 m/s).

The results show that the power required for the plastic deformation of the layer being removed in its transformation into the chip is the greatest. Therefore, the major objective in the selection of the tool optimum geometry is to reduce this power and thus assure cutting with minimum plastic deformation of the layer being removed. This results in increased tool life and improved integrity of the machined surface. Obviously, this objective is achieved concurrently with the selection of the optimal machining regime.

**Table A.1.** Example of calculations: Work materials –Aluminum alloy 2024 T6 (90.7–94.7%Al, 3.8–4.8%Cu, 1.2–1.8%Mg, 0.3–0.9%Mn), Hardness HB 125; Tensile strength, ultimate – 185MPa , Tensile strength, yield – 86MPa, elongation at break – 5%, Shear strength 125MPa,  $K=0.220\text{GPa}$ ,  $n=0.16$ ; Tool – standard inserts SNMG 432-MF2 TP2500 Materials Group 4 (SECO Tools) installed into a tool holder 453-120141 R1-1 (Sandvik). The tool-in-machine tool geometry parameters are: the tool cutting edge angle =  $45^\circ$ , tool minor cutting edge angle =  $45^\circ$ , nose radius = 1mm, radius of the cutting edge = 0.3mm, normal flank angle =  $7^\circ$ , the normal rake angle =  $-7^\circ$

Cutting Speed (m/s)	Feed (mm/rev)	Depth of cut (mm)	CCR	$P_{pd}$ (KW)	$P_{fR}$ (KW)	$P_{pd} + P_{fR}$ (KW)	$P_{Tot}$ (W)
1	0.45	4	4.96	1.242	0.284	1.526	1.596
3	0.45	4	3.84	1.702	0.539	2.241	2.595
5	0.45	4	2.65	1.954	0.746	2.700	3.270
7	0.45	4	1.92	1.716	0.889	2.605	3.458
3	0.75	4	2.82	2.093	0.758	2.851	3.544
3	0.50	3	3.75	1.397	0.439	1.836	2.290
3	0.50	2	3.82	0.940	0.291	1.231	1.539
3	0.30	4	3.94	1.169	0.366	1.535	1.984

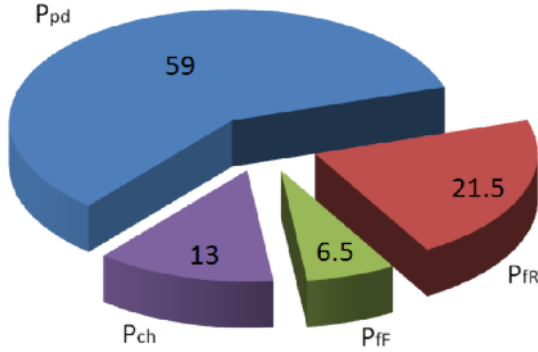


**Fig. A.13.** Relative impact of the powers on the cutting force for steel 52100

Although the power required for the plastic deformation is the greatest in machining ductile materials, its relative impact lessens with the cutting speed. The greater the cutting speed, the greater powers spent on the rake and flank faces of the cutting tool. When the cutting speed is 1m/s, the power of the plastic deformation,  $P_{pd}$  is 67% while the power spent at the tool-chip interface,  $P_{fR}$  is 18% and the power spent at the tool-workpiece interface,  $P_{ff}$  is 9%. When the cutting speed is 4 m/s then  $P_{pd}$  is 45%,  $P_{fR}$  is 25, and  $P_{ff}$  is 22%, i.e., the sum of powers spent on the tool-chip and tool-workpiece interfaces is greater than the power spent



for the plastic deformation. The power spent in the formation of new surfaces  $P_{ch}$  is 6% in both considered case although the frequency of chip formation is much greater when  $v = 4\text{m/s}$ .



**Fig. A.14.** Relative impact of the powers on the cutting force for aluminum 2024

**Table A.2.** Data for 52100 steel and 2024 aluminum used in the calculations

Variable	Symbol	Unit	Value (St52100)	Value (Al 2024)
Depth of cut	$d_w$	m	5.00E-03	4.00E-03
Cutting feed per revolution	$f$	m/rev	2.00E-04	7.50E-04
Strength coefficient	$K$	$\text{N/m}^2$	1.34E+09	2.20E+08
Hardening exponent	$n$		2.50E-01	1.60E-01
Chip compression ratio	$\zeta$		3.1	2.82E+00
Cutting speed	$v$	m/s	1.50E+00	3.00E+00
Ultimate tensile strength of the work material	$\sigma_{UTS}$	$\text{N/m}^2$	8.50E+08	1.85E+08
Tool nose radius	$r_n$	m	1.00E-03	1.00E-03
Tool cutting edge angle	$\kappa_r$	rad	7.85E-01	7.85E-01
Normal rake angle	$\gamma_n$	rad	-1.22E-01	-1.22E-01

**Table A.2.** (Continued)

Radius of the cutting edge,	$\rho_{ce}$	m	5.00E-05	1.00E-04
Shear strength of the work material	$\sigma_y$	N/m <sup>2</sup>	5.20E+08	1.25E+08
Normal flank angle	$\alpha_n$	rad	1.22E-01	1.22E-01
Cohesive energy per unit fracture area	$E_{fr-u}$	J/m <sup>2</sup>	4.00E+04	8.00E+03
Frequency of chip formation	$f_{cr}$	Hz	1.60E+03	6.20E+03

## References

- [1] Boothroyd G, Knight WA (2006) Fundamentals of machining and machine tools, Third ed. CRC, Boca Raton
- [2] Usachev YG (1915) Phenomena occurring during the cutting of metals, (in Russian). Izv. Petrogradskogo Politechnicheskogo Inst. XXIII(1):321–338
- [3] Zorev NN (1966) Metal Cutting Mechanics. Pergamon Press: Oxford
- [4] Shaw MC (2004) Metal Cutting Principles, 3rd Edition. University Press, Oxford
- [5] Sreejith PS, Ngoi BKA (2000) Dry machining: machining of the future. J. of Mat. Proc. Tech. 101:287–291
- [6] DeVries WR (1992) Analysis of material removal processes, New York: Springer-Verlag
- [7] Altintas, Y. (2000) Manufacturing automation. Metal cutting mechanics, machine tool vibrations, and cnc design. Cambridge University Press, New York
- [8] Anselmetti B, Chep A, Mognol P (1995) Minimal database for the cutting parameters in con manufacturing systems. Int. Journal of Computer Integrated Manuf. 8(4):277–285
- [9] Yoon MC, Kim YG (2004) Cutting dynamic force modelling of endmilling operation. J. of Mat. Proc. Tech. 155-156:1383-1389
- [10] Konig W, Langhammer K, Schemmel V (1972) Correlations between cutting force components and tool wear. Annals of the CIRP 21(1):19–20
- Chang, TC, Wysk RA (1984) An Introduction to automated process planning systems. Prentice Hall, Englewood Cliffs, NJ
- [11] Stenphenson DA, Agapiou JS (1996) Metal Cutting Theory and Practice, Marcel Dekker, New York
- [12] Astakhov VP (2006) Tribology of metal cutting. Elsevier, London:
- [13] Ivester RW (2004) Comparison of machining simulations for 1045 steel to experimental measurements. SME Paper TPO4PUB336:1–15

- [14] Astakhov, VP, Shvets SV (2001) A novel approach to operating force evaluation in high strain rate metal-deforming technological processes. *J. of Mat. Proc. Tech.* 117(1-2):226–237
- [15] Astakhov VP, Xiao X (2008) A methodology for practical cutting force evaluation based on the energy spent in the cutting system *Machining Science and Technology* 12:325–347
- [16] Astakhov VP (1998/1999) *Metal cutting mechanics*, Boca Raton, FL: CRC Press
- [17] Astakhov, VP, Shvets S (2004) The assessment of plastic deformation in metal cutting. *J. of Mat. Proc. Tech.* 146:193–202
- [18] Shet C., Chandra N. (2002) Analysis of energy balance when using cohesive zone models to simulate fracture process. *ASME J. of Eng. Mat. and Tech.* 124(4):440–450
- [19] Astakhov VP, Outeiro JC (2008) *Metal cutting mechanics, finite element modeling*. In Davim PJ(ed) *Machining: fundamentals and recent advances*, Springer: London
- [20] Astakhov VP (2004) The assessment of cutting tool wear. *Int. J. of Mach. Tools and Manuf.* 44:637–647

## Appendix B

---

### ANSI and ISO Turning Indexable Inserts and Holders

*What you see is what you get.*

Flip Wilson, Term borrowed by computer engineers  
abbreviated to WYSIWYG

Comedian and television actor, starred in The Flip Wilson Show (1933–1998)

**Abstract.** This appendix aims to help specialists in tool design and end users to make proper selection of the standard cutting inserts and tool holders. It walks a potential reader through particularities of ISO and ANSI standards, explaining differences between these standards and clarifying specific issues. It points out important discrepancies between these standards and their interpretations found in the catalogs of tool manufacturers. Examples provided in this appendix helps one to understand the selection process and its results clearly.

#### B.1 Indexable Inserts

Cutting tool nomenclatures are defined by ANSI and ISO standards for indexable (cutting) inserts and tool holders. These standards represent the inserts and holders in certain codes consisting of letters and numbers. Those code letters and numbers can be deciphered to reveal a wealth of information about indexable inserts.

Tool users are exposed regularly to various indexable-insert nomenclature and identification codes. For many who try to find the right tool for their job, these identification systems can be a confusing assortment of letters and numbers. And with the increasing use of superhard (for example, PCD, and PCBN) cutting tools, the tool nomenclatures have evolved still further. Polycrystalline cutting tools often have unique identifying codes that are supplier-dependent. These only add to the size and scope of an already extensive string of identification code letters and numbers.

Most of the world's insert manufacturers use either the American National Standards Institute (ANSI) indexable-insert identification system or the International Organization of Standards (ISO) system (ISO1832: 2004). The ANSI

system is confined mainly to the United States and is available as ANSI B212-4. Most of the rest of the world uses the ISO identification system, although it is used in the United States as well. Some European and Asian cutting tool suppliers use ISO codes in their U.S. sales efforts, and U.S. tool exporters often code their products in ISO standard for overseas sales and distribution. This global distribution of cutting tools makes it important to understand both systems.

**B.1.1 ANSI Code**

The current ANSI code consists of up to 10 positions; each position defines a characteristic of the insert in the following order: 1 – shape; 2 – clearance; 3 – tolerance class; 4 – type; 5 – size; 6 – thickness; 7 – cutting-point configuration; 8 – edge preparation; 9 – hand; 10 – facet size. Figure B.1 shows an example of the ANSI indexable insert code.

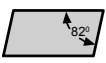




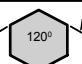
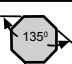






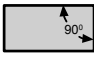
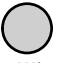



**Fig. B.1.** Example of the ANSI code for an indexable insert

*B.1.1.1 Shape*

A letter symbol is used to identify the shape. Insofar as possible, this letter is descriptive of the shape, as shown in Table B.1.

**Table B.1.** Shape

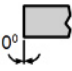
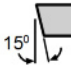
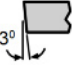
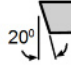

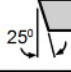
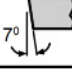


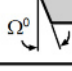
SHAPE			
<p style="font-size: 1.5em; font-weight: bold;">A</p>  <p>Parallelogram</p>	<p style="font-size: 1.5em; font-weight: bold;">E</p>  <p>Diamond</p>	<p style="font-size: 1.5em; font-weight: bold;">M</p>  <p>Diamond</p>	<p style="font-size: 1.5em; font-weight: bold;">S</p>  <p>Square</p>
<p style="font-size: 1.5em; font-weight: bold;">B</p>  <p>Parallelogram</p>	<p style="font-size: 1.5em; font-weight: bold;">H</p>  <p>Hexagon</p>	<p style="font-size: 1.5em; font-weight: bold;">O</p>  <p>Octagon</p>	<p style="font-size: 1.5em; font-weight: bold;">T</p>  <p>Triangle</p>
<p style="font-size: 1.5em; font-weight: bold;">C</p>  <p>Diamond</p>	<p style="font-size: 1.5em; font-weight: bold;">K</p>  <p>Parallelogram</p>	<p style="font-size: 1.5em; font-weight: bold;">P</p>  <p>Pentagon</p>	<p style="font-size: 1.5em; font-weight: bold;">V</p>  <p>Diamond</p>
<p style="font-size: 1.5em; font-weight: bold;">D</p>  <p>Diamond</p>	<p style="font-size: 1.5em; font-weight: bold;">L</p>  <p>Rectangle</p>	<p style="font-size: 1.5em; font-weight: bold;">R</p>  <p>Round 360°</p>	<p style="font-size: 1.5em; font-weight: bold;">W</p>  <p>Trigon</p>

*B.1.1.2 Clearances (Flank Angles)*

The second position is a letter denoting the relief angles. These angles are the differences from 90° measured in a plane normal to the cutting edge generated by

the angle between the flank and top surface of the insert. Table B.2 shows the meaning of code letters.

**Table B.2.** Flank (clearance) angles

CLEARANCE	
N 	D 
A 	E 
B 	F 
C 	G 
P 	O 

#### *B.1.1.3 Tolerance Class*

The third position is a letter that indicates the tolerances that control the indexability of the insert. Tolerances specified do not imply the method of manufacture. Dimensions are established prior to supplemental edge or coating modification. Letters for tolerances are shown in Table B.3.

#### *B.1.1.4 Type*

The fourth position is a letter to show differences in design not specifically provided for in the other sequence positions. The most common differences are the existence of fixing holes, countersinks, and special features on rake surfaces as shown in Table B.4. A space may be used after the fourth position to separate the shape-describing portion from the following dimensional description of the insert and is not to be considered a position in the standard description.

#### *B.1.1.5 Size*

##### *Regular Polygon and Diamond (Rhombic) Inserts*

The fifth position is a significant one- or two-digit number indicating the size of the inscribed circle (I.C.) for all inserts having a true I.C. such as Round, Square, Triangle, Trigon, Pentagon, Hexagon, Octagon, and Diamond. This position designates the number of eighths of an inch in the nominal size of the I.C. and will be a one- or two-digit number when the number of eighths of an inch in the I.C. is a whole number. It will be a two-digit number carried to one decimal place when it is not a whole number. (For examples, see Table B.5, Odd Numbers: 0.5, round up; Even Numbers: 0.5 round down).

**Table B.3.** Letters for tolerances

<b>TOLERANCE CLASS</b>						
				VALID FOR SHAPE D ONLY		
Tolerance on Dimensions (± from nominal)				IC	A	B
					Class	Class
					J, K, L, M, N	M, N
Tolerance Letter	Dimension			7/32	0.002	0.004
	B	A	T			
A	0.0002	0.0010	0.001	1/4	0.002	0.004
B	0.0002	0.0010	0.005	5/16	0.002	0.004
C	0.0005	0.0010	0.001	3/8	0.002	0.004
D	0.0005	0.0010	0.005	1/2	0.003	0.006
E	0.0010	0.0010	0.001	5/8	0.004	0.007
F	0.0002	0.0005	0.001	3/4	0.004	0.007
G	0.0010	0.0010	0.005	VALID FOR SHAPE V ONLY		
H	0.0005	0.0005	0.001	IC	A	B
J	0.0002	*	0.001		Class	Class
K	0.0005	*	0.001		J, K, L, M, N	M, N
L	0.010	*	0.001	7/32	0.002	0.004
M	*	*	0.005	1/4	0.002	0.004
U	*	*	0.005	5/16	0.002	0.004
N	*	*	0.001	3/8	0.002	0.004
				1/2	0.003	0.006
				5/8	0.004	0.007
				3/4	0.004	0.007

\* see charts below

*Rectangles or Parallelograms*

On rectangle and parallelogram inserts, the width and length dimensions are used in place of the I.C. A two-digit number is necessary because these do not have an inscribed circle.

The first digit indicates the number of eighths of an inch in the width and the second digit indicates the number of fourths of an inch in the length of the insert.

*Rectangles or Parallelograms*

On rectangle and parallelogram inserts, the width and length dimensions are used in place of the I.C. A two-digit number is necessary because these do not have an inscribed circle.

The first digit indicates the number of eighths of an inch in the width and the second digit indicates the number of fourths of an inch in the length of the insert.

Table B.4. Letters for insert type

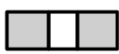
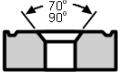

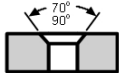
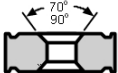
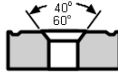
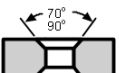
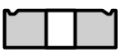
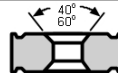


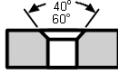

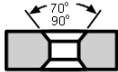
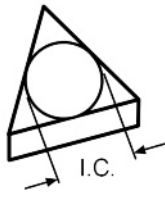
TYPE		
<p><b>A</b></p>  <p>With hole, without chip grooves</p>	<p><b>H</b></p>  <p>With hole, one countersink (70°-90°) and chip groove on one rake face</p>	<p><b>R</b></p>  <p>Without hole, with chip grooves on one rake face</p>
<p><b>B</b></p>  <p>With hole, without chip grooves, and one countersink (70°-90°)</p>	<p><b>J</b></p>  <p>With hole, two countersinks (70°-90°) and chip grooves on two rake faces</p>	<p><b>T</b></p>  <p>With hole, one countersink (40°-60°) and chip groove on one rake face</p>
<p><b>C</b></p>  <p>With hole, without chip grooves, and two countersinks (70°-90°)</p>	<p><b>M</b></p>  <p>With hole and chip groove on one rake face</p>	<p><b>U</b></p>  <p>With hole, two countersinks (40°-60°) and chip grooves on two rake faces</p>
<p><b>F</b></p>  <p>Without hole, with chip grooves on two rake faces</p>	<p><b>N</b></p>  <p>Without hole, without chip grooves</p>	<p><b>W</b></p>  <p>With hole, without chip grooves, and one countersink (40°-60°)</p>
<p><b>G</b></p>  <p>With hole, with chip grooves on two rake faces</p>	<p><b>Q</b></p>  <p>With hole, without chip grooves, and two countersinks (70°-90°)</p>	<p><b>X</b></p> <p>With dimensions or detailed explanation, a sketch or additional specifications</p>

Table B.5. Numbers for the fifth position

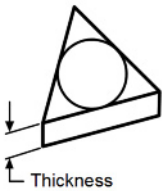
SIZE (I.C.)	
 <p>For equal sided inserts this indicates the inscribed circle (I.C.) in 1/8 of an inch.</p>	<p>Examples:</p> <ul style="list-style-type: none"> <li>1/8" = 1</li> <li>5/32" = 1.2</li> <li>3/16" = 1.5</li> <li>7/32" = 1.8</li> <li>1/4" = 2</li> <li>5/16" = 2.5</li> <li>3/8" = 3</li> <li>1/2" = 4</li> <li>5/8" = 5</li> <li>3/4" = 6</li> <li>7/8" = 7</li> <li>1" = 8</li> <li>1-1/4" = 10</li> </ul>
<p>For rectangles and parallelograms two digit are necessary</p> <p>1st digit = number of 1/8" in width</p> <p>2nd digit = number of 1/4" in length</p>	



*B.1.1.6 Thickness*

The sixth position is a significant one- or two-digit number indicating the number of sixteenths of an inch in the thickness of the insert. As shown in Table B.6, this position will be a one-digit number when the number of sixteenths of an inch in the thickness is a whole number. It will be a two-digit number carried to one decimal place when it is not a whole number.

**Table B.6.** Number for the sixth position

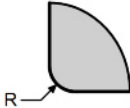
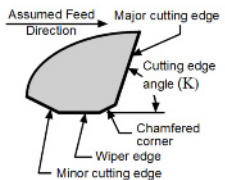
THICKNESS	
	<p>Examples:</p> <p>1/16" = 1</p> <p>5/64" = 1.2</p> <p>3/32" = 1.5</p> <p>1/8" = 2</p> <p>5/32" = 2.5</p> <p>3/16" = 3</p> <p>7/32" = 3.5</p> <p>1/4" = 4</p> <p>5/16" = 5</p> <p>3/8" = 6</p> <p>7/16" = 7</p> <p>1/2" = 8</p> <p>9/16" = 9</p> <p>5/8" = 10</p>
<p>This indicates the insert in 1/16 of an inch.</p> <p>Measured from:</p> <p>Cutting edge to opposite pad on inserts types F, G, J, &amp; U</p> <p>Cutting edge to bottom on types H, M, R, &amp; T</p> <p>Top to bottom on types A, B, C, N, O &amp; W</p>	

*B.1.1.7 Cutting-point Configuration*

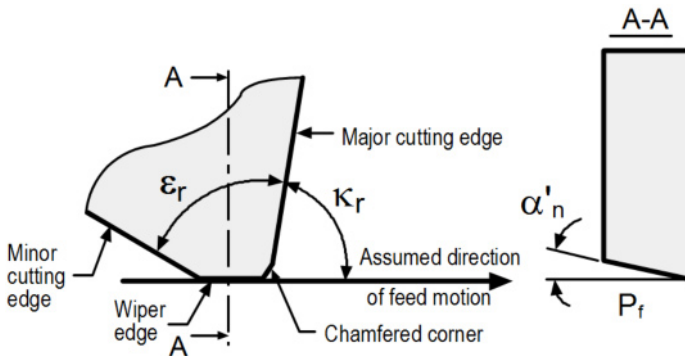
The cutting point configuration, indicated by the seventh position, will be shown by either a significant number indicating a radius, tangent to the adjacent sides, or two letters indicating the details of the primary facet as indicated in Table B.7. In the case of a radius, the number designates the number of sixty-fourths of an inch in the radius as shown in Table B.7. In the case of a facet, two letters will be used. The first designates the facet angle and the second designates the facet clearance angle as shown above. Secondary facets and radii in place of secondary facets are not defined by this standard and shall be manufacturer's standard.

One should clearly realize that the insert corner radius is a very critical dimension as CNC programs are written around a specific insert nose radius. As a result, if a nose radius changes, the corresponding corrections should be made to the CNC program on the machine (line, manufacturing cell, etc.). Moreover, when using ISO (metric) inserts, one must verify that the nose radius on the insert matches the nose radius used in the part program. If in doubt, convert the number to find the equivalent inch size. This conversion can be done by using the conversion factor of 1" = 25.4 mm.

**Table B.7.** Numbers and letters for the seventh position

<b>CUTTING POINT</b>										
 <p>This indicates the form of the cutting point in 1/64 of an inch for those with radius.</p> <p>Examples:</p> <p>0.002" = 0            0.004" = 0.2            0.008" = 0.5            1/64" = 1            1/32" = 2            3/64" = 3            1/16" = 4            5/64" = 5            3/32" = 6            7/64" = 7            1/8" = 8            5/32" = 10            3/16" = 12            7/32" = 14            1/4" = 16            any other = x</p>	<p><b>DP</b> For those with a facet</p> <p>Facet Angle (K) 1st letter            A = 45°            D = 60°            E = 75°            G = 87°            P = 90°            Z = any other edge angle</p>  <p>Facet Clearance (primary facet) 2nd letter</p> <table border="1" style="width: 100%; text-align: center;"> <tr> <td>A = 3°</td> <td>B = 5°</td> <td>C = 7°</td> </tr> <tr> <td>D = 15°</td> <td>E = 20°</td> <td>F = 25°</td> </tr> <tr> <td>G = 30°</td> <td>N = 0°</td> <td>P = 11°</td> </tr> </table> <p>Z = any other</p>	A = 3°	B = 5°	C = 7°	D = 15°	E = 20°	F = 25°	G = 30°	N = 0°	P = 11°
A = 3°	B = 5°	C = 7°								
D = 15°	E = 20°	F = 25°								
G = 30°	N = 0°	P = 11°								

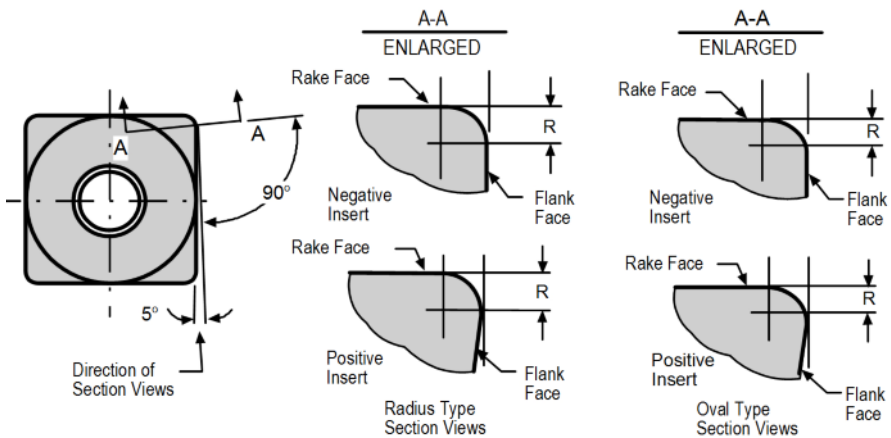
According to ANSI B standard B212-4, the wiper edge is a part of the minor cutting edge as shown in Fig. B.2. Inserts with wiper edge may or may not have chamfered corners, depending on their type. The designation for indexable inserts gives no information as to whether the inserts have or do not have chamfered corners. For standardized inserts, this information is given in dimensional standards; for nonstandardized inserts, it is given in suppliers' catalogues. It is intended that all nose radii be essentially tangent to the included angle on both sides of the form.



**Fig. B.2.** Wiper edge is a part of the minor cutting edge

*B.1.1.8 Edge Preparation*

The eighth position shall be a letter. It shall define special conditions, such as edge treatment and surface finish, as shown in Table B.8. Figure B.3 shows the direction of measurement of hone (dimension  $R$ ) on the flank face. Although this figure shows only a square insert, the same edge preparation conditions apply for any shape insert. According to standard ANSI B212.4, the type of hone – oval or radius – is the manufacturers’ option. The latter have never being acknowledged in the literature on metal cutting even though a particular shape of hone together with its dimension  $R$  play an important role in the cutting process as discussed in the body of this book. Moreover, the standard does not specify the  $R$ -dimensions for any other than shown cross-sections. In other words, this dimension can vary over the nose radius and straight part of the major cutting edge depending upon the kinematics and the setup of the machine used for edge preparation.



**Fig. B.3.** Radius and oval types of the rounded cutting edge

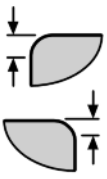







*B.1.1.9 Hand*

When the geometry dictates a handed condition, the letters “R”, “L”, or “N” must be used in the ninth position to indicate right hand, left hand, or neutral as show in Table B.9.

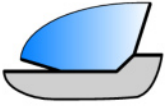
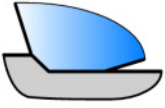

*B.1.1.10 Facet Size*

The tenth position is only used if there are letters in the seventh position. It shall be a significant number representing the nominal sixty-fourths of an inch in length of the primary facet as shown in Table B.10.

**Table B.8.** Letters for the eight position

EDGE PREPARATION		
 <p>Honed edge (Rounded Corner)</p> <p>A = 0.0005" to less than 0.003" B = 0.003" to less than 0.005" C = 0.005" to less than 0.007"</p>	<p>E = Rounded edge</p> 	<p>P = Double chamfered and rounded cutting edge</p> 
	<p>F = Sharp edge</p> 	<p>S = Chamfered and rounded cutting edge</p> 
	<p>J = Polished to 4 microinches AA. Rake face only</p> 	<p>P = Chamfered cutting edge</p> 
	<p>K = Double chamfered cutting edge</p> 	

**Table B.9.** Letters for the ninth position

HAND	
 <p>R = Right Hand</p>	 <p>L = Left Hand</p>
<p>N = Neutral</p> 	

### B.1.2 ISO Code

According to ISO 1832: 2004/2005, the designation code comprises nine symbols for designating the dimensions and other characteristics; the first seven symbols (symbols (1) to (7) shall be used in every designation. Symbols (8) and (9) may be used when necessary).

For tipped inserts in accordance with ISO 16462 and ISO 16463, the designation code comprises 12 symbols for designating the dimensions and other characteristics; symbols (1) to (7) as well as (11) and (12) shall be used in every designation. Symbols (8), (9), and (10) may be used when necessary. Symbols (11) and (12) shall be separated from symbols by a dash. In addition to the standardized designation for indexable inserts and for tipped inserts, a supplementary symbol (13), consisting of one or two characters, may be added by the manufacturer for

a better description of his product (e.g., different chip breakers), provided that this symbol is separated from the standardized designations by a dash and that it does not contain the letter specific for reference (8), (9), and (10).

**Table B.10.** Meaning of numbers in the tenth position

FACET SIZE	
	<p>This indicates the length of the primary facet in approximately 1/64 of an inch.</p> <p>Used only a double letter in the 7th position</p> <p>Examples:</p> <p>1/64" = 1            1/32" = 2            3/64" = 3            1/16" = 4            5/62" = 5            3/32" = 6            7/64" = 7            1/8" = 8            9/64" = 9            5/32" = 10</p>

Examples of metric and inch designation are shown in Fig. B.4. Each symbol defines a characteristic of insert according to Table B.11.

Metric designation	<b>T</b>	<b>P</b>	<b>G</b>	<b>N</b>	<b>16</b>	<b>03</b>	<b>08</b>	<b>E</b>	<b>N</b>	—	□
	1	2	3	4	5	6	7	8	9		13
Inch designation	<b>T</b>	<b>P</b>	<b>G</b>	<b>N</b>	<b>3</b>	<b>2</b>	<b>2</b>	<b>E</b>	<b>N</b>	—	□
	1	2	3	4	5	6	7	8	9		13

**Fig. B.4.** Examples of the ISO code for indexable inserts

*B.1.2.1 Symbols*

*Symbol for Insert Shape – Reference (1)*

Symbols for insert shape are shown in Table B.12.

*Symbol for Normal Clearance – Reference (2)*

Symbols for insert shape are shown in Fig. B.8.

**Table B.11.** Significance of the symbols constituting the ISO designation

<b>1</b>	Letter symbol identifying	Insert shape	} Compulsory symbols for indexable inserts	} Compulsory symbols for tipped inserts in accordance with ISO 16462 and ISO 16463, except as noted
<b>2</b>	Letter symbol identifying	normal clearance		
<b>3</b>	Letter symbol identifying	tolerance class		
<b>4</b>	Letter symbol identifying	fixing and/or chip breakers		
<b>5</b>	Number symbol identifying	insert size		
<b>6</b>	Number symbol identifying	insert thickness		
<b>7</b>	Letter or number symbol identifying	insert corner configuration		
<b>8</b>	Letter symbol identifying	cutting edge condition		
<b>9</b>	Letter symbol identifying	cutting direction		
<b>10</b>	Number symbol identifying	size of cutting edge condition		
<b>11</b>	Letter symbol identifying	style of tipped or solid cutting edge and number of tipped corners		
<b>12</b>	Letter or number symbol identifying	length of tipped cutting edge		
<b>13</b>	Manufacturer's symbol or cutting material designation in accordance with ISO 513			

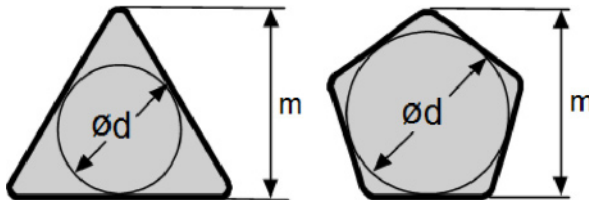
*Symbol for Tolerance Class – Reference (3)*

Symbols for insert shape are shown in Table B.13.

The dimensions concerned are  $d$  (nominal diameter of the inscribed circle of the insert),  $s$  (thickness of the insert), and  $m$ . For this last dimension, the three cases represented in Fig. B.5 through Fig. B.7 are distinguished.











Tolerances on  $d$  for tolerance classes J, K, L, M, N and U for inserts of shapes H, O, P, S, T, C, E, M, W, and R and tolerances on  $n$  for tolerance classes M, N, and U for inserts with an included angle of  $60^\circ$  or more, of shapes H, O, P, S, T, C, E, M, and W are shown in Table B.14.

In the case of rhombic inserts with an included angle of  $55^\circ$  (shape D) and  $35^\circ$  (shape V), the values for tolerance classes M and N on  $d$  and  $m$  are indicated in Table B.15.



**Fig. B.5.** Case 1. Inserts with an odd number of sides and rounded corners

**Table B.12.** Significance of the symbols for reference (1)

Type	Letter symbol	Description of shape	Included angle, $\epsilon_f$	Figure
I Equilateral and equiangular inserts	H	Hexagonal inserts	$120^0$	
	O	Octagonal inserts	$135^0$	
	P	Pentagonal inserts	$108^0$	
	S	Square inserts	$90^0$	
	T	Triangle inserts	$60^0$	
II Equilateral but not equiangular inserts	C	Rhombic inserts	$80^{0a}$	
	D		$55^{0a}$	
	E		$75^{0a}$	
	M		$86^{0a}$	
	V		$35^{0a}$	
	W	Trigon inserts	$80^{0a}$	
III Non-equilateral but equiangular inserts	L	Rectangular inserts	$90^{0a}$	
IV Non-equilateral and non-equiangular inserts	A	Parallelogram-shaped inserts	$85^{0a}$	
	B		$82^{0a}$	
	K		$55^{0a}$	
V Round inserts	R	Round inserts	-	
<sup>a</sup> The included angle considered is always the smaller angle				

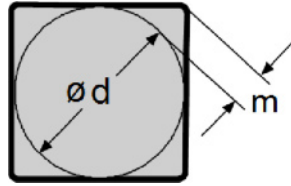


Fig. B.6. Case 2. Inserts with an even number of sides and rounded corners

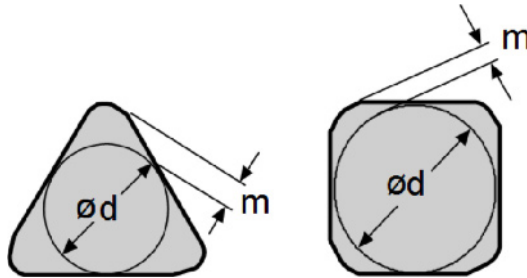


Fig. B.7. Case 3. Inserts with wiper edges

<b>Letter symbol</b>																					
For normal clearance, choose, from the symbol listed below, the one which corresponds to the major cutting edge (see the figure).																					
If (in spite of different clearances) all the cutting edges have to be used as major cutting edges, the symbol to be used for the designator of the normal clearance shall be the symbol applicable to the normal clearance of the longer cutting edge, which is also considered as the major cutting edge for the indication of the insert size (see reference ⑤).																					
	<table border="0"> <tr><td><b>A</b></td><td>- 3°</td></tr> <tr><td><b>B</b></td><td>- 5°</td></tr> <tr><td><b>C</b></td><td>- 7°</td></tr> <tr><td><b>D</b></td><td>- 15°</td></tr> <tr><td><b>E</b></td><td>- 20°</td></tr> <tr><td><b>F</b></td><td>- 25°</td></tr> <tr><td><b>G</b></td><td>- 30°</td></tr> <tr><td><b>N</b></td><td>- 0°</td></tr> <tr><td><b>P</b></td><td>- 11°</td></tr> <tr><td><b>O</b></td><td>- Other normal clearances requiring a special specification.</td></tr> </table>	<b>A</b>	- 3°	<b>B</b>	- 5°	<b>C</b>	- 7°	<b>D</b>	- 15°	<b>E</b>	- 20°	<b>F</b>	- 25°	<b>G</b>	- 30°	<b>N</b>	- 0°	<b>P</b>	- 11°	<b>O</b>	- Other normal clearances requiring a special specification.
<b>A</b>	- 3°																				
<b>B</b>	- 5°																				
<b>C</b>	- 7°																				
<b>D</b>	- 15°																				
<b>E</b>	- 20°																				
<b>F</b>	- 25°																				
<b>G</b>	- 30°																				
<b>N</b>	- 0°																				
<b>P</b>	- 11°																				
<b>O</b>	- Other normal clearances requiring a special specification.																				

Fig. B.8. Significance symbols for reference (2)

*Symbol for Fixing and/or for Chip Breakers – Reference (4)*

Symbols for fixing and/or for chip breakers are shown in Table B.16.



**Table B.13.** Tolerances 1

Let	Tolerances in millimeters			Tolerances in inches		
	<i>D</i>	<i>m</i>	<i>s</i>	<i>d</i>	<i>m</i>	<i>s</i>
<b>A<sup>a</sup></b>	±0.025	±0.005	±0.025	±0.001	±0.0002	±0.001
<b>F<sup>a</sup></b>	±0.013	±0.005	±0.025	±0.0005	±0.0002	±0.001
<b>C<sup>a</sup></b>	±0.025	±0.013	±0.025	±0.001	±0.0005	±0.001
<b>H</b>	±0.013	±0.013	±0.025	±0.0005	±0.0005	±0.001
<b>E</b>	±0.025	±0.025	±0.025	±0.001	±0.001	±0.001
<b>G</b>	±0.025	±0.025	±0.13	±0.001	±0.001	±0.005
<b>J<sup>a</sup></b>	From ±0.05 <sup>(b)</sup> to ±0.15	±0.005	±0.025	From ±0.002 <sup>(b)</sup> to ±0.006	±0.0002	±0.001
<b>K<sup>a</sup></b>	From ±0.05 <sup>(b)</sup> to ±0.15	±0.013	±0.025	From ±0.002 <sup>(b)</sup> to ±0.006	±0.0005	±0.001
<b>L<sup>a</sup></b>	From ±0.05 <sup>(b)</sup> to ±0.15	±0.025	±0.025	From ±0.002 <sup>(b)</sup> to ±0.006	±0.001	±0.001
<b>M</b>	From ±0.05 <sup>(b)</sup> to ±0.15	From ±0.08 <sup>(b)</sup> To ±0.2	±0.13	From ±0.002 <sup>(b)</sup> to ±0.006	From ±0.003 <sup>(b)</sup> to ±0.008	±0.005
<b>N</b>	From ±0.05 <sup>(b)</sup> to ±0.15	From ±0.08 <sup>(b)</sup> to ±0.2	±0.025	From ±0.002 <sup>(b)</sup> to ±0.006	From ±0.003 <sup>(b)</sup> to ±0.008	±0.001
<b>U</b>	From ±0.08 <sup>(b)</sup> to ±0.25	From ±0.13 <sup>(b)</sup> to ±0.38	±0.13	From ±0.003 <sup>(b)</sup> to ±0.01	From ±0.005 <sup>(b)</sup> to ±0.015	±0.005
<sup>a</sup> The tolerance classes normally apply to indexable inserts with wiper edges <sup>b</sup> The tolerance is dependent upon the insert size (see also Tables A.14 and A.15) and should be indicated for insert according to the corresponding dimensional standard						

*Symbols for Insert Size – Reference (5)*

Symbols for insert size are shown in Table B.17.









*Symbols for Insert Size – Reference (6)*

Symbols for insert size are shown in Table B.18. The thickness, *s*, of an insert is defined as the distance between the cutting edge of the corner and the opposing supporting surface of the insert as shown in Fig. B.9.

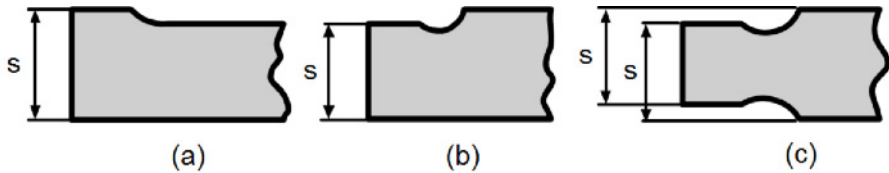
**Table B.14. Tolerances 2**

Diameter of inscribed circle <i>d</i>		Tolerances on <i>d</i>				Tolerances on <i>m</i>			
		Classes J, K, L, M, N		Class U		Classes M and N		Class U	
mm	in	mm	in	mm	in	mm	in	mm	in
4.76	3/16								
5.56	7/32								
6 <sup>a</sup>	-								
6.35	1/4	±0.05	±0.002	±0.08	±0.003	±0.08	±0.03	±0.13	±0.005
7.94	5/16								
8 <sup>a</sup>	-								
9.525	3/8								
10 <sup>a</sup>	-								
12 <sup>a</sup>	-								
12.7	1/2	±0.08	±0.003	±0.13	±0.005	±0.13	±0.005	±0.2	±0.008
15.875	5/8								
16 <sup>a</sup>	-								
19.05	3/4	±0.1	±0.04	±0.18	±0.007	±0.15	±0.006	±0.27	±0.011
20 <sup>a</sup>	-								
25 <sup>a</sup>	-								
25.4	1	±0.13	±0.005	±0.25	±0.01	±0.18	±0.007	±0.38	±0.015
31.75	1 1/4								
32 <sup>a</sup>	-	±0.15	±0.006	±0.25	±0.01	±0.2	±0.008	±0.38	±0.15

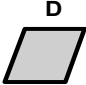

	H	O	P	S	T	H, E, M	W	H (tolerance on <i>d</i> only)
Shape of the insert concerned								

<sup>a</sup> Applies only for round inserts



**Fig. B.9. Thickness of an insert**

**Table B.17.** Tolerances 3

Diameter of inscribed circle, d		Tolerance on d		Tolerance on m		Shape of the insert concerned
mm	in	mm	in	mm	in	
5.56 6.35 7.94 9.525	7/32 1/4 5/16 3/8	±0.05	±0.002	±0.11	±0.004	
12.7	1/2	±0.08	±0.003	±0.15	±0.006	
15.875 19.05	5/8 3/4	±0.1	±0.004	±0.18	±0.007	
6.35 7.94 9.525	1/4 5/16 3/8	±0.05	±0.002	±0.16	±0.006	

*Symbols for Insert Size – Reference (7)*

Symbols for insert size are shown in Fig. B.10.

*B.1.2.2 Optional Symbols for Indexable Inserts*

*General*

The compulsory designation for indexable inserts other than specified in ISO 16462 and ISO 16463 comprises the seven symbols given in Section B.1.2.1. As stated above, references (8) and (9) may be used when necessary.

If only one symbol is needed (cutting edge condition or cutting direction), it shall occupy position (8). If both cutting edge condition and cutting direction are to be specified, the two symbols should occupant positions (8) and (9), respectively.

*Symbols for Cutting Edge Condition – Reference (8)*

These are given in Table B.19.

*Symbols for the Cutting Direction and the Application of the Insert (Direction of Feed Motion) – Reference (9)*


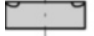
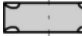
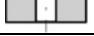










These are given in Table B.20.

*B.1.2.3 Additional Symbols for Tipped Inserts*

*General*

Symbols (11) and (12) shall be used for designating tipped inserts in accordance with ISO 16462 and ISO 16463. Symbol (10) may be used when necessary. Symbols (11) and (12) shall be separated from symbol (10) by a dash.

**Table B.16.** Symbols for reference (4)

Letter symbol	Fixing	Chip breakers <sup>a</sup>	Figure
<b>N</b>	Without fixing hole	Without chip breakers	
<b>R</b>		Chip breakers on one face only	
<b>F</b>		Chip breakers on both faces	
<b>A</b>	With cylindrical fixing hole	Without chip breakers	
<b>M</b>		Chip breakers on one face only	
<b>G</b>		Chip breakers on both faces	
<b>W</b>	With partly cylindrical fixing hole, 40–60° countersink on one side only	Without chip breakers	
<b>T</b>		Chip breakers on one face only	
<b>Q</b>	With partly cylindrical fixing hole, 40–60° countersink on both sides	Without chip breakers	
<b>U</b>		Chip breakers on both faces	
<b>B</b>	With partly cylindrical fixing hole, 70–90° countersink on one side only	Without chip breakers	
<b>H</b>		Chip breakers on one face only	
<b>C</b>	With partly cylindrical fixing hole, 70–90° countersink on both sides	Without chip breakers	
<b>J</b>		Chip breakers on both faces	
<b>X<sup>b</sup></b>	With dimensions or details requiring detailed explanation, a sketch, or additional specifications		—
<p><sup>a</sup> For the definition of chip breakers, see ISO 3002-1</p> <p><sup>b</sup> Non-equilateral inserts shall always be designated in reference (4) by X because the indication of width (measured perpendicularly on the major cutting edge or perpendicularly on the longer edge) and details concerning special features of construction are necessary</p> <p>The letter symbol X cannot be used for those insert shapes which are not defined under reference (1).</p>			

**Table B.17.** Symbols for reference (5)

Type	Number symbol
<p>I – II Equilateral inserts</p>	<p>In countries using the metric system, choose the values of the side length as the symbol of designation and disregard any decimals. If the resulting symbol has only one digit, it shall be preceded by a zero.</p> <p>EXAMPLE    Edge length                    15.5 mm                   Symbol of designation            15                   Edge length                            9.525                   Symbol of designation            09</p> <p>In countries using the Imperial (inch) system, choose the value of the inscribed circle as the symbol of designation The symbol is the numerator of the fraction measure in 1/8 in.</p> <p>1) It is a one-digit symbol when the numerator is a whole number</p> <p>EXAMPLE    Diameter of inscribed circle    1/2 in                   Symbol of designation            4 (1/2 = 4/8)</p> <p>2) It is a two-digit symbol when the numerator is not a whole number</p> <p>EXAMPLE    Diameter of inscribed circle    5/16 in                   Symbol of designation        2.5 (5/16 = 2,5/8)</p>
<p>III-IV Non- equilateral inserts</p>	<p>The symbol of designation for the insert size is always given for the major cutting edge or the longer cutting edge. The indication of other dimensions shall be made by means of sketch or detailed explanation, indicated in position 4 by the symbol X.</p> <p>In countries using the metric system, the symbol of designation is the length, disregarding any decimals</p> <p>EXAMPLE    Length of the main edge            19.5 mm                   Symbol of designation            19</p> <p>In countries using the Imperial (inch) system, the symbol of designation is the numerator of the fraction for the value in 1/4 in</p> <p>EXAPMPLE   Length of the main edge            3/4 in                   Symbol of designation            3</p>
<p>V Round inserts</p>	<p>In countries using the metric system, choose the values of the diameter as the symbol of designation and disregard any decimals.</p> <p>EXAMPLE    Insert diameter                        15.575 mm                   Symbol of designation            15</p> <p>For inserts having rounded metric diameter, the same rule is valid, combined with a special symbol at reference (7) (see Table B.19)</p> <p>In countries using the Imperial (inch) system, proceed as for equilateral inserts (types I – II).</p>

**Table B.18.** Symbols for reference (6)

Number symbol		
In countries using the metric system, take the numerical value of the thickness as the symbol for the insert thickness, disregarding any decimals. If the resulting symbol has only one digit, it shall be preceded by 0 (zero).		
EXAMPLE	Insert thickness	3,18 mm
	Symbol of designation	03
As an exception for inserts having thickness of 1.96 mm and 3.97 mm, in order to distinguish them from those having thickness 1.59 mm (symbol 01) and 3.18 mm (symbol 03), precede the digit by the letter T.		
EXAMPLE	Insert thickness	3.97 mm
	Symbol of designation	T3
In countries using the Imperial (inch) system, the symbol of designation for the insert thickness is the numerator of the fraction for the value in 1/16 in		
1) It is a one digit symbol when the numerator is the whole number		
EXAMPLE	Insert thickness	1/8 in
	Symbol of designation	2 (1/8=2/16)
2) It is two-digit symbol when the numerator is not the whole number		
EXAMPLE	Insert thickness	3/32 in
	Symbol of designation	1.5 (3/32=1.5/16)

*Size of Cutting Edge Condition – Reference (10)**Maximum Symbol*

Maximum symbol is a five-digit number dependant of the cutting edge conditions.

*E = rounded*

A rounded cutting edge is shown in Fig. B.11. No coding of the size.

Example: SNMA150608E

*T = chamfered*

five-digit symbol

$b_\gamma$	-	T-land size in 1/100mm	three digit
$\gamma_b$	-	T-land angle	two digit.

Parameters  $b_\gamma$  and  $\gamma_b$  are shown in Fig. B.12 and the symbols for their designation are given in Table B.21.



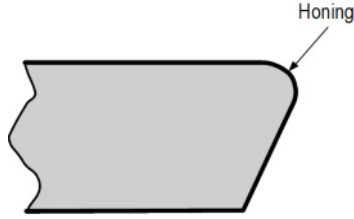








Fig. B.11. Illustration of a rounded cutting edge

Table B.19. Symbols for reference (8)

Letter symbol	Cutting edge condition	Figure
F	Sharp cutting edges	
E	Rounded cutting edges	
T	Chamfered cutting edges	
S	Chamfered and rounded cutting edges	
K	Double chamfered cutting edge	
P	Double chamfered and rounded cutting edge	

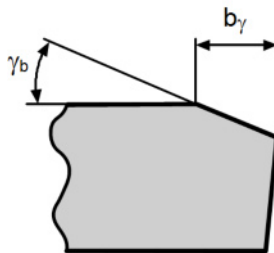


Fig. B.12. Illustration of a chamfered edge



EXAMPLE: SNMA150608T05020

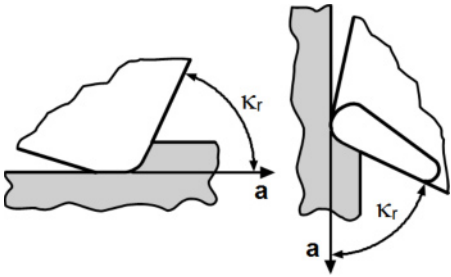
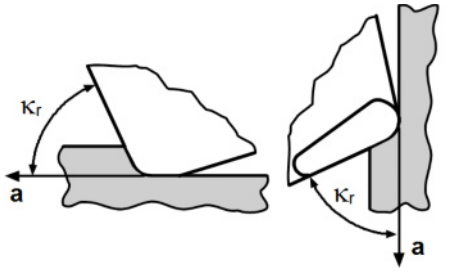
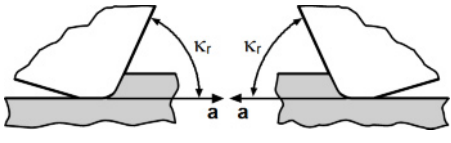
*S = chamfered and rounded*

five-digit symbol

- $b_\gamma$  - T-land size in 1/100mm      three digit
- $\gamma_b$  - T-land angle                      two digit.
- rounded                                      no code

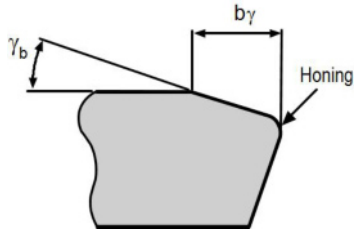
Parameters  $b_\gamma$  and  $\gamma_b$  are shown in Fig. B.13 and the symbols for their designation are given in Table B.22.

**Table B.20.** Symbols for reference (9)

Letter symbol	Corner type	Application of the insert	Figure
<b>R</b>	Right-hand insert	For non-equilateral and non-equiangular inserts and for all inserts with asymmetrical corners and/or asymmetrical chip breaker, permitting the use of the insert in only one direction of the feed motion	 <p style="text-align: center;">a – direction of feed motion</p>
<b>L</b>	Left-hand insert		 <p style="text-align: center;">a – direction of feed motion</p>
<b>N</b>	Neutral insert	For all inserts with symmetrical corners and symmetrical chip breaker, permitting the use of the insert in both directions of the feed motion	 <p style="text-align: center;">a – direction of feed motion</p>

**Table B.21.** Symbols for a chamfered edge

Symbol	$b_\gamma$ (mm)	Symbol	$\gamma_b$ (mm)
005	0.05	05	05°
010	0.10	10	10°
015	0.15	15	15°
020	0.20	20	20°
025	0.25	25	25°
030	0.30	30	30°
050	0.50		
070	0.70		
100	1.00		
150	1.50		
200	2.00		



**Fig. B.13.** Illustration of a chamfered and rounded cutting edge

EXAMPLE: SNMA150608S05020

*K = double chamfered*

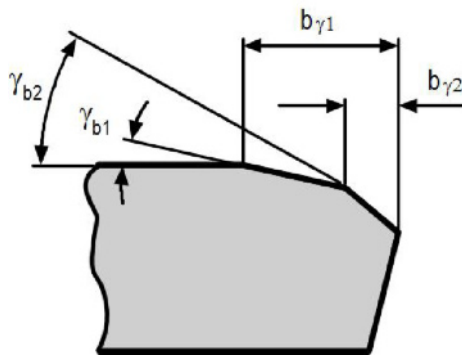
Five-digit symbol

- $b_{\gamma 1}$  – T-land size in 1/100mm      three digit
- $\gamma_{b1}$  – T-land angle      two digit.
- $b_{\gamma 2} \times \gamma_{b2}$  dependant on  $b_{\gamma 1} \times \gamma_{b1}$

**Table B.22.** Symbols for a chamfered and rounded edge

Symbol	$b_\gamma$ (mm)	Symbol	$\gamma_b$ (mm)
005	0.05	05	05°
010	0.10	10	10°
015	0.15	15	15°
020	0.20	20	20°
025	0.25	25	25°
030	0.30	30	30°
050	0.50		
070	0.70		
100	1.00		
150	1.50		
200	2.00		

Parameters  $b_{\gamma 1}$ ,  $b_{\gamma 2}$ ,  $\gamma_{b1}$  and  $\gamma_{b2}$  are shown in Fig. B.14 and the symbols for their designation are given in Table B.23.



**Fig. B.14.** Illustration of a double chamfered cutting edge

EXAMPLE: SNMA150608K15010

**Table B.23.** Symbols for a double chamfered cutting edge

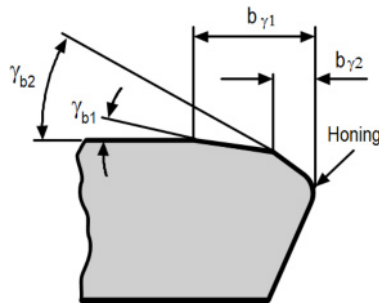
Symbol	$b_{\gamma_1}$ (mm)	$\gamma_{b1}$	$b_{\gamma_2}$ (mm)	$\gamma_{b2}$
05015	0.50	15 <sup>0</sup>	0.10	30 <sup>0</sup>
07015	0.70	15 <sup>0</sup>	0.15	30 <sup>0</sup>
10015	1.00	15 <sup>0</sup>	0.20	30 <sup>0</sup>
15010	1.50	10 <sup>0</sup>	0.25	30 <sup>0</sup>
20010	2.00	10 <sup>0</sup>	0.25	30 <sup>0</sup>

*P* = double chamfered and rounded

five-digit symbol

- $b_{\gamma_1}$  – T-land size in 1/100mm three digit
- $\gamma_{b1}$  – T-land angle two digit.
- $b_{\gamma_2} \times \gamma_{b2}$  dependant on  $b_{\gamma_1} \times \gamma_{b1}$
- rounded no code

Parameters  $b_{\gamma_1}$ ,  $b_{\gamma_2}$ ,  $\gamma_{b1}$  and  $\gamma_{b2}$  are shown in Fig. B.15 and the symbols for their designation are given in Table B.24.



**Fig. B.15.** Illustration of a double chamfered and rounded cutting edge

EXAMPLE: SNMA150608P15010

*Style of Tipped or Solid Cutting Edge and Number of Tipped Corners – Reference (11)*

Single digit letter symbol – see Table B.25.

Table B.26. Symbols for reference (11).

*Length of Tipped Cutting Edge – Reference (12)*

This symbol may appear on letter symbols A, B, C, D, G, H, J, K, L, M, N, P, Q, R, T, U, V, W, X, Y, Z contained in Table B.26.

There are two options:

Single digit letter symbol – see Table B.26. Designates the length of the cutting edge in comparison to the standard length.

or three-digit symbol if the tip length is not equal to with the standard length. When this is the case, the effective length shall be indicated as a three-digit number symbol which gives the length in 1/10 mm. If the tip length is smaller than 10,0 mm, the symbol shall be prefixed by zero(s) (0) (e.g. tipped cutting edge length 4.5 mm = 045; tipped cutting edge length 10.7 mm = 107).

**Table B.24.** Symbols for a double chamfered cutting edge

Symbol	$b_{\gamma_1}$ (mm)	$\gamma_{b1}$	$b_{\gamma_2}$ (mm)	$\gamma_{b2}$
05015	0.50	15°	0.10	30°
07015	0.70	15°	0.15	30°
10015	1.00	15°	0.20	30°
15010	1.50	10°	0.25	30°
20010	2.00	10°	0.25	30°

*Example B.1.*

*Problem:* Find the parameters of an insert SHMA-15068S05020-BL

*Solution:* Insert with 90° included angle (S), normal clearance angle 0° (N), tolerance class (M), with cylindrical fixing hole and no chip breakers (A), cutting edge length 17.875 mm (15), insert thickness 6.36 mm (06), corners radius 0<8 mm (08), cutting edge condition chamfered and rounded (S), T-land size 0.5 mm (050), T-land angle 20° (20), tipped on one side with two corners (B), tip length  $l_t = 3.00$  mm (L).

End of Example B.1.

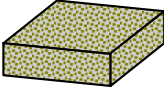
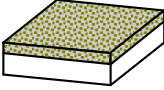
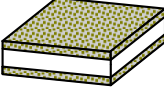
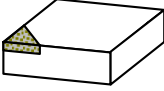
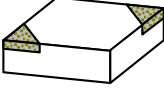
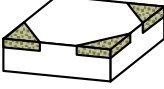
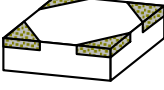
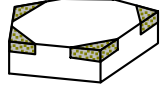
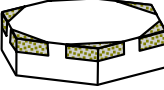
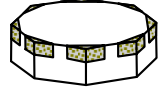
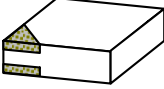
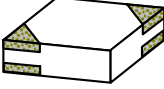
*Example B.2.*

*Problem:* Find the parameters of an insert SHMA-15068S05020-B045.

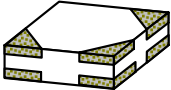
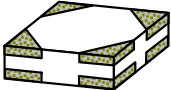
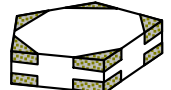


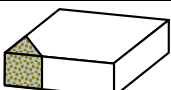
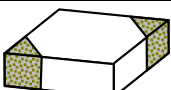


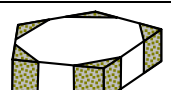

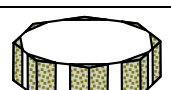
*Solution:* Insert with 90° included angle (S), normal clearance angle 0° (N), tolerance class (M), with cylindrical fixing hole and no chip breakers (A), cutting edge length 17.875 mm (15), insert thickness 6.36 mm (06), corners radius 0<8 mm (08), cutting edge condition chamfered and rounded (S), T-land size 0.5 mm (050), T-land angle 20° (20), tipped on one side with two corners (B), tip length  $l_t = 4.5$  mm (045).

End of Example B.2.

**Table B.25.** Symbols for reference (11)

Symbol	Picture	Description
S		Solid
F		Full face – one-sided
E		Full face – two-sided
A		Tipped – one-sided – one corner
B		Tipped – one-sided – two corners
C		Tipped – one-sided – three corners
D		Tipped – one-sided – four corners
G		Tipped – one-sided – five corners
H		Tipped – one-sided – six corners
J		Tipped – one-sided – eight corners
K		Tipped – two-sided – one corner
L		Tipped – two-sided – two corners

**Table B.25.** (Continued)

Symbol	Picture	Description
M		Tipped – two-sided – three corners
N		Tipped – two-sided – four corners
P		Tipped – two-sided – five corners
Q		Tipped – two-sided – six corners
R		Tipped – two-sided – eight corners
T		Tipped – full thickness – one corner
U		Tipped – full thickness – two corners
V		Tipped – full thickness – three corners
W		Tipped – full thickness – four corners
X		Tipped – full thickness – five corners
Y		Tipped – full thickness – six corners
Z		Tipped – full thickness – eight corners

**Table B.26.** Symbols for reference (11)

Symbol	Description	Cutting edge length $l_1$ (mm)
L	Long	See ISO 16482 and ISO 16483
S	Short	

## B.2 Tool Holders for Indexable Inserts (Single Point Tools)

The standard designation of tool holders and some interpretations of this designation taken by leading tool manufactures are considered in this section. The emphasis is placed only on the features that affect tool geometry while other parameters (for example, holders' dimensions, insert clamping mechanisms and hand) are briefly considered.

Standards ISO 5608:1995 Turning and copying tool holders and cartridges for indexable inserts – Designation defines the designation and dimensions of tool holders. The designation code comprises 10 symbols for the designation of dimensions and other characteristics of the tool and the insert, of which the first 9 symbols shall be used in any designation. The last symbol may be used when necessary. In addition to the standardized designation (Symbols in positions (1) to (10)), a supplementary symbol consisting of a maximum of three letters, and/or numbers may be added by the manufacturer for a better description of his products, on condition that this symbol is separated from the standardized designation by a dash and that it does not contain letters specified for position (10).

No addition to or extension of the code specified in this International Standard shall be made without consultation with Technical Committee ISO/TC 29 and its agreement. Rather than adding symbols not provided for in this system, it is preferable to add to the designation conforming with this International Standard all necessary explanations in detailed sketches or specifications.

The meaning of the nine compulsory symbols and one optional symbol constituting the code is as follows:

- (1) Letter symbol identifying the method of holding the insert.
- (2) Letter symbol identifying insert shape.
- (3) Letter symbol identifying tool style.
- (4) Letter symbol identifying insert normal clearance.
- (5) Letter symbol identifying hand of tool.
- (6) Number symbol identifying tool height (shank height of tool holders and height of cutting edge).
- (7) Number symbol identifying tool holder shank width or, for cartridges, the letter C followed by a letter symbol identifying the cartridge type.
- (8) Letter symbol identifying tool length.
- (9) Number symbol identifying indexable insert size.
- (10) Letter symbol indicating special tolerances.



Figure B.16 shows an example of tool holder code for ISO indexable insert.

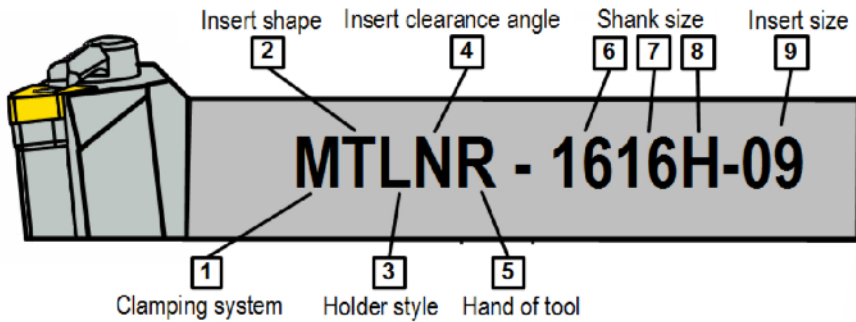


Fig. B.16. Example of the standard code for a tool holder

Although various tool manufacturers should use the same structure of the designation code for tool holders, the meaning of the letters and numbers included are not the same as defined by Standards ISO 5608:1995. Moreover, the designations codes are often different for ANSI and ISO inserts and the differences are more than simple in/mm conversions. These codes as presented in the catalogs of leading tool manufacturers are not strictly clear so some experience is required to understand the real meaning of such codes.

**B.2.1 Symbol for the Method of Holding Horizontally Mounted Insert – Reference Position (1)**

The first position has the same meaning for various tool manufactures, namely, it defines (generically) a type of insert clamping system (a method of holding inserts in the holder’s pocket) used. Table B.27 shows the symbols defined by the standard while Fig. B.17 present example of practical realization of various holding methods.

Table B.27. Symbols for holding method

Letter symbol	Method of holding the insert
C	Top clamping (insert without hole)
M	Top and hole clamping (insert with hole)
P	Hole clamping (insert with hole)
S	Screw clamping through hole (insert with hole)

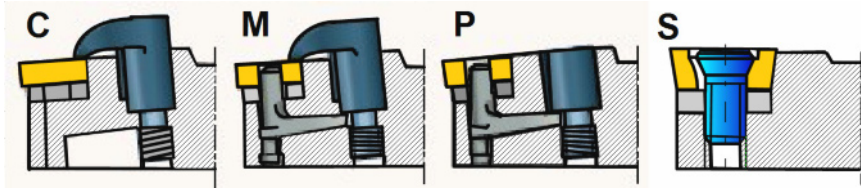


Fig. B.17. Examples of realization of holding methods

Tool manufacturers add some additional designation symbols particular to their design of insert holding methods and mechanisms. For example, Sandvik Coromant uses symbol D to designate the top and hole clamping (the so-called rigid clamping); Kennametal uses symbol D to designate KENCLAMP, which is a combination of the top and screw clamping; Seco Tools introduces symbol T which designates T-Lock clamping; ISCAR uses symbol W to designate a top wedge lock clamping, etc.

### B.2.2 Symbol for Insert Shape – Reference Position (2)

This letter symbol should be the same as the first letter symbol of the insert code – see Fig. B.1, Sect. B.1.1.1 and Fig. B.4 and Sect. B.1.2.1.1.

### B.2.3 Symbol for Tool Style – Reference Position (3)

Tool style position relates not only to a particular tool holder but rather to the assembly “tool holder-insert.” Figure B.18 shows the symbols defined by the standard. As seen, this symbol uniquely defines the tool cutting edge angle  $\kappa_r$  according to its definition given in Sect. 1.4.2, i.e., as the acute angle between the projection of the main cutting edge into the reference plane and the  $x$ -direction (direction of the cutting feed). Angle  $\kappa_r$  is always positive and it is measured in a counter-clockwise direction from the position of the assumed working plane.

Although the standard designation for this position is seemingly simple and straightforward, there are a number of discrepancies in the catalogs of tool manufacturers. According to Sandvik Coromant, this position relates to “holder style” (not to tool style as per the standard). ISCAR refers to this position as “Approach angle” while showing the tool cutting edge angle in the table as per standard. According to Bohler, this position is to designate “tool holder shape” while description table relates to the proper standard designation of the tool style. Kennametal designates this position as “tool style or lead angle” showing the lead angles in the table instead of standard tool cutting edge angles.

In the author’s opinion, however, the use of non-standard terminology with the additional features not assigned by the standard adds a lot of confusion in the selection of the tool style. Figure B.19 present two fragments of the tables that assign the letter codes for reference position (3) in the tool holders designation. Comparing the corresponding symbols in these tables with that shown in Fig. B.18, one can easily recognize significant discrepancies. Non-standard terminology as “side cutting edge angle,” “lead side cutting edge angle,” etc. just adds more confusion to the matter.

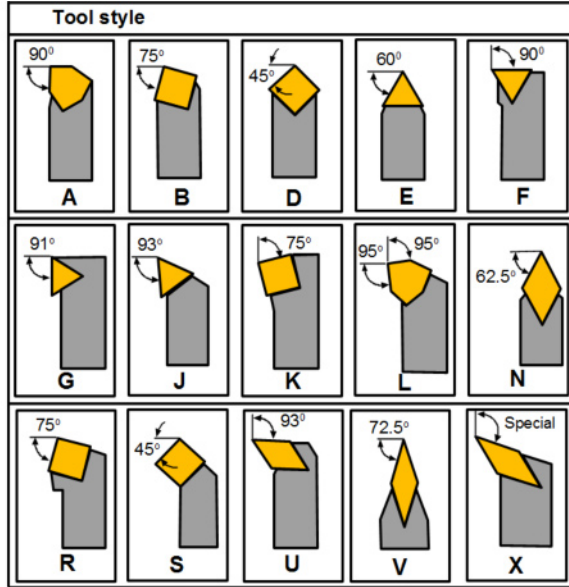


Fig. B.18. Letter symbols for tool styles

**B.2.4 Letter Symbol Identifying Insert Normal Clearance – Reference Position (4)**

The Codes (4) is the letter symbol in accordance with ISO 1832, i.e., should correspond to the insert’s code position (2) as shown in Fig. B.4 and Table B.14. Although most manufacturers follow this, some provide their own interpretations for this reference position. For example, Fig. B.20 shows Valenite symbols for reference position (4) for metric tool holders. As can be seen, it does not follow the standard recommendation and it is not clear if the clearance angle is attributed to the indexable insert or to the tool holder.

**B.2.5 Symbol for Tool Hand – Reference Position (5)**

Figure B.21 shows the letter symbols for this position.

**B.2.6 Symbol for Tool Height (Shank Height of Tool Holders and Height of Cutting Edge) – Reference Position (6)**

In countries using the metric system, reference position (6) is two-digit number that shows the height of the shank  $h$  in mm as shown in Fig. B.22. If the shank height is less than 10mm, the first digit is 0. For single-point tools with indexable insert, the height of the tool point,  $h_1$  (Fig. B.22) is equal to the shank height,  $h$ .

3. Toolholder style		Holder Style	
A	= Straight shank with 0° side cutting edge angle.	A	0° side cutting angle, no offset (90°)
B	= Straight shank with 15° side cutting edge angle.	B	15° lead side cutting angle, no offset (75°)
C	= Shank with 0° end cutting edge angle.	C	0° lead end cutting angle (90°)
D	= Straight shank with 45° side cutting edge angle.	D	45° lead side cutting angle, no offset
E	= Straight shank with 30° side cutting edge angle.	E	30° lead side cutting angle (60°)
F	= Offset shank with 0° end cutting edge angle.	F	0° lead end cutting angle offset (90°)
G	= Offset shank with 0° side cutting edge angle.	G	0° lead side cutting angle offset (90°)

Fig. B.19. Fragments of the letter codes for reference position (3) by: (a) Seco Tools, and (b) Valenite

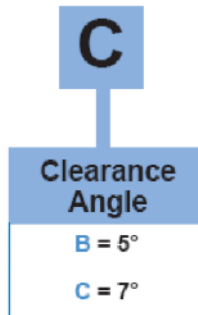


Fig. B.20. Valenite symbols for reference position (4) for metric inserts toolholders.

**B.2.7 Number Symbol Identifying Tool Holder Shank Width – Reference Position (7)**

In countries using the metric system, reference position (7) is a two-digit number that shows the width of the shank *h* in mm as shown in Fig. B.23. If the shank height is less than 10mm, the first digit is 0.

**B.2.8 Number Symbol Identifying Tool Length – Reference Position (8)**

Reference position (7) is a letter symbol that defines tool length (Fig. B.24). Table B.28 shows the symbols defined by the standard.

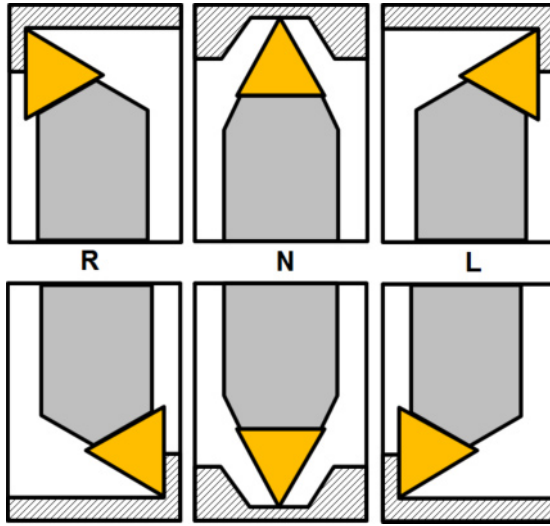


Fig. B.21. Symbols for tool hand

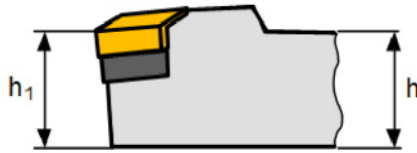


Fig. B.22. Meaning of tool height

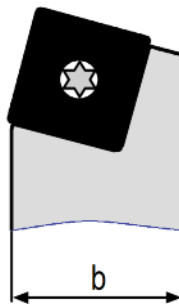
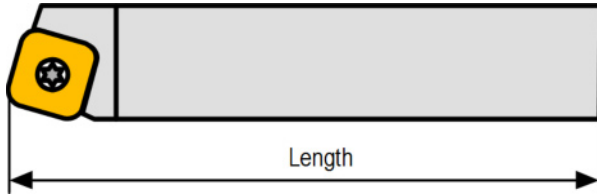


Fig. B.23. Shank width



**Fig. B.24.** Tool length

**Table B.28.** Symbols for tool length

Symbol	<b>A</b>	<b>B</b>	<b>C</b>	<b>D</b>	<b>E</b>	<b>F</b>	<b>G</b>	<b>H</b>	<b>J</b>	<b>K</b>	<b>L</b>	<b>N</b>
Length, mm	32	40	50	60	70	80	90	100	110	125	140	150
Symbol	<b>P</b>	<b>Q</b>	<b>R</b>	<b>S</b>	<b>T</b>	<b>U</b>	<b>V</b>	<b>W</b>	<b>Y</b>	<b>X</b>		
Length, mm	170	180	200	250	300	350	400	450	500	Special		

### **B.2.9 Letter Symbol Identifying Indexable Insert Size – Reference Position (9)**

The Codes (9) is the letter symbol in accordance with ISO 1832, i.e., should correspond to the insert’s code position (5) as shown in Table B.17.

## Appendix C

---

### Basics of Vector Analysis

*In mathematics you don't understand things, you just get used to them.*  
John von Neumann (1903–1957)

**Abstract.** This appendix presents the basics of vector analysis to help potential readers to comprehend the analysis of the tool geometry in the book. The concepts of vector and scalar quantities are explained. Starting with trivial vector operations as vector summation and subtraction, the text walks a potential reader through the dot and cross and scalar triple products of vectors as the fundamental operations used in the analysis of tool geometry. Suitable exemplifications are provided for each of these vector operations.

#### C.1 Vectors and Scalars

A vector is a mathematical object that has magnitude and direction, and satisfies the laws of vector addition. Vectors are used to represent physical quantities that have a magnitude and direction associated with them. For example:

- The velocity of an object is a vector. The direction of the vector specifies the direction of travel, and the magnitude specifies the speed.
- The force acting on an object is a vector. The direction of the vector specifies the line of action of the force, and the magnitude specifies how large the force is.

Other examples of vectors include position, acceleration, electric field, electric current flow, heat flow, and the normal to a surface. Examples of quantities that are not vectors include mass, temperature, electric potential, volume, and energy. These can all be described by their magnitude only (they have no direction) and so are scalars.

To comprehend the principle difference between a vector and scalar quantities, one can consider the velocity and speed of a moving car. Speed, for example 120

km/h, is a scalar because no direction is attached. Although this particular value can be used to compare with the velocity allowed on a given road and thus to avoid getting a speeding ticket, it does not tell the driver where he is heading. An example of a vector quantity is velocity. This speed in a particular direction is velocity. An example of velocity might be 120 km/h due north.

Vector quantities are extremely useful in many engineering applications as their use significantly simplifies engineering analyses. The important characteristic of a vector quantity is that it has both a magnitude (or size) and a direction. Both of these properties must be given in order to specify a vector completely. An example of a vector quantity is a displacement. This tells one how far away we are from a fixed point (for example, home), and it also tells one the direction relative to that point.

## C.2 Definition and Representation

### C.2.1 Definitions

A vector is defined as a quantity that has magnitude and direction and that is commonly represented (Fig. C.1) by a directed line segment whose length represents the magnitude and whose orientation in space represents the direction. Thus,  $AB$  designates the vector represented by an arrow from point  $A$  to point  $B$ , while  $BA$  designates a vector of equal magnitude in the opposite direction, from  $B$  to  $A$ . In order to compare vectors and to operate on them mathematically, however, it is necessary to have some reference system that determines scale and direction. Cartesian coordinates are often used for this purpose. In the plane, two axes and unit lengths along each axis serve to determine magnitude and direction throughout the plane.

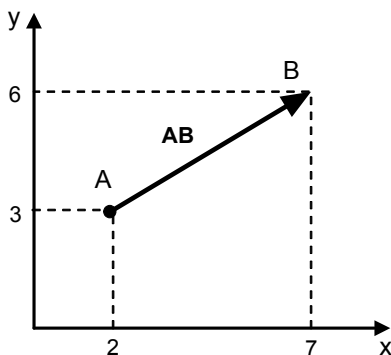


Fig. C.1. Representation of a vector



*Example C.1.*

*Problem:* Point A mentioned above has coordinates (2,3) and point B has coordinates (7,6) as seen in Fig. C.1. Find the size and position of the vector AB.

*Solution:* The size of this vector in the x-direction is found by projecting the vector onto the x-axis, i.e., by dropping perpendicular line segments to the x-axis. The length of this projection is simply the difference between the x coordinates of the two points A and B, or  $7 - 2 = 5$ . This is called the x-component of the vector. Similarly, the y-component of the vector is found to be  $6 - 3 = 3$ . A vector is frequently expressed by giving its components with respect to the coordinate axes; thus, vector AB becomes [5,3].

Knowledge of the components of a vector enables one to compute its magnitude – in this case, 5.83, from the Pythagorean theorem  $[(5^2 + 3^2)^{1/2} = 5.83]$  – and its direction from trigonometry, once the lengths of the sides of the right triangle formed by the vector are known. (Trigonometry can also be used to find the component of the vector as projected in some direction other than the x-axis or y-axis). Since the vector AB points from A to B, both its components are positive; if it pointed from B to A, its components would be  $[-5, -3]$  but its magnitude and orientation would be the same.

End of Example C.1.

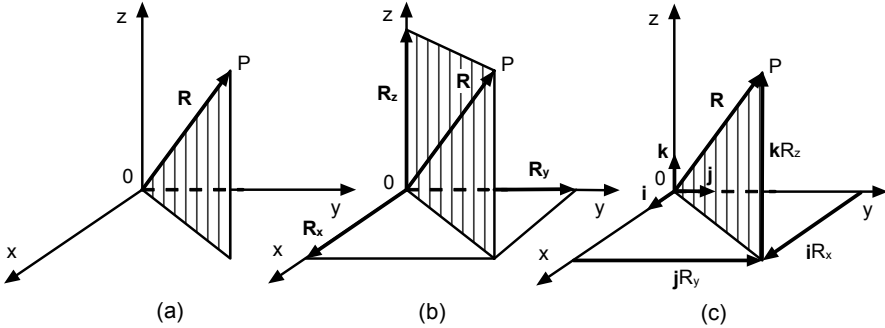
It is obvious that an infinite number of vectors can have the same components [5,3], since there are an infinite number of pairs of points in the plane with x- and y-coordinates whose respective differences are 5 and 3. All these vectors have the same magnitude and direction, being parallel to one another, and are considered equal. Thus, any vector with components  $a$  and  $b$  can be considered as equal to the vector  $[a,b]$  directed from the origin (0,0) to the point (a,b). The concept of a vector can be extended to three or more dimensions. Although there are a number of books discussing vectors, vector analysis, and their application in engineering (for example [1]), it is instructive to review here some basic principles of such an analysis that are used in the body of the book.

A vector is a form of graphical representation of a quantity in which both the magnitude and the direction must be stated for its full description. As such, a vector is a straight line whose length is the magnitude of the quantity it represents on a certain known scale and whose orientation in the selected and thus always known coordinate system represents the direction. Therefore, a vector makes sense only in a well-defined coordinate system.

Let the location of point  $P$  in the xyz coordinate system be described by a vector extending from the origin  $O$  of this system to the point. Point  $P$  in Fig. C.2a is located by the vector  $\mathbf{R}$ . The x-, y-, and z-coordinate axes in that figure are mutually perpendicular. Any motion of  $P$  will result in a change in the vector  $\mathbf{R}$ , either in its magnitude or direction or both.

A line through  $P$  perpendicular to the x-axis intersects this axis at a distance  $R_x$  from the origin  $O$  (Fig. C.2b). The distance  $R_x$  is called the projection of the vector  $\mathbf{R}$  on the x-axis, or the x component of  $\mathbf{R}$ . The projections of  $\mathbf{R}$  on the y-axis and z-axis are labeled  $R_y$  and  $R_z$ . Vectors  $\mathbf{i}$ ,  $\mathbf{j}$  and  $\mathbf{k}$  are unit vectors in the x, y, and z

directions, respectively, as shown in Fig. C.2c. That is, each has unit length and is normally used only to assign a direction. Vectors  $\mathbf{i}$ ,  $\mathbf{j}$  and  $\mathbf{k}$  are also called the coordinate vectors. In the  $xyz$  coordinate system, their coordinates are  $\mathbf{i} = (1,0,0)$ ,  $\mathbf{j} = (0,1,0)$ ,  $\mathbf{k} = (0,0,1)$ .



**Fig. C.2.** Basics of vector analysis: (a) vector  $\mathbf{R}$  locates the position of point  $P$  in the coordinate system, (b) vector  $\mathbf{R}$  is resolved into components along the  $x$ -,  $y$ -, and  $z$ - axes, and (c) each component is considered as the product of a unit vector times the scalar magnitude of the component

The scalar length  $R_x$  multiplied by the unit vector  $\mathbf{i}$  gives us the vector  $\mathbf{i}R_x$  of length  $R_x$  parallel to the  $x$ -axis (Fig. C.2c). Forming the vector sum of the three components times their corresponding unit vectors, one obtains the original vector as

$$\mathbf{R} = \mathbf{i}R_x + \mathbf{j}R_y + \mathbf{k}R_z \tag{C.1}$$

The magnitude of the vector  $\mathbf{R}=(R_x,R_y,R_z)$ , also called its length or norm, is defined by

$$\|\mathbf{R}\| = \sqrt{R_x^2 + R_y^2 + R_z^2} \tag{C.2}$$

Vectors can be defined in any number of dimensions, though in the consideration of tool geometry and its motions one should clearly focus only on 3D-space. When drawing a vector in 3D-space, the position the vector along its directional line is unimportant; the vector's essential properties are just its magnitude and its direction. Two vectors are equal if and only if corresponding components are equal.

A vector of norm 1 is called a unit vector. The coordinate vectors are examples of unit vectors. The zero vector,  $\mathbf{0} = (0,0,0)$ , is the only vector with magnitude 0.

## C.2.2 Basic Vector Operations

Basic vector operations are: (1) resolution into components (addition and subtraction), (2) scalar (dot) product, and (3) vector (cross) product. Although these basic operations are well-described in the literature, it is instructive to remind here some definitions.

Vector addition – the sum of two vectors  $\mathbf{a} = (a_x, a_y, a_z)$  and  $\mathbf{b} = (b_x, b_y, b_z)$  is defined as  $\mathbf{a} + \mathbf{b} = (a_x + b_x, a_y + b_y, a_z + b_z)$ . Figure C.3 shows geometric interpretation of vector addition where  $\mathbf{a} = (4, 1)$ ,  $\mathbf{b} = (2, 3)$ , and  $\mathbf{a} + \mathbf{b} = (6, 4)$ .

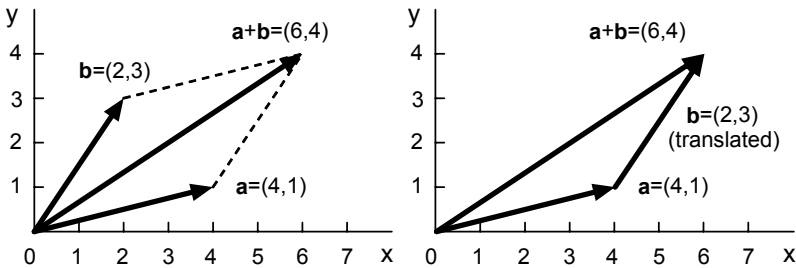


Fig. C.3. Geometric interpretation of vector addition

Vector subtraction – the difference of two vectors  $\mathbf{a} = (a_x, a_y, a_z)$  and  $\mathbf{b} = (b_x, b_y, b_z)$  is defined as  $\mathbf{a} - \mathbf{b} = (a_x - b_x, a_y - b_y, a_z - b_z)$ . One should remember that the vector  $\mathbf{a} - \mathbf{b}$  is the vector from  $\mathbf{b}$  to  $\mathbf{a}$ . Figure C.4 shows geometric interpretation of vector subtraction where  $\mathbf{a} = (4, 1)$ ,  $\mathbf{b} = (2, 3)$  and  $\mathbf{a} - \mathbf{b} = (-2, 2)$ .

Vector scaling – the product of the vector  $\mathbf{a} = (a_x, a_y, a_z)$  and the scalar  $c$  is defined as  $c\mathbf{a} = (ca_x, ca_y, ca_z)$ .

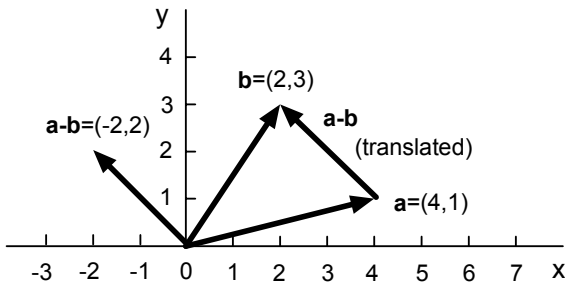


Fig. C.4. Geometric interpretation of vector subtraction

Scalar or dot product – the scalar product of two vectors  $\mathbf{a} = (a_x, a_y, a_z)$  and  $\mathbf{b} = (b_x, b_y, b_z)$  is defined as

$$\mathbf{a} \cdot \mathbf{b} = (a_x b_x + a_y b_y + a_z b_z) = \begin{cases} \|a\| \|b\| \cos \tau & \text{if } \mathbf{a} \neq 0, \mathbf{b} \neq 0 \\ 0 & \text{if otherwise} \end{cases} \quad (\text{C.3})$$

where  $\tau$  is angle between these two vectors.

It follows from Eq. C.3 that the scalar product of two perpendicular vectors  $\mathbf{a}$  and  $\mathbf{b}$  is equal to zero, i.e.,

$$\mathbf{a} \cdot \mathbf{b} = \|a\| \|b\| \cos \tau = \|a\| \|b\| \cos 90^\circ = 0 \quad (\text{C.4})$$

The difference between all other operations and the scalar product is that the result is a number, not a vector.

Using Eq. C.3 one can calculate the angle between two vectors as

$$\cos \tau = \frac{\mathbf{a} \cdot \mathbf{b}}{\|a\| \|b\|} = \frac{a_x b_x + a_y b_y + a_z b_z}{\sqrt{(a_x^2 + a_y^2 + a_z^2)(b_x^2 + b_y^2 + b_z^2)}} \quad (\text{C.5})$$

The scalar product is very useful to determine the angle between two lines, for example 1 and 2 as shown in Fig. C.5. To do that, the corresponding directional vectors along these lines should be assigned and the angle between these lines is determined as the angle between these vectors using Eq. C.5.

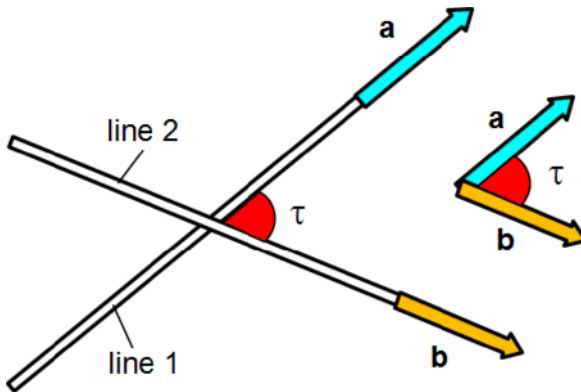


Fig. C.5. Finding the angle between two lines using the scalar product

*Example C.2.*

*Problem:* Suppose that first vector  $\mathbf{a} = 2\mathbf{i} - 3\mathbf{j} + \mathbf{k}$  and second vector  $\mathbf{b} = 4\mathbf{i} + \mathbf{j} - 3\mathbf{k}$  are given. Find the angle between these vectors.

*Solution:* Using Eq. C.5, one can calculate the angle as

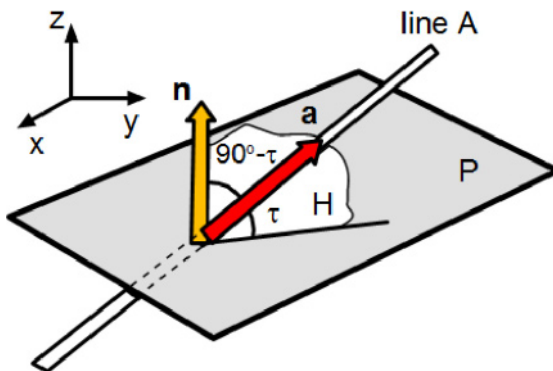
$$\tau = \arccos \frac{\mathbf{a} \cdot \mathbf{b}}{\|\mathbf{a}\| \|\mathbf{b}\|} = \arccos \frac{a_x b_x + a_y b_y + a_z b_z}{\sqrt{(a_x^2 + a_y^2 + a_z^2)(b_x^2 + b_y^2 + b_z^2)}} =$$

$$\arccos \frac{2 \times 4 + (-3) \times 1 + 1 \times (-3)}{\sqrt{(2^2 + (-3)^2 + 1^2) \times (4^2 + 1^2 + (-3)^2)}} = 84^\circ$$

End of Example C.2.

Another great use of the scalar product is for determining the angle between a line and a plane as shown in Fig. C.6. As can be seen, the normal vector  $\mathbf{n}$  is set by its tail at the point of intersection with line  $A$  with plane  $P$ . At the same point, direction vector  $\mathbf{a}$  is set along line  $A$ . Then  $\mathbf{n}$  and  $\mathbf{a}$  together define plane  $H$  which is perpendicular to plane  $P$ . The angle which line  $A$  makes with plane  $P$  is  $\tau$  and the angle between vectors  $\mathbf{n}$  and  $\mathbf{a}$  is  $90^\circ - \tau$  as  $\mathbf{n}$  is perpendicular to plane  $P$ . Using Eq. C.4 one can write  $\mathbf{n} \cdot \mathbf{a} = \|\mathbf{n}\| \|\mathbf{a}\| \cos(90^\circ - \tau) = \|\mathbf{n}\| \|\mathbf{a}\| \sin \tau$  so the angle between line  $A$  and plane  $P$  calculates as

$$\tau = \arcsin \frac{\mathbf{n} \cdot \mathbf{a}}{\|\mathbf{n}\| \|\mathbf{a}\|} = \frac{n_x a_x + n_y a_y + n_z a_z}{\sqrt{(n_x^2 + n_y^2 + n_z^2)(a_x^2 + a_y^2 + a_z^2)}} \quad (\text{C.6})$$



**Fig. C.6.** Finding the angle between a line and a plane using the scalar product

Dot products of unit vectors are

$$\begin{aligned} \mathbf{i} \cdot \mathbf{i} = \mathbf{j} \cdot \mathbf{j} = \mathbf{k} \cdot \mathbf{k} &= 1 \\ \mathbf{i} \cdot \mathbf{j} = \mathbf{j} \cdot \mathbf{k} = \mathbf{k} \cdot \mathbf{i} &= 0 \end{aligned} \tag{C.7}$$

Some useful properties of the dot product are

$$\begin{aligned} \mathbf{a} \cdot \mathbf{b} &= \mathbf{b} \cdot \mathbf{a} \\ \mathbf{a} \cdot (\mathbf{c} + \mathbf{d}) &= (\mathbf{a} \cdot \mathbf{c}) + (\mathbf{a} \cdot \mathbf{d}) \\ \mathbf{a} \cdot \mathbf{a} &= \|\mathbf{a}\|^2 \end{aligned} \tag{C.8}$$

The vector or cross product of two vectors  $\mathbf{a} = (a_x, a_y, a_z)$  and  $\mathbf{b} = (b_x, b_y, b_z)$  is defined as

$$\mathbf{c} = \mathbf{a} \times \mathbf{b} = (a_y b_z - a_z b_y) \mathbf{i} + (a_z b_x - a_x b_z) \mathbf{j} + (a_x b_y - a_y b_x) \mathbf{k} = \begin{vmatrix} \mathbf{i} & \mathbf{j} & \mathbf{k} \\ a_x & a_y & a_z \\ b_x & b_y & b_z \end{vmatrix} \tag{C.9}$$

In a three-dimensional Euclidean space, with the usual right-handed coordinate system, it is defined as a vector  $\mathbf{c}$  that is perpendicular to both  $\mathbf{a}$  and  $\mathbf{b}$ . Figure C.7 shows plane  $P$  containing vectors  $\mathbf{a}$  and  $\mathbf{b}$ . Vector  $\mathbf{c}$  is perpendicular to this plane, i.e., in the direction of normal  $\mathbf{n}$  to this plane. The exact direction of  $\mathbf{c}$  is given by the right-hand rule as shown in Fig. C.8.

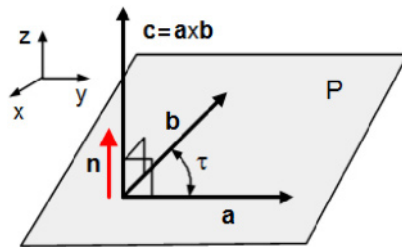
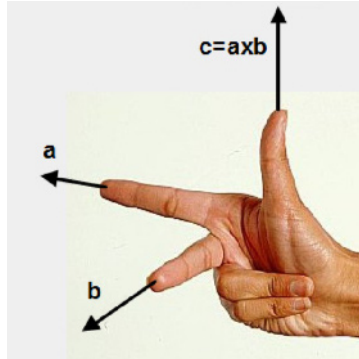


Fig. C.7. Illustration of the cross-product in respect to a right-handed coordinate system

The magnitude of the cross product calculates as

$$\|\mathbf{c}\| = \|\mathbf{a} \times \mathbf{b}\| = \|\mathbf{a}\| \|\mathbf{b}\| \sin \tau \text{ if } \|\mathbf{a}\| \neq 0 \text{ and } \|\mathbf{b}\| \neq 0 \tag{C.10}$$

where  $\tau$  is angle between vectors  $\mathbf{a} = (a_x, a_y, a_z)$  and  $\mathbf{b} = (b_x, b_y, b_z)$  as shown in Fig. C.7.



**Fig. C.8.** Finding the direction of the cross product by the right-hand rule

Using Eq. C.9, one can calculate the angle between two vectors as

$$\sin \tau = \frac{\|\mathbf{a} \times \mathbf{b}\|}{\|\mathbf{a}\| \|\mathbf{b}\|} \quad (\text{C.11})$$

Combining Eqs. C.4 and C.10, one can obtain

$$\tan \tau = \frac{\|\mathbf{a} \times \mathbf{b}\|}{\mathbf{a} \cdot \mathbf{b}} \quad (\text{C.12})$$

Cross products of unit vectors are

$$\begin{aligned} \mathbf{i} \times \mathbf{j} &= \mathbf{k} & \mathbf{j} \times \mathbf{i} &= -\mathbf{k} \\ \mathbf{j} \times \mathbf{k} &= \mathbf{i} & \mathbf{k} \times \mathbf{j} &= -\mathbf{i} & \mathbf{i} \times \mathbf{i} &= \mathbf{j} \times \mathbf{j} = \mathbf{k} \times \mathbf{k} = 0 \\ \mathbf{k} \times \mathbf{i} &= \mathbf{j} & \mathbf{i} \times \mathbf{k} &= -\mathbf{j} \end{aligned} \quad (\text{C.13})$$

Some important properties of the cross product are

$$\begin{aligned} \mathbf{a} \times \mathbf{b} &= -(\mathbf{b} \times \mathbf{a}) \\ \mathbf{a} \times (\mathbf{c} + \mathbf{b}) &= (\mathbf{a} \times \mathbf{c}) + (\mathbf{a} \times \mathbf{b}) \\ \mathbf{a} \times \mathbf{a} &= 0 \end{aligned} \quad (\text{C.14})$$

The cross product has a number of remarkable properties underutilized in theory and practice of the cutting tool design. Among them, the following are of prime importance.

The angles that constitute the tool geometry are actually the angles between planes as discussed in Chap. 2. As known [2, 3], the angle between planes is defined as that between the normal vectors to the said planes. If any two vectors in

a plane are known, say  $\mathbf{a} = (a_x, a_y, a_z)$  and  $\mathbf{b} = (b_x, b_y, b_z)$ , then the normal vector  $\mathbf{n}$  to this plane is defined as

$$\mathbf{n} = \mathbf{a} \times \mathbf{b} = \begin{vmatrix} \mathbf{i} & \mathbf{j} & \mathbf{k} \\ a_x & a_y & a_z \\ b_x & b_y & b_z \end{vmatrix} \quad (\text{C.15})$$

Using normal vectors instead of actual plane, one can significantly simplify tool geometry calculations.

One of the very useful properties of the cross product in analyzing the tool geometry is the ability to determine the direction of the intersection lines of two planes as shown in Fig. C.9.

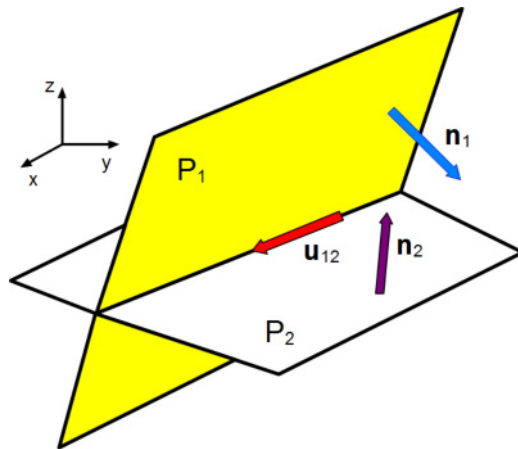


Fig. C.9. Intersection of two planes

In this figure,  $\mathbf{n}_1 = (n_{1x}, n_{1y}, n_{1z})$  and  $\mathbf{n}_2 = (n_{2x}, n_{2y}, n_{2z})$  are normal vectors of planes  $P_1$  and  $P_2$ , respectively. The position of their intersection line is defined by directional vector determined as

$$\mathbf{u}_{12} = \mathbf{n}_1 \times \mathbf{n}_2 =$$

$$(n_{1y}n_{2z} - n_{1z}n_{2y})\mathbf{i} + (n_{1x}n_{2z} - n_{1z}n_{2x})\mathbf{j} + (n_{1x}n_{2y} - n_{1y}n_{2x})\mathbf{k} = \begin{vmatrix} \mathbf{i} & \mathbf{j} & \mathbf{k} \\ n_{1x} & n_{1y} & n_{1z} \\ n_{2x} & n_{2y} & n_{2z} \end{vmatrix} \quad (\text{C.16})$$

The scalar triple product of three vectors is defined as the dot product of one of the vectors with the cross product of the other two. It is a scalar (more precisely, it can be either a scalar or a pseudoscalar). Geometrically, this product is the (signed)



volume of the parallelepiped formed by the three vectors given. It can be evaluated numerically as

$$\mathbf{a} \cdot (\mathbf{b} \times \mathbf{c}) = \begin{vmatrix} a_x & a_y & a_z \\ b_x & b_y & b_z \\ c_x & c_y & c_z \end{vmatrix} = (b_y c_z - b_z c_y) a_x + (b_x c_z - b_z c_x) a_y + (b_x c_y - b_y c_x) a_z \quad (\text{C.17})$$

Another useful property of the scalar triple product is that, if it is equal to zero, the three vectors  $\mathbf{a}$ ,  $\mathbf{b}$ , and  $\mathbf{c}$  are coplanar, i.e. vectors  $\mathbf{a}$ ,  $\mathbf{b}$ , and  $\mathbf{c}$  belong to the same plane. This property of the scalar triple product is very useful in tool geometry analysis.

### C.3 Application Conveniences

Each of the basic geometry planes introduced in Figs 2.11 and 2.12 contains at least two known lines in the tool-in-hand coordinate system. For example, the assumed working plane (Fig. 2.11) contains the cutting speed and the cutting feed vectors; the cutting edge plane contains the cutting speed vector and directional vector of the cutting edge; the orthogonal plane contains the cutting speed vector and directional vector of the trace of the rake face in the considered point, etc. Therefore, the normal vectors to these plane can easily be determined using Eq. C.15 and then any of the tool geometry angles (Fig. 2.11) can be defined using Eq. C.5.

The neatest method to simplify the use of vectorial analysis in tool geometry calculations by utilizing the basic properties of the unit vectors can be explained as follows. Figure C.10 shows the cutting edge  $AB$ . To represent this cutting edge in the vectorial form for use in the analysis of the tool geometry, a vector  $\mathbf{r}_{AB}$  should be drawn from  $A$  to  $B$  and then this vector should be set in the tool coordinate system as shown in Fig. C.10. Then, projections  $r_x$ ,  $r_y$ , and  $r_z$  are determined and the cutting edge  $AB$  is represented as  $\mathbf{r}_{AB} = (r_x, r_y, r_z) = r_x \mathbf{i} + r_y \mathbf{j} + r_z \mathbf{k}$ . Such a representation, however, complicates further analysis in terms of the representation its results as the mentioned components will appear as numbers in the relationships among the angles of the cutting tool geometry.

Analyzing the tool geometry using vectors, Rodin [4] proposed a simplification the essence of which can be explained as follows. Cutting edge  $AB$  is considered in the tool coordinate system in its “natural” location, i.e., as assigned by the tool designer. Figure C.11 shows the cutting edge of a drill as an example. The angle which this edge makes with the  $y$ -axis in the  $yz$  coordinate plane is known as the approach angle  $\varphi_p$ . A directional vector  $\mathbf{m}$  is set along  $AB$  in such a way that its projection into the  $y$ -axis is equal to the length of the unit vector  $\mathbf{j}$ . Then, the projection of  $\mathbf{m}$  into the  $z$ -axis is  $\tan \varphi_p$ . Therefore, cutting edge  $AB$  is fully represented by directional vector

$$\mathbf{m} = \mathbf{j} + \mathbf{k} \tan \varphi_p \quad (\text{C.18})$$

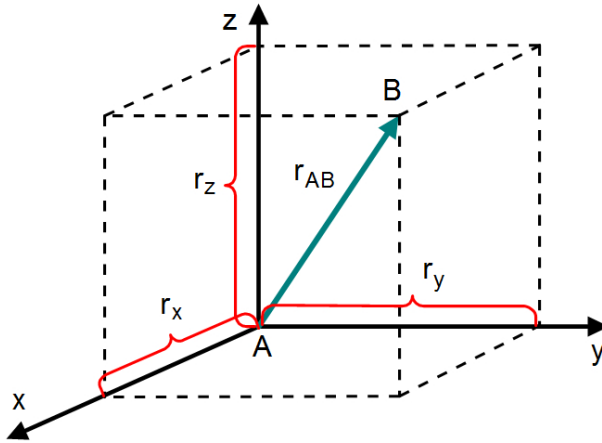


Fig. C.10. Conventional way of representing cutting edge AB as a vector

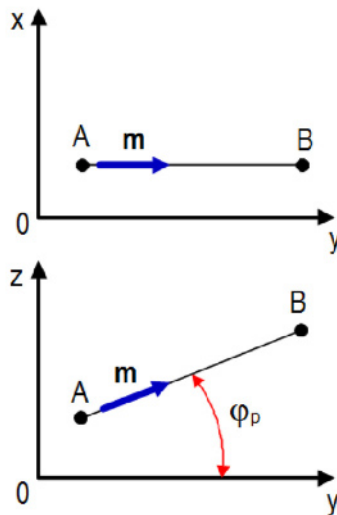


Fig. C.11. Simplified method of representing cutting edge AB as a vector

As demonstrated in the body of the book, such a representation significantly simplifies obtaining the basic relationships among the angles of the tool geometry.

*Example C.3.*

*Problem:* Let the coordinate system shown in Fig. C.11 is T-mach-S of a drill while cutting edge  $AB$  is a part of the major cutting edge (Chapter 4). Let the approach angle  $\phi_p = 30^\circ$ . Find a directional vector of the cutting edge  $AB$ .

*Solution:* Using Eq. C.18, one obtains  $\mathbf{m}_{AB} = \mathbf{j} + \mathbf{k}\tan 30^\circ = \mathbf{j} + \mathbf{k}0.5774$ .

End of Example C.3.

*Example C.4.*

*Problem:* Let the same cutting edge  $AB$  be provided with the normal T-hand-S flank angle  $\alpha_n = 8^\circ$  as shown in Fig. C.12. Using the cross product, define the normal vector  $\mathbf{n}$  to this flank plane.

*Solution:* To define the normal vector using Eq. C.15, one needs to know two vectors in the flank plane. One vector  $\mathbf{m}_{AB} = \mathbf{j} + \mathbf{k}\tan 30^\circ = \mathbf{j} + \mathbf{k}0.5774$  is defined in the previous example. To define the second vector, one needs consider SECTION C–C shown in Fig. C.12. In this section, a vector  $\mathbf{p}$  of unit length is drawn as shown. As seen, its projections on the z-axis is  $\sin \alpha_n \cos \phi_p = \sin 8^\circ \cos 30^\circ = 0.1205$ , on the y-axis is  $-\sin \alpha_n \sin \phi_p = -\sin 8^\circ \sin 30^\circ = -0.0696$ , and its projection on the x-axis is  $-\cos \alpha_n = -\cos 8^\circ = -0.9903$ . Therefore,  $\mathbf{p} = -\mathbf{i}0.9903 - \mathbf{j}0.0606 + \mathbf{k}0.1205$ .

Using Eq.C.11, one can define the normal vector to the flank plane as

$$\mathbf{n} = \mathbf{p} \times \mathbf{m} = \begin{vmatrix} \mathbf{i} & \mathbf{j} & \mathbf{k} \\ p_x & p_y & p_z \\ m_x & m_y & m_z \end{vmatrix} = \begin{vmatrix} \mathbf{i} & \mathbf{j} & \mathbf{k} \\ -0.9903 & -0.0696 & 0.1205 \\ 0 & 1 & 0.5774 \end{vmatrix} = \begin{matrix} -\mathbf{i}0.1607 + \mathbf{j}0.5718 - \mathbf{k}0.9903 \end{matrix} \quad (\text{C.19})$$

End of Example C.4.

Table C.1 summarizes some useful properties of the vector dot and cross products.

## C.4 Rotation: Linear and Angular Velocities

### C.4.1 Planar Linear and Angular Velocities

Most metal cutting operations involve rotational motion applied to the workpiece or to the tool or to both. As the parameters of rotational motion directly correlate with the tool geometry, their understanding provides the proper assessment of the parameters of the tool geometry. Seemingly simple and straightforward, the

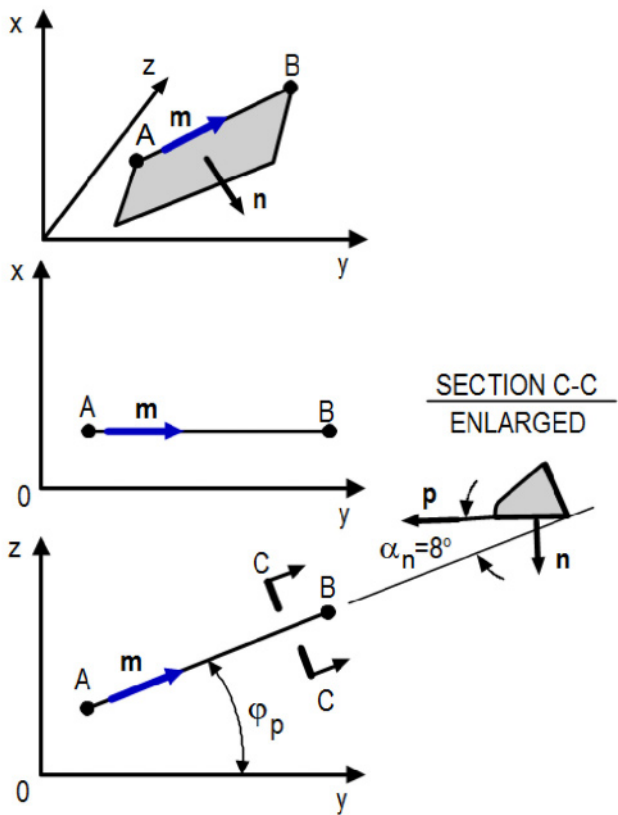


Fig. C.12. Cutting edge AB is provided with the flank plane

Table C.1. Some useful properties of the vector dot and cross products

Dot Product (is a scalar)		Cross Product (is a vector)	
$\mathbf{v} \cdot \mathbf{u} = \mathbf{u} \cdot \mathbf{v}$	Commutative	$\mathbf{v} \times \mathbf{u} = -\mathbf{u} \times \mathbf{v}$	Anti-commutative
$ \mathbf{v} \cdot \mathbf{u}  =  \mathbf{v}   \mathbf{u}  \cos \alpha$	Angle		Angle
$(a\mathbf{v}) \cdot \mathbf{u} = a(\mathbf{v} \cdot \mathbf{u})$	Linearity	$ \mathbf{v} \times \mathbf{u}  =  \mathbf{v}   \mathbf{u}  \sin \alpha$	linearity
$(\mathbf{u} + \mathbf{v}) \cdot \mathbf{n} = \mathbf{u} \cdot \mathbf{n} + \mathbf{v} \cdot \mathbf{n}$	Distributivity	$(a\mathbf{v}) \times \mathbf{u} = a(\mathbf{v} \times \mathbf{u})$	distributivity
$\frac{d}{dt}(\mathbf{u} \cdot \mathbf{v}) = \dot{\mathbf{u}} \cdot \mathbf{v} + \mathbf{u} \cdot \dot{\mathbf{v}}$	Product rule	$(\mathbf{u} + \mathbf{v}) \times \mathbf{n} = \mathbf{u} \times \mathbf{n} + \mathbf{v} \times \mathbf{n}$	
		$\frac{d}{dt}(\mathbf{u} \times \mathbf{v}) = \dot{\mathbf{u}} \times \mathbf{v} + \mathbf{u} \times \dot{\mathbf{v}}$	Product rule

determination of these parameters as related to the tool geometry often presents a great challenge even to experienced tool designers and users. Therefore, this section aims to clarify some important issues.

Figure C.13 shows the  $xy$  coordinate system with the origin at point 0 which coincides with the center of rotation. Consider point  $A$  (Fig. C.13) that travels along the circular path starting from position  $A_x$  in the counterclockwise direction. A straight line that connects point  $A$  and the center of rotation is termed the radius of rotation. The length  $OA$  is  $r_A$ . The angle between the  $x$ -axis at the starting position of rotation and the current position of radius  $r_A$  is designated as  $\theta$ .

The angular velocity is the change in the angular position over time, i.e., the rate of changing  $\theta$  which is

$$\frac{d\theta}{dt} = \omega \quad (\text{C.20})$$

Note that the angular velocity does not depend on the radius so it is the same for any point of the body that rotates about the center. Angular velocity,  $\omega$  is measured in radians per second (rad/s),

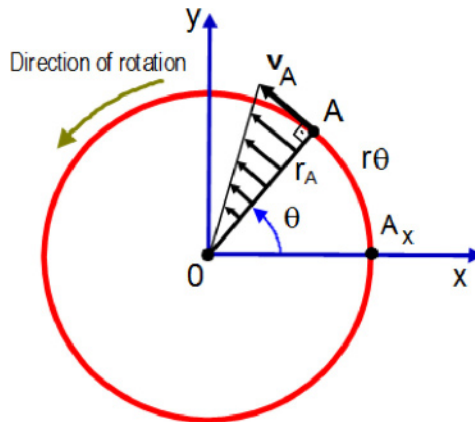


Fig. C.13. Rotation of point  $A$  about center  $O$

In industry, the rotational speed,  $n$  measured in r.p.m. (revolutions per minute) is often used. As a revolution is defined to be one complete turn, and one complete turn is defined to be  $360^\circ$  then  $1 \text{ rev} = 360^\circ = 2\pi$  radians. Owing to the fact that  $1 \text{ min.} = 60 \text{ sec.}$ , one can obtain the relationship between these two parameters as

$$\omega = \frac{2\pi n}{60} = \frac{\pi n}{30} \quad (\text{C.21})$$

For example, if the spindle rotational speed is  $n = 5,600 \text{ rpm}$  then its angular velocity is  $\omega = 3.141 \times 5600 / 60 = 293.16 \text{ (rad/s)}$ .

Referring to Fig. C.13, the distance covered by point  $A$  along its circumferential path  $A_xA$  is  $r\theta$ . The linear velocity of point  $A$  is the rate of change of this distance, i.e.,

$$v = \frac{d}{dt}(r\theta) = r \frac{d\theta}{dt} \quad (\text{C.22})$$

where the fact that radius  $r$  of point  $A$  is constant is used. Combining Eqs. C.21 and C.22, one can obtain an equation for the linear velocity:

$$v = r\omega \quad (\text{C.23})$$

Recalling that the diameter of a rotating point calculates as  $D = 2r$  and is commonly given in millimeters and that the cutting speed is commonly measured in m/min (1 min = 60 s), one can combine Eqs. C.21 and C.23 to obtain the known expression to calculate the cutting speed:

$$v = \frac{\pi Dn}{1000} \text{ (m/min)} \quad (\text{C.24})$$

where  $D$  is in mm and  $n$  is in r.p.m.

Several important outcomes of the foregoing consideration should be pointed out:

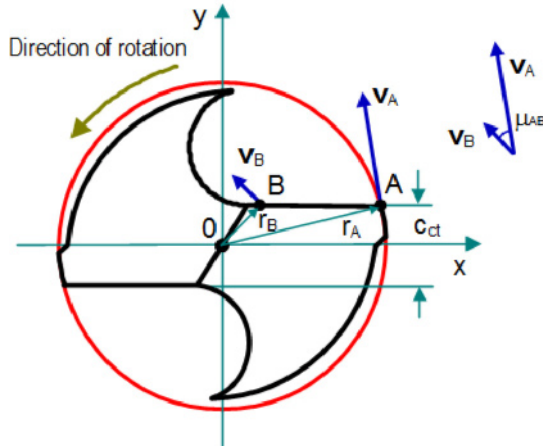
- Linear velocities of a body rotating with respect to the fixed center are not the same as the linear velocity proportional to the radius of rotation. The further a point is from the center of rotation, the greater its linear velocity.
- The linear velocity of the rotating point is always perpendicular to the radius of rotation.

Although this sounds simple and straightforward, it is not always obvious for the designer of axial tools when they assign the flank angles along the radial cutting edges. Figure C.14 shows an example of a twist drill that rotates at  $n$  (rpm) about center  $O$ . As seen, the cutting speed (the linear speed with respect to the center of rotation  $O$ ) for two considered points  $A$  and  $B$  calculates as  $v_A = \frac{\pi 2r_A n}{1000}$  and

$v_B = \frac{\pi 2r_B n}{1000}$ , respectively. However, the vectors  $\mathbf{v}_A$  and  $\mathbf{v}_B$  are not parallel.

Because the reference plane is defined as to be perpendicular to the vector of the cutting speed (Fig. 2.11) and the cutting edge plane is defined to be perpendicular to the reference plane, the cutting edge planes for point  $A$  and  $B$  are not parallel and thus not the same. Rather, the angle between these plane is  $\mu_{AB}$ . As defined in Chap. 2 (Fig. 2.13), the flank angle is the angle between the tool cutting edge plane and the intersection line formed by the tool flank plane and (for the normal flank angle) the cutting edge normal plane. Therefore, if the considered drill is ground

with a constant flank angle in the T-hand-S as it is in the most common case, the actual flank angles at  $A$  and  $B$  differ by  $\mu_{AB}$ . In other words, the flank angle in the T-mach-S varies along the cutting edge.



**Fig. C.14.** Difference in the magnitude and direction of the cutting speed vectors for points A and B of the drill cutting edge

#### C.4.2 Rotation: The Angular Velocity Vector

In the previous section, the plane rotational motion is considered. However, a real tool is a three-dimensional rigid body so it has rotating points of which the rotational planes may not coincide with the coordinate planes. Moreover, when complicated tool motions is considered which may include several rotations and translations, the angular velocity considered as a scalar does not allow one to apply vectorial analysis to such cases. To do this in a concise way, it is useful to define a vector called the angular velocity vector

$$\boldsymbol{\omega} = \omega \mathbf{n} \quad (\text{C.25})$$

where  $\mathbf{n}$  is a unit vector perpendicular to the plane of rotation as shown in Fig. C.15.

The direction of the angular velocity vector  $\boldsymbol{\omega}$  is given by the right-hand rule as shown in Fig. C.16. The magnitude of the angular velocity vector  $\boldsymbol{\omega}$  is the angular velocity  $\omega$ .

There is a very useful expression for the linear velocity in terms of the angular velocity vector:

$$\mathbf{v} = \boldsymbol{\omega} \times \mathbf{r} \quad (\text{C.26})$$

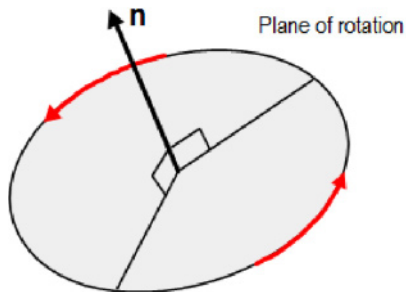


Fig. C.15. Sense of  $\mathbf{n}$

The sense of this cross product is shown in Fig. C.17.

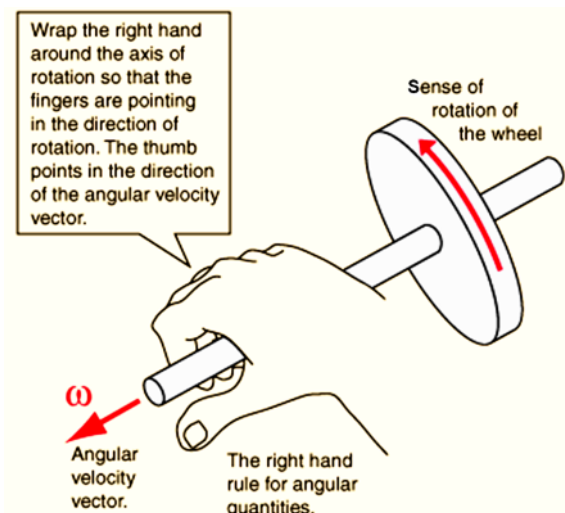
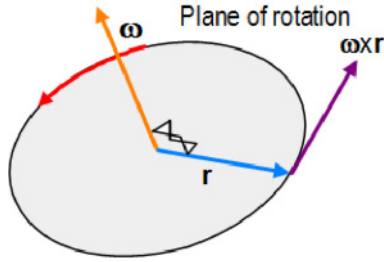


Fig. C.16. Determining the direction of the angular velocity vector  $\omega$

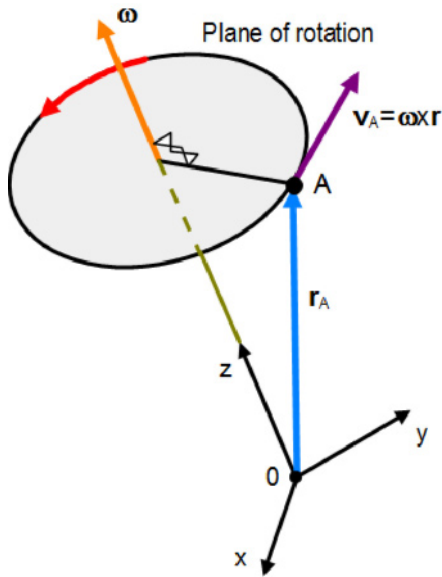
The introduced angular velocity vector  $\omega$  is particularly useful when the rotation of a three-dimensional rigid body, such as, for example, a drill, is considered. Equation C.26 is valid for this case where  $\mathbf{r}$  should be considered now as the position vector of a considered point of the rotating body. Therefore, one does not have to measure it from the center of rotation. Rather, it can be measured from the origin of the tool coordinate system that simplifies geometry considerations. Figure C.18 shows example of determining the linear velocity of point A in the xyz tool coordinate system. Here,  $\mathbf{v}_A = \omega \times \mathbf{r}_A$ . Figure C.19 shows that, in the xyz tool coordinate system, points of interest of the rotating tool can be selected, for example 1, 2, and 3, and their linear velocities calculate

$$\text{as } \mathbf{v}_i = \omega \times \mathbf{r}_i \quad i = 1, 2, 3 \dots \tag{C.27}$$





**Fig. C.17.** Sense of the linear velocity vector of the cross product of  $\omega$  and  $\mathbf{r}$



**Fig. C.18.** Determining the linear velocity of point A in the xyz tool coordinate system

*Example C.5.*

*Problem:* Suppose in the known coordinate system a body rotates with angular velocity  $\omega = (2\mathbf{i}, (-1)\mathbf{j}, 4\mathbf{k})$  (rad/s). Find the instantaneous linear velocity of point

$P$  of this body if the radius of rotations of this point is  $\mathbf{r} = ((-1)\mathbf{i}, 10\mathbf{j}, 20\mathbf{k})$  (mm).

*Solution:* The linear velocity of point  $P$  is given by

$$\mathbf{v} = \omega \times \mathbf{r} = \begin{vmatrix} \mathbf{i} & \mathbf{j} & \mathbf{k} \\ \omega_x & \omega_y & \omega_z \\ r_x & r_y & r_z \end{vmatrix} = \begin{vmatrix} \mathbf{i} & \mathbf{j} & \mathbf{k} \\ 2 & -1 & 4 \\ -1 & 10 & 2 \end{vmatrix} = \mathbf{i}(-42) + \mathbf{j}(19) + \mathbf{k}19 \text{ (mm/s)}$$

This linear velocity is perpendicular to the plane containing vectors  $\boldsymbol{\omega}$  and  $\mathbf{r}$ , and its magnitude is

$$\|\mathbf{v}\| = \sqrt{v_x^2 + v_y^2 + v_z^2} = \sqrt{(-42)^2 + (-8)^2 + 19^2} = 66.79 \text{ mm/s}$$

End of Example C.5.

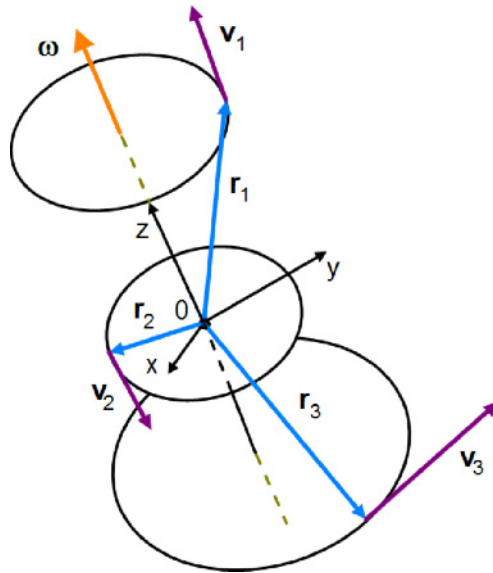


Fig. C.19. Velocities of various points of the rotating body

## References

- [1] Beer FP, Johnston ER Jr., Eisenberg ER, Clausen WE (2006) Vector mechanics for engineers: statics and dynamics. McGraw-Hill, New-York
- [2] Hoffmann, B. (1975) About vectors. Dover Publications Minneola, NY
- [3] Hausner M (1998) A vector space approach to geometry. Dover Publications Minneola, NY
- [4] Rodin PR (1972) Basics of shape formation by cutting (in Russian). Visha Skola, Kyev

## Appendix D

---

### Hydraulic Losses: Basics and Gundrill Specifics

*Experience does not ever err. It is only your judgment that errs in promising itself results which are not caused by your experiments.*

Leonardo da Vinci, Notebooks

Italian engineer, painter, and sculptor (1452–1519)

**Abstract.** This Appendix discusses MWF pressure losses in the hydraulic circuit of the gundrilling system. An electrical analogy of this hydraulic system is used to explain the essence of these losses. To fulfil *Design Rule No. 3* introduced in Chap. 5, namely, to maximize the MWF pressure in the bottom clearance space, all hydraulic losses are distinguished as ‘bad’ (reduce the pressure) and ‘good’ (increase the pressure in the bottom clearance space) losses. The concept and significance of the critical and optimal MWF velocity and flow rate as applicable to chip transportation in the V-flute are introduced and explained with an example.

#### D.1 Hydraulic Pressure Losses – General

To calculate hydraulic losses in terms of hydraulic head, Bernoulli’s equation for incompressible flow can be written for any two section of a hydraulic conduit as [1]

$$\frac{P}{\rho g} + \frac{V^2}{2g} + Z = C \quad (\text{D.1})$$

where each term of Eq. D.1 has dimension of length, or “head” of flowing fluid. The individual terms are:  $P/\rho g$  is the head due to local static pressure;  $V^2/2g$  is the head due to local dynamic pressure (kinematic energy per unit mg of flowing liquid);  $Z$  is the elevation head;  $C$  is the constant total head for the flow.

Equation D.1 can be written for any two cross-sections, for example for sects. 1 and 2, of a flow conduit that yields

$$\frac{P_1}{\gamma} + \frac{V_1^2}{2g} + Z_1 = \frac{P_2}{\gamma} + \frac{V_2^2}{2g} + Z_2 + H_{ls} \quad (\text{D.2})$$

where subscripts 1 and 2 refer to the section of the hydraulic circuit between which the equation is applied;  $P_1$  and  $P_2$  are the static pressure at these sections;  $\gamma$  is specific gravity of the liquid under consideration;  $V_1$  and  $V_2$  are the velocities of the liquid through the considered sections;  $g$  is the gravity constant;  $Z_1$  and  $Z_2$  are the vertical coordinate of sections 1 and 2, respectively, with respect to a certain horizontal reference plane;  $H_{ls}$  is the overall hydraulic head loss between the considered sections.

Expressing Eq. D.2 in terms of head loss and assuming section 1 and 2 locate at the same vertical distance from the reference plane (i.e.,  $Z_1 = Z_2$ ), one can obtain

$$H_{ls} = \frac{P_1 - P_2}{\gamma} + \frac{V_1^2 - V_2^2}{2g} \quad (\text{D.3})$$

Equation D.3 provides a method to determine  $H_{ls}$  experimentally by measuring static pressures and velocities at sections 1 and 2 .

Total head loss,  $H_{ls}$  is regarded as the sum of major losses,  $h_l$  due to frictional effects in fully developed flow in constant-area tubes, and minor losses,  $h_m$  due to entrances, fittings, area changes, and so on:

$$H_{ls} = h_l + h_m \quad (\text{D.4})$$

The terms ‘major’ and ‘minor’ are conditional. They originated from traditional pipe hydraulics where the frictional losses are much greater than those due to local resistances. In analyzing local hydraulic conduits, it often happens that minor losses are much larger than major.

### D.1.1 Major Losses: Friction Factor

The friction losses are usually calculated using the Darcy-Weisbach formula [1]:

$$h_f = f_f \frac{L}{D} \frac{V^2}{2g} \quad (\text{D.5})$$

where  $f_f$  is the friction factor;  $L$  and  $D$  are the length and diameter of the pipe, respectively;  $V$  is the velocity of the liquid.

It must be emphasized that the friction factor  $f_f$  is empirical and can only be determined through experiments because it depends upon many parameters, e.g.,

velocity, diameter, density, viscosity and pipe surface roughness. For smooth laminar and turbulent flow in circular ducts, this friction factor is a function of Reynolds number  $Re$  only. It calculates as:

For laminar flow

$$f_f = \frac{64}{Re} \quad (D.6)$$

For turbulent flow

$$f_f = \frac{0.3164}{Re^{0.25}} \quad (D.7)$$

In these equations, the Reynolds number is calculated as

$$Re = \frac{VD}{\nu} \quad (D.8)$$

where  $\nu$  is kinematic molecular viscosity ( $L^2/t$ ).

The constants 64 and 0.3164 in Eqs. D.6 and D.7 are referred to as Blasius constants and valid only for tubular cross sections. Because in gundrills, the shank and the tip have irregular cross sections, these constants should be determined experimentally to calculate pressure losses in gundrilling.

### D.1.2 Minor Losses (Losses Due to Form Resistance)

The flow in the piping system may need to pass through a variety of fittings, bends, or abrupt changes in area. Additional head losses are encountered primary as a result of flow separation because violent mixing in the separated zones eventually dissipates energy. The minor head losses may be expressed as

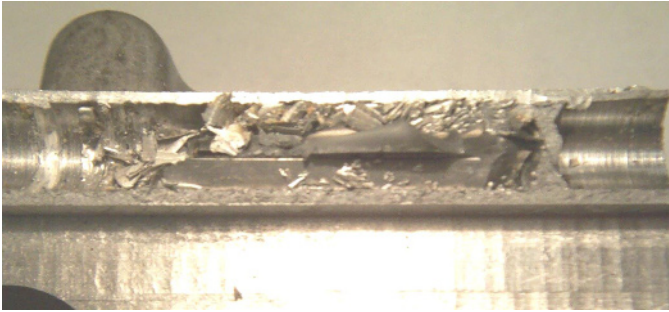
$$h_m = K \frac{V^2}{2g} \quad (D.9)$$

where the loss coefficient,  $K$  must be determined experimentally for each situation.

## D.2 Concept of the Critical MWF Velocity and Flow Rate

Reliable chip removal is one of the first and foremost requirements of any gundrilling application. The MWF (coolant) is supplied to a gundrill and then, after performing its cooling and lubricating actions in the machining zone, it carries away the chips through the V-flute toward the chip box. As a result, after the machining zone, a two-phase flow, i.e., the chip-coolant mixture, should be

considered. When the MWF flow rate is insufficient to transport the formed chip, the chip clogs the V-flute. If gundrilling is not stopped at this point, the drill fails due to excessive torque. Figure D.1 shows a common drill failure that happens in this case. The shown region adjacent to the terminal end of the drill tip is the most common place for chip clogging.



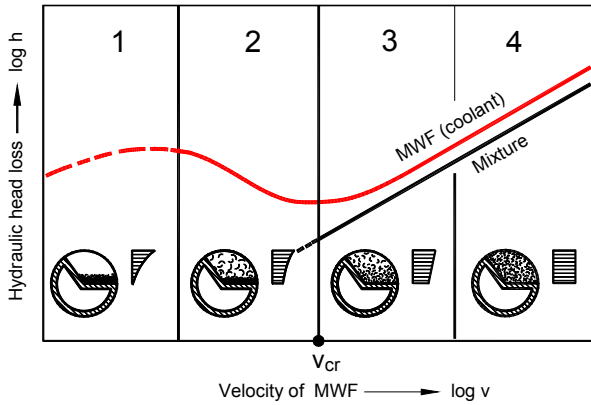
**Fig. D.1.** Gundrill failure due to chip clogging

The flow of the chip-coolant mixture through the chip removal passage may occur in different transportation modes. Figure D.2 shows the influence of the MWF velocity on the chip transportation and the velocity profiles of the mixture in the V-flute located horizontally. When the MWF velocity is low (zone 1 in Fig. D.2), the MWF does not have any effect on the chip accumulated in the V-flute. As such, the velocity profile shows that the MWF moves while the chip does not. Increasing the MWF velocity leads to its interaction with the chip (zone 2 in Fig. D.2). When it happens, part of the chip layer moves with the MWF while the other part forms a slow moving (gliding) layer in the V-flute. This transportation mode is called heterogeneous with a gliding layer. Because a lot of chips concentrate at the bottom of the V-flute, there is a possibility of formation of chip clog in the V-flute. Further increase in the MWF velocity leads to the heterogeneous transportation mode where the coolant-chip mixture forms (zone 3 in Fig. D.2). When heterogeneous flow takes place, reliable chip removal is achieved. Therefore, this transportation mode should be assured in gundrilling by supplying a sufficient MWF flow rate. Although the further increase in the MWF flow rate leads to the pseudohomogeneous flow mode (zone 4 in Fig. D.2), coolant pressure losses become significant. Moreover, achieving this regime requires great coolant flow rates that are not feasible in gundrilling unless the gundrilling system is equipped with a high-pressure unit.

As can be seen in Fig. D.2, when the heterogeneous flow mode of the mixture takes place, reliable chip removal is achieved. Therefore, this transportation mode should be assured in gundrilling by applying a sufficient MWF flow rate. The coolant-chip mixture velocity corresponding to the beginning of the heterogeneous mode is referred to as the critical velocity,  $v_{cr}$ . Observations reveal that, when the velocity of the mixture is less than  $v_{cr}$ , the formed chips clog the V-flute that, in turn, eventually leads to drill failure.

### D.2.1 MWF Flow Rate Needed for Reliable Chip Transportation

To calculate the MWF flow rate needed for reliable chip transportation along the V-flute, special analysis is needed. This analysis aims to define  $v_{cr}$ . The analysis is based on a known fact that transportation of a particle in any hydraulic passage takes place if the media velocity exceeds the particle's setting velocity. Therefore, the setting velocity is to be determined theoretically/experimentally.



**Fig. D.2.** Chip-coolant transportation modes: (1) two-phase flow, (2) heterogeneous flow with a gliding (slow moving) chip layer, (3) heterogeneous flow, and (4) pseudo-homogeneous flow

For any particle in the MWF, the settling rate is a function of the gravitational force (downward) and the frictional resistance (opposite). Because the mass of a particle increases proportionally to the cube of its average radius, but drag surface area only increases proportionally to the square of the radius, larger particles settle faster and, therefore, their removal requires higher velocity of the MWF.

To estimate the setting velocity, consider the equilibrium condition for a piece (particle) of the chip setting in the MWF. This equilibrium can be thought of as achieved when the gravitation force is equal to that of friction resistance. From Newton's second law

$$m_{ch} \frac{dV_s}{dt} = F_g - F_b - F_d \quad (D.10)$$

where  $m_{ch}$  is the mass of the particle,  $V_s$  is the settling velocity, and the right side of Eq. D.10 shows forces due to  $F_g$  - weight,  $F_b$  - buoyancy and  $F_d$  - drag.

The gravitational force calculates as

$$\text{Gravitational Force} = F_g - F_b = (\rho_{ch} - \rho_v) g V_p \quad (D.11)$$

where  $\rho_c$  is the density of MWF,  $\rho_{ch}$  is the density of the chip (the work material),  $g$  is the acceleration due to gravity, and  $V_p$  is the volume of particle.

The drag force is calculated as

$$F_d = \frac{C_D A_p \rho_c V_s^2}{2} \quad (D.12)$$

where  $C_D$  is the drag coefficient, and  $A_p$  is the average particle area.

Equation D.10 can be re-written as

$$m_{ch} \frac{dV_s}{dt} = (\rho_{ch} - \rho_c) V_p g - \frac{C_D A_p \rho_c V_s^2}{2} \quad (D.13)$$

After an initial transient period, the system reaches its steady-state so that

$$(\rho_{ch} - \rho_c) V_p g = \frac{C_D A_p \rho_c V_s^2}{2} \quad (D.14)$$

From Eq. D.14 one may obtain an expression for  $V_s$  as

$$V_s = \sqrt{\left[ \frac{2g(\rho_{ch} - \rho_c)}{C_D \rho_c} \right] \frac{V_p}{A_p}} \quad (D.15)$$

If the particle of the chip can be considered as spherical then

$$V_p = \frac{\pi d_p^3}{6} \quad \text{and} \quad A_p = \frac{\pi d_p^2}{4} \quad (D.16)$$

If it is further assumed that the setting velocity is so that the Reynolds (Re) number is less than 0.1, then the drag coefficient according to Stokes approximation is

$$C_D = \frac{24}{\text{Re}} = \frac{24\mu}{\rho_c V_s d_p} \quad (D.17)$$

Finally, substituting Eqs. D.16 and D.17 into Eq. D.15, one can obtain

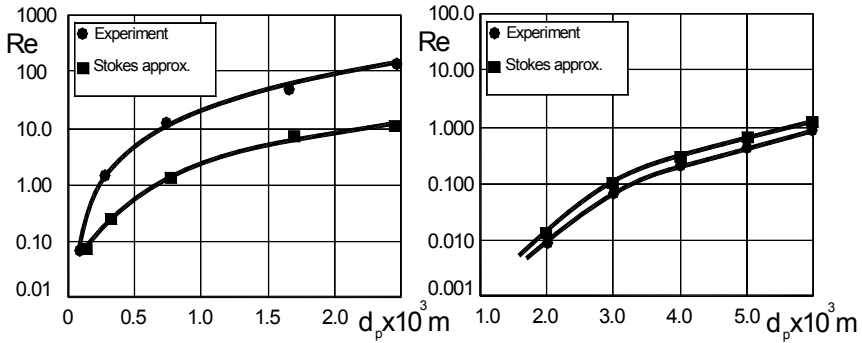
$$V_s = \sqrt{\frac{4g(\rho_{ch} - \rho_c)d_p}{3 \left( \frac{24\mu}{\rho_c V_s d_p} \right) \rho_c}} = \frac{(\rho_{ch} - \rho_c) d_p^2}{18\mu} \quad (D.18)$$

where  $\mu$  is the dynamic viscosity of MWF, and  $d_p$  is the particle diameter.



Many of the real-world chip particle characteristics which do not entirely conform to the assumptions used in this analysis include: (1) non-spherical particles, (2) variable particle density, (3) uneven flow through the V-flute, (4) size fractionations and (5) particle contact, with large chip elements interfering with smaller ones. Besides, the Reynolds number should be less than 0.1 to use the Stokes approximation.

A comparison between the Stokes approximation and the complete iterative solution for the setting velocity of aluminum chips is provided in Fig. D.3. As can be seen, the Stokes approximation provides fairly good results compare to the results of experiments particularly in the to deep-hole machining range of Re.



**Fig. D.3.** Comparison between the Stokes approximation and the experimental data for the setting velocity of aluminum chips

The critical velocity is calculated using the following formula [2, 3]:

$$v_{cr} = 8.4 \left[ C_v \left( \frac{\rho_{ch}}{\rho_c} - 1 \right) g D_{5-5} V_s \right]^{1/3} \quad (D.19)$$

where  $C_v$  is the weight concentration of the chips in the coolant expressed as fraction of unity; for reliable gundrilling  $C_v = 0.015-0.017$ ;  $D_{5-5}$  is the hydraulic diameter of the chip removal passage (in the considered case, the V-flute), mm;  $\rho_{ch}$  and  $\rho_c$  are specific densities of the chip and coolant, respectively,  $\text{kg/m}^3$ .

Our observations showed [3] that the reliable chip removal is achieved when the MWF velocity in the V-flute is

$$v_{c-opt} = v_{cr} \frac{8.54}{|\ln C_v|} \quad (D.20)$$

This velocity is referred to as the optimal MWF velocity and the MWF flow rate that assures this velocity is the optimal MWF flow rate.

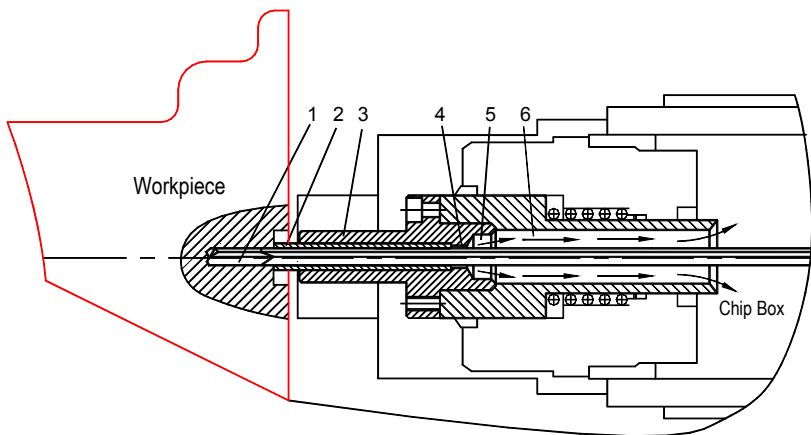
The minimum flow rate that has to be supplied to the gundrill to assure the critical MWF velocity in the V-flute then calculates as

$$Q_{cr} = v_{cr} A_v \quad (D.21)$$

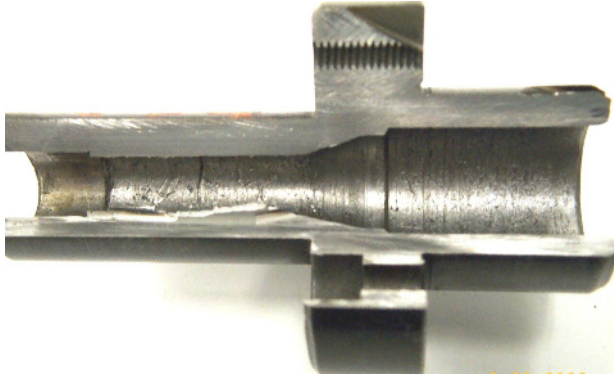
where  $A_v$  is the cross-sectional area of the V-flute.

As can be seen from this equation, the optimum MWF velocity increases with the chip concentration. In other words, the use of higher feed rates requires increase in the MWF flow rate to assure reliable chip removal. Unfortunately, this is not the case in practice. The author's analysis of many gundrilling systems reveals many gundrill machines suffer from a common design flaw in their chip removal channels. The essence of this flaw is in the fact that the chip removal channel is usually made of sections having progressively increasing diameters. As such, it becomes not possible to provide  $v_{c-opt}$  for each passage in the whole chip removal system of the drilling machine.

The example of such a design is shown in Fig. D.4. Gundrill 1 penetrates into the workpiece from starting bushing 2 held in bush holder 3. The MWF-chip mixture begins its way into the V-flute, where its optimal velocity defined by Eq. D.20 is maintained by supplying sufficient MWF flow rate. However, the mixture eventually leaves the flute flowing through passages 4, 5, and 6 having progressively increasing diameters. Because the MWF flow rate is kept the same, the MWF velocity decreases proportionally to increasing cross-sectional areas. At certain cross section, this velocity becomes less than the critical velocity that theoretically ceases chip removal. Practically, the chips move due to the push from incoming chips from the V-flute. As a result, the walls of the discussed chip removal channels are covered by the built-up of the workpiece material because the rotating drill imposes an additional high-speed rotating motion on the slowly sliding chip and thus the chips rub the walls leaving the discussed built-up. Figure D.5 shows a cross-section of the bushing holder having chip-removal channels with the built-up of the work material.

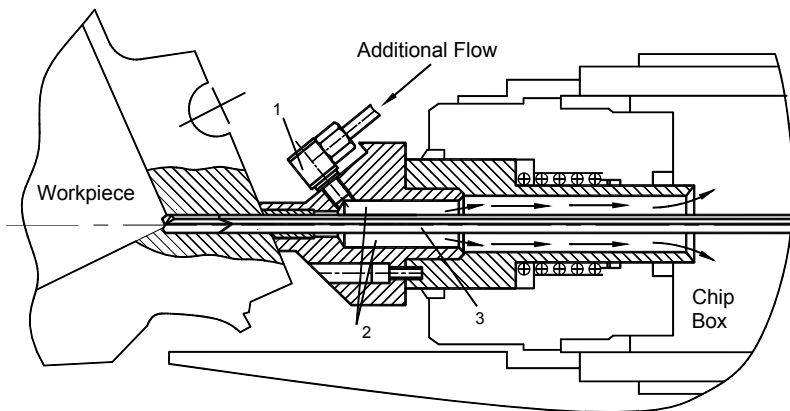


**Fig. D.4.** Typical design of the chip removal passage used in production line machines in the automotive industry



**Fig. D.5.** Cross-section of the bush holder showing aluminum build-up on the wall of the chip removal passage

Trying to avoid the discussed problem, some gundrill machine manufactures try to introduce an additional MWF flow to the chip removal channel. Figure D.6 shows a common solution used in the automotive industry. As can be seen, an additional MWF flow is introduced in the place where the chip removal passage becomes significantly larger. In the practice, however, the introduction of the additional flow in this manner makes chip removal even less reliable. As a result, it is common that the hydraulic lines with the additional MWF flow are closed down. The reason for that is that the additional MWF flow has much higher flow rate than that of the MWF–chip mixture so the introduced flow has much higher velocity. In practical terms it means that a high-velocity jet from the MWF fitting 1 enters the chip removal channel 2 creating a flow ‘shield’ for the mixture. The latter may move only when it is covered by the rotating gundrill 3, i.e., when the V-flute faces down.



**Fig. D.6.** Improper introduction of an additional MWF flow onto the chip removal passage

### D.2.3 Example D.1

*Problem:* Calculate the optimal MWF flow rate for the following conditions:

Gundrill: 8 mm diameter, workpiece material: aluminum alloy 319 having density  $\rho_{ch} = 2,829 \text{ kg/m}^3$ , maximum equivalent diameter of the chip is determined by Eq. D16 using actual chip  $d_p = 0.0048 \text{ m}$  (4.8 mm). Drill rotational speed is 8,000 rpm, feed rate is 0.99 m/min (990 mm/min). MWF is a water-soluble coolant having 8% concentration. MWF mass density  $\rho_c = 980 \text{ kg/m}^3$ .

*Solution:* The kinematic and dynamic viscosity of the MWF has to be defined. Because MWF is a water-soluble mixture, the resultant kinematic viscosity of the MWF,  $v_c$  can be calculated as

$$v_c = \frac{n_w v_w + n_{oil} v_{oil}}{100} \quad (\text{D.22})$$

where  $v_w$  and  $v_{oil}$  are kinematic viscosities of water and oil (dissolved in it), respectively;  $n_w$  and  $n_{oil}$  are volume contents (in %) of water and oil, respectively.

It is worthwhile to point out here that the kinematic velocity of water and oil is a temperature dependant parameter. Assuming that the mean temperature of the coolant is  $37.8^\circ\text{C}$ ,  $v_w = 0.68 \text{ cSt}$ . In the same way, the kinematic velocity of the oil is determined to be  $v_{oil} = 33 \text{ cSt}$  (at the same temperature). Because the coolant has 8% oil concentration,  $n_w = 92\%$  and  $n_{oil} = 8\%$ . Therefore, the resultant kinematic viscosity is

$$v_c = \frac{92 \times 0.68 + 8 \times 33}{100} = 3.27 \text{ cSt} = 3.27 \times 10^{-6} \text{ m}^2/\text{s}$$

Dynamic viscosity is calculated as

$$\mu = \rho_c v_c = 980 \times 3.27 \cdot 10^{-6} = 3.21 \times 10^{-3} \text{ kg} / (\text{s} \cdot \text{m})$$

The setting velocity is calculated using Eq. D.18

$$V_s = \frac{(\rho_{ch} - \rho_c) d_p^2}{18\mu} = \frac{(2829 - 980) \times 0.0048^2}{18 \times 3.21 \times 10^{-3}} = 0.74 \text{ m/s}$$

Cross-section area of the V-flute is determined graphically as  $A_v = 15 \text{ mm}^2$ , its wet perimeter: is  $P_v = 15.75 \text{ mm}$ . Then its hydraulic diameter calculates as

$$D_{s-s} = \frac{4A_v}{P_v} = \frac{4 \times 15}{15.75} = 3.8 \text{ mm}$$

The critical velocity is calculated using Eq. D.19:

$$v_{cr} = 8.4 \left[ 0.015 \left( \frac{2829}{980} - 1 \right) \times 9.81 \times 3.8 \times 0.74 \right]^{1/3} = 7.75 \text{ m/s}$$

The optimal MWF velocity is calculated using Eq. D.20:

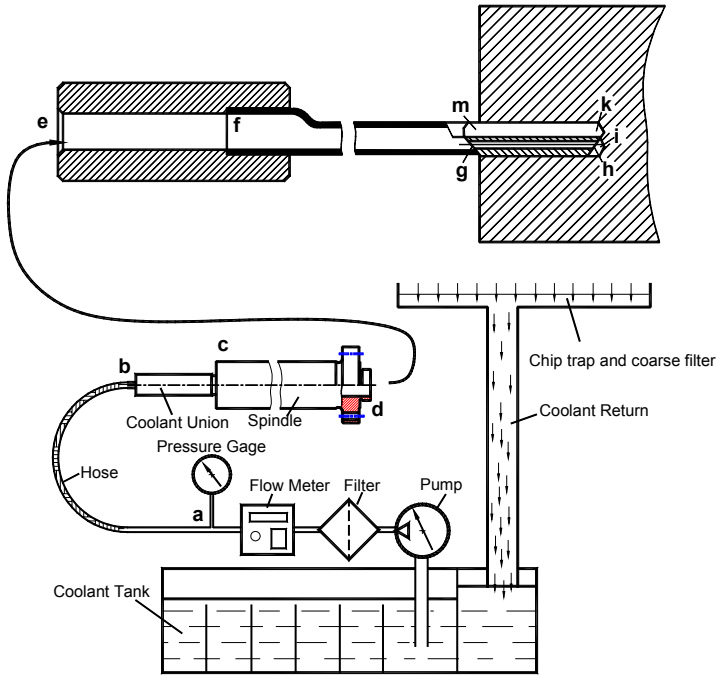
$$v_{c-opt} = v_{cr} \frac{8.54}{|\ln C_v|} = 7.75 \frac{8.54}{|\ln 0.015|} = 15.76 \text{ m/s}$$

and thus the optimal MWF flow rate that assures the optimum MWF velocity in the V-flute is calculated as

$$Q_{opt} = v_{c-opt} A_v = 15.76 \times 15 \times 10^{-6} = 236.4 \times 10^{-6} \text{ m}^3/\text{s} = 13.91 \text{ l/min}$$

### D.3 Inlet Coolant Pressure

Because the physical meaning of the inlet MWF pressure is the most misunderstood issue in gundrilling and in any cutting tool with internal MWF supply, this section aims to clarify this issue in simple terms. To do this, let us consider the complete hydraulic circuit of a gundrilling machine shown in Fig. D.7. The MWF tank provides the main coolant storage. It could be installed next to a deep-hole machine or one MWF tank and pump(s) can serve a group of machines. The pump has to generate MWF pressure while supplying a certain flow rate. A filter shown in Fig. D.7 is a fine-grade filter that cleans the MWF to be supplied into the drilling system. Usually the pump and the filter are located on the MWF supply system regardless of its relative location with respect to the gundrilling machine. The flow meter (unfortunately only a few many gundrilling and drilling machines are equipped with this important device) is to measure the MWF flow and the pressure gage is to measure its pressure. Additionally, properly designed gundrilling MWF supply systems should have a temperature gage that measures the MWF temperature. The MWF delivery system is connected to the spindle by a flexible high-pressure hose. To introduce the MWF into the rotating spindle, a high-pressure coolant union (rotating joint) is used. Passing the spindle (and possibly a spindle extension which is so popular in the automotive industry), the MWF flows into a drill holder (in Fig. D.7 it is shown as a collet chuck) and then it reaches the gundrill driver. Passing the driver, the MWF flows through the shank and then the tip reaching the bottom clearance space. From this space, the MWF flows through the region of the shoulder deb-off into the V-flute. Here, the MWF picks up the chip and transports it along the V-flute. Leaving the gundrill and passing through coarse filters, the MWF returns to the “dirty” section of the coolant tank.



**Fig. D.7.** A simplified schematic of a typical hydraulic circuit of a deep-hole machine

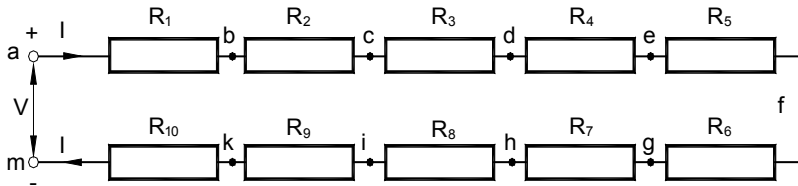
The MWF basic parameters (flow rate, pressure, and temperature) are called the inlet parameters. It should be clear to everybody who deals with the design of drilling systems and tools that the MWF flow rate does not change along the hydraulic circuit of a (gun)drilling machine (i.e., it is the same in any considered point of MWF circuit) while the MWF pressure and temperature do change. As such, the pressure only decreases starting from the pressure gage while temperature may decrease and increase. In any cutting tools with internal MWF supply, the MWF pressure serves as a mean to deliver sufficient flow rate into the machining zone. It could serve as a measure of the efficiency of the hydraulic circuit of a machine – higher efficiency means lower pressure is needed to deliver the same flow rate.

To understand the concept of the MWF pressure in gundrilling, an electric circuit analogy is used. As such, the MWF flow rate,  $Q$  is associated with the electric current,  $I$ , pressure,  $p$  – with voltage (electrical tension),  $U$ , and the hydraulic resistance,  $\xi$  (which includes, major,  $\lambda$  and minor,  $\zeta$  losses) – with electrical resistance,  $R$ . Using this analogy, the hydraulic system shown in Fig. D.7 can be represented as an electrical circuit shown in Fig. D.8.

In Fig. D.8, the following designations are adopted:

- point  $a$  corresponds to the pressure gage,  $R_l$  represents the hydraulic resistance of the flexible hose.

- point  $b$  corresponds to the inlet of the coolant unit,  $R_2$  represents its resistance.



**Fig. D.8.** Electric analogy of the gundrilling hydraulic circuit

- point  $c$  corresponds to the inlet of the spindle and  $R_3$  represents its resistance
- point  $d$  corresponds to the inlet of the tool holder (chuck) and  $R_4$  represents its resistance
- point  $e$  represents the inlet of the driver and  $R_5$  represents its resistance
- point  $f$  represents the inlet of the shank and  $R_6$  designates its resistance
- point  $g$  correspond to the inlet of the coolant hole (orifice) in the gundrill tip and  $R_7$  represents its hydraulic resistance
- point  $h$  corresponds to the inlet of the bottom clearance space and  $R_8$  represents its resistance
- point  $i$  corresponds to the inlet of the space limited between shoulder deb-off flank of the gundrill and the bottom of the hole being drilled and  $R_9$  represents its hydraulic resistance
- point  $k$  corresponds to the inlet of the V-flute and  $R_{10}$  represents its hydraulic resistance
- point  $m$  represents open space having the atmospheric pressure

For the model shown in Fig. D.8, Ohm's law is valid, i.e.,

$$I = \frac{V}{R_{\Sigma}} \left( Q = \frac{p}{R} \right) \quad (\text{D.23})$$

where  $I$  is the electric current (flow rate,  $Q$ ),  $V$  is the potential difference between points  $a$  and  $m$  (pressure,  $p$ ),  $R$  is the total electrical resistance (the total hydraulic resistance).

Because the resistors  $R_i$  are connected in series, the total resistance (electric and hydraulic) calculates as

$$R_{\Sigma} = R_1 + R_2 + R_3 + R_4 + R_5 + R_6 + R_7 + R_8 + R_9 + R_{10} = \sum_{i=1}^{10} R_i \quad (\text{D.24})$$

For a given gundrilling system (gundrilling machine and gundrill)  $R_{\Sigma} = \text{Const.}$  If  $Q_{cr}$  (Eq. D.24) is the flow rate corresponding to the critical MWF velocity to be delivered then the inlet pressure,  $p_m$  calculates from Eq. D.23 as follows:

$$p_{in} = Q_{cr} R_{\Sigma} \quad (D.25)$$

Knowing the hydraulic resistances  $R_i$ , the actual static pressure in any desirable point can be calculated easily knowing the fact that the MWF pressure at point  $m$  is equal to zero (the atmosphere pressure). Amongst the points shown in Fig. D.8, point  $h$  presents highest practical interest because the static pressure in the bottom clearance space determines the efficiency of the MWF to perform its cooling and lubricating functions in the machining zone. This pressure defined MWF flows in the bottom clearance space and its penetration into the drill's flank and supporting pad contact surfaces. In Chap. 5, Rule 3 is introduced which states that this pressure should be as high as possible.

The next issue is how to calculate this pressure to assure its maximum under the given MWF flow rate. A common perception is to increase inlet pressure (as measured at point  $a$  (Figs. D.7 and D.8) by introducing high-pressure MWF systems. It is no surprise that this measure does not help to achieve the goal simply because the perception is incorrect. Foregoing analysis suggests that the MWF pressure in the bottom clearance space calculates as

$$p_i = (R_9 + R_{10}) Q_{cr} \quad (D.26)$$

Comparison of Eqs. D.24 and D.26 shows that hydraulic resistances  $R_1 - R_8$  are 'bad' resistances because they decrease the MWF pressure in the bottom clearance space under a given inlet pressure. Indeed,

$$p_h = p_{in} - (R_1 + R_2 + R_3 + R_4 + R_5 + R_6 + R_7) Q_{cr} \quad (D.27)$$

Therefore, all means and measures to reduce  $R_1 - R_8$  should be considered in the design of gun-drills and gun-drilling systems.

In contrast, hydraulic resistances  $R_9 - R_{10}$  are regarded as 'good' resistances because, according to Eq. D.26, they determine the MWF pressure in the bottom clearance space. Unfortunately, this fact has never been properly understood in the gun-drilling industry where the opposite treatment of the mentioned hydraulic resistance is the case.

Although the discussed analogy is of great help to understand the principles of the hydraulic system of gun-drilling and thus serves its purpose, the physics of resistance is more complicated. In reality, Eq. D.2 holds in electric circuits but not in hydraulic ones because the hydraulic resistance is not linear with respect to the flow rate. Rather it is proportional to  $Q^2$  that makes the whole picture a bit more complicated although the discussed principle is perfectly valid. This dependence makes the design of gun-drilling hydraulic circuits even more sensitive to the smallest changes in the design parameters.

An important issue is the fact the hydraulic resistance defined in Eqs. D.23 through D.27 cannot be measured using available apparatuses while the electrical resistance can be measured using a simple ohmmeter. Therefore, a more practical analogue of Eq. D.24 having absolutely identical physical meaning can be written as



$$p_{in} = \gamma_c (h_1 + h_2 + h_3 + h_4 + h_5 + h_6 + h_7 + h_8 + h_9 + h_{10}) \quad (D.28)$$

where  $\gamma_c$  is the specific gravity of the coolant ( $\text{N/m}^3$ ), and  $h_i, i=1 \dots 10$  are hydraulic head loss of the corresponding regions 1–10 (m).

In terms of Eq. D.28, Eqs. D.26 and D.27 can be re-written as

$$p_i = \gamma_c (h_9 + h_{10}) \quad (D.29)$$

$$p_h = p_{in} - \gamma_c (h_1 + h_2 + h_3 + h_4 + h_5 + h_6 + h_7 + h_8) \quad (D.30)$$

The next logical question to be answered is about the extent that the tool designer has to control these hydraulic resistances.

## D.4 Analysis of Hydraulic Resistances

### D.4.1 Analysis of Hydraulic Resistances Over Which the Designer Has No or Little Control

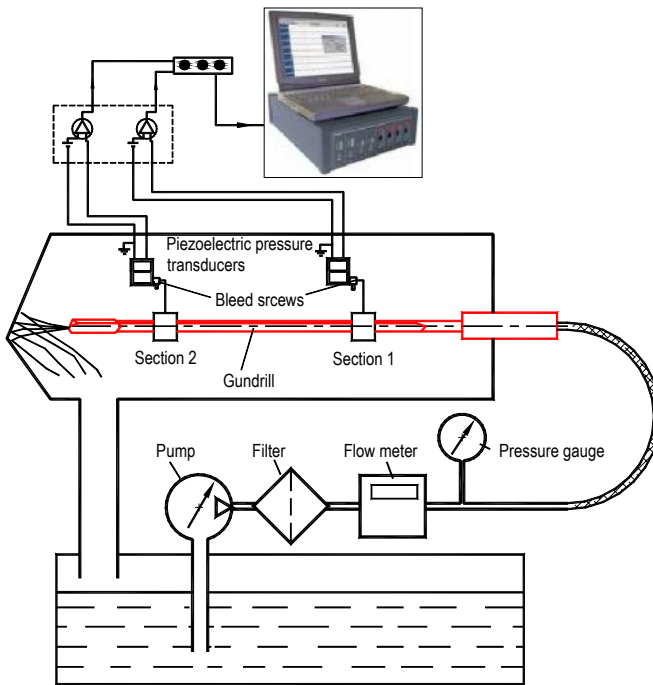
#### D.4.1.1 Invariable Resistances $h_1-h_5$

For a given gundrilling machine, particular values of hydraulic resistances  $h_1-h_5$  depend on MWF flow mode [1] because their design and cross-sectional areas are given. For a relatively narrow range of gundrill diameters (for example, 5–8 mm) and for the same MWF type (water soluble or oil-based), the MWF flow mode would be the same and thus these resistances are constants, i.e., do not depend on the particular design of a gundrill used. In other words, the tool designer cannot change these resistances. If the pressure sensor is installed directly on the coolant union, the hydraulic resistance  $h_1$  should not be considered and thus particular location of the coolant system with respect to the machine has no influence. The experimental results show that resistances  $h_1-h_5$  are small compare to other hydraulic resistances (less than 5%). Experience shows that the sum of these pressure losses is normally in the range of 0.1–0.3MPa.

#### D.4.1.2 Hydraulic Resistance of the Shank, $h_6$

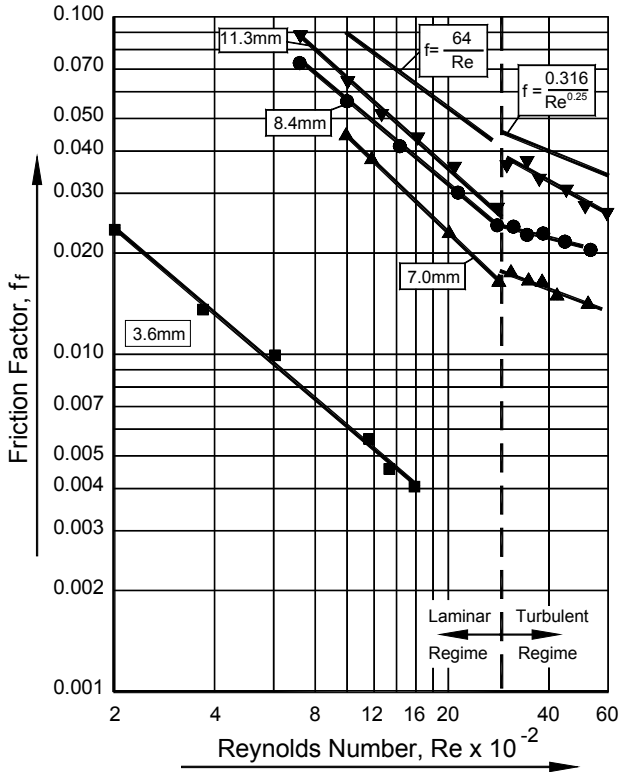
Hydraulic resistance of the shank,  $h_6$  is a function of its cross-sectional area and length, surface roughness of its internal passage, and the MWF flow mode. The cross-sectional area is determined by the diameter of the shank, its wall thickness, and V-flute profile. To the first approximation, the shank diameter, its wall thickness, and V-flute profile are almost the same (in terms of hydraulic resistance) for different gundrill designs of the same diameter. Therefore, hydraulic resistance of the shank,  $h_6$  is a function of its length providing that other parameters are given. According to Eq. D.5, this resistance is directly proportional to the shank length. As a result, for a given tool layout, where the gundrill diameter and its length are set, resistance  $h_6$  should also be considered as a constant. Note, this parameter does not depend on the gundrill designer excluding some exotic cases where the gundrill designer can select ‘perfect shank parameters’ for a given application.

A specially designed set-up has been used for the measurements of energy losses in gundrill shanks of different diameter. Figure D.9 shows the schematic diagram of the over-all flow circuit. The variable displacement piston pump was capable of delivering flow up to 320 L/min at the maximum pressure of 45.5MPa. A precision turbine flow meter was used to measure the flow rate to an accuracy of  $\pm 0.5\%$ . The pressure drop across the sections was monitored with pressure transducers to an accuracy of  $\pm 0.1\%$ . The measuring sections were located after allowing necessary entrance length to establish fully developed flow. The temperature of the MWF was recorded at the inlet and then used in the calculation to adjust the actual coolant properties. The coolant used in experiments was Shell Tellus Oil 25 with kinematic viscosity at 37.8°C of 33.0 centistokes and mass density of 876 kg/m<sup>3</sup>.



**Fig. D.9.** Experimental setup to assess pressure losses in the shank

The experimental data are presented in Fig. D.10 in the form of friction factor-Reynolds number charts. For the purpose of comparison, the lines representing the results of calculation for the corresponding flow regimes (Eqs. D.5 and D.7) are also shown. As seen, the friction factors obtained experimentally are considerably less than those for circular tubes in both flow regimes particularly for small shank diameters. For 7.0 mm shank diameter, circular-tube solution overestimates the friction factor by 50% while for 11.3 mm shank – by 20%. For 3.6 mm, the kidney-like passage of the shank is so narrow that the flow is always in the laminar regimes.



**Fig. D.10.** Friction factor vs Reynolds number

#### D.4.1.3 Hydraulic Resistance of the V-flute $h_{10}$

Hydraulic resistance of the V-flute,  $h_{10}$  is the function of the V-flute profile and its length. The V-flute profile is a standard feature of a gundrill. The length of the V-flute is given by the tool layout. Therefore, this resistance should be considered as a constant providing that the flow rate sufficient to transport the chip along this flute is supplied. Although  $h_{10}$  is considered as 'good' resistance, the tool designer should not attempt to increase this resistance because it always means deterioration of chip removal. Moreover, to facilitate chip removal, this resistance should be as small as possible. To achieve this, the V-flute should not have any steps or bumps (usually present at the tip-shank joint), should have very sharp corner radii to prevent chip trapping between these corners and the wall of the hole being drilled, and should be polished. It is important that hydraulic resistance  $h_{10}$  is relatively small compare to other hydraulic resistance (less than 1%).

## D.4.2 Variable Resistances Over Which the Designer Has Control

### D.4.2.1 Resistance of the Coolant Passage in the Tip $h_7$

The hydraulic resistance of the coolant hole in the gundrill's tip,  $h_7$  is one of the most ignored parameters in gundrilling although this resistance is often the highest. Gundrill manufacturers have adopted different shapes of the coolant hole in the tip, namely one round hole, two round holes and a kidney hole as shown in Fig. D.11.



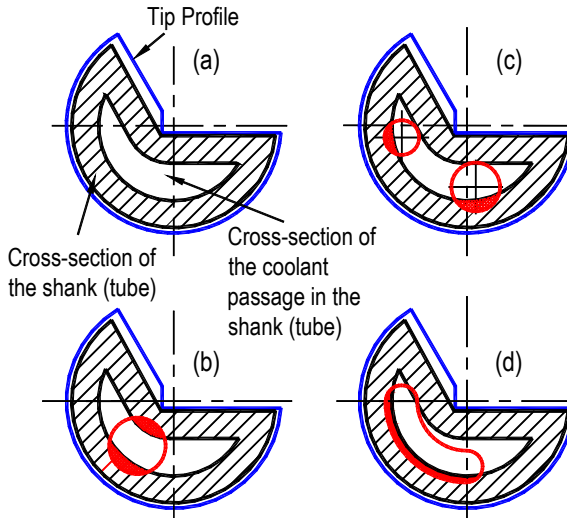
**Fig. D.11.** Different shapes of the coolant passage adopted by gundrill manufactures: one round hole, two round holes, and a kidney-shaped hole.

It is interesting to note that all the mentioned shapes are in use today although their dimensions and locations differ from one carbide (and thus gundrill) manufacturer to another. Moreover, the same gundrill manufacturer often produces gundrills with different shapes and sizes of this coolant hole. This is particularly true when a gundrill producer uses different carbide (rods or preforms) suppliers. In practice, not much attention is paid to this design particularity. Gundrills having various coolant holes are used interchangeably for the same job on the same machine. The most conservative practitioners, however, are of the strong opinion that a kidney-shaped coolant passage weakens the tip.

According to the author's experience, a simple switch from one gundrill design to another having different parameters of coolant hole may cause significant although not yet understood problems. For example, consider consequence of changing a gundrill having a kidney-shaped coolant hole in the tip to a gundrill having one hole (all other parameters are kept the same). As such, if the inlet pressure is kept the same (this is the most practical case because most of gundrilling machines control only the inlet pressure), the flow rate through the second gundrill may reduce by 25–30% that often causes the problem with reliable chip transportation. As a result, there is a good chance that the second gundrill fails due to chip clogging in the V-flute. The considered case is not hypothetical. Rather, it happens every day in gundrilling practice.

To clarify the issue further, Fig. D.12a shows the overlapped profiles of the tip and the shank. As can be clearly seen from this figure, the coolant passage in the shank has a crescent shape. Figure D.12b shows the overlapped profiles of the tip, the shank, and the coolant passage made as a single round hole. As clearly seen in this figure, the apparent cross-sectional area (measured as  $A_{c-a} = \pi d_c^2 / 4$  where  $d_c$  is the diameter of the coolant hole) of this coolant passage is greater than the effective area,  $A_{c-e}$  equal to the apparent cross-sectional area minus the areas of two

crosshatched segments. Figure D.12c shows typical locations of holes in the case of two-hole coolant passage in the tip. As can be seen, the effective area is smaller than the apparent area. Figure D.12d shows the typical location of the kidney-shaped coolant hole. When properly designed and positioned, the apparent cross-sectional area of the kidney-shaped passage is close to the effective area.



**Fig. D.12.** Scaled overlapped view of the shank, tip, and coolant passage

As an example, Table D.1 shows the results of actual measurements made on standard gundrills. As can be seen, the difference between the apparent and effective areas can be significant. Moreover, this difference is not consistent and varies from one drill diameter to another. Unfortunately, the leading gundrill and gundrilling system manufacturers as well as end users pay little attention to this important issue.

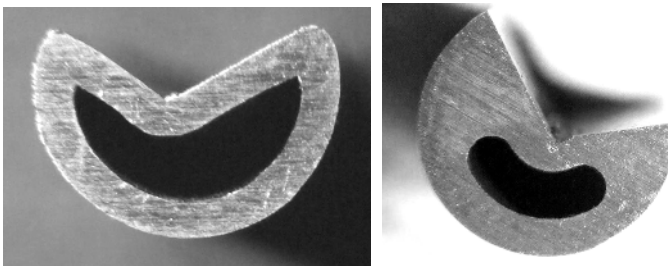
Specialists and practitioners in the field of any kind of drilling with internal MWF supply should realize that significant pressure losses occur due to changes in the shape and cross-sectional areas of the coolant passage in the shank and that in the tip. As can be clearly seen in Fig. D.12, the tip having a kidney-shaped coolant passage should have the minimum pressure losses of the coolant flow because the shape of the passage is closer to that in the shank and the cross-sectional area of the kidney-shaped passage in the tip is largest. In practice, however, it is not the case where the actual shape and area of the kidney-shaped coolant passage varies from one manufacturer of the carbide blanks for gundrills to another. In any case, it is still much smaller than the cross-sectional area of the coolant passage in the shank as can be clearly seen in Fig. D.13.

Figure D.13 shows the scaled comparison of these two areas for a gundrill of 8mm widely used in the automotive industry. Moreover, it happens quite often that the same carbide blank supplier manufactures the same diameter of carbide sticks for gundrilling with different cross-sections of the kidney-shaped hole with no apparent reason. To support this statement, Fig. D.14 shows the cross-sections of

two carbide sticks of the same diameter (8.85 mm meant for gundrills of 8 mm diameter) manufactures by the same reputable supplier.

**Table D.1.** Comparison the apparent and effective areas of coolant passage in the gundrill tip

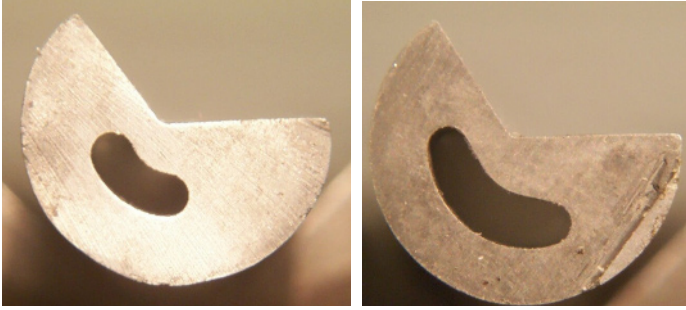
Drill dia (mm)	Area of small hole (mm <sup>2</sup> )	Area of bigger hole (mm <sup>2</sup> )	Apparent (total) area, (mm <sup>2</sup> )	Effective area, (mm <sup>2</sup> )	Area reduction (%)
2.8	0.4418	0.63618	1.07803	0.7940	26.35
3.2	0.44184	0.79891	1.15075	0.8415	26.85
3.6	0.50752	1.00300	1.57050	0.9350	40.40
4.1	0.84960	1.13112	1.98072	1.3090	34.26
4.6	0.96780	1.49590	2.46370	1.5895	35.48
5.0	1.28696	1.76737	3.05433	1.9635	35.69
5.5	1.32750	2.01088	3.33838	2.4500	26.61
6.0	1.53960	2.27010	3.80960	3.3420	12.27
6.5	1.74390	2.54500	4.28890	3.6344	15.04
7.0	2.01090	3.20510	5.21600	4.2300	18.82
7.5	2.24350	3.80180	6.04530	4.7300	21.16
8.0	2.65940	4.48670	7.14610	6.0700	15.05



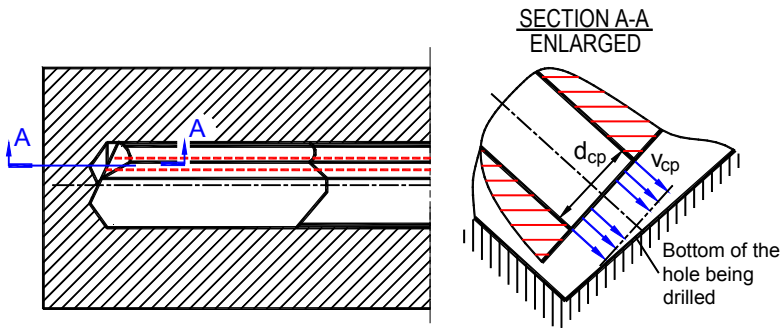
**Fig. D.13.** Cross-sections of the coolant passages: (a) in the shank, and (b) in the tip

#### D.4.2.2 Resistance of the Bottom Clearance Space $h_8$

In the author's opinion, this is the most important (as normally it accounts for 30–40% of the total pressure losses in gundrilling) and one of the least understood issues in gundrilling. The MWF pressure loss in the bottom clearance space is mainly due to the interaction of the MWF jet from the coolant passage in the tip.



**Fig. D.14.** Cross-sections of two carbide sticks having the same diameter (8.85 mm)



**Fig. D.15.** Interaction of the MFF jet leaving the coolant passage in the tip with the bottom of the hole being drilled

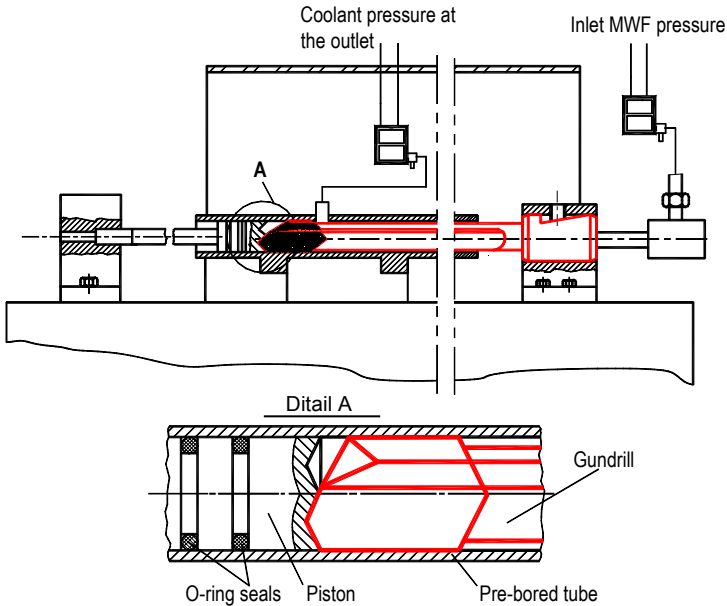
and the bottom of the hole being drilled. This is because the outlet of the coolant passage in the tip locates very close to this bottom as shown in Fig. D.15

Using the control volume method and the force balance equation, the author developed the model of MFF pressure loss in the bottom clearance space [4]. According to this model, this loss is proportional to the MFF jet velocity  $v_{cp}$ , diameter of the coolant passage  $d_{cp}$ , and the location of the coolant passage with respect to the bottom of the hole being drilled.

In the author's opinion, the major problem with the MFF supply in many existing gundrilling systems is insufficient inlet MFF pressure to assure the optimal flow rate. This is because the pressure loss  $R_\delta$  is not accounted for in research and practice of gundrilling. As such, the flow rate vs pressure in gundrilling is assessed using setups similar to that shown in Fig. D.9 where there is no resistance  $R_\delta$  [5].

To assess the pressure losses in the tip and the bottom clearance space, an improved experimental set-up was used to simulate better the flow in a gundrill. Figure D.16 shows the schematic diagram of this set-up. The gundrill was placed into the tube, which was pre-bored with the drill under test. A piston with two O-rings was installed to simulate the bottom of the hole being drilled as shown in Fig. D.16. A steel rod fixed at one end, and screwed to the piston at the other end, kept

the piston at fixed position. The side of the piston facing the drill tip was machined with the drill under test so it was shaped exactly the same as the bottom of the hole being drilled. The drill was clamped at the driver point and close contact was maintained between the piston and the tip. Although a full simulation of the chip removal has not been achieved because there were no chips in the V-flute, the study was mainly intended to assess the pressure loss in different types of drill tips.



**Fig. D.16.** Improved experimental setup

Figure D.17 shows an example of flow rate vs inlet pressure charts obtained using the improved set-up. As can be clearly seen, the pressure losses do not change significantly with the gundrill length. It means that, when properly measured, the pressure losses in the shank are relatively small compared to that in the tip and in the bottom of the hole being drilled. Unfortunately this important fact is completely unknown for gundrill manufacturers and end users.

#### *D.4.2.3 Pressure in the Bottom Clearance Space*

As discussed above, the pressure in the bottom clearance space is determined by hydraulic resistance  $h_9$  as the hydraulic resistance of the V-flute should be kept at minimum possible.

## **D.5 Practical Implementation in the Drill Design**

The importance of maintaining a high MWF pressure in the bottom clearance space is explained in Chap. 5. When this pressure increase by twofold complying with the design rules introduced in Chap. 5, tool life increases up to four times [2, 4, 6].



As such, the feed rate can be increased by 30–40% without compromising quality parameters of drilled holes [2]. The results obtained, however, also have methodological significance for the designers and users of gundrills. One of interesting uses of the obtained results is presented in this section for the sake of exemplification.

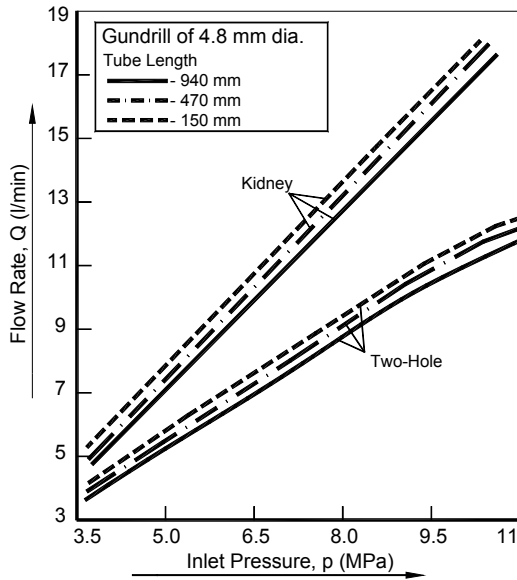


Fig. D.17. Flow rate vs inlet pressure

Consider one of the unusual gundrill designs which, in the author’s opinion, was the best attempt to improve tool life, chip control, and quality in gundrilling of difficult to machine materials (US Patent No. 4,092,083 (1978)). Such a design termed the double-jet gundrill is shown in Fig. D.18.

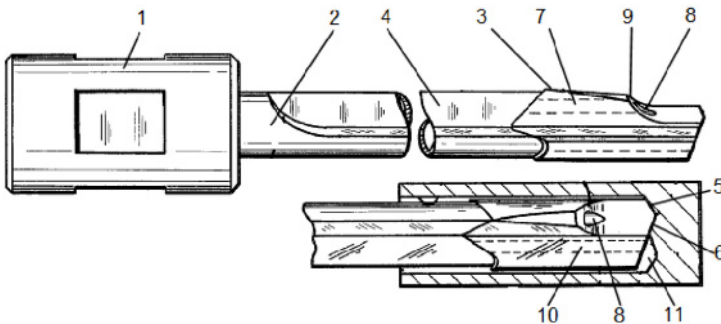
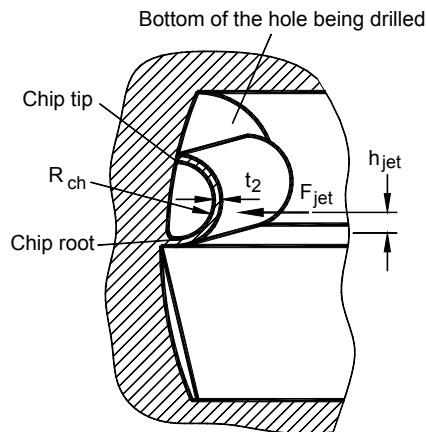


Fig. D.18. Double-jet gundrill (US Patent No. 4,092,083 (1978))

The gundrill shown in Fig. D.18 consist of a driver 1, shank 2, tip 3, and a V-flute 4. The terminal end of the tip 2 has the inner 5 and outer 6 cutting edges. The tip has two coolant passages. One is of smaller diameter, 7 which is directed into the cutting edges. Its outlet orifice, 8 is located on the inclined surface 9 formed on the tip at a certain distance from the cutting edges. The inclined surface cooperates with the hole being drilled to form a relief passage communicating with the pocket formed in the drill between the cutting edge and the outlet orifice so as to prevent chips from packing the pocket and plugging the this outlet orifice so as to endanger the tool. The second coolant passage, 10 has its outlet orifice on the flank surface of the inner cutting edge and thus is meant to supply MWF in the bottom clearance space 11.

Unfortunately, practical application of this design did not show any advantages anticipated by the authors. Moreover, the performance of this drill was even worse than that of drills having the standard design. As a result, this great, in the author's opinion, design was abandoned. This is the price to pay for not knowing the MWF flow modeling presented in this Appendix and in Chap. 5.

To correct the design mistakes in the drill shown in Fig. D.18 using the above-discussed principle, consider what was the intent of this design. As discussed in Chap. 5, a common gundrill does not have any chip breaker. The chip breaks when it collides with the rotating bottom of the hole being drilled. It happens, however, when the chip has sufficient thickness,  $t_2$  so that it bends to a certain radius  $R_{ch}$ . When it happens, the chip tip collides with the bottom of the hole being drilled. Such a collision results in chip breakage at its root because the bottom and the chip move relative to each other. This mechanism is shown in Fig. D.19.

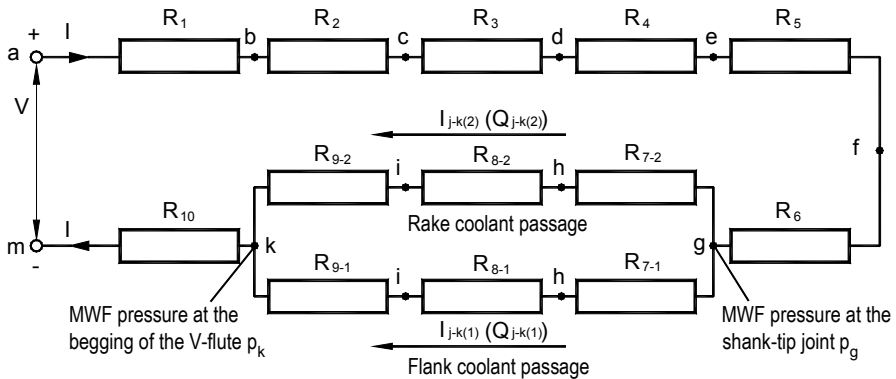


**Fig. D.19.** Mechanism of chipbeaking in gundrilling

In drilling difficult-to-machine materials, relatively small feeds are used due to high cutting forces. As a result, the chip thickness  $t_2$  is small so that the chip may not curve in the manner shown in Fig. D.19. To improve chip control, an MWF jet of high velocity that applies the additional force  $F_{jet}$  to facilitate its curving is very beneficial. When such a force is great enough, tight chip control is possible even in

machining with shallow cutting feeds. Moreover, curving the chip, the additional force  $F_{jet}$  reduces the tool-chip contact length and improves the cooling conditions at the tool-chip interface that is of vital importance in machining of difficult-to-machine materials. This was the rationale behind the gundrill design shown in Fig. D.18.

To understand why this gundrill did not fulfil expectations, one should turn to the electrical analogy of the gundrilling flow circuit discussed in Sect. D.3. Figure D.20 shows electrical analogy circuit for the double-jet gundrill while Fig. D.21 shows the design of the parallel part of this circuit. As can be seen, the pressure in the coolant passage of the shank just before the tip is  $p_g$ . The MWF flow rate is separated into two flows. One having the flow rate  $Q_{j-k(1)}$  goes through the large coolant passage made in the tip into the bottom clearance space. The second one having flow rate  $Q_{j-k(2)}$  goes through the smaller coolant passage made in the tip to interact with the partially formed chip on the rake face. Because, hydraulic resistances  $R_{7-1}$  and  $R_{7-2}$  are approximately the same (one passage has larger diameter while other has smaller length) as well as hydraulic resistances  $R_{8-1}$  and  $R_{8-2}$ . Because the outlet section of the bottom clearance space (see Chap. 5) has great cross-section, its hydraulic resistance is low. As a result,  $Q_{j-k(1)} \gg Q_{j-k(2)}$ , i.e., the flow rate  $Q_{j-k(2)}$  is even nearly insufficient to be able create kinetic energy to interact with the partially formed chip effectively. This explains why the double-jet gundrill did not show its intended advantages.



**Fig. D.20.** Electric analogy for the MWF circuit of the double-jet gundrill

To solve the problem, the pressure in the bottom clearance must be increased to the point where flow rate  $Q_{j-k(2)}$  effectively affects the chip control. This increase can be achieved by controlling the cross-sectional area of the MWF outlet of the bottom clearance space (US Patent No.7,147,411 (2006)). The re-designed double-jet gundrill should have the configuration similar to that shown in Fig. D.22. The maximum advantage of the double-jet design is achieved, however, when this is combined with the additional coolant passage along the side cutting edge (US Patent No. 7195428 (2007)) as discussed in Chap. 5. As such, no MWF stagnation zones due to flow loops occur in the bottom clearance space.

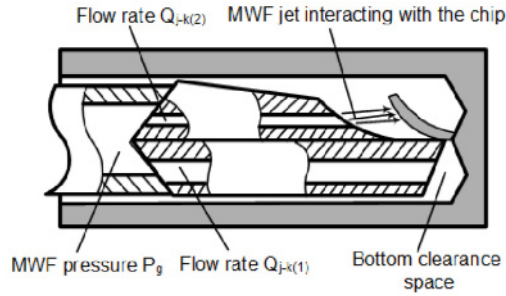


Fig. D.21. The section of the gundrill where the MWF separates into two flow

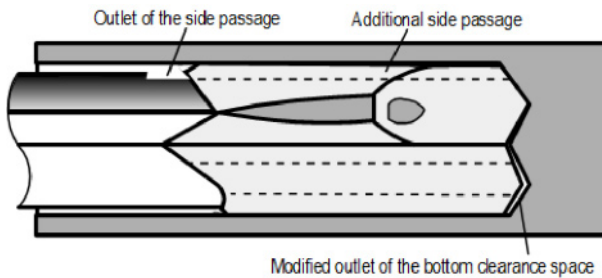


Fig. D.22. Modified double-jet gundrill

## References

- [1] Fox RW, McDonald AT (1985) Introduction to fluid mechanics. John Wiley, New York
- [2] Astakhov VP, Galitsky VV, Osman MOM (1995) A novel approach to the design of self-piloting drills with external chip removal, Part 2: Bottom clearance topology and experimental results. ASME J. of Eng. for Ind. 117:464–474
- [3] Astakhov VP, Subramanya PS, Osman MOM (1995) An investigation of the cutting fluid flow in self-piloting drills. Int. J. of Machine Tools and Manuf. 35(4):547-563
- [4] Astakhov VP, Frazao J, Osman MOM (1994) On the experimental optimization of tool geometry for uniform pressure distribution in single edge gundrilling. ASME J. of Eng. for Ind. 118:449–456
- [5] Osman MOM, Chahil GS (1979) A theoretical and experimental investigation of coolant flow in gundriling. Int. J. Mach. Tool Des. Res. 19:145–155
- [6] Astakhov VP, Osman MOM (1996) On the improvement of tool life in self-piloting drilling with external chip removal. Journal of Eng. Manufacture, Part B, Proceeding of the I. Mech. E 210:243–250

## Appendix E

---

### Requirements to and Examples of Cutting Tool Drawings

*There are no big problems, there are just a lot of little problems.*  
Henry Ford, My Life and Work – An Autobiography of Henry Ford

**Abstract.** This Appendix argues that probably the most important stage in the implementation of optimized tool geometry is its assigning on the tool drawings. To assign this tool geometry properly, a tool designer should be a well-seasoned specialist with an advanced degree having a broad knowledge in the design, manufacturing, implementation, failure analysis, and many other surrounding subjects. As this is not the case today, the common flaws with exemplification of some common tool drawings are discussed. The Appendix sets the basic requirements of tool drawings with examples of proper tool drawings.

#### E.1 Introduction

In the author's opinion, the inadequate cutting tool drawings practice is the most important issue affecting tool design, manufacturing and performance although not many specialists in the tool industry as well as end users realize this problem. Moreover, manufacturing and process engineers, for example in automotive plants, are used to the existing tool drawings and do not see any problem with them so that there is no sense of urgency to change or to improve these important documents.

An engineering drawing is a type of drawing that is technical in nature, used to define fully and clearly requirements for engineered items, and is usually created in accordance with standardized conventions for layout, nomenclature, interpretation, appearance (such as typefaces and line styles), size, etc. Its purpose is to capture accurately and unambiguously all the geometric features of a product or a component. The end goal of an engineering drawing is to convey the all required information that will allow a manufacturer to produce that component; an inspector to properly inspect the produced component and thus fill an inspection report;

a user to verify if the component is suitable for its application; a maintenance specialist to maintain the components in working conditions; and an application specialist to carry out a reliability and/or failure analysis (if failure occurs). Therefore, an engineering drawing should be a self-sufficient engineering document which contains all the information needed over the manufacturing and service time of a product. As a saying goes, “You can't staple your tongue to the drawing” – it must say it all.

Drawings convey the following critical information:

- Geometry – the shape of the object; represented as views, how the object will look when it is viewed from various standard directions, such as front, top, side, etc.
- Dimensions – the size of the object is captured in accepted units.
- Tolerances – the allowable variations for each dimension and shape.
- Material – represents what the item is made of and its properties with reference to the corresponding standard(s).
- Finish – specifies the surface quality of the item, functional or cosmetic. Ideally, it should contain all information on surface integrity parameters needed to intended part performance.

## **E.2 Tool Drawings – the Existant Practice**

Unfortunately, there is a definite lack of information on cutting tool drawing available in the literature on tool design. Moreover, according to the existing in industry practice, a tool designer may not be even an engineer but rather a draftsman with a community college education with some practical experience. Moreover, application and tool performance specialists in many tool manufacturing companies do not have advanced degrees.

According to existing notions [1, 2], the practice of tool design is as follows. Once the necessary concept and descriptive information have been transmitted to the tool designer via the tool order, concept sketch, the existing drawing (with some comments) and verbal communication from the ordering department, it becomes a tool designer responsibility to communicate adequately with the toolmaker. The primary medium of that communication is the formal tool drawing. As recommended [1, 2], beyond standard drafting practice, tool designers should observe the following practices to assist in communications and reduce tool cost:

1. Tool drawing should describe the tool completely and also specify optimal construction wherever possible.
2. Tool tolerances should be specified as loosely as possible, with every attempt made to avoid extremely tight tolerances.
3. Tool drawing should be dimensioned completely so the scaling is not required by toolmakers.

4. A complete bill of materials should be part of the assembly drawing. The tool designer has to select these materials from the list of the recommended materials (tool manufacturer specific) whenever possible.
5. Proper tool identification, the drawing number, and current revision data should be provided.

When a tool drawing is completed and checked, it is sent for approval to the customer. Upon receiving the approval, with possible corrections, the tool designer finalizes the drawing and then sends it to the tool manufacturing facilities.

In the author's opinion, this practise is incomplete as it misses a number of important steps and the role of the tool designer is highly undermined. It is not understood that the tool drawing is the only document for many involved in the tool manufacturing and application:

- It is used by purchasing to order the proper materials needed to manufacture the tool so the complete information on these materials should be included in the drawing.
- It is used by the manufacturing/process engineer to design the whole manufacturing process including suitable machinery, workholding fixtures, tools, gages, etc., so the information to assure manufacturing quality while keeping low manufacturing costs should be a part of the tool drawing.
- It is used by the inspector to check the quality of the manufacturing tool so that the information to make this inspection simple and cost effective while assuring the quality needed should also be provided by the tool drawing.
- The tool drawing should also be used by the tool packing and handling personnel so the corresponding information on packing and handling should be a part of the tool drawing.
- The tool drawing should be used by the customer's manufacturing personnel for multiple purposes: tool pre-setting, setting the machining regime favourable for the designed tool, setting the tool life on the machines in automated manufacturing environment (production lines and manufacturing cells), set the parameters of MWF (for example, flow rate), meet safety requirements and many other facets of modern manufacturing.
- The tool drawing is the prime document to investigate tool failure if it occurs. In this context, tool failure is understood in a broad sense. It includes premature tool failure before achieving the intended tool life, quality problems with the machined parts (surface finish, dimensional and/or form and position tolerances, chatter marks, burr, spiraling, etc.), tool handling failure (cracking, chipping, etc.), high cost per unit, low reliability of the tools that cause unscheduled stoppage of the manufacturing lines for replacement. Because the tool failure investigator should find the root cause of the failure, he should be able to verify all information related to the failure. As such, the information provided by the drawing is always a starting point to verify if: (1) tool design is proper, (2) tool material is suitable, (3) tool geometry is correct, (4) correspondence of the dimensioning and tolerancing on the tool drawing and those provided by the inspection report, etc. Unfortunately, in practice, the information provided by the drawing to the tool failure investigator to carry out a

failure analysis is normally incomplete and often misleading. As a result, the tool manufacturer is always blamed for any tool failure even though this failure may have little to do with the tool itself.

To be able to provide the listed information on the tool drawing to optimize tool design accounting for the particular application conditions and requirements, the tool designer should be a well-seasoned specialist with an advanced degree and with a decisive voice in any tool manufacturing company. Unfortunately, this is not the case today.

### E.3 Tool Drawing Requirements

Tool drawings additionally should:

- *General*: Compliance with the drawing standards (ISO) and with the Drawing Manual set by the customer; compliance with ISO Standards on tolerances and fits.
- *Specific*: Compliance with ISO Standards on tool geometry and with particular requirements set by the customer.
- *Performance*: As a tool drawing is actually a set of drawings that includes a tool layout, the machining regime and the intended tool life should be indicated. In future, the cutting tool R&R (repeatability and reproductibility) standards should be developed.

The first and foremost feature that must appear on any tool drawing is the datum [3–5] which distinguishes a drawing from a sketch (picture). In order to ensure the quality of tool produced, the datum features should be clearly indicated. It assures proper inspection, selection of the proper tool holder, pre-setting, and tool proper performance. In reality, however, this is not the case as the vast majority of tool drawings stored in the tooling database of automotive companies do not indicate any datum and does not adhere (even partially) to the above requirements.

To exemplify the last point, consider a few examples of drawing of tool common in the automotive industry. Figure E.1 shows a drawing of the most common PCD cartridge, Fig. E.2 shows a drawing of a typical PCD reamer, and Fig. E.3 shows a drawing of a typical PCD interpolated milling tool as found in a typical drawing database of an automotive company.

Although these tools are different and were designed by different well-known tool manufacturing companies, there are a number of similarities what can be observed in these drawings:

- The datum is not indicated by any means that automatically downgrades these drawings to pictures.
- No tool geometry is shown according to the ISO [6] and/or ANSI [7] standards for tool geometry. No edge preparation conditions are mentioned (microgeometry parameters) although this is vitally important for PCD tools.



- Although all the shown tools are assemblages, no bill of material is provided. In other words, no indication of the tool, tool shank, and brazing filler materials are mentioned.
- No shape and location tolerances are indicated including the runout of the working part with respect to HSK holder as probably the most important shape tolerance.

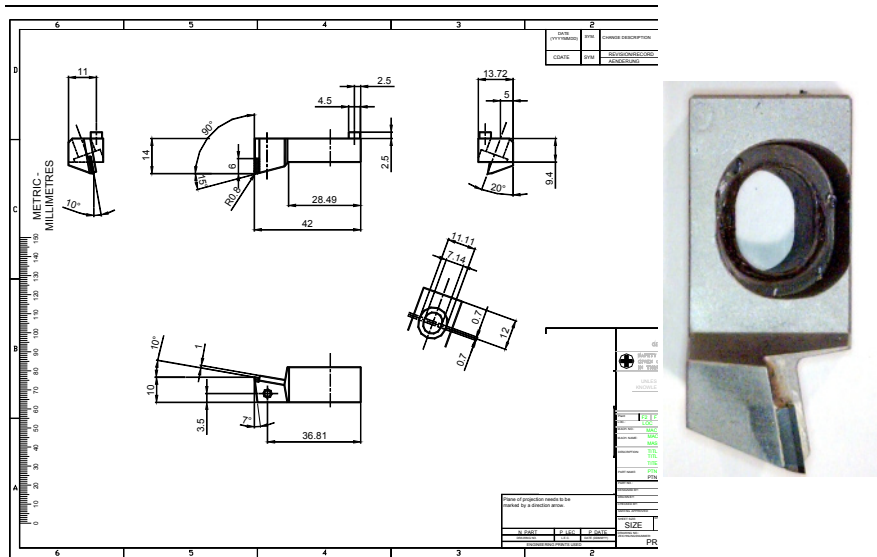


Fig. E.1. PCD cartridge

- No surface finish is mentioned.
- No particular sizes of PCD inserts, including their thickness as well as the thickness of the carbide substrate are shown.
- There is no indication of how the cutting inserts are secured in the body. Technically, a paper glue can be used and this would not violate the drawing requirements.
- Many projections and cross-sections are not to the drawing standards.

For the reamer and the milling tools shown in Figs. E.2 and E.3, respectively, the flute profiles are not dimensioned so that one may wonder whether there is enough space for chip evacuation. Moreover, the diameters and locations of the coolant holes are not indicated. Although some means for balancing is graphically shown, no one balancing procedure and/or requirement is set by these drawings.



The total absence of the most critical technical information on the tool drawing is one of the most critical issues in manufacturing in the automotive industry. It makes it impossible to optimize tool design and geometry, select and test advanced tool materials suitable for a given application, carry out tool failure analysis, and commonize cutting tools for similar applications at various manufacturing facilities. A tool application specialist becomes useless as he cannot perform his basic functions due to the almost complete absence of relevant information which should be primarily provided by the tool drawings.

Tool manufactures are very reluctant to submit proper tool drawings to their customers. The prime reason for that (always put forward in any meeting on the matter) is that they want to protect their designs from being copied by others (i.e., from knockoffs). Although it might sound convincing, it is a very shallow excuse. This is because modern laser scanning equipment (used in rapid prototyping and in the car aftermarket business) and CMM machines (available in any automotive powertrain plant) allow obtaining a complete digital image of any complicated product with precise geometry of all intricate details in a short time. Sophisticated metal analysers widely available today (for example, XL3t Analyzer by Thermo Fisher Scientific) allow obtaining composition of any alloy while any engineering metallography analysis can be conducted in the materials laboratories which are imbedded in any powertrain plant. The only logical explanation for not having the vital information on tool drawings is the fear of responsibility to follow the requirements set by these drawings.

The absence of vital information on a tool drawing does not allow generation any meaningful inspection report for this tool. This is because Dimensional Inspection (also known as metrology services, validation, verification, product evaluation, contract inspection, and layout inspection) is performed to compare the actual condition of a manufactured part (tool) or component to the nominal condition as defined by engineering drawings. If, for example, the normal flank angle is not shown in this drawing, it is not inspected as it is a common case today.

The minimum requirements of the tool drawing are as follows:

1. In order to ensure the quality of tool produced, the datum features should be clearly indicated. This assures proper inspection, selection of the proper tool holder, pre-setting, and performance. Out of common datum features used, namely design, manufacturing, inspection, pre-setting, working datum features, a tool drawing submitted for approval should have the inspection and pre-setting datum features. All shape tolerances should be specified with respect to these datum features.
2. Proper dimensioning and tolerancing with respect to the selected datum features. Besides the required lengths and diameters, particular attention should be paid to the:
  - Profile and location (relative to the datum features) of the chip-removal flutes.
  - Profile, dimensions, spatial location and location of the outlet nozzles of the coolant holes.
  - Tool body dimensions that define the strength and rigidity.

3. Properly defined surface integrity including surface finish. The primary ISO standard dealing with surface finish, ISO 1302:1992 is concerned with the methods of specifying surface texture symbology and additional indications on engineering drawings. This and all ISO standards are expressed in SI metric units, with commas (,) used as decimal points. Other ISO standards are referenced for constituent provisions, but not directly discussed in the ISO 1302 standard. For instance: ISO 468:1982 Surface roughness: Parameters, their values and general rules for specifying requirements, ISO 4287:1997 Surface texture: Profile method, terms, definitions and surface texture parameters, ISO 4288:1996 Surface texture: Profile method, rules and procedures for the assessment of surface texture, ISO 8785:1998 Surface imperfections: Terms, definitions and parameters.
4. Proper specification of the tool geometry according to the standards: ISO 3002/1 “Basic quantities in cutting and grinding – Part1: Geometry of the active part of cutting tools – General terms, reference systems, tool and working angles, chip breakers. Second Edition 1982-08-01”, American National Standard B94.50 “Basic Nomenclature and Definitions for Single-Point Cutting Tools.”
6. Proper specification of the tool material(s), its properties and coating. Although standard ISO 513:1991 “Application of hard cutting materials for machining by chip removal – Designations of the main groups of chip removal and groups of application” defines different groups of tool materials, its intent *is not* the specification of a particular tool material on the tool drawing. This is because the standard defines the *application* groups so considerable different tool materials can fall into the same application group. Therefore, it is of great importance to specify tool material and coating on the drawing. Although the exact specifications for various tool materials are yet to be developed, it is reasonable to set the following requirements at this stage:
  - For carbides: Exact grade and manufacturer. For example, TCN 20 PlanceeTizit. If the edge preparation is used, it should be shown in a separate view with proper dimensions.
  - For PCDs: Exact grade and manufacturer, edge preparation parameters. For example, DA90 Sumitomo Electric. For CBNs: Exact grade and manufacturer, edge preparation parameters. For example, IB50 ISCAR.
  - For HSS: Exact grade, manufacturer, hardness, place to check hardness. For example, CPM4 Crucible, HRC 66-68. Metallurgical data (grain size, maximum allowable phosphorus and sulfur etc) may be very helpful.
7. The required MWF (coolant) flow rate and pressure for tools with internal coolant supply. MWF brand, concentration and other parameters (for example pH, particle count) can also be included when they are critical to tool performance.

For the drawing submitted for approval when new design is to be tested, the additional information should include:

8. Suggested machining regime: cutting speed (spindle r.p.m.), cutting feed (feed per revolution and feed per tooth for multi-tooth tools), depth of cut, cycle diagram.
9. The required coolant flow rate and pressure to assure reliable chip removal and intended tool life.
10. Criterion (criteria) of tool life and its assessment.
11. Expected tool life.
12. Tool reliability data. This important issue should be a subject to a special meeting as one of the most important. This is because a prematurely failing tool may cause a great losses. For example, on a transmission case line in the automotive industry, a failed reamer causes up to 40 scraped cases and 1.5h lost in production time.

## E.4 Examples of Tool Drawing

Figures E.4–E.8 show examples of tool drawings where the above-listed concepts are realized. Figure E.4 shows a typical PCD cartridge as an example of single-point tools. A simple comparison of this drawing with that shown in Fig. E.1 reveals the differences. First and foremost, datum A and datum B are assigned to the base surface of the cartridge used for the tool location in the holder. The T-hand-S geometry is specified according to the basic notions presented in Chap. 2.

Figure E.5 shows a drawing of a typical straight-flute drill used in the automotive industry. The complete T-hand-S geometry is specified that makes the tool grinding and inspection simple and straightforward. The longitudinal axis of the tool shank is selected as the datum because this datum is actually the design, manufacturing and working datum simultaneously. Particularities of the drill point grind, location of the coolant holes, and flute geometry are completely specified. The notes provide clear instructions including tool handling and shipping.

Figure E.6 shows a simple (due to the paper size limitation) yet common PCD-tipped drill used in the automotive industry. As with other tools, the tool geometry is completely described in the T-hand-S. The longitudinal axis of the tool shank is selected as the datum because this datum is actually the design, manufacturing and working datum simultaneously. Bill of materials shows the complete description of the materials used to manufacture this tool. Important particularities of PCD tool design are also shown in corresponding sections and views.

Figure E.7 shows a design of a high-penetration rate gundrill used in the automotive industry. As it was an experimental tool, the complete description of the conditions of its production testing as well as the expected tool life and expected tool reliability are also shown on the drawing. Figure E.8 shows the T-hand-S geometry of the terminal end of the drill used for its point grind.

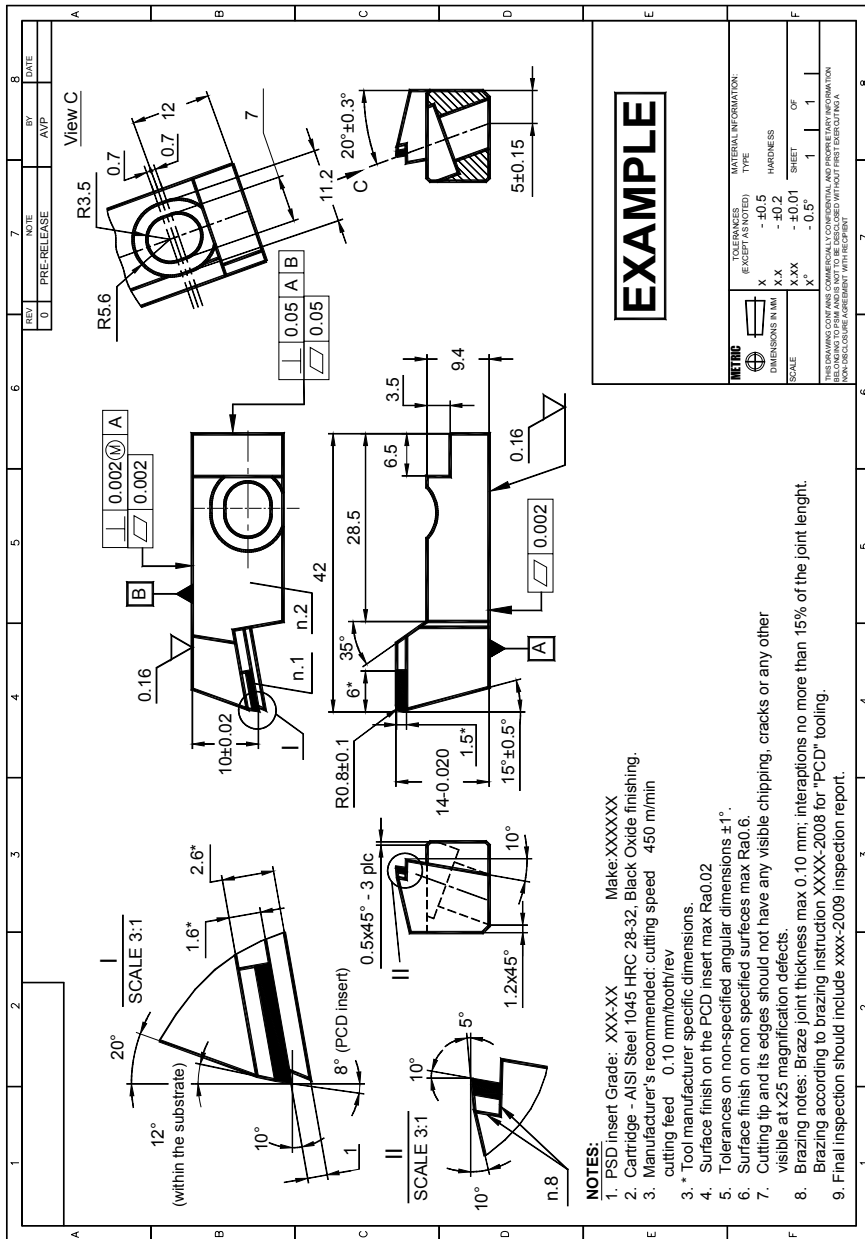


Fig. E.4. PCD cartridge drawing – an example



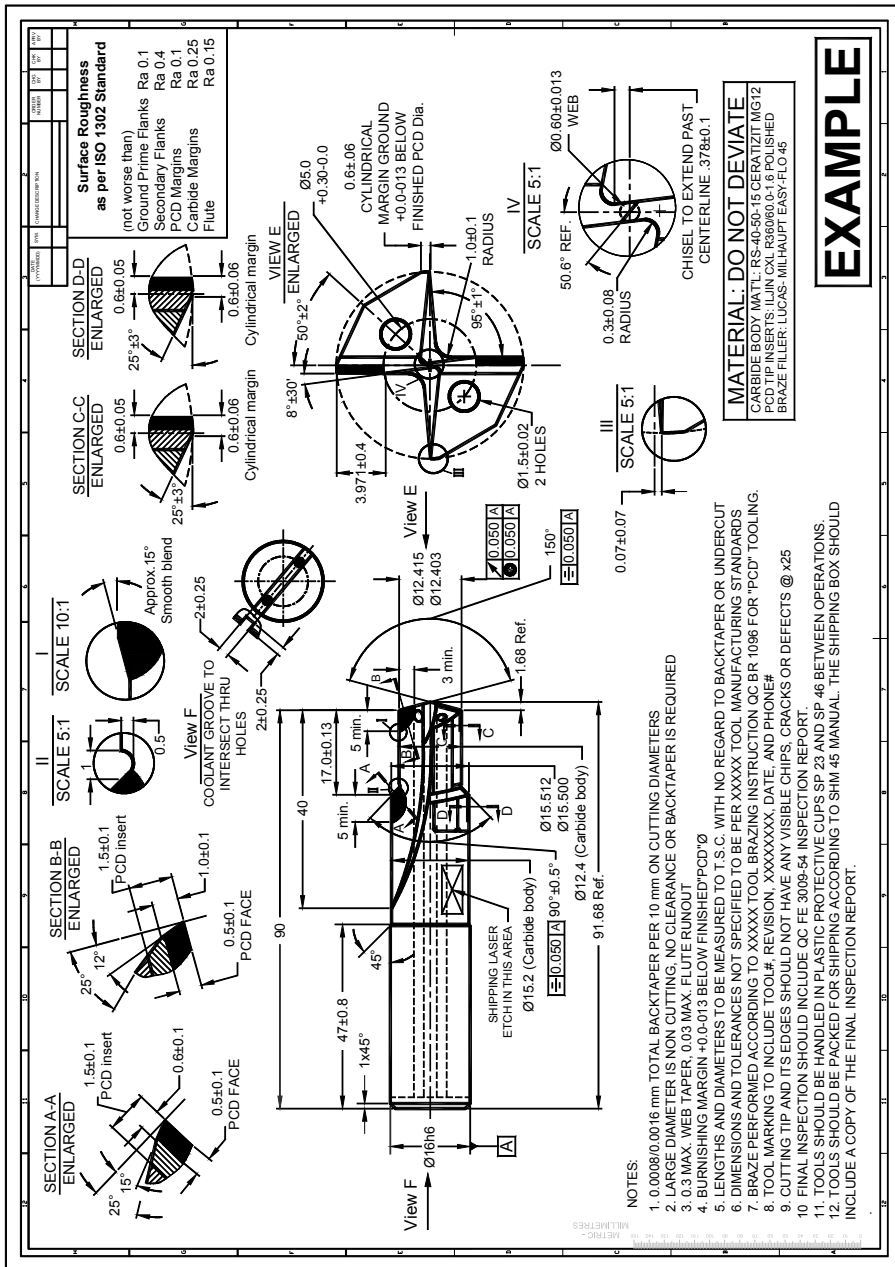


Fig. E.6. PCD-tipped drill – an example



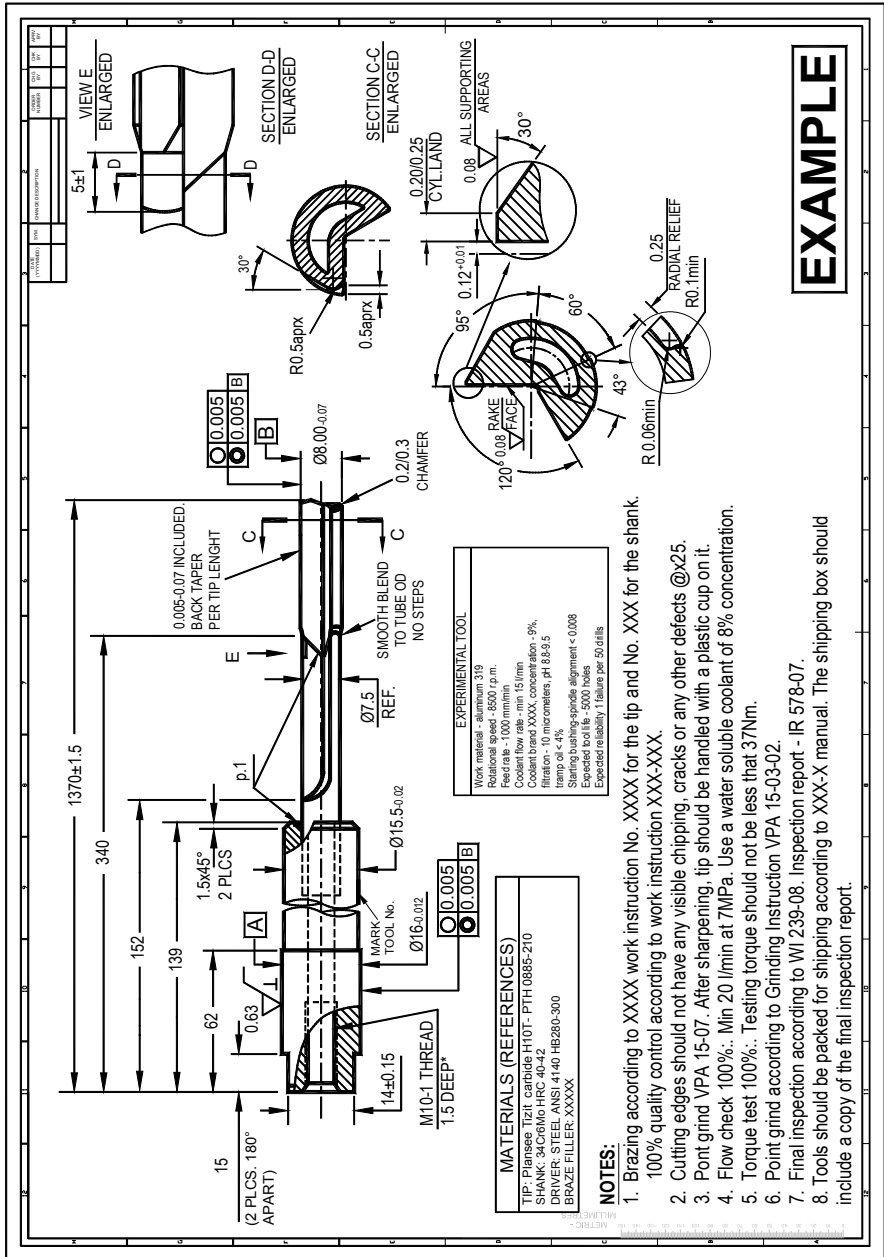


Fig. E.7. High-penetration rate gundrill – an example

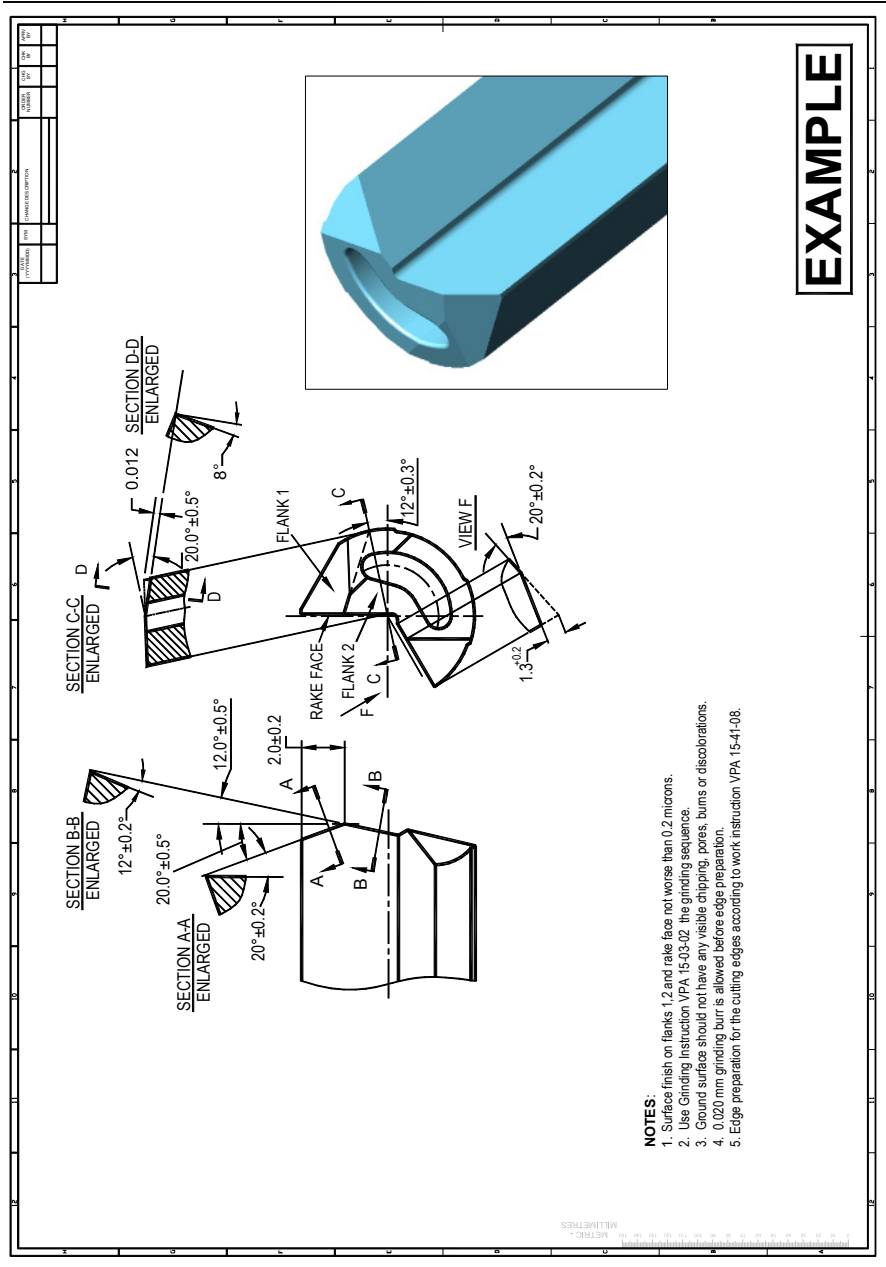


Fig. E.8. Point grind of the gundrill shown in Fig. E.7

## References

- [1] Tanner JP (1990) Manufacturing Engineering: An Introduction to the Basic Functions. 2nd. ed. Marcel Dekker, New York
- [2] Mutter CS (1996) Product tooling and equipment. In: J.M. Walker (Ed) Handbook of manufacturing engineering. Marcel Dekker, New York
- [3] Mathematical definition of dimensioning and tolerancing principles (1994) ASME Standard Y14.5.1M-1994
- [4] Geometrical Product Specification (GPS) – Masterplan. 1995, ISO.
- [5] Meadows JD (1995) Geometric dimensioning and tolerancing. Marcel Dekker, New York
- [6] International Standard ISO 3002-1 Basic quantities in cutting and grinding. Part 1: Geometry of the active part of cutting tools - general terms, reference systems, tool and working angles, chip breakers. 1982.
- [7] American National Standard ANSI B94.50-1975 Basic nomenclature and definitions for single-point cutting tools. 1975 (reaffirmed 1993).

---

## Index

### A

Alignment 218, 351, 352, 355–359, 365, 411, 412  
Angle of twist 217, 219, 359  
Angular velocity 119–124, 288, 314, 327, 376, 513, 515–517  
Approach angle 60, 68, 113, 142, 270, 275, 292, 370, 372, 372, 376, 378, 380, 382, 385, 387–389, 392, 393, 407, 428–430, 433, 435–436, 438, 440, 493, 509, 511  
Axial force 6, 133, 198, 213, 214, 217, 218, 220–225, 229, 231, 238, 244, 245, 250, 253, 255, 256, 258, 269, 299, 306, 222, 342, 345, 347, 384, 429, 453, 454  
Axial force-torque coupling 221–223

### B

Backtaper 150, 152–158, 395  
    Definition 150  
    Significance 152–158  
Basic kinematic scheme of drilling 350–353  
Bending moments, gundrill 391–394  
Boring 82, 87, 444–449

Bottom clearance space 264–267, 397–399, 415–417, 420–424, 430, 529, 531, 532, 538–540, 542, 543  
    Definition 397  
    MWF pressure management 413  
    Topology 399  
Briks criterion 164, 455  
Broaches 197–198  
Built-up Edge (BUE) 4, 16, 33, 143, 153, 155, 178, 181, 242, 243, 262, 299, 300, 423

### C

Chibreakers 179, 250  
Chip 3  
    Silver white 181  
Chip compression ratio (CCR) 3, 4, 11, 22, 37–39, 41–46, 132, 146, 165, 169, 175, 176, 182, 183, 188, 249, 261, 427, 455, 456, 459, 460  
Chip flow 59, 249, 434  
    Angle 136, 137, 180, 181, 199, 280  
    Direction 69, 92, 98, 136, 137, 178, 180, 193–195, 197, 300, 339, 249, 280

Chip structure 12, 13, 27, 29  
 Chip thickness 3, 11, 22, 38, 39, 45, 56, 92, 185, 188, 427, 542  
 Chip velocity 3, 4, 29, 44, 280  
 Chisel edge 209–213, 220–249, 257, 260, 270, 280, 295–300  
 Combined point grind 365  
 Conical point grind 315–321  
 Coolant holes 260  
     Location and size 263, 264, 345, 536, 549, 551, 553  
 Cutting 2–49  
     Free 3, 59  
     Feed 66, 84, 85, 100, 129, 134, 139, 141–144, 148, 149, 159, 160, 167–169, 185, 218, 219, 229, 287, 325, 326, 375, 376, 380, 427, 428, 434–438, 443, 448, 451, 509  
     Force 1–9, 9, 23–28, 133–135, 145–147, 164–169, 174, 175, 177, 178, 186, 190, 191, 213–225, 345–350, 453–459  
     Non-free 55, 59, 60  
     Orthogonal 25, 42, 57, 58  
     Oblique 58, 59  
     Speed 3, 4, 13, 35, 44, 57, 58, 66, 67, 91, 98, 112, 119, 125, 273, 283, 287, 329, 366–369, 371, 379, 448–459  
     Cutting edge 3, 11, 12, 23, 24, 56–77, 108–117  
         Major 56, 57, 60, 66, 69, 77, 85, 86, 103, 105–111  
         Minor Major 56, 57, 60, 66, 69, 77, 85, 86, 103, 105–108  
     Cutting edge inclination angle 35, 58, 59, 69, 81, 87, 88, 96, 99, 103, 107, 109, 11, 193–195, 197–201, 249, 280, 281  
     Cutting edge radius 35, 163–171, 429  
     Cutting tool selection 74–77  
     Cutting tool surface and elements 3, 56  
         Flank face 3, 57  
         Rake face 3, 57  
         Shank 57, 359

**D**

Deep-hole machining operations 343  
     Gundrill type 343  
     BTA type 344  
     Ejector type 344, 345  
 Deformation mode 2–5  
 Deformation zone 24, 29, 30, 168  
     State of stress 30, 183, 454  
 Depth of cut 56, 60, 129, 135–139, 145, 146, 445, 449–451  
 Dovetail forming tool 117–119  
 Drill 206  
     Basic terms 208–211  
     Classification 206–208  
     DIN Classification 223, 224  
     Point 223  
     Point angle 63, 150, 209, 270, 278, 288–292, 315  
     Point geometry 229, 230, 234, 238, 235, 303  
     With partitioned cutting edge 347–350  
     With single cutting edge 345–347  
 Drill-to-diameter ratio (L/D) 341, 342  
 Drilling force system 213  
 Drilling system 353–362  
 Drilling torque, 213–217

**E**

Edge preparation 160–172  
     hone radius 163  
     finish 169  
     methods 172  
 Elastic recovery (see also springback) 83, 151–158, 164,  
 Energy partition 166, 455–461

**F**

Feed motion 12, 56–58, 65, 66, 84, 90, 92, 95–97, 102, 186, 314, 444–453  
 Feed rate 58, 95, 218, 434, 448–451

Flank angle 3, 68–108, 112–125, 191–193, 278, 281–292, 315–324, 370–390, 407–409, 464, 465  
 Back 68, 104–107, 370–390  
 Normal 68, 104–108, 269, 369, 428–429  
 Optimal 82, 192, 193  
 Orthogonal 68, 88, 104–108, 117–119, 370–390, 437, 438  
 Side 68, 104–108, 370–390  
 Flank face 3, 16, 57, 92–96, 104–107, 160, 167, 191, 264, 270–324, 416, 417  
 Flute 206–21  
 Modification 247–254  
 Profile 208, 245–254  
 Width ratio 245, 246  
 Fracture 9–18, 22–49  
 Frequency of chip formation 457–461  
 Friction force at the tool-workpiece interface 166  
 Fundamental laws  
 First Metal-Cutting Law (Makarow's law) 32  
 Second law of metal cutting (the deformation law) 35, 36

**G**  
 Gundrilling system 354–362  
 Common issues 356–363  
 Gundrill geometry 362–439

**H**  
 Helix angle 207–210, 222, 227, 275–277  
 Helical flank face 239, 246, 321–324  
 Helical point 321–324, 364  
 Helical rake face 275–279

**I**  
 Indexable cutting inserts 74–84  
 ANSI code 464–471  
 Geometry parameters 77–84  
 ISO code 471–491  
 Inner angle 363, 392

Interference 70, 94–96, 100, 158, 159, 290–292, 398–400, 405  
 Condition of free penetration 290–292, 398–405  
 Model 290–292

**K**

Kinematic angles 92–101  
 Flank angle 92–101  
 Inclination angle 99  
 Rake angle 96, 99

**M**

Machining regime 448, 449  
 Mean shear stress at the tool chip interface 177  
 Metal cutting, definition 28, 29  
 Metal working fluid (MWF) 154, 155, 157, 186, 190, 205, 218, 263–267, 342–345, 357–359, 397–399, 413–425, 519–544  
 Critical velocity 523–526  
 Critical flow rate 521–526  
 Flow rate 523, 526–529  
 Inlet pressure 529–533, 541  
 Optimal velocity 524–526  
 Pressure 413–425  
 Milling tools 198–201  
 Model of chip formation 3, 4

**N**

Nose radius 56, 60, 78, 108, 137–146, 457, 468, 470

**O**

Optimization of tool geometry 439–441  
 Original coordinate system 271, 272, 292, 365, 366, 370, 375, 385, 386  
 Outer angle 363, 392

**P**

Penetration rate 212, 213–223  
 Constrains 218  
 Measures to increase 224–259

Plastic deformation 3–11, 15–22,  
35–44, 164–177, 458–460  
Point grinds, gundrill 414–418  
Poletica criterion 175–176  
Power spent on plastic deformation  
455, 458–460  
Primary motion 57, 58, 66, 68, 90,  
97, 443–452

## R

Rake angle 3, 56, 68, 70–74, 77, 78,  
88, 89, 92–99, 104, 112, 167,  
167–169, 172–191, 225–230,  
272–279, 332–337  
  Back 68, 103–108  
  Effective 183–191  
  Extremely high 173, 188–190  
  Neutral 79, 92, 173–178  
  Negative 79, 173–175  
  Normal 68, 104–109  
  Orthogonal 69, 89, 104–109  
  Side 68, 104–109  
  Origin of the term 173  
  Positive 79, 173  
References planes 66, 67  
  Assumed working 66  
  Cutting edge normal 67  
  Main reference 66  
  Orthogonal 67  
  Tool back 66, 67  
  Tool cutting edge 66  
Relative Tool Sharpness (RTS)  
164–167  
Resultant cutting motion 58, 91  
Rotary tools, turning 195–196  
  Self-propelled 196  
  Spinning 195–196  
Rule No. 1 in drill design 392  
Rule No. 2 in drill design 393  
Rule No. 3 in drill design 398,  
423–424  
Rule No. 4 in drill design 399

## S

Self-centering 218, 254–259  
Self-piloting drill (SPD) 345–350  
Self-piloting tool 345–350

Shear angle 3, 4, 20  
Shear plane 3, 4  
Shear strain 11–13, 39, 40  
Shoulder deb-off 364, 413–422  
  Length 417–419  
Side passage 413, 414–422  
  Outlet cross-sectional area  
414–422  
  Auxiliary 423, 424  
Single point cutting tool, 56  
Single-shear plane model 3, 22–28  
Split-point geometry 234–238  
Springback (see elastic recovery)  
Stagnation zone 417, 418  
Static equilibrium 213–216  
Straight-flute drill 269–275  
Stress-strain diagram 152  
String 367–369  
  Deflector 369  
System approach 211–213, 353–362  
System consideration 354–362  
System objective 212  
Systems of consideration of the tool  
geometry 61  
  tool-in-hand (T-hand-S) 61,  
64–68, 74  
  tool-in-machine (T-mach-S) 61,  
64, 65, 90  
  tool-in-use (T-use-S) 61,  
90–101  
Summation of motions 119–125  
Supporting pads 346

## T

Tensile test 183–187  
  elongation 185  
  neck down 185  
  frusto-conical section 185  
Tool–chip contact length (length of  
the tool–chip interface) 175–177,  
178–183  
  elastic part 181, 182  
  natural 178  
  plastic part 181, 182  
  restricted 178–183

Tool cutting edge angle 66, 73–78, 81–89, 132–150, 270, 276, 298, 315, 216, 330, 334, 335, 465

Tool drawing 545

- Critical information 544
- Examples 553–558
- Existent practice 546–548
- Requirements 548–553

Tool failure 351

Tool geometry

- selection 129
- ideal 130–132
- experimental evaluation 132
- Influence in edge preparation 167–169

Tool holder 75–83

- Geometry parameters 77–83
- ISO code 491–487

Tool life 8, 12, 30, 171, 186, 187, 192, 221, 324, 327–330, 191, 427–435

- Correlation equation, gundrill 425
- Criterion 423
- Test 427–435

Tool life, overall 394

Tool minor (end) cutting edge angle 66, 85, 106–108, 146–160

Treading taps 197

Tool wear patterns 395–397

Turning 444–446

## U

Ultimate tensile strength 177

Uncut chip cross-sectional area 8, 134, 135

Uncut (undeformed) chip thickness 3, 8, 11, 38, 56, 133–141, 146, 159, 167, 168, 175, 325–327

Uncut chip width 56, 136–141, 166

## V

Vector 102–125, 499

- Definition 500
- Analysis 500
- Magnitude 500
- Unit 502
- Resolution into components 502

Vectors 503

- Addition 503
- Angle between vectors 504
- Angle between line and plane 504
- Cross-product 506–509
- Scalar (dot) product 502
- Scalar triple product 509

## W

Waterfall edge preparation 163

Wear curves 431

Wear pattern 11, 12

Web 211

- Conventional 244
- Eccentricity/lip index error 260, 261
- Thickness 211, 222, 247
- Thickness ratio 246
- Thinning 231–233
- Wide 244

Wedge angle 68

- Back 68
- Normal 68
- Orthogonal 68
- Side 68

Wiper insert 108–110

Work material

- Brittle 14
- Constitutive model (flow curve) 26, 36, 43
- Ductile 14
- Properties in cutting and in FEA 25

Workpiece surfaces 56